Library Declaration and Deposit Agreement

1. STUDENT DETAILS

Full name: Chris Charlesworth

University ID number: 0755705

2. THESIS DEPOSIT

2.1 I understand that under my registration at the University, I am required to deposit my thesis with the University in BOTH hard copy and in digital format. The digital version should normally be saved as a single pdf file.

2.2 The hard copy will be housed in the University Library. The digital version will be deposited in the University's Institutional Repository (WRAP). Unless otherwise indicated (see 2.3 below) this will be made openly accessible on the Internet and will be supplied to the British Library to be made available online via its Electronic Theses Online Service (EThOS) service.

[At present, theses submitted for a Master's degree by Research (MA, MSc, LLM, MS or MMedSci) are not being deposited in WRAP and not being made available via EthOS. This may change in future.]

2.3 In exceptional circumstances, the Chair of the Board of Graduate Studies may grant permission for an embargo to be placed on public access to the hard copy thesis for a limited period. It is also possible to apply separately for an embargo on the digital version. (Further information is available in the *Guide to Examinations for Higher Degrees by Research*.)

2.4 *If you are depositing a thesis for a Master's degree by Research, please complete section (a) below. For all other research degrees, please complete both sections (a) and (b) below:*

(a) Hard Copy

I hereby deposit a hard copy of my thesis in the University Library to be made publicly available to readers immediately

I agree that my thesis may be photocopied. **YES**

(b) Digital Copy

I hereby deposit a digital copy of my thesis to be held in WRAP and made available via EThOS.

Please choose one of the following options:

My thesis can be made publicly available online. **YES**

3. GRANTING OF NON-EXCLUSIVE RIGHTS

Whether I deposit my Work personally or through an assistant or other agent, I agree to the following:

Rights granted to the University of Warwick and the British Library and the user of the thesis through this agreement are non-exclusive. I retain all rights in the thesis in its present version or future versions. I agree that the institutional repository administrators and the British Library or their agents may, without changing content, digitise and migrate the thesis to any medium or format for the purpose of future preservation and accessibility.

4. DECLARATIONS

(a) I DECLARE THAT:

I am the author and owner of the copyright in the thesis and/or I have the authority of the authors and owners of the copyright in the thesis to make this agreement. Reproduction of any part of this thesis for teaching or in academic or other forms of publication is subject to the normal limitations on the use of copyrighted materials and to the proper and full acknowledgement of its source.

The digital version of the thesis I am supplying is the same version as the final, hard-bound copy submitted in completion of my degree, once any minor corrections have been completed.

I have exercised reasonable care to ensure that the thesis is original, and does not to the best of my knowledge break any UK law or other Intellectual Property Right, or contain any confidential material.

I understand that, through the medium of the Internet, files will be available to automated agents, and may be searched and copied by, for example, text mining and plagiarism detection software.

(b) IF I HAVE AGREED (in Section 2 above) TO MAKE MY THESIS PUBLICLY AVAILABLE DIGITALLY, I ALSO DECLARE THAT:

I grant the University of Warwick and the British Library a licence to make available on the Internet the thesis in digitised format through the Institutional Repository and through the British Library via the EThOS service.

If my thesis does include any substantial subsidiary material owned by third-party copyright holders, I have sought and obtained permission to include it in any version of my thesis available in digital format and that this permission encompasses the rights that I have granted to the University of Warwick and to the British Library.

5. LEGAL INFRINGEMENTS

I understand that neither the University of Warwick nor the British Library have any obligation to take legal action on behalf of myself, or other rights holders, in the event of infringement of intellectual property rights, breach of contract or of any other right, in the thesis.

Please sign this agreement and return it to the Graduate School Office when you submit your thesis.

Student's signature: [redacted] Date: 19/04/1012

Ultrasonic phased array testing in the power generation industry; Novel wedge development for the inspection of steam turbine blades roots

by
Chris Charlesworth

Thesis submitted to the University of Warwick
for the degree of Doctor of Engineering

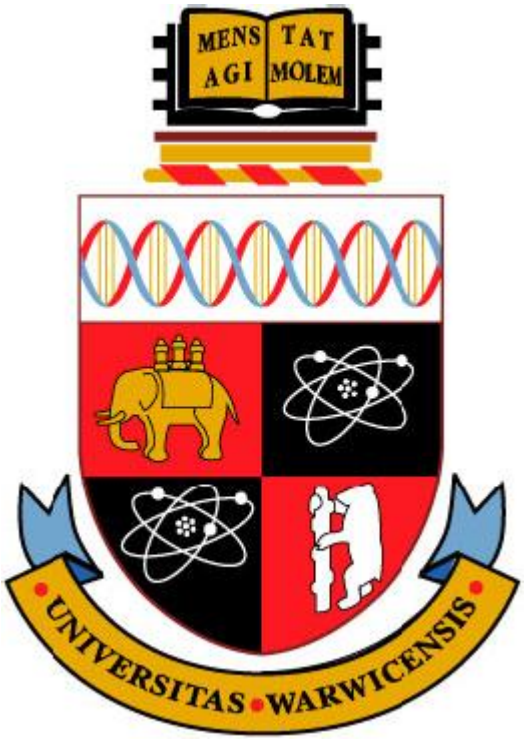

School of Engineering
University of Warwick
November 2011

Table of Contents

List of Figures

List of Tables

Acknowledgements

I would like to offer special thanks to RWE npower (my sponsoring company and employer) but in particular Kevin Stamps who has been an inspiration on many occasions whilst being a mentor and friend. Also to Paul Crowther (My Boss) who has supervised this project from the beginning and offered level headed intelligent feedback and advice at every stage. To Roger Lyon (retired) for giving me the opportunity to do the EngD and Bob Spenser (soon to be retired) for giving his continued financial support.

To my supervisors at Warwick, Duncan Bilson and Dave Hutchins, who have been a calming influence and given me guidance, feedback, and more importantly the confidence when needed.

Chris Scruby for seeing my potential and allowing me to join the course, and the entire Academic and support staff involved in the RCNDE, who through taught courses and events have furthered my knowledge over the wider field of NDT.

My sincere thanks go to the other EngD students who have offered support and friendship along the way, but in particular to the guys in Cohort 3.

My amazing daughter Lily who's first birthday was in the week I started the course and who's fifth birthday will be in the week I complete, she has endured weekend after weekend of Daddy working at his computer. Her smile and wonderful personality got me through.

Finally Jenny, my wife, you have been my rock.

Declaration

The work presented in this thesis has been carried out by the author, except where otherwise stated. It has been performed in my role as development engineer at RWE npower and in the School of Engineering at the University of Warwick. No part of this work has previously been submitted to the University of Warwick, or any other academic institution for consideration for a higher degree. All publications to date arising from this work are listed in the publications section in the end.

Summary

The thesis presented herein comprises of the work undertaken to research novel methods of Phased array ultrasonic inspection of complex steam turbine blade roots as found in the power generation industry. The research was conducted as part of the Engineering Doctorate scheme, administered by the Research Centre for Non-Destructive Evaluation (RCNDE), in conjunction with RWE npower and the University of Warwick.

Steam turbine blades, and in particularly last stage blades of low pressure steam turbines, are amongst the most highly stressed components on a power generating plant. Two of the most common blade root fixing types include 'curved axial entry fir tree roots' (CAEFTR), and axial pinned roots, both of which are prone to cracking due to the high stresses to which they are subjected under operating conditions. Failure of the blade root fixings of such components, leading to the release of the blades, has historically led to the catastrophic failure and destruction of the whole turbine; the cost of collateral damage to plant components and the loss in generating income are seconded only by the risk these failures pose to life. Due to the high price of failure, NDT plays a critical part in the support and management of engineering maintenance, offering insight into the condition and integrity of turbine components through regular planned inspection regimes.

It will be shown in this thesis how the invention of a novel continuous wedge, used to refract ultrasound into the critical regions of the blade roots, has significantly improved the ability to detect defects. Combined with the development of bespoke scanning frames these wedges facilitate the efficient and accurate acquisition of scanned data to assess the integrity of the component. By combining the latest reverse engineering, modelling and simulation tools with novel application of rapid prototyping, the author has been able to demonstrate significant reduction in design cycles whilst improving accuracy, sensitivity and repeatability of the applied inspections. Furthermore, application of this design philosophy has led to the development of inspection techniques which have facilitated the inspection of remote regions of the blade roots where manual access is limited or impossible.

The developments and techniques invented during this research have been successfully deployed across numerous RWE npower and customer projects, leading to estimated savings in excess of £1m.

Chapter 1. Introduction, aims and objectives

1.1 Introduction

This thesis investigates the use of advanced ultrasonic non-destructive evaluation methods as applied to the power generation industry, and mainly but not exclusively to rotating plant such as steam turbine rotors. The main focus is the development of ultrasonic phased array inspection techniques, utilised in the search for cracking defects in the root fixings of steam turbine blades. It will be shown how research into blade root inspection and development of complex refractive wedges has led to the design and implementation of novel inspection techniques applied to in-situ and ex-situ steam turbines, increasing inspection coverage whilst significantly reducing service costs and downtime. Furthermore, the invention of a continuous wedge, for which a patent application has been filed (page 242), and novel use of rapid prototyping has led to further improvements in defect detection, improved inspection reliability, and reduced inspection time.

The research has been carried out on behalf of RWE npower, a leading UK electrical power generation company, in conjunction with Warwick University, and the Research Centre for Non-Destructive Evaluation (RCNDE).

1.2 Company profile

RWE ranks among Europe's largest industrial corporations by implementing a multi-utility strategy, combining three core businesses in the fields of electricity, gas and environmental services. RWE is one of the leading companies in these industries in Germany, Great Britain and Central Eastern Europe, and supply electricity to more than 16 million customers and gas to 8 million[1].

In the UK, RWE npower is made up of three main subsidiary companies: - Generation and Renewables, npower, and npower Cogen.

1.2.1 npower Cogen

npower Cogen is the cogeneration division of RWE npower, being one of the leading developers of industrial Combined Heat and Power (CHP) in the UK[2]. CHP is the simultaneous generation of electricity and useful heat from a single fuel source, and can increase overall energy efficiency to between 70 and 90 %, resulting in significant energy cost savings, and real environmental gains through reduced CO_2 emission[3]. There is currently a portfolio of 16 plants across the UK and Republic of Ireland saving an estimated 1.7million tonnes of CO_2 from the environment in 2004.

1.2.2 npower Retail

RWE npower's retail business, npower, is one of the UK's largest suppliers of electricity and gas, and includes household names such as Yorkshire Electricity and Northern Electric.

1.2.3 Generation and Renewables (G&R)

G&R Technology Services division operates within the Generation business providing support and specialist services to other power plant operators and owners around the world, in addition to supporting RWE's own generation assets. G&R expertise is in improving power station reliability, efficiency, and environmental management to deliver optimal commercial performance. In addition to providing this expertise to third parties, Technical Services provides support to the UK generating capacity of over 8,000 MW of coal, oil and gas-fired power stations over eight sites, as well as renewable and cogeneration plants.

A requirement of the power industry is that by 2015 renewable energy should account for 15 % of the total generation capacity. RWE are leaders in the development of new energy resources and are innovating technology in Hydro Plant and Wind power to meet future requirements. The portfolio of Hydro Plant and On/Off-Shore Wind Generation, account for 550 MW of generating potential[4].

1.2.4 Asset Operation and Support (AOS)

Asset Operation and Support (AOS), formerly known as 'Plant Life and Integrity (PLI), is a sub-division of G&R consisting of Boiler Engineering, Metallurgy, Technical Services Group (TSG), and Inspection Management (IM). Much of the UK's generation plant is 'Life Expired', meaning that most plant components have worked and continue to work beyond their original design life[5]; so there are stringent controls over the integrity of plant against catastrophic failure with both physical and financial risks associated with such events. Therefore NDE plays an integral part in the ongoing challenge of keeping plant running both safely, and efficiently, long after the design life. There is also the predicted boom in energy demand across Europe and indeed the world, where the proliferation of renewable, gas fired, and nuclear power generation will drive the demand for ever more challenging NDT[6]. The drive to develop new technologies for power generation, where super critical materials and higher temperatures are utilised to increase efficiency, will ensure that NDT and Inspection Management command a leading role in future Plant Integrity.

1.2.5 Inspection Management (IM)

The Inspection Management team is responsible for all NDT activities within RWE npower. It is made up of around 16 full time company employees, and around 40 full time contract staff working on a rolling one-year basis. The department is broken down into 4 main areas of responsibility:-

Outage management –Support on site during power station outages for the provision of standard NDT disciplines (UT, MPI, DPI). Typical inspections include boiler tube corrosion surveys and inspection of steam pipe welds etc

Specialist NDE – Provision of high integrity inspections for specific applications, mainly using advanced NDE methods such as phased array, TOFD, and AutoUT etc. Typical

applications would include turbine rotor inspections, generator rotor wedge bars or end rings to name a few.

Development – This is where new technology and innovative inspections are developed and proven before deployment on site. This involves creation of techniques to meet specific requirements and ensures that industry leading technology is applied where required across the company and customers sites.

Workshop NDE – This team are based at Ferrybridge and provide NDT services to the Technical Services Group (TSG), whose role is to provide workshop services. These include fabrication and repair to all manner of power station ancillary plant and steam turbine rotors from fossil or nuclear fuelled power stations.

1.3 Industrial challenge and project aims

Power plants use steam turbine rotor trains to extract the maximum potential from the steam created in a nuclear reactor, coal fired boiler, or gas turbine heat recovery boilers. These rotor trains include high pressure (HP), intermediate pressure (IP), and low pressure (LP) steam turbines, which extract energy from the high temperature, high pressure steam. The steam turbines are each constructed from up to twenty rows of radial-mounted aerofoil blades which become incrementally larger from the first row at the inlet to the last row at the outlet. The steam gives up its potential energy as it expands through successive rows of blades, expanding through the HP rotor, which exhausts into a reheat cycle in the boiler, then through the IP rotor which exhausts into the LP rotors. LP rotors are constructed from the largest aerofoil blades, the last and largest stage of which can consist of more than 100 individual blades, each measuring 1m in length and weighing in excess of 40 kg. When rotating under full load at 3000 rpm, the LP rotor's last stage blades (LSB) can be subjected to around 1Million Newtons (1000 kN) of force at their roots, leading to stresses calculated at around 120 Newtons per millimetre squared (N/mm^2). In simple terms this is the

equivalent of 80 Mini Coopers at 1200 kg each on the end of each blade[7]. Due to the astonishing stresses induced by such extreme forces, there are very specific and common methods of blade attachment to rotor disks, designed to withstand the harsh environment in which they operate.

Despite the efforts afforded to the careful design and production of steam turbine rotor blades, and the margins of safety built into them, there are well documented instances of un-availability of plant or catastrophic failure due to stress corrosion cracking and fatigue cracking to the blade root fixings of various types[8 9]. This has led to stringent limits on operating regimes across the power industry, and has forced operators to undergo regular plant outages in which steam turbines are inspected for cracking using a number of NDT techniques. These issues are not limited to life expired turbine designs, as cracking has been experienced even in the latest turbine designs, often where operating conditions have been less than ideal, or due to transient events where turbines have experienced out of specification running conditions for even very short periods[10].

As direct visual access to root cracking is not possible, the most common technique requires decommissioning of the rotor and blade removal in order to perform Eddy Current Testing (ECT) or magnetic particle inspection (MPI). MPI is the most sensitive and comprehensive method of inspection but can be prohibitively expensive due to the cost of decommissioning and the loss in generation due to extended down time. In a recent project to inspect blades at one of RWE npower's gas fired power stations, utilising techniques developed by the author as part of this project, it was estimated that circa £1M in cost savings was achieved; the in-situ phased array inspection that was carried out prevented the need to remove the turbine casings, covers, diaphragms, and all ancillary services, and reduced the turbine non-availability from 20 days down to 8 days, see Table 1-1. The direct cost savings alone were estimated at £625K whilst only several days in lost generation were gained due to unrelated maintenance work on the boiler. It will be shown how the

alternative to MPI utilises ultrasonic testing (UT) which allows limited in-situ inspections of the rotor for early detection of root cracking.

		Removal and reinstallation					NDT Inspection	Totals
		Ancillary plant and connections	Inner covers and diaphragms	Turbine	Blade removal and reinstallation	Scaffold for access		
Surface inspection methods ex-situ	Cost (£K)	100	200	200	50	150	10	710
	Time (days)	4	4	2	4	4	2	20
Phased array volumetric inspection in situ	Cost (£K)	0	0	0	0	50	35	85
	Time (days)	0	0	0	0	4	4	8
Savings	Cost (£K)	100	200	200	50	100	-25	625
	Time (days)	4	4	2	4	0	-2	12

Table 1-1 Estimation of cost savings due to in situ blade root inspection

Techniques developed by RWE npower[11], Siemens[12, 13], GE, Alstom, and Zetec[14], utilise a combination of UT inspections including phased array (PA) and single element ultrasonic testing, using fixed jigs, manipulators and mechanised scanners.

The main aim of the project was to research and critically assess the available methods of turbine root inspection, then to develop techniques which would ultimately improve coverage, sensitivity, repeatability and reliability, whilst removing the costs of decommission and extended outages, by inspecting in-situ.

1.4 Specific objectives

There are significant cost savings to be achieved by the deployment of inspection techniques which would reliably inspect the critical regions of the blade roots, and offer coverage which was equivalent to surface inspection methods. Driven directly by the industrial challenge, and very focussed on producing practical and deployable techniques, the objectives were set out as follows:-

- Research, and as far as practicable, evaluate the state of the art in the inspection of turbine blade root fixings. The main focus of such inspections should be on two common types of blade fixing which are historically prone to cracking:-
    - Pinned Roots
    - Curved Axial Entry Fir Tree Roots
- Overcome the technical challenges of applying phased array ultrasonic techniques to complex geometry with limited refraction surfaces, and/or limited access.
- Establish techniques which overcome the engineering challenges of inspecting LP turbine last stage blades whilst in-situ, with the aim of:-
    - Increased coverage, sensitivity, repeatability, and reliability
    - Utilising the current portfolio of RWE inspection equipment and retaining portability where possible
    - Utilising, primarily but not exclusively, phased array technology
    - Developing mechanical means of access to inspection surfaces where manual manipulation is prohibitively space limited
- Adopt a design and development methodology which is transferable between varying rotor designs, allowing rapid and controllable deployment of new application challenges

1.5 Contents of the thesis

This thesis will describe new and novel research into the aspects outlined in section 1.4. Chapter 2 provides context by detailing background on power plants and steam turbines, and the ways in which the problems that arise have been addressed to date. Chapter 3 then covers the various methods used for ultrasonic inspection, detailing the properties of wave propagation and the construction and operation of phased arrays.

Chapter 4 describes how rapid prototyping and Rexolite jigs have been used in a new way to study parts with complex geometry, to solve some of the difficult inspection problems faced in the power generation industry. Chapter 5 then goes on to describe the way in which scanning frames had to be developed to facilitate the inspection of unsighted and inaccessible regions of the components. Validation of these scanning frames is then investigated experimentally.

Chapter 6 introduces the concept, design and simulation of a continuous wedge which, with novel design elements, promises to lead to major advances in inspection techniques in the power industry. Chapter 7 then goes on to experimentally validate the continuous wedge.

A final chapter concludes the thesis and suggests further work.

Please note that various aspects of this work have already been published; details will be given in the relevant chapters.

Chapter 2. Background

2.1 Power plant and steam turbine construction and operation

2.1.1 Basic operation

The most modern fossil fuel power stations in the UK, burning coal and oil, were designed in the 1960s and commissioned in the early 1970s; their design gave maximum efficiencies through multiple economiser and reheat configurations in the boiler. The typical layout of a coal fired boiler, as seen in Figure 2-1, is a complex system of pipes carrying water through various heating stages; pumped by the main boiler feed pump (MBFP) the water is heated to 560 ºC at 166 bar[15]. The steam turbines labelled 17, 19, and 20 in Figure 2-1, which consist of a train of five rotors and powered by steam from the boiler, are coupled together to form a single drive shaft which drives the generator rotor. Main steam lines from the boiler super heaters supply steam to the high pressure (HP) turbine via steam chests which regulate 565 ºC steam to both sides of the turbine at 156 bar. After expanding through and driving the HP turbine, the steam is exhausted at 360 °C, 42 bar, and is returned via cold reheat pipes to the boiler's primary re-heater. The steam is reheated through various secondary boiler stages and is fed via hot re-heat pipes to the intermediate pressure (IP) steam chests. The IP steam chests regulate 565 ºC steam to both sides of IP steam turbine at 40.2 bar. After expanding through and driving the IP turbine, steam, which is at 306 ºC and 6.32 bar is exhausted to feed three low pressure (LP) Turbines. So that the maximum amount of energy is extracted through the LP turbines, the exhaust pressure is kept very low, just 50 millibar above a complete vacuum. Finally exhaust from the LP turbines is fed directly into banks of condensers that cool the water which is fed back to the MBFP and the cycle starts over.

1. Rail Unloading House
2. Junction House
3. Coal Conveyor
4. Boiler Coal Bunker
5. Bucket Wheel Machine
6. Coal Feeder
7. Pulverising Mill
8. Primary Air Fan
9. Boiler Burner
10. Boiler
11. Forced Draught Fan
12. Air Heater
13. Electrostatic Precipitator
14. Induced Draught Fan
15. Main Chimney
16. Super Heater
17. High Pressure Turbine
18. Boiler Reheater
19. Intermediate Pressure Turbine
20. Low Pressure Turbine
21. Rotor
22. Stator
23. Generator Transformer
24. Condenser
25. Condensate Extraction Pump
26. Low Pressure Feed Heaters
27. Deaerator
28. Boiler Feed Pump
29. High Pressure Feed Heaters
30. Economiser
31. Steam Drum
32. Cooling Tower
33. Circulating Water Pumps
34. Circulating Water Make-Up Pumps
35. FGD Absorber Tower

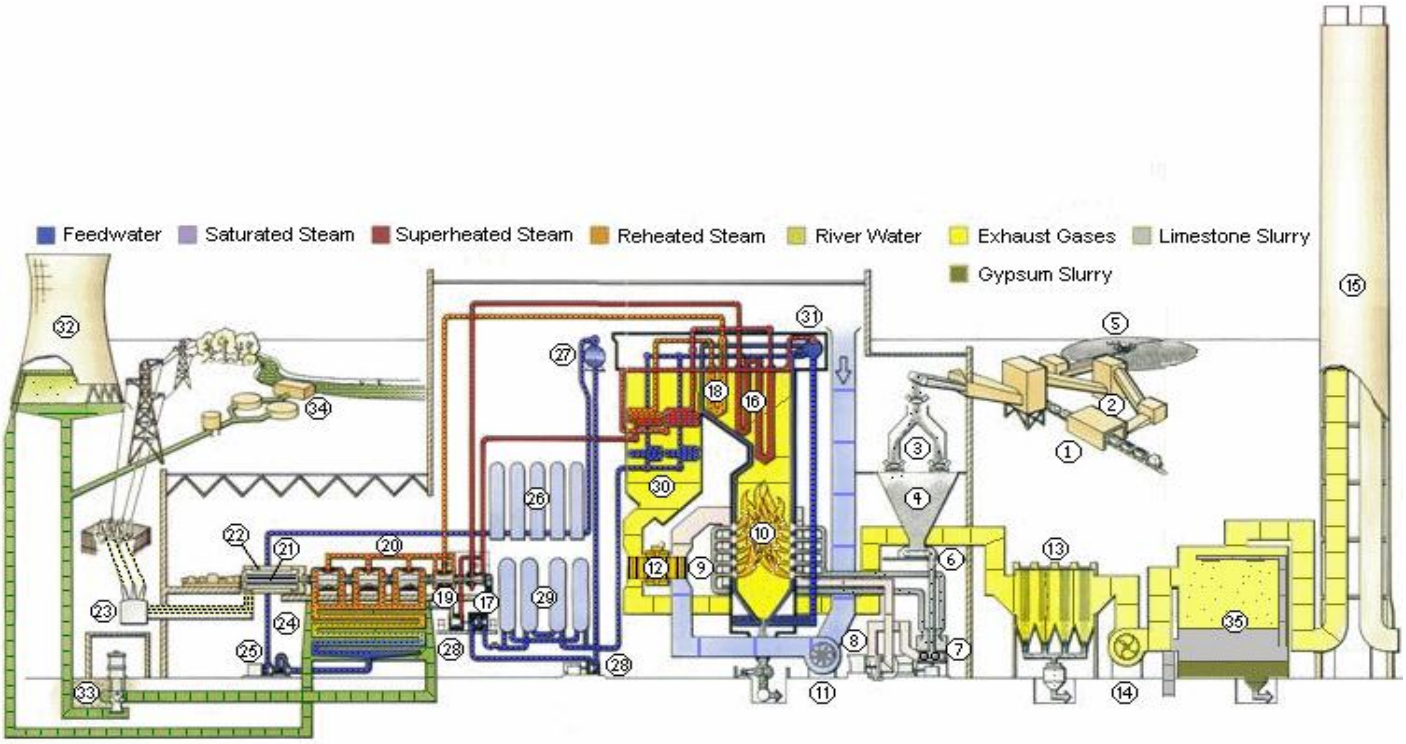

Courtesy of DRAX Group PLC

Figure 2-1 Layout of a typical coal fired power station boiler[15]

2.1.2 Steam turbine rotors

Depending on the capacity of a given coal fired boiler, the steam turbine rotor train consists of the HP, IP, up to three LP rotors, and the generator rotor. The rotor shafts are coupled together to form a single shaft which rotates at 3000 rpm to generate electricity at 50 Hz (UK) or at 3600 rpm to generate electricity at 60 Hz (North America). Each rotor consists of multiple wheels of radial-mounted aerofoil blades (known as stages), which become incrementally larger from the first stage at the inlet to the last stage at the outlet. Between each rotating stage of blades, a static wheel of blades known as the diaphragm, acts

upon the steam exiting the previous stage to optimise the flow of steam onto the subsequent stage. Most turbine designs incorporate a dual flow construction where steam is fed into the centre of the rotor and expands outward through incrementally larger stages to the outer ends (outlets). However many turbines can incorporate a single flow design where steam enters at the inlet end through subsequently larger stages to the outlet end.

The typical HP turbine, pictured in Figure 2-2, is subject to steam with the highest pressures of 156 bar at 565 ºC, and is therefore constructed with the smallest turbine blades (buckets) which increase in size through subsequent stages as the steam gives up its energy. This type of turbine acts predominantly as an impulse turbine where the fixed veins (diaphragm) act as nozzles to direct high velocity steam, which has significant kinetic energy, onto the buckets to create turning force in the rotor[16]. The blade design of these turbines tend to be of short aerofoils with fixed cross section along their entire length and shroud rings tying the full wheel of blades together at their tips; the shroud rings also incorporate sealing rings to prevent steam leakage around the outside of each stage[17].

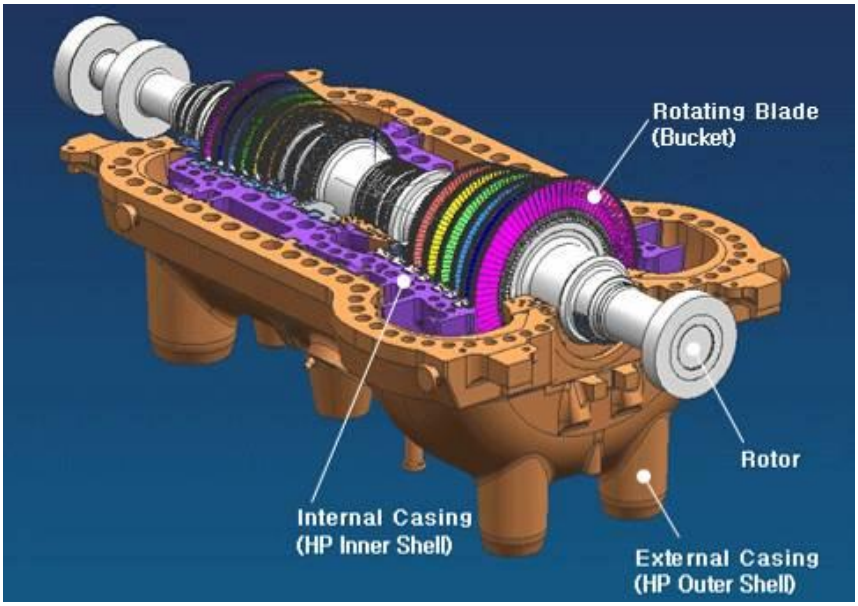

Figure 2-2 Typical dual flow high pressure (HP) turbine[17]

The typical IP rotor, pictured in Figure 2-3, is subject to steam at 565 ºC but at a relatively lower pressure of 40.2 bar; this means that it is of similar but scaled up design to the HP

rotor. The dual flow configuration has steam supplied to the centre of the rotor and expands through subsequently larger stages to the exhaust at the outer ends. As in the HP turbine, the IP turbine acts predominantly as an impulse turbine where the diaphragm creates nozzles to direct steam onto the rotating buckets of the rotor, imparting the kinetic energy of the steam to rotation of the rotor. However, in the latter stages of more modern rotors, where the kinetic energy of the steam reduces as the pressure reduces, the aerofoils are designed such that they act as reaction turbines. Reaction turbine blades of these latter stages employ advanced aerodynamic features so that they react with the flow of steam over their profile; this creates a pressure differential which produces rotational torque similar to the lift created by an airplane wing. These stages of blades therefore act as impulse turbines at their base and have some features of reaction turbines at their tips[18].

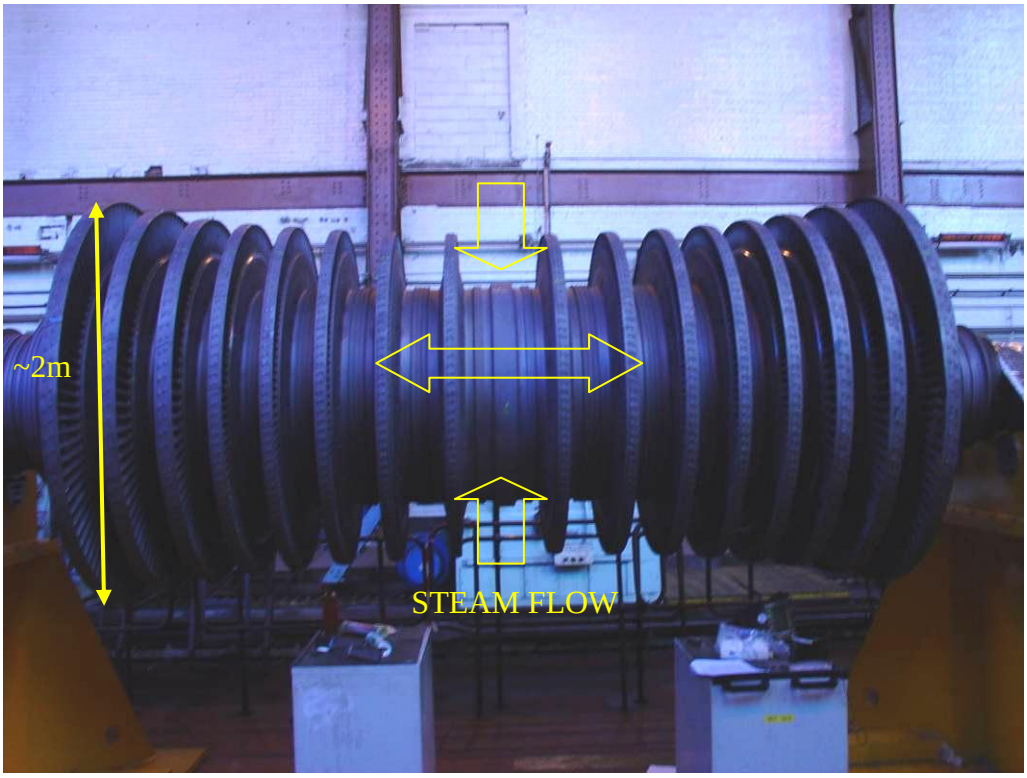

Figure 2-3 Photograph of a dual flow intermediate pressure turbine

The typical LP rotor, pictured in Figure 2-4, is powered by the exhaust steam at 306 ºC and 6.32 bar, from the IP rotor. The rotor train might consist of up to 3 LP turbines which

are critical to the efficiency of power production and can typically produce up to 40 % of the total power[15]. As the pressure of the steam has reduced significantly the stages of blades are markedly larger in both length and width, creating a much larger surface area. The LP rotor has a significantly different design where the first four stages act mainly as impulse turbines having some aerodynamic features to produce reaction forces toward their tips (similar to the latter stages of the IP rotor). However the last two or three stages of blades consist of free standing aerofoils designed to work together as a system; acting predominantly as reaction turbines over the length of the blades. This design employs advanced aerodynamic features including meridional flow path contouring, axial and tangential compound lean of the L-0 nozzle, and tailored exit profiles from the L-1 stage to allow optimum radius ratio in the L-0 blade[18 19].

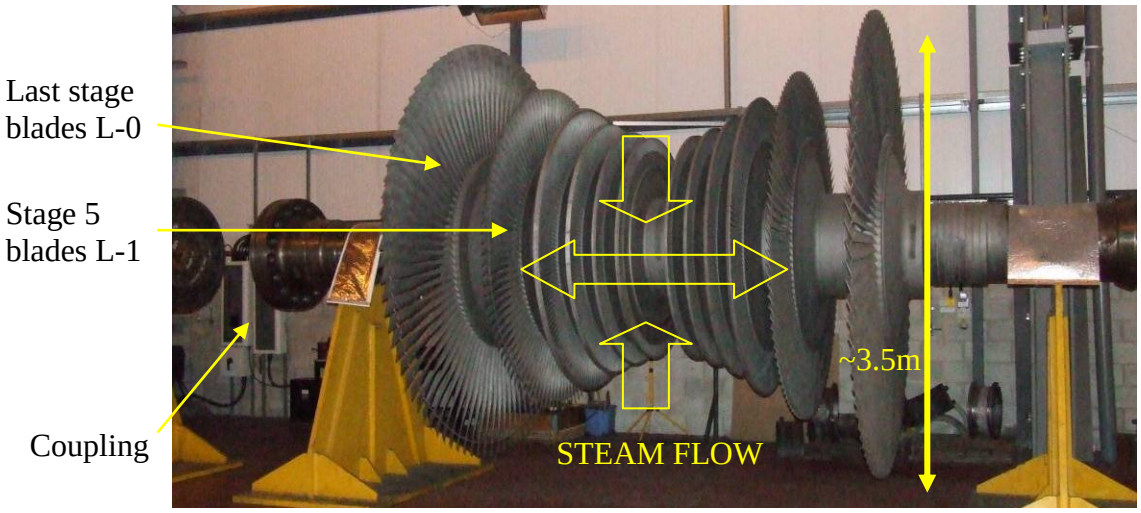

Figure 2-4 Photograph of dual flow low pressure turbine

During service, the last stage blades of an LP rotor, which are typically greater than 1 m long, and can weigh around 40 kg each, will rotate at 3000 rpm (50 Hz); the enormous centrifugal forces exerted upon these blades mean that they are among the most highly stressed components in a power station. Damage such as cracking in the root fixings of turbine blades can be caused by the start-up loading stresses, thermal stresses, residual manufacturing stresses, and normal loading stresses due to the centrifugal forces acting on

the blades. The root areas of the blades are subjected to the highest stresses and can be damaged over time during normal running conditions, but more susceptible to damage due to non-ideal conditions occurring during running; such events as loss of vacuum or over speed are factors leading to the initiation of cracking. Any such cracking will propagate under normal running loads, but under transient loading, such as start-up and shut-down cycles, cracks propagate readily leading to subsequent failure[20]. Failure of even a minor stage blade of a steam turbine rotor can lead to significant damage to the rotor as it is ejected through subsequent stages. The loss of a last stage blade of an LP rotor can lead to the total destruction of the LP, and generator rotors, due to the chain of events which occur after the sudden loss of balance in the rotor train. Figure 2-5 illustrates the catastrophic damage which occurred after a last stage blade was ejected through the 400 mm thick steel casing of the LP turbine, crashing through the roof of the turbine hall, and subsequently landing in a lay-down yard 100 metres away. The sudden unbalance of the LP turbine led to the rotor train coming to a full stop from 3000 rpm in several seconds. The force broke the 500 mm diameter main rotor shaft, damaging the generator turbine casing, which exploded, destroying both the LP and generator rotors. The cost to the utility company ran into millions of pounds for the replacement of the rotors and loss of generation. No lives were lost due, in main, to it occurring in the early hours of the morning.

Figure 2-5 Catastrophic failure of LP rotor last stage blade

2.1.3 Steam turbine rotor design

Historically steam turbines were constructed with a single large forging to create the main hub of the rotor, onto which fixing mechanisms (disc heads) were machined to accommodate blade wheel attachment. The cost and shortage of large forgings around the world, due to the extensive lead times from foundries and high demand, led rotor manufacturers to utilise smaller forgings and machine separate rotor segments; these segments are then bolted together with tie rods or welded around their circumference to form the rotor hub, see Figure 2-6. Welded rotors have in fact become the preferred manufacturing method for many OEM turbine manufacturers such as Mitsubishi Heavy Industries Ltd who note that the use of smaller materials enabled a shift to larger capacity and shorter delivery times[21].

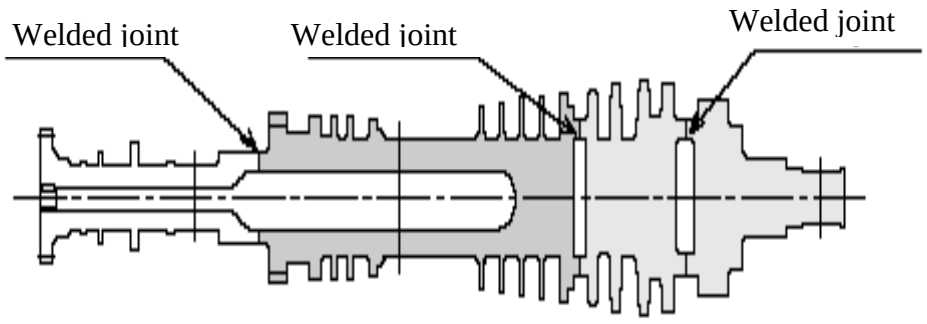

Figure 2-6 Typical welded rotor construction

The disc heads, designed to hold the wheels of blades to the rotor hub, consist of a variety of different fixing designs, none of which are exclusive to a single rotor, see Figure 2-9. Many of the fixing designs for smaller blades utilized in HP, IP, and the smaller stages of LP rotors, are seen in Figure 2-7. Straddle, Internal T, and pinned type blade roots are attached to circumferential mating tenons or mortises in the disc head, utilizing one or more insertion points at which locking blades are inserted during assembly, see Figure 2-8. Internal Tree and Dovetail blade roots are attached to axial mortises machined in the disc

head and are individually locked in place by various mechanical methods including pins or keys.

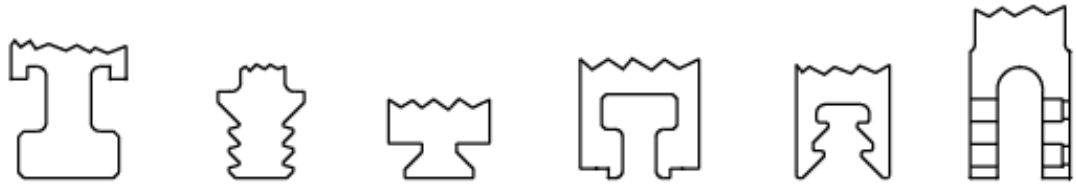

Figure 2-7 Typical blade root configurations

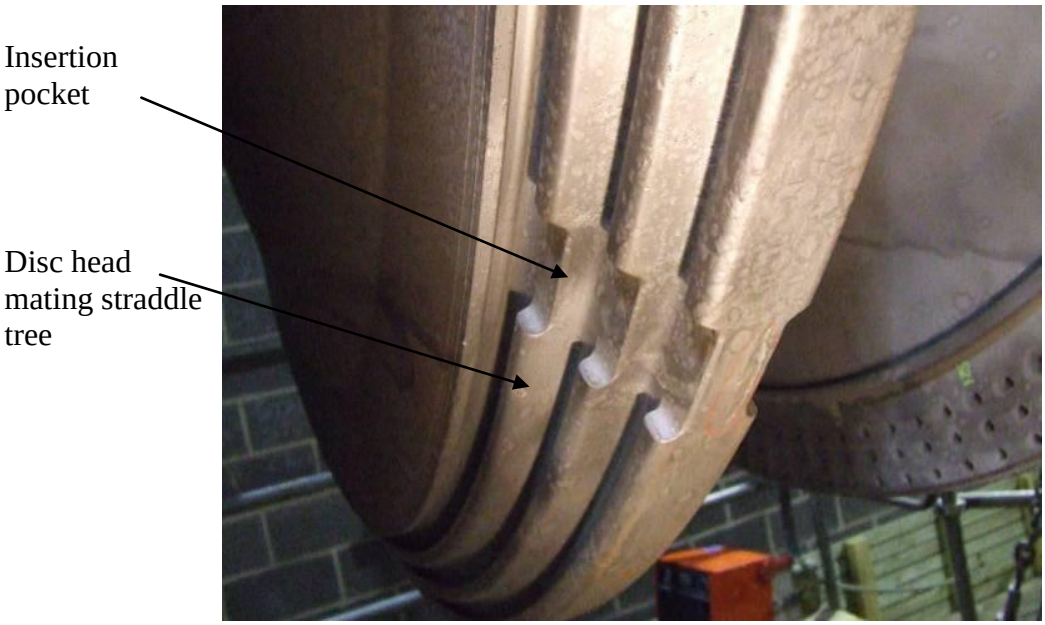

Figure 2-8 Straddle fir tree disc head with insertion point

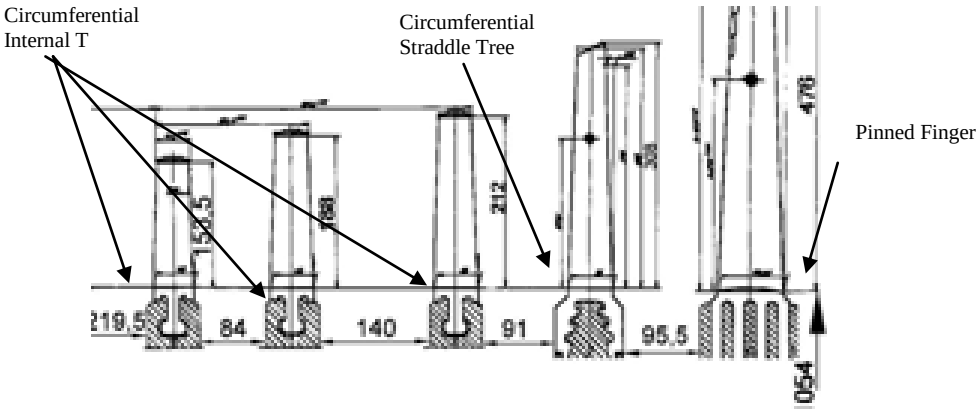

Figure 2-9 Schematic of typical steam turbine root configurations

For the larger turbine blades in LP rotors, such fixing methods are not sufficient to withstand the centrifugal forces at full rotational speeds. Common methods of large blade attachment include; pinned finger roots, axial entry fir tree roots, and curved axial entry fir tree roots, see Figure 2-10, Figure 2-11, and Figure 2-12 respectively.

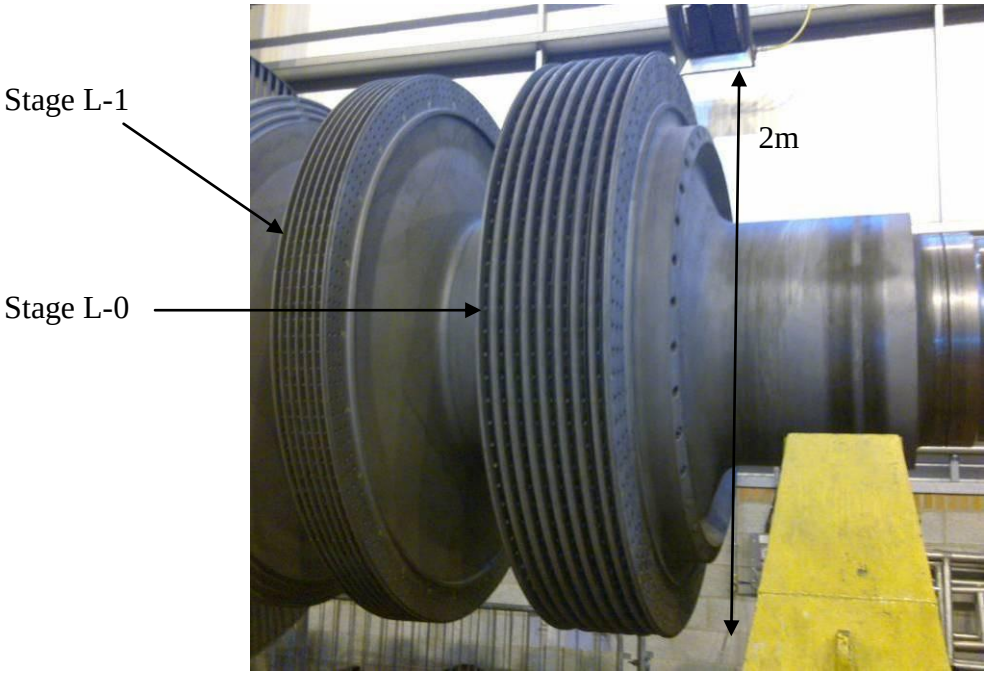

Figure 2-10 De-bladed LP rotor with pinned finger roots L-0 and L-1

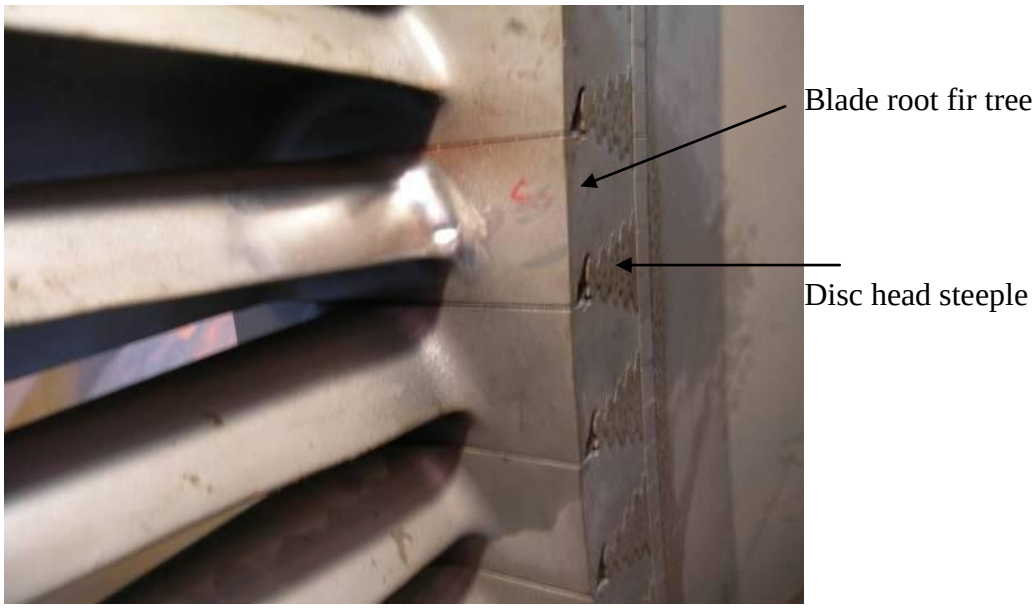

Figure 2-11 Axial entry fir tree roots

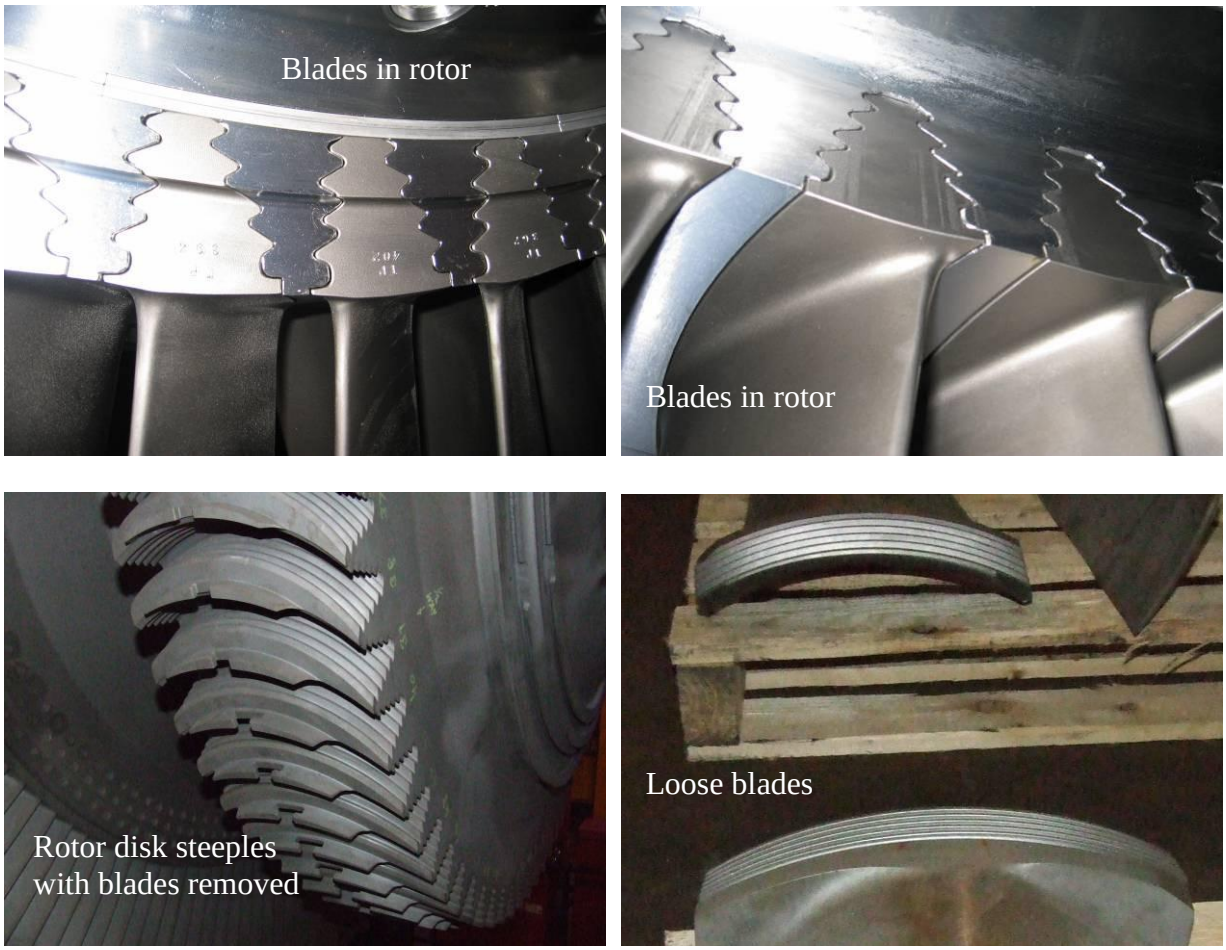

Figure 2-12 Curved axial entry fir tree roots

Historically, pinned finger root fixings were utilised for large blades of LP rotors but were susceptible to finger hole cracking induced by low or high cycle fatigue and stress corrosion cracking. The major contributing factor to high crack initiation rates was the presence of multiple stress raising points created by the corners of the pin holes in the fingers. Axial entry fir tree roots were designed to spread the high loads and reduce the occurrence of high stress points at the sharp changes of section in pin holes. Advances in design methodologies has led to the implementation of curved axial entry fir tree roots being the preferred configuration[19 22]. The curvature of the root attachment allows more flexibility in the aerodynamic design of the aerofoil, with improved inter-blade spacing. The drive for bigger last stage blades in LP rotors has stemmed from the need to improve turbine efficiency; in

central generating plants the LP rotors can account for 40 – 50 % of the total generating capacity, and improvements of 3-4 % efficiency can have drastic effects on profitability.

2.2 Conventional inspection of steam turbine blade roots

2.2.1 Introduction

The remit of this research is the inspection of blade root fixings. Due to operational demands during the course of this research, pinned roots on IP rotors, and curved axial entry fir tree roots on LP rotors became the main focus of the research. The various techniques deployed for the inspection of these blade roots, can be very specific to the types of defect sought but not often used in isolation. Many inspections are developed in response to failures or the discovery of new failure mechanisms, and many are deployed as a matter of routine during maintenance periods. This section focuses on the state of the art and routine inspection techniques for Pinned root attachments and curved axial entry fir tree root attachments.

2.2.2 Pinned roots

Pinned roots are a common attachment method for steam turbine rotor blades of many sizes, from smaller stages of IP turbines to the largest stages on LP turbines. The main feature of this type of fixing is a series of up to eight circumferential slots machined into the disc head, with corresponding fingers machined into the root of the blade (refer to Figure 2-10). The blade fingers are inserted into the disk head slots and locked in place with axial pins which are either hot or cold riveted through holes in both the up-stands and blade fingers. Common issues with this design include cracking from the pin holes in the disc head fingers; often limited to the heat affected zone around the pin hole, created during the process of hot riveting, but have been known to propagate extensively, see Figure 2-13. Detection of these defects is limited to the accessible outer disc finger, utilising enhanced

visual inspection such as magnetic particle inspection (MPI), or eddy current testing (ECT), both of which are sensitive to surface breaking cracks. However, cracking to the blade root, which is not accessible by visual inspection or ECT means, can be found to be emanating from the pin holes. Figure 2-14 shows a typical blade which was removed from a customer rotor and was found to be cracked full through wall, leading to detachment from the root altogether. The ability of this blade root to withstand the forces in full load operation was severely diminished and could have led to the destruction of the rotor had it been released.

The challenge for inspection of these particular blade roots, which were taken from a Siemens/Parsons 200 MW IP Rotor, is the ability to carry out volumetric inspection, in search of crack initiation sites, with severely limited access from the blade root platforms.

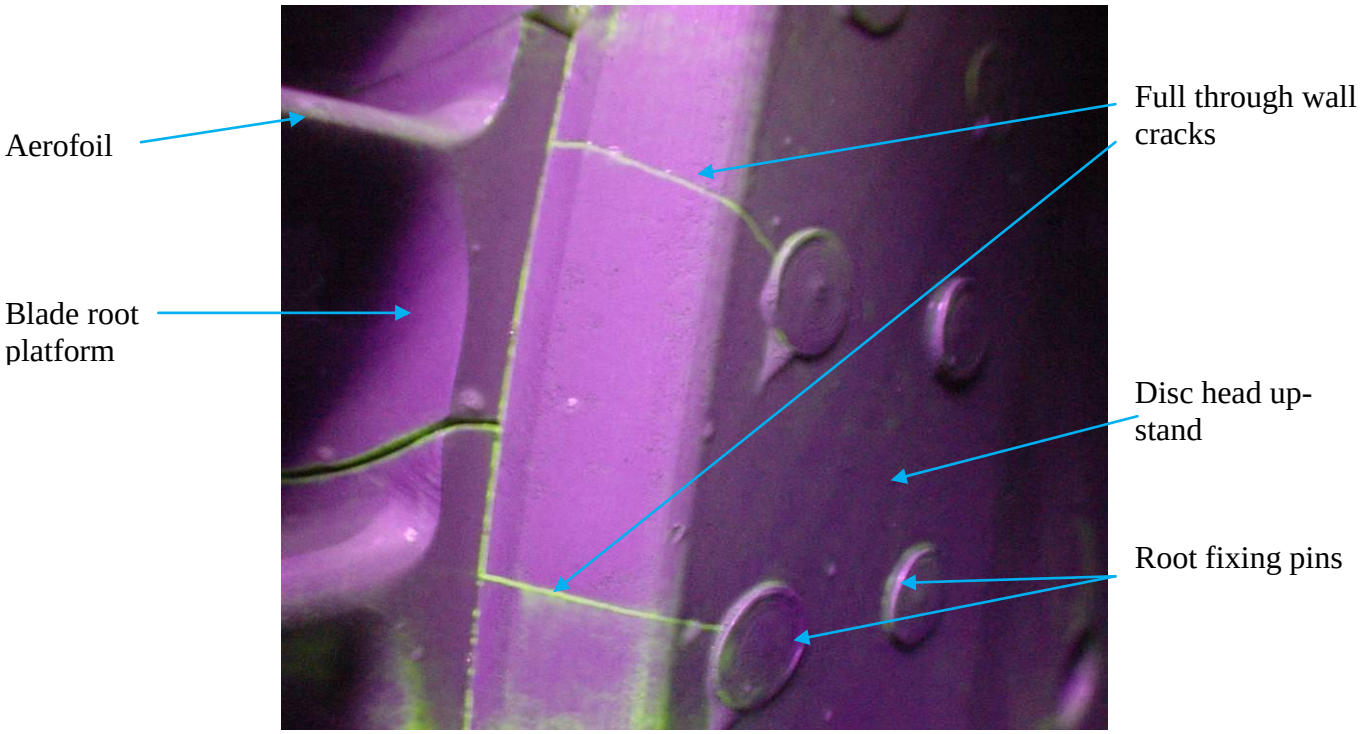

Figure 2-13 Example of up-stand cracking to IP steam turbine

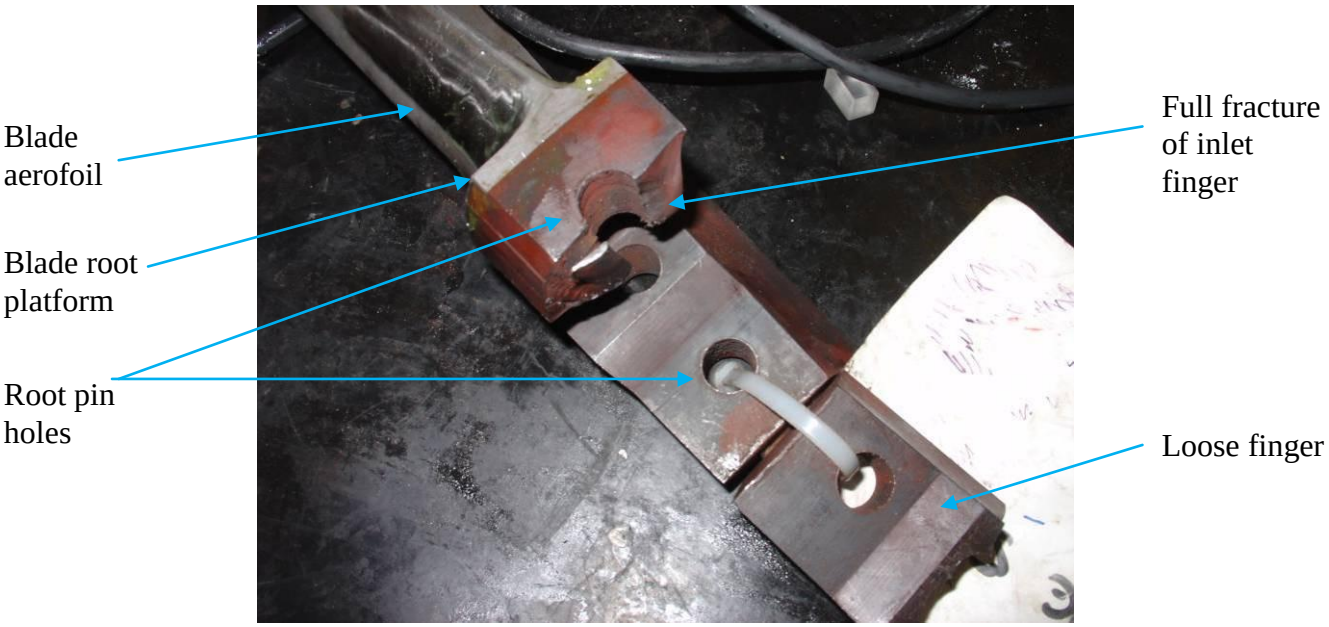

Figure 2-14 Pinned root cracking to IP turbine blade

2.2.2.1 Defects Sought

Metallurgical analysis of failed blades had identified a number of crack initiation sites around the pin holes and sharp section changes of the root, see Figure 2-15 and Figure 2-16.

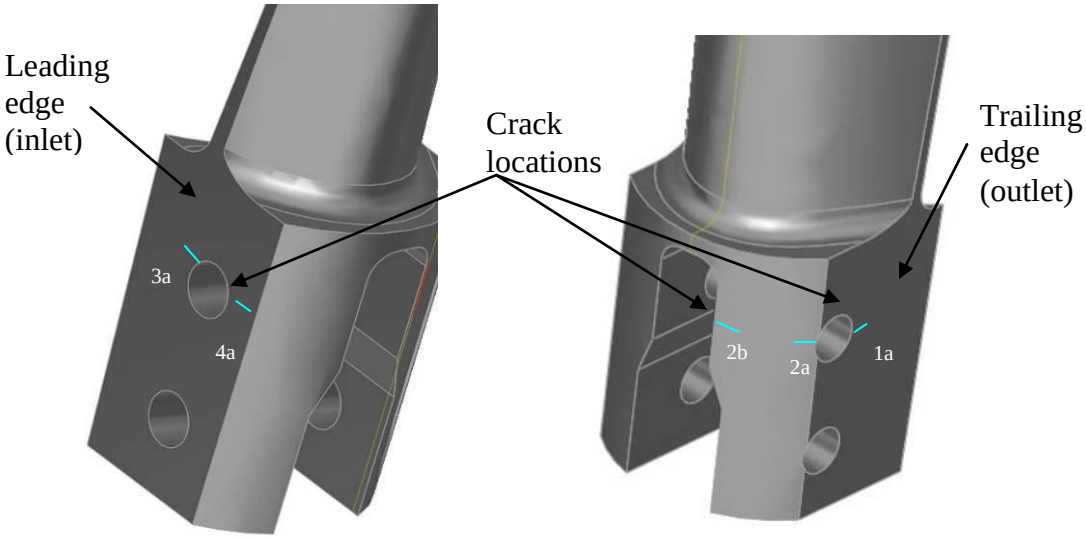

Figure 2-15 IP blade root crack locations

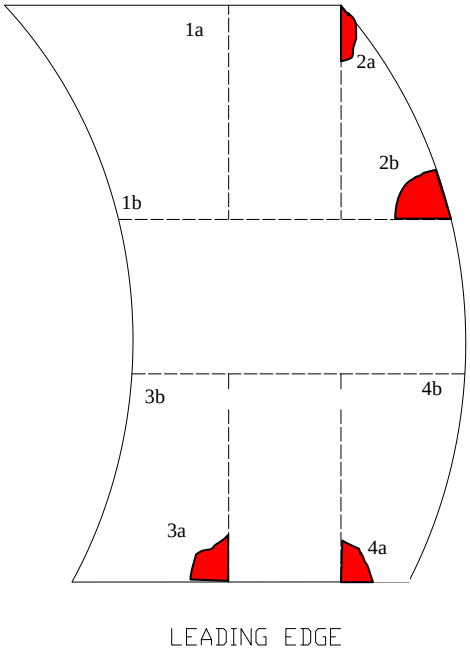

Figure 2-16 Section through blade root illustrating crack initiation points

It was reported that cracking in these initiation sites had occurred early in the life of the rotor and had propagated rapidly during transient periods such as stop/start cycles, and over-speed runs[23.]

2.2.2.2 Pinned root inspection techniques employed by RWE npower

The approach taken by RWE npower, for the detection of pinned-root cracking, utilises Panametrics M203, 10 MHz 3 mm diameter ultrasonic transducers, used in conjunction with a digital A-Scan flaw detector. The inspection utilises the very limited flat lands at the aerofoil root block transition, introducing compression waves into the root block in search of geometric responses from the pin holes and back walls in zones 2a, 3a, and 4a, see Figure 2-19 and Figure 2-19. Further coverage of the 2b position is achieved by use of a Panametrics A6015, 5 MHz 4x4 mm, sub miniature single element 45º shear wave transducer, and refracting ultrasound across to the saddle corner region at zone 2b, see Figure 2-17. Zone 1a was not inspected due to the lack of flat land from which to refract ultrasound. These techniques require the use of thick grease couplant and the manipulation

of the probe to various skews to achieve coverage of the root pin hole. The orientation of the rotor in relation to the operator is also critical, and inspections have to be carried out with the blading and inspector positioned with optimum access for ease of probe manipulation. Optimal access is only possible if the rotor can be rotated freely, and where this requirement is not met then the probability of defect detection will be significantly reduced[24]. Furthermore, the quality and sensitivity of this technique relies heavily on the operator being methodical and meticulous about how the probes are positioned and manipulated.

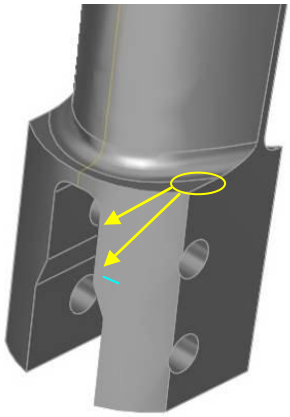

Figure 2-17 Shear wave inspection for position 2b

2a

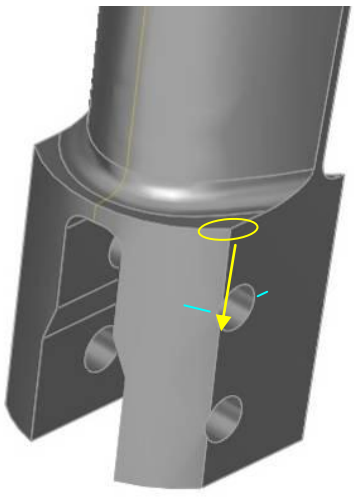

3a

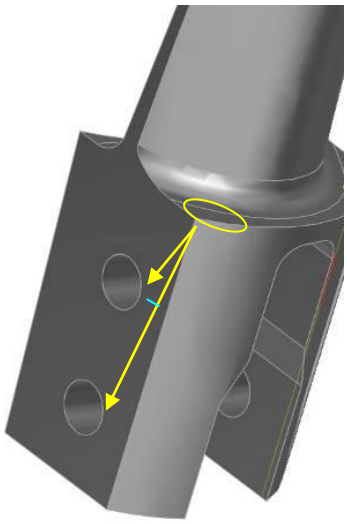

Figure 2-18 Compression wave inspection for positions 2a and 3a

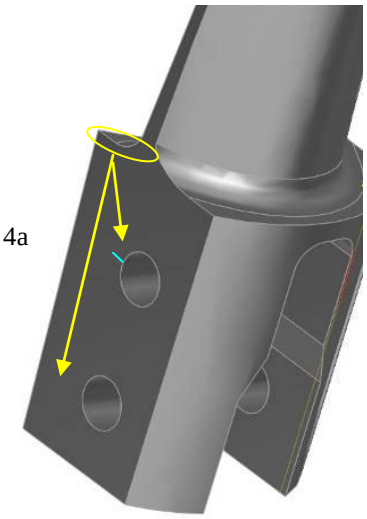

Figure 2-19 Compression wave inspection for position 4a

2.2.2.3 Validation and technical appraisal of current RWE pinned root technique

To provide a valid measure of the quality and sensitivity of this method, the author organised and carried out a blind trial on a live rotor which was crucial in understanding the limitations of the current technique. A full stage of blades was inspected using the current technique, and all defects found were reported by the operators involved[25]. Following the inspection, the entire stage was de-bladed in the workshop, the loose blades grit blasted to remove service contaminants, and fluorescent MPI was carried out on the blade roots; all defects were recorded in detail and reported[26]. The ultrasonic inspection reported cracks to 16 blades out of the 98 blades inspected, whilst MPI confirmed that 20 blades contained cracks:-

- 15 of the cracks were in zone 2a or 2b, and of these 7 were also cracked in zone 1.
- 3 blades were cracked in zones 3a and 4a.
- 2 cracks were found in zone 1 where there were no other defects in other zones.

In summary, 16 cracked blades were positively detected by the UT inspection but 2 cracked blades with defects were missed due to the crack responses being difficult to resolve from the geometric responses. The missed cracks consisted of a 10mm by 18mm crack and

3mm by 4mm crack (when measured along the surfaces of the root fingers), but were severely masked by the geometric response from the saddle shoulder when viewed on an A-scan display. Two cracked blades were not detected due to cracks occurring in zone 1 alone which is not inspected. Although this trial was not a rigorous reliability study of the current RWE npower technique, it highlighted that significant defects in the critical regions could be missed due to the limitations of the inspection technique.

2.2.2.4 Inspection techniques employed outside RWE

The types of inspection techniques deployed by outside companies, including power operators, turbine manufacturers, and inspection companies, is dictated almost entirely on the type and design of turbine, the capabilities of the said companies, and by the constraints laid out with regard to outage regimes and budgets. The geometry of specific pinned root designs dictates the available scanning surfaces from which to refract ultrasound and dominates the inspection approach taken. British Energy for example, have utilised bespoke miniature wafer probes designed to fit into the limited spaces available, but using the same principles as used by RWE npower[27]. Their probes were evaluated and due to their frequency of 5 MHz and would be less likely to provide good resolution to small defects whilst being less capable of resolving signals close to the main geometric responses during application. They were also found to be more easily manipulated due to their size and design but less flexible in manipulating the ultrasound trajectories and therefore limited potential coverage. Other companies such as Siemens have deployed phased array techniques for the inspection of pinned roots of larger blades, where access can be gained from blade root shoulders, utilising linear scans to achieve coverage[12 13 28]. Siemens report that defects of the same order of size at similar locations around the pin holes are positively detected. Their approach has been tested through simulation techniques published by Zetec, who show that it is possible to skip linear phased array ultrasound off inner fingers to achieve coverage of the root pin under test[29].

2.2.2.5 Discussion

It has been found that very specific solutions must be sought in achieving coverage and sensitivity to defects in the pinned root design in question. By performing a technical appraisal and validation of the current RWE npower technique, albeit not rigorous, it was shown that very small defects or those in particular positions could be missed by the technique. The difficulties arise in trying to apply single element pulse-echo ultrasonic techniques which are required to cover wide zones from very limited probe positions; added to this, the amount of manipulation required to perform a sensitive inspection and the need to rotate the rotor to keep optimum inspector positioning, would lead to inconsistencies and poor repeatability. Phased array ultrasonic technology might allow the manipulation of beam trajectory to be controlled electronically, removing some of the requirement for probe manoeuvring, but would be restricted by the availability of scanning surfaces from which to test. Some techniques are published for particular designs of rotor with specific challenges, but these were found to be inappropriate for the pinned root design under investigation.

2.2.3 Curved axial entry fir tree roots

The main feature of curved axial entry fir tree roots is that of a ‘fir tree’ root profile, known as such due to the shape being similar to that of a fir tree or Christmas tree. This profile is extruded around a fixed radius to produce the curved axial shape which allows for optimum aerofoil design, Figure 2-20. Mating fir tree slots are machined into the rotor disk head, known as disk steeples, into which the blades are axially inserted and fixed with various types of locking keys, as seen in Figure 2-21.

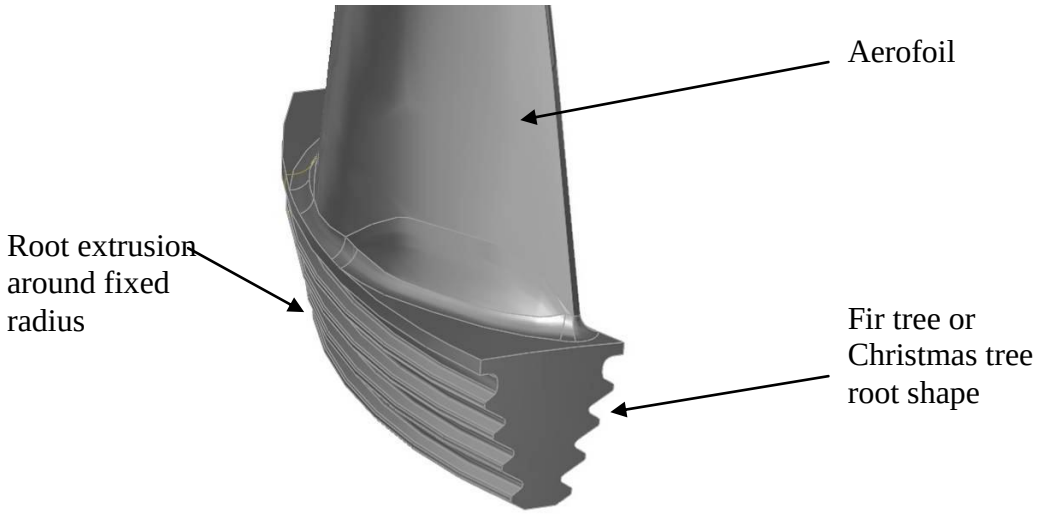

Figure 2-20 Curved fir tree blade root design

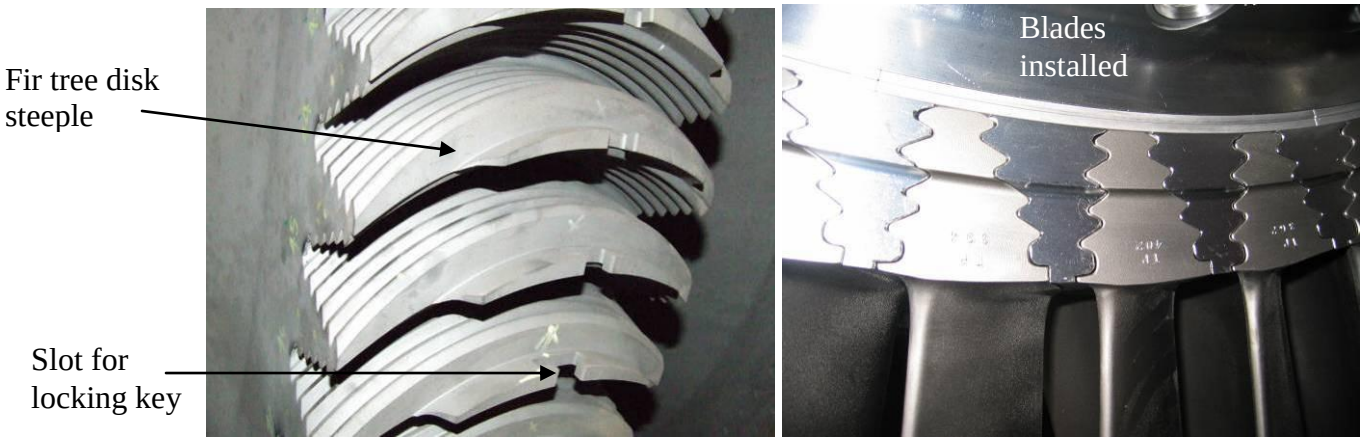

Figure 2-21 Disk head steeple curved fir tree root slots

The fir tree design allows for a significant increase in surface area of the attachment region and therefore spreads the loading exerted on the blade during full load operation.

2.2.3.1 Defects sought

Defect locations have been established by finite element analysis (FEA) and known historic defects on various blade root designs. Stress corrosion cracking has been the most prevalent type of defect, induced where environmental conditions or poor water chemistry have been evident. The efficient running of thermal power plants rely heavily on clean deaerated water used to raise steam, but contaminants such as dissolved oxygen, Silica, Sodium Phosphate, Ammonia and Chloride all have detrimental effects on the physical

condition of the plant; these contaminants react aggressively in the hostile environment and can lead to rapid failure of the system[30, 31]. There are also instances of fatigue cracking which, due to their tendency to propagate rapidly, are more serious and present the potential for blade detachment from the turbine.

Finite element analysis (FEA) was carried out by RWE engineering team and it suggested that the top serration is the most highly stressed area of the blade root; see Figure 2-22 and Figure 2-23, representing the region where cracking is most likely to lead to total blade detachment from the turbine[32]. In some cases however, FEA suggests that the second serration down is the most highly stressed, see Figure 2-24. However in all cases the FEA suggests that the most highly stressed areas reside towards the centre of the convex root, and towards the outer ends of the concave root.

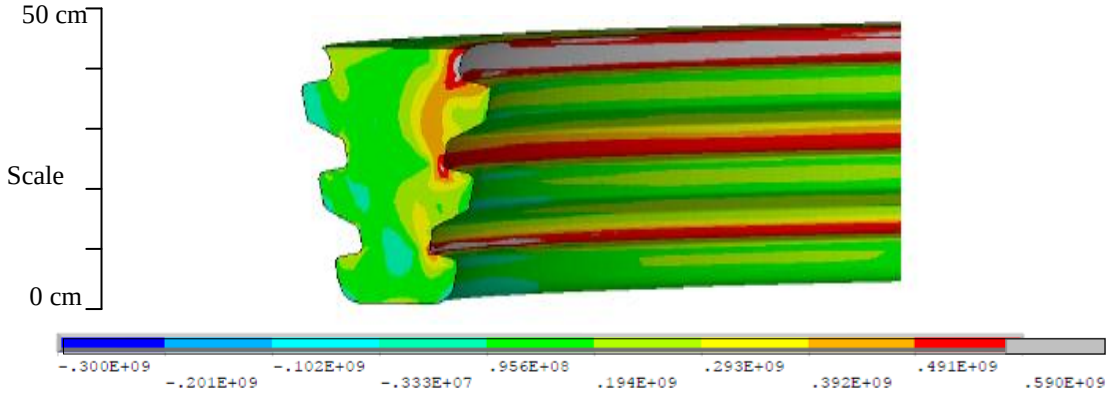

Figure 2-22 Blade root concave: Von Mises equivalent tension [MPa] [32]

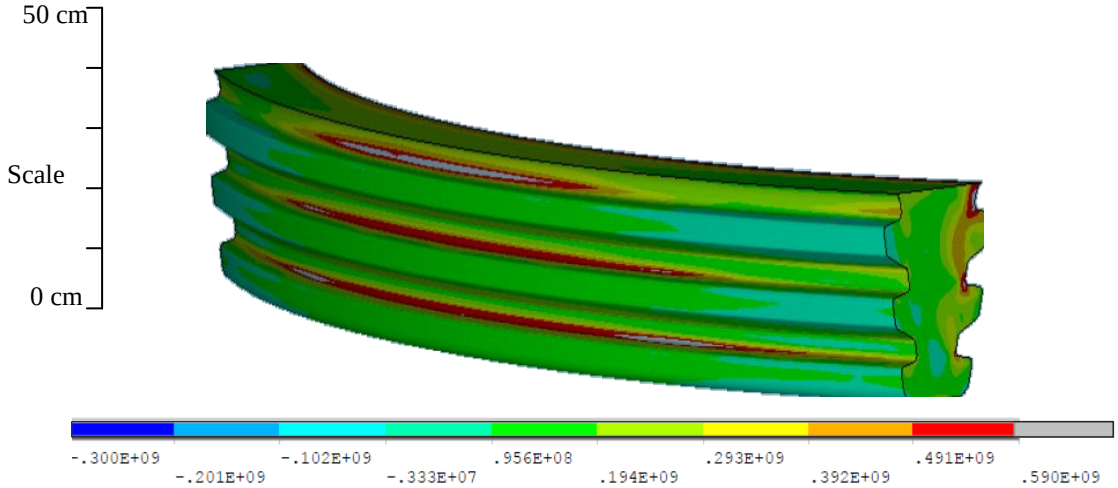

Figure 2-23 Blade root convex: Von Mises equivalent tension [MPa][32]

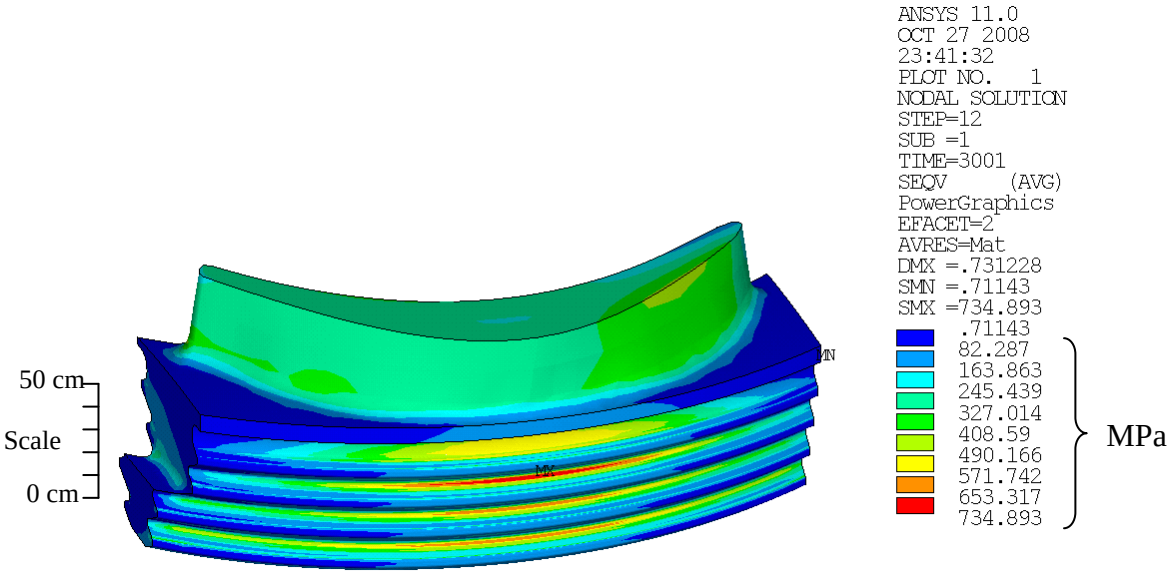

Figure 2-24 Blade root convex: Von Mises equivalent tension [MPa] [32]

Operational experience has shown that defects have the tendency to initiate in the first serration down from the aerofoil-root platform, in the centre of the convex side, and the extreme ends of the concave side[13] [33]. Typical examples of defects found in several different rotor designs are illustrated in Figure 2-25 showing concave side cracking, and Figure 2-26 showing convex side cracking.

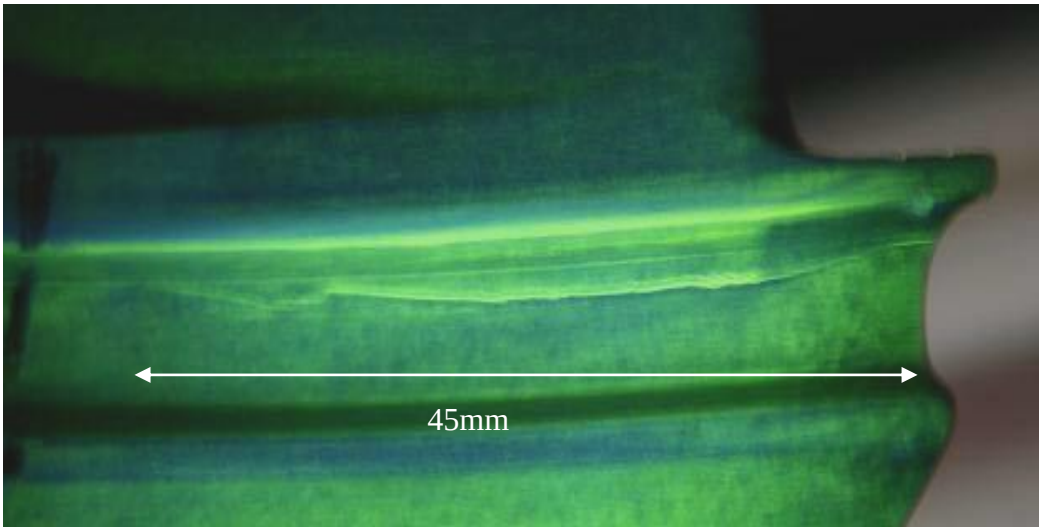

Figure 2-25 Crack propagating in the top serration of the concave side

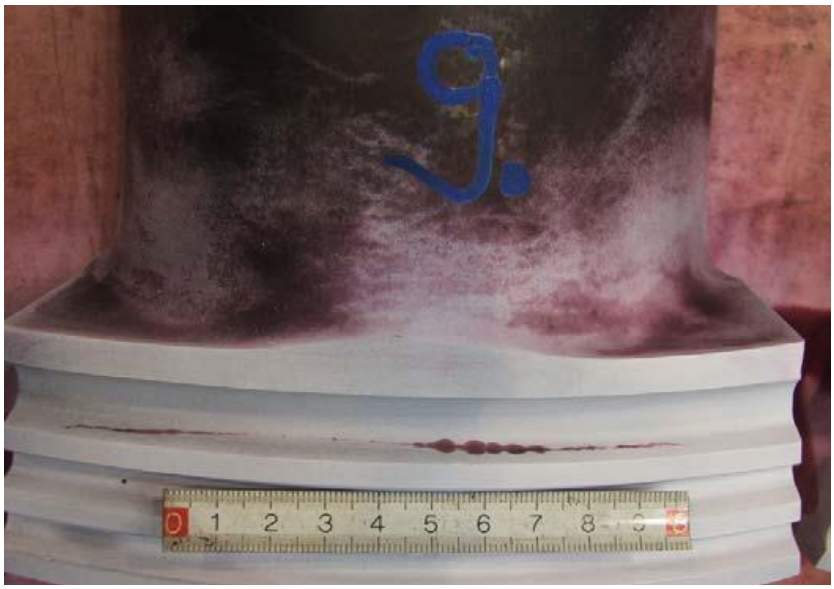

Figure 2-26 Crack propagating in the top serration from the centre of the convex side 2 (Ruler scale in centimetres)

There have been many instances of cracking to curved axial entry fir tree root designs, which have in some instances led to failure and catastrophic damage to the turbine and surrounding plant items[8]. Significant changes to inspection regimes were introduced to one RWE npower site after a failure at Duvha power station in South Africa destroyed the whole turbine train[13]. Samples, provided to RWE npower at the time, had cracking to the centre of the top root serration of the convex side (Primary crack location), and cracking to the outer ends of the top serration to the concave side (Secondary crack location). Other turbine failures have occurred where the primary crack location has been the outer ends of the concave top serration, and in the case of the GEC (Alstom) LD66 945 last stage blade, significant modifications were made to rotor trains around the world[34]. So in summary the main target locations for any blade root inspection would have to include:-

- Coverage of the concave top serration toward the outer ends of the root block, Figure 2-27.
- Coverage of the convex top serration toward the centre of the root block, Figure 2-28.

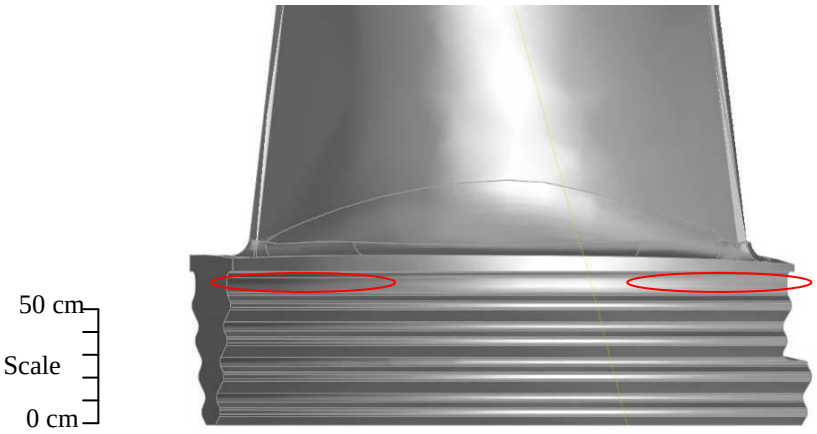

Figure 2-27 Target regions of concave side root

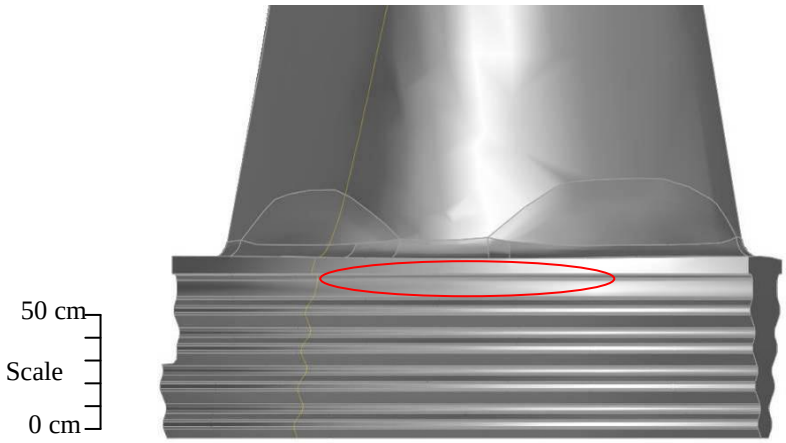

Figure 2-28 Target regions of convex side root

2.2.3.2 Inspection techniques employed by RWE

Due to the complex geometry associated with curved root designs, there are limited available lands from which to perform ultrasonic testing, varying from one blade design to another; some having generous platforms from which to scan whilst others have almost none. Common to all curved root inspection techniques, the aerofoil offers the main scanning surface from which the majority of coverage is attained; see Figure 2-29 and Figure 2-30.

Due to the shape of the aerofoil in relation to the root, limitations to the coverage exist, requiring further scanning from any available platforms (Figure 2-31), or end faces of the root block, (Figure 2-32).

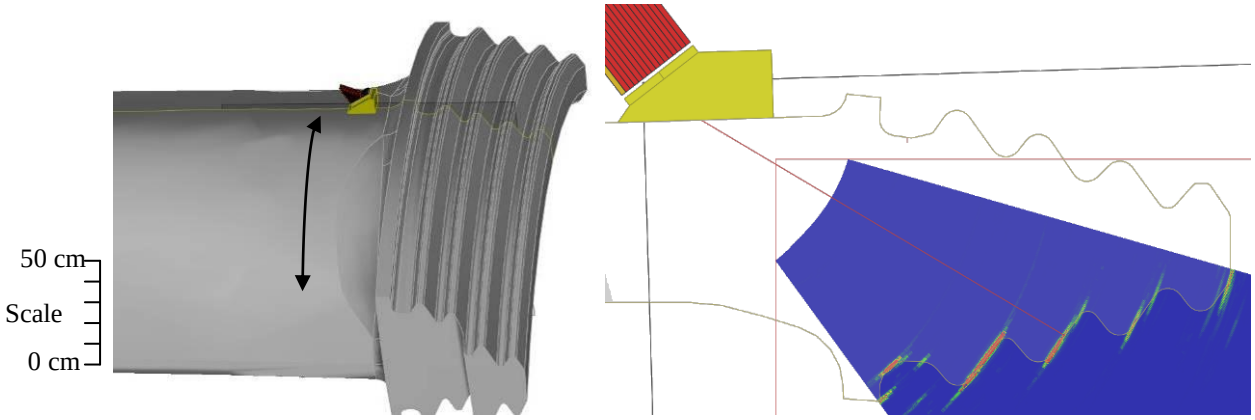

Figure 2-29 Root inspection from convex aerofoil

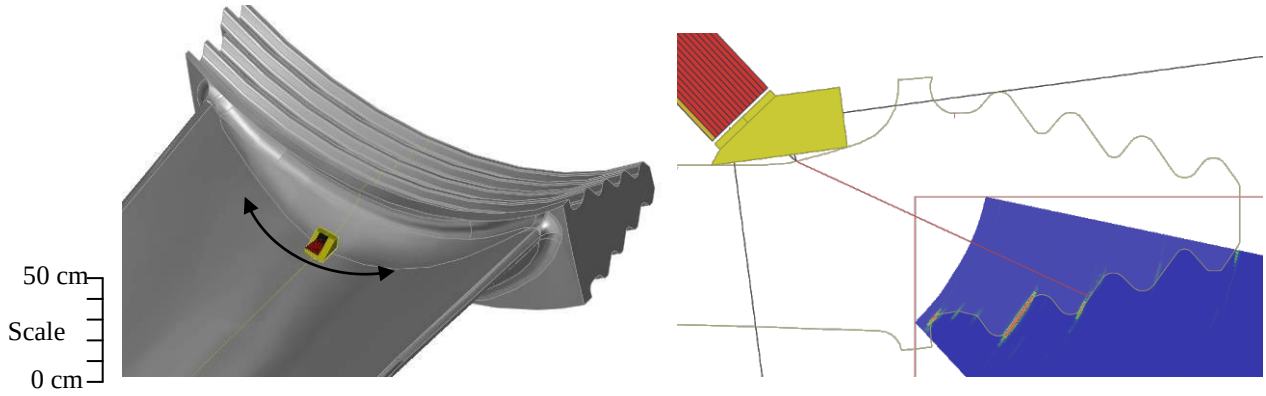

Figure 2-30 Root inspection from concave aerofoil (Gap under probe due to CIVA graphical representation)

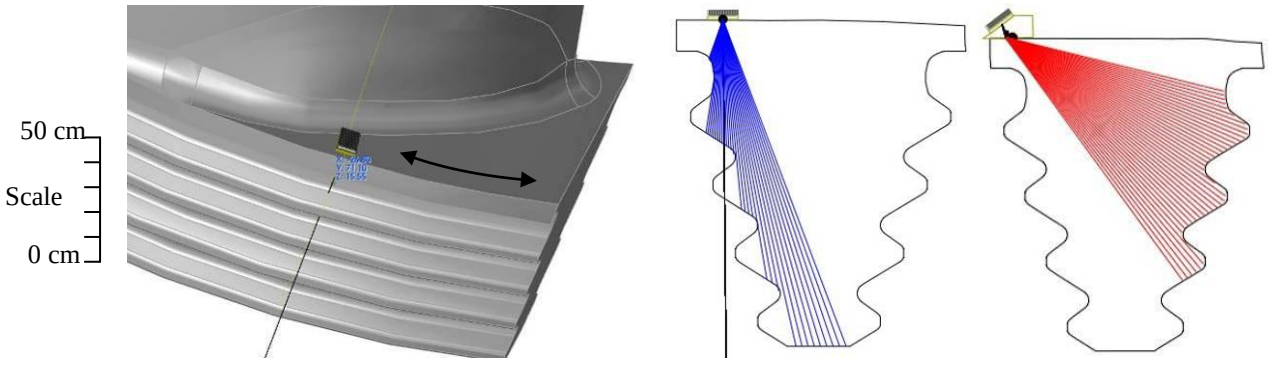

Figure 2-31 Root inspections from platforms

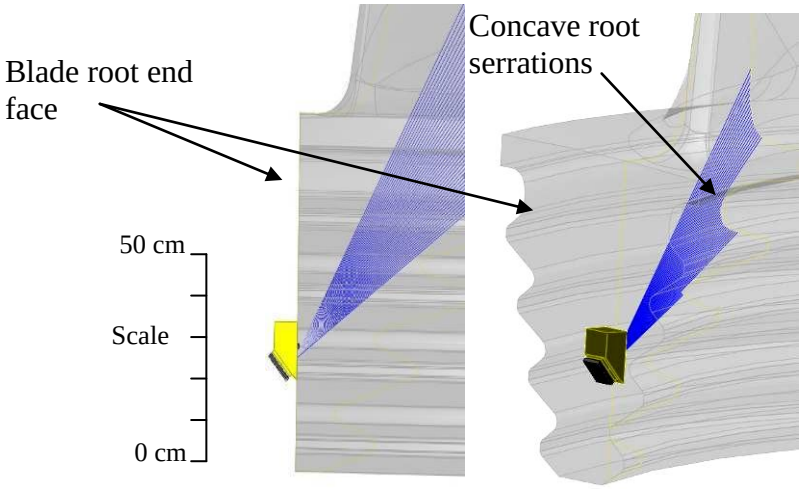

Figure 2-32 Root shear wave inspection from end face

Combinations of both phased array ultrasonic testing and manual pulse echo ultrasonic testing are commonly deployed to inspect various types of curved root designs, but the ability to achieve comprehensive coverage is limited almost entirely by the geometry of the blade and inter-blade spacing. Axial coverage of the blade roots is achieved by careful manipulation of the ultrasonic transducer along the aerofoils, platforms, and end face lands, as seen above. In order that the critical inspection areas are interrogated in the most efficient and comprehensive way, phased array ultrasonic testing (PAUT) is utilised. PAUT is constrained by the same physical limitations as conventional pulse echo ultrasonic testing (UT) but offers superior control over ultrasound transduction; having the ability to steer the ultrasonic beam over many angles of trajectory, many times per second, and enables sectorial images to be built up, offering the inspector a clear view within the volume of the material. PAUT also offers the ability to focus the ultrasonic beam at distances shorter than the natural focal depth of the transducer, by introducing time delays into the firing sequence of the individual elements. In order to take full advantage of the capabilities of PAUT it is necessary to very accurately position the transducer on the available inspection surfaces in a reliable and repeatable manner.

There are a number of difficulties in performing aerofoil scanning, as manual manipulation of the PAUT transducer is limited almost entirely by the inter-blade spacing. Skewing of the ultrasonic beam or transducer is necessary to compensate for the geometric mismatch between the aerofoil and the blade root (Figure 2-33); thereby optimising the geometric reflections and maximising sensitivity to defects in the serrations. Skewing of the beam has the effect of normalising the ultrasound trajectory to the root serrations and, although straightforward with manual manipulation of the transducer, is very challenging where access is limited. One of the major limitations of the current techniques, where in-situ inspection is required, is the ability to place transducers at the leading edge of the blade aerofoil or platform in a reliable manner.

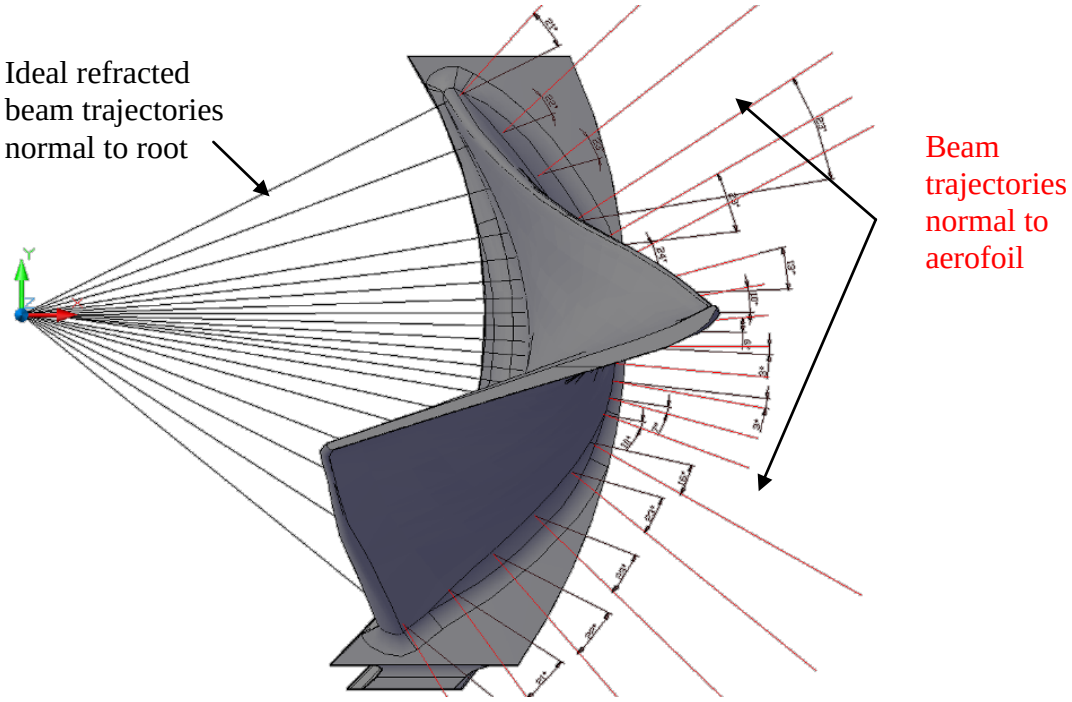

Figure 2-33 Aerofoil – blade root geometric mismatch

2.2.3.3 Inspection techniques employed outside RWE npower

Siemens, GEC Alstom, GE and Ansaldo are some of the biggest suppliers of steam turbine rotors in the world. Siemens have published papers regarding their development of

techniques for in-situ inspection of low pressure (LP) steam turbine roots[12 13 35]. A common approach was taken where production of test samples were procured with electro discharge machining (EDM) slots in critical 'at risk' areas of the first two root serrations. Siemens then targeted specific areas of the root region with single element probes (compression and 60° shear), fixed in a geometrically matched jig to facilitate accurate and repeatable positioning, see Figure 2-34.

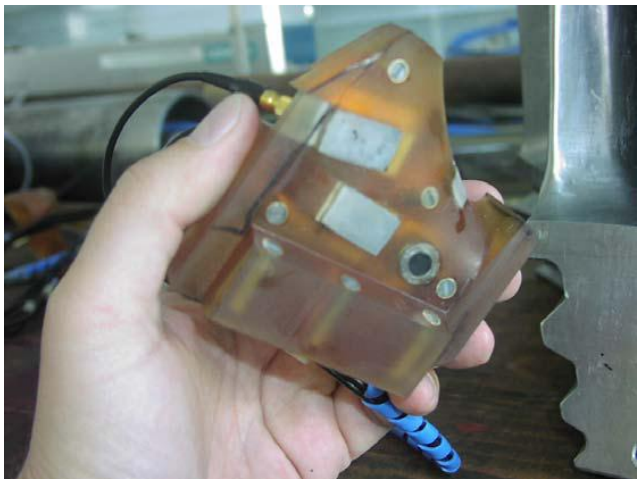

Figure 2-34 Multi probe jig fixture

It was reported by Siemens that several approach angles were required to confirm detection of each reference reflector and as such, several jigs were required to satisfy the detection of all reference reflectors. By utilising a four channel ultrasonic instrument, each jig would contain up to 4 single element probes, allowing 4 channels of data for a single interrogation. This method addressed the problem of access to in-situ rotors because the jigs are locatable, and can be pushed through the available gap and easily positioned. However this approach means that only the exact locations of the reference reflectors are targeted, so 100 % coverage is not achieved. This approach is very effective for the targeted inspection at the extremities of the blade roots, where access for manual manipulation is prohibitive. A drawback however is the inability to manipulate the ultrasonic signals, which would improve characterisation of defects based on echo dynamic responses; this is critical when

attempting to distinguish between mechanical damage and cracking. The sound trajectory, which is not normal to the target region, could lead to problems with detection of tight fatigue cracks; the technique is validated on relatively wide EDM slots designed to provide corner reflectors.

From trials carried out on nuclear LP turbines, Siemens concluded that this method of inspection was rapid, cost effective, and valid for critical areas of blade roots whilst the turbines were in-situ[35].

Developments over many years for the inspection of complex blade root designs have been published by Peter Ciorau from Ontario Power Generation (OPG) in Canada. His extensive development work has led to techniques very similar to those currently employed by RWE npower; applying phased array ultrasonic inspection to the blade roots from the aerofoils, root platforms and end faces[36 37]. Significantly, little or no consideration is made to the geometric mismatch between the blade root and aerofoil surfaces as described in section 2.2.3.2, and the scan data published in the literature shows variation of sensitivity to defects in the critical regions. Further work has been done by Peter to quantify the reliability, repeatability, and contribution made by phased array to the inspection of such complex components[38 39]. Further work is on-going through the Electrical Power Research Institute (EPRI) who, through their coordinated research with industrial partners, have been addressing the issue of blade root failure and the inspection strategies associated with such rotor designs[40].

2.2.3.4 Inspection techniques developed by third parties

Third party equipment suppliers such as Zetec, Olympus, and Phoenix have historically partnered with OEMs and end-users to develop complex manipulators and scanners to perform mechanised inspection of plant. Scanners which are clamped to the adjacent blade

are designed to place a shear wave phased array probe on the aerofoil surface looking down into the root area, see Figure 2-35.

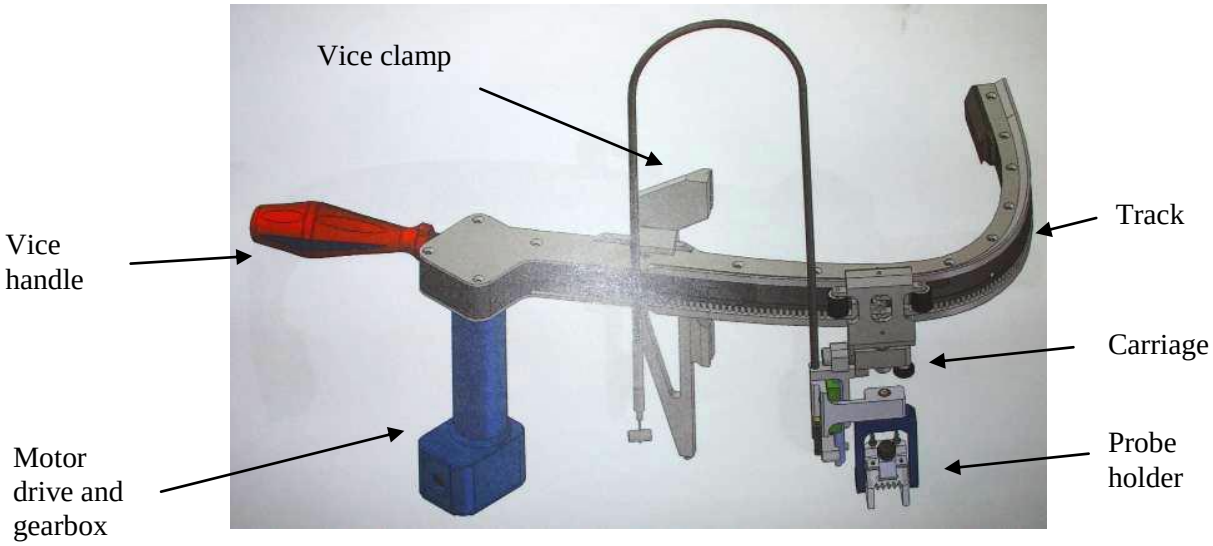

Figure 2-35 Illustration of typical scanner (courtesy of Zetec)

The coverage achieved can be similar to that achieved with manual manipulation of the probes, but takes no account of the geometric mismatch between the aerofoil and the blade root so can only be applied where the mismatch is minimal. A benefit of mechanised scanners is that more stable and repeatable results can be obtained, and that encoded 'C', and 'D' scans can be recorded for further analysis, and potentially leading to more sensitive detection. However, the use of motorised scanners requires all the added complexity of the motor drive units and ancillary equipment. Due to the curvature of the aerofoil being different to that of the root form, it would be necessary to skew the probe in order to keep the ultrasound beam normal to the root serrations and therefore potential defects. To achieve this, the automated scanner would be required to perform multiple scans with varying pre-set skews. To date scanners have only been developed to inspect blade designs where the mismatch is minimal and where detection of defects is possible without the need to skew or offset the ultrasonic beam. Another obstacle to the fully automated scanner is the presence of locking keys, designed to prevent axial movement of the blade root, which obstruct the

scan path of the probe around the aerofoil. Zetec's solution to this was to provide a lifting mechanism to raise the probe over the keyway and to break the inspection into two halves, one for each side of the keyway. The number of scans required to achieve coverage, with high sensitivity has increased from one pass, using RWE npower's technique, to many passes using the automated system.

2.2.3.5 Discussion

It has been found during the course of this review that there are many approaches taken by different companies with varying challenges and constraints being set out to the development engineers and technicians alike. The use of phased array technology is long established in this sector, but there are a number of approaches, each having advantages and disadvantages. Where access is severely limited and thereby omitting the ability to apply manual scanning, mechanised methods must be sought which can achieve the same kind of dexterity of probe manipulation as though in the hand of an operator. Furthermore it has been seen how jigs can be utilised to aid inspection of remote locations on the blade root, but are so far limited to specific targeted regions with multiple jigs being adopted to increase coverage with single element ultrasonic testing. Another significant issue with all methods outlined so far, is the quality of ultrasonic coupling; the use of Rexolite and Perspex wedges is common in ultrasonic testing to aid refraction of the ultrasound beam in the test material. In order to acquire maximum transfer of ultrasound from the wedge into the test material, coupling mediums such as water or Sonagel are used, but also require that the wedge contact face matches the component surface very closely. Where a wedge has been profiled in this way it will only match the component geometry at one position and coupling is severely disrupted where skewing of the transducer is applied. The result is that the shape of any wedge, designed to refract ultrasound into the component, must be a compromise and provide reasonable coupling properties for a range of different surface geometry.

2.2.4 Conclusions

The inspection of complex blade root geometry has taken many forms and is in itself a complex balance of financial, physical, and technological challenges, with each separate blade design requiring special consideration, with no single solution to fit all. Some of the limits set out early on by RWE (the sponsoring company) included the use of their current arsenal of ultrasonic and phased array technology, with the desire to keep inspections portable for deployment in very confined and difficult situations. Based on the research of current methods, it is the intention of the author to investigate and develop methods of ultrasonic inspection which take advantage of modern modelling and simulation techniques, and the best offered by 1D phased array technology. For the purposes of this body of work, 2D phased array was discounted based on the remit of the sponsoring company; the requirement to utilise current equipment, which was limited to 32 element phased array pulsers and 1D arrays. In order to achieve the aims of the research, it would be necessary to investigate the use of mechanical means to achieve highly sensitive coverage of blade roots, including the use of fixtures, jigs, scanners, and novel complex wedge design. These aspects will be described in detail in later chapters of this thesis.

Chapter 3. Ultrasonic testing in NDE

3.1 Introduction

This chapter explores some of the physical properties of ultrasound, and the use of ultrasonic testing in NDE. In this thesis the author will be researching the use of novel wedge design and utilisation of novel mechanical methods of improving coverage and sensitivity to defects in turbine blade roots. The main focus of the research takes advantage of phased array technology, using current equipment available in the sponsoring company. It is therefore useful to cover some of the basic physics of ultrasound and ultrasonic inspection, and attempt to describe how a wave will interact with a component, i.e. how it reflects or transmits through an interface, the amount of refraction which occurs at an interface, and the efficiency of transmission of ultrasound through the point of contact.

3.2 Basic ultrasonic theory

Ultrasound falls into a branch of physics associated with the origin, propagation and reception of sound or pressure waves travelling in media such as gas, liquid or solids. It resides in a band of frequencies above the audible (or sonic range) of approximately 20 kHz to 150 MHz[41], see Figure 3-1 below.

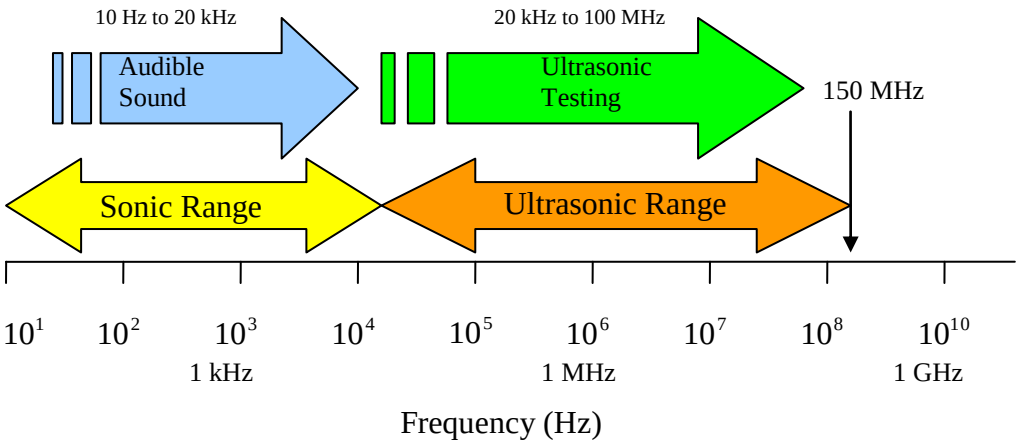

Figure 3-1 Frequency range of sound waves

Ultrasound travels in a medium as a series of pressure waves or oscillations at a velocity dictated by the mechanical properties of the medium through which it propagates, and a wavelength dictated by the frequency of the oscillations and velocity of the material. Ultrasound is produced by mechanical vibrations of the particles throughout the medium, which are analogous to a mass damper system in which displacement of the mass from its rested or mean position will oscillate about its equilibrium[42]. The displacement of the mass from the mean position, as a function of time, forms a sine wave.

3.2.1 Elastic wave propagation

The propagation of ultrasonic waves within a mass media is due to the elastic properties of the material, having the ability to sustain ultrasonic vibrations and so being commonly termed elastic waves. A wave travelling in a material does so at a velocity determined by the material properties and reflects from surfaces, refracts when travelling through interfaces, diffracts from edges and around obstacles, and is scattered by particles or rough surfaces. As sound is a stress wave however, it relies on a body in intimate contact with another body to propagate. Therefore unlike light and electromagnetic waves it cannot travel through a vacuum[43]. Sound waves propagate through a body because as a force (disturbance) is applied to one particle of the medium, it then imparts some energy to its neighbouring particle, which in turn imparts energy to its neighbour, and so on. This disturbance passes from particle to particle, therefore propagating through the medium until the energy is used and dissipates[44]. The elements of mass are elastic and deform under stress, therefore an individual wave that maintains constant phase propagates through the medium at the phase velocity (c_p) the media[45]. Alternatively, where multiple waves of similar velocity propagate through a medium, such as with wideband transmission of ultrasound, the acoustic energy propagates at an average velocity of the group, termed 'group velocity' (c_g) [45].

The velocity of sound varies from media to media dependent on a number of factors associated with that media: -

- Type of disturbance (oscillating motion), i.e. compression waves, shear waves, surface waves, and many other wave modes.
- The elastic properties of the media.
- Density of the material
- Temperature

Gasses are only capable of supporting compression (longitudinal) waves, whereas liquids can also support surface waves. Solids are capable of supporting compression, shear, surface, and many other wave modes.

3.2.2 Velocity of sound in solids

Considering all the various parameters, the phase velocity (c_p) of sound in a given media is fixed dependent on the wave mode being transmitted through it. For example the approximate phase velocity of sound in steel is 5950ms^{-1} for compression waves and 3300ms^{-1} for shear waves. The speed of sound in gasses, fluids, and solids can be expressed as acoustic velocity:

$$c_p = \sqrt{\left(\frac{\partial p}{\partial \rho}\right)}, \qquad (1)$$

where ∂p = Change in pressure (Pa or Psi)

$\partial \rho$ = Change in density (kg/m)

c_p = Phase velocity (m/s)

However, it is more common to express the velocity of sound in a given material based on that materials modulus of elasticity which can be seen in several forms. These include the 'bulk modulus', 'Young's modulus', and 'shear modulus', all of which are related to each other by 'Poisson's ratio'.[46 47 48]

Starting at the beginning and analysing a typical stress/strain curve, Figure 3-2, there is an elastic region up to the yield strength (elastic limit) where the curve is linear (conforming to Hook's Law). Within this elastic region a material under strain will return to its original shape with no lasting changes to its structure. However, strain applied above the elastic limit, will cause permanent deformation of the material thereby permanently changing its shape.

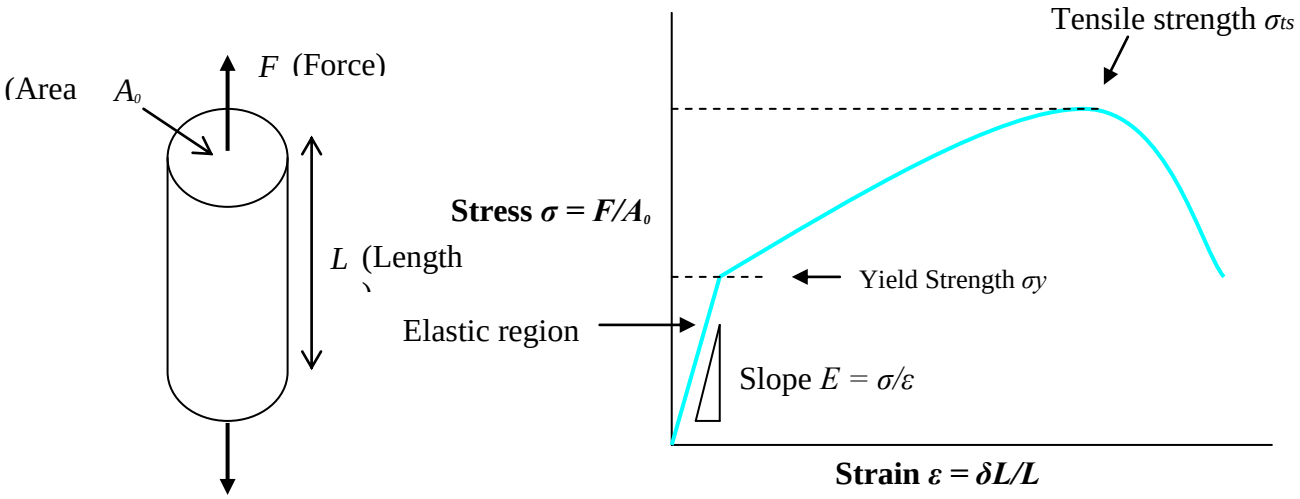

Figure 3-2 Tensile stress strain curve

Within the elastic region, an applied stress (σ) results in a proportional strain (ε) where Young's modulus (E) is the constant of proportionality.

$$\sigma = E\varepsilon \qquad (2)$$

In a similar way shear stresses (σ_s) applied in the elastic region result in proportional shear strain (γ) where Shear Modulus (G) is the constant of proportionality.

$$\sigma_s = G\gamma \qquad (3)$$

In a similar way, if pressure (p) is applied in the elastic region then a proportional volume change (Δ) results, where Bulk Modulus (K) is the constant of proportionality.

$$p = K\Delta \qquad (4)$$

The same units of stress apply to all three moduli, being that of force per unit area (N/m² or GPa) and they can all be related by another quantity known as 'Poisson's Ratio' (v)[48]. This is the ratio between lateral or transverse strain (ε_{trans}) to the axial strain (ε_{axial}) in tensile loading, where, if a material is stretched in one direction, it will tend to contract in the other two directions, Figure 3-3.

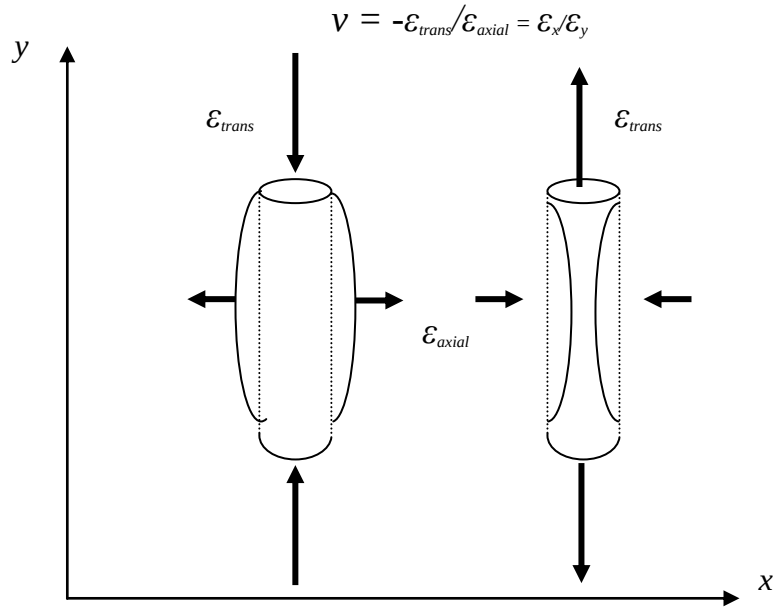

Figure 3-3 Poisson's ratio illustrated

For isotropic materials a deformation in the direction of one axis will produce a deformation of the material along the other axis in 3 dimensions. Thus it is possible to generalise 'Hooks Law' into 3 dimensions: -

$$\varepsilon_x = \frac{1}{E}\left[\sigma x - v(\sigma y + \sigma z)\right] \quad (5a)$$

$$\varepsilon_y = \frac{1}{E}\left[\sigma y - v(\sigma x + \sigma z)\right] \quad (5b)$$

$$\varepsilon_z = \frac{1}{E}\left[\sigma z - v(\sigma x + \sigma y)\right] \quad (5c)$$

Where ε_x, ε_y, and ε_z are strain in the direction of the x, y, and z axis, σ_x, σ_y, and σ_z are stress in the direction of the x, y, and z axis.

For homogeneous isotropic materials, simple relations exist between elastic constants (Young's modulus *E*, shear modulus *G*, bulk modulus *K*, and Poisson's ratio *v*) that allow calculating them all as long as two are known:

For example: -

$$E = 2G(1+v) = 3K(1-2v) \quad (6a)$$

$$G = E/2(1+v) \quad (6b)$$

$$K = E/3(1-2v) \quad (6c)$$

It is possible to generate sound waves of different velocities in solids dependent on the mode. A longitudinal wave, which produces volumetric deformation of the material, travels at a speed calculated using 'Young's modulus' (*E*) for longitudinal waves in a rod:

$$c_p = \sqrt{E/\rho} \quad (7)$$

where ρ (rho) is equal to the density of the material.

A shear wave producing shear deformation of the material travels at a velocity calculated using the 'Shear Modulus' (*G*) for shear waves in a bulk solid:

$$c_p = \sqrt{G/\rho} \quad (8)$$

In liquids, shear forces cannot be sustained due to zero stiffness to volumetric deformation, and so the velocity of sound is calculated using 'Bulk Modulus' (*K*) for longitudinal waves in a liquid:

$$c_p = \sqrt{K/\rho} \quad (9)$$

In a solid rod where the axial dimension is very small relative to the wavelength of the propagating compression wave, there are little or no lateral constraints imposed by the material of the rod. Therefore the compressions and tensions in the axial direction give rise to expansions and contractions in the plane of the cross section by the amounts set by Poisson's Ratio (*v*), Figure 3-3. Therefore 'Young's Modulus' which represents uni-axial

elastic modulus can be used to calculate the velocity of waves travelling in the rod. Where the bulk of the material is much larger in cross section than the wavelength of the sound propagating through it, there is now non-zero stiffness to volumetric deformation. In other words, the lateral strains arising from longitudinal stresses are opposed by the inertia of the bulk of the material affecting the speed at which the waves travel. This gives rise to much more complicated relationships between tensile stress and strain and depends on the relationship between Young's Modulus and Poisson's Ratio. The more appropriate elastic modulus which can be now used to calculate velocity in this case is known as 'axial modulus' or plane wave modulus (*M*). This can be shown to be given by:

$$M = K + 4G/3 \tag{10}$$

where Bulk Modulus (K) = $E/3(1-v)$ and Shear Modulus (G) = $E/2(1+v)$

By substitution it can be shown that:-

$$M = E\frac{(1-v)}{(1+v)(1-2v)} \tag{11}$$

Therefore velocity (c):-

$$c_p = \sqrt{M/\rho} \tag{12}$$

The velocity of sound in media is therefore determined by the elastic properties, density, temperature, and geometry of any particular material, and is generally independent of frequency and ultrasound intensity. Table 3-1 shows some examples of common material phase velocities.

Material	Compression Wave Velocity (ms^{-1})		Shear Wave Velocity (ms^{-1})
	Bulk	Rods	
Steel	5900	4800	3230
Aluminium	6400	5100	3100
Perspex	2700	2100	1300
Water	1500	N/A	N/A

Table 3-1 Example material velocities

3.2.3 Acoustic impedance

The relationship between stress (force) and velocity of sound is described as 'Impedance' (z). The acoustic impedance of a given material dictates how a sound wave interacts with an interface, i.e. how it reflects and transmits at an interface. Acoustic impedance is the ratio of sound pressure (p) to particle velocity (v), but is also the product of material density (ρ (rho)) and the velocity of sound for that material (c_p). The unit of acoustic impedance is the Rayl and is measured in pascal-second per meter ($Pa \cdot s \cdot m^{-1}$), or equivalently newton-second per cubic meter ($N \cdot s \cdot m^{-3}$), which in SI base units ($kg \cdot s^{-1} \cdot m^{-2}$) [49]. Acoustic impedance can be shown:-

$$Z = \rho.c \qquad (13)$$

where : ρ (rho) = density of the medium kg/m^3
c = speed of sound (the acoustic velocity) in m/s.

It is therefore possible to calculate the acoustic impedance of steel for example, knowing the acoustic velocity (c) for compression waves being approximately 5900 ms^{-1} and the density being 7800 Kg/m^3.

$$Z = \rho.c = 5900 \times 7800 = 46020000 \text{ Rayl} = 46.02 \text{ MRayl}$$

Examples for the acoustic impedance for common materials which might be encountered in non-destructive testing can be seen in Table 3-2 [49].

Acoustic impedance is important in acoustics, and more specifically to ultrasonic inspection, as it determines the reflection or transmission of ultrasound energy which is incident on a given material surface or interface between different materials. The choice of damping material and matching layer material in the construction of ultrasonic transducers is directly related to the acoustic impedance of the transducer element, component under test and said materials.

Material	Longitudinal velocity c_p(ms^{-1})	Material Density ρ (Kg.$^{m-3}$)	Acoustic Impedance Z (MRayls)
Aluminium rolled	6420	2.70	17.33
Araldite 502/956 20 phe	2540	1.39	3.52
Brass 70cu 30 Zn	4700	8.64	40.6
Concrete	3100	2.6	8.0
Copper rolled	5010	8.93	44.6
Iron	5900	7.69	46.4
Iron cast	4600	7.22	33.2
Lead	2200	11.2	24.6
Molybdenum	6300	10.0	63.1
Nickel	5600	8.84	49.5
Steel mild	5900	7.8	46.0
Steel stainless	5790	7.89	45.7
Titanium	6100	4.48	27.3
Tungsten	5200	19.4	101.0
Vanadium	6000	6.03	36.2

Table 3-2 Acoustic impedance of common materials for compression waves

3.2.4 Reflection and transmission coefficients

When ultrasonic energy is incident on a boundary between two materials, some energy is reflected back into the source material, and some is transmitted into the material across the boundary. When taking no account of losses, the incident energy at a boundary is equal to the sum of the reflected and transmitted energy. For a boundary between two non-absorbent materials, 1 and 2, the wave equations for acoustic pressure and particle velocity can be written[44]:-

$$p_i = A_1 \sin(\omega t - k_1 x) = u_i Z_1 \quad (14)$$

$$p_r = B_1 \sin(\omega t - k_1 x) = -u_i Z_1 \quad (15)$$

$$p_t = A_2 \sin(\omega t - k_2 x) = u_t Z_2 \quad (16)$$

where: p_i, p_r, p_t, are acoustic pressure (stress) for incident, reflected, and transmitted waves
u_i, u_r, u_t, are particle velocity for incident, reflected, and transmitted waves
A_1, B_1, and A_2 are the pressure amplitudes
k_1 and k_2 are the wave numbers of the respective materials ($2\pi/\lambda$)

Z_1 and Z_2 are the acoustic impedance of the respective materials
x is zero when it's direction is that of the incident beam

Two boundary conditions apply at all times:-

- The pressure (p) at both sides of a boundary should be the same at all times to preserve continuity –

$$p_t = p_i + p_r \tag{17}$$

- The particle velocities normal to the boundary should be the same at both sides so that the materials stay in contact with one another –

$$u_t = u_i + u_r \tag{18}$$

By making x = 0 at the boundaries, these equations become:-

$$A_2 = A_1 + B_1$$

and $$Z_1A_2 = Z_2(A_1 - B_1)$$

thus $$p_t / p_i = A_2/A_1 = 2Z_2 / (Z_1 - Z_2)$$

and $$p_r / p_i = B_1/A_1 = (Z_2 - Z_1) / (Z_1 + Z_2) \tag{19}$$

The ratio $r = \boldsymbol{B_1/A_1}$ defines the 'Amplitude (pressure) reflection coefficient'.

Now because the intensity of the wave is proportional to the square of the acoustic pressure (amplitude), the 'Intensity reflection coefficient' α_r can be written as :-

$$r^2$$

so:- $$\alpha_r = I_r/I_i = r^2 = B_1^2/A_1^2 = (Z_2 - Z_1)^2 / (Z_1 + Z_2)^2$$

Now the Transmission coefficient α_t can be written:-

$$\alpha_r + \alpha_t = 1$$

thus $$\alpha_t = 1 - \alpha_r = 4Z_1.Z_2 / (Z_1 - Z_2)^2 \tag{20}$$

Both α_r and α_t can be written as a percentage of the incident energy by multiplying by 100. It is also common to express the reflection or transmission coefficients in decibels (dB) to allow large changes in signal strength to be expressed. The amplitude reflection and

transmission coefficients can be converted to the dB scale by taking the log of the coefficients multiplied by 20. The intensity or power reflection and transmission coefficients are converted by taking the log of the coefficients and multiplying by ten.

$$r = -20\log(Z_2 - Z_1) / (Z_1 + Z_2) \text{ dB} \quad (21a)$$

$$\alpha_r = -10\log(Z_2 - Z_1)^2 / (Z_1 + Z_2)^2 \text{ dB} \quad (21b)$$

In order for the transmission of ultrasonic energy to be 100 % with no reflection, the impedances of each material must be equal, or matched. In ultrasonic inspection it is therefore critical that impedance matching is considered to maximise the transmission of ultrasound into and out of the components under test.

3.2.5 Modes of propagation

There are numerous ways in which ultrasonic waves propagate through a medium, known as wave modes; Table 3-3 shows many of the more common modes of propagation.

Wave Types in Solids	**Particle Vibrations**
Longitudinal	Parallel to wave direction
Transverse (Shear)	Perpendicular to wave direction
Surface - Rayleigh	Elliptical orbit - symmetrical mode
Plate Wave - Lamb	Component perpendicular to surface (extensional wave)
Plate Wave - Love	Parallel to plane layer, perpendicular to wave direction
Stoneley (Leaky Rayleigh Waves)	Wave guided along interface
Sezawa	Antisymmetric mode

Table 3-3 Common ultrasonic wave modes

Only two types of wave mode are supported in the bulk of a medium: - longitudinal and transverse waves[50]. The particle motion or mode of vibration of longitudinal waves occur in parallel to the direction of propagation, and are produced by the compression forces on the material particles. The particle motion or mode of vibration of transverse waves occur in the perpendicular direction to wave motion, and are produced by the shear forces applied to the

particles. Longitudinal (compression) and transverse (shear) waves are most commonly utilised in NDE as they are generally non dispersive, i.e. usually have constant velocities dependant on material properties and independent of frequency, and are therefore easy to identify and understand. Rayleigh waves, discovered by John William Strutt who later became the third Baron Rayleigh[51 52], are another wave mode which occurs in a medium when a compression wave is incident on an interface at the third critical angle. The Rayleigh wave combines longitudinal and shear wave modes, creating an elliptical particle motion which is restricted to the near surface of the media, with significant displacement within one wavelength of the surface. In isotropic media these waves are non-dispersive and are therefore easily utilised for the detection of surface or near surface defects in solids.

Another group of wave modes, which occur when restricted or guided by boundaries, are known as guided waves and travel through wave guides such as thin plates or pipes. There are a number of different modes of propagating plate waves including Lamb waves, Love waves, and Stoneley waves, which all propagate between boundaries. Guided waves can be utilised to inspect large areas of a structure from one position, but are complicated by the existence of at least two modes at any frequency, and are dispersive in that their velocity is dependent on frequency over a nonlinear dispersion curve[53].

As described in the previous section, the velocity of a wave travelling in a medium is dependent on the elastic properties of that medium, and in the case of bulk waves, this velocity is generally independent of frequency due to the non-dispersive nature of longitudinal and transverse wave modes. It is therefore possible to describe the wavelength of a propagating wave based on the phase velocity and frequency of the ultrasound by:-

$$\lambda = \frac{c_p}{f} \tag{22}$$

where: λ = wavelength
c_p = phase velocity
f = frequency

This equation is derived from the mathematical representation of a sinusoidal wave traveling in a medium[54], in terms of its velocity (c) (in the x direction), frequency (f) and wavelength (λ) as:

$$y(x,t) = A\cos(2\pi(\frac{x}{\lambda} - ft)) = A\cos(\frac{2\pi}{\lambda}(x - ct)) \quad (23)$$

where: y is the value of the wave at any position x and time t, and
A is the amplitude of the wave.

Also commonly expressed in terms of radians

$$y(x,t) = A\cos(kx - \omega t) = A\cos(k(x - ct)) \quad (24)$$

where: k is the wavenumber (2π times the reciprocal of wavelength)
ω is angular frequency (2π times the frequency)

Wavelength and wavenumber are related to velocity and frequency as:

$$k = \frac{2\pi}{\lambda} = \frac{2\pi f}{c} = \frac{\omega}{c} \quad (25)$$

or

$$\lambda = \frac{2\pi}{k} = \frac{2\pi c}{\omega} = \frac{c}{f} \quad (26)$$

Wavelength is therefore seen to be proportional to frequency and is the distance between the zero crossing points of the sinusoidal disturbance travelling at a given velocity, see Figure 3-4.

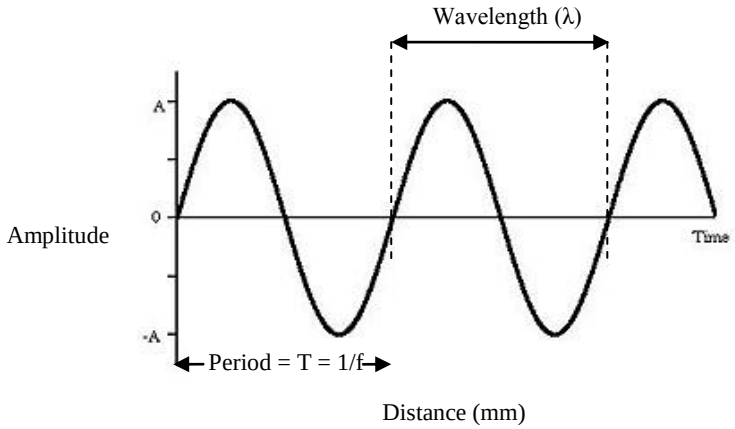

Figure 3-4 Wavelength of a sinusoidal ultrasound wave

3.2.6 Refraction of ultrasound

Refraction occurs to any wave which is incident but not normal to an interface or boundary between two substances with different acoustic velocities. This is true for electromagnetic waves such as light or x-ray, but also for acoustic waves such as ultrasound[55]. The measure of refraction between two materials can be described by the refractive index which is fixed for a given pair of materials and is given by:-

$$N = c_1/c_2 \quad (27)$$

where: N = Refractive Index
c_1 = Acoustic velocity of material 1
c_2 = Acoustic velocity of material 2

In 1621, the Dutch physicist, Willebrord Snell, is credited for deriving the relationship between the incident angle and refracted angle of light as it passes through the interface between two transparent media. Light is refracted from one medium to another and is bent according to Snell's law which states:

$$N_i \,.\, \sin(\theta_i) = N_r \,.\, \sin(\theta_r) \quad (28)$$

where:- N_i is the refractive index of the medium the light is leaving
θ_i is the incident angle between the light ray and the normal to the medium - medium interface,
N_r is the refractive index of the medium the light is entering,
θ_r is the refractive angle between the light ray and the normal to the medium to medium interface.

Thus:

$$Ni/Nr = \sin(\theta r)/ \sin(\theta i) \quad (29)$$

and

$$N_i / N_r = V_r / V_i \quad (30)$$

where: c = speed of light in a vacuum
V_i = velocity of light in medium 1 (Incident media)
V_r = velocity of light in medium 2 (Refracted media)

From Snell's law it is possible to write the relationship between an ultrasonic wave, which is incident at an oblique angle (θ_i) to an interface between two media, and the wave which is refracted into the second media at the refracted angle (θ_r) by:

$$V_r / V_i = \sin\theta r / \sin\theta i$$

and

$$V_i / \sin\theta i = V_r / \sin\theta r \qquad (31)$$

Figure 3-5 illustrates Snell's law when the velocity of sound for a longitudinal wave (V_{Li}) is represented in vector form. The incident angle (θi) of the reflected wave ($V_{Li'}$) is equal to that of the incident wave, as the ultrasonic wave is reflected back into the medium of the same velocity and no refraction occurs. However the angle (θr) of the refracted wave (V_{Lr}) has now changed due to the difference in acoustic velocity of the two media, and is set by Snell's law.

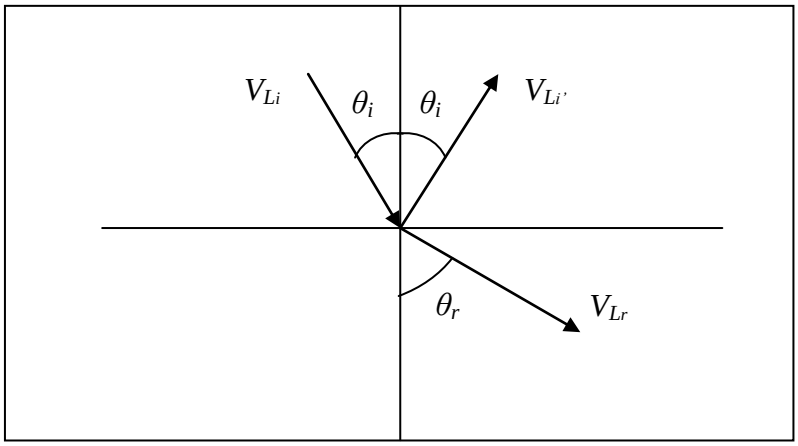

Figure 3-5 Vector representation of the refraction of a longitudinal wave on an interface between two media of different acoustic velocity

At some point when a longitudinal wave refracts from a slower material to a faster material, the angle of the refracted wave (θ_r) becomes 90º and mode converts into a surface wave known as a longitudinal creep wave. This incident angle is known as the first critical angle and can be calculated by making θ_r equal to 90º.

3.2.6.1 Mode conversion to creeping longitudinal wave

As the refracted longitudinal wave approaches the first critical angle, it mode converts to a longitudinal creeping wave. The creeping wave propagates just under the component surface and the energy is concentrated within a few millimetres and parallel to the surface. The creep wave rapidly loses energy in the form of a 33º indirect shear, or 'head', wave as it propagates[56]. The head waves further mode convert on contact with a parallel inner surface of the component into a back wall surface creep wave.

3.2.6.2 Mode conversion to shear waves

When a longitudinal wave is normal to an interface, only longitudinal waves are transmitted into the second medium. However, as soon as the longitudinal wave is incident to the interface at an oblique angle, some of the energy creates transverse excitation of the particles, inducing the propagation of transverse (shear) waves, both in reflection and transmission into the second material. This phenomenon is represented in the vector diagram in Figure 3-6, clearly showing that the shear wave (V_{Sr}) is refracted less than the longitudinal wave (V_{Lr}). This is because shear waves travel more slowly than longitudinal waves and so there is much less difference in velocity between the two media, leading to less refraction of the wave.

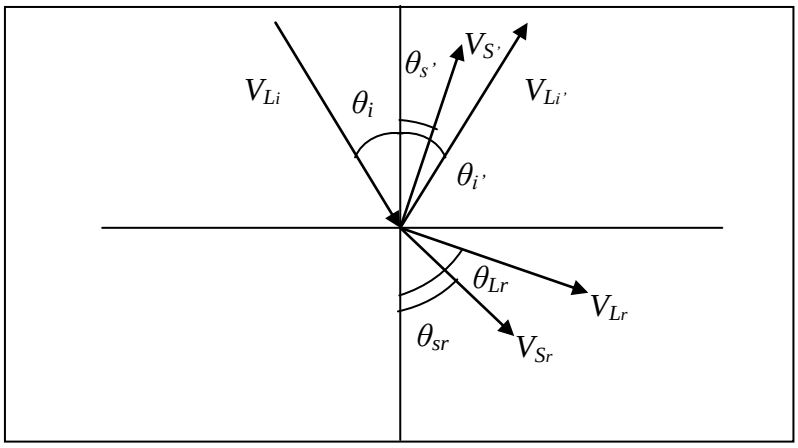

Figure 3-6 Vector representation of the refraction of a longitudinal and Shear waves on an interface between two media of different acoustic velocity

Beyond first critical angle only shear waves are refracted into the bulk medium, simplifying the issue of discerning two different wave modes travelling at different speeds. For this reason transverse waves beyond the first critical angle are among the most widely used.

3.2.6.3 Mode conversion to creeping transverse waves

At some point when the longitudinal wave refracts from a slower material to a faster material, the angle of the refracted shear wave (θ_{Sr}) becomes 90º and mode converts into a surface wave known as a transverse creep wave. This incident angle is known as the second critical angle and can be calculated by making θ_{Sr} equal to 90º .

3.2.6.4 Mode conversion to Rayleigh waves

By further increasing the incident angle θ_i beyond the second critical angle, Rayleigh waves are produced as a true surface propagating wave, combining longitudinal and transverse wave modes to produce an elliptical particle motion. The acoustic velocity of a propagating Rayleigh wave (V_{Rr}) is approximately 0.9Vs_r. Mode conversion of reflected waves

As in the cases outlined above where mode conversion occurs with refraction through interfaces, mode conversion also occurs on reflected waves, see Figure 3-7.

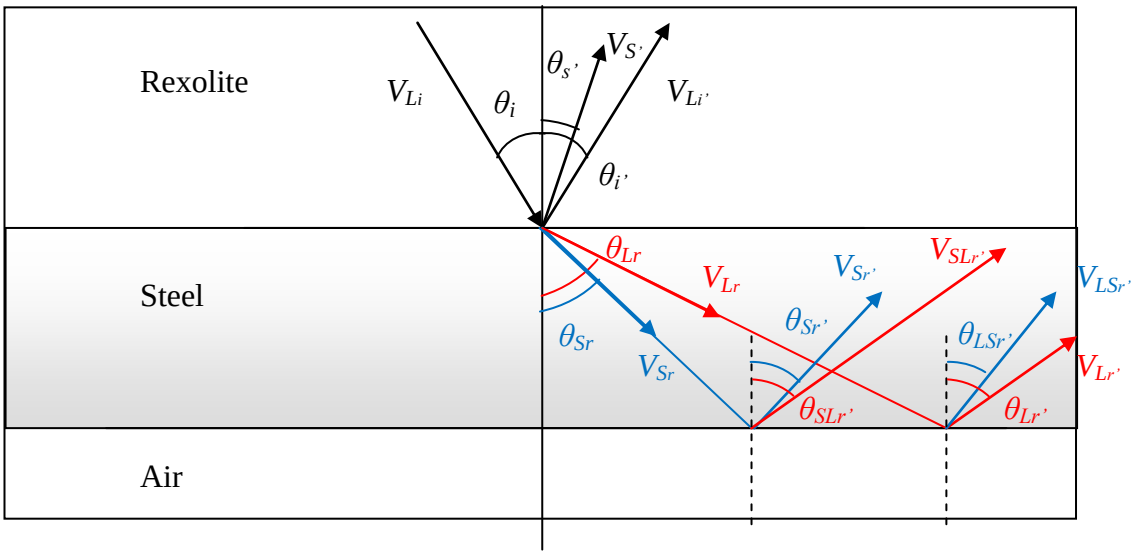

Figure 3-7 Mode conversion on reflected waves

The relationship between the incident waves, refracted waves, and reflected waves can all be similarly described by Snell's law:-

$$\frac{\sin\theta_i}{V_{Li}} = \frac{\sin\theta_{i'}}{V_{Li'}} = \frac{\sin\theta_{Lr}}{V_{Lr}} = \frac{\sin\theta_{Sr}}{V_{Sr}} = \frac{\sin\theta_{S'}}{V_{S'}} = \frac{\sin\theta_{Sr'}}{V_{Sr'}} = \frac{\sin\theta_{SLr'}}{V_{SLr'}} = \frac{\sin\theta_{Lr'}}{V_{Lr'}}$$

As it can be seen, mode conversion occurs every time a wave of any type interacts with an interface between materials of different velocities. To discern all the different wave modes propagating in the bulk of a medium, at different velocities, can be very complicated and confusing. However, a shear wave refracted above the first critical angle ensures that compression waves are no longer present in the bulk of the medium; neither does a mode change to a longitudinal wave occur on a parallel back wall reflective surface. For this reason ultrasonic inspection is most often carried out using the transverse wave mode.

3.3 Specific theory of ultrasonic testing

As early as 1928 the pioneers of ultrasonic testing were looking at ways in which to use ultrasound to detect flaws in materials, the use for which was first suggested by Soviet scientist Sergei Y Sokolov in 1928 [57] [58]**. T**he first pulse echo technique was developed by Dr Floyd Firestone in 1940 [59]. The onset of fracture mechanics as an engineering field, able to predict failure mechanisms and growth rates of known defects, led to the philosophy of 'damage tolerant' design. This new philosophy required not only the detection of defects in a structure, but the ability to accurately size and characterize defects. Advances have been made throughout the past 6 decades, but the onset of the microchip and modern computing since the 1980s has seen the biggest advancements in the use of ultrasonic testing in industry.

All ultrasonic testing is based on the properties of sound waves, propagating through media and being reflected off, or attenuated by features such as flaws and geometry in the

component under test. Short pulses of relatively high-frequency ultrasound are transmitted into the component using piezoelectric transducers. Ultrasonic waves are then detected by a receiving transducer and displayed for analysis by various types of electronic equipment. Because the velocity of sound is constant for a given homogenous material using bulk waves, it is possible to analyse signals returning to the transducer based on the amount of time it takes them to reach it. For example, thickness testing can be carried out by measuring the time it takes for the transmitted pulse to return after being reflected from the back surface of the component; conversely the velocity of a material can be measured if the actual thickness is known. There are two main ways in which ultrasound is used for the inspection of components: - Pulse echo, where reflections (echoes) from component features and flaws are characterised. Pitch-catch (through transmission), where the attenuation of an ultrasonic wave transmitted through a component is characterised.

Pulse-echo is commonly used to search for manufacturing defects such as cracks or lack-of-fusion in welds for example, whilst pitch-catch can be used to test for good quality bonding in brazed components or composites. Other more advanced techniques have been developed over many years including Time-of-Flight-Diffraction (TOFD), developed in the 1970s by the UK Atomic Energy Authority[60], and being capable of detecting diffracted waves emanating from the extremities of very tight defects, making it very accurate at measuring the through-wall depth of cracks. Phased array Ultrasonic Testing (PAUT) is another advanced ultrasonic technique, using specialised transducers with multiple elements which can be fired in sequences to electronically focus or steer the ultrasonic beam.

3.3.1 Transducers

A transducer is a device which converts a signal in one form of energy into a signal of another form of energy. An electric motor which converts electrical energy into mechanical energy, or a microphone which converts sound energy (pressure waves) into electrical

energy, are both types of transducer. In ultrasonic testing, transducers are designed to convert electrical energy into ultrasonic energy, and inversely to convert ultrasonic energy into electrical energy.

There are a number of different transducer types including piezoelectric, electromagnetic, electrostatic, magnetostrictive, laser and optical, and various specialist transducers, all with very specific properties used in different applications[44]. Piezoelectric transducers are by far the most widely used in non-destructive testing as they are reversible (transmit and receive), are cost effective, and provide good quality performance[61]. As the mechanical vibrations are created in the piezoelectric material, a coupling medium is required in contact with the component under test in order to induce ultrasound in the component. Where this is not possible or desirable due to high temperatures or hostile environments, then alternative transducers which induce vibrations directly in the component such as magnetostrictive types are deployed[62]. The piezoelectric effect is a naturally occurring characteristic in crystals such as quartz and lithium sulphate, in some semiconductors such as cadmium sulphate and zinc oxide, and also occurs in suitably prepared ceramics such as barium titanate, lead zirconate (PTZ), and lead meta-niobate[44].

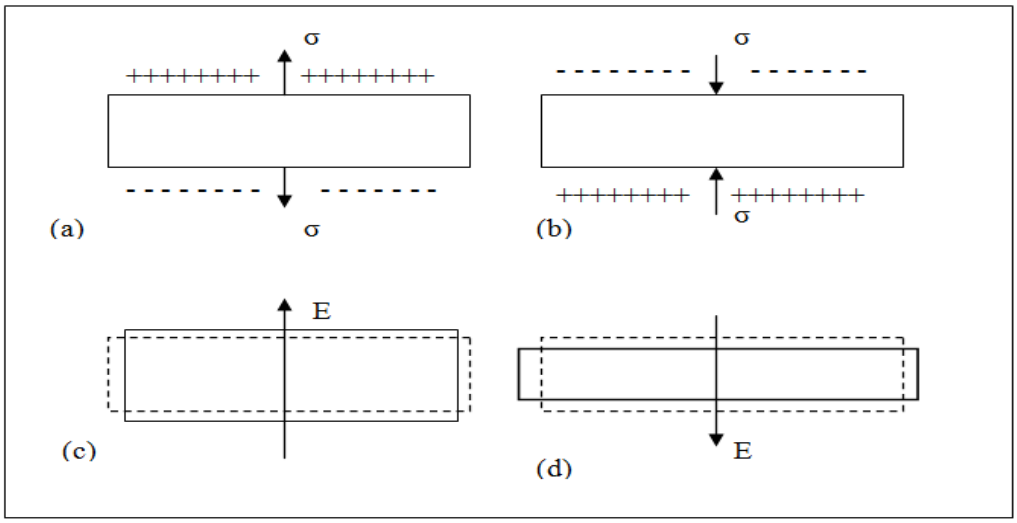

Figure 3-8 The piezoelectric effect: (a) effect of tensile stress σ; (b) effect of compressive stress σ; (c) expansion due to applied electric field F; (d) contraction due to reversal of field E; the dashed lines in (c) and (d) represent the transducer dimensions when not in operation.[44]

3.3.2 Probes

Piezoelectric ceramic transducers used in ultrasonic testing are most commonly used in assemblies known as probes; these consist of the piezoelectric ceramic element, backing material (damping), electrical connections, housing, and matching layer or wear plate[63 64], see Figure 3-9. The transducer illustrated in Figure 3-9(a) acts as both a transmitter and receiver with a common alternative, known as a twin element transducer illustrated in Figure 3-9(b), containing separate receiving and transmitting transducer elements. The delay lines and acoustic barrier prevent cross talk and interference due to side lobes in the ultrasound beam. Twin element transducers can also be designed to focus the ultrasonic beam by toeing in the two elements and providing better near surface detection and resolution.

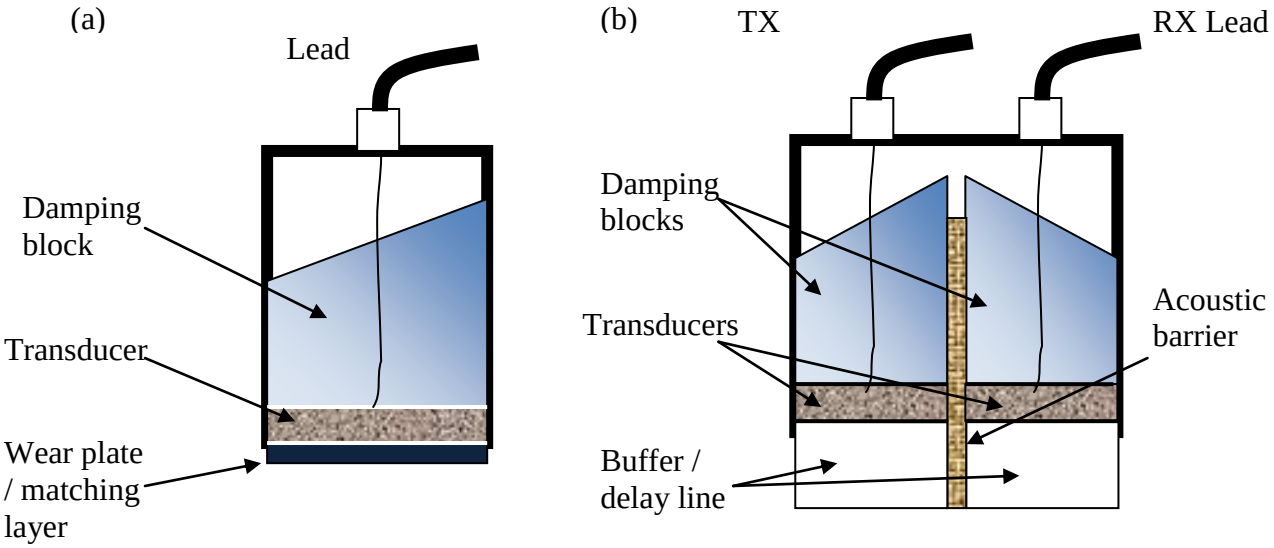

Figure 3-9 Typical ultrasonic compression wave probe assemblies: (a) single crystal compression wave probe; (b) dual or twin crystal compression wave probe.

Shear wave probes are created by use of simple compression wave transducers mounted on angled wedges above the first critical angle (section 3.2.6), made of materials such as Perspex or Rexolite, see Figure 3-10. The most common probes are manufactured and marked with shear wave angles for refraction of ultrasound in steel and adjustments must be

made for inspection of materials with differing velocities. Because the wedge is designed above the first critical angle, only shear waves are predominantly produced making interpretation of returning signals simpler.

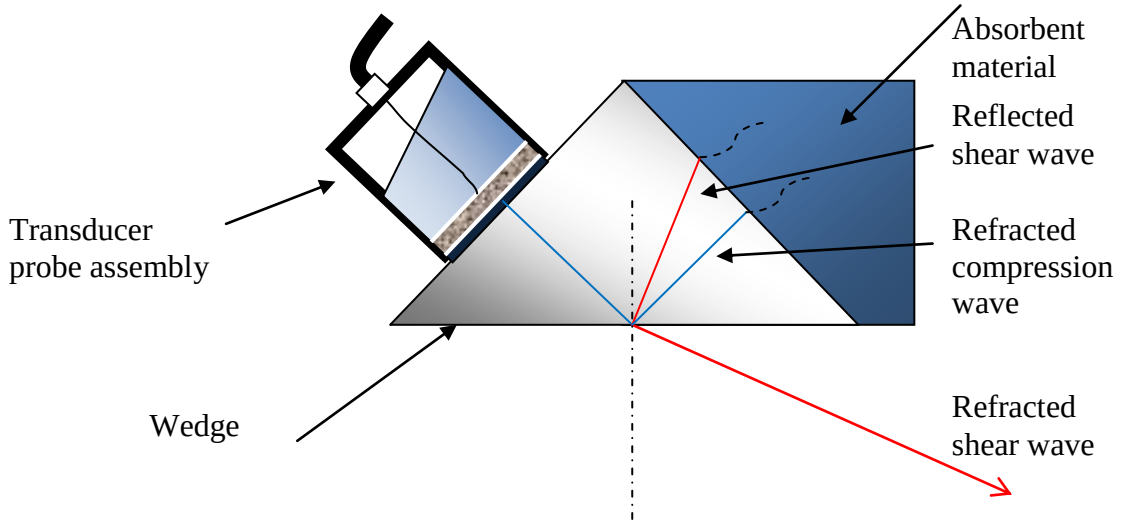

Figure 3-10 Typical shear wave probe

3.3.3 Pulse echo

Pulse echo is the most widely used ultrasonic testing method, where ultrasound is transmitted into a component and reflections (echoes) from features and flaws are detected, either by a second receiving transducer or the same transducer in receive mode. Figure 3-11 illustrates a very simple application of pulse echo ultrasonic flaw detection in a component. A single transducer is used for both transmission and reception of the ultrasound and produces a compression wave normal to the surface. Transducer (a) is being held over a defect-free region of the test piece, while transducer (b) is being held over a crack which is positioned at mid-wall of the component.

Using a calibrated A-scan display, which plots amplitude of the ultrasonic waves over time, the returning ultrasonic wave is displayed as a peak (response) on the screen, see Figure 3-12 . The multiple responses seen from the defect are due the crack being faceted,

creating reflections (echoes) of different amplitudes across its width; the shape or echo dynamic of the response is indicative that this flaw is a crack-like defect[65].

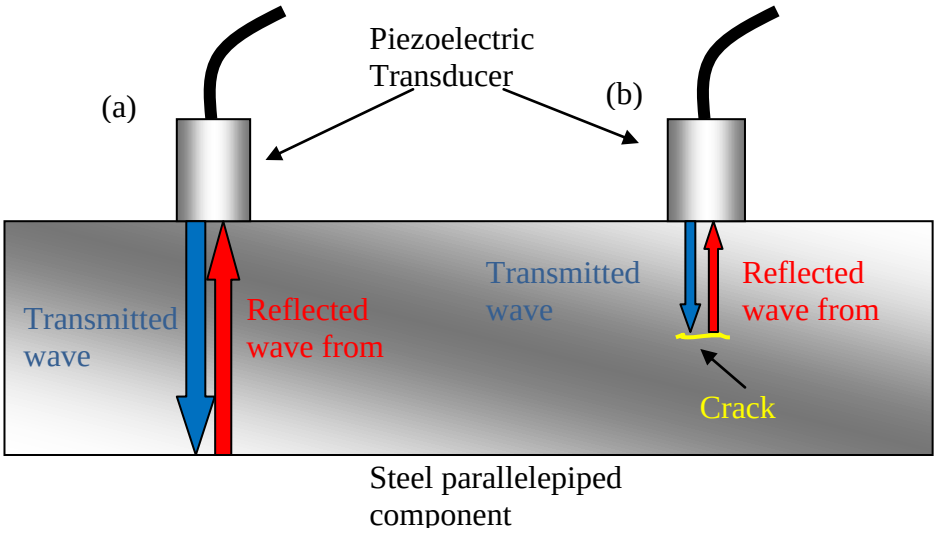

Figure 3-11 Illustration of simple ultrasonic application: (a) transducer over defect free region of component; (b) transducer over mid-wall defect

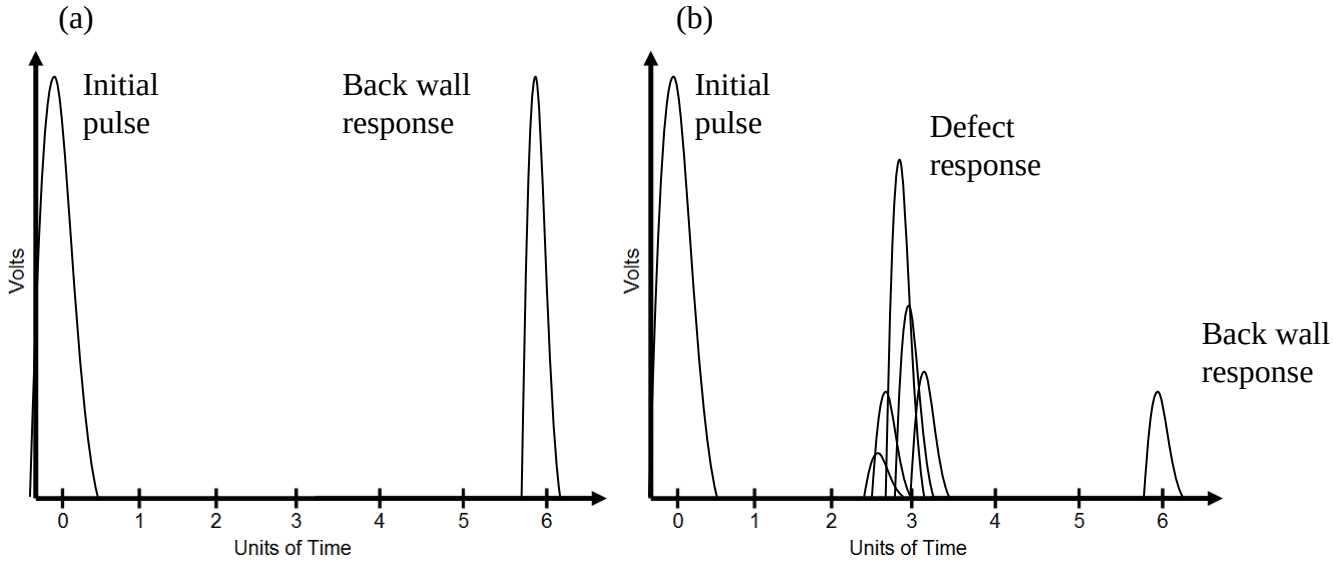

Figure 3-12 The A-Scan display: (a) Defect free region of component giving back wall reflection; (b) loss of back wall with defect response

The reflections from the defect reaching the transducer are entirely dependent on its shape and orientation to the inspection surface. Angled compression waves or more often shear waves are used in order to create ultrasound trajectories which create detectable reflections when they encounter a flaw. Figure 3-13 illustrates a component which has a vertical crack

emanating from the back surface; it is interrogated by a zero degree compression wave transducer and an angled shear wave transducer. Figure 3-14 illustrates how choice of the wrong technique for a given defect type could lead to non-detection.

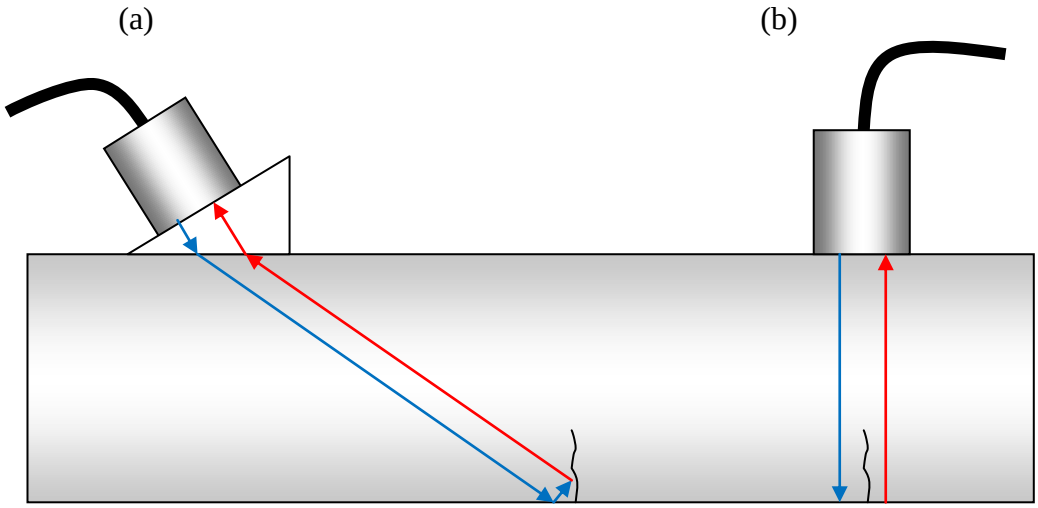

Figure 3-13 Crack detection illustration: (a) Angled compression or angled shear wave transducer; (b) 0º compression wave transducer

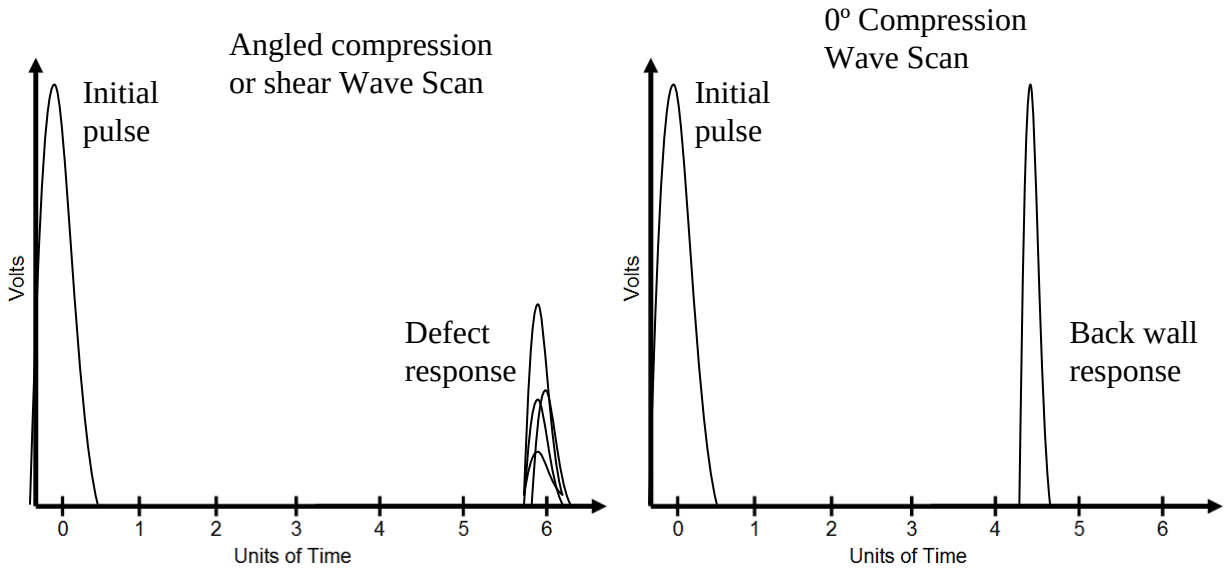

Figure 3-14 A-Scans of cracked component

3.3.4 Pitch-Catch (through transmission)

Through transmission uses a transmitting transducer and a receiving transducer which are configured so that ultrasound is transmitted through a component from one transducer

directly to the other. The amplitude of the received ultrasonic pulse is calibrated for ideal transmission, for example through a perfectly bonded (e.g. brazed) interface; a reduction in amplitude of the received pulse, when applied to the component under test, is an indication of the quality of the bonded interface, see Figure 3-15 and Figure 3-16.

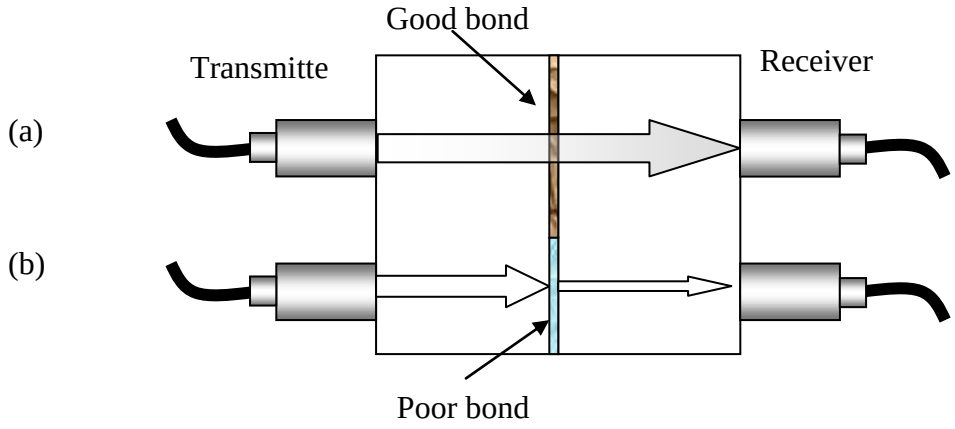

Figure 3-15 Illustration of bond testing using the through transmission technique: (a) good bond; (b) poor bond

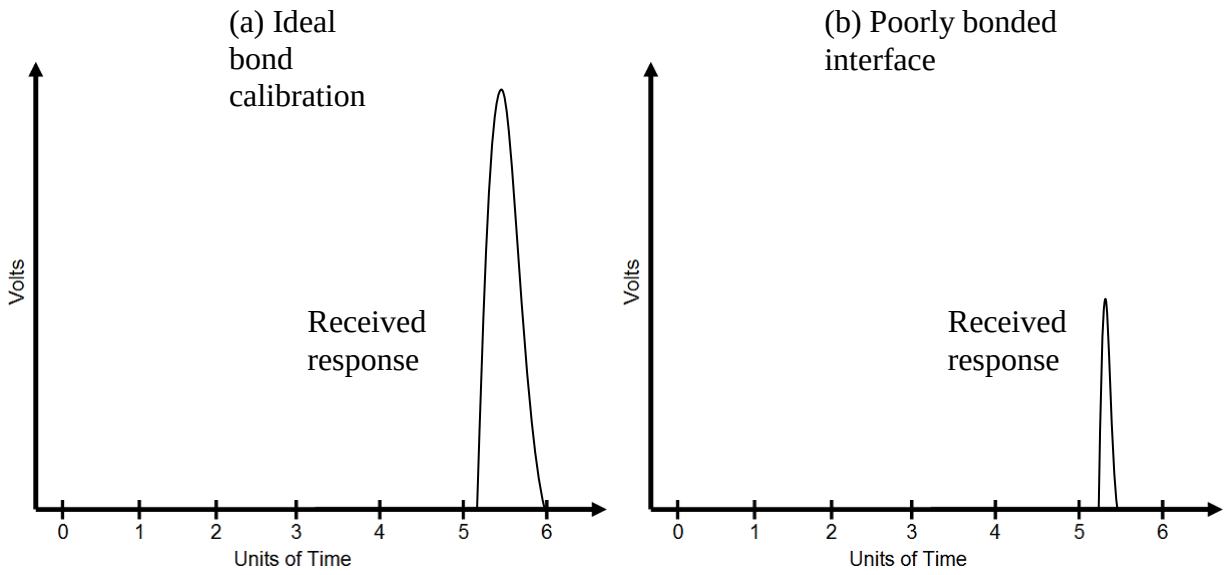

Figure 3-16 A-scan responses from through transmission bond test: (a) Perfect bond for calibration; (b) poorly bonded region of component under test.

3.4 Phased array Ultrasonic Testing (PAUT)

3.4.1 Introduction and brief history

In 1678 the Dutch physicist Christiaan Huygens (1629 – 1695) first described the principle of diffraction in his treatise called '*Traite de la Lumiere'* on the wave theory of light[66]. In it he states that "Every point of a wave front may be considered the source of secondary wavelets that spread out in all directions with a speed equal to the speed of propagation of the waves". In basic terms Huygens had theorized that a wave front was made up of a number of point sources creating a series of wavelets which combine constructively or destructively together to form a propagating wave front (Figure 3-17). When incident on a boundary between two different media the resulting reflection and refraction can be described using this principle, where the resulting wave front is the tangent through all the individual circular wavelets acting as point sources of sound or light (Figure 3-18). If the second medium has a velocity of sound that differs from the first medium then the speed of the wavelets changes and the resulting tangent wave front changes direction (refraction)[67].

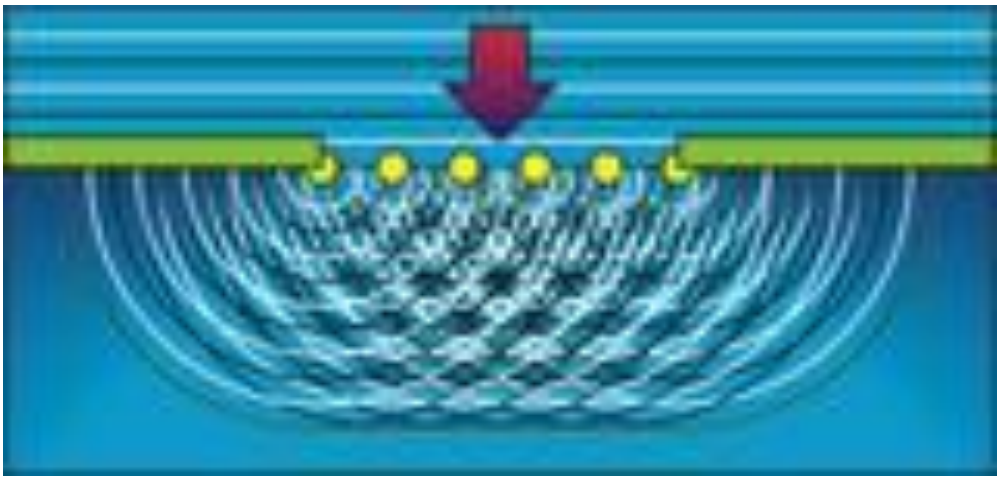

Figure 3-17 Illustration of Huygens' Principle[68]

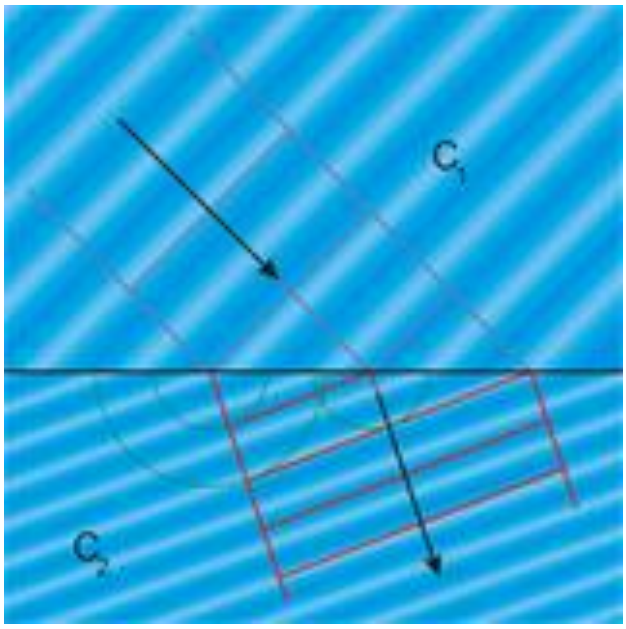

Figure 3-18 Illustration of Huygens' principle of refraction[68]

In the early 19th century (between 1801 and 1805) Thomas Young conducted his famous 'Double Slit' experiment which seemed to prove that light was indeed a wave based on Huygens' Principle. This experiment revitalized the interest in Huygens' principle and had a profound impact on 19th century physics[68 69]. In 1861 Scottish physicist and mathematician James Clerk Maxwell published a four-part paper, "On Physical Lines of Force", which provided a solid theoretical basis on which to prove the principles of wave propagation, first theorized by Huygens. He created a set of partial differential equations (Maxwell's Equations) which, along with Lorentz force law, form the basis for modern electrodynamics, optics, and electric circuits. Also Ampere's law and Faraday's law later predict that every point in an electromagnetic wave acts as a source of the continuing wave, which is perfectly in line with Huygens' analysis[68]. Huygens' principle is commonly used in modern modelling techniques for the analysis of wave propagation and forms the basic principle used in phased array ultrasonic testing (PAUT). [71 72]

Phased arrays see their roots in the medical field where, since the middle of the twentieth century, ultrasonography was used for the detection of foetal activity or brain and abdominal

diagnosis. It was in the late 1940's when Dr Douglass Howry pioneered mechanical scanners which guided pulse-echo ultrasonics to produce two dimensional B-mode images of body tissue[73]. By 1951 Howry, with the help of engineers William Roderic Bliss and Gerald J Posakony, had produced the 'immersion tank ultrasonic system', the first two dimensional B-mode linear compound scanner[74]. Their work culminated in the production of the Somascope in 1954, the details of which were published in 'Life magazine' in 1954[75]. Further work was carried out with the support of the U.S. public health service to fabricate compound contact scanners which removed the need for immersion testing.

The concept of multi element linear electronic arrays, which could remove the need to use complex scanners to produce B-mode scans, were first described by Werner Buschmann in 1964 for an ophthalmologic application; it consisted of ten transducers mounted in an arc shape designed to fit over the eyes[76]. Further advances to this concept were made in 1971 by Nicolaas Bom from the Netherlands who produced a 20 element probe capable of producing 20 scan lines at 3MHz and sweeping 150 frames per second[77]. The first commercial system called the 'Multiscan System' aimed at cardiac investigation was launched in 1972. Around the same time Rokuro Uchida at Aloka, Japan, independently researched array technology and published papers in 1971 illustrating a 200 element transducer which was electronically driven to produce a 20 element linear scan configuration to produce two dimensional images with a depth of field of 20cm[78]. The first prototype was not made commercially available but an updated version was launched in 1976. In that same year Toshiba corporation also launched their first commercial real time linear array, the SSL-53H for abdominal applications[79]. Friederich (Fritz) Thurstone, Olaf Von Ramm and H Melton Junior at the Duke University published important work on the electronic focussing of annular arrays between 1971 and 1974[80]. Albert Macovski[81] at the Stanford University filed patent in 1974 for a circular array generating dynamically focussed beams whilst George Kossoff[82] and William Beaver[83] filed patents in 1973 and 1975

respectively on linear array systems incorporating electronic delays for focussing and steering of ultrasound. The advances throughout the next decade in electronic engineering across the United States and Japan saw a boom in commercial equipment for medical ultrasonography including ADR, Hitachi, Toshiba and Aloka.

Phased array for use in industrial applications opened up a whole host of different challenges when compared to medical ultrasonography. The diversity of materials used in industrial applications offered different challenges when it came to material properties acoustic velocity, impedance matching and grain structure. The first industrial applications for phased array ultrasonic inspection were reported in the early 1980s where the advantages offered by phased arrays suited the power generation industry, particularly the nuclear power industry[84] . Advances in both electronic and computer technology saw the introduction of the first portable phased array system in the mid-1990s and are manufactured and supplied by all the main vendors of ultrasonic equipment throughout the world. PAUT is now accepted across industry as primary NDT technology and the applications are well reported in the literature[85 86]. The advantages of the phased array over traditional single element ultrasonic inspection has been iterated many times in the literature with applications for the inspection of complex components such as turbine blades, complex weldments and forgings[87 88].

Advances in computing and refinement in the manufacture of transducer technology has seen the biggest changes to phased arrays over recent years. Linear arrays are still by far the most common configuration but two dimensional arrays have been developed which allow for the steering and focussing of the ultrasonic beam in both the active and passive plane. By segmenting the elements in both the active and passive plane of the transducer, the delays can be phased such that steering of the beam is produced in both dimensions. Due to the increase in complexity and number of elements these arrays require specialised equipment to drive them but have led to developments in new techniques such as full matrix capture

(FMC), and the total focussing method (TFM). FMC is a technique where each individual element of a matrix probe is fired whilst data is collected on every other individual element. This is repeated for every element of the array so that a data set is collected for every combination of element firings. Post processing of this data set allows any focal law to be reproduced and reconstruction of any emission beam can be achieved[89]. TFM uses the same concept as FMC but using post processing algorithms reconstructs delay laws to focus at every point throughout the whole volume of the component under test. Both methods have been developed to aid in the inspection and characterisation of defects in anisotropic materials such as single crystal turbine blades[90].

3.4.2 Phased array operation

PAUT uses special transducers made up of multiple piezoelectric, piezo-ceramic, or piezo-composite elements which can be likened to the individual point sources producing circular wavelets in Huygens' principle. By phasing the excitation of these individual elements, or delaying the time at which elements are fired relative to each other, the resulting tangential wave front can be controlled in terms of its direction and focal distance. This principle allows for the resulting phased array beam to be steered or focused (Figure 3-19).

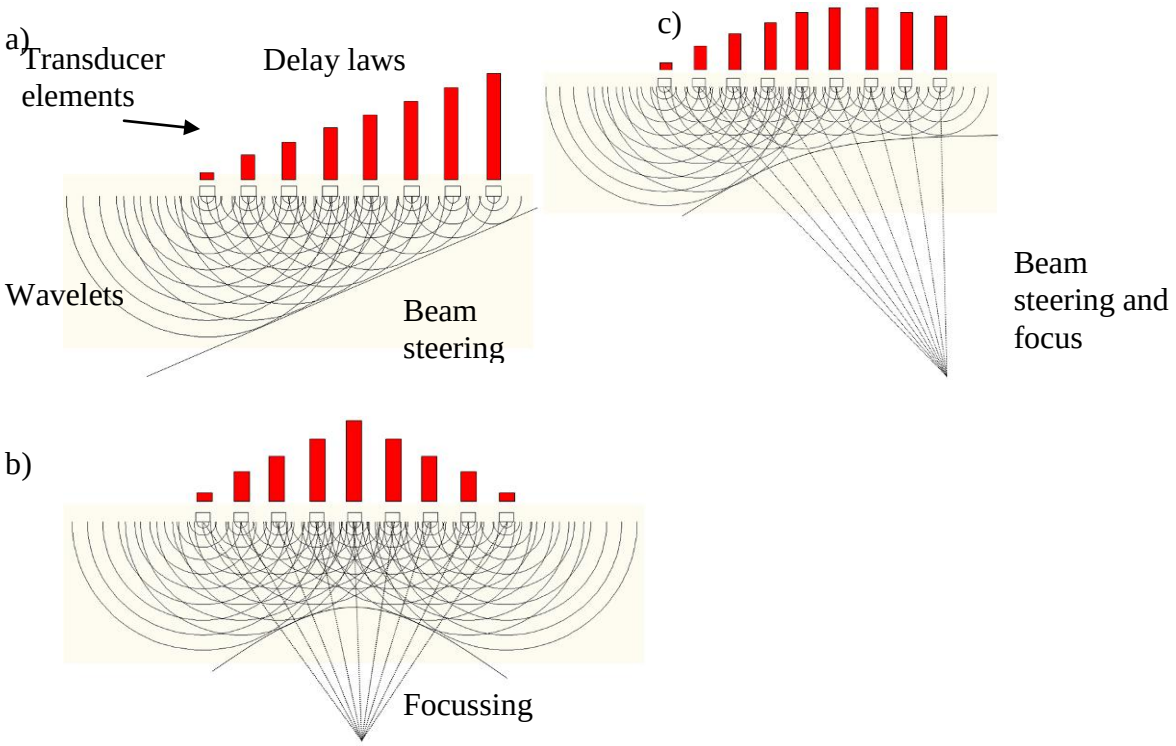

Figure 3-19 Phased array beam steering and focusing:– a) Beam steering created when element excitation is delayed incrementally from element 1 to element n, b) Beam focusing created when element excitation is delayed incrementally from the outer elements 1 and n to the middle element n/2, c) Beam steering with focus created when element excitation combines the delays for both steering and focusing

3.4.3 Phased array transducers

There are a number of transducer configurations, each with specific characteristics and applications. These include the most common which is the 1D linear array, but also 1D Annular, 2D Matrix, 2D Annular, and Circular arrays[91], see Figure 3-20.

1. 1D Linear array
2. 1D Annular array
3. 2D Matrix array
4. 2D Annular array
5. Circular array

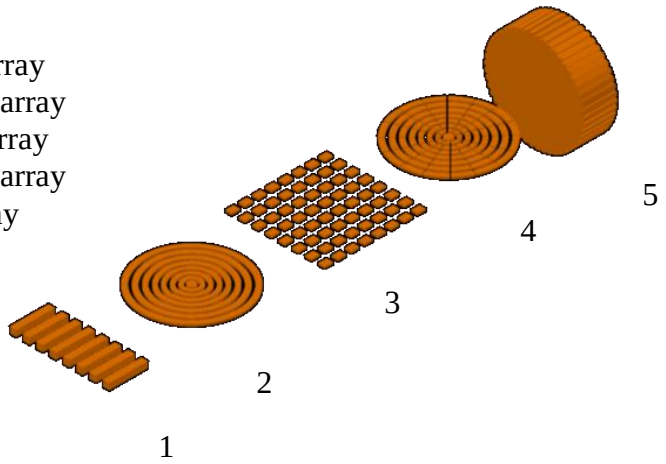

Figure 3-20 Phased array transducer configurations

3.4.3.1 1D Linear array

These Arrays are constructed with multiple juxtaposed elements aligned along a single axis and allow for beam steering, focusing, and scanning in one dimension.

3.4.3.2 1D Annular array

Constructed of concentric circular elements, each having equal surface area and therefore consecutively thicker toward the centre[91], allowing the beam to be focussed at different depths along a single perpendicular axis.

3.4.3.3 2D Matrix and Annular arrays

These consist of either square chequer board or sectored rings of elements divided up in two dimensions and allow for beam steering, focusing, and scanning in three dimensions.

3.4.3.4 Circular arrays

These arrays can consist of multiple juxtaposed elements arranged around the outer or inner surface of a cylinder (as in Figure 3-20 - 5), or in a daisy type configuration arranged around the axis of symmetry. These are used to create beam steering and focusing for tube inspection.

The solutions developed by the author which are discussed in this thesis were developed around the utilisation of 1D linear arrays, and so will form the basis of discussion throughout the remainder of this chapter.

3.4.4 Transducer design constraints

Phased array transducers and ultrasonic beam formation are constrained by the same physical limitations as conventional single element ultrasonic testing, but there are many parameters which need to be considered in the design of an effective transducer. Elements size and pitch have significant effect on performance, as do frequency, number of elements,

and aperture[92]. Figure 3-21 illustrates the dimensional parameters which have influence over performance of linear phased array transducers.

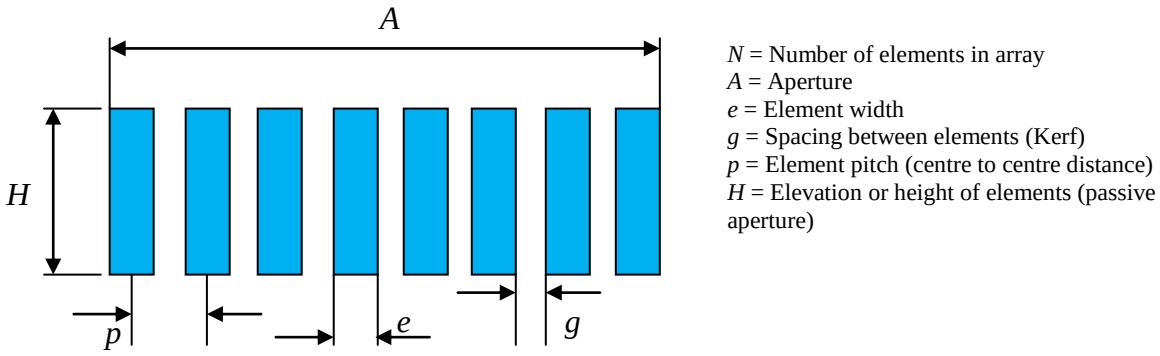

Figure 3-21 Phased array transducer dimensional parameters[93]

The choice of transducer is dependent on the requirements of a given inspection and limitations in the hardware equipment available. The main considerations include the amount of beam steering, beam path to inspection zone, and size of defect sought, which are all influenced by the probe frequency, elementary pitch, and aperture.

3.4.4.1 Active aperture and near field

The total active aperture of the transducer is the total length from the start of the first element to the end of the last element, and can be described by the following equations[93]:-

$$A = (n \times e) + (g \times (n\text{-}1)) \quad (32)$$

or

$$A = (p \times n) - g \quad (33)$$

where A = active aperture
n = number of elements
e = element width
g = gap between adjacent elements
p = element pitch.

In most cases probes are specified and engraved with the number of elements, frequency, and element pitch, and because the element spacing is an order of magnitude smaller than the element pitch, it can be ignored and the aperture approximated by:-

$$A \approx p \times n \quad (34)$$

The active aperture is important as it has a direct influence on the focal capabilities of the transducer. All ultrasonic transducers form a beam of ultrasound which, from the source of emission to just before a region known as the far field, is subject to variations in intensity due to diffraction effects of the constructive and destructive interference of the multiple waves originating from the transducer surface[94 95]. At the limit of the near field the beam forms a natural convergence to a point of natural focus beyond which the beam forms a uniform wave and tends to diverge in the far field, see Figure 3-22. The same effect is apparent with a phased array probe when all elements are fired simultaneously (as a single element); in the far field, beyond the natural focus of the transducer, phasing of the elements has no effect on the beam, so focussing of the beam is only effective within the near field[96].

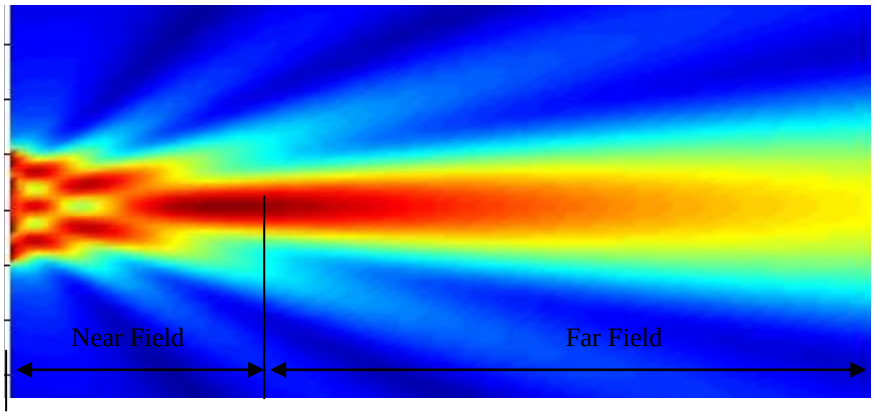

Figure 3-22 Intensity field of a 4 MHz, 10 mm diameter transducer

The size of the near field is dependent on the probe frequency, material velocity, and probe aperture, and can be calculated in single element transducers by:

$$N = k(A^2 - \lambda^2)/4\lambda \qquad (35)$$

where: N = Near field (Fresnel zone)
k = Near field width to length correction factor.
A = Aperture (Diameter for round transducers)
λ = Wavelength = velocity of sound divided by frequency (v/f)

The correction factor (k) relates to the ratio between the active and passive apertures in rectangular transducers, and for width to length ratios ≤ 0.5 then k approximates to 1.

Also for probes with $A/\lambda > 10$, the near field distance can be approximated by:-

$$N \approx A^2/4\lambda \qquad (36)$$

It can be seen that an increase in aperture or increase in frequency (reducing λ) would lead to increased near field and so improved focal range of the resulting transducer. Considering that the near field is the limit of focus for a phased array transducer then this parameter has a significant bearing transducer design.

3.4.4.2 Effective aperture and near field

When calculating the near field the active aperture of both conventional single element transducers and phased array transducers can only be considered for a 0° compression wave beam where the full aperture is seen if looking back up the beam toward the transducer. However, when an angled beam is created within a component, the aperture which is actually apparent, when looking back toward the transducer along the refracted beam path, is smaller and is known as the effective aperture, see Figure 3-23.

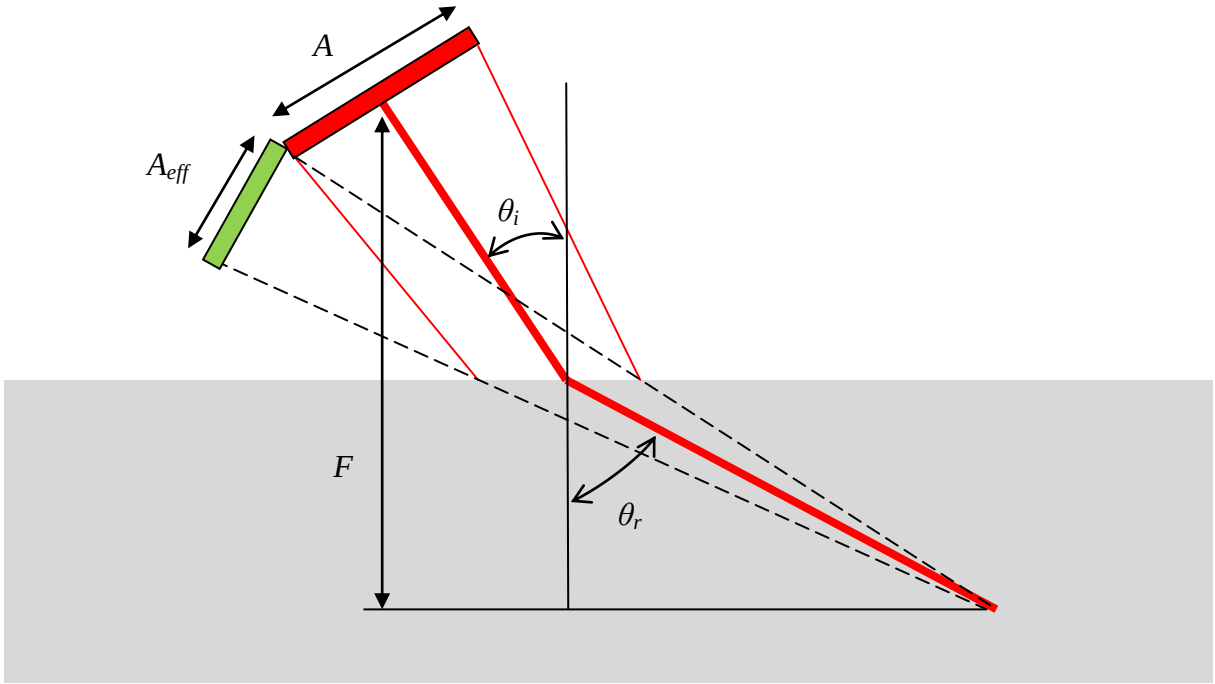

Figure 3-23 Illustration of effective aperture (A_{eff})

The effective aperture can be calculated by:-

$$A_{eff} = A \times \cos\theta_r / \cos\theta_i \qquad (37)$$

where: A_{eff} = Effective aperture
A = Active aperture
θ_i = Incident angle
θ_r = Refracted angle

Hence, when considering the near field of a phased array transducer, and therefore the focal range, it is necessary to consider the maximum refracted angle required and calculate the near field by substituting A in the near field equation with A_{eff}. Where the transducer is mounted on a Rexolite wedge some of the near field is contained within the wedge material and so the effective near field in the test piece will be shorter as shown by:-

$$N = \frac{k \times A_{eff}^{\ 2}}{4\lambda} - \frac{BP_i \times v_i}{v_r} \qquad (38)$$

Where: N = Near field (Fresnel zone)
k = Near field width to length correction factor.
A_{eff} = Effective aperture
λ = Wavelength = velocity of sound divided by frequency (v/f)
BP_i = Beam path length in wedge
v_i = Wedge velocity
v_r = test piece velocity

The right hand side subtraction in the equation ($BP_i \times v_i/v_r$) is the proportion of the near field contained within the wedge and corrected by the ratio of velocities in the two materials. When considering probe selection the effective aperture has a significant bearing on focal range and leads to larger apertures being required to achieve large near fields at higher steering angles.

3.4.4.3 Element size

Element size and frequency have a direct effect on beam divergence and therefore limit the maximum steering angle (θ_{st}) of the phased array beam; the relationship between them can be approximated by the equation[93]:-

$$\theta_{st} = \sin^{-1}(0.514\lambda/e) \quad (39)$$

It can be seen that as element width (e) decreases or wavelength increases, the ability to steer the ultrasonic beam increases. If each element was considered to be a point source from which circular wavelets emanate, the amplitude of the wavelet around the full 180 degrees in the half space would be constant. Therefore the ultrasonic beam would have no drop off in intensity when measured at any angle relative to the centre of the beam normal to the surface, having a beam spread of 90 degrees in both directions. However, in practice phased array transducer elements have finite width (e) and therefore produce wavelets which are relatively plane and higher in intensity towards the centre of the element whilst curving with lesser intensity towards the edges of the element. The resultant beam exhibits reduced divergence when measured as a 6 dB reduction in intensity relative to the centre of the beam. As wavelength (λ) increases, the element size becomes smaller in relative terms and therefore also results in increased beam divergence. Figure 3-24 shows the effect on beam steering when the number of elements remains constant but the element width changes for a 5 MHz transducer refracting compression waves in steel.

$$V_{steel} = 5900 \text{ ms}^{-1} \text{ therefore} \quad \lambda = 5.9\times10^{6}/5\times10^{6} = 1.18 \text{ mm}$$

Hence when $e = 0.7$ mm: $\theta_{st} = \sin^{-1}(0.514\times1.18/0.7) = 60°$

$e = 1$ mm: $\theta_{st} = \sin^{-1}(0.514\times1.18/1) = 37°$

$e = 2$ mm: $\theta_{st} = \sin^{-1}(0.514\times1.18/2) = 17°$

It is noted that an element size of less than $\lambda \times 0.514$ produces angles beyond 90°. A decrease in element width (e) leads to an increase in divergence and therefore smaller elements are desirable for achieving high steering angles, leading to either larger kerf (g), or more elements to compensate for the reducing aperture size[97].

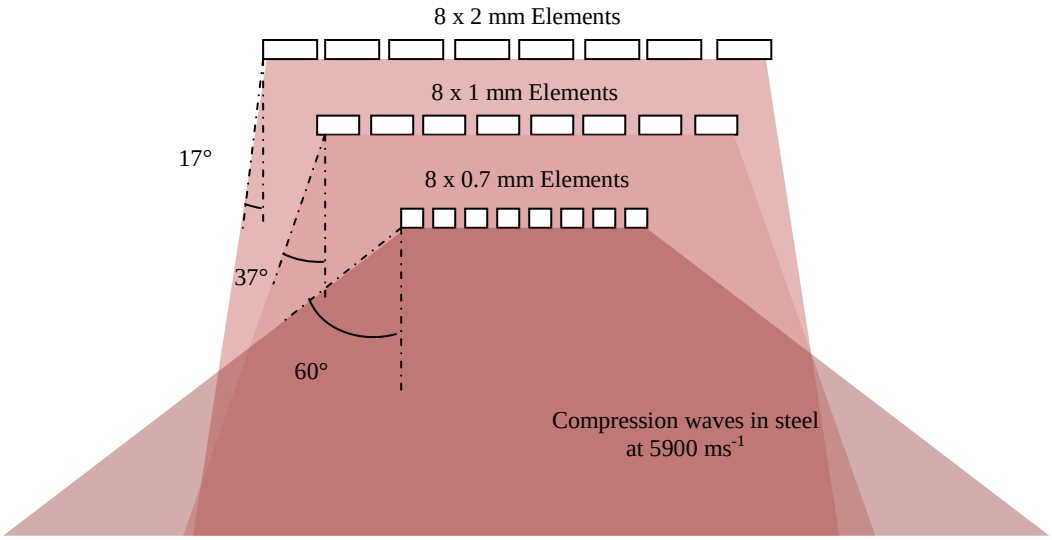

Figure 3-24 Illustration of the effect of element size on beam steering capability[93]

Frequency has a similar effect on beam divergence and if the element size is kept constant at 1 mm, it is seen that for the same compression wave in steel:-

When $f = 5$ MHz $\theta_{st} = \sin^{-1}(0.514 \times 1.18/1) = 37°$

$f = 7.5$ MHz $\theta_{st} = \sin^{-1}(0.514 \times 0.79/1) = 23°$

$f = 10$ MHz $\theta_{st} = \sin^{-1}(0.514 \times 0.59/1) = 17°$

In this case an increase in frequency has the effect of reducing the beam divergence and therefore reducing the ability to steer the beam. To compensate for frequency, the element size could be reduced further requiring larger kerf (g) or more elements to increase apertures.

Steering of the beam is aided by use of angled wedges but the range of angles through which the ultrasonic beam can be steered is still limited by the divergence achievable for a given element width (e).

3.4.4.4 Element pitch and grating lobes

Element pitch is determined by the width of the elements (e) and the kerf (g) and has dramatic effect on the size and angle of grating lobes. As discussed in the previous sections,

it is important that elements are small to facilitate high beam divergence at higher frequencies and produce the steering capabilities in a phased array transducer. This leads to the requirement for higher numbers of elements and therefore more pulser channels in the equipment, or reduction in aperture size and compromised focal range. Grating lobes are generated due to the periodic symmetry of the transducer; the constructive and destructive interference which creates the primary lobe (electronically driven beam) can also interact constructively at other angles and produce grating lobes[98] . In certain instances these grating lobes can be higher in intensity than the primary lobe and when interacting with the component under test can cause significant spurious echoes.

Grating lobes are however predictable and periodic in both amplitude and angle relative to the electronically driven lobe (main beam). The angle and position of the grating lobes can be calculated by:-

$$\sin\theta_k = k \times \lambda / (p - \sin\theta) \qquad (40)$$

where θ = refracted angle of the main beam
θ_k = refracted angle of the grating lobe
k = integers ±1, ±2, ±3, ±4..... ±n
p = inter-element pitch (p) of the linear transducer
λ = wavelength in the medium under consideration

The amplitude of the grating lobes is significantly affected by the driven angle and the elementary pitch; it can be seen when analysing the equation that:-

- If $p < \lambda/2$, no grating lobe is generated regardless of driven angle.
- If $p > \lambda$, at least one grating lobe generated regardless of driven angle
- If $\lambda/2 < p < \lambda$ grating lobes appear progressively according to the angle of the main beam.

The maximum pitch to avoid grating lobes is given by the formula:

$$p < \lambda / (1 + \sin\theta)$$

Beam simulations were carried out using Huygens principle in Matlab, representing a 10 MHz compression wave being electronically driven at 45° with fixed aperture of 9 mm, but varying element count to change the elementary pitch. Table 3-4 shows the parameters used for each simulation.

Element Pitch	λ/2	λ/1.8	λ/1.6	λ/1.3	λ	1.87λ
Element Pitch (mm)	0.30	0.33	0.38	0.45	0.60	1.13
Element Count	30	27	24	20	15	8
Aperture	9.00	9.00	9.00	9.00	9.00	9.00
Element Spacing	0.001	0.001	0.001	0.001	0.001	0.001
Element Size	0.30	0.33	0.37	0.45	0.60	1.12

Table 3-4 Parameters used in Huygens' Matlab simulations

Considering the beam simulations shown in Figure 3-25 it can be seen in the first plot that when the elementary pitch is equal to $\lambda/2$ the main lobe is generated as desired with no sign of grating lobes. However in the second plot where the elementary pitch has increased to $\lambda/1.8$ the main lobe is generated as before with the addition of a grating lobe of comparable amplitude being emitted behind the transducer. As the elementary pitch is increased through subsequent simulations, the plots show that the grating lobe becomes increasingly larger in amplitude and is refracted at steeper angles into the component. Ultimately when the simulation was carried out with the elementary pitch set to 2λ, shown in the final plot, a second grating lobe is generated and the primary lobe is essentially gone.

In practice standard probes which can be purchased off the shelf from Imasonic or G.E. have common element counts of 16, 20, 32, 64, 128 etc and typical elementary pitches of:-

f = 10 MHz, p = 0.25 mm - 0.31 mm

f = 7.5 MHz, p = 0.5 mm - 0.6 mm

f = 5 MHz, p = 0.6 - 1 mm

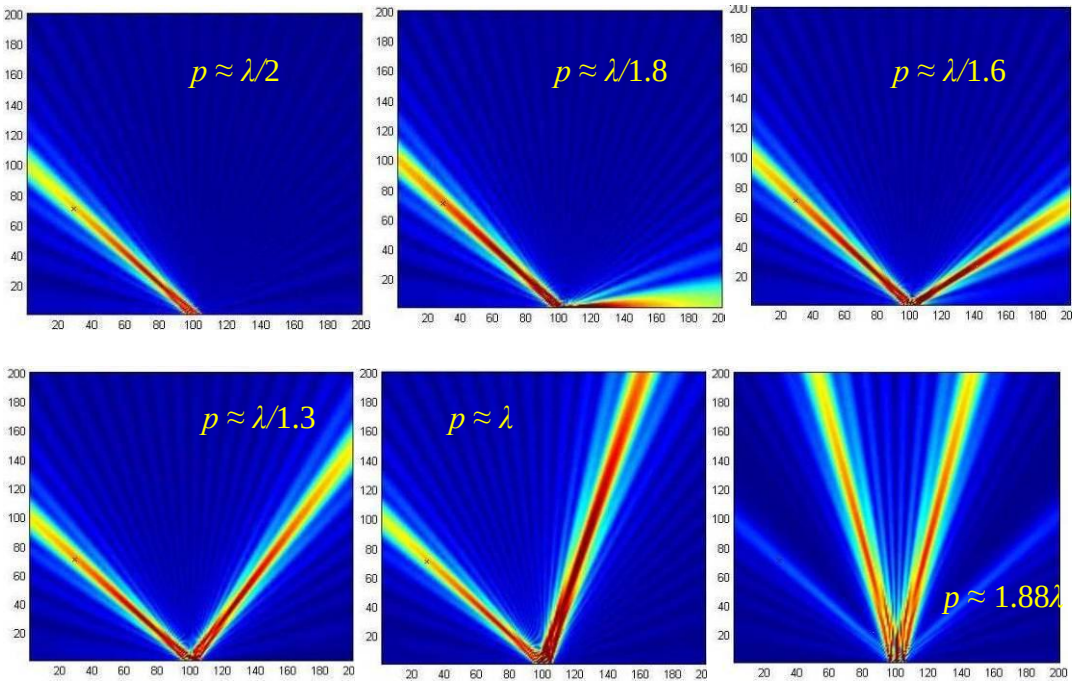

Figure 3-25 Simulations of a 45° beam from a 9 mm aperture at 10 MHz, using Matlab

3.4.5 Phased array transducers summary

All the transducer parameters discussed in this section are used in designing the optimum probe for a given inspection, and are ultimately a compromise. Large aperture size gives large near field to improve focal capability, offset against the requirement to reduce element size to improve beam divergence and reduce grating lobes. The number of pulser channels available in the test equipment, the space available for contact with the component, the depth of inspection zone, and defect size will all influence the choice of transducer.

3.4.6 Delay laws and phased array configurations

Delay laws, or focal laws, simply describe the time delays and amplitude for each individual element of a transducer, which together form the function to create a particular beam shape, direction or focus. Conveniently, modern phased array inspection tools calculate these laws based on the transducer parameters, material velocity, frequency, and the desired scan type, but can be manually calculated. Firstly an element is chosen to have

zero delay (centre element) and the delay of the other elements calculated relative to that. If the law was designed to create a focus at a given depth and angle then the relative laws can be calculated as seen in Figure 3-26.

Using simple maths the delays can be calculated for each individual element relative to the others to create focussing and beam steering.

There are a number of different configurations when using phased arrays which allow for high productivity and advanced imaging of the components under test.

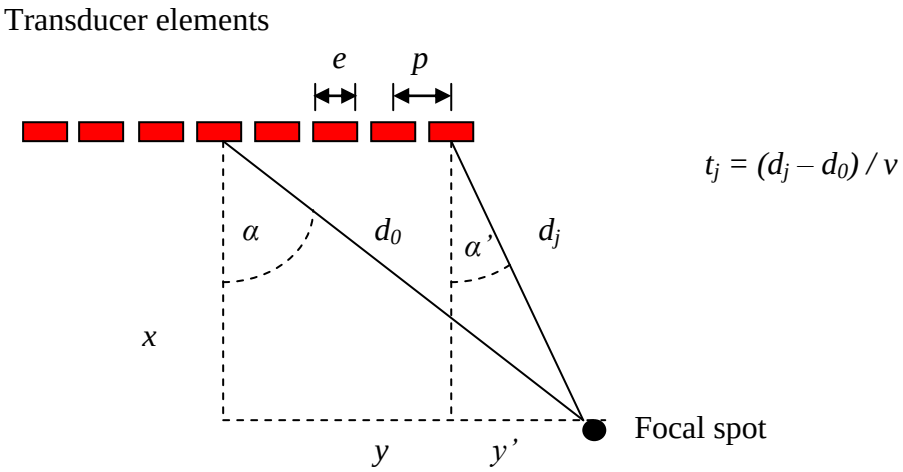

Figure 3-26 Calculating delay laws within the near field[93]

The values for d_0 and d_j can be calculated:

$$d_0 = x / \cos\alpha$$

$$d_j = x / \cos\alpha'$$

3.4.6.1 Sectorial (Azimuthal) scanning

The ability to phase the elements and produce ultrasonic beams of different refraction angles allows a component to be interrogated through many refraction angles almost instantaneously, giving a large field of coverage from a single position (Figure 3-27). If delay laws were produced to scan angles between 35° and 70°, in 1° increments then an A-scan image representing each angle would be recorded. By representing the amplitude of

each A-scan response in a colour map and stacking them sequentially, an image of the covered region can be created. The image is corrected for volume so that each scan is imaged at its true orientation angle and a sectorial or azimuthal scan image is created. Figure 3-28 shows a volume corrected sector scan with the original component overlaid to show how responses from geometry are imaged. Within the phased array inspection equipment, individual A-scan images can be displayed to aid defect characterisation, plus on screen measuring gates are available to aid defect sizing.

It is also possible to scan the phased array probe with the aid of encoding devices, to feedback relative position, and collect sectorial scans at fixed intervals to build up D-scan or C-scan images. The three types of scan form a full 3 dimensional image of the component under test and are commonly used for inspection of large components such as welds[99].

In addition to producing multiple angled beams in a single sectorial scan it is possible to focus those beams (within the near field) in various ways. The most common focussing schemes can be seen in Figure 3-29, and include true depth focussing where the focus of all laws are set to a particular through wall depth, projection focus where all the laws are focussed along a projected line, half path focussing where the focal distance is fixed at a given beam path $(x^2+z^2)^{0.5}$, and focal plane focussing where all laws are focussed along a linear plane ($z = ax+b$). The choice of focussing method is based almost entirely on the requirement of the inspection and the types of defect sought.

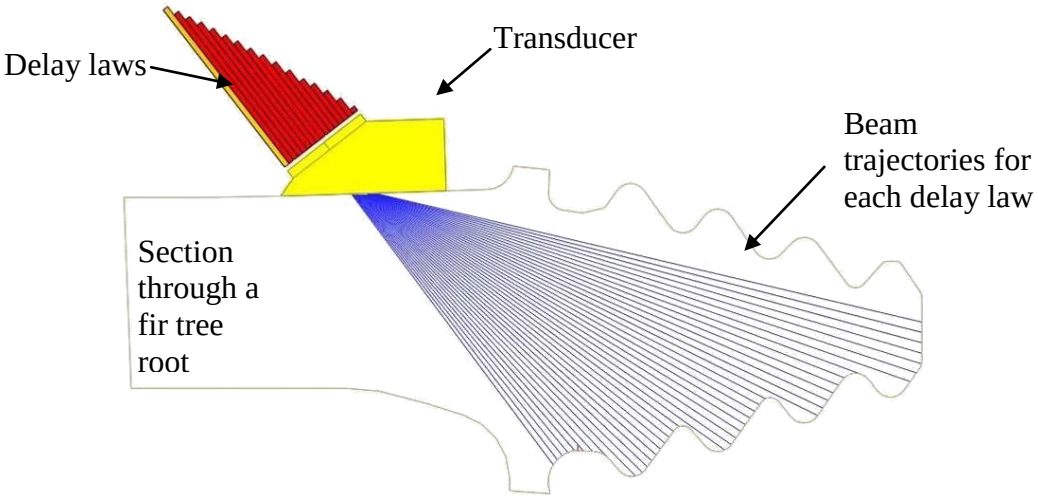

Figure 3-27 Ray tracing representation of 35° to 75° azimuthal scan

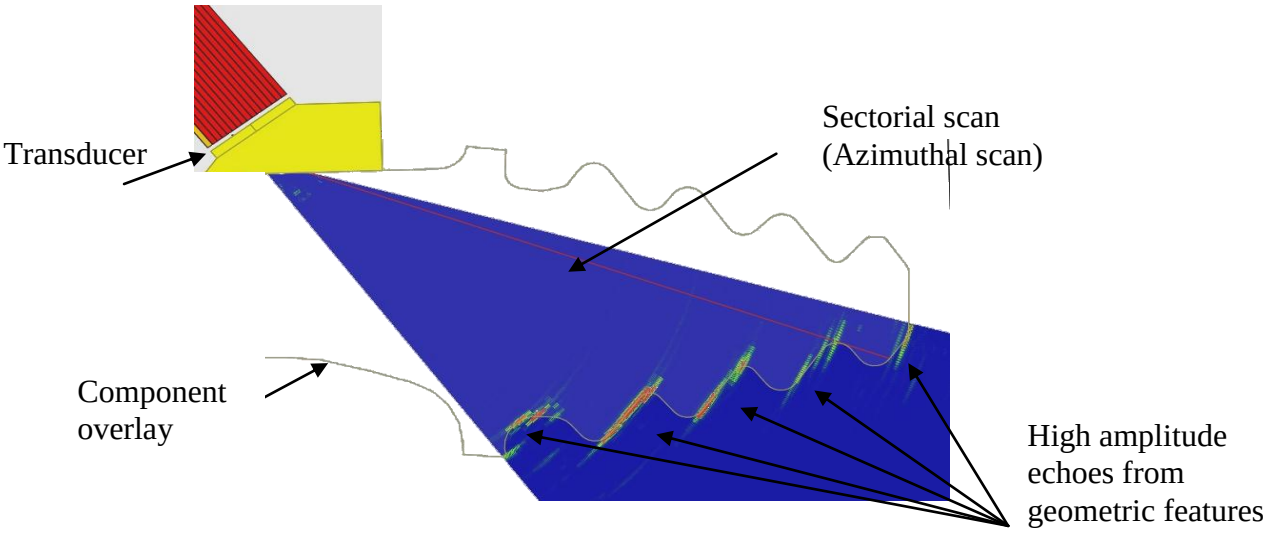

Figure 3-28 Imaging with azimuthal sector scans

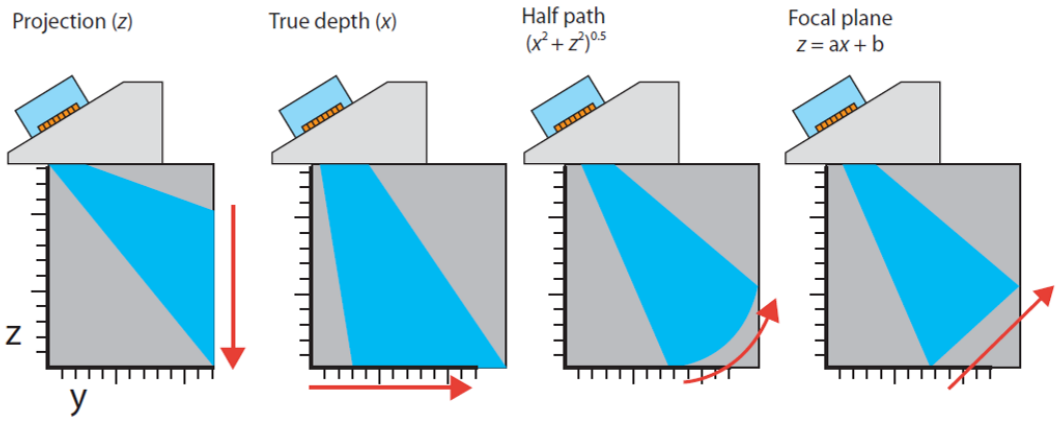

Figure 3-29 Focussing methods for linear phased array probes[100]

3.4.6.2 Electronic linear scanning

Another common mode of operation is the use of electronic scanning which, rather than phasing the delay laws to produce multiple angles, produces fixed beam angles which are electronically scanned along the probe aperture. An electronic scan utilises a block of adjacent elements (active aperture) to form a delay law at some angle and focal depth which is multiplexed along the full aperture of the probe. For example, a 64 element probe could be configured with an 8 element active aperture to form a 0° compression wave focused at 20 mm through wall; the active aperture is incrementally scanned through all 64 elements using elements 1 to 8, 2 to 9, 3 to10, 4 to 11, through 57 to 64, see Figure 3-30. The method records the A-scan for each firing which is colour mapped for amplitude and sequentially stacked to form a sectorial scan image. This method allows large regions under the probe to be electronically scanned to form a B-scan image without the need to raster the probe. Typical applications include rapid corrosion mapping, and fixed angle beam weld inspection.

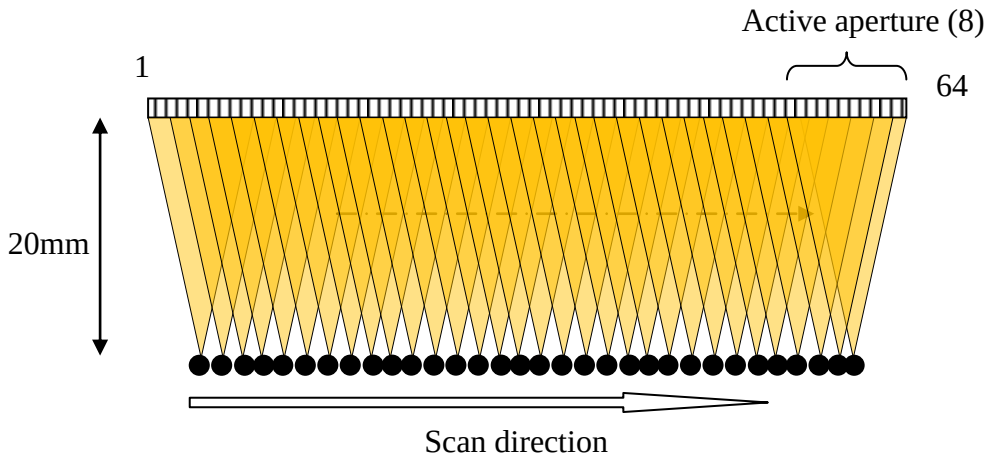

Figure 3-30 Electronic linear scanning

3.5 Ultrasonic refraction using wedges

Ultrasonic wedges are used for a variety of applications and primarily provide the appropriate incident angle at a component surface to refract ultrasound at the desired angle within the component. Wedges used with conventional ultrasonic testing facilitate the production of angled compression waves, and angled shear waves, determined by the refractive index of the wedge material and component material using Snell's law of refraction (3.2.6). Wedges can also be shaped to produce focussing at predetermined depths or shaped to match the surfaces of the component under test. Wedges are used for phased array ultrasonic testing in much the same way and limit the amount of steering done by phasing the elements. For instance, an azimuthal scan generating angles between 35° and 75° would benefit from a wedge with a natural refracted angle of 55°, thereby limiting the electronic steering to ±20°. Discussed in section 3.4.4, which describes transducer design constraints, element size directly affects the maximum steering angles achievable with a phased array transducer, so choosing the correct wedge can offset some of the compromises on other design parameters. Phased array probes can be purchased with integral wedges, with a predetermined natural refraction angle in steel, but are more commonly supplied separately and coupled to a variety of wedges depending on application.

3.5.1 Phased array wedge parameters

In order to accurately generate delay laws to achieve the desired refraction angles in the component using a wedge, the varying sound paths in the wedge must be considered to offset the delay laws. Figure 3-31 shows the typical parameters which are required to calculate the correct beam paths within the wedge, and establish index points.

ω = wedge angle
H_i = Height of middle of first element
H_w = wedge height (back)
P = Ultrasound half path (in wedge)
α_i = Incident angle
β_R = Refracted angle
E_h = Height of middle of probe
p = Elementary pitch
n = Number of elements
I_i = Index point from back of wedge
v_i = Velocity of wedge material
v_r = Velocity of component

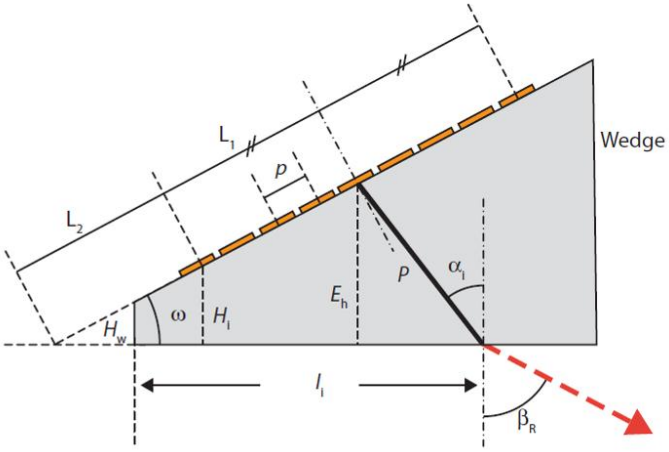

Figure 3-31 Parameters required to calculate wedge delay[100]

Calculations can be made as follows:

Incident angle for a given refracted angle (Snell's law):-

$$\alpha_i = \sin^{-1}\left(\frac{v_i}{v_r} \times \sin\beta_R\right) \quad (41)$$

Height of the middle of the probe:-

$$E_h = (L_1 + L_2)\sin\omega \quad \text{where} \quad L_2 = H_i/\sin\omega, \quad L_1 = p(n-1)/2$$

hence $$E_h = H_i + (p(n\text{-}1)/2\sin\omega) \quad (42)$$

Ultrasound path in wedge:-

$$P = E_h/\cos\alpha_i \quad (43)$$

Wedge delay:-

$$D_{wedge} = 2P/v_i \quad (44)$$

Index point from back of wedge (refracted angle dependent):-

$$I_i = (L_1 + L_2)\cos\omega - H_w\tan\omega + P\sin\alpha_i \quad (45)$$

It can be shown that the index point (I_i) changes depending on the incident angle being generated by the probe, and is described as index point migration. Modern phased array equipment and law calculating software make law creation simple as they do all the calculations automatically with as little as the values for: - H_i, v_i and ω.

3.5.2 Types of beam deflection

There are a number of ways in which a phased array probe might be configured on a wedge, leading to different beam deflection trajectories.

Parallel deflection is the most common and involves the probe being mounted on a wedge as illustrated in

Figure 3-32, where the angle of the wedge contributes to the active steering direction of the transducer, i.e. the passive aperture of the probe is parallel to the front of the wedge.

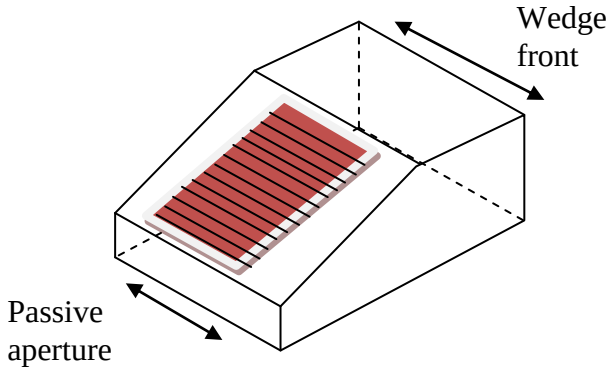

Figure 3-32 Parallel deflection wedge configuration

Lateral deflection involves the probe being mounted so that the active aperture is perpendicular to the front of the wedge, where the wedge angle determines a fixed angle refracted beam in the component in the passive elevation of the probe. Electronic beam steering done by the probe acts along the width or lateral axis of the wedge, see Figure 3-33.

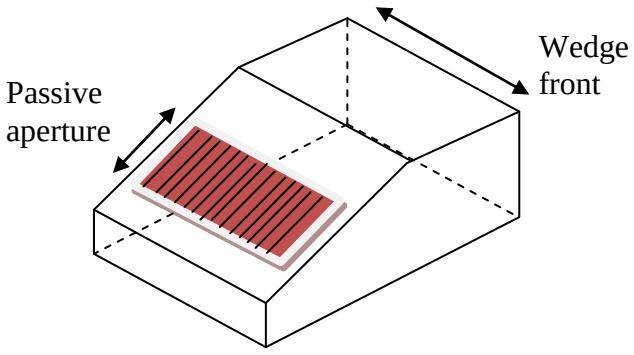

Figure 3-33 Lateral deflection wedge configuration

Skew deflection or roof angled deflection involves mounting the probe in the conventional parallel configuration with the passive aperture of the probe parallel to the front of the wedge. However, the surface of the wedge on which the probe is mounted is tilted around the tilt axis to produce a roof angle and therefore skewed deflection into the component, see Figure 3-34.

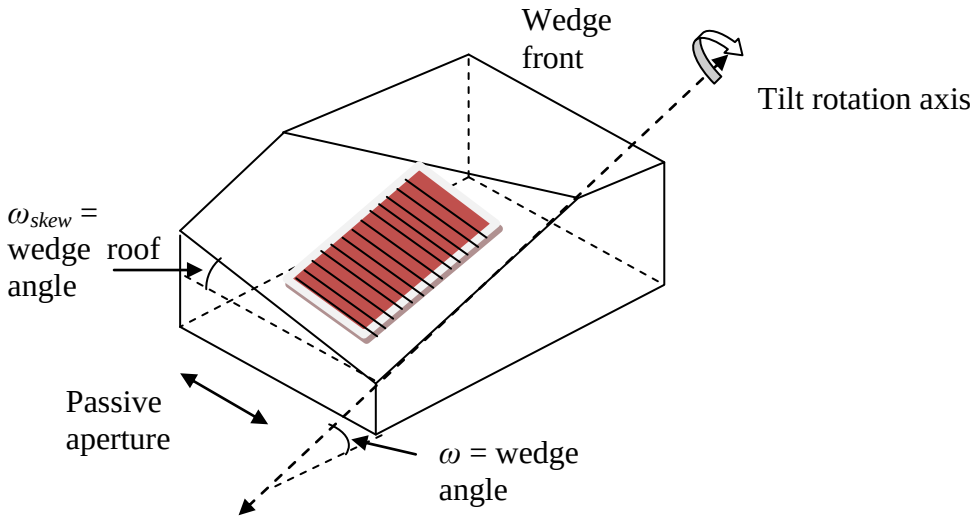

Figure 3-34 Skew roof angle deflection wedge configuration

3.5.3 Shaped and conformable wedges

There are a number of applications where the wedge plays a major part in coupling the phased array probe to a complex surface where sufficiently large flat surfaces are not available. Examples include radii, curved or wavy surfaces where the bottom side of the wedge is matched exactly to the surface under test, leading to distortion of the ultrasonic beams in the component. By careful design of the phased array laws it is possible (to a certain degree) to compensate for the distortion and to control the refracted beams. Figure 3-35 shows an example of a fixed wedge machined to fit a wavy surface; compared to the result of a scan carried out to a flat test plate (Figure 3-36), the image of the defects in the

wavy plate are distorted (Figure 3-37). After optimisation of the delay laws, to take account of the surface, the resulting image is much closer to the flat plate reference scan and with significantly less distortion (Figure 3-38). The ability to optimise the focal laws is not straightforward and is limited by the laws of refraction; in certain positions of the wavy surface some elements do not contribute optimally to the formation of the ultrasonic beam[101].

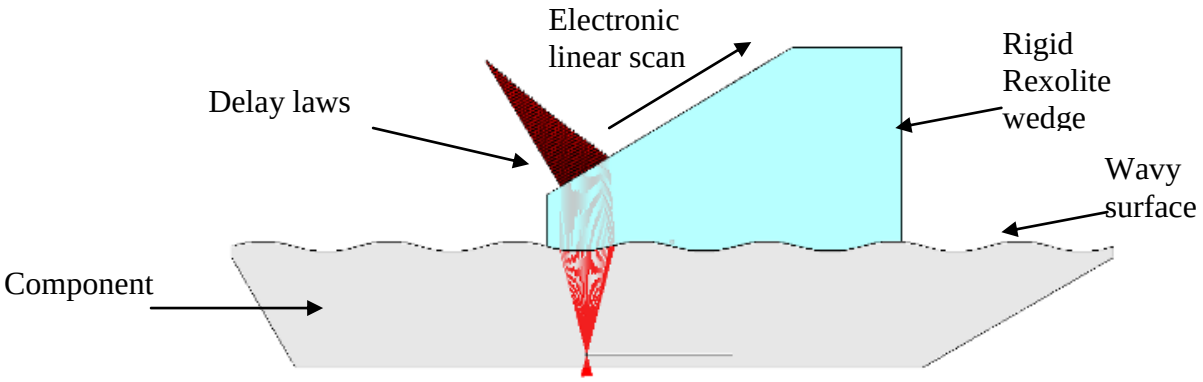

Figure 3-35 Fixed Rexolite wedge machined to fit exactly to a wavy surface[101]

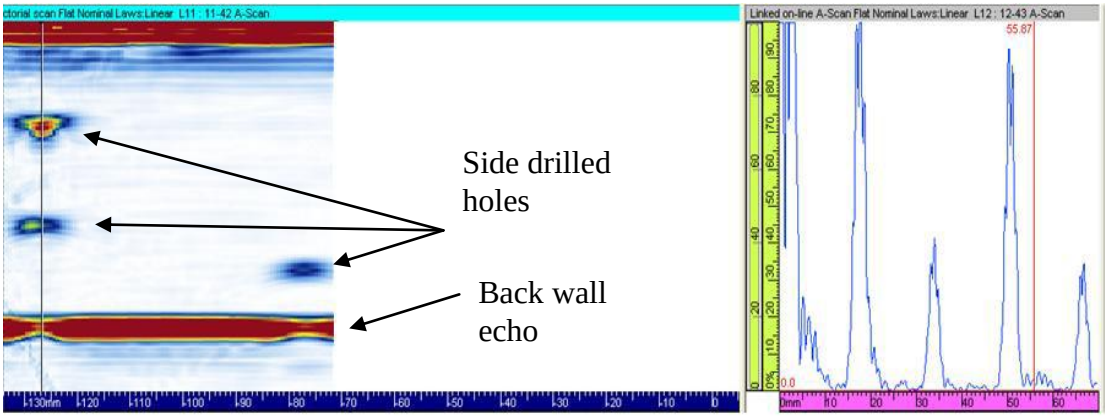

Figure 3-36 Reference electronic B-scan on flat geometry[101]

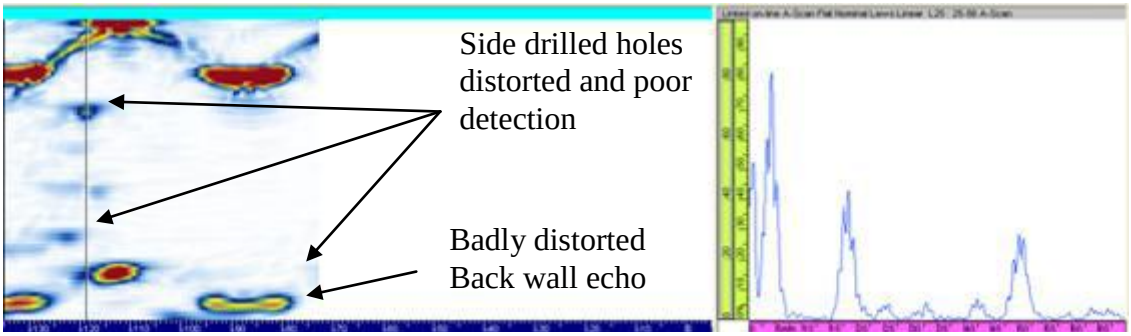

Figure 3-37 Electronic B-scan on wavy surface with no delay law optimisation[101]

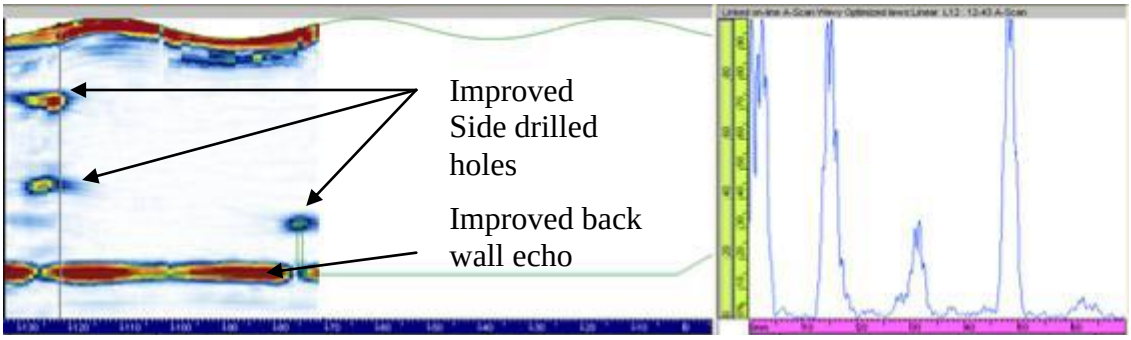

Figure 3-38 Electronic B-scan of wavy surface with optimised delay laws[101]

Conformable wedges, designed to conform to the shape of the component under test as seen in Figure 3-39, have similarly complex delay law optimisation. Added to this there is the requirement to measure the surface distortion under the wedge prior to calculating the delay laws. Bespoke software is used to transmit ultrasonic signals onto the wedge face and measure the deflection upon it and the main delay laws are then optimised to compensate for the change in surface geometry[102].

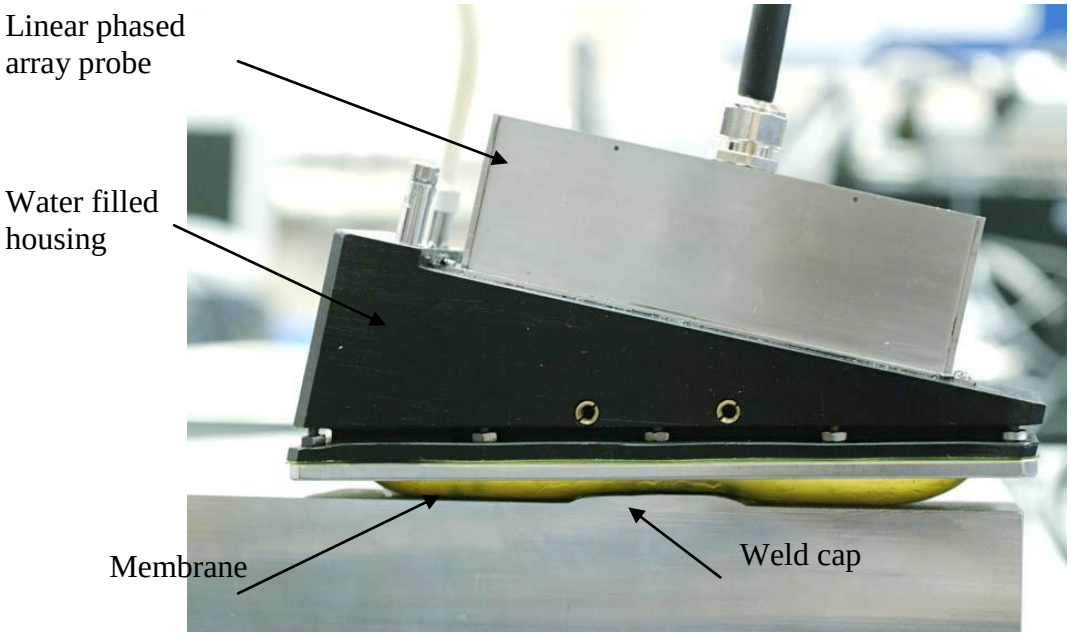

Figure 3-39 2nd generation membrane coupled conformable phased array device[102]

3.5.4 Wedge materials

The choice of wedge material has a bearing on the efficiency in which ultrasound is refracted into the component. There are a number of key factors which influence the material choice including: - velocity of sound, acoustic impedance, and attenuation coefficient. The velocity of sound controls the refractive index of the wedge relative to the component under test, whilst the acoustic impedance has to be optimised to match that of the component for efficient transmission and reception of ultrasound. The attenuation coefficient is important because it is frequency dependant and can be a significant influence at higher frequencies. The two most common wedge materials include Rexolite, a cross linked polystyrene plastic, and Perspex, a transparent thermoplastic also known as Plexiglass or Lucite[103]. Rexolite is commonly used in probe design where a reduction in size is required as it has a lower acoustic velocity than Perspex and can generate shear waves at lower incident angles. Rexolite also has very low attenuation coefficient and so is well adapted for use with higher frequency transducers[103]. Perspex however is much harder

wearing and so is commonly used in conventional angled compression and shear wave probes.

3.6 Conclusions

Mechanical disturbances (waves) propagating through a medium do so due to the elastic properties of the particular material. It has been shown that the velocity of sound waves propagating through gasses, liquids or solids is determined by the density, elastic modulus and temperature of the material. Importantly, the type of medium dictates the type of wave mode which is supported and gasses, liquids and solids all support varied types of waves, propagating at velocities determined by various moduli. Important parameters such as acoustic impedance determine the efficiency of transmission or reflection of waves at boundaries, and significant detail has been given to illustrate the effect of refraction at boundaries. Mode conversion occurs at particular incident angles as a wave refracts through or reflects from a boundary between different materials and this is utilised depending on the type if inspection required. The knowledge of these properties is used to develop real world ultrasonic inspection techniques which are commonly deployed in non-destructive evaluation.

Phased array ultrasonic testing has transformed the way in which materials are interrogated in search of defects. It offers critical control over beam formation in terms of focus and trajectory while advanced imaging of the volume of the component offers improved coverage, detection and characterisation of defects. Transducer parameters critically effect the operation of phased arrays, affecting the focal range, beam size and production of parasitic lobes among others. All these parameters must be considered when designing probes in order to achieve the desired results and valid inspection techniques. Refracting wedges can be utilised to optimise beam trajectories in the test material, which

combined with optimised phased array laws offer control over the refracted beam in 2 dimensions and facilitate inspection of non-flat complex geometries.

Chapter 4. Solution for the inspection of complex geometry utilising Rexolite jigs and rapid prototyping

4.1 Introduction

As explained in Chapter 2, it is clear that individual blade root designs require very specific and targeted techniques to fulfil the detection requirements of specific defects. More challenging however is the requirement to place transducers in accurate and repeatable positions on very limited inspection surfaces of a variety of differing geometries. It was shown in section 2.2.2.3 that current single element pulse echo techniques used for the inspection of pinned roots could miss critical defects. The reasons for this might include: - Operator skill level, optimised operator positioning, severely limited access, probe manipulation, and a basic lack of repeatability of the inspection. One of the proposals for improvement of the current techniques is the deployment of phased array ultrasonic inspection, which through electronic steering of the beam, offers a wider and potentially more comprehensive coverage of the regions under test. The inspection of pinned roots and curved axial entry fir tree roots differ in their individual difficulties of application. The approach taken by the author was generic to both and offered solutions to the challenges set out. This chapter discusses the development steps taken which have led to the deployment of bespoke inspection jigs which address the issues of repeatable and sensitive inspection using phased array technology. It will be shown that the use of modern modelling and simulation tools, coupled with rapid prototyping has led to significant improvement in the detection of defects in the complex root geometry of the most common blade fixing types.

4.1.1 Pinned root inspection challenges

The major limitation for the phased array inspection of many minor stage pinned roots is the lack of available space and scanning surfaces from which to refract ultrasound into the targeted regions. The choice of inspection philosophy was previously dictated by this, where the smallest practical transducers were selected and applied in a slightly hap-hazard approach, requiring significant manual manipulation of the refracted beam. This led to varied levels of sensitivity affected by operator dexterity, quality of coupling and position. Although phased arrays can offer electronic control over the beam trajectory (in the active plane) and focussing, they have previously proven difficult to apply in a prescriptive manner due to the relative size of transducers compared to the available space and scanning surfaces. The main challenge therefore was to find a way to apply phased array in a practical and repeatable technique where access was severely limited on complex geometric features.

4.1.2 Curved axial entry fir tree root inspection challenges

In most cases the available scanning surfaces offered by large curved blade roots is significantly more generous than those offered by the much smaller pinned roots of blades from minor stages. However there are significant challenges in applying techniques which rely heavily on accurate probe positioning in regions where manual manipulation of such probes is impractical. The complexity of the blade geometry can also lead to severe limitations to coverage of critical regions of the root serrations and require accurate a repeatable probe positioning. The challenge was to find an inspection methodology which allowed accurate and repeatable targeted inspections of critical regions of the blade roots in un-reachable and often un-sighted regions of the scanning surfaces whilst in-situ.

4.2 Development of bespoke Rexolite jigs for IP rotor pinned root inspection

Due to major inspection requirements following cracking of stage 6 blades on Parsons 200MW Intermediate Pressure (IP) rotors, this blade design was singled out for the initial development of bespoke wedges. As described in section 2.2.2 there are very specific defect locations which must be targeted with very limited surfaces from which to refract ultrasound, refer back to Figure 2-16 and see Figure 4-1. The defects which had been identified as fatigue cracking ranged in size from approximately 1 mm to 20 mm through wall extent. In order to control the refraction of ultrasound into the target regions it would be necessary to use the flat platform regions on the root block which at their widest measure only 5 mm across. Choice of phased array probe would be the first critical decision in balancing functionality with form factor and allow a basis on which to develop suitable wedges.

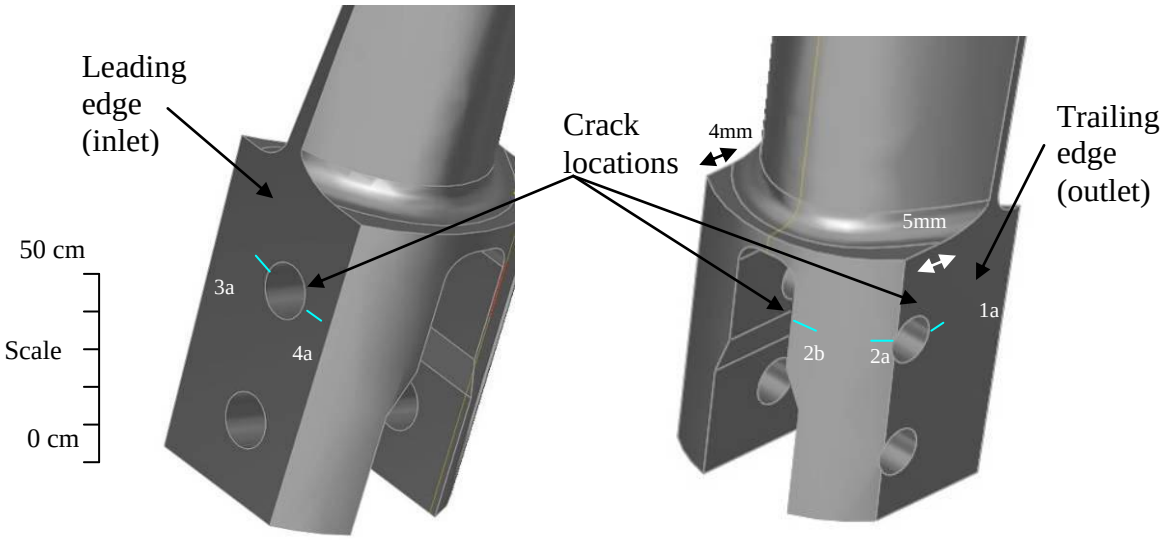

Figure 4-1 Defect locations and limited scanning surfaces from which to refract

4.2.1 Imasonic 20 element 10 MHz phased array probe

In partnership with Imasonic, a 20 element 10 MHz phased array probe was designed to provide the small form-factor required for such limited geometric applications. The probe

having an active aperture of 6.2 mm and passive aperture of just 5 mm (refer to section 3.4.4) with cases size of just 9 × 7 mm was an ideal candidate for the inspection of the IP blade roots, see Figure 4-2. Extensive calculations were carried out to establish the potential performance of the probe as laid out in Appendix B, where parameters such as focal potential, resolution and beam dimensions were approximated. It was found that although the inspection zones were outside of the near field of the transducer, the approximated beam field would lead to extremely good sensitivity and resolution, well within the requirements of the inspection.

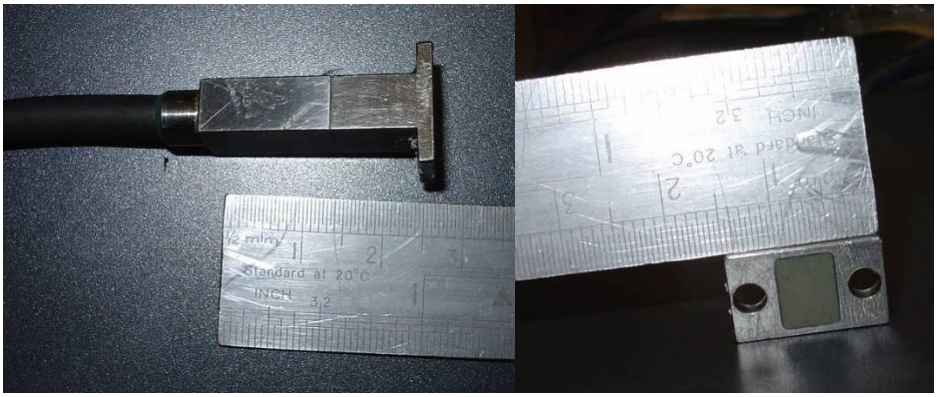

Figure 4-2 Imasonic 6822 E101 - 10 MHz, 20 element phased array probe

4.2.2 Beam simulations

Beam simulations were carried out using CIVA beam computation tools; CIVA is a comprehensive development and simulation tool developed by the French company CEA in conjunction with several industrial and academic partners. CIVA facilitates full ultrasonic beam simulation with 3D CAD models along with defect response analysis for phased array, TOFD, pulse echo, and tandem techniques. CIVA is able to accurately simulate the wave field of an ultrasonic transducer by discretizing a series of source points over the transducer surface. The contribution from each elementary source is obtained through a high frequency approximation (pencil method) from which the impulse responses are computed and convoluted with the input response[104]. Development of defect interaction simulation in

CIVA uses a model which is fundamentally based on a 'Priori' field computation for radiation and reception[104]. The field is simplified to the form:

$$\Phi(M,t) = A(M)s(t\text{-}tof(M)) \quad (46)$$

where Φ is the scalar potential (for P-waves) while vector potential is used for SV-waves, A(M) the amplitude distribution (value of scalar potential), and $s(t - t_{of}(M))$ the waveform delayed by the time of flight between the probe and the computation point of the defect[105]. The wave field interaction with the defect is based on either the Kirchhoff approximation or the Geometric theory of diffraction. Many papers have been published regarding the validity and accuracy of the CIVA simulation tools and have become and accepted method of ultrasonic method validation[106].

Figure 4-3 shows the results of a 2D beam simulation carried out to confirm the performance of the 20 element 10 MHz phased array probe, when utilised to produce compression waves on a Rexolite wedge with no beam focusing.

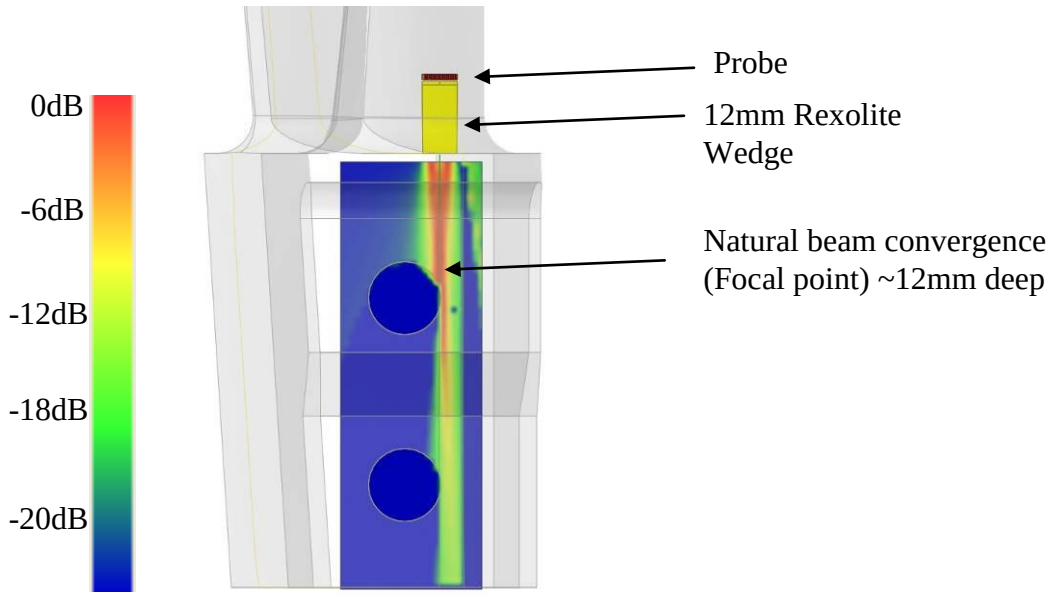

Figure 4-3 Beam simulation of 20 element 10 MHz phased array compression probe; hot colours represent regions of highest intensity

It can be seen that the near field beam convergence for the unfocused beam is comparable to the calculated value of 11.56 mm from Table B-2. The beam profile, (seen as peak

amplitude), exhibits low beam divergence after the natural focal point, and the inspection zone falls well within the region of high intensity. Due to the narrow beam profile it was also noted that reasonable coverage of the inner pin hole might be expected.

Figure 4-4 shows the results of a 2D beam simulation of the 20 element 10 MHz probe mounted on a 30.5º Rexolite wedge to produce shear waves at 25º, 45º, and 65º. Again no beam focusing was utilised in the phased array laws.

It can be seen that the target inspection region was in the far field of the phased array beam, but due to low beam divergence the beam width is relatively small. The simulation also shows that the region of highest intensity occurred at the 45º angle which is the region of highest defect occurrence.

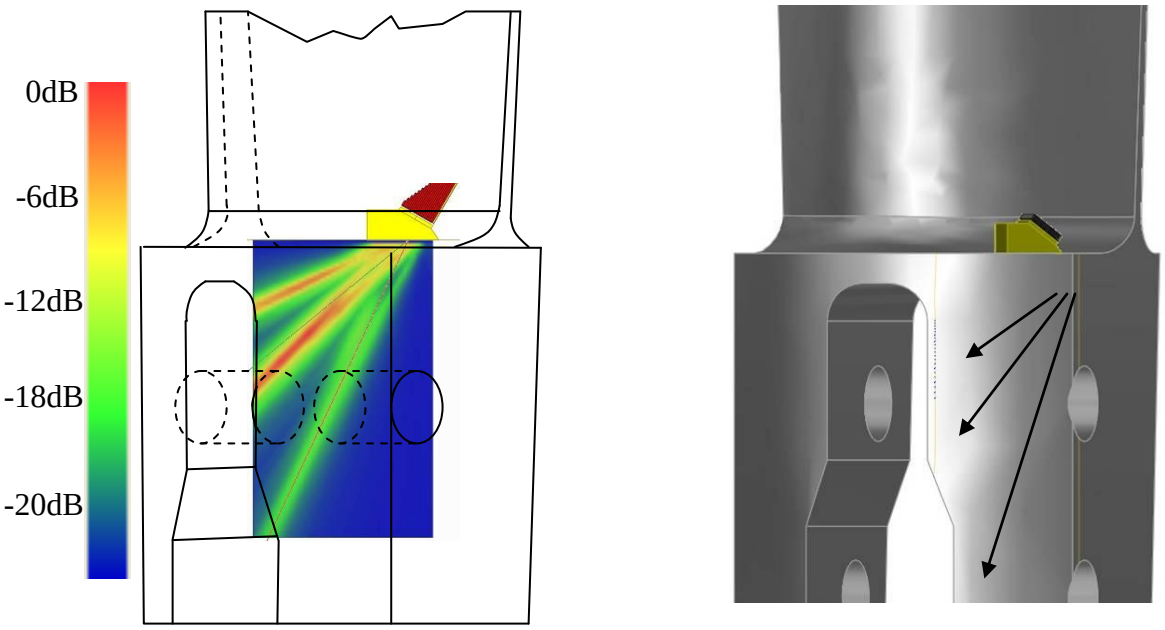

Figure 4-4 Beam simulation of 20 element 10 MHz phased array shear wave probe; hot colours represent regions of highest intensity

4.2.3 Rexolite inspection jigs

As the available flat lands from which to refract ultrasound into the inspection zones of the blade roots were so limited, there was no way of coupling the phased array probe efficiently to the component. Therefore a Rexolite wedge would be required to effectively

couple the probe for compression waves and also to provide the appropriate refraction angles for shear waves. The contact face of the wedges would be required to accurately match the radii and contours of the blade root platform and would therefore be difficult if not impossible to manufacture without taking account of the blade geometry. Positioning of such wedges would also be critical in order to ensure that refraction through the correct portion of platform was achieved repeatedly. The production of bespoke jigs was therefore necessary to accommodate the complex shape of the root platform to both position the phased array transducer accurately, and to produce the ultrasonic refraction required by the inspection.

The initial approach by the author was the development of Rexolite jigs which involved the production of jig blanks, modelled in a CAD environment and manufactured using advanced five axis CNC machines in the RWE workshops. Several blank wedges were produced with the negative profile of the convex side aerofoil and root platform radius, but with no specific profile for the transducer contact face, see Figure 4-5 and Figure 4-6.

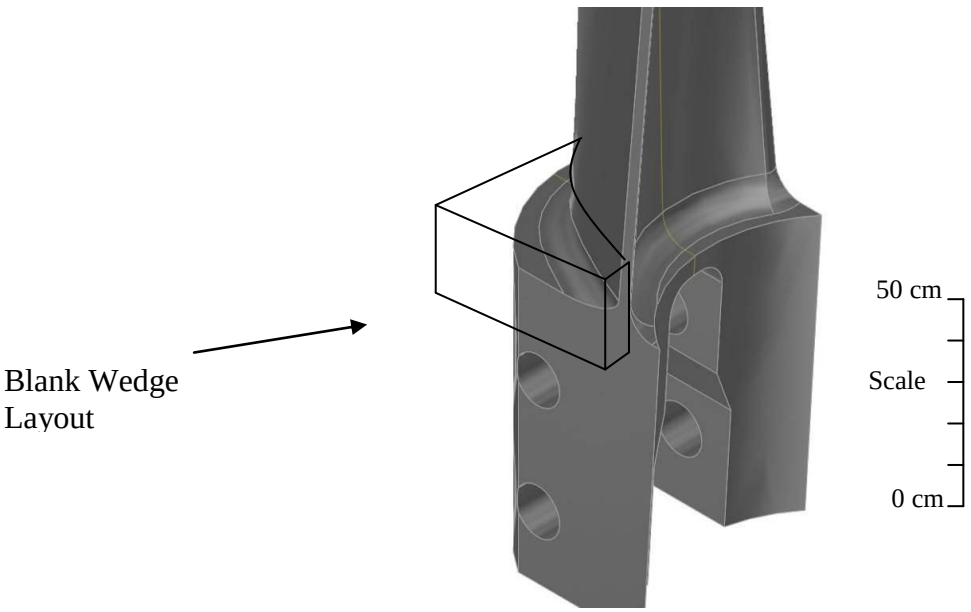

Figure 4-5 CNC wedge layout

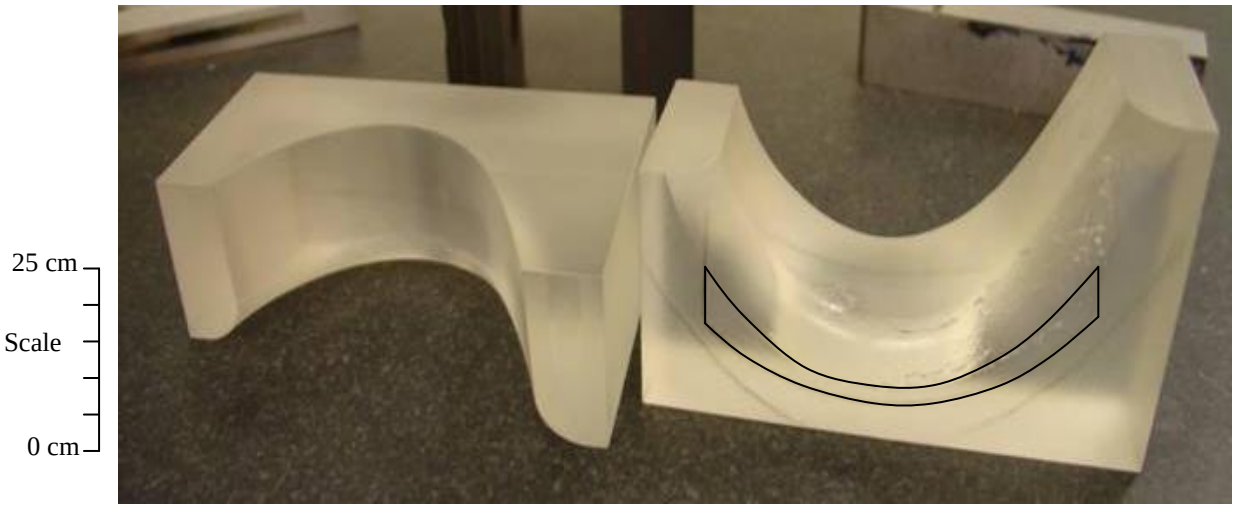

Figure 4-6 Blank CNC wedges

The minimal flat land available on the root platform can be clearly seen on the jig blanks as highlighted in Figure 4-6, along with the exact profile of the aerofoil and the root platform radius, giving a very accurate fit to the component. The next stage involved using the CIVA simulation tools to assess the ideal probe positioning for the shear wave inspection of zone 2b, see Figure 4-7. It was determined that a skew angle of 45º to the side face was optimal with a mechanical wedge angle of 30.5º to provide a natural refracted angle of 45º. The compound angle produced by the skew and refraction angle was then milled into the blank wedge to provide a scanning surface on which to mount the probe. The wedge was coupled to a test sample containing EDM notches in the 2b position using sonagel couplant. The 20 element 10 MHz phased array probe was positioned and coupled to the surface of the jig and manoeuvred to optimise the responses from the EDM notch. The optimum position was marked and the probe mounted to the partially finished jig, see Figure 4-8.

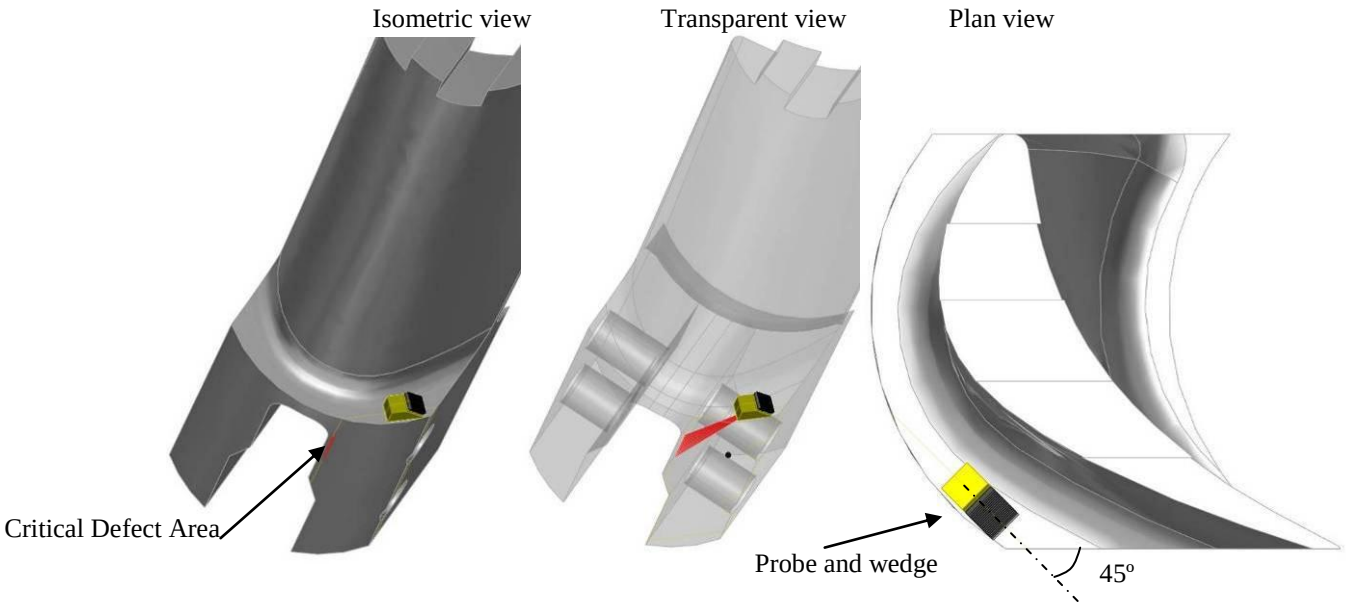

Figure 4-7 CIVA model of shear probe positioning

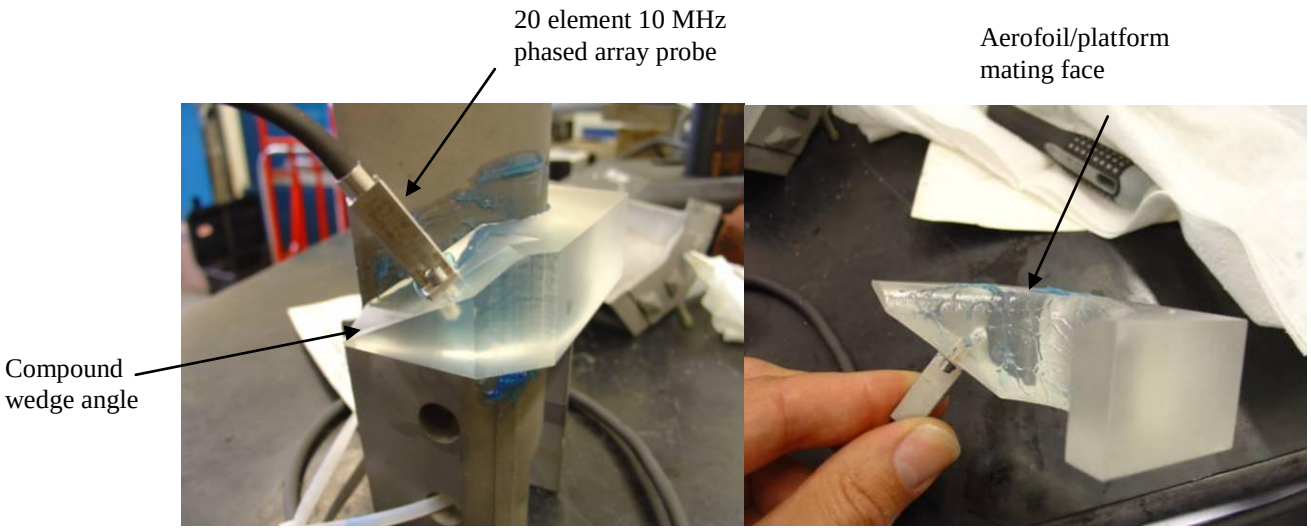

Figure 4-8 Initial wedge angle and skew in blank wedge

The prototype wedge was tested on two blades containing defects of 3 mm and 8 mm through-wall respectively, emanating from the target area, see Figure 4-9. The resulting sector scans were recorded as seen in Figure 4-10 and Figure 4-11. As it can be seen, very positive results were attained with large measurable responses from the defects.

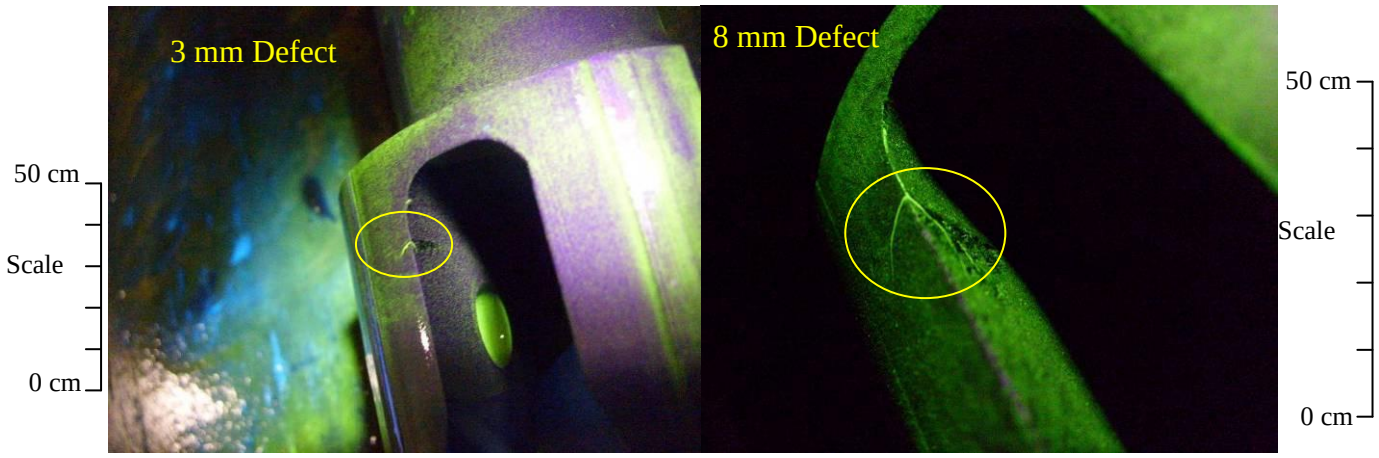

Figure 4-9 MPI images of 3 mm and 8 mm defects to position 2b

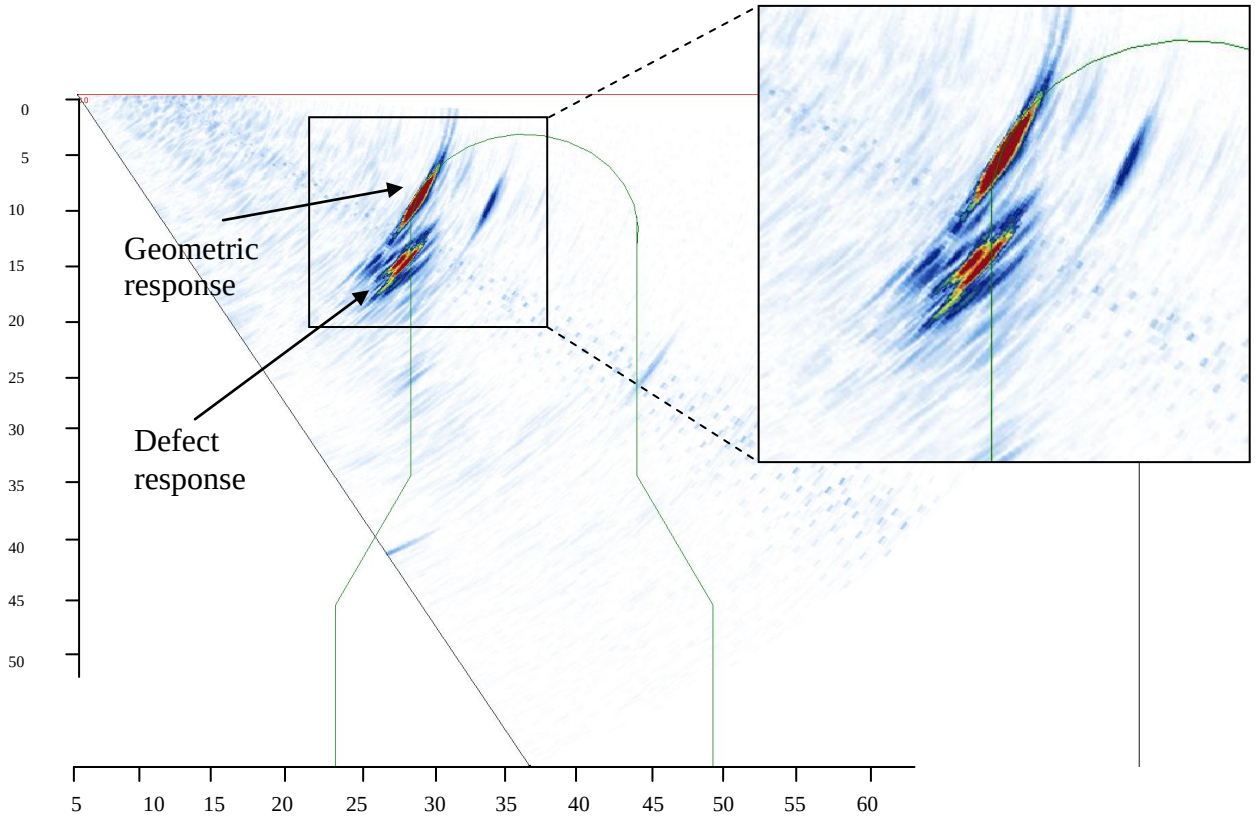

Figure 4-10 Sector scan of 3 mm defect to position 2b

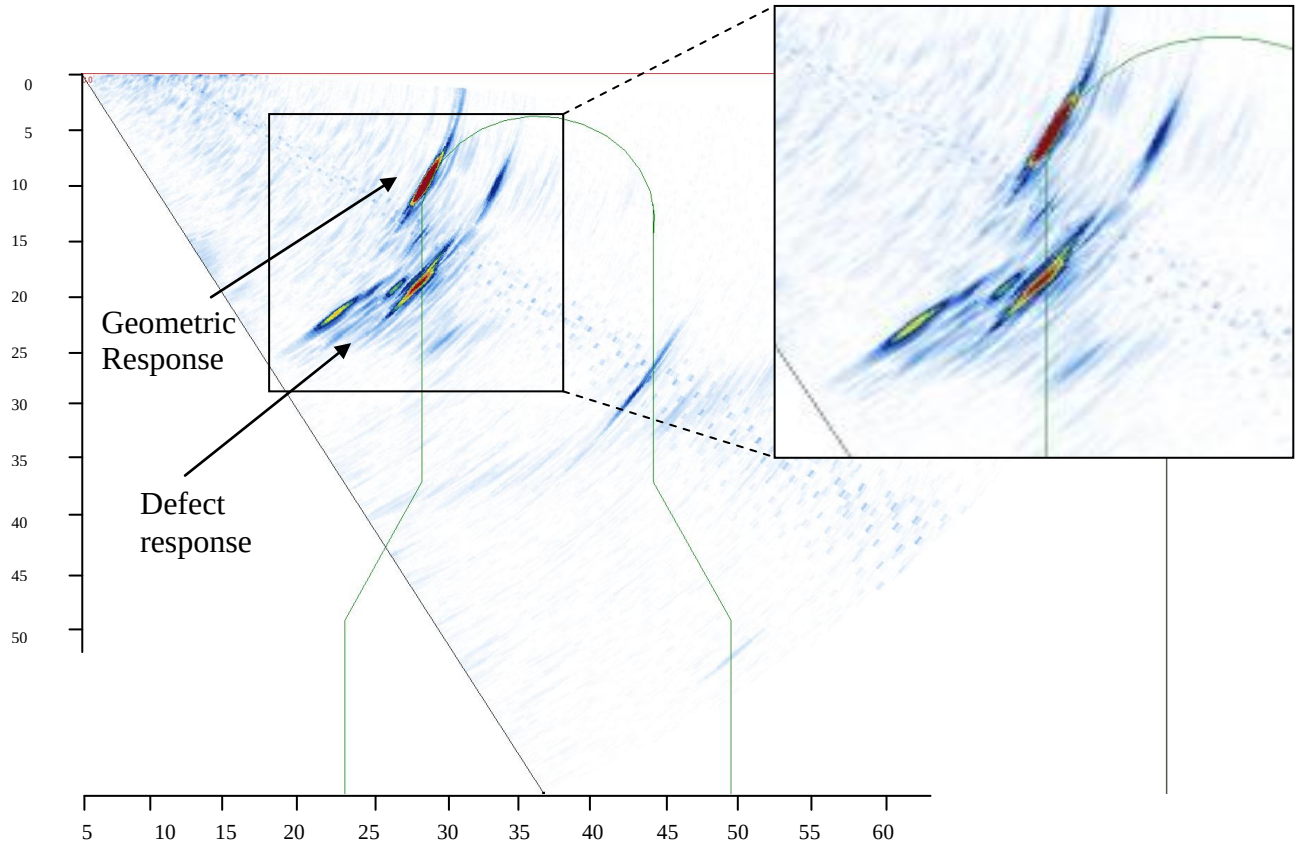

Figure 4-11 Sector scan of 8 mm defect to position 2b

The jig was finished by removing excess material to enable its insertion between adjacent blades. The final jig consisted of a small strip of flat refracting interface to make contact with the root platform, the radius and profile of the aerofoil, see Figure 4-12.

Figure 4-12 Zone 2b shear wave inspection jig

The whole process was then repeated to create wedges to facilitate the inspection using compression waves in Zones 2, 3, and 4. Each jig matched the profile of the blade with sufficient flat surface to refract sound into the available land on the blade root platforms, see Figure 4-13 to Figure 4-15. Taking account of the outer hole centre being 25 mm deep and the inner hole centre being 50 mm deep the wedge heights were chosen which would result in the wedge delay response being imaged at around 35 mm deep to avoid masking around the holes. By taking the ratio of the velocity of rexolite compared to the longitudinal velocity of steel this was done by:-

$$H_i = v_r/v_s \times 35 = 2320/5900 \times 35 = 13.7 \text{ mm}$$

where: H_i = height of the first element
v_r = longitudinal velocity of Rexolite
v_s = longitudinal velocity of steel

Figure 4-13 Zone 2a compression wave inspection jig

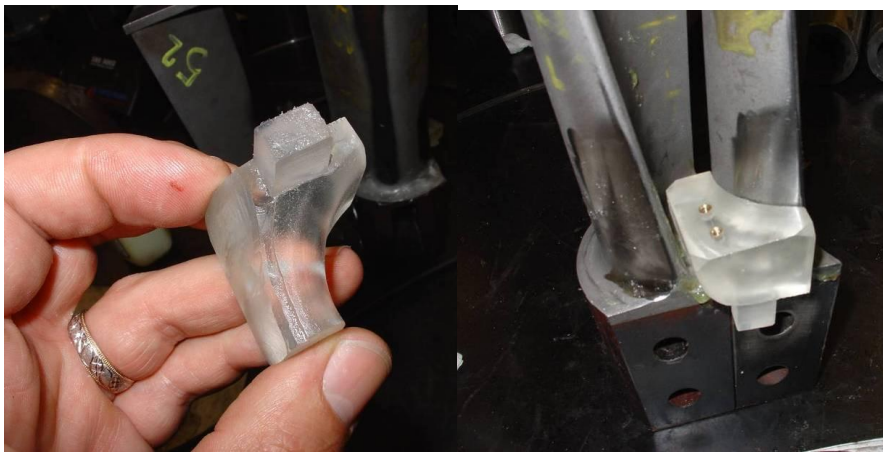

Figure 4-14 Zone 3 compression wave inspection jig

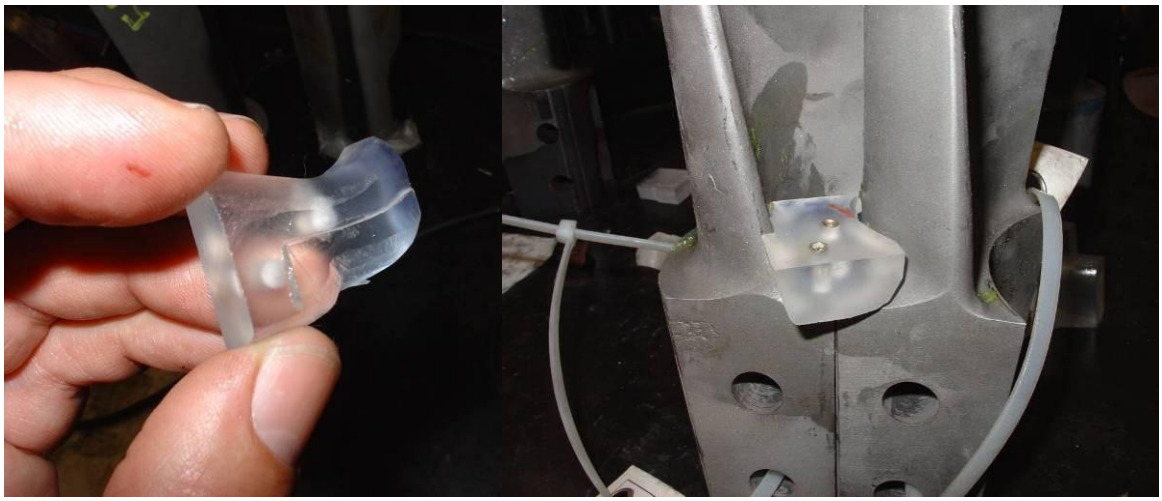

Figure 4-15 Zone 4 compression wave inspection jig

Initial bench tials with multiple cracked blades were carried out followed by full validation on a live inspection rotor as outlined in Appendix C.

The bench trials concluded that all EDM notches were detected using the jigs in the various inspection zones as discussed in section C.1.1 and tabulated in Table C-1. Subsequent inspection trials on service rotors were further carried out as detailed in Appendix C and further discussed and analysed in section C.1.3, C.1.4 and C.1.5.

4.2.4 Discussion – IP rotor pinned root inspections using rexolite jigs

During the validation process a very high detection rate was achieved and after the addition of an inspection to zone 4b, and slight modifications to the technique, 115 out of 117 defective blades could be positively identified as containing defects. The two blades with cracking that could not be positively detected were in zone 3b where no current inspection was possible due to lack of inspection surfaces from which to refract ultrasound. It has been shown that the novel approach utilising CNC wedges led to a more sensitive, rapid and repeatable inspection technique, applying the latest in phased array probe technology and proving the jig concept. The technique for inspection of the Parsons 200MW

IP rotor was subsequently deployed across both RWE and customer sites and has been successful in detecting confirmed defects in each deployment.

There were significant gains made in the process of producing Rexolite jigs for the accurate and repeatable positioning of phased array probes to inspect both complex and severely limited inspection surfaces. There were some drawbacks to the process of producing such jigs however, which were seen by the author as limitations to their deployment across other complex inspection challenges. Where design cycles were short and budgets limited these drawbacks which include a combination of financial and technical considerations were apparent: -

- The manufacture of solid Rexolite wedges proved to be expensive due to the requirement for 5 axis CNC machines, and small items are challenging to manufacture.
- Significant hand finishing was required to produce the final jig shape with some experimental tweaking to establish final probe positioning.
- Lead times for wedge manufacture could be long, and design tweaks would require expensive and time consuming remanufacture.
- Larger jigs required for the inspection of large blade roots would use significant amounts of expensive Rexolite while the manufacturing process wastes significant material.

A more fundamental issue however created an unforeseen but significant obstacle to producing precise jigs which accurately fit the complex components. It was found in further jig developments that the accuracy of the original CAD models of the components under test was not sufficient for the purposes of phased array ultrasonic development. For the reasons listed above and to provide significantly improved accuracy in jig design the author pursued an alternative design and manufacturing technique as discussed in the following sections.

4.3 Laser scanning and production of component CAD models

4.3.1 Introduction

An issue discovered during a second development of Rexolite jigs was the lack of accuracy of the CAD models used to produce the jig designs. The issue was the reverse engineering methodology used at the time, as opposed to the accuracy of the coordinate measuring machine (CMM) which was used for data point collection. In regions of the component where very low tolerances (<0.025 mm) were required for fitment to other components, very high density of data points would be collected. Other regions such as the aerofoil of a turbine blade would be sampled at relatively high resolution around the perimeter but at low resolution along its length, and a CAD method known as lofting used to interpolate those points to produce the aerofoil shape. The radii formed at the transition between the root platform and aerofoil would be produced in the CAD model at a normalised dimension which would fit quite well across the whole root block. In the manufacture of the original blades there can be variations to the radius region due to variations in the forging process of different batches; some blades are subject to hand blending to remove blemishes. For that reason the absolute accuracy of the re-engineered model compared to the original blade is not seen as critical in these regions and lower resolution of the coordinate point map is used. The result of the lower data point resolution and lack of specific tolerances in these regions meant that the aerofoil to root block radii in the CAD model might be significantly different to the service blades. The aerofoil and radius at this transition however are the regions where high accuracies are required for the production of jigs which fit snugly, and essential if refraction through the radius is required. A couplant layer of up to 0.25 mm thick between the Rexolite wedge and the component was deemed to be acceptable in terms of compensating for slight variations between blades and so a reverse engineering system with scanning accuracy better than 0.25mm was sought.

In order to collect the maximum amount of surface data points a number of laser scanning systems were evaluated which could achieve the desired accuracy whilst being cost effective as an alternative to using the CMM system in the workshops.

In the interest of accuracy and in order to have full control over the CAD model production process, a NextEngine desk top laser scanning system was procured. This scanner was adopted as the primary method for CAD model production for use in NDT development.

4.3.2 NextEngine desktop laser scanner

The NextEngine Desktop 3D Scanner and ScanStudio™ software were designed and developed in Santa Monica, CA by NextEngine Inc. Founded in 2000 the privately-held company invented a new technology with an all new electro-optical architecture; using sophisticated new algorithms and an array of lasers scanning in parallel along with photo imaging. The scanner has become the number one selling 3D scanner in the world at $1/10^{th}$ the cost of equivalent performance scanners[107]. The performance and cost of other systems on the market can be seen in Table 4-1 which illustrates clearly the performance/cost point benefits of this system.

When considering the 0.25 mm accuracy described in 4.3.1 it was clear that a number of systems met this criteria but, based purely on price, the NextEngine was clearly the most cost effective. The nearest comparable system in terms of accuracy and price is the Konica Minolta VIVID 3D Laser system which starts at $25,000[108] ; this compared to the NextEngine system which was procured for $5990 including all the development tools required to produce parametric CAD models from the scan data.

The scanner is capable of scanning the component surface and collecting a point cloud of millions of points in a matter of minutes to an accuracy of 0.005 inches (0.127 mm). The point cloud can be exported into multiple CAD formats or manipulated within the

ScanStudio™ and RapidWorks™ CAD tools to produce parametric solid models or NURBS surface models.

The methodology preferred and utilised by the author involved laser scanning and point cloud collection using ScanStudio HD™ followed by mesh manipulation and native feature extraction for production of parametric solid models using RapidWorks™.

Scanner Type	Image	Accuracy	Price
NextEngine Desktop 3D Scanner		0.127 mm	$2995 to $5990
Mantis Vision's F5		0.5 mm	$45,000 to $60,000
Basis Software Surphaser		0.2 mm	$90,000 to $150,000
Dimensional Imaging DI3D & DI4D		0.5 mm	$20,000 to $140,000
ViALUX z-Snapper 3D CameraKonica		0.0254 mm	$25,000 to $50,000
Minolta Range7 3D Digitizer		0.0301 mm	$80,000 up
Konica Minolta VIVID 3D Laser		0.127 mm	$25,000 to $55,000
LDI SLP Laser Scanner		0.057 mm	$16,900 to $22,900
FARO Laser ScanArm		0.0508 mm	$30,000 to $40,000
Kreon Zephyr Laser Scanner		0.0254 mm	$60,000 to $75,000

Table 4-1 Comparison of available laser scanning systems[108]

4.3.3 Model production of Siemens LP stage 4 blade

In the process of developing inspection jigs for a similar inspection technique to that describe in section 4.2, an accurate CAD model was required as a prerequisite to jig design. The stage 4 blade from a Siemens low pressure rotor was laser scanned using the NextEngine scanner and modelled using RapidWorks™ software.

4.3.3.1 Laser scanning and point cloud generation

The blade sample was coated with standard white powder developer used in dye penetrant inspection to provide a high contrast non reflective background. Datum markers in the form of small red dots were added at random intervals around the component to provide markers for scan alignment later in the process. As this blade was relatively small it was scanned using the encoded turn table which is supplied with the scanner. A 360° panoramic scan was enacted producing eight fixed position scans (A1 to A8) around the blade which was aligned automatically based on encoder position, see Figure 4-16 and Figure 4-17.

Figure 4-16 360° eight segment panoramic scan of stage 4 blade

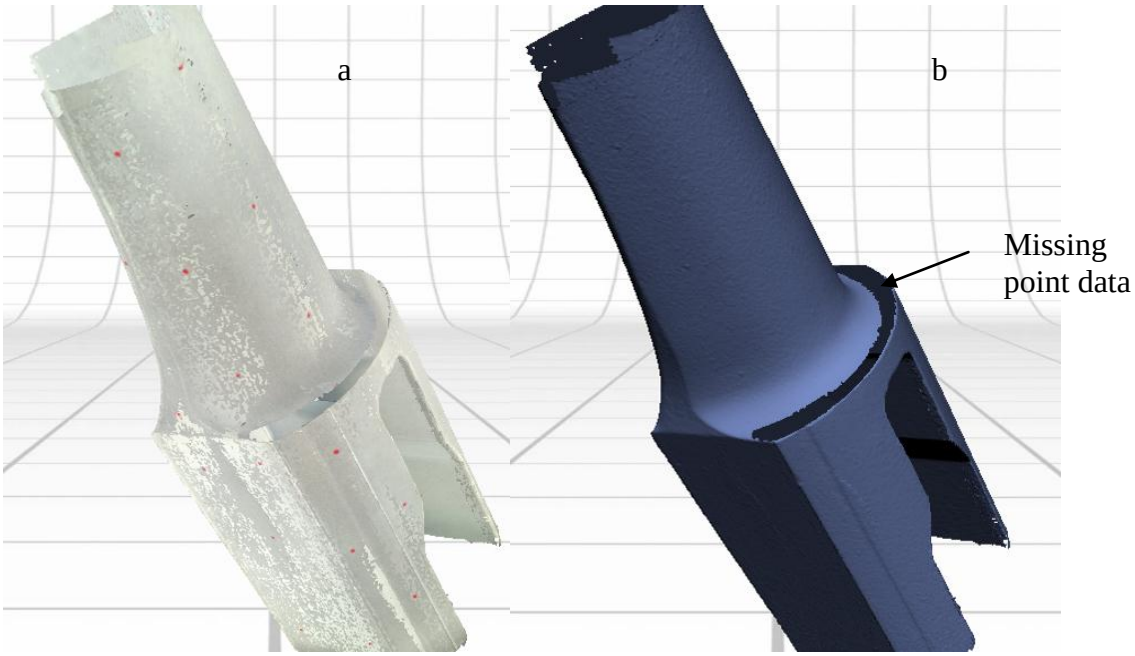

Figure 4-17 Aligned panoramic scans - a: photo image, b: Shaded image

It can be seen that point data from the flat platform region was not collected due to it being parallel to the laser trajectory. A further single point scan was taken with the blade oriented to make the platform more normal to the beam trajectory to fill in the gap left from the first scan, see Figure 4-18.

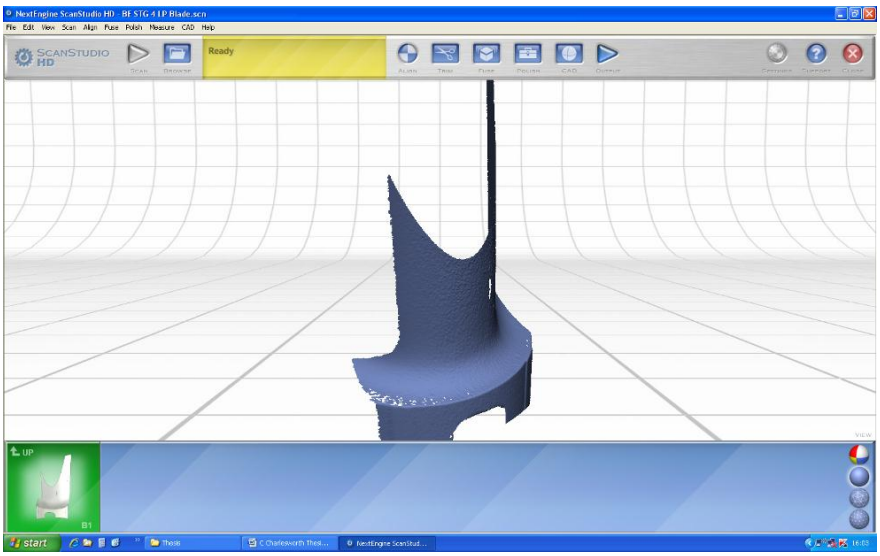

Figure 4-18 Extra platform scan

Utilising the datum points applied at the outset, the platform scan and the panoramic scan were aligned using a tool which allows placement of coloured balls to cross reference the same points in each scan as seen in Figure 4-19 and Figure 4-20.

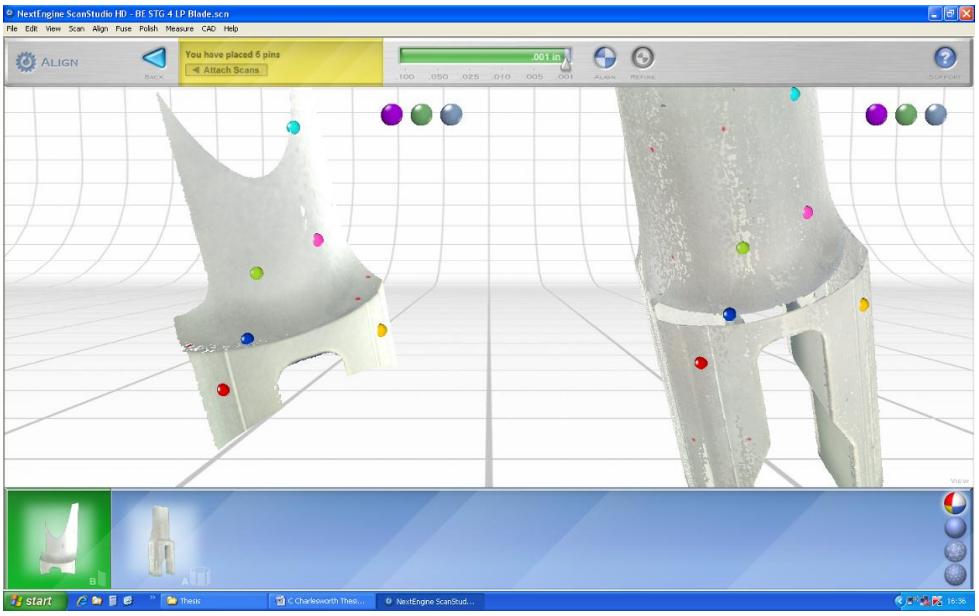

Figure 4-19 Scan alignment tool

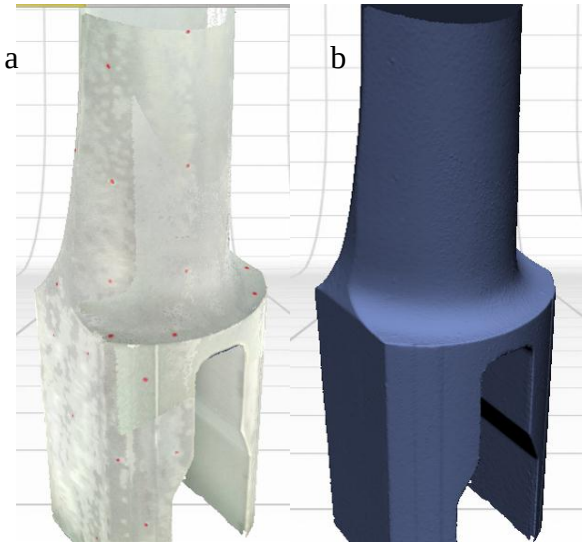

Figure 4-20 Aligned scans - a: photo image, b: shaded image

The scans were then finally fused and simplified to produce a point cloud with all the overlapping mesh detail from the different scans averaged to produce a simple mesh, see Figure 4-21. The point cloud was then imported into RapidWorks™ for parametric modelling.

a

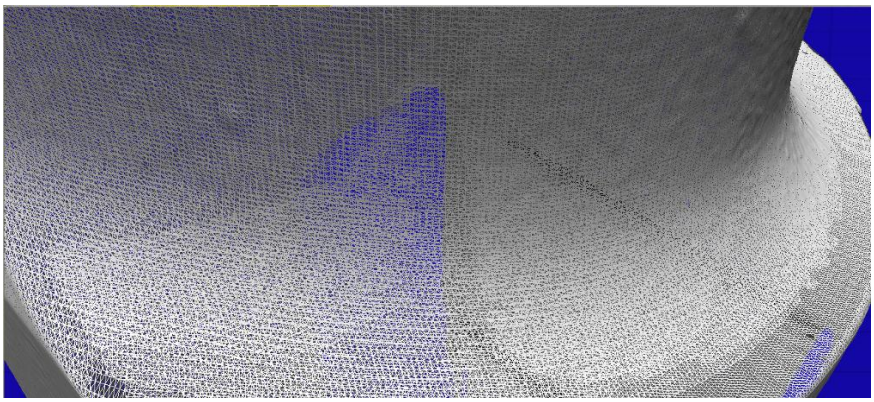

b

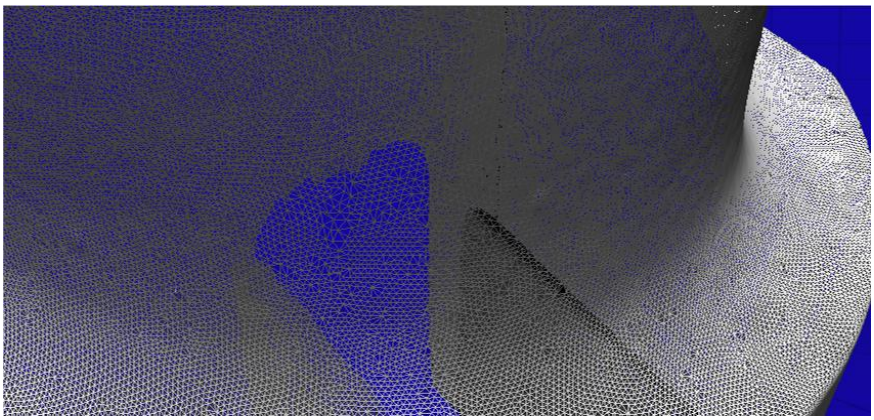

Figure 4-21 Final point cloud data - a: non fused, b: fused and simplified

4.3.3.2 Parametric modelling with RapidWorks™

RapidWorks™ is a proprietary modelling tool which is based on the RapidForm XOR CAD engine but adapted for direct use with the NextEngine 3D scanner. It uses a sketch based design environment to enable the production of full parametric models with full feature tree whilst offering special tools to recognise native features and points in the scan data cloud[107].

Once the scan data from Scan Studio was imported, the first operation was carried out to globally re-mesh the data and even out the mesh triangle size and filling in minor holes in the mesh. The surface was then segmented to highlight and separate native features such as radii, cylinders, planes, and revolutions etc., shown in different colours in Figure 4-22.

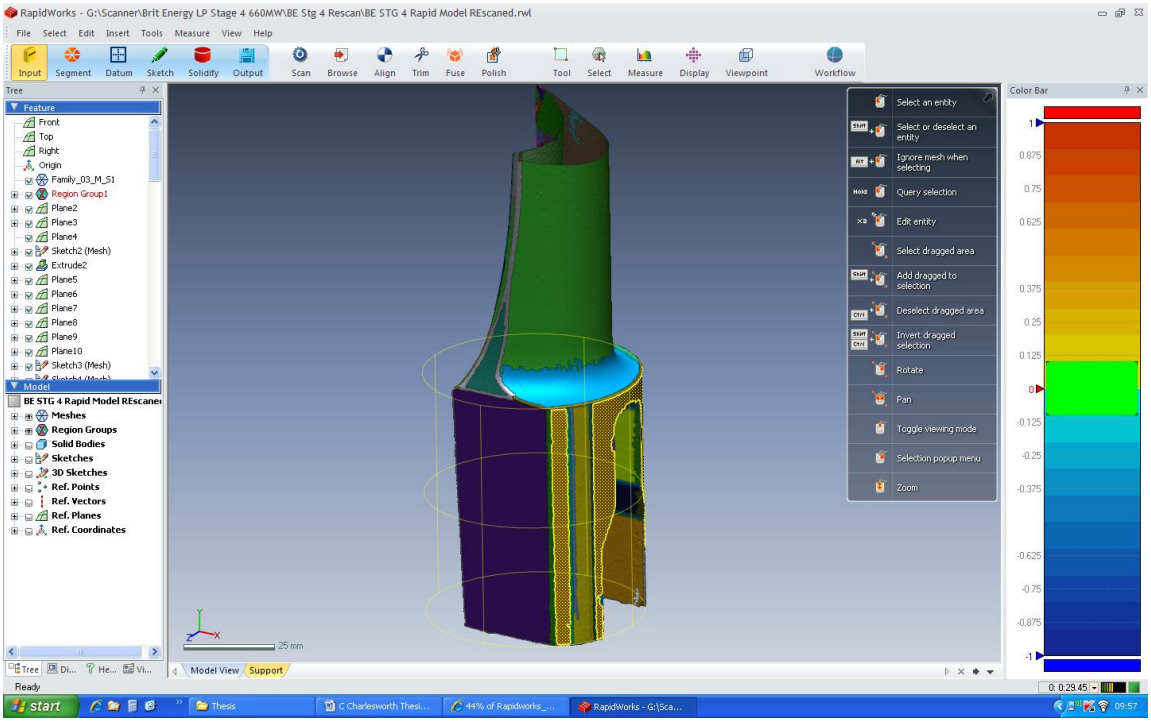

Figure 4-22 Segmented surface of data point cloud illustrating separate native features in different colours

The process of building up the solid model features was then continued by aligning the scan data to a sensible coordinate system and adding the basic building blocks of each feature. By taking sketch planes through significant features of the cloud, points in the cloud which intersect those planes (in pink) are extracted and used to fit sketch features such as lines, curves or splines, see Figure 4-23. These sketch features are measured for precision by use of a vector multiplier which can be multiplied up to 1000 times the preset tolerance, in the case illustrated being 0.01 mm.

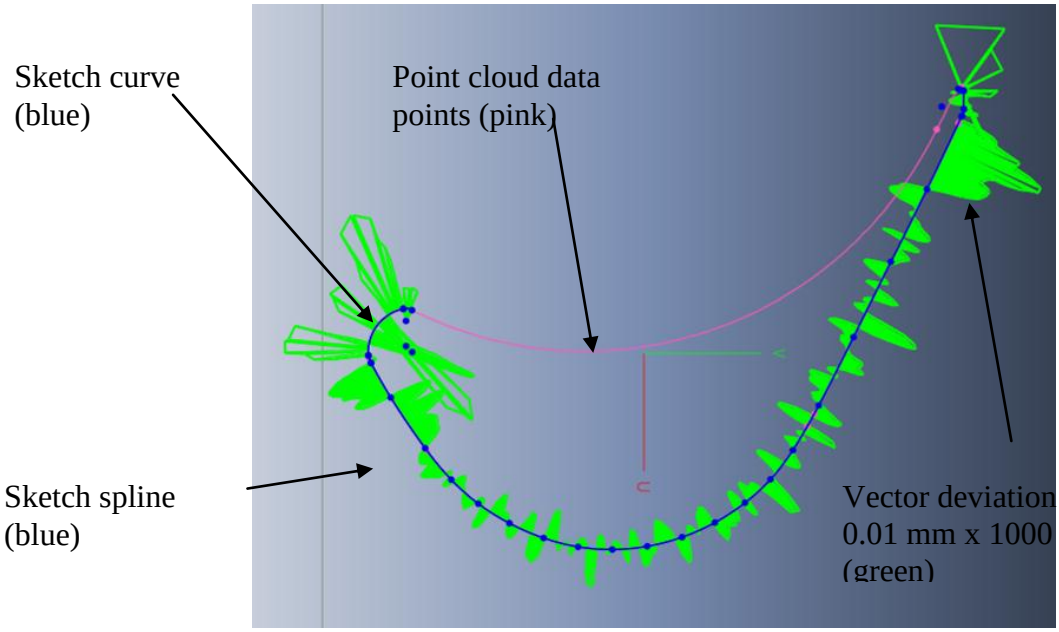

Figure 4-23 Sketch plane of aerofoil with 1000x vector multiplier to measure precision to original point cloud (pink)

After creating a solid cylinder to represent the disk made up of all the blades in a rotor stage, the aerofoil was modelled using sketches extracted from the point cloud along its length to produce a disk with single solid aerofoil, see Figure 4-24. The most important aerofoil to root block radius was then created using the fillet tool and the surface deviation tool to ensure accuracy to the original point cloud data, see Figure 4-25.

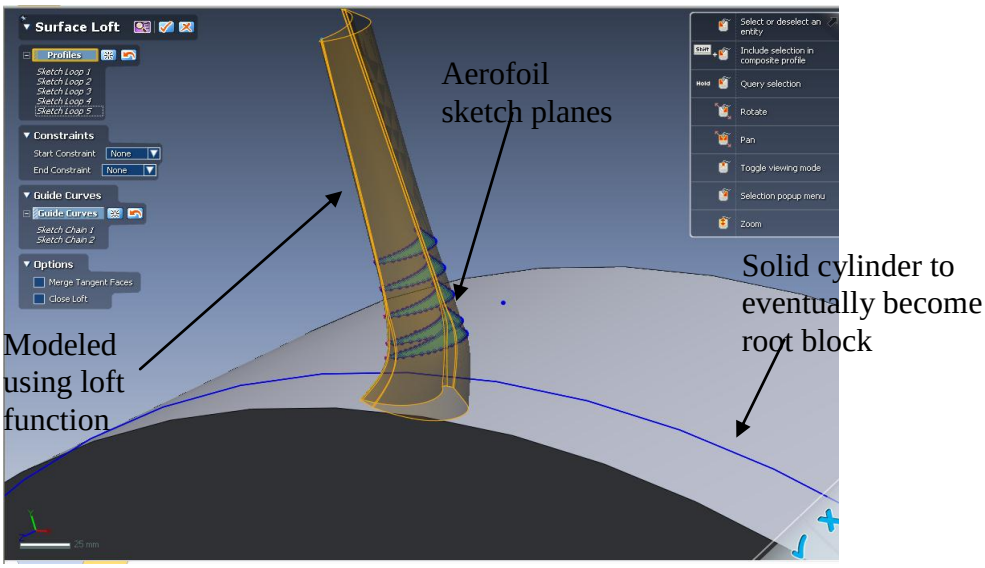

Figure 4-24 Lofting of aerofoil from sketch planes

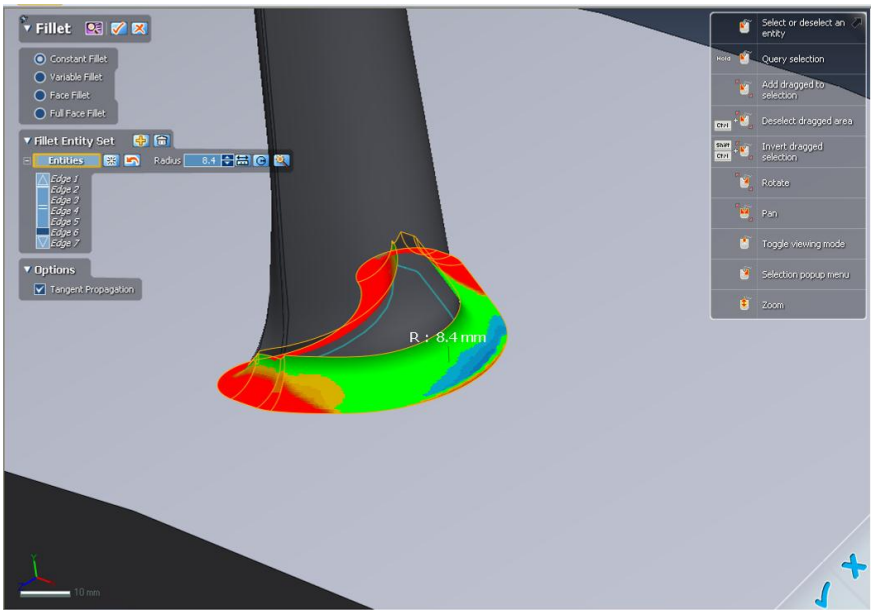

Figure 4-25 Creation of aerofoil to root radius – green represents regions within tolerance of deviation from point cloud data

The root block was then shaped by creating sketch planes and extrusions which represented the curvature and features of the root block, see Figure 4-26 and Figure 4-27.

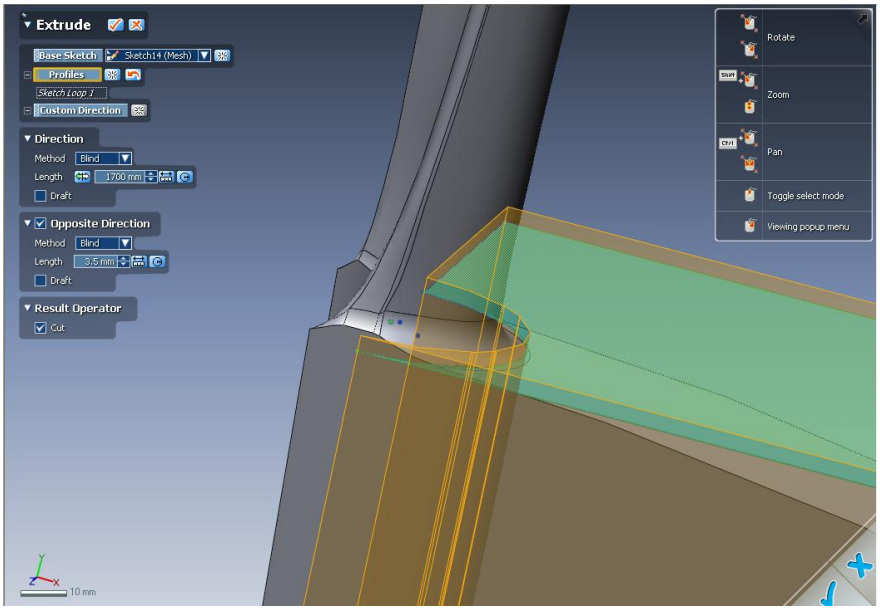

Figure 4-26 Extruding and cutting out the root block geometry

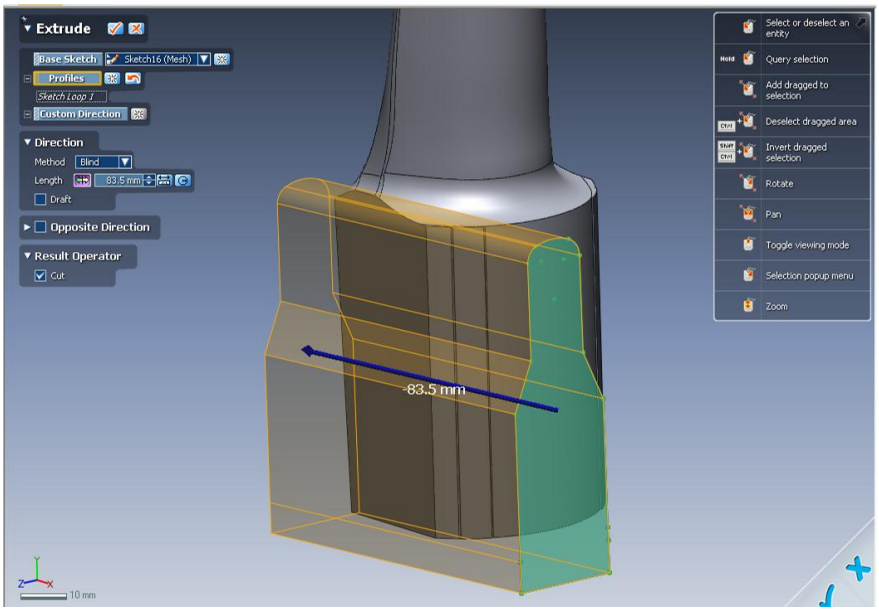

Figure 4-27 Extruding and cutting of saddle feature

Finally small features like corner fillets were added and the deviation tool used to compare the model with the original scan data to within a tolerance of 0.1 mm, see Figure 4-28, and exported as a STEP formatted CAD file for use in the simulation tools, Figure 4-29.

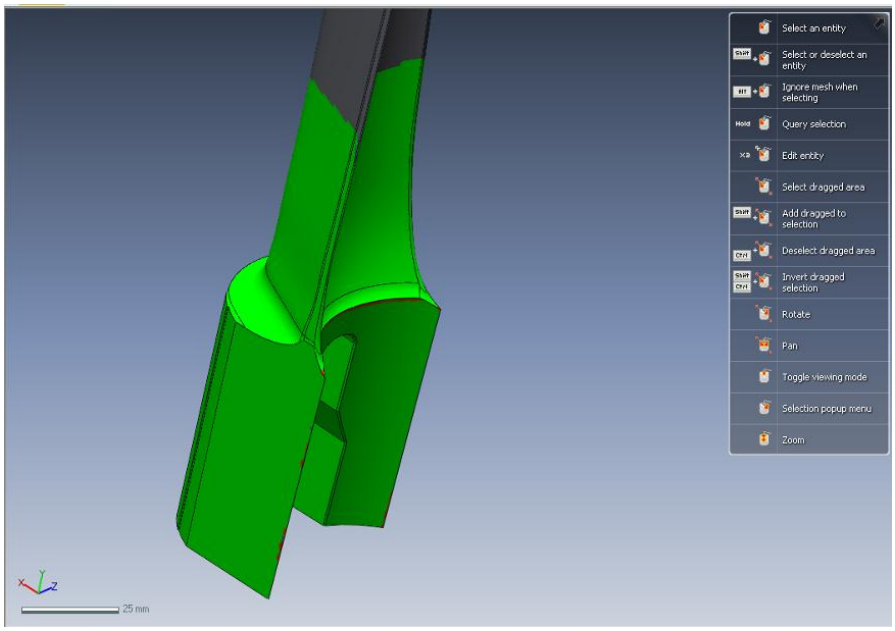

Figure 4-28 Final solid model compared to scan data representing tolerance of <0.1 mm shown in green

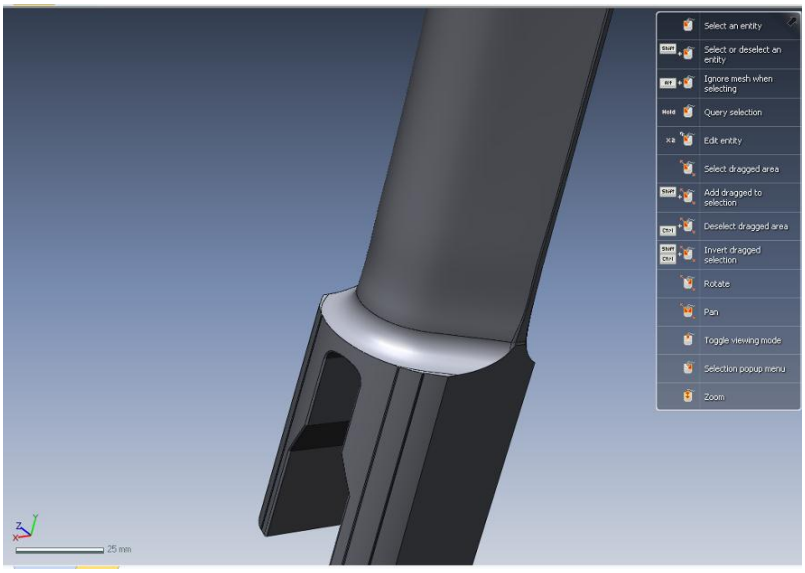

Figure 4-29 Final parametric solid model of stage 4 LP blade

4.3.4 Discussion – Production of accurate CAD component models

It has been shown that accurate CAD models of components of interest can be produced by means of laser scanning and parametric modelling. The NextEngine laser scanner offered a solution which was both accurate and affordable, offering the facility to produce models with greater precision in the regions of interest for the development phased array techniques using positioning jigs. It was found that the models produced using traditional CMM point data for re-engineering and production of spare components, provided extremely tight tolerances for clearance fits for installation, but was lacking accuracy in the more subjective regions such as the platform radii and aerofoil transition of CAEFTR blades. The application of the laser scanning system and subsequent parametric modelling allowed for an order of magnitude increase in data points collected which could be used to accurately model the inspection regions of the component. Subsequent design of inspection techniques using positioning jigs made directly from these CAD models will show how this improvement in accuracy has led to the deployment of previously impracticable inspections.

4.4 Development of novel jigs utilising rapid prototyping techniques

4.4.1 Introduction

For the reasons laid out in 4.2.4 pertaining to cost, manufacturing lead times, and accuracy of probe positioning, a new design philosophy was pursued which would overcome these obstacles and facilitate deployment across a wider range of inspection challenges. The main challenge was to develop a design methodology which would allow total control over the jig and wedge design and manufacture them both quickly and cheaply.

The complexity of applying phased arrays to blade root geometries required accurate models, as described in the previous section, combined with advanced CAD modelling tools and ultrasonic ray tracing simulation software. CIVA, which was utilised by the author throughout this project and described in section 4.2.2, offered a method of simulation by ray tracing but was limited because it allows only one complex CAD model to be manipulated and offers only simplistic refracting wedge shapes to be created for simulation. Furthermore CIVA is unable to provide transferable wedge positioning data or skew angle data relative to the refraction surface which would be critical in accurate CAD modelling of positioning jigs. By combining phased array vector ray tracing and beam profile simulation into the AutoCAD environment, Zetec's 3D simulation package offered the solution for designing jigs for precise phased array probe positioning on complex geometric problems.

4.4.2 Zetec 3D simulation tools

Although obsolete in the Zetec product line up, having been replaced and integrated into UltraVision 3^{TM}, the advanced 3D simulator had some significant advantages which were critical in its application to this project. The package is integrated into the Autodesk AutoCAD environment and was originally designed by David Reilly and marketed under the NDTSoft banner before being bought by Zetec. The significant advantage it offers is that it

facilitates full ultrasonic ray tracing capabilities within the CAD environment and allows simulation of rays through multiple interfaces of multiple complex CAD models. In practice what this means is that complex wedge designs, like the Rexolite jigs described in section 4.2.3, can be precisely modelled against the components allowing ultrasonic beam paths to be simulated through the various contact interfaces. Rather than utilising the basic parameterised wedges offered in CIVA, which are manipulated into position without actually graphically matching the surface and offering no output to a CAD environment, the Zetec simulator facilitates full design and modelling capabilities within the package. Rexolite jigs or rapid prototyped jigs (described later in the thesis) could be designed and positioned in the complex component and simulated to finely tune their accuracy. Without this capability the validity of probe and wedge positioning within the jig could only be proven after production.

For ray tracing no special algorithms or specific mathematical methods are used to generate the simulations. Instead rays are propagated and Snell's law is used to calculate mode converted and transmitted paths. The 'special' feature, for AutoCAD and UltraVision, is the interaction and visualisation with specimens and defects[109 110].

4.4.3 Rapid prototyping

Combined with the ability to design and simulate complex wedge geometries, rapid prototyping techniques were adopted to quickly and cheaply manufacture the inspection jigs required to position these wedges accurately. Ideally the material from which the rapid prototypes are manufactured would be used as the refracting wedge material, thereby allowing mono-block jigs similar to the Rexolite wedges described in section 4.2.3. This would facilitate an extremely effective solution to the disadvantages of Rexolite jig manufacture, but was not feasible due to the poor ultrasonic properties of the materials used. Rapid prototyping is a form of additive manufacture where a CAD model is segmented into

a series of virtual horizontal layers which are laid down one by one in various types of manufacturing process to produce the finished object, see Figure 4-30.

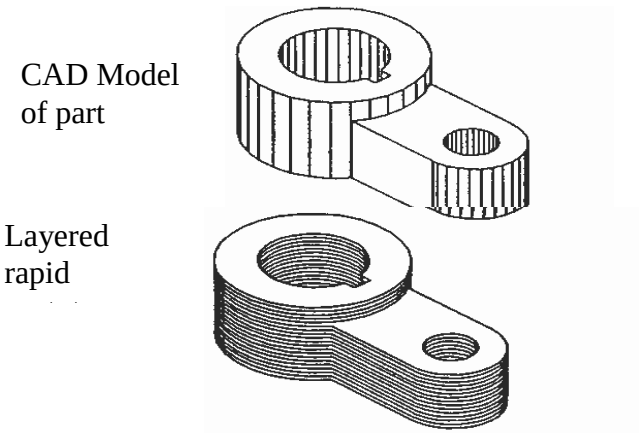

Figure 4-30 Illustration of layered manufacturing process

The advantage of this type of manufacturing process is the ability to produce virtually any shape or feature which might prove difficult to machine, extrude, cast, or forge, see Figure 4-31. First developed in the late 1980s for the production of prototype models[111], the development of new materials and even metals has seen these manufacturing techniques used in rapid manufacture. Where limited production runs are required the technique offers robust parts with very fast time to market and reduced tooling costs.

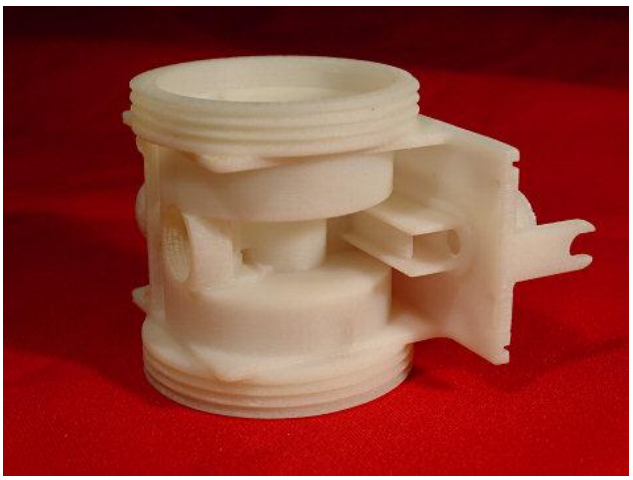

Figure 4-31 Example of a complex component manufactured by rapid prototyping

There are a number of different rapid prototyping technologies using various types of liquids, powders, metals or paper to produce models of the original CAD solid. Different products as listed in Table 4-2 offer different mechanical properties and accuracy so have their individual applications.

Prototyping technologies	Base materials
Selective laser sintering (SLS)	Thermoplastics, metals powders
Direct Metal Laser Sintering (DMLS)	Almost any alloy metal
Fused deposition modelling (FDM)	Thermoplastics, eutectic metals.
Stereolithography (SLA)	photopolymer
Laminated object manufacturing (LOM)	Paper
Electron beam melting (EBM)	Titanium alloys
3D printing (3DP)	Various materials

Table 4-2 Types of rapid prototyping technologies

The two main methods considered by the author were Selective laser sintering (SLS) and Stereolithography (SLA) each with advantages and disadvantages when considered in the context of jig manufacture.

4.4.3.1 Selective Laser Sintering (SLS)

The SLS method involves cutting the CAD model into 0.1 mm thick slices where each slice is “sintered” by a heating laser which draws the shape of the layer into the powdered material, melting the powder particles and bonding them together. The part is lowered by one layer thickness (0.1 mm) and the next layer is drawn and sintered by the heat laser, bonding it to the previous layer. This process continues until the entire part emerges after the last sintering layer. Fully enclosed regions within the part will remain full of un-sintered powder which requires extraction via drainage holes included in the model or added later and subsequently filled.

The latest process used by leading rapid prototyping manufacturers uses nylon Innov'PA 1550 for superior surface finish straight from the machine when compared to others such as Duraform PA, GF, EX, or EOS PA2200, and PA3200[113]. The resulting components can be used as functional prototypes, being strong, durable, water tight, chemical resistant, and high temperature resistant. Further increases in rigidity and stiffness can be acquired by use of Aluminium and glass filled Innoc'PA2550 which is mechanically similar to moulded Talc-filled polypropylene which is widely used as an engineering plastic[113].

4.4.3.2 Stereolithography (SLA)

The SLA method is the most widely used technology for prototyping and is generally considered to provide the greatest accuracy[112**Error! Reference source not found.**]. SLA is commonly used for aesthetic and conceptual models and masters for casting processes such as Polyurethane or Quickcast™ investment patterns. The SLA method again involves cutting the CAD model into 0.1 mm thick slices where each slice is "cured" by a UV laser which draws the shape of the layer onto a liquid resin. Where the laser hits the liquid a chemical reaction is set off, turning the liquid to solid. The part is lowered by one layer thickness (0.1 mm) and the next layer is drawn and cured by the UV laser, bonding it to the previous layer. This process continues until the entire part emerges after the last curing layer. Large models can be produced on a SLA5000 machine using Somos 11120 Watershed™ resin[113]. This resin has properties that match ABS plastic, which is widely used throughout the manufacturing industry. The Watershed™ resin has low water absorption properties meaning it is not affected by high humidity or wet environments. The published accuracy for the Somos 11120 Watershed™ states that standard for SLA models could be expected to be[114]:

In X/Y: about +/- 0.1225 mm for the first 25 mm, +/- 0.0.0245 mm for the each 25 mm thereafter.

In Z: about +/- 0.245 mm for the first 25 mm, +/- 0.049 mm for each 25mm thereafter.

Part geometry and build orientation can have a significant effect on the accuracy of produced parts and therefore should be considered.

It was found after procuring a sample of each material that finer details such as 0.5 mm diameter holes were not formed correctly with the SLS process but successfully formed using SLA. Also SLA resulted in a semi-transparent component compared to a solid cream coloured component from SLS. The transparency was seen as an advantage as it enabled easier seating of the phased array transducer when inserted into blind holes, and the ability to visually confirm that subsequent jigs were correctly seated on a component. The surface finish of SLA was also superior to that of SLS as it was smooth compared to a slightly grainy finish. The target accuracy for production jigs was 0.25 mm which was deemed to be an acceptable couplant layer thickness. Combining the accuracy of the laser scanning system with that of the SLA process should result in jigs with accuracy of approximately:-

Laser Scan tolerance ± 0.125 mm added to SLA tolerance ± 0.1225 mm giving an estimated tolerance of ± 0.2475 mm.

For these reasons it was decided that the SLA method would be adopted for the creation of inspection jigs.

4.4.4 Design of precision inspection jigs for critically limited geometry

The precision required to produce sensitive and repeatable phased array inspections of critically limited complex components such as the LP rotor stage 4 blades, which were laser scanned and modelled as described in section 4.3, was facilitated by a combination of simulation, CAD modelling and rapid prototyping. The inspection regions of this blade were essentially identical to those of the IP blades for which Rexolite wedges were developed, as described in section 4.2. However, the stage 4 blade was approximately half the size of the IP blades meaning that the available inspection surfaces were critically small. Any jigs

designed to position probes on this blade design would be required to be as accurate as possible, so taking the tolerance of the laser scanning system coupled with the errors in the SLA process it was estimated that the jigs would be accurate to ±0.2475 mm. Figure 4-32 shows the ray tracing simulation carried out to inspect the saddle root corner from the platform of the root block. It can be seen that there was no sufficient flat land from which to refract ultrasound which led to the radius being used to achieve coverage. The roof angle and disorientation of the wedge and probe were tuned to align the azimuthal scan. Once the position and shape of the wedge was modelled and tuned, a positioning jig was designed around it with a recess for the wedge and probe. It can be seen in Figure 4-33 that the wedge was designed to be wider by 1 mm either side of the probe. This was to facilitate the retro-fitting of a 9 mm by 9 mm Rexolite block, with its end machined perfectly flat and square, to sit snugly on the ledges formed in the jig by the oversized hole.

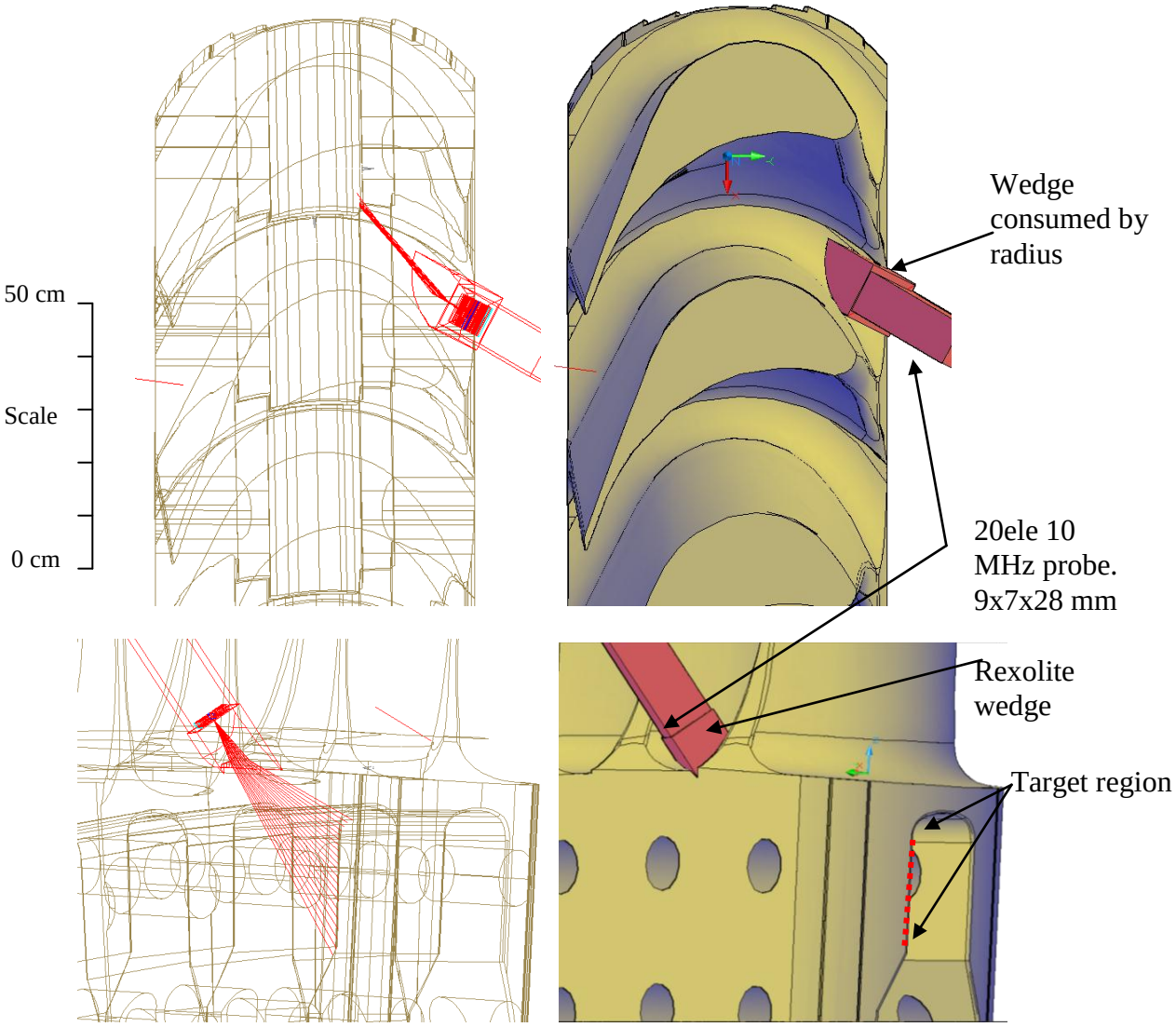

Figure 4-32 Ray tracing simulation of leading edge saddle corner

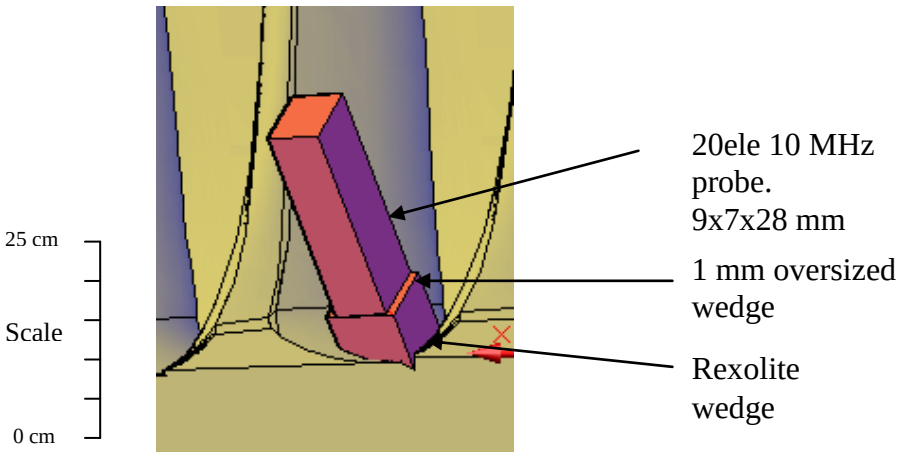

Figure 4-33 Illustration of oversized wedge to facilitate accurate retrofitting

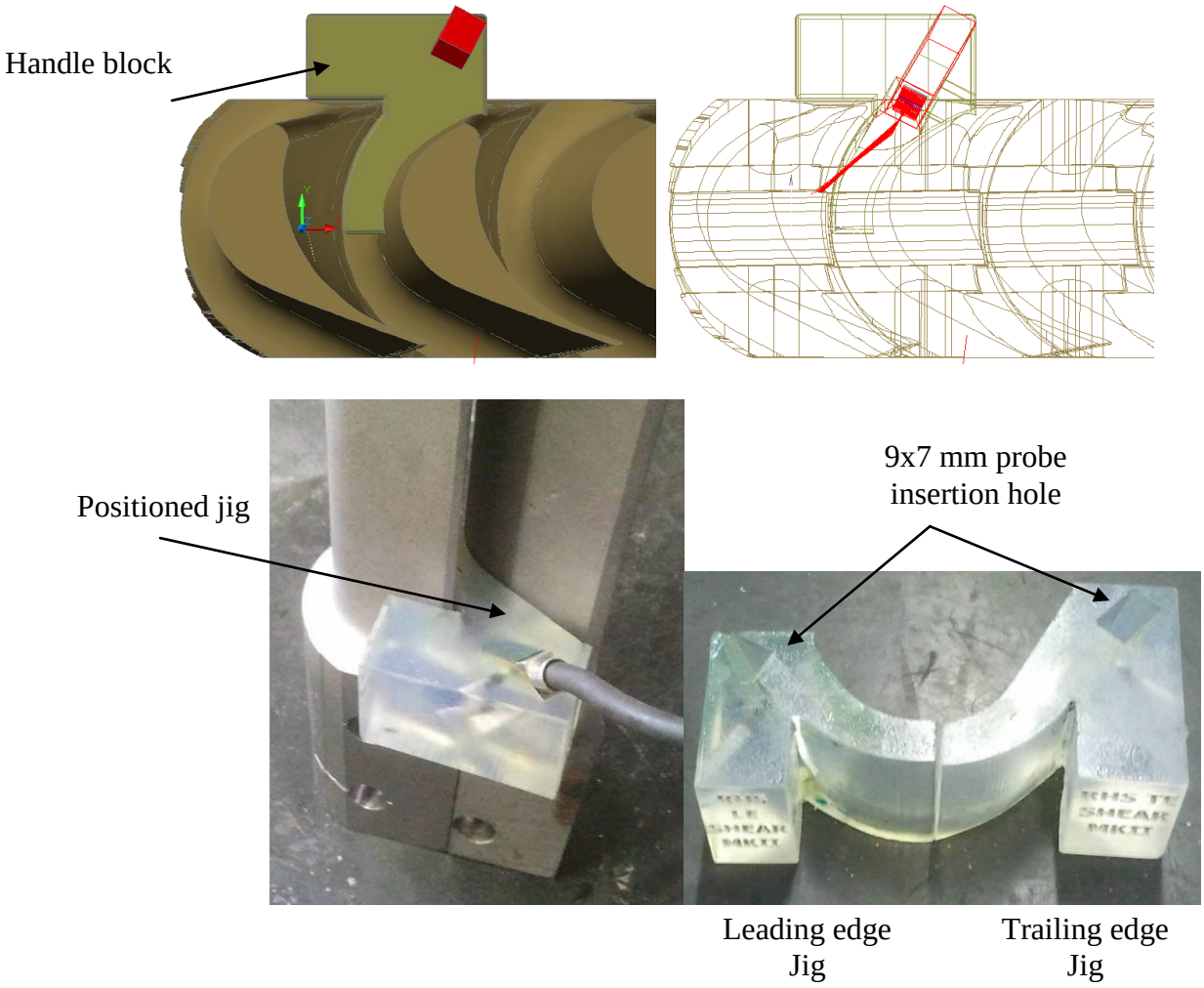

Figure 4-34 Positioning jig designed around probe and wedge position

Figure 4-34 shows how the jig was designed to fit snugly against the aerofoil and root block geometry of the blade, with clearance to the adjacent blade and a handle block for easy manipulation. The jig design included a square recess into which the 20 element phased array probe (Appendix B) with its fixing lugs removed could be inserted. Clamping screws, couplant exhaust holes, and the wedge identifier were embossed on the final model as seen in Figure 4-35. After manufacturing using SLA Watershed^{TM}, the final process was to thread the clamping hole and fix the square Rexolite block using epoxy; blending the protruding end of the wedge to match the complex shape of the jig completed the manufacture of the jig.

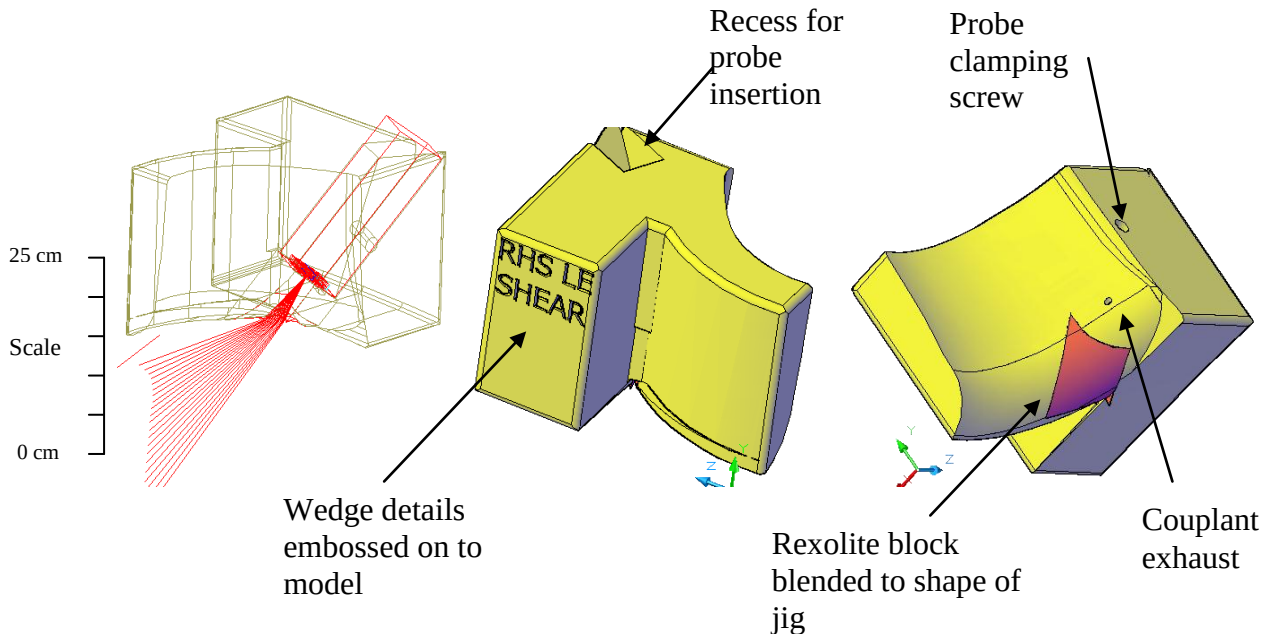

Figure 4-35 Finished jigs with retrofit Rexolite wedge and embossed

The final jig design requires a small amount of couplant to be placed onto the 20 element 10 MHz probe which is inserted snugly into the square hole on the jig. The couplant exhaust allows the excess couplant to be cleared while the clamping screw holds the probe firmly in position. The jig was tested against a reference blade containing an EDM notch across the saddle corner as illustrated in Figure 4-36.

The phased array laws were configured to produce an azimuthal shear wave scan between 35° and 75° in 0.5° steps. The resulting sector scan of the reference blade can be seen in Figure 4-37.

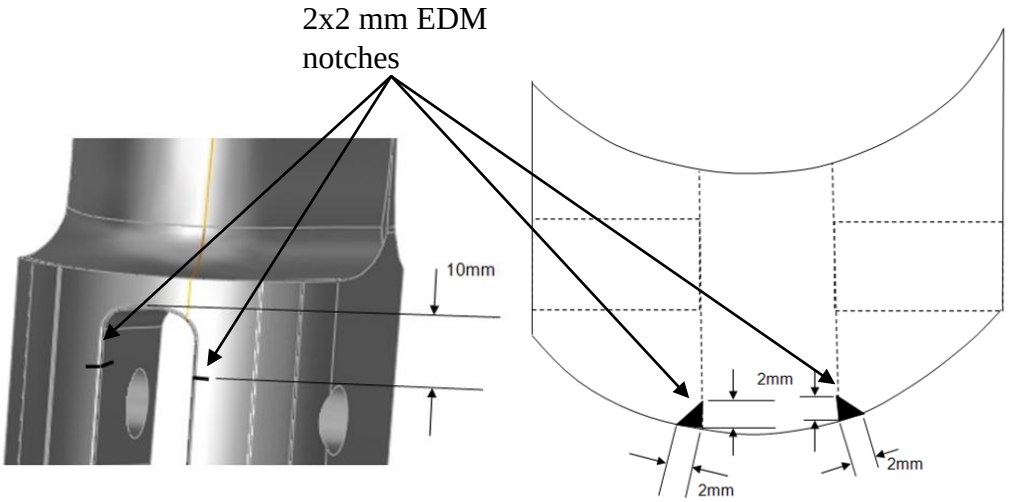

Figure 4-36 2 mm EDM notch in stage 4 LP rotor reference sample blade

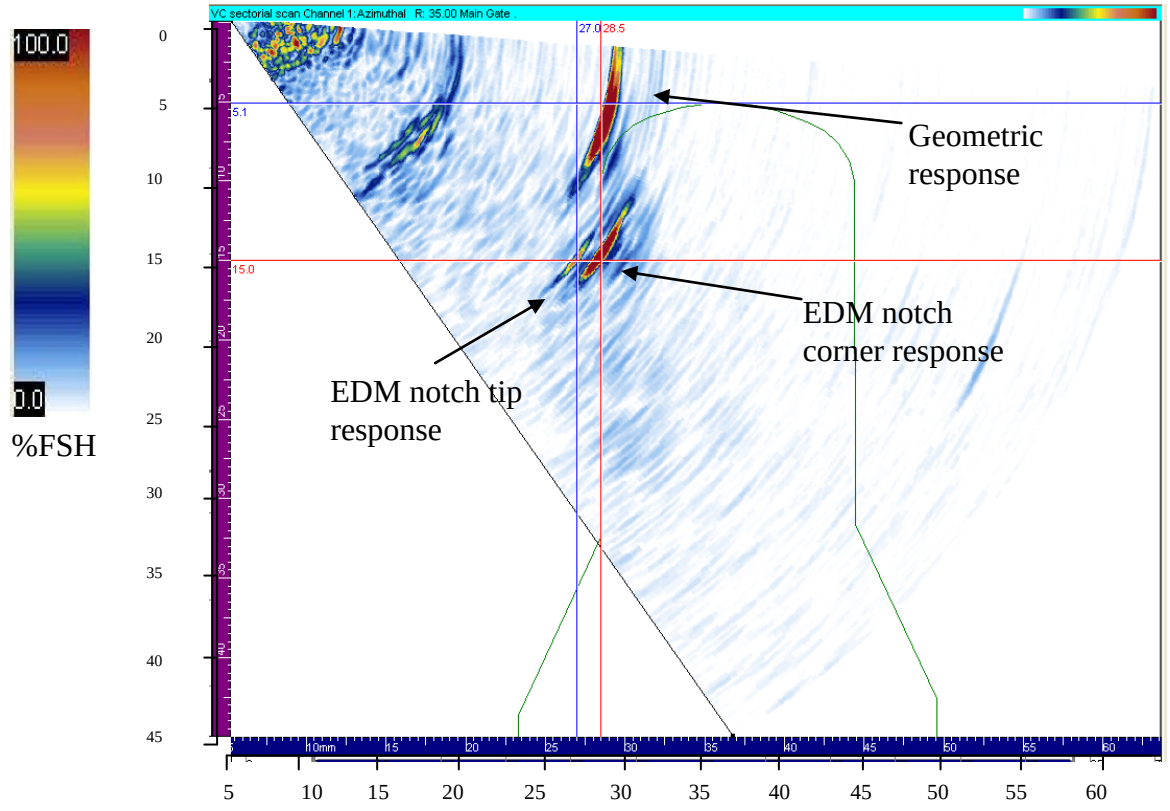

Figure 4-37 Sector scan of reference blade using rapid prototyped inspection jig (scale in mm)

It can be seen that the response from the EDM notch was clearly detected and sized with a high level of accuracy. Using the cursors on the sector scan the defect was measured at 10 mm beneath the saddle radius with a through wall extent of 1.5 mm, matching the true depth

of the defect which was √2 mm (1.41 mm). The geometric response appeared slightly distorted due to the ultrasound being refracted entirely through the radius of the root block.

4.4.5 Design of precision inspection jigs for inaccessible geometry

Further application of the design philosophy used for the inspection of critically limited complex geometry was also used to improve the extent of coverage for curved axial entry fir tree roots (CAEFTR) on the large last stage blades of low pressure (LP) rotors. The challenge in these cases was not necessarily the absence of generous inspection surfaces, but the inability to apply precision but straightforward inspections in regions with no physical access for manual probe manipulation. It was described in section 2.2.3 how critical regions prone to cracking on CAEFTRs include the inlet and outlet end concave root serrations and the centre of the convex root serrations as illustrated in Figure 4-38. During in-situ inspection access is limited to the outlet side of the blade, creating the problem of manipulating phased array probes towards the inlet side. In order to address this problem the same CAD based simulation and modelling environment was used to produce precision positioning jigs manufactured by rapid prototyping.

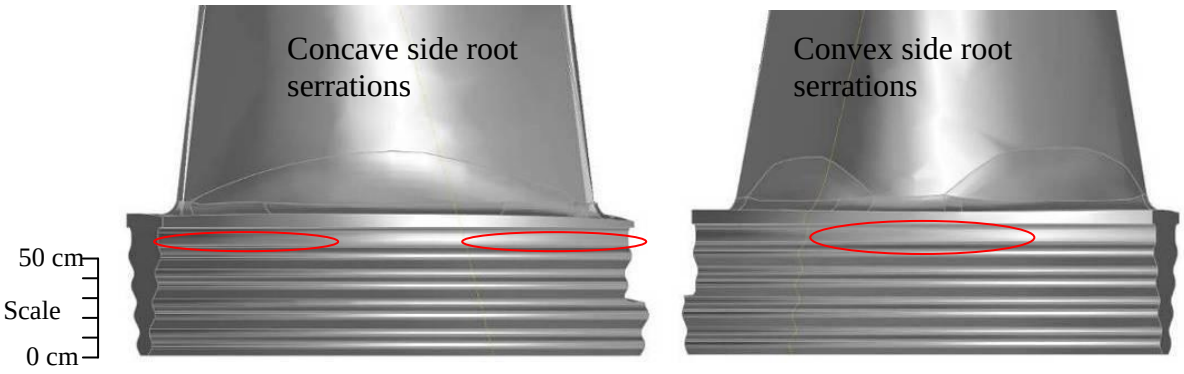

Figure 4-38 Critical defect regions of the curved axial entry fir tree root

In many CAEFTR designs the blade root platforms offer significant surfaces from which to interrogate the target regions. Within the CAD environment Rexolite wedges were modelled to target critical regions and tuned using ray tracing simulation, see Figure 4-39.

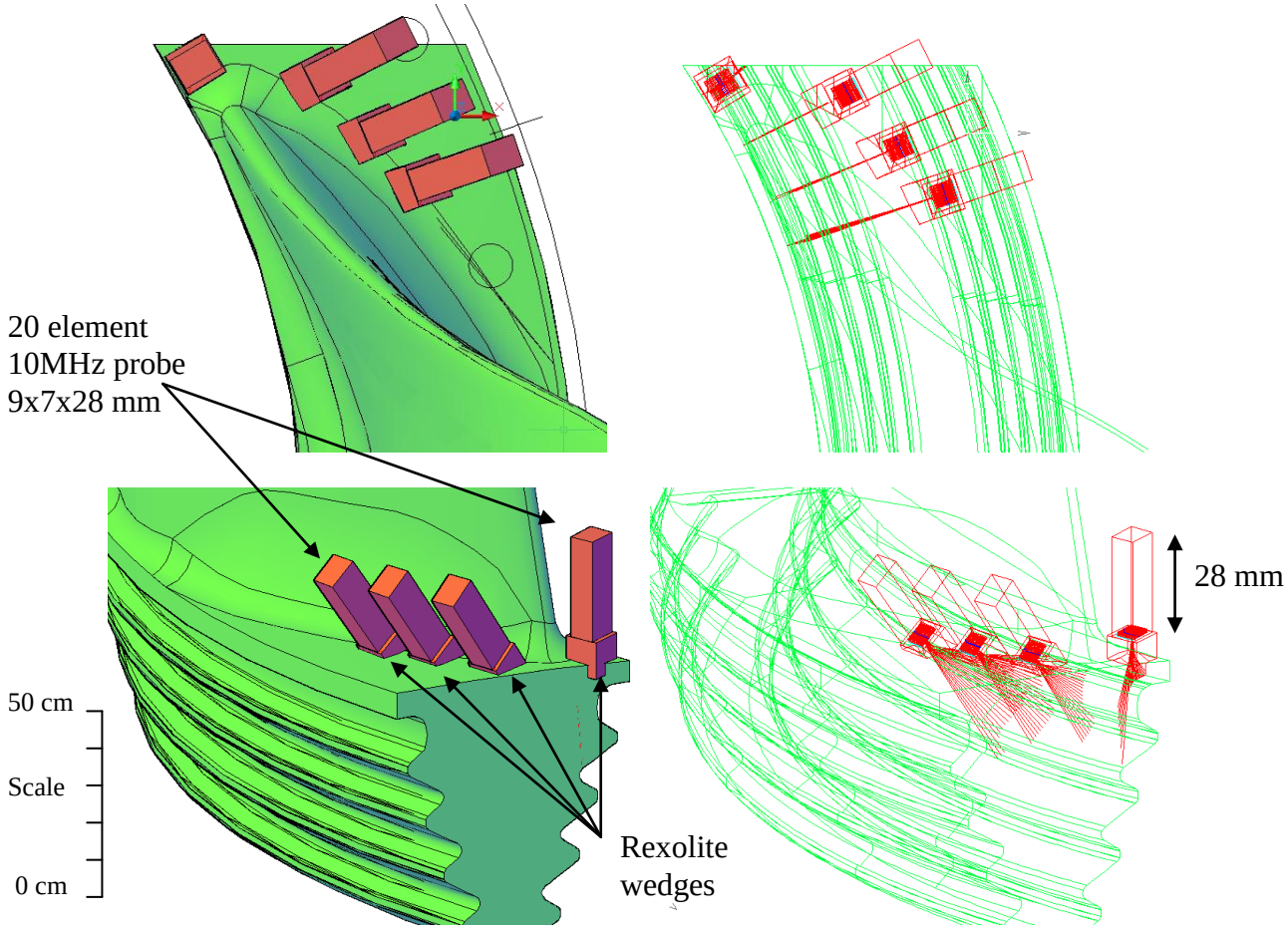

Figure 4-39 Ray tracing simulation to interrogate inlet end concave root serrations

With three shear wave positions and one compression wave position established a jig was modelled to fit exactly around the leading edge of the aerofoil and into the platform and radius, see Figure 4-40. An oversize recess was created for incorporation of the Rexolite wedge leaving 1 mm ledges to facilitate accurate retrofitting. Square holes were added to accommodate insertion of the 20 element 10 MHz probe, along with clamping screw holes and couplant exhaust holes, see Figure 4-41. As this jig would be used on the remote inlet edge of the blade it was necessary to incorporate couplant feeds to allow pumped liquid couplant to be fed to the surface of the component. A single couplant connection was created on the top of the jig feeding into a three branch manifold within the jig volume to feed each wedge position, see Figure 4-42.

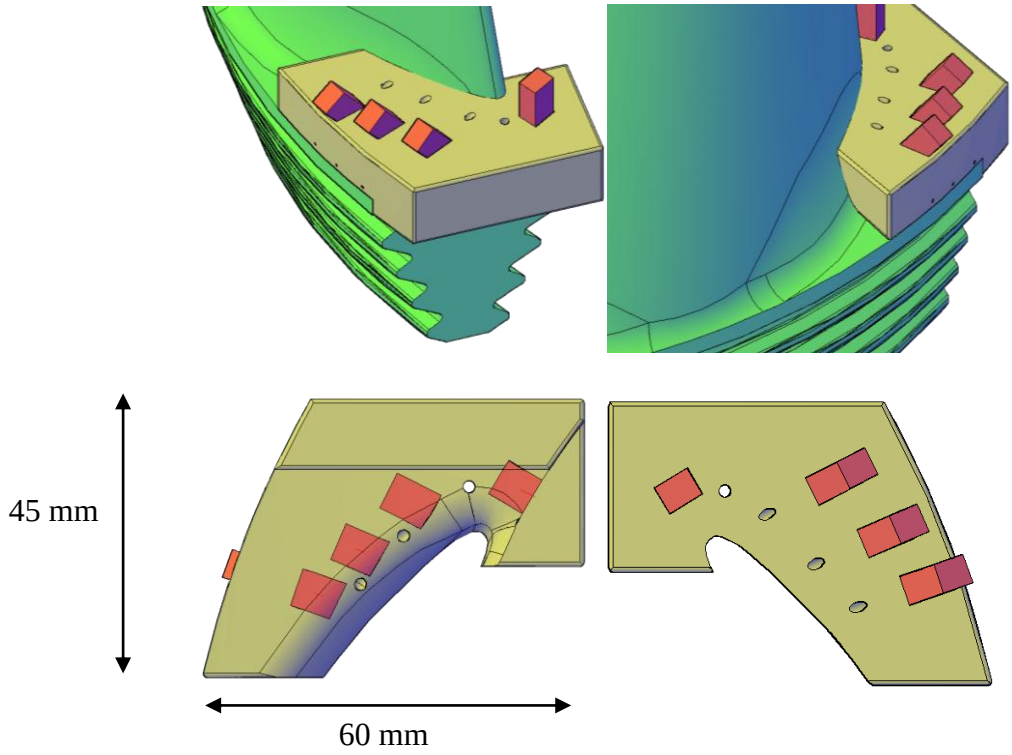

Figure 4-40 Wedge modelled to fit the inlet geometry of the blade

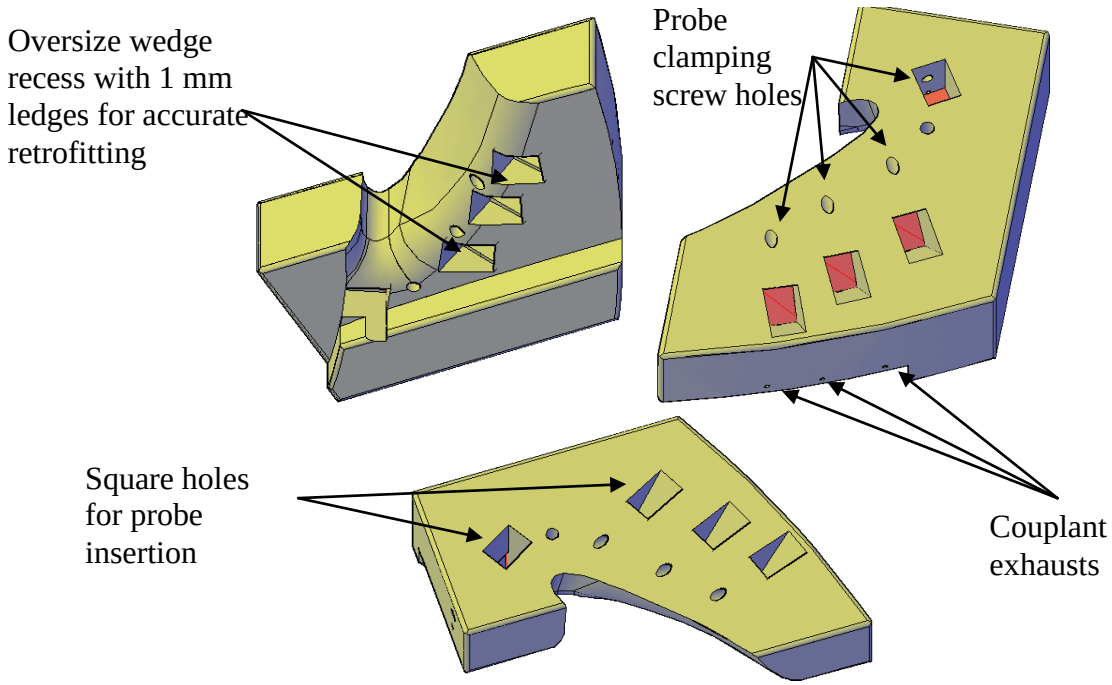

Figure 4-41 Inlet side inspection jigs with clamping screw holes and couplant exhausts

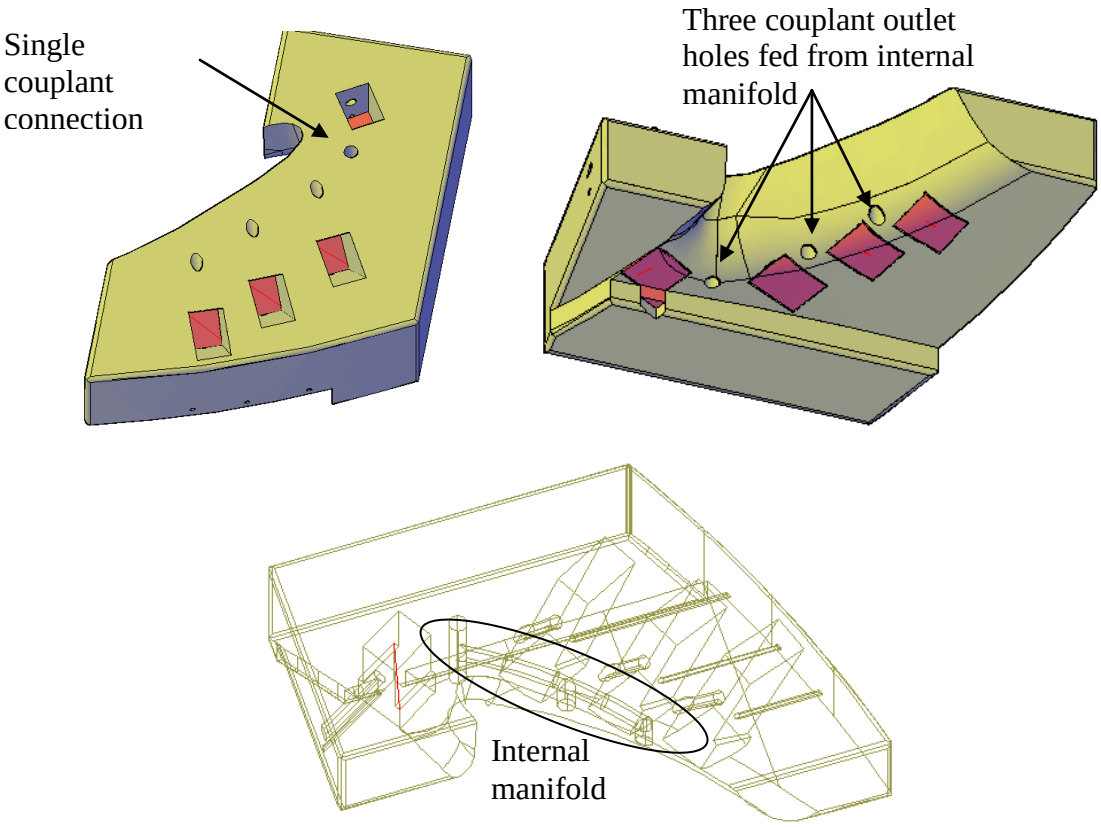

Figure 4-42 Incorporation of couplant feed manifold for remote coupling

After manufacturing using SLA Watershed^{TM}, the square Rexolite blocks were retrofitted using epoxy and profiled to match the complex shape of the jig. The clamping holes were threaded, couplant feed attached, magnets added to aid positioning, and a semi-flexible con-rod and handle were fitted to enable access to the inlet edge, see Figure 4-43. The final jig was able to facilitate the inspection of the concave root serrations from the platform with access from the outlet side of the blades, see Figure 4-44.

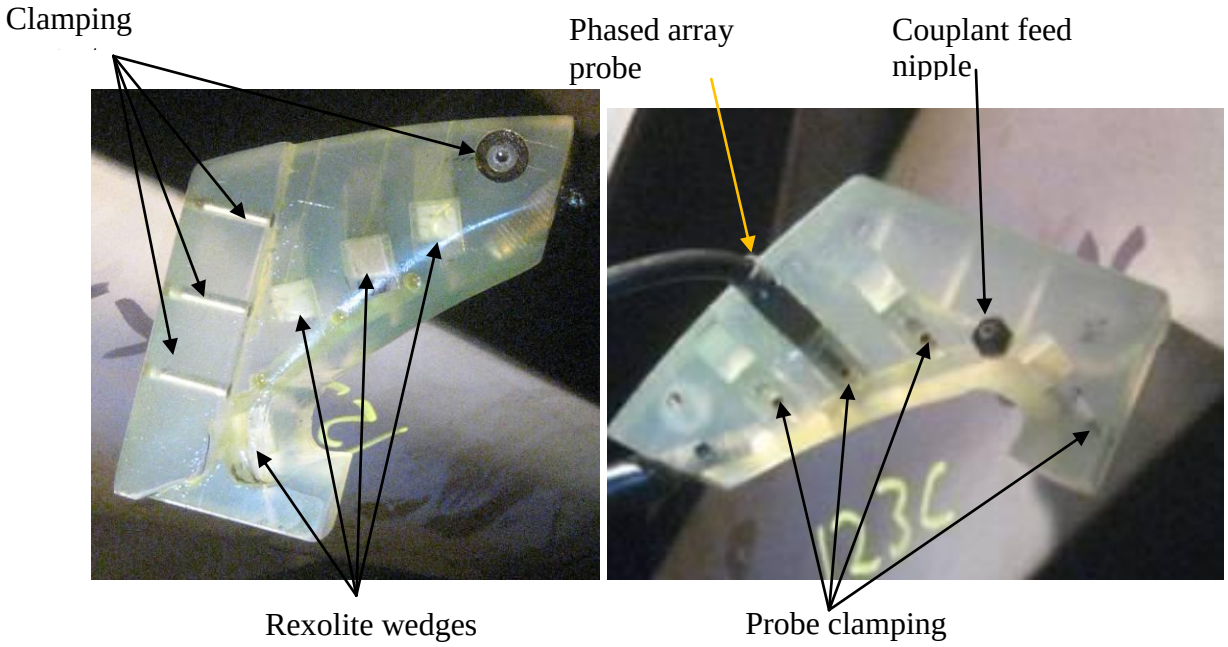

Figure 4-43 Final inspection jig complete with magnets, couplant feed, Rexolite wedges, phased array probe with clamping screws (for dimensions see Figure 4-40)

Figure 4-44 Finished leading edge inspection jig showing insertion from trailing edge to access the leading edge of blade root

The jig was tested against a reference sample containing 5 mm long by 0.5 mm deep

EDM notches in the target region as illustrated in Figure 4-45 and Figure 4-46.

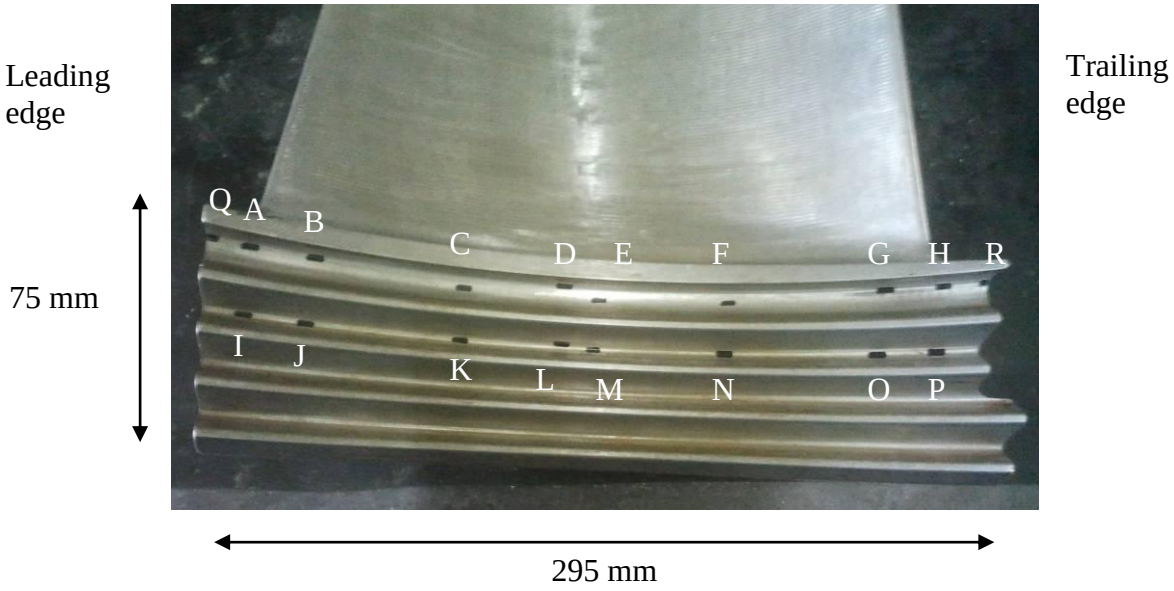

Figure 4-45 Reference sample containing 5 mm by 0.5 mm EDM notches

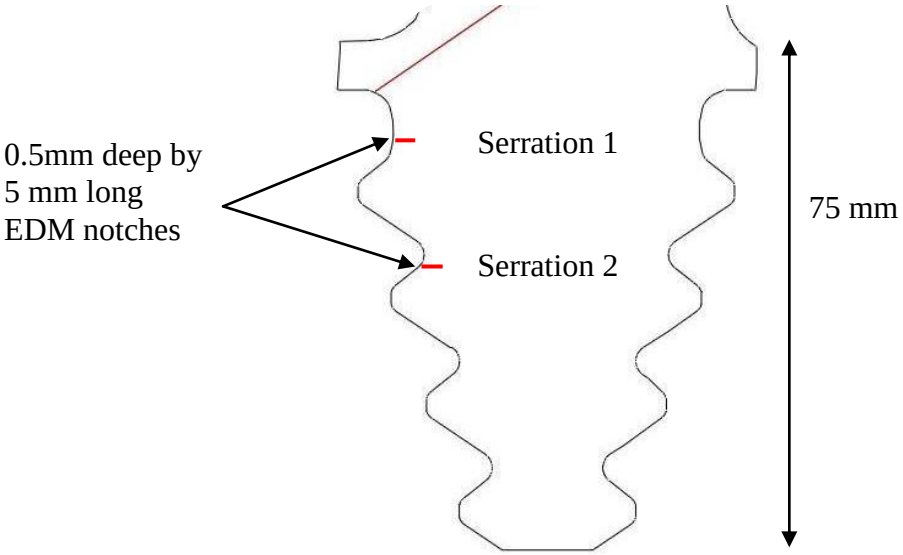

Figure 4-46 Sectional view of reference sample containing EDM notches

The phased array laws were configured to produce an azimuthal compression wave scan between -10° and 20° in 0.5° steps to interrogate notch Q and a shear wave scan between 35° and 75° in 0.5° steps to interrogate reference notches A, B, I and J. The responses from each notch were recorded as seen in the sector scans shown in Figure 4-47 to Figure 4-50. It can be seen that detection of each notch was positive and well resolved from the main

geometric responses. Because the probe positions in the jig were fixed to target a specific axial position around the root serrations, there would be blind spots in the axial coverage between each probe position around the serration. Although lateral beam spread might produce a reduction in this blind spot, it would still be necessary to ensure that the root serrations were interrogated around their full extent within the confines of this inspection. Rather than producing multiple jigs, each with the probe positions offset compared to the other for increased axial interrogation of the serrations, it was found that applying a small axial scan of the jig from its natural design position facilitated overlapping of the interrogated regions, see Figure 4-51. Coverage of this region was verified by detection of EDM notches which were offset from the design position of the jig, confirming that the blind spot regions were being sufficiently interrogated.

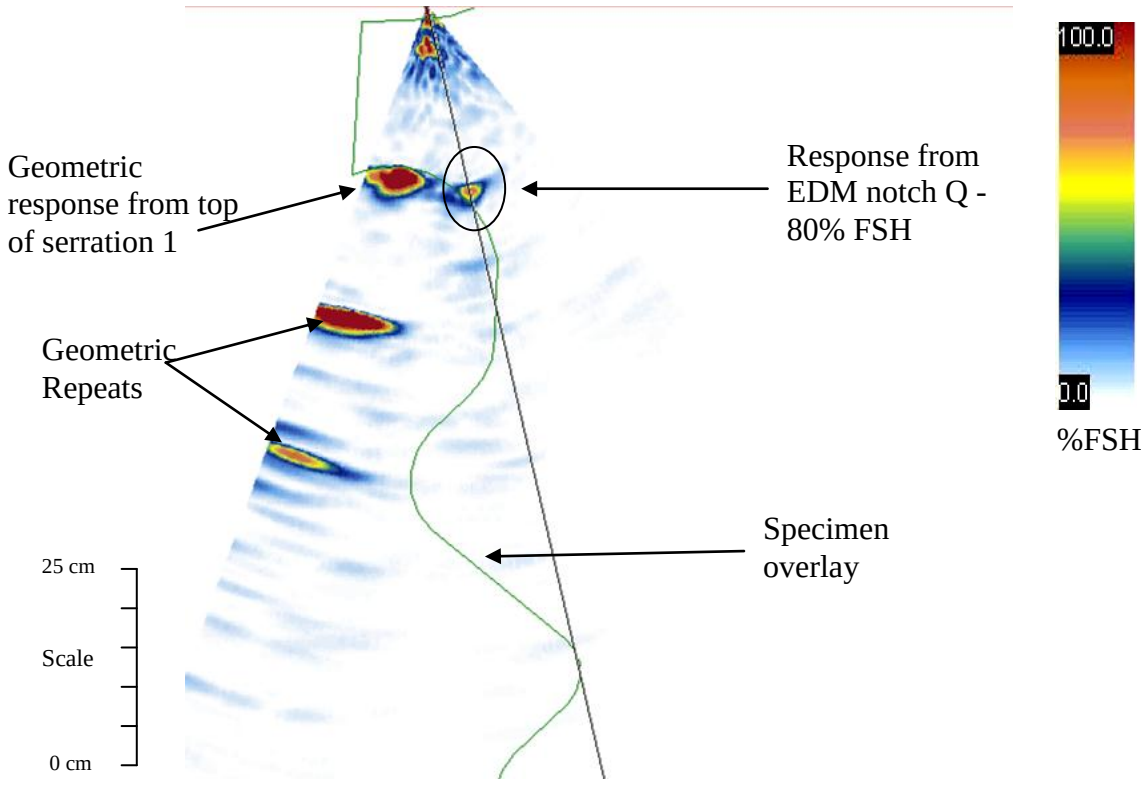

Figure 4-47 Phased array compression wave sector scan of reference notch 1

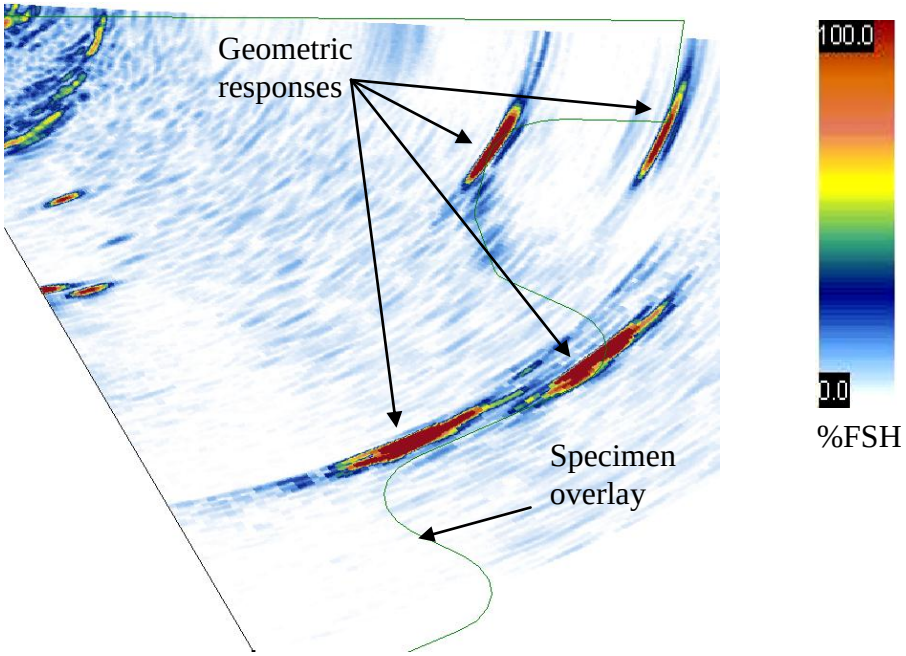

Figure 4-48 Phased array shear wave sector scan of defect free region

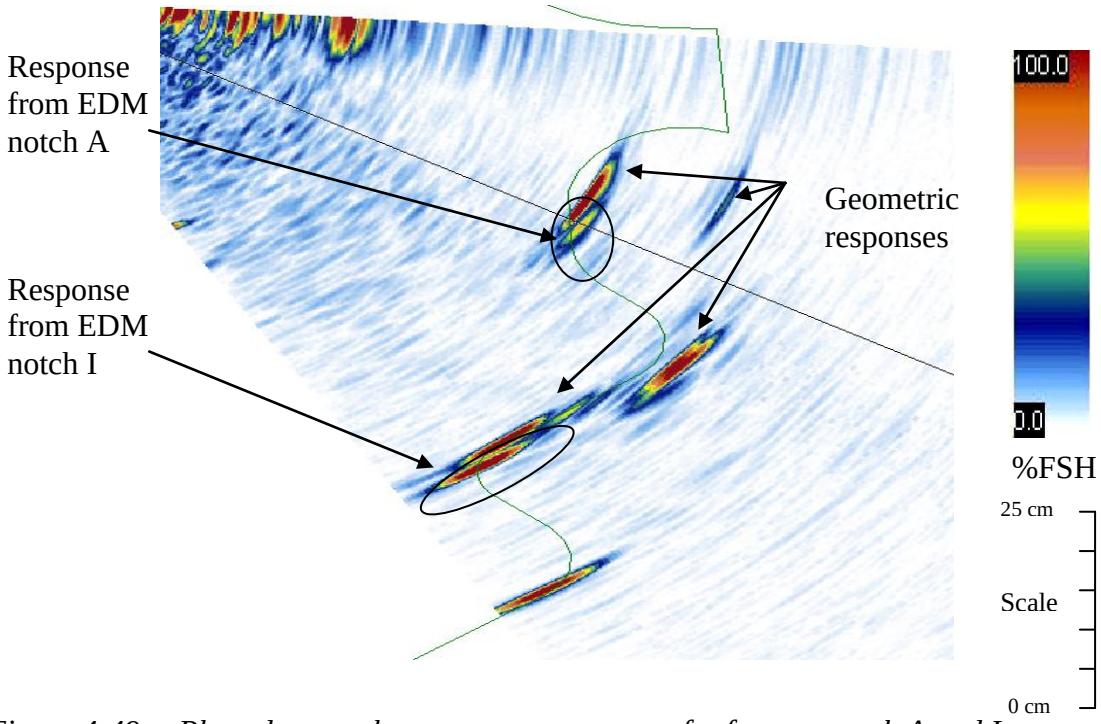

Figure 4-49 Phased array shear wave sector scan of reference notch A and I

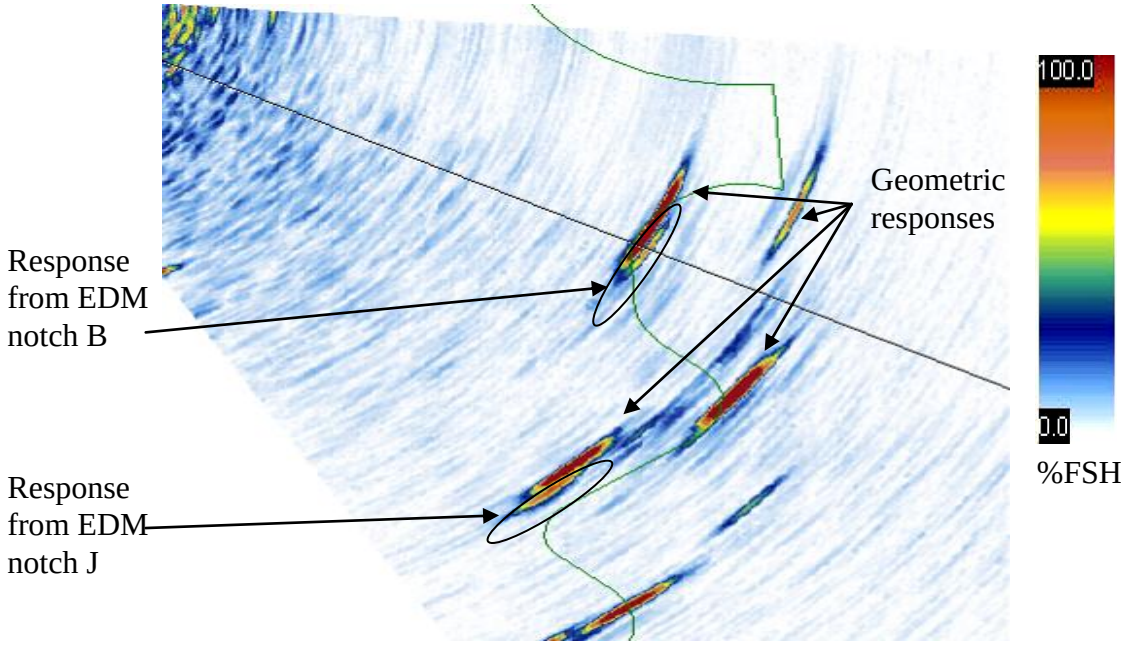

Figure 4-50 Phased array shear wave sector scan of reference notch B and J

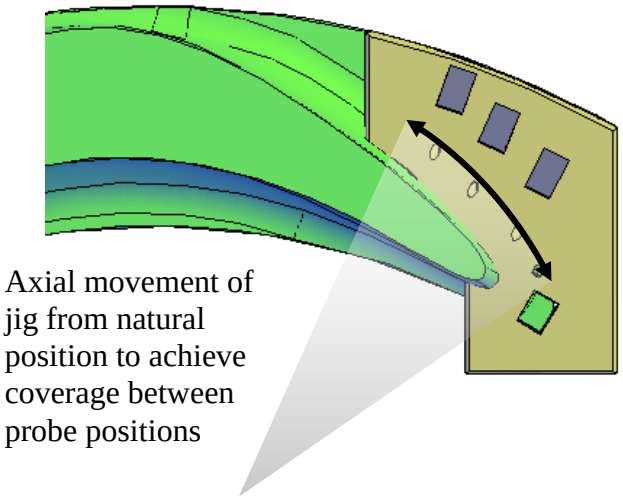

Figure 4-51 Axial scanning of jig to facilitate overlapping axial interrogation of the root serrations between probe positions

4.4.6 Discussion – Production of accurate positioning jigs

It has been shown that due to the accuracy of the CAD models produced from laser scanning and simulation tools built into the CAD environment, precision jigs have been designed to refract ultrasound into very limited and complex surfaces.

There were drawbacks to the process of producing jigs from solid Rexolite as described in section 4.2, which were seen by the author as limitations to their deployment across other complex inspection challenges. Short design cycles, limited budgets and technical shortcomings were addressed by developing the rapid prototyping methodology for jig design:-

- Rapid prototyping facilitated the production of any complex component, including very small items, both quickly and cheaply.
- Extremely precise probe positioning is set at the modelling stage and all significant features of the finished jigs are incorporated in the final design before manufacture.
- Time to market is extremely short and design tweaks can be incorporated and re-manufactured using rapid prototyping in a matter of days rather than weeks.

The cost of producing the Rexolite blanks described in section 4.2.3 was approximately £1400 which included modelling and manufacture of two blanks which were then used to produce 4 jigs. The lead time was two weeks and subsequent jig finishing added another two man days. To produce four equivalent rapid prototyped jigs the modelling would take one half man day and the production would cost approximately £150 with a two day lead time, adding another one half man day to retrofit the Rexolite blocks. In total, the rapid prototype jigs can be designed and manufactured in 3 working days for £150 compared to Rexolite jigs being designed and manufactured in 10+ working days for a cost of £1400.

4.5 Conclusions

The challenge set out was the application of ultrasonic phased array inspection, to improve coverage and defect characterisation on complex geometric components, with severely limited access or scanning surfaces. Conventional ultrasonic inspection techniques offered access to these complex components by use of miniature transducers, but suffered

critical deficiencies in detecting and characterising small defects and could be both complex and time consuming to apply. There were also severe limitations to the inspection of CAEFTR blade root designs when access in-situ was limited to the outlet side and prevented any kind of manual manipulation of probes at the inlet side.

It has been shown by careful specification of the phased array transducer, which offered functionality and small form factor, that inspection of components with severely limited access and space was facilitated. The initial approach, which took advantage of the bespoke transducer by using solid Rexolite wedges to appropriately refract ultrasound whilst doubling up as positioning jigs, proved to be a successful solution. The inspection of complex components with limited scanning surfaces and space was facilitated by this design approach, but was seen by the author as having a number of drawbacks. The approach was time consuming and expensive to deploy, was inflexible to design changes and there were doubts about the absolute accuracy of probe positioning.

A combination of accurate CAD model production by laser scanning, modelling and simulation within the CAD environment, and production via rapid prototyping, led to higher precision, shorter design cycles and cheaper more efficient production of inspection jigs. The methodology has enabled sensitive, repeatable and rapid inspection of small complex components and also facilitated the coverage of components where manual access is impossible and precision is required. This solution has been validated and utilised across numerous RWE and customer inspection techniques; and has prevented the need to remove LP rotors from their machines on two occasions, saving the company in excess of £1M [115] at the time of writing.

Chapter 5. Development of scanning aids for in-situ inspection of curved axial entry fir tree roots

5.1 Introduction

As briefly discussed in section 2.2.3.2, the aerofoils of most curved axial entry fir tree root designs offer significant scanning surfaces from which to interrogate the blade root serrations. The ability to perform such inspection techniques however is limited almost entirely by the inter-blade spacing, which in many cases severely restricts access for manual manipulation of ultrasonic transducers. Another significant factor which complicates inspection from the aerofoil is the mismatch in geometry between the aerofoil surface and the root serrations under test. This mismatch results in the ultrasonic beam which is transmitted into the component being refracted at trajectories which are not normal to the root geometry and therefore severely compromising sensitivity to defects. The critical 'at risk' regions of the blade root shown in Figure 2-27 and Figure 2-28, which include the first serration of the concave root towards the inlet and outlet ends and the first serration of the convex root toward the centre, are subject to the most severe geometric variations and require careful transducer manipulation to achieve coverage. Restricted inter-blade spacing and access limited to the outlet end of the blades whilst in-situ, coupled with the complex manipulation required to achieve sensitive coverage, has historically limited the extent of inspections available without costly removal of the rotor.

This chapter will discuss how innovative solutions were developed to accommodate the geometric mismatch of the aerofoil and root serrations, offering remote control of the phased array probes and facilitating in-situ inspection of CAEFTR designs. Experimental comparisons were carried out which show that a manual remote control scanner performed comparably to the manual application of phased array ultrasonics to detect EDM notches in

a reference sample. The development of these solutions also served to highlight shortcomings of the aerofoil inspection techniques leading directly to the invention of an innovative continuous wedge which is introduced in Chapter 6 and experimentally validated in Chapter 7.

5.2 Inspection coverage from aerofoils

It can be shown that significant coverage of the blade root serrations is achieved from the aerofoil. Figure 5-1 and Figure 5-2 illustrate the results of CIVA simulations carried out to assess coverage from the aerofoils of a common Alstom CAEFTR blade root. It can be seen that all serrations of the blade root appear to be well covered by the spread of phased array laws which form the sector scans. However this does not take account of the mismatched geometric shape of the blade root when compared to the aerofoil. One of the major features of the CAEFTR design is that the root region, consisting of fir tree serrations, is curved to a fixed continuous radius, allowing it to be axially located by sliding into matching steeples on the rotor disc. The curvature of the blade aerofoil does not match the radius of the root serrations and is in fact made up of continually changing radii, see Figure 5-3.

It can be seen that the aerofoil curvature of this particular design can be approximated by at least three different radii of different size and centres (shown as blue circles). Figure 5-4 shows how the mismatch affects the trajectory of the refracted ultrasound which is significantly less than 90° and not perpendicular to the root inspection zone. Reflections from root geometry and potential defects would occur at a trajectory away from the transducer and therefore produce poor sensitivity and non detection. To overcome the disorientation whilst performing manual manipulation, the probe is skewed to normalise the refracted beam to the root geometry. The effect of skew is illustrated in Figure 5-5 where the probe has been skewed by 15° to achieve a trajectory which is normal to the root geometry.

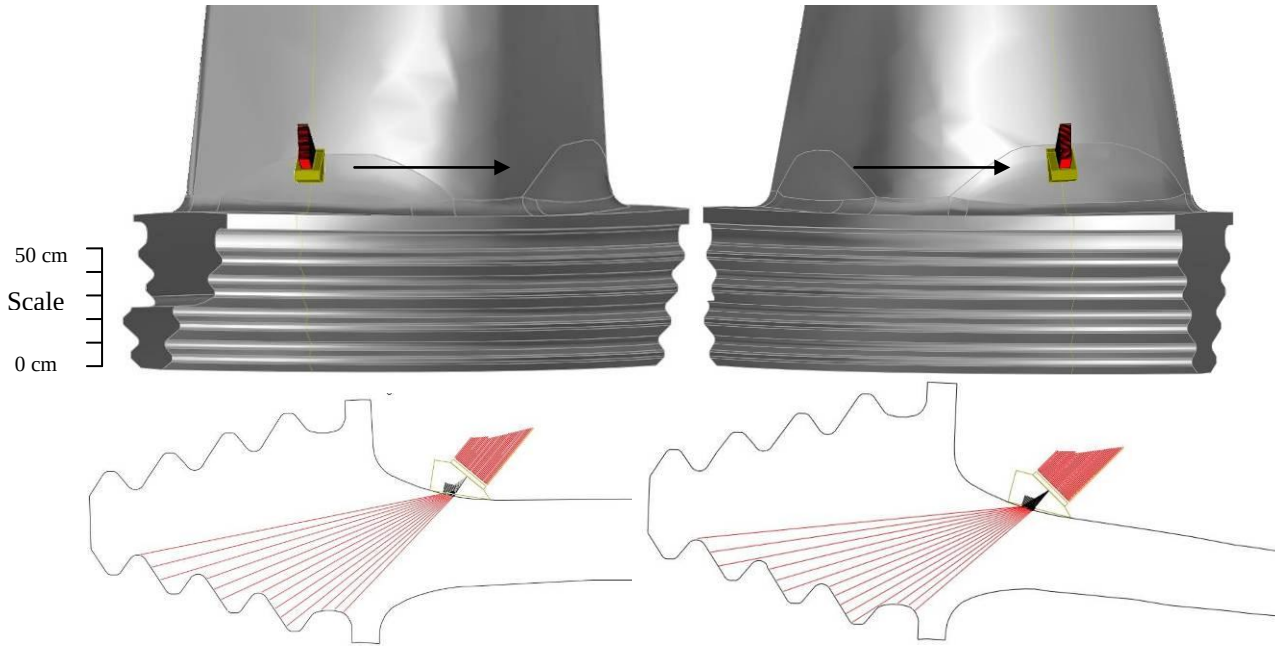

Figure 5-1 Simulated inspection coverage of the concave root from the convex aerofoil illustrating the phased array laws making up the sector scan

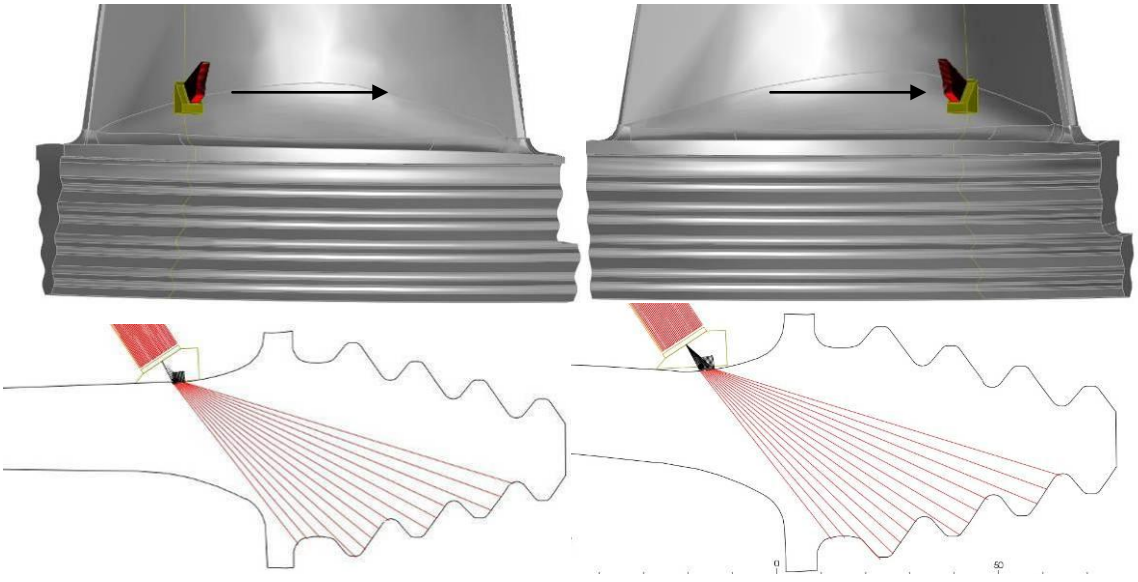

Figure 5-2 Simulated inspection coverage of the convex root from the concave aerofoil illustrating the phased array laws making up the sector scan

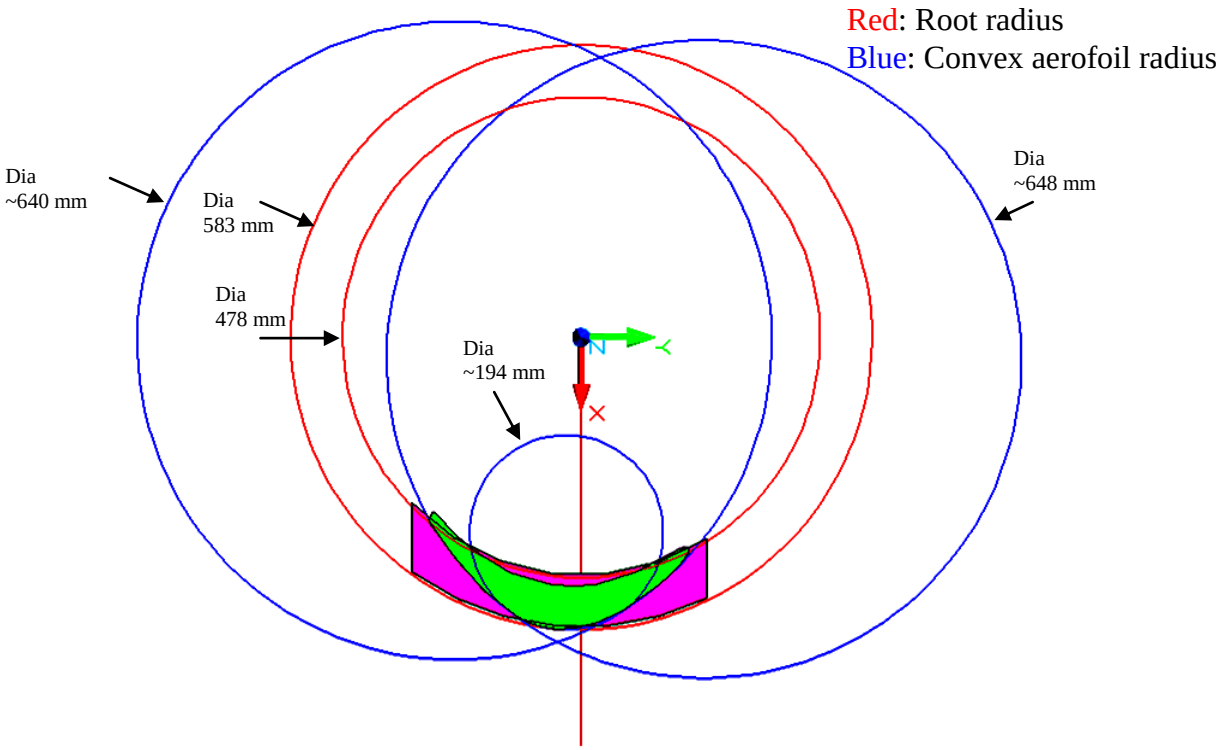

Figure 5-3 Geometric mismatch between blade root and aerofoil showing that the convex aerofoil can be approximated to three entirely different radii

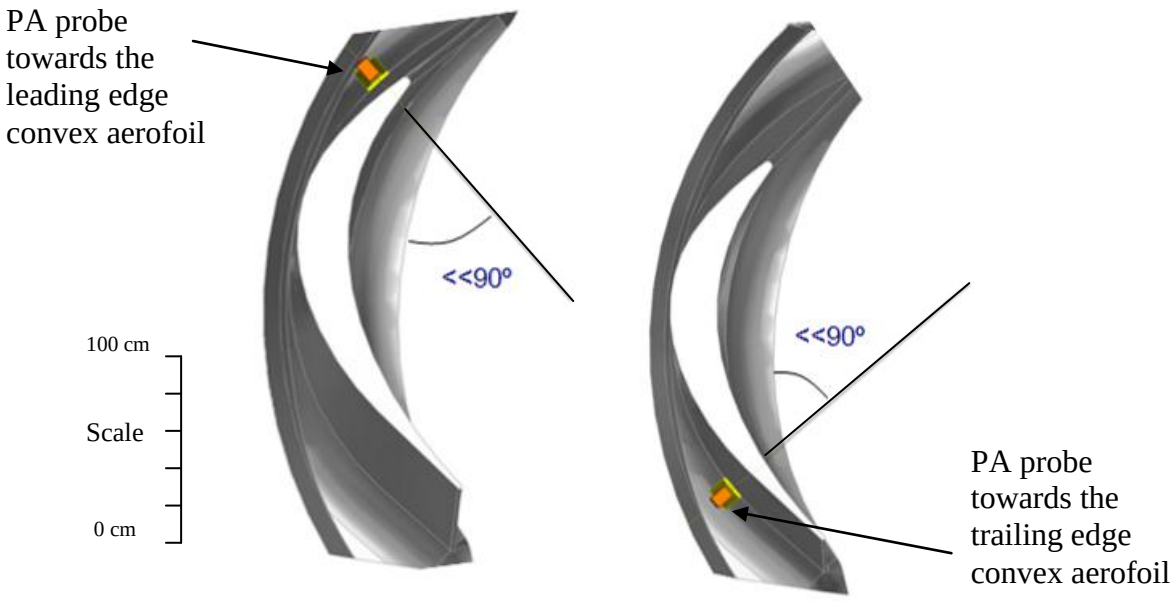

Figure 5-4 Illustration of non perpendicular beam trajectories due to aerofoil and root geometric mismatch

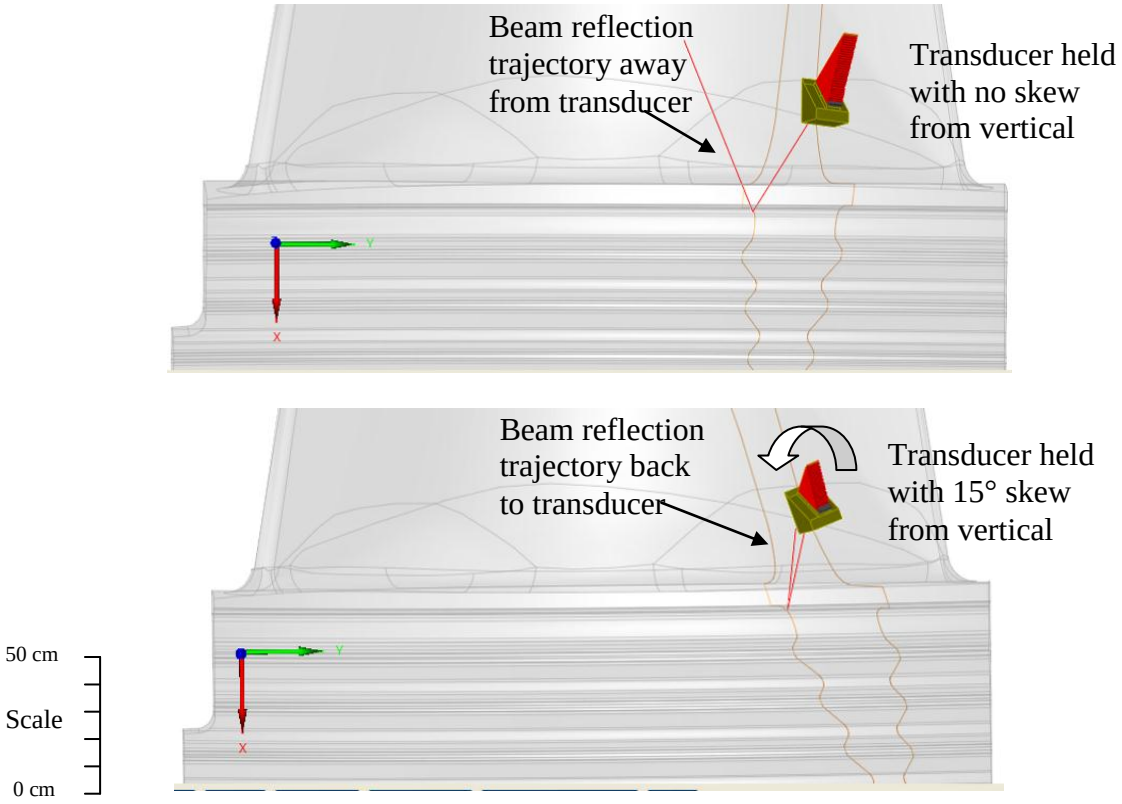

Figure 5-5 Simulation to determine the required probe skew which normalises the beam trajectories at the inlet end of the aerofoil interrogating the concave root

Application of mechanical skew is straightforward during manual scanning along the aerofoil surface; given that feedback from geometric responses on the sector scan display is used to maximise sensitivity to defects. Manual manipulation of the transducer however is restricted by the available space between adjacent aerofoils and is in many cases impossible.

The amount of skew required varies dramatically depending on the physical position around the aerofoil and also varies from one blade design to the next depending on the amount of geometric mismatch between the root and the aerofoil.

5.3 Bespoke scanning frames (Zetec)

An inspection aid was required which could facilitate the mechanical manipulation of the phased array probe around the aerofoil of the blade whilst providing the means to remotely skew the probe. It was shown in section 2.2.3.4 that mechanised systems, which utilise

encoded scanning frames driven by motors, have been developed for some blade root designs which have very limited aerofoil to blade root geometric mismatch. The overhead in extra equipment required to drive and control automated scanning equipment was seen as a significant disadvantage, as they would be deployed in confined spaces working from scaffold platforms within the steam space of the rotor. In order to provide a solution for inspecting blade roots from the aerofoil with no manual access and significant geometric mismatch, Zetec were commissioned by the author to design and manufacture a pair of manual scanning frames to fulfil certain specifications. Simulations were carried out to determine the positional height of the probe which would provide best coverage of serrations 1 and 2 of the concave and convex roots, see Figure 5-6 to Figure 5-11. It was found that a height of 25 mm above the platform would provide best coverage around the full extents of the inspection.

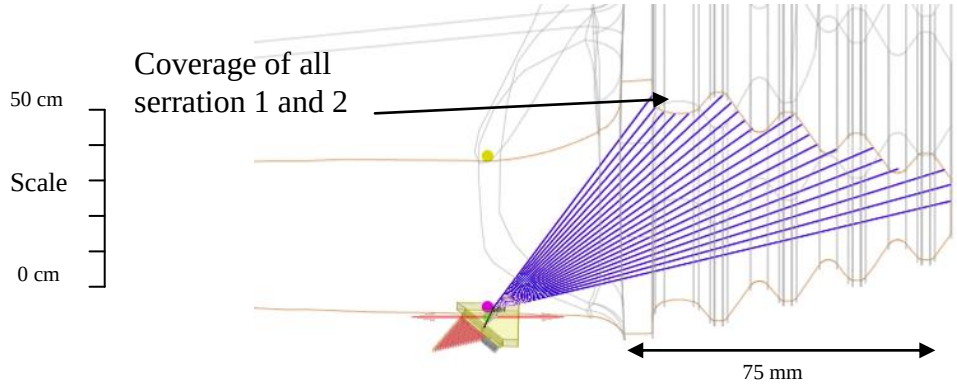

Figure 5-6 Simulation - Centre of concave root from convex aerofoil 25 mm above platform

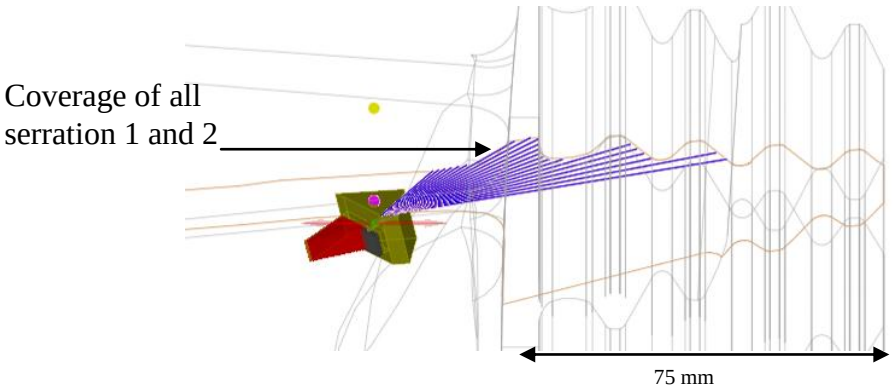

Figure 5-7 Simulation – Outlet end of concave root from convex aerofoil 25 mm above platform

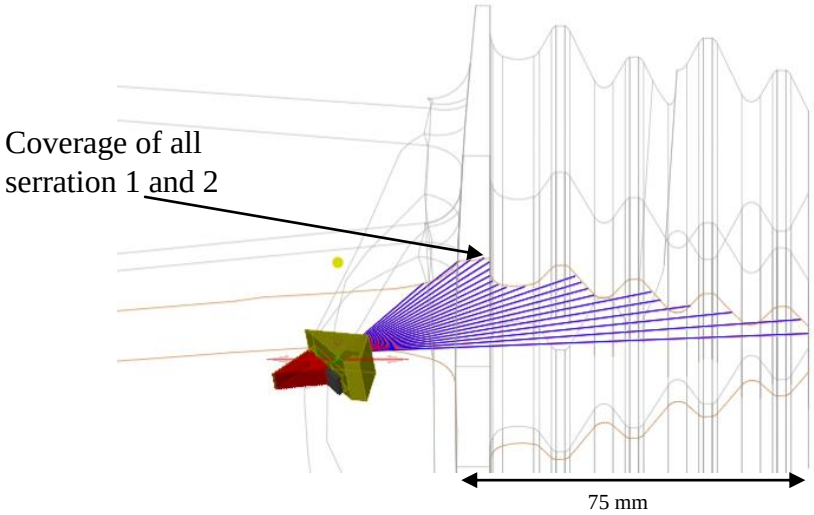

Figure 5-8 Simulation – Inlet end of concave root from convex aerofoil 25 mm above platform

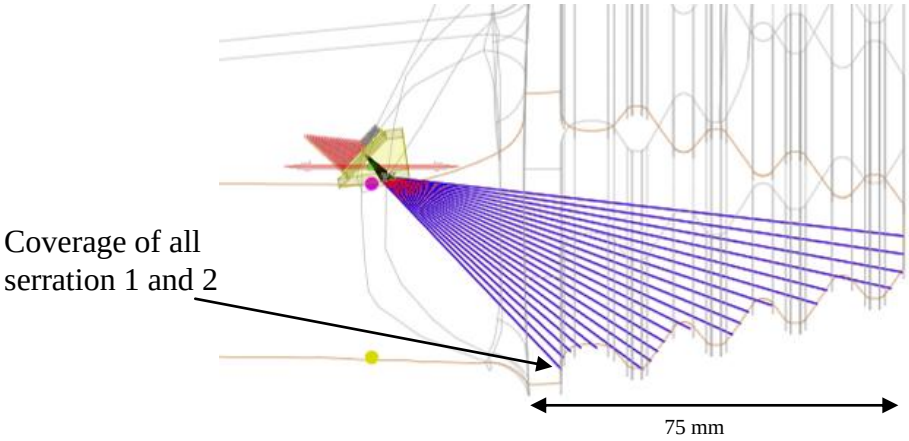

Figure 5-9 Simulation – Centre of convex root from concave aerofoil 25 mm above platform

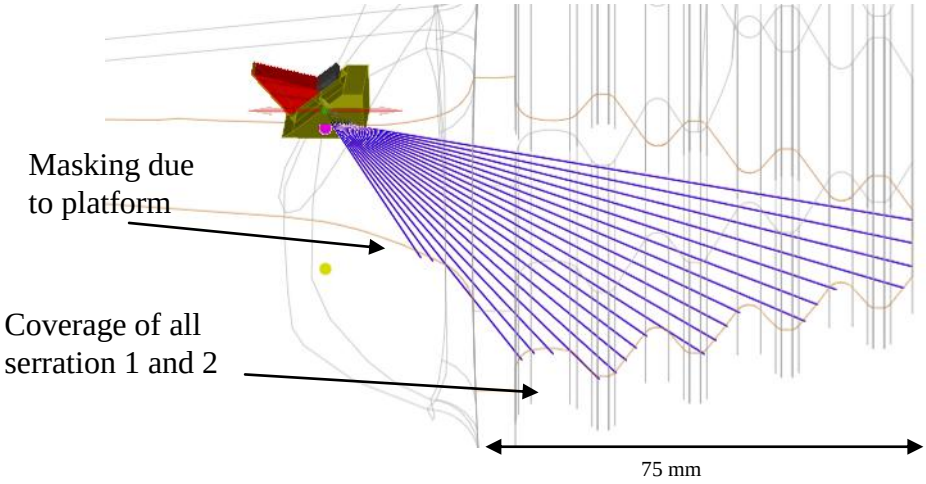

Figure 5-10 Simulation – Outlet end of convex root from concave aerofoil 25 mm above platform

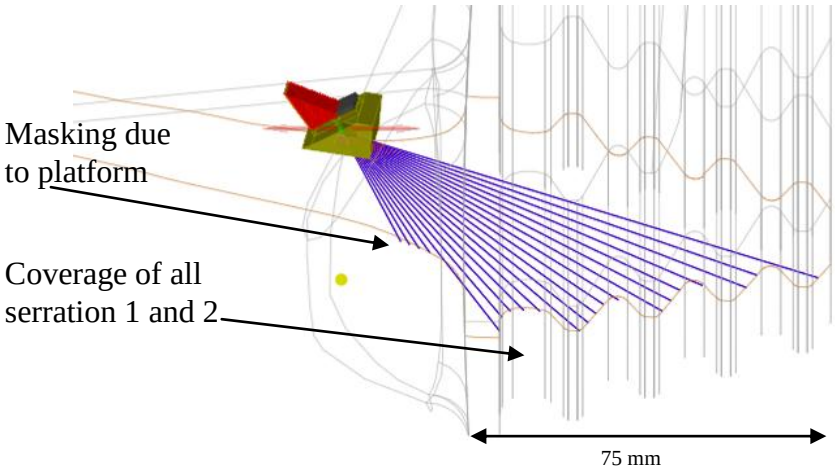

Figure 5-11 Simulation – Inlet end of convex root from concave aerofoil 25 mm above platform

5.3.1 Specifications

The design of the manual scanning frame, for the inspection of an Alstom 37 inch last stage blade which is common in the RWE fleet, was specified below; see Figure 5-12 and Figure 5-13.

- Scanner to be fixed and operated from outlet the end of blade
- Probe to be capable of scanning the full extent of both concave and convex aerofoil from the outlet edge to leading edge.
- The overhang of the frame at the leading edge shall be less 90 mm.
- Probe height adjustment to allow the front of the wedge to be between 0 and 30 mm from blade platform.
- Probe skew capability ±15º.
- Manual mechanical axial drive
- Encoder output

All other aspects of the design were left to Zetec and agreed at various design review stages over a period of four months.

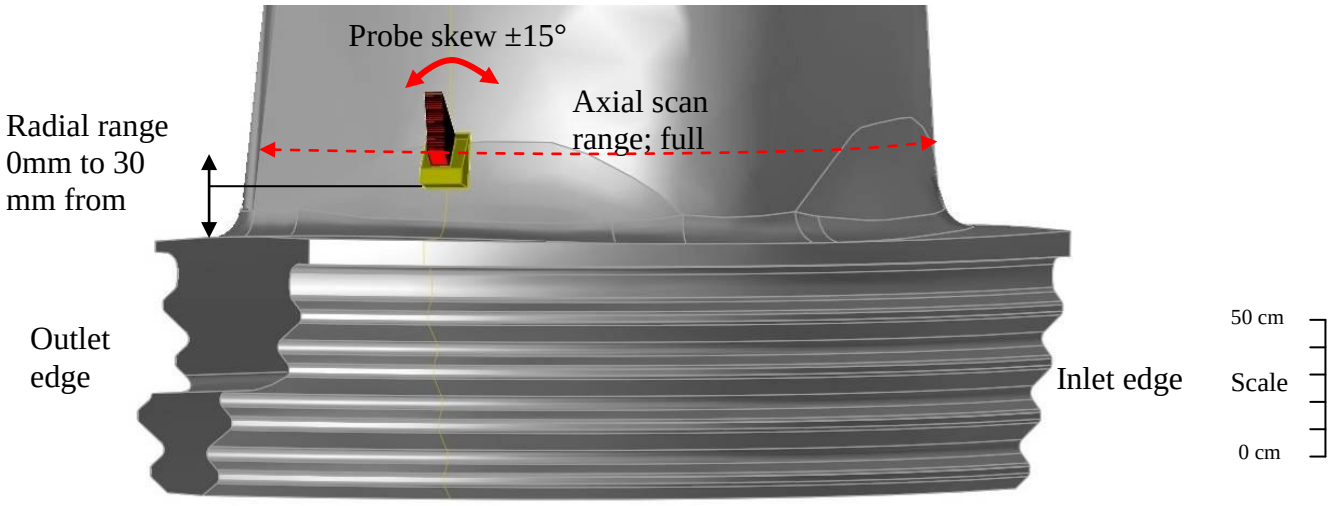

Figure 5-12 Convex side aerofoil Alstom 37inch CAEFTR

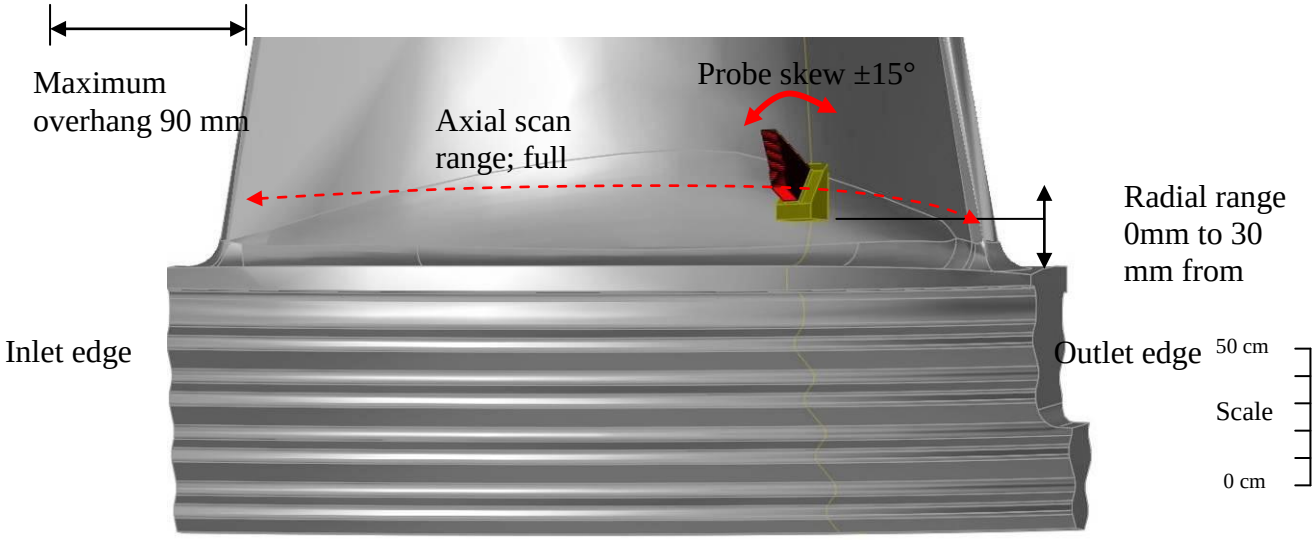

Figure 5-13 Concave side aerofoil Alstom 37 inch CAEFTR

5.3.2 Final design review

The final design review was carried out with a complete scanner specification document which incorporated any changes requested at previous reviews. The scanner and its primary features are seen in Figure 5-14 to Figure 5-20 below.

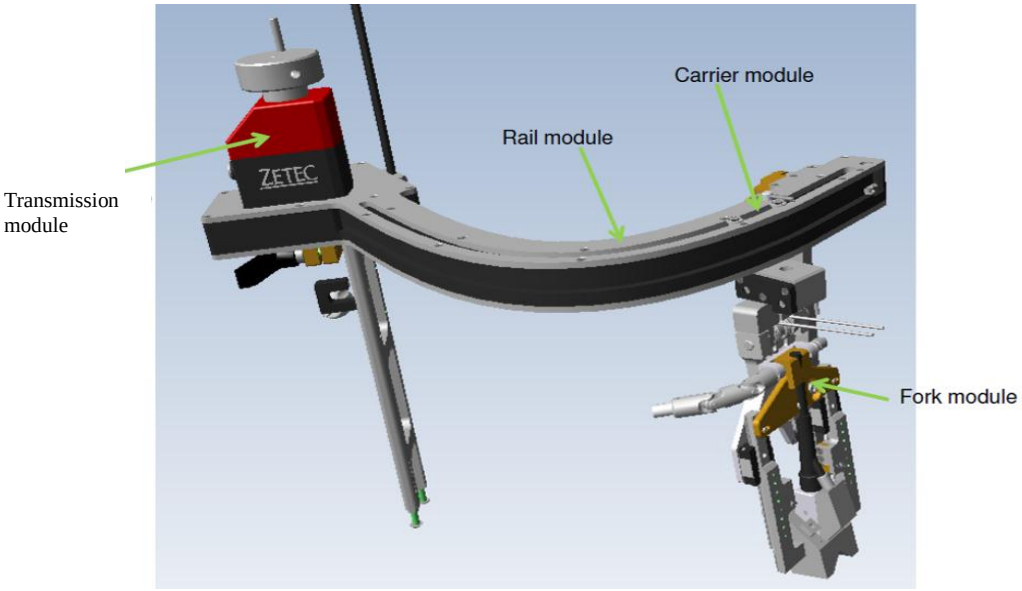

Figure 5-14 Rear view of Zetec manual scanning frame

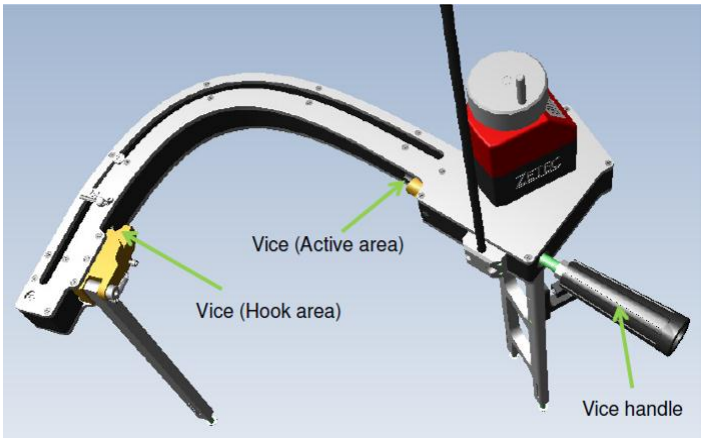

Figure 5-15 Top view of Zetec manual scanning frame

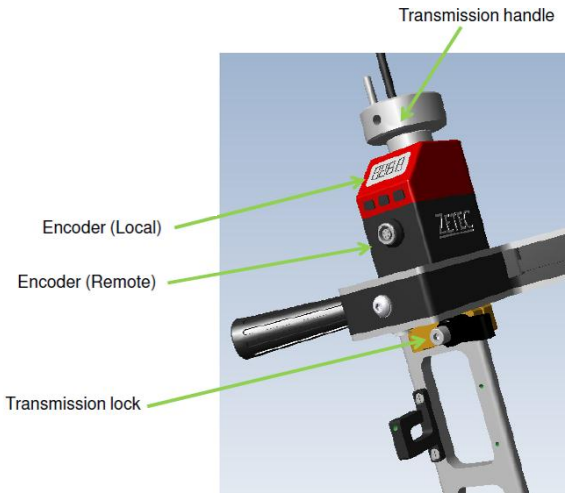

Figure 5-16 Manual drive encoded transmission module

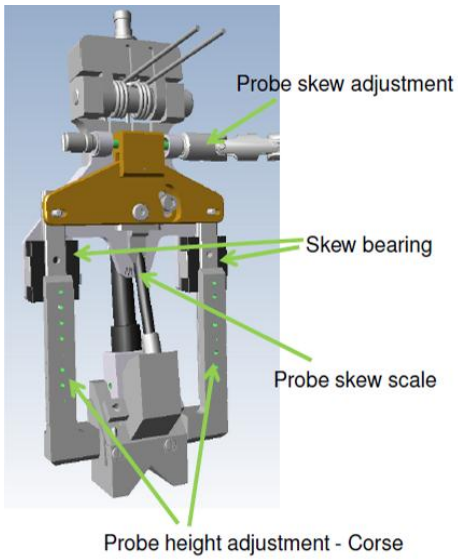

Figure 5-17 Probe carriage fork module with skew adjuster

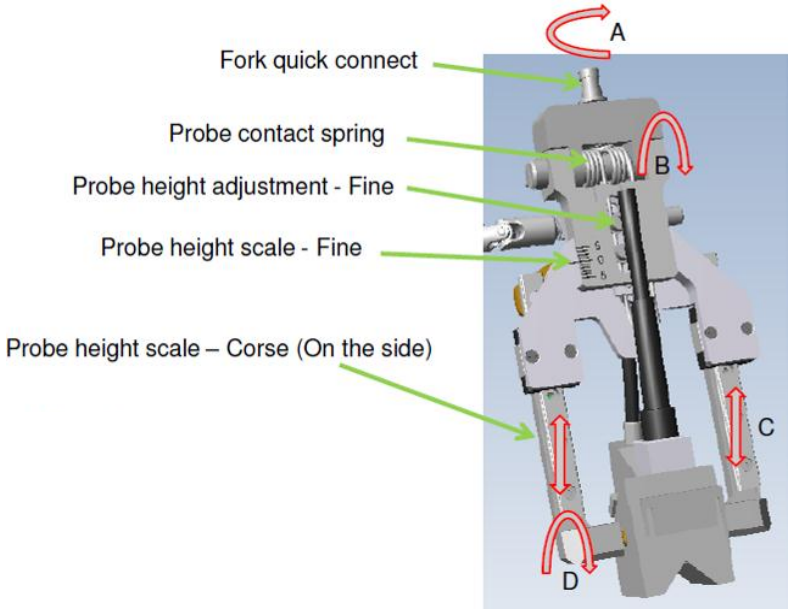

Figure 5-18 Probe carriage fork module height adjustment and articulation

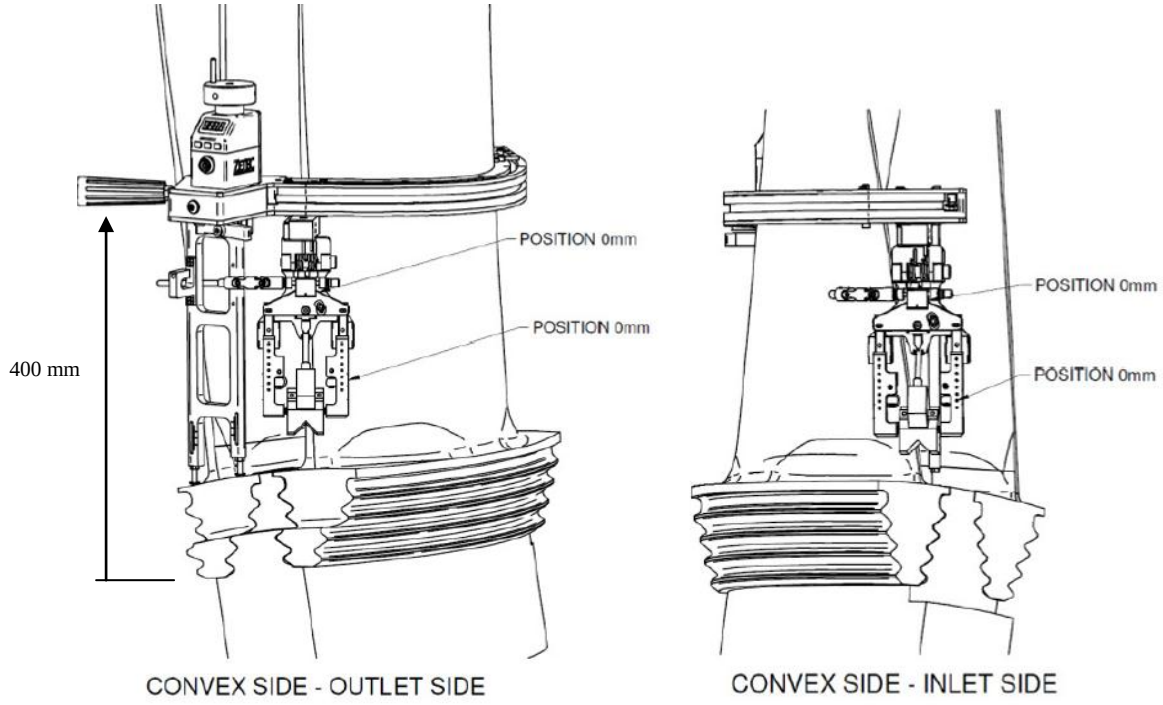

Figure 5-19 Convex side scanner positioning and axial scan range

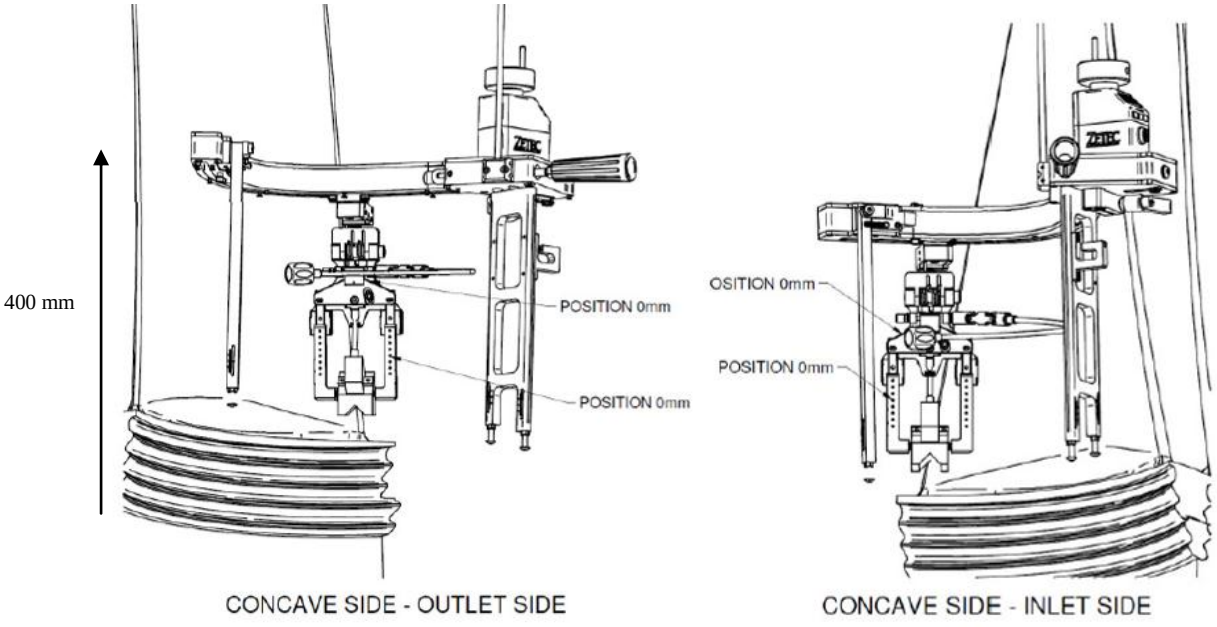

Figure 5-20 Concave side scanner positioning and axial scan range

The main features of the scanning frame include an encoded manual transmission module which allows the operator to precisely drive the probe carriage axially around the aerofoil, whilst the skew adjustment rod allows active control over the amount of skew applied to the probe. Due to the rugged construction and positioning feet, the scanning frame can be inserted accurately and clamped to the aerofoil in an efficient and repeatable manner, see Figure 5-21. Articulation via gimbals on the fork module allows the probe to be sprung down onto the aerofoil surface in a consistent manner regardless of position around the scan. Full adjustment of both the positioning feet and the fork module allow the radial height to be adjusted up to 30 mm above the blade platform, and fine adjustment to tune the scan position. The digital encoder built in to the transmission module provides an instantaneous measurement of axial probe position whilst the remote encoder output provides a quadrature signal for use in the phased array inspection equipment.

Figure 5-21 Images of scanning frame positioned on a rotor in-situ

5.3.3 Phased array wedge design

The scanning frame was designed to enable the operator to carry out a manual scan of the blade root; the phased array probe is scanned around the aerofoil whilst continual adjustment of the skew normalises the beam trajectory to maximise geometric responses from root serrations. The profile of the phased array wedge has a significant effect on the reliability of the coupling interface to the aerofoil and is complicated by the variation in surface geometry at different parts of the scan. Figure 5-22 illustrates the variation in wedge shape when profiled to match various axial positions on the aerofoil.

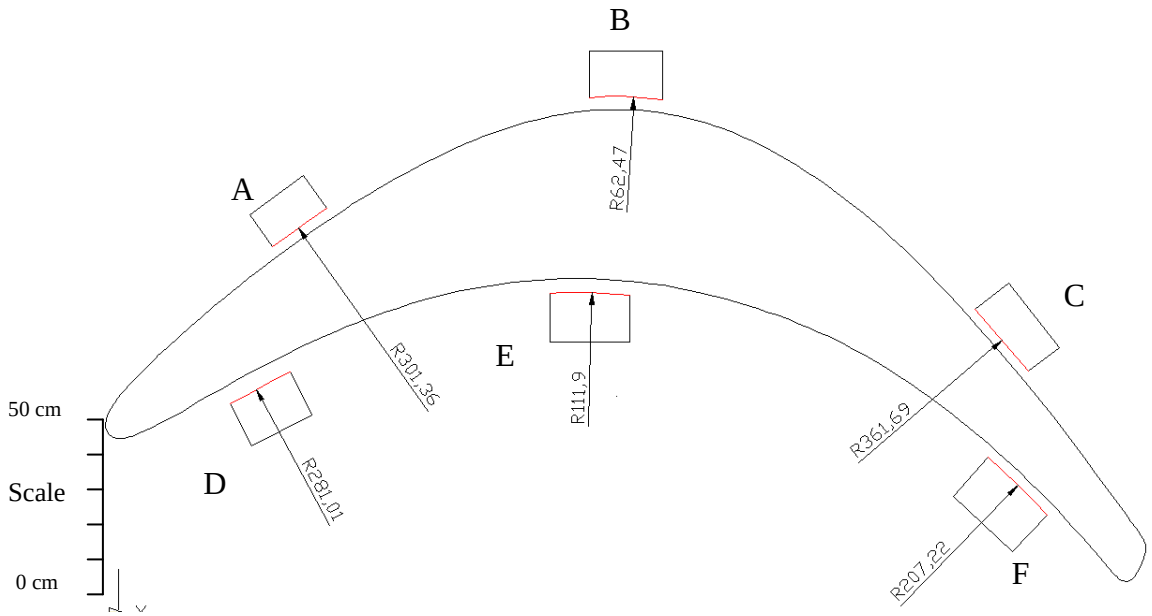

Figure 5-22 Illustration of wedge profiling

It can be seen that the radius at the apex of the convex aerofoil (B) is 62.47 mm compared to the radius at the trailing edge (C) of 361.69 mm and leading edge (A) of 301.36 mm. A similar but far less severe variation is present on the concave aerofoil where the centre (E) has a radius of 111.9 mm compared to the trailing edge (F) of 207.22 mm and leading edge (D) of 281.01 mm. This shows that no single profiled wedge can facilitate perfect coupling for all positions around either the concave or convex aerofoil. When utilising the scanning

frame the only adjustment available to optimise coupling is the axial drive and probe skew; the dexterity and fine control offered by manual manipulation is not afforded by the scanner, so the shape of the wedges was critical. Coupling of the probe was further complicated on the concave aerofoil by the skewing of the probe. The wedge couples to the aerofoil on a contact patch which is diagonal across the wedge surface; the corners of the wedge surface collide with the concave curvature of the aerofoil lifting the wedge and decoupling the ultrasound, see Figure 5-23.

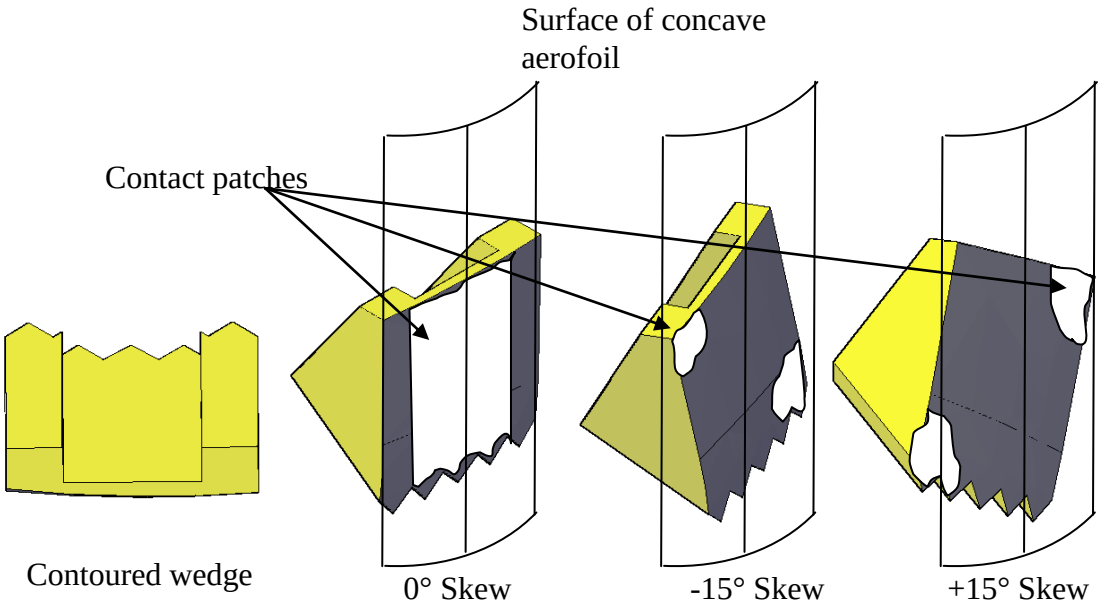

Figure 5-23 Illustration of wedge seating with skew applied

To produce efficient coupling around the axial extent of the concave aerofoil a wedge was designed to match the smallest radius at the centre and the corners were chamfered to reduce the effect of decoupling when skewed, see Figure 5-24. The resulting wedge matched the concave aerofoil precisely at the centre whilst interrogating the critical convex root regions (Figure 2-28) where little skew is required. Efficient coupling was also achieved on the larger radius toward the ends of the concave aerofoil whilst interrogating the less critical convex root regions, where the corner chamfers facilitated the greater skew angle required for normalised the beam trajectories.

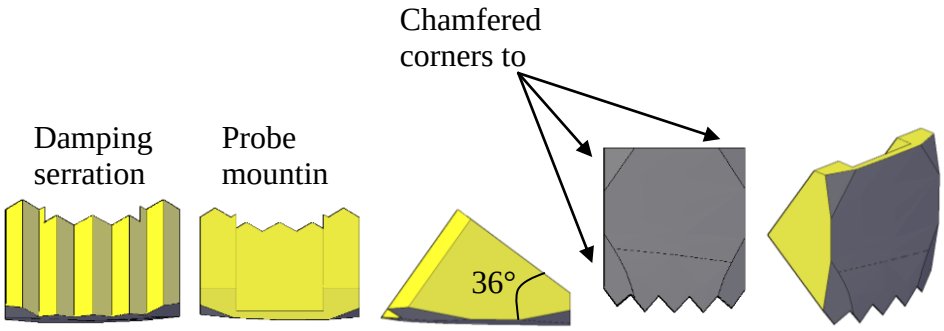

Figure 5-24 Concave wedge design with profiled face and chamfered corners

As the critical regions for inspection on the concave root were towards the inlet and outlet ends of the root (Figure 2-27), the ideal wedge profile in those regions would consist of a radius between 300 mm and 400 mm to match the convex aerofoil. However the requirement to skew the probe up to 15° at these positions meant that the corners of the wedge lifted and decoupled the ultrasound in a similar way to that of the concave wedge. It was found that using a flat wedge on the convex aerofoil was the best compromise because skewing did not decouple the probe and good coupling was achieved in the flatter critical regions where most skew was required. The disadvantage of utilising a flat wedge was that the contact patch available in the centre of the convex aerofoil was reduced significantly so that viscous gel type couplant was required to achieve good results.

5.3.4 Operation of scanning frame

The operation and functionality of the bespoke scanning frames were tested on a reference sample containing 5 mm long by 0.5 mm deep EDM notches in serrations 1 and 2 at various positions around the concave and convex roots, see Figure 5-25 and Figure 5-26. Each EDM notch was interrogated with the phased array transducer and wedge manipulated on the aerofoils by hand to find the ideal detection baseline (experiment 1 and 2). The blade sample was then mounted in a steeple test block assembly along with a plastic blade model to simulate a real blade installation, see Figure 5-27. Each EDM notch was then interrogated

using the transducer and wedges mounted in the bespoke scanner to compare the results to the baseline (Experiments 3 and 4).

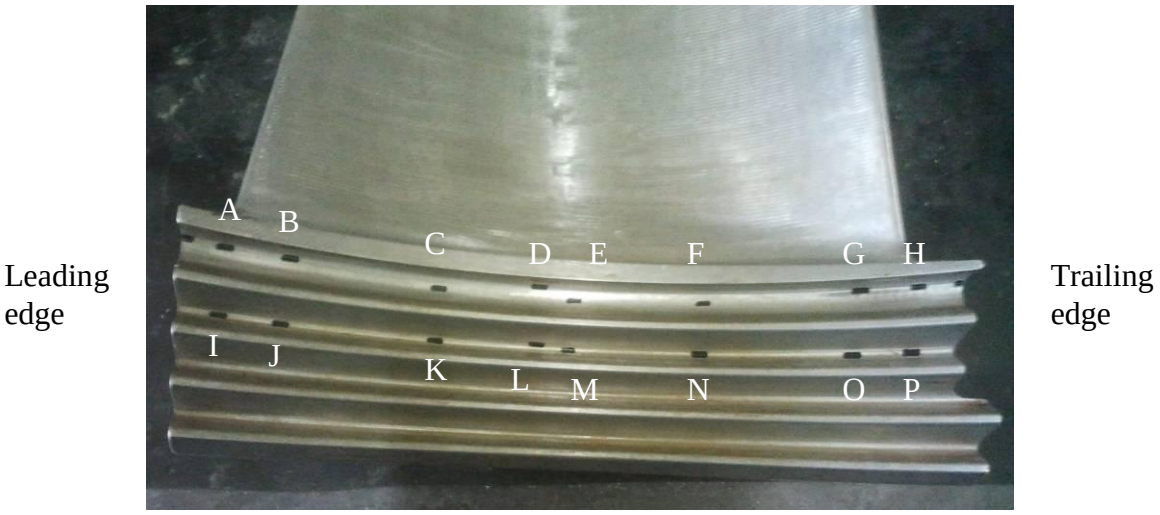

Figure 5-25 Reference sample S1 – concave root EDM notches

Figure 5-26 Reference sample S1 – convex root EDM notches

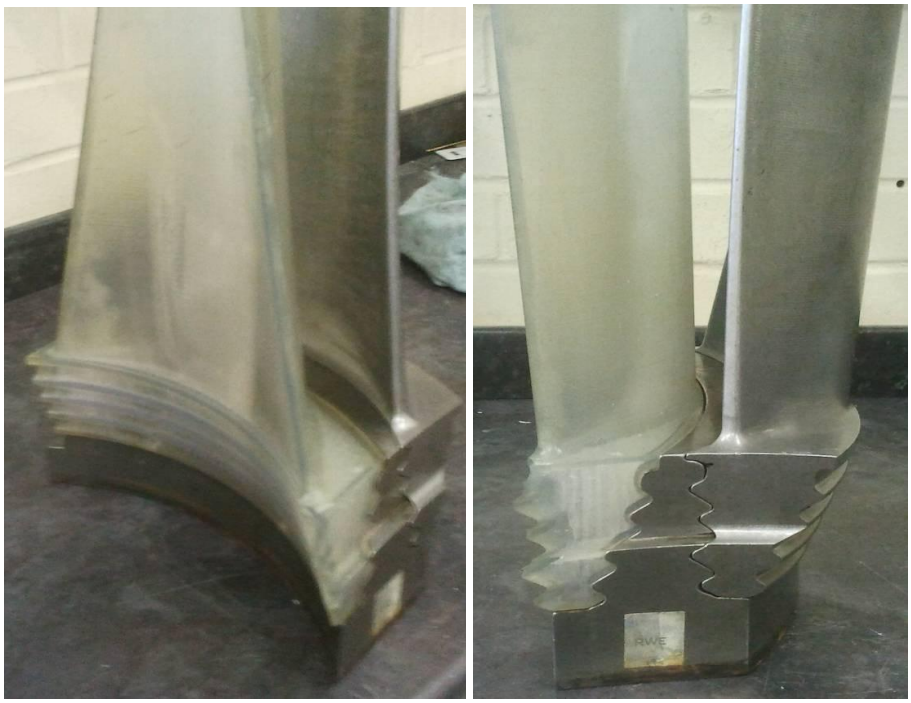

Figure 5-27 Reference sample and steeple assembly

5.3.4.1 Delay law configuration

CIVA simulations, as seen in Figure 5-6 to Figure 5-11, established that the required range of angles in the phased array laws to cover the root serrations in all axial positions would be 35º to 85º. The minimum reasonable angular resolution to ensure that defects would not be passed over between subsequent law angles was approximated at one half beam width at the appropriate beam path and angle. By taking the longest beam path to the 4th serration at approximately 70º shear waves the beam width was estimated at 6mm in the active plane. The angular step required to stay within one half of this value would be approximately 2º. However, in the interest of image quality and improved resolution an angular step of 0.5º was chosen; this would be within the total number of laws available in the equipment and still provide sufficient acquisition rate for reasonable data collection and refresh rate. Focussing of the beam at a fixed depth which was equivalent to the deepest portion of the blade root was chosen; only half skip responses were relevant in the inspection and so focusing beyond this would have no advantage. Filters were chosen so that the centre frequency of the probe fell roughly in the middle of the high and low pass limits.

All other parameters were set based on the physical dimensions of the probe and wedges used in the experiments.

5.3.4.2 Experimental equipment

Zetec Omniscan phased array unit (serial No NP1056), laptop running Ultravision 1.2R4, Imasonic 5L16E16-10 phased array probe (serial No L289C101), 36° flat Rexolite wedge (HoFE 8 mm), 36° contoured Rexolite wedge (HoFE 8 mm), Zetec bespoke scanning frame, reference sample S1, calibration block C1 with vertically aligned 1.5 mm side drilled holes (SDH) at 5 mm intervals from 10 mm deep to 60 mm deep, Sonagel couplant.

5.3.4.3 Ultravision phased array parameters

Shear wave velocity (steel): 3230ms^{-1}, wedge longitudinal velocity: 2320ms^{-1}, wedge angle: 36°, Height of First Element (HoFE): 8 mm, scan axis offset: 7 mm, sector scan: 35° to 85° at 0.5° steps, focussing: true depth at 40 mm, band pass filters: 3.3 MHz to 7.5 MHz, number of elements: 16, element pitch: 1 mm, elevation: 10 mm, centre frequency: 5 MHz.

5.3.4.4 Procedure for experiments 1 and 2:

Reference sensitivity was set by maximising the response from the reference notches and calibrating to 80 % FSH. The gain level, beam angle, and depth were recorded. The relative sensitivity to the equivalent 1.5 mm SDH at the same depth and beam angle were measured using calibration block B1. Responses from all relevant notches were maximised in turn setting them to 80 % FSH; gain level, beam angle, and depth were recorded. Notches D, L, E and M were excluded as they are designed for a complementary inspection.

Screen shots of all sector scans were recorded.

5.3.4.5 Experiment 1 – Base line manual scan of concave root from convex aerofoil

5.3.4.5.1 Reference sensitivity:

Notch E to 80 % full screen height (FSH)

5.3.4.5.2 Results:

The recorded sector scan of the reference Notch E can be seen in Figure 5-28 below and the recorded sector scans for each of the other notches can be found in Appendix D. Table 5-1 shows a summary of the results for each EDM notch.

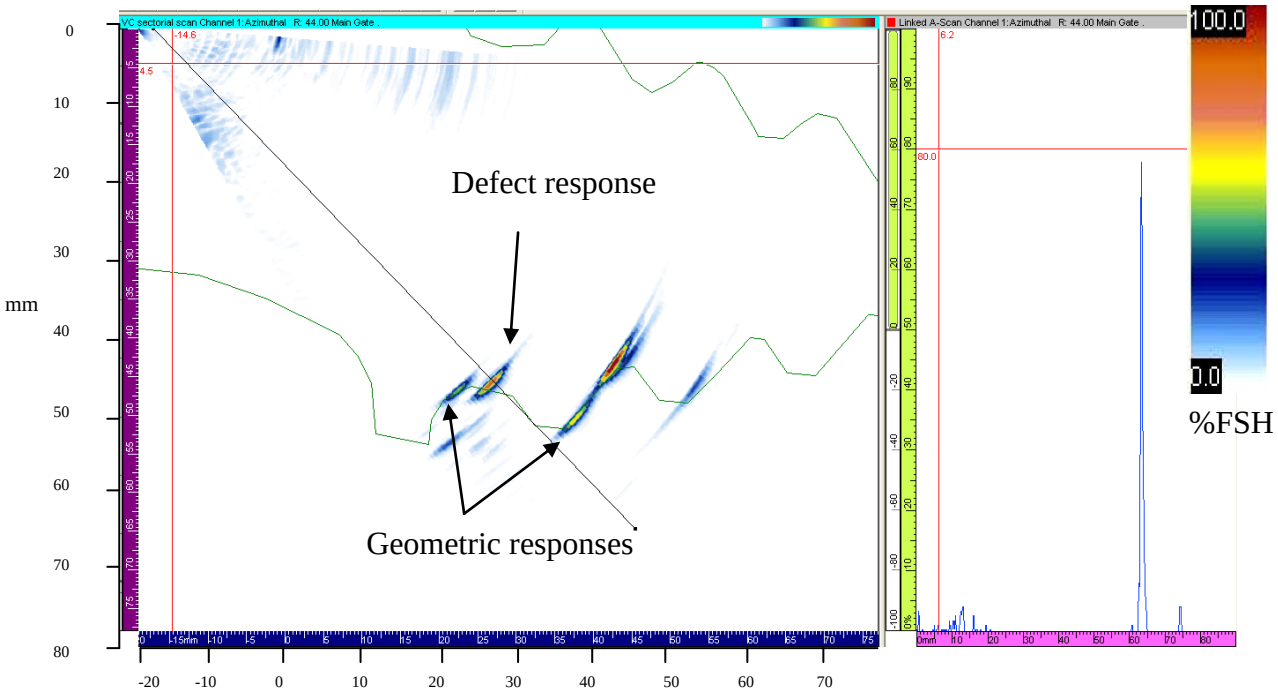

Figure 5-28 Sector scan of concave Notch E – 80 % FSH, 21dB, 44°, and 45.6 mm deep

	Base Line results - concave root from convex aerofoil				
	EDM Notch Position	Gain at 80 % FSH (dB)	Beam Angle (°)	Depth ±0.5 (mm)	Deviation from reference (dB)
	SDH Equivalent	24	44	45	+3
Serration 1	A	No Detection out of range			
	B	28	73.5	10.4	+7
	C	21	59	27.6	0
	E (reference)	21	44	45	0
	F	23	49	32	+2
	G	28	68.5	10.1	+7
	H	No Detection out of range			
Serration 2	I	No Detection out of range			
	J	No Detection out of range			
	K	32	69	23.7	+11
	M	25	49	42.6	+4
	N	34	66	26.1	+13
	O	No Detection out of range			
	P	No Detection out of range			

Table 5-1 Experiment 1 baseline results concave root

5.3.4.5.3 Discussion of results

It can be seen from Table 5-1 that the extent of coverage from the convex aerofoil was between notch B at the leading edge and notch G at the trailing edge in serration 1. The limit of coverage in serration 2 was shown to extend past notch K but not as far as notch J at the leading edge and past notch N but not as far as notch O at the trailing edge. It was noted during the experiment that a skew level which would provide sensitivity to defects in the first serration would not necessarily be sensitive to defects in the second serration. Therefore during manual manipulation the probe skew must be continually varied between the first and second serration to achieve sensitive coverage. It was also noted that away from the centre of the aerofoil there was very little geometric response from the second serration to provide feedback that the skew level was correct. It was also noted that significant skewing was required immediately after the probe was axially moved away from the apex of the aerofoil.

Sensitivity to defects in the first serration varied only by 7dB compared to the reference sensitivity level from notch E and defects in the second serration varied by as much as 13dB. The decrease in sensitivity was due to the increasing beam angles presented to the inspection regions as the offset between the aerofoil and roots decreased towards the inlet and outlet ends.

5.3.4.6 Experiment 2 – Base line manual scan of convex root from concave aerofoil

5.3.4.6.1 Reference sensitivity:

Notch D to 80 % Full screen height (FSH)

5.3.4.6.2 Results:

The recorded sector scan of the reference Notch D can be seen in Figure 5-29 below and the recorded sector scans for each of the other notches can be found in Appendix D. Table 5-2 shows a summary of the results for each EDM notch.

5.3.4.6.3 Discussion of results

It can be seen from Table 5-2 that the extent of coverage from the concave aerofoil was between notch C at the leading edge and notch F at the trailing edge in serration 1. The main limitation was set by the overhang of the root platforms blocking the beam trajectories beyond these notches. The limit of coverage in serration 2 was shown to extend to all notches in the second serration. The sensitivity to notches away from the centre of serration 1 was improved compared to the reference notch D where a variation of up to -5dB was measured. The variation in sensitivity to notches in the second serration was also very small ranging from -2dB at best and +8dB at worst. It can be seen that the beam trajectories and depths were more consistent from the concave aerofoil which led to the smaller variation in sensitivity and the requirement to skew the probe much less.

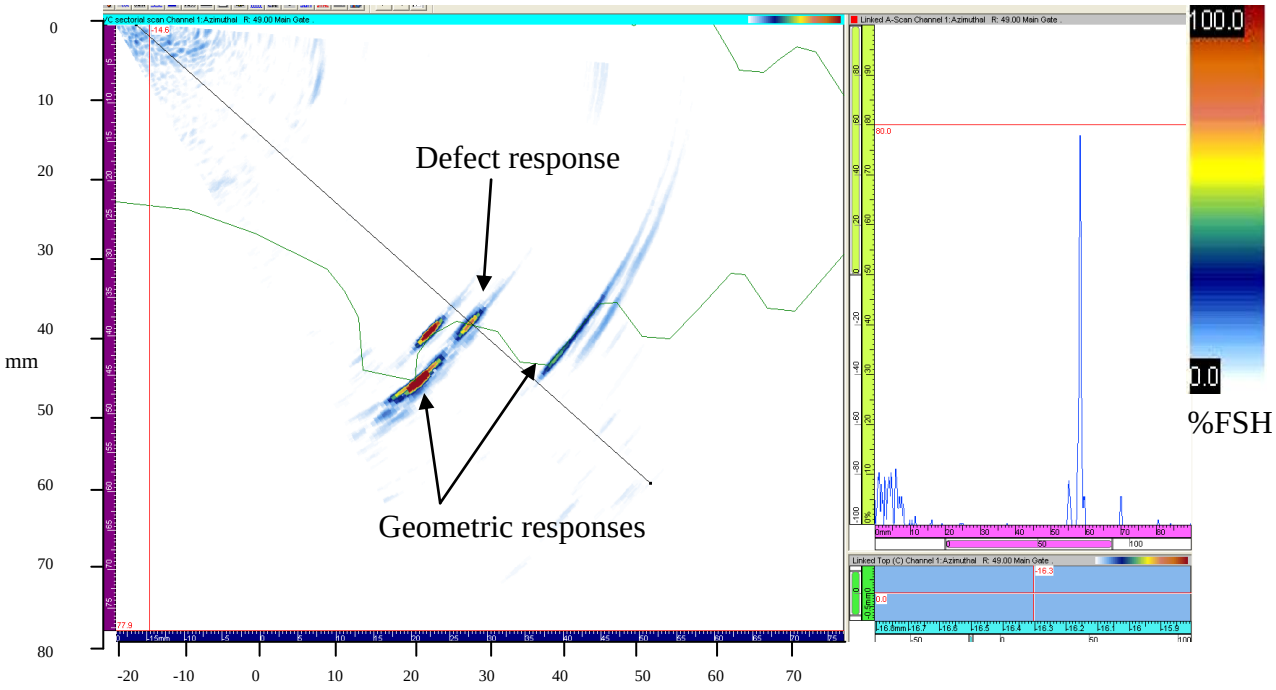

Figure 5-29 Sector scan of convex Notch D – 80 % FSH, 22dB, 48.5°, and 38.6 mm deep

	Base Line results - convex root from concave aerofoil				
	EDM Notch Position	Gain at 80 % FSH (dB)	Beam Angle (°)	Depth ±0.5 (mm)	Deviation from reference (dB)
	SDH Equivalent	25	48.5	40	+3
Serration 1	A	No Detection blocked by platform			
	B	No Detection blocked by platform			
	C	17	48.5	40	-5
	D (reference)	22	48.5	38.6	0
	F	19	54.5	36.1	-3
	G	No Detection blocked by platform			
	H	No Detection blocked by platform			
Serration 2	I	29	48	45	+7
	J	21	57	41.8	-1
	K	22	57	38.6	0
	L	27	57	35	+5
	N	25	61.5	34	+3
	O	20	59	36.1	-2
	P	30	57.5	36.7	+8

Table 5-2 Experiment 2 baseline results convex root

5.3.4.1 Procedure for experiments 3 and 4:

The bespoke scanning frame was configured to inspect the concave root as seen in Figure 5-30 and the convex root as seen in Figure 5-31 . The appropriate contoured wedges were attached and the height of the scanner was adjusted so that the front of the wedge was measured at 15 mm from the top of the root platform. Reference sensitivity was set by maximising the response from the reference notches and calibrating to 80 % FSH. The gain level, beam angle, and depth were recorded. Responses from all relevant notches were maximised in turn setting them to 80 % FSH; gain level, beam angle, and depth were recorded. Notches D, E, L and M were excluded as they are designed for a complementary inspection.

Screen shots of all sector scans were recorded.

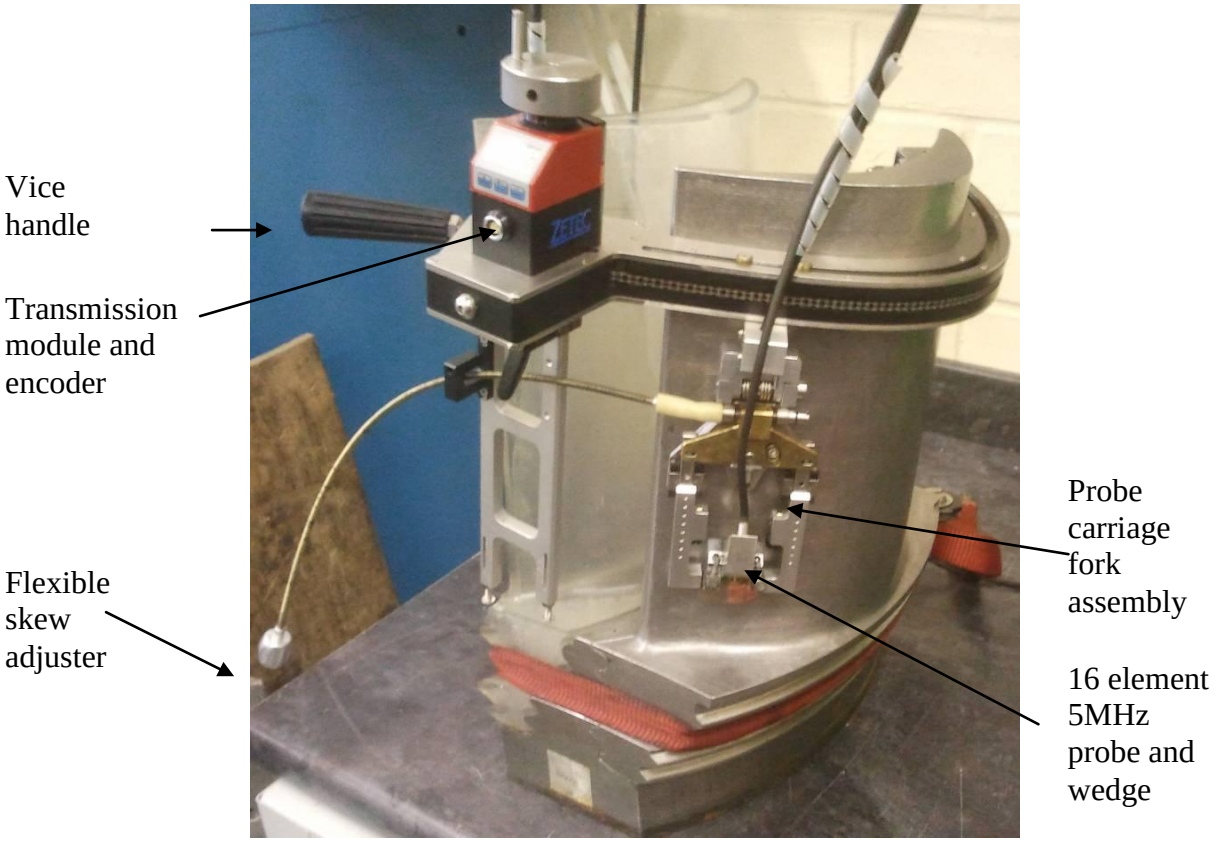

Figure 5-30 Bespoke scanning frame configured to scan the concave root from convex aerofoil

Figure 5-31 Bespoke scanning frame configured to scan the convex root from concave aerofoil

5.3.4.2 Experiment 3 – Bespoke frame, scan of concave root from convex aerofoil

5.3.4.2.1 Reference sensitivity:

Notch E to 80 % Full screen height (FSH)

5.3.4.2.2 Results:

The recorded sector scan of the reference Notch E can be seen in Figure 5-32 below and the recorded sector scans for each of the other notches can be found in Appendix D. Table 5-3 shows a summary of the results for each EDM notch.

5.3.4.2.3 Discussion of results

It can be seen from Table 5-3 that the extent of coverage from the convex aerofoil was again between notch B at the leading edge and notch G at the trailing edge in serration 1. The limit of coverage in serration 2 was shown to extend past notch K but not as far as notch J at the leading edge and past notch N but not as far as notch O at the trailing edge. Sensitivity to defects in the first serration varied by 11dB compared to the reference sensitivity level from notch E and defects in the second serration varied by as much as 15dB.

It was found that all the notches detected using the manual technique in experiment 1 were detected using the scanning frame but sensitivity was compromised due to the fixed height setting and responses could not be optimised by movement of the probe down the aerofoil. Compared to the manual manipulation of the probe by hand, the scanner required much more care in maximising responses from notches. This was due to the compromise in coupling whilst skewing where the subtleties in probe manipulation were not afforded by the scanner. This was particularly difficult towards centre of the scan at the apex of the aerofoil where the flat wedge tended to rock and lose coupling when driven and skewed.

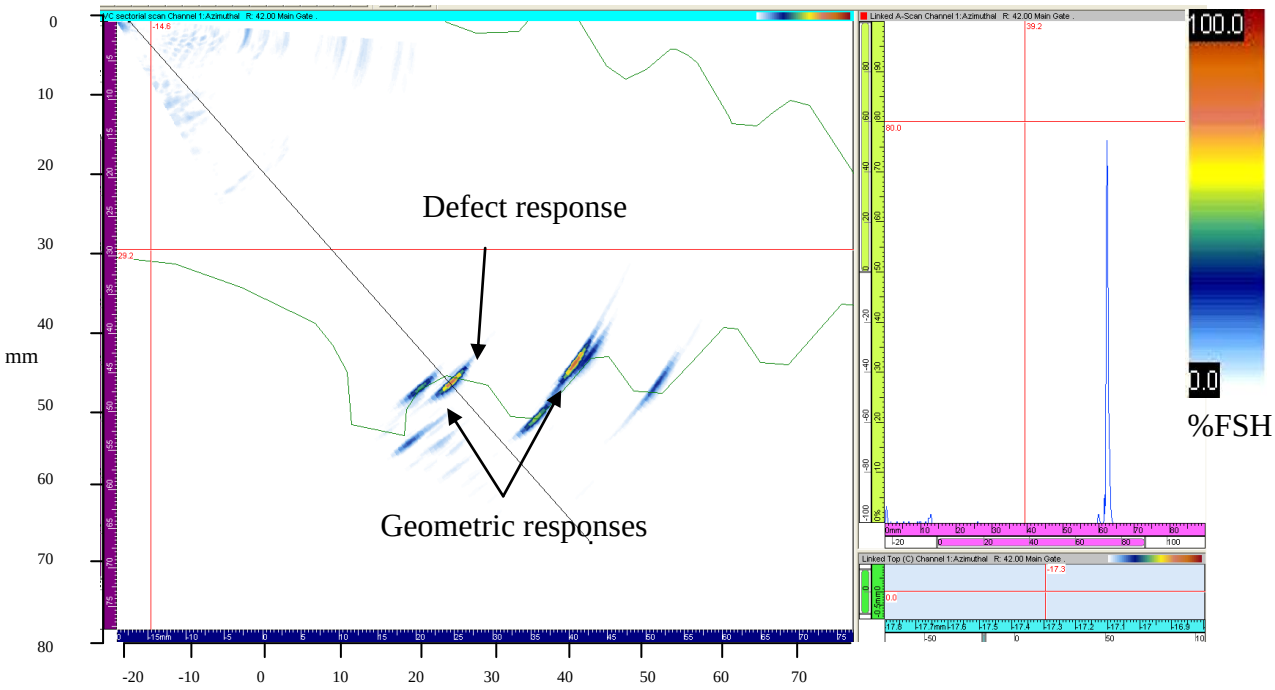

Figure 5-32 Sector scan of concave Notch E from bespoke scanning frame – 80 % FSH, 21dB, 42°, and 46 mm deep

	Scanner results - concave root from convex aerofoil				
	EDM Notch Position	Gain at 80 % FSH (dB)	Beam Angle (°)	Depth ±0.5 (mm)	Deviation from reference (dB)
Serration 1	A	No Detection out of range			
	B	30	76	9	+9
	C	23	56	29	+2
	E (reference)	21	42	46	0
	F	24	59	28	+3
	G	32	70	9	+11
	H	No Detection out of range			
Serration 2	I	No Detection out of range			
	J	No Detection out of range			
	K	36	68	25	+15
	M	26	42	43	+5
	N	35	67	25	+14
	O	No Detection out of range			
	P	No Detection out of range			

Table 5-3 Experiment 3 bespoke scanner results concave root

5.3.4.3 Experiment 4 – Bespoke frame, scan of convex root from concave aerofoil

5.3.4.3.1 Reference sensitivity:

Notch D to 80 % Full screen height (FSH)

5.3.4.3.2 Results:

The recorded sector scan of the reference Notch D can be seen in Figure 5-33 below and the recorded sector scans for each of the other notches can be found in Appendix D. Table 5-4 shows a summary of the results for each EDM notch.

5.3.4.3.3 Discussion of results

It can be seen from Table 5-4 that the extent of coverage from the concave aerofoil was between notch C at the leading edge and notch F at the trailing edge in serration 1. The main limitation was set by the overhang of the root platforms blocking the beam trajectories beyond these notches. The limit of coverage in serration 2 was shown to extend to all notches in the second serration. The sensitivity to notches away from the centre of serration 1 was improved compared to the reference notch D where a variation of up to -3dB was measured. The variation in sensitivity to notches in the second serration was also very small for notches J to O ranging from -3dB at best and +9dB at worst. However a significant reduction in sensitivity was found for notches I and P which were 16dB and 21dB respectively worse than the reference notch. This was attributed to the inability to push the probe down the aerofoil from its fixed height to maximise the responses. It can be seen that the beam trajectories and depths were again consistent from the concave aerofoil which led to the small variation in sensitivity and the requirement to skew the probe much less.

It was found that all the notches detected using the manual technique in experiment 2 were detected using the scanning frame and sensitivity was comparable apart from notches I and P. It was found that, unlike the difficulty manipulating the flat wedge on the convex aerofoil, the profiled wedge on the concave aerofoil was more easily controlled and responses were maximised efficiently.

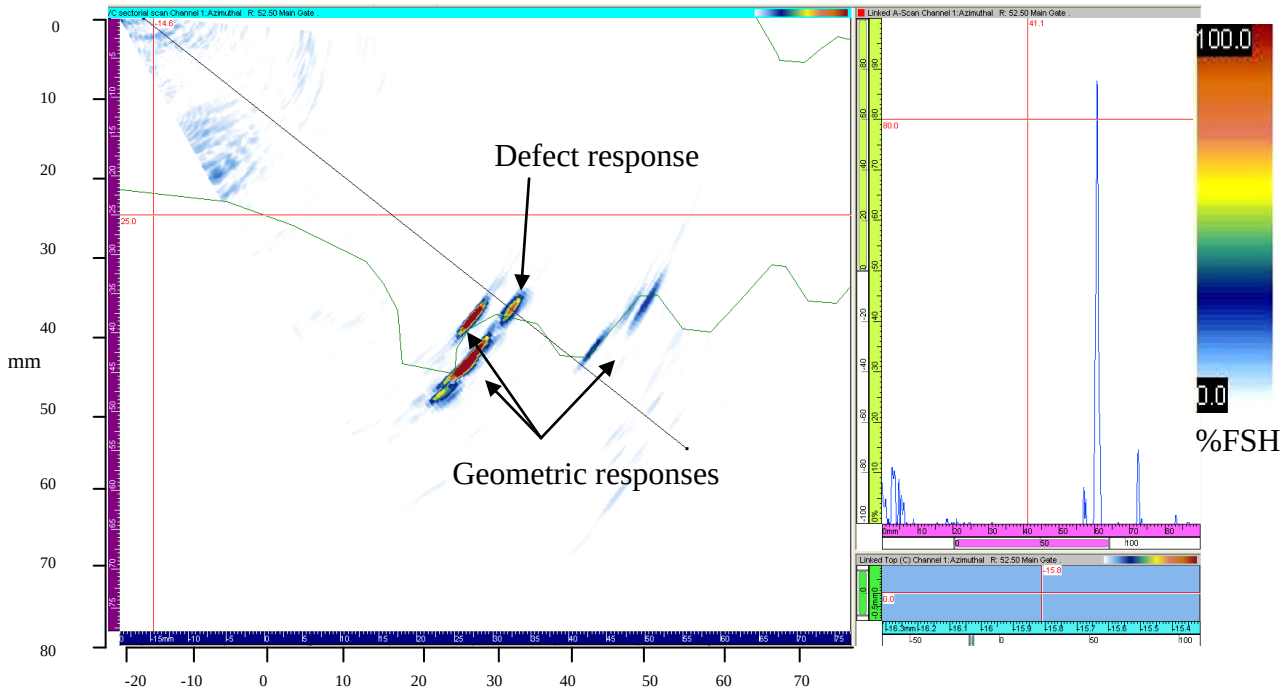

Figure 5-33 Sector scan of convex Notch D from bespoke scanning frame – 80 % FSH, 24dB, 52.5°, and 37 mm deep

	Base Line results - convex root from concave aerofoil				
	EDM Notch Position	Gain at 80 % FSH (dB)	Beam Angle (°)	Depth ±0.5 (mm)	Deviation from reference (dB)
Serration 1	A	No Detection blocked by platform			
	B	No Detection blocked by platform			
	C	21	49.5	41	-3
	D (reference)	24	52.5	37	0
	F	21	52.5	37	-3
	G	No Detection blocked by platform			
	H	No Detection blocked by platform			
Serration 2	I	40	51	45	+16
	J	23	56.5	42	-1
	K	25	60	38	+1
	L	33	61	36	+9
	N	26	63	33	+1
	O	22	62	35	-3
	P	45	62.5	33	+21

Table 5-4 Experiment 4 bespoke scanner results convex root

5.3.4.4 Discussion and conclusions

Table 5-5 shows a direct comparison of all the sensitivity measurements taken through experiments 1 to 4. The comparison shows the potential reduction in sensitivity between

manually manipulating the probe on the aerofoil surfaces, with the freedom to tilt or skew at varied heights above the platform, compared to the limited manipulation at fixed heights using the scanning frame. It is clear that the delta gain levels (Δ dB) are in most cases positive, showing that the restricted manipulation of the probe afforded by the scanner has reduced sensitivity. However, apart from the extreme inlet and outlet ends of the convex root (notches I and P) where the platform begins to block the beam from the second serration, the delta gain is <= 4 dB, which would be well within an acceptable variation.

	Sensitivity Comparison 80 % FSH (dB)						
	EDM Notch Position	Convex Root deviation from reference (dB)			Concave Root deviation from reference (dB)		
		Manual	Scanner	Δ dB	Manual	Scanner	Δ dB
Serration 1	A						
	B				7	9	2
	C	-5	-3	2	0	2	2
	D	0 (reference)	0 (reference)	0	N/A		
	E	N/A			0 (reference)	0 (reference)	0
	F	-3	-3	0	2	3	1
	G				7	11	4
	H						
Serration 2	I	7	16	9			
	J	-1	-1	0			
	K	0	1	1	11	15	4
	L	5	9	4	N/A		
	M	N/A			4	5	1
	N	3	1	-2	13	14	1
	O	-2	-3	-1			
	P	8	21	13			

Table 5-5 Comparison of sensitivity measurements comparing manual manipulation to scanner

It was noted that the inspection of the concave root required significant skewing of the probe immediately away from the apex of the aerofoil to combat the mismatch between the aerofoil and root geometries. This made manipulation of the probe more complex during the rapid transition from the apex towards the ends, which was trivial to control manually but difficult using the scanner. One of the main issues was the tendency for the flat wedge to rock as it was driven axially around the apex of the aerofoil, causing problems with coupling

and making it much more time consuming to apply. A profiled wedge designed to match the curve of the apex would solve the problem of rocking and improve stability but prevent efficient coupling whilst skewing the probe.

Stability problems whilst scanning from the concave aerofoil were not experienced and due to the reduced amount of mismatch between the aerofoil and root, less skew was required. This in turn led to a more even sensitivity across all positions apart from notches I and P which were in fact at the very limit of coverage due to the probe running off the end of the aerofoil.

Given the situation where no manual access is available between blades for manipulation of the probe, the experiments showed that the scanning frames could successfully facilitate the remote inspection of the roots with equivalent coverage and similar sensitivity. Scanning around the apex of the convex aerofoil was however problematic due to poor stability and coupling and would require further consideration.

In the experiments it was seen that there were a number of regions in which coverage was limited and that certain regions were out of range for inspection from the aerofoils. The following section briefly describes the development of further scanning aids which fulfilled the requirement for full coverage of serration 1 and 2.

5.4 Rapid prototyped platform scanning frames and jigs

It was shown in the previous section how significant coverage of both the concave and convex roots was achieved by scanning from the aerofoil. It was also seen that certain regions towards the leading and trailing edges of the blade root were either out of range or significantly lacking sensitivity when interrogated from the aerofoils. Table 5-6 shows a list of EDM notches which were not effectively detected from the aerofoil.

EDM notch concave root	Reason for limitation	EDM Notch convex root	Reason for limitation
A	Out of range	A	Masked by platform
H	Out of range	B	Masked by platform
I	Out of range	G	Masked by platform
J	Out of range	H	Masked by platform
O	Out of range	I	Reduced sensitivity
P	Out of range	P	Reduced sensitivity

Table 5-6 EDM notches not covered effectively from aerofoil

The solution for coverage of all the notches in the concave root was previously described in section 4.4.5 with the production of rapid prototyped jigs for precise inspection from the root platforms, see Figure 5-34. It can be seen that both the leading and trailing edge jigs contain three probe positions for shear wave inspections, and one compression wave inspection targeting serrations 1 and 2 of the concave root. It was also shown that axial movement of the jigs facilitated coverage of the roots between the fixed probe positions.

Coverage of all the notches in the convex root from Table 5-6 was facilitated by the production of probe scanners designed to precisely guide a phased array probe around the root platform above the convex serrations at the leading and trailing edges, see Figure 5-35. The scanners were modelled and manufactured using rapid prototyping with the same process described in section 0. The scanner consists of a probe manipulator with a clamp to hold the 20 element 10 MHz phased array probe (section B.2) and tenon designed to locate and slide in a matching groove in the jig fitted to the blade platforms. Magnets in the tenon pull the probe onto the platform to ensure positive coupling. The phased array probe was configured to generate a compression wave sector scan looking down at the root serrations. Figure 5-36 and Figure 5-37 show the recorded sector scans of notches A and I to illustrate the detection capabilities of the technique. As the axial path of the scan is constant in relation to the root curvature, the detection of all convex root notches listed in Table 5-6 was facilitated with identical sensitivity levels.

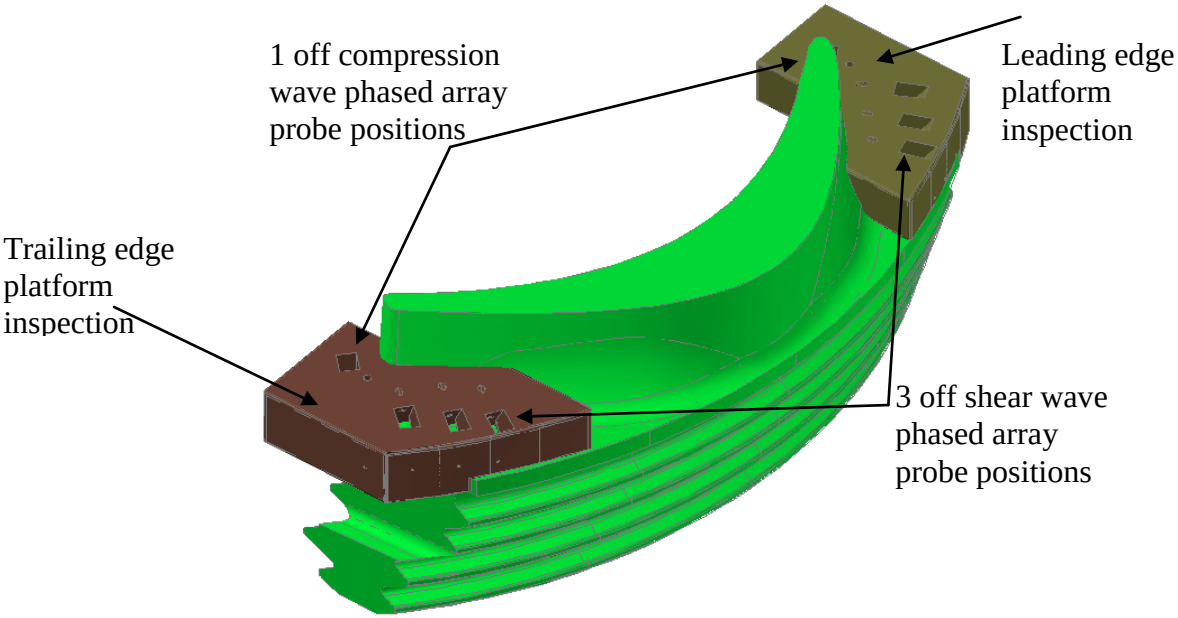

Figure 5-34 CAD model of rapid prototyped platform inspection jigs

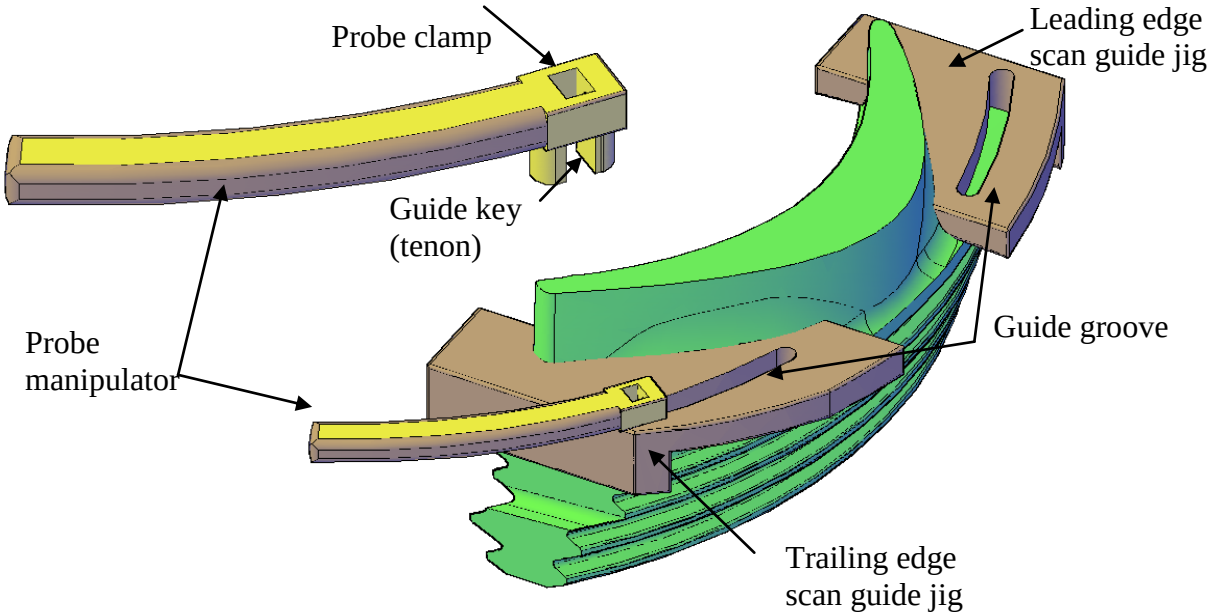

Figure 5-35 Platform scanning guides for inspection of convex root

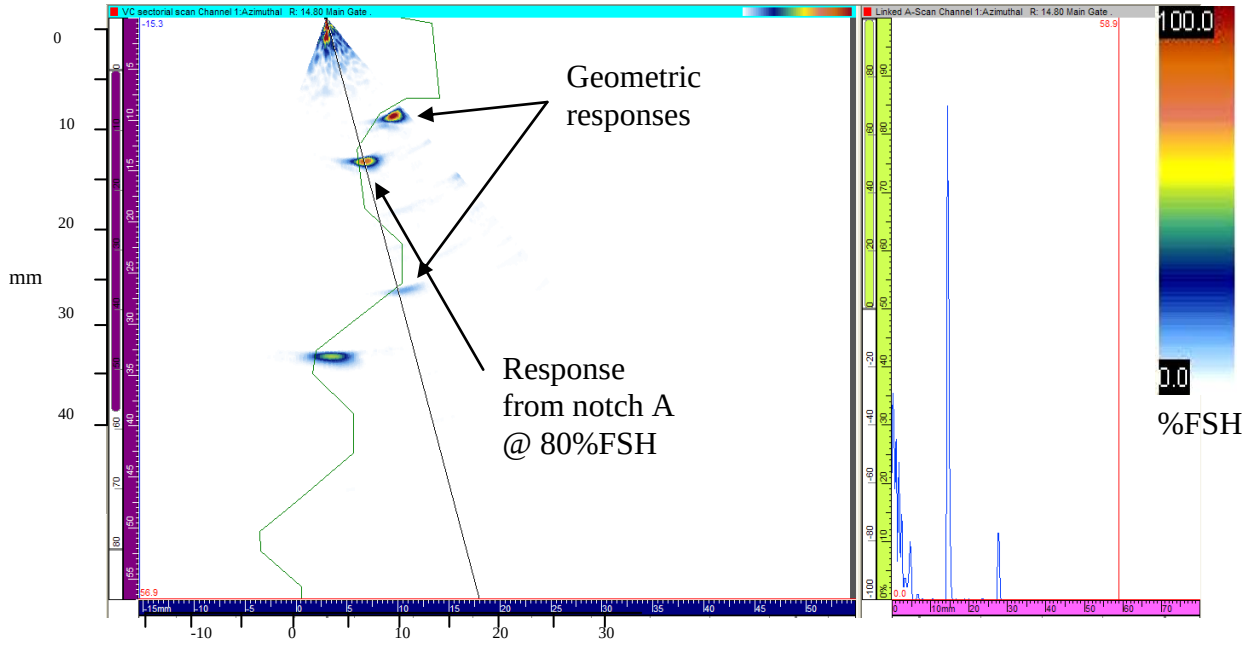

Figure 5-36 Sector scan of convex Notch A from platform scan guides – 80 % FSH, 24dB, 14.8°, and 14 mm deep

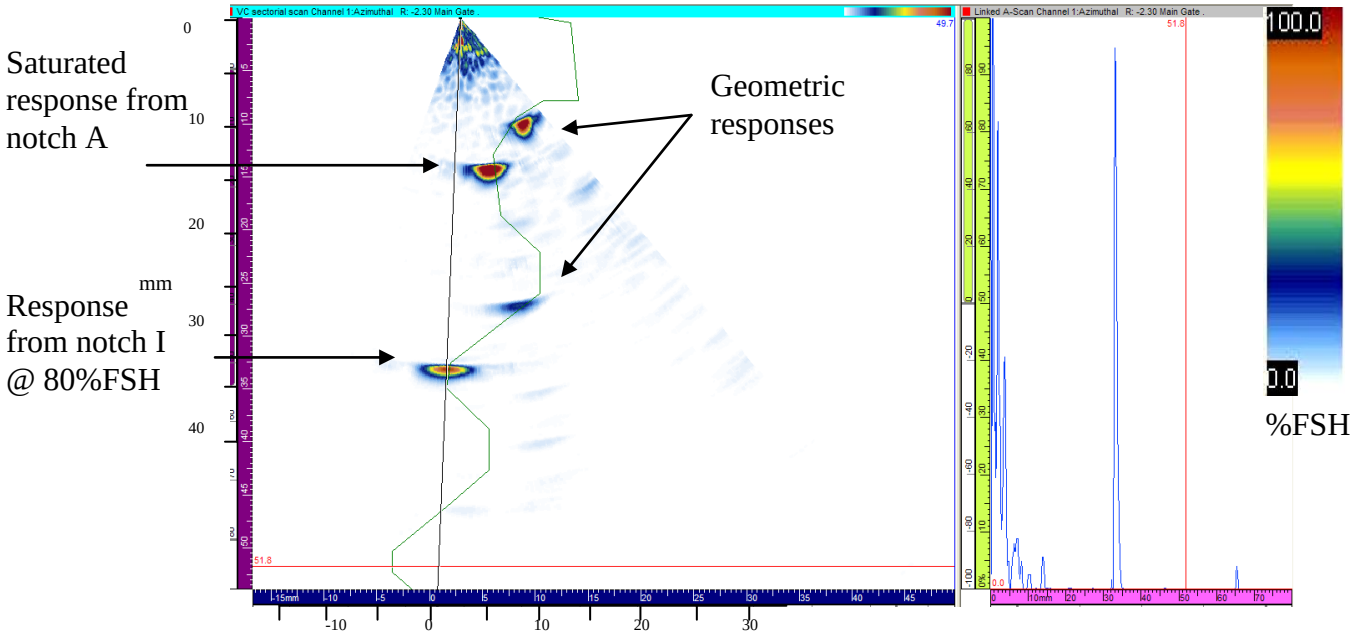

Figure 5-37 Sector scan of convex Notch I from platform scan guides – 80 % FSH, 32dB, -2.3°, and 33 mm deep

5.5 Conclusions

It has been shown how the blade aerofoil provides significant coverage of the first two serrations in both the concave and convex roots. The complex shape of the aerofoil compared to the constant radii of the roots creates a mismatch which complicates the

application of ultrasound and affects the sensitivity to small defects. It has been shown that careful profiling of the refracting wedges and the application of probe skew, combined with complimentary inspections using the rapid prototyped jigs, enabled consistent detection of reference notches in the critical target regions. The complex manipulation of the probe, which is trivial when carried out by hand, is not possible where limited inter-blade spacing is available; the development, design and manufacture of novel bespoke scanning frames has facilitated remote control of the probe on the aerofoil and has been shown to produce comparative sensitivity. The success of this development has culminated in its deployment on two separate last stage blade inspections of Franco Tosi built low pressure rotors which were otherwise impossible to inspect effectively.

It was found however, through the deployment and experimental validation of the technique, that the subtle control afforded by manual manipulation of the probe was not possible with the scanning frame. The instability and coupling problems at critical parts of the scan range meant that the application of the technique and detection of the reference notches was more difficult and time consuming, requiring care to replicate the base line results. The need to skew at various angles along the scan also prevented the application of encoded line scans; this would facilitate collection of inspection data of the whole blade root to produce ‘C’ and ‘D’ scans for permanent records of the root volume and offline analysis.

The following chapters describe an innovative wedge invention which has overcome the issues of geometric mismatch between the aerofoil and root whilst addressing the coupling problems and facilitating the application of line scans.

Chapter 6. Novel wedge design, the continuous wedge

6.1 Introduction

In the previous chapter it was shown how mechanical skewing of the phased array probe was used to compensate for the geometric mismatch between the aerofoil and root geometry when applying inspection techniques to the aerofoils of CAEFTR designs. It was seen that the process of skewing the probe led to disruption of the coupling between the refracting wedge and the component, resulting in compromises to the wedge design. Furthermore it was seen that the application of encoded line scans would not be practicable as the variation in required skew would render data collection with consistent sensitivity across the whole scan path impossible.

This chapter describes the invention, for which a patent has been applied (see page 242), of an innovative continuous Rexolite wedge which overcame the issues described by removing the requirement to skew the probe and optimising the coupling efficiency between the aerofoil and wedge. Rather than refracting ultrasound into the component using a probe mounted on a wedge, which together are scanned along the component, the invention makes use of a single continuous wedge which is coupled to the component and remains static; the phased array probe is then scanned along the wedge in a single continuous scan. It will be shown how careful modelling of the Rexolite wedge ensures that it perfectly fits the contour of the blade and produces skew deflection to compensate for the geometric mismatch without the need to mechanically skew the probe. It will also be shown how the invention facilitates the application of cost effective 1D phased array technology and provides the potential to enact encoded line scanning of the root. This chapter describes the continuous wedge concept in detail along with the design and modelling process used to produce it. Simulations are then shown which validate the functionality of the wedge before Chapter 7 describes the experimental validation of the first prototypes which were manufactured.

6.2 Concept of the continuous wedge invention

A Rexolite wedge with an exact negative of the surface of the component would provide the perfect coupling interface for the refraction of ultrasound into the component. By then including an appropriate scanning surface to the top of the wedge, a phased array probe could be scanned along it to inspect the component. As the wedge is static on the component, coupling is consistent with no variation due to the scan movement. The scan surface of the wedge is controlled and machined to a smooth finish ensuring that positive and consistent coupling of the probe to the wedge is attained. Figure 6-1 illustrates the single wedge concept on a simple geometric block.

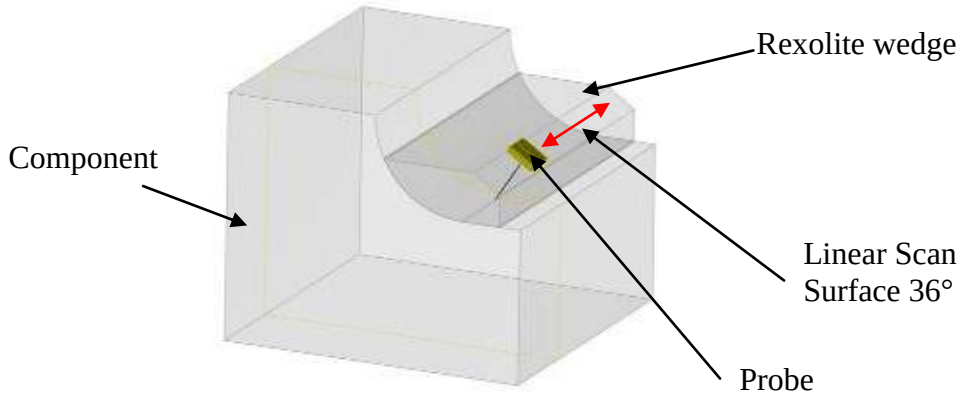

Figure 6-1 Illustration of the continuous wedge invention

The significant premise of the continuous wedge design, along with the ability to control coupling efficiency, is that the wedge shape is carefully controlled to steer the ultrasonic beam in the passive direction as well as the active direction. By the addition of skew deflection or roof angle, as described in section 3.5.2 and illustrated in Figure 3-34, the beam trajectory in the lateral direction can be controlled. The incident beam in the wedge refracts through the wedge-component interface in some direction not parallel with the active aperture of the transducer producing ultrasonic waves in 3 dimensional space. A continuous Rexolite wedge could be designed to match the geometry of the blade aerofoil

and root platform whilst the scanning surface is shaped to produce varying amounts of skew deflection based on the geometric mismatch. The effect of this would be that the phased array probe could be scanned along the wedge with no application of mechanical skew and result in all beam trajectories being normal to the root serrations at any given point along the scan. Figure 6-2 illustrates the detailed design concept of the invention and shows how the gradual thickening of the continuous wedge forms an effective roof angle as the probe is scanned around the scanning surface.

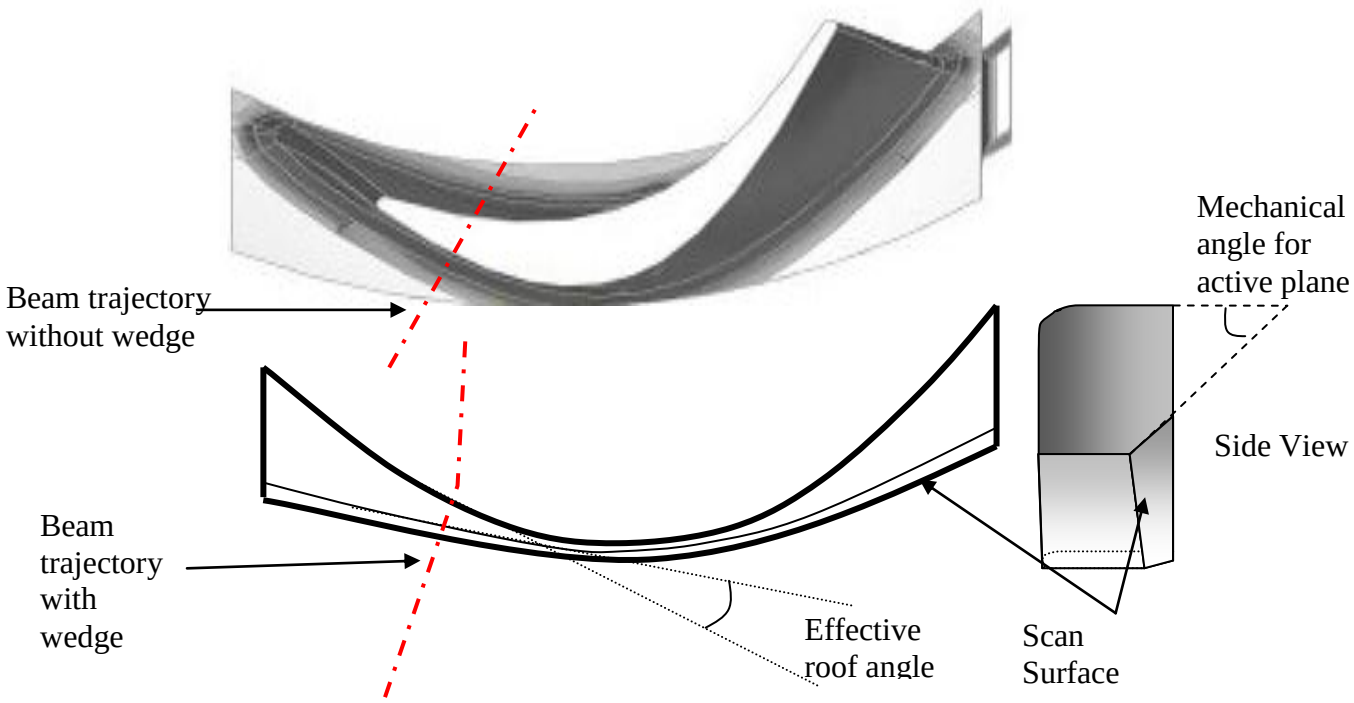

Figure 6-2 Design concept of the continuous Rexolite wedge as applied to blade root inspection

6.1 Calculation of skew deflection

Due to the complex nature of the blade geometry the skew deflection required at different positions around the aerofoil would need to be calculated accurately. Equations were derived which could calculate the skew deflection attained using a roof angled wedge following the convention illustrated in Figure 6-3.

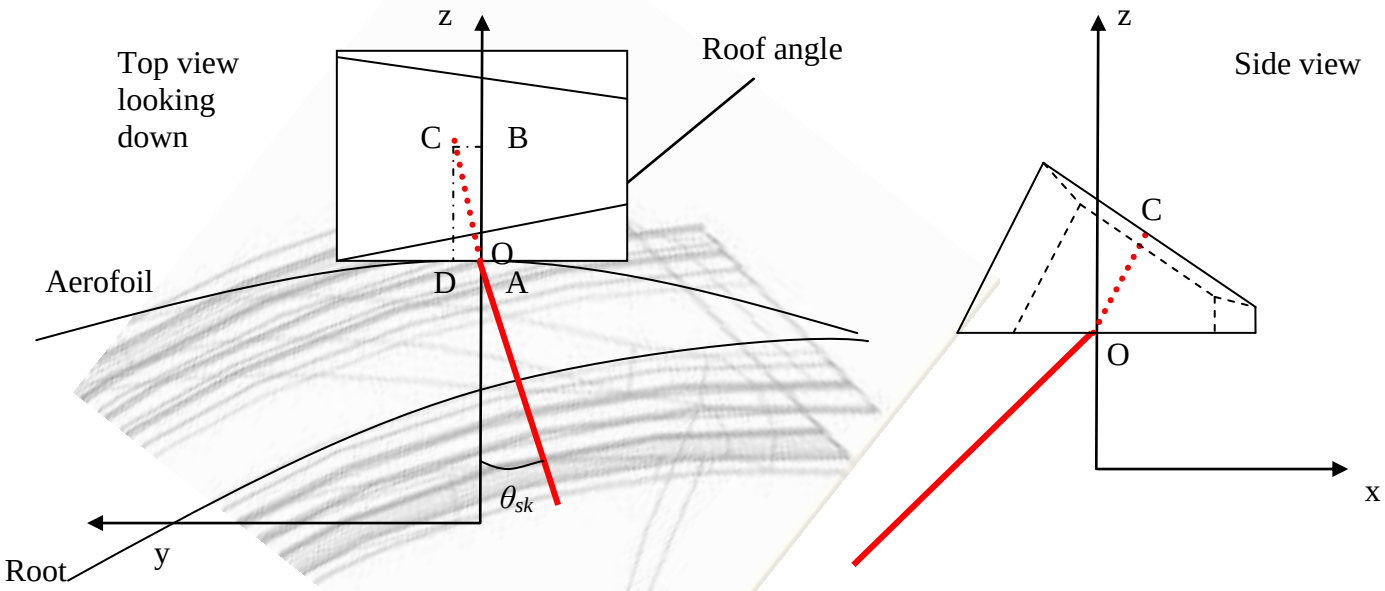

Figure 6-3 Coordinate convention for roof angle calculations

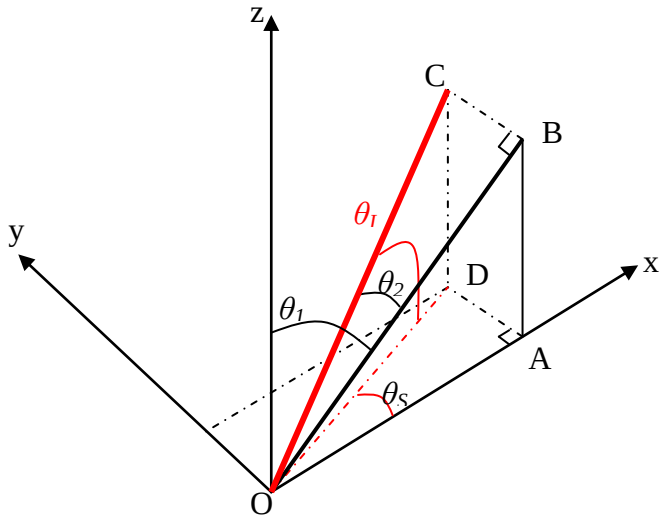

θ_1 = Active wedge angle
θ_2 = Roof angle
θ_S = Projected x-y plane angle

OC = 1 (unit vector)

$OB/OC = \cos\theta_2$	thus	$OB = \cos\theta_2$
$BC/OC = \sin\theta_2$	thus	$BC = \sin\theta_2$
$OA/OB = \sin\theta_1$	thus	$OA = OB.\sin\theta_1$ $OA = \cos\theta_2.\sin\theta_1$
$AB/OB = \cos\theta_1$	thus	$AB = \cos\theta_1.\cos\theta_2$

Figure 6-4 Vector diagram of beam trajectories developed within roof angled wedge

The unit vector 'OC' shown as red in Figure 6-4 represents a vector which is normal to and projected from the probe face of a roof angled wedge. The incident angle (θ_I) can be calculated by:

$$\cos\theta_I = AB/OC \qquad \text{so} \qquad \cos\theta_I = AB = \cos\theta_1 \,.\, \cos\theta_2$$

Thus $\theta_I = \cos^{-1}(\cos\theta_1 \,.\, \cos\theta_2)$ (47)

The skew angle (θ_S) in the x-y plane can be calculated by:

$$\tan\theta_S = AD/OA = BC/OA = \sin\theta_2/(\cos\theta_2.\sin\theta_1)$$

Thus $\theta_S = \tan^{-1}(\sin\theta_2/ (\cos\theta_2.\sin\theta_1))$ (48)

Using Snells law to calculate the refracted angle (θ_R):

$$\theta_R = \sin^{-1} (\sin\theta_I \, V_R/V_I)$$ (49)

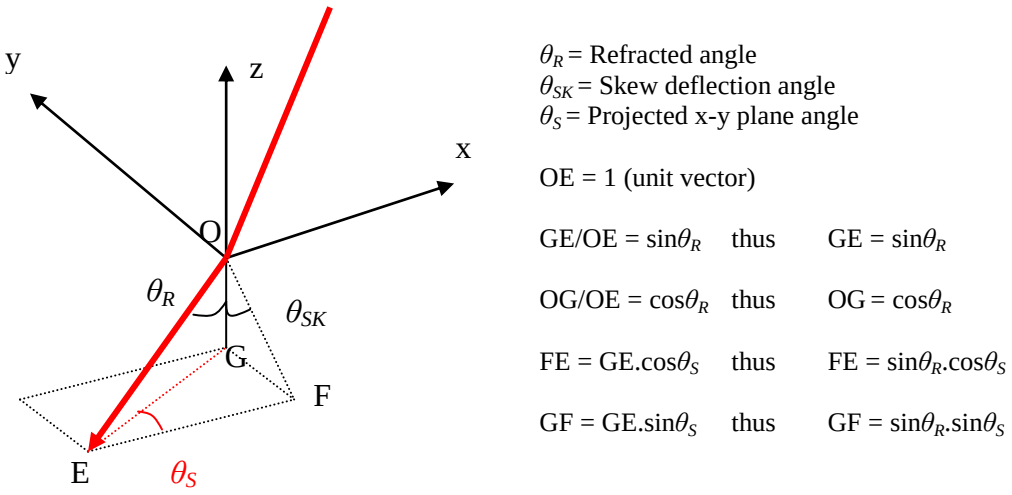

Figure 6-5 Vector diagram of beam trajectories developed within component

In can be seen in Figure 6-5 that the skew deflection angle (θ_{SK}) can be calculated by:

$$\tan\theta_{SK} = GF/OG = \sin\theta_R.\sin\theta_S / \cos\theta_R$$

To simplify $\tan\theta_{SK} = \tan\theta_R.\sin\theta_S$

Thus $\theta_{SK} = \tan^{-1}(\tan\theta_R.\sin\theta_S)$ (50)

6.1.1 Worked example

The skew deflection for a Rexolite wedge with an active angle (θ_1) of 36° and roof angle (θ_2) of 12° can be calculated as follows:

$$\theta_I = \cos^{-1}(\cos 36 \,.\, \cos 12) = 37.6893°$$

$$\theta_S = \tan^{-1}(\sin 12 / (\cos 12 . \sin 36)) = 19.88°$$

$$\theta_R = \sin^{-1}(\sin 37.6893 \times 3230/2320) = 58.34°$$

$$\theta_{SK} = \tan^{-1}(\tan 58.34 . \sin 19.88) = 28.87°$$

Hence the ultrasonic beam will be refracted at 58.34° in the active plane at a skew deflection of 28.87°. The values for skew deflections for different probe parameters can be seen in Table 6-1.

Active Angle					
31°		**36°**		**41°**	
Roof Angle	**Skew deflection**	**Roof Angle**	**Skew deflection**	**Roof Angle**	**Skew deflection**
0.5	1.00	0.5	1.21	0.5	1.71
1	2.00	1	2.42	1	3.42
1.5	3.00	1.5	3.63	1.5	5.13
2	3.99	2	4.84	2	6.83
2.5	4.99	2.5	6.05	2.5	8.54
3	5.99	3	7.26	3	10.24
3.5	6.99	3.5	8.47	3.5	11.94
4	7.99	4	9.68	4	13.63
4.5	8.99	4.5	10.89	4.5	15.32

Table 6-1 Calculated skew deflections for various wedge angles

6.2 Continuous wedge design

To begin the design process the amount of skew deflection required at various positions around the scan was measured. This was done by taking a section through the aerofoil at the relevant inspection height and through the blade root between serrations 1 and 2. Vectors normal to the root section were created at angular intervals converging at the centre point of the root radius and representing the trajectories of ideal refraction to the root. Vectors were then created normal to the aerofoil section at similar intervals to represent the incident beam

trajectories of the aerofoil with no correction. The angle between overlapping incident and refraction vectors were then measured at each angular interval and the required skew deflection was calculated at each point, see Figure 6-6.

The points of convergence for 3 groups of aerofoil incident vectors were established and represented by three separate circles which approximate the profile of the aerofoil, see Figure 6-7. These centres were used as reference points for production of the wedge profile.

A blank wedge block was created by carrying out a Boolean subtraction from the blade model to create the coupling interface between the wedge and blade, see Figure 6-8. Starting at the centre of convergence point 2, the coordinate system was aligned to the centre point, rotated around Z to align the X axis to the first vector, rotated around Y by 36° to create the active wedge angle, and finally rotated around X by the calculated roof angle for that vector, see Figure 6-9. The blank wedge was then sliced in the Y-Z plane to produce the probe contact surface. This process was repeated at each vector for convergence point 1 using the apparent intersection from the previous slice for the position coordinate, see Figure 6-10. The process was repeated for each convergence point on all vectors to produce the approximate probe scan surface. If the process had been carried out without the X coordinate rotation to the required roof angle, then the result would be a wedge with an active 36° angle which followed the shape of the aerofoil. However, the roof angle rotation results in the wedge thickening towards the inlet and outlet ends of the aerofoil which represents the varying roof angle required to produce skew deflection, see Figure 6-11.

A similar process was repeated to produce a wedge for the concave aerofoil; this time the wedge thinned towards the inlet and outlet ends due to the roof angle producing skew deflection in the opposite direction, see Figure 6-12.

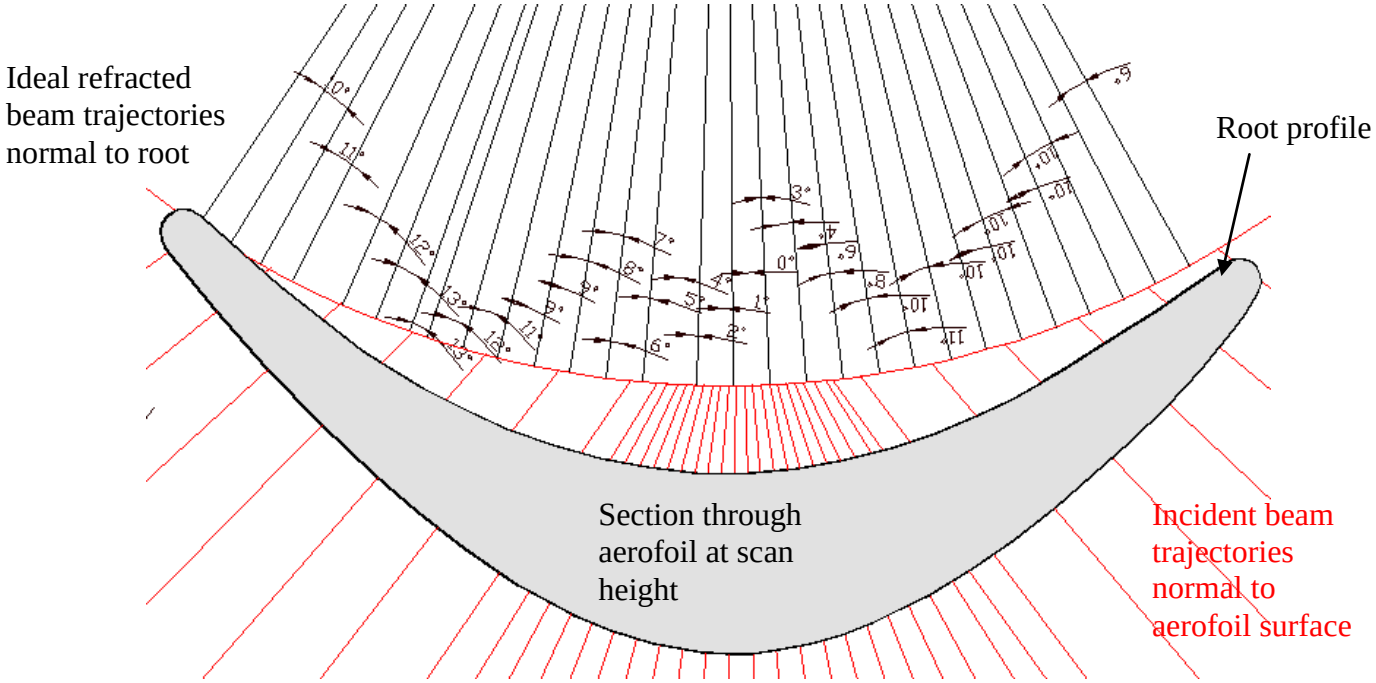

Figure 6-6 Wedge Design, Measurement of required skew deflection comparing aerofoil normal incidence and ideal refracted angles

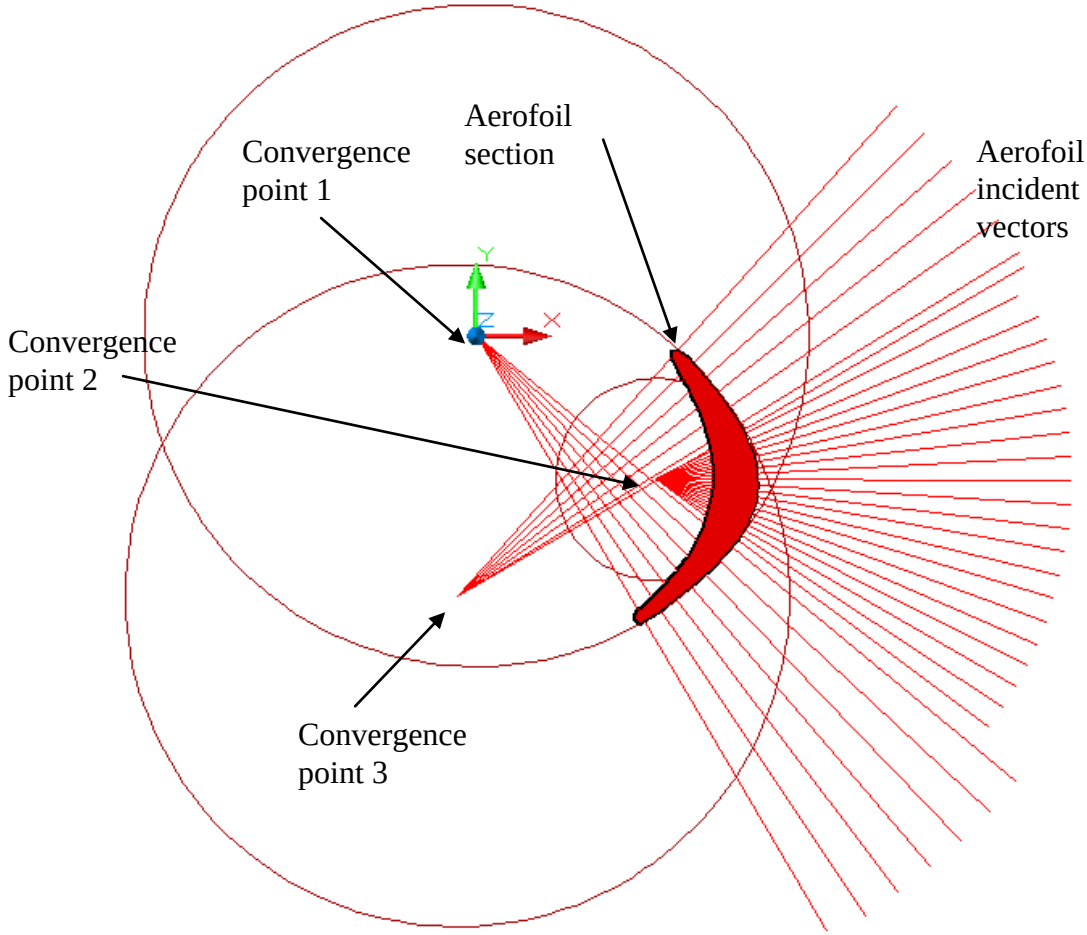

Figure 6-7 Centres of convergence for aerofoil incident vectors

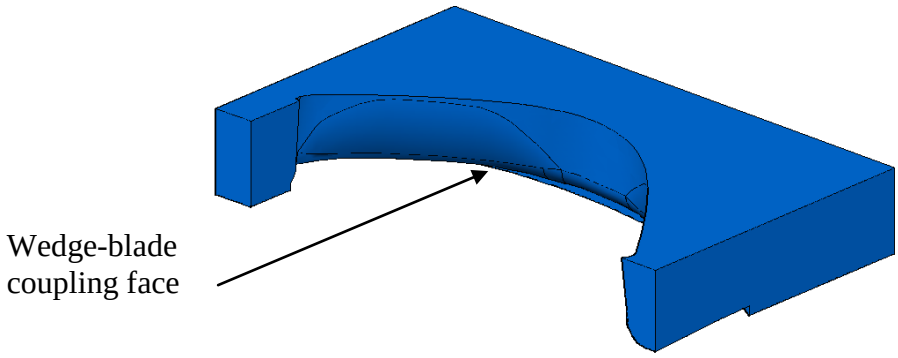

Figure 6-8 Blank wedge block created by Boolean subtraction to match blade

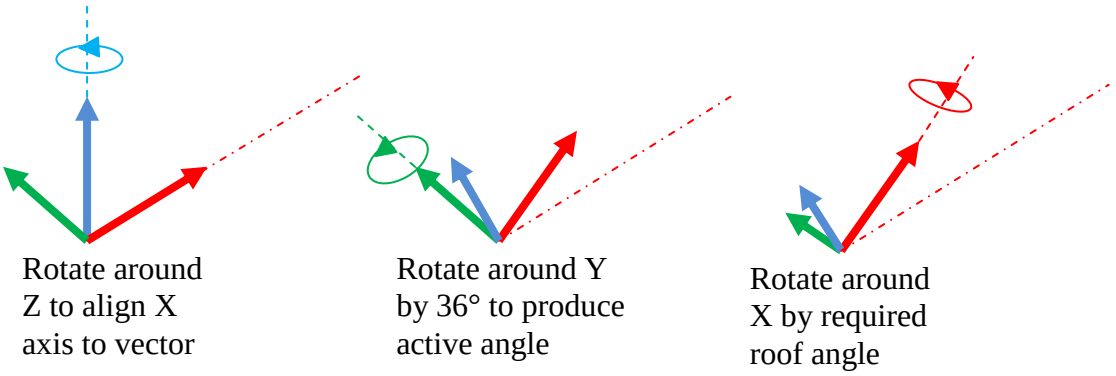

Figure 6-9 Illustration of the coordinate system settings for wedge modelling

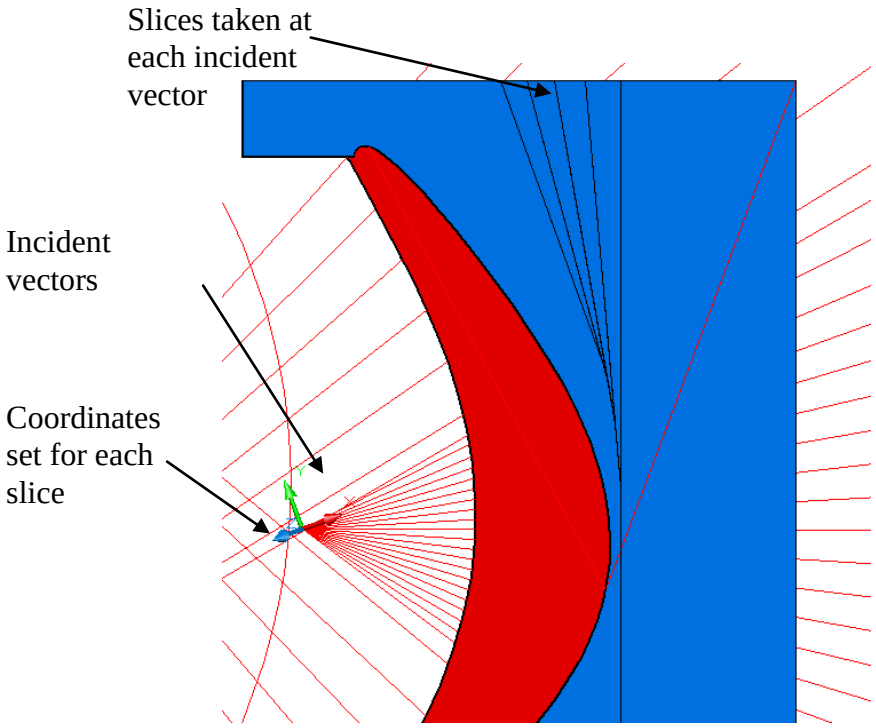

Figure 6-10 Sliced segments being removed from blank wedge at each incident vector

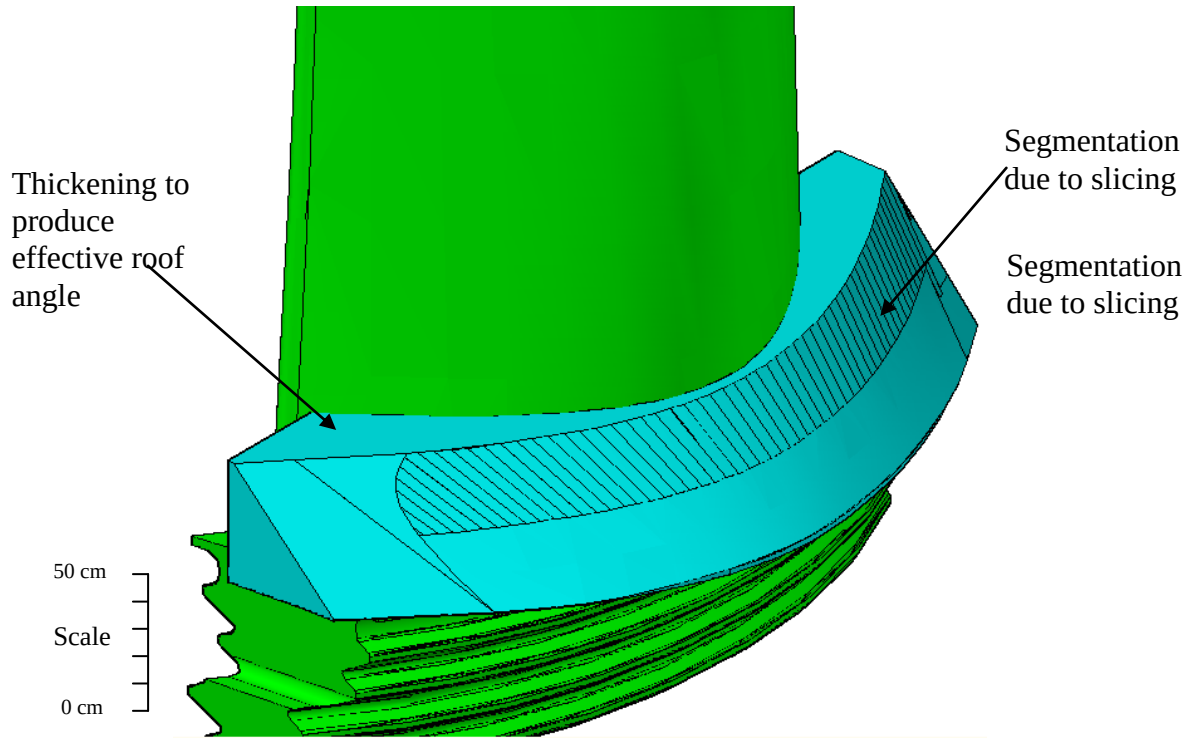

Figure 6-11 Convex side wedge resulting from slicing at each incident vector

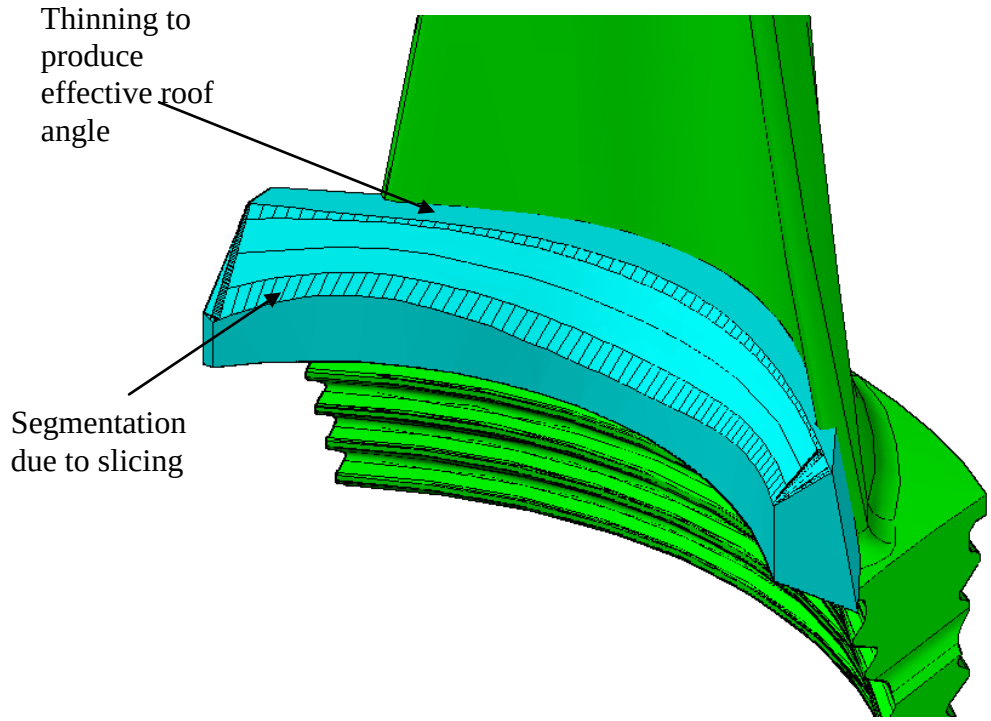

Figure 6-12 Concave side wedge resulting from slicing at each incident vector

The final process for both wedges was to smooth the probe contact surface to interpolate out all the segmentation created in the modelling process. The probe scan surfaces on both wedges produced a 36° angle for refraction in the active direction of the probe, and the effective roof angle which varies subject to axial position has the effect of normalising the beam to the root serrations by skew deflection.

6.3 Simulated validation of continuous wedges

Zetecs' 3D simulation tools, which allow ray tracing to be performed through multiple CAD models, were used to test the performance of the modelled wedges. Arrays of beams were projected onto the probe-scan surface around the full axial extent of the wedge and aerofoil. The simulation was used to check that the skew deflection created by the wedge refracted the beams so that they were normal to the root profile. Figure 6-13 and Figure 6-14 show the simulations carried out to the concave wedge interrogating the convex root. Figure 6-15 and Figure 6-16 show the simulations carried out to the convex wedge interrogating the concave root.

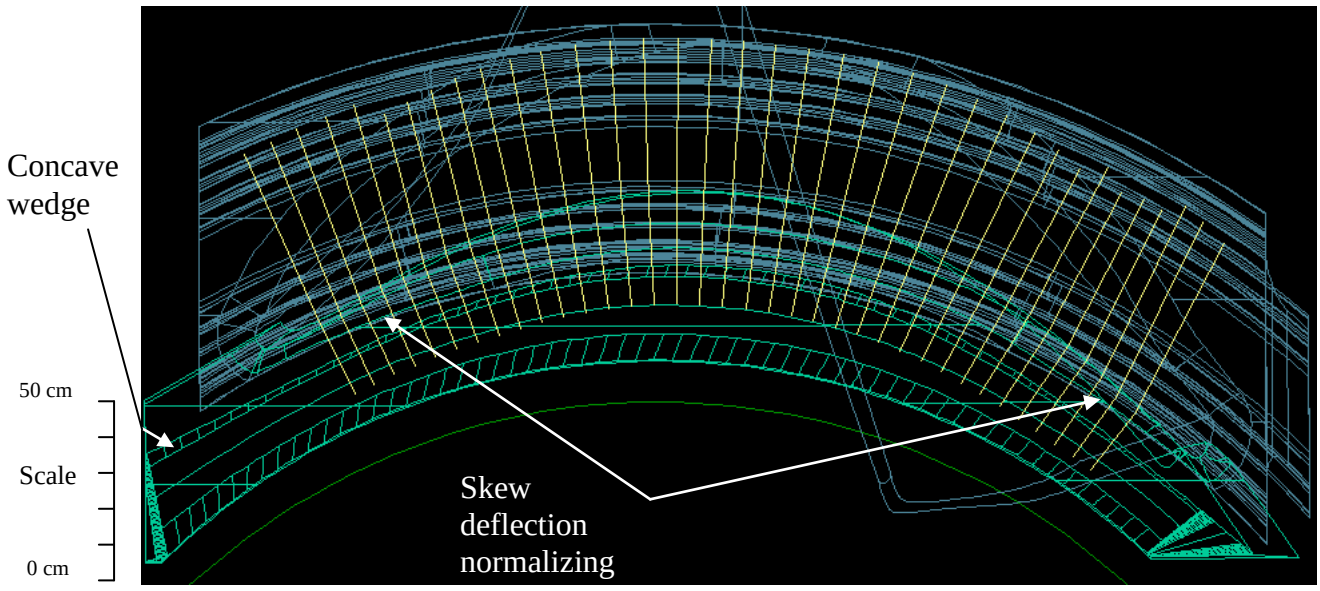

Figure 6-13 Ray tracing simulation of concave wedge interrogating convex root (top view)

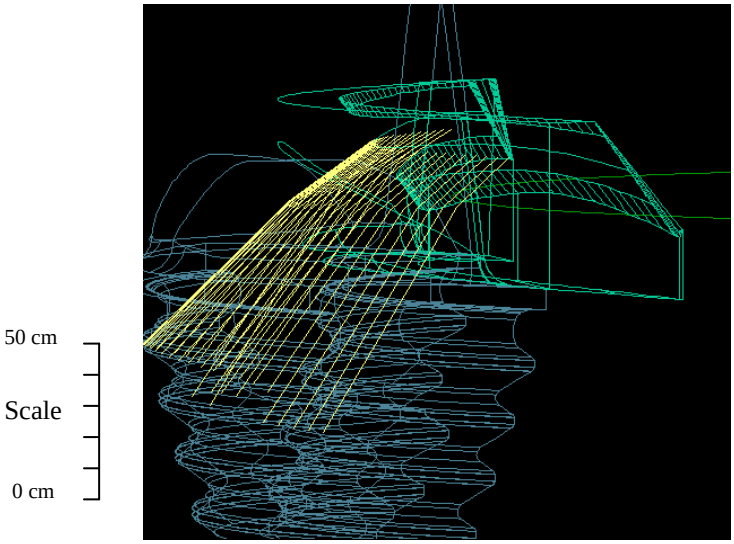

Figure 6-14 Ray tracing simulation of concave wedge interrogating convex root (side view)

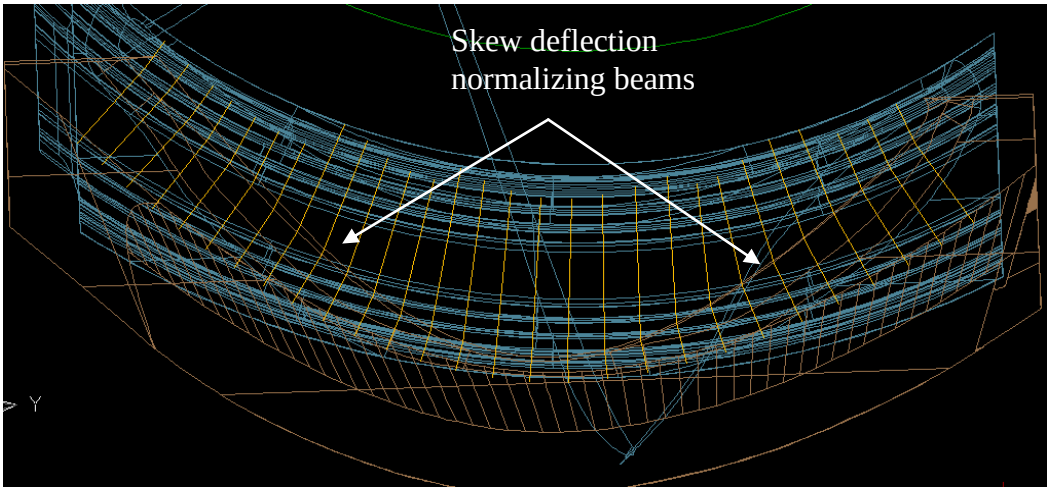

Figure 6-15 Ray tracing simulation of convex wedge interrogating concave root (top view)

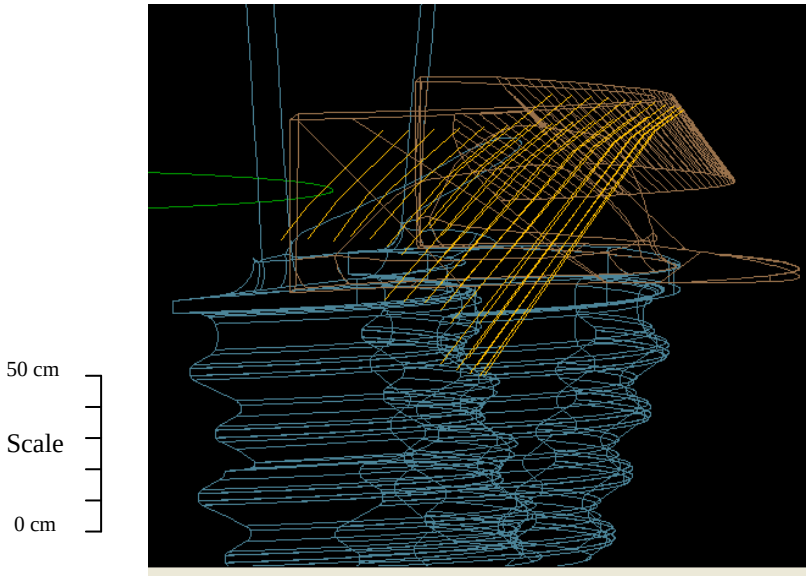

Figure 6-16 Ray tracing simulation of convex wedge interrogating concave root (side view)

It can be seen that the wedges create the refraction in the active plane whilst successfully creating skew deflection to normalise the beam trajectories to the root profiles. Further simulations were carried out generating phased arrays at several positions around the wedges. It can be seen in Figure 6-17 and Figure 6-18 that successful skew deflection for all the separate laws was created.

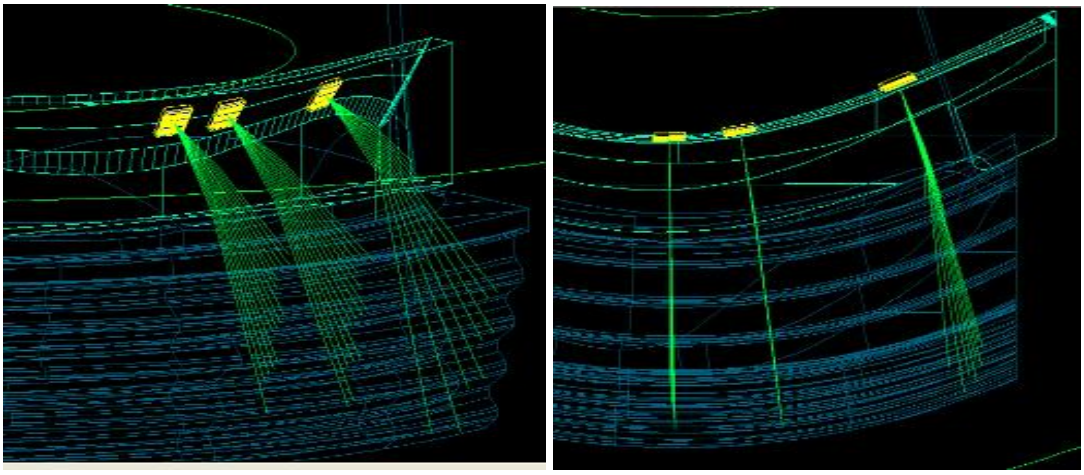

Figure 6-17 Phased array ray tracing simulation of concave wedge interrogating convex root

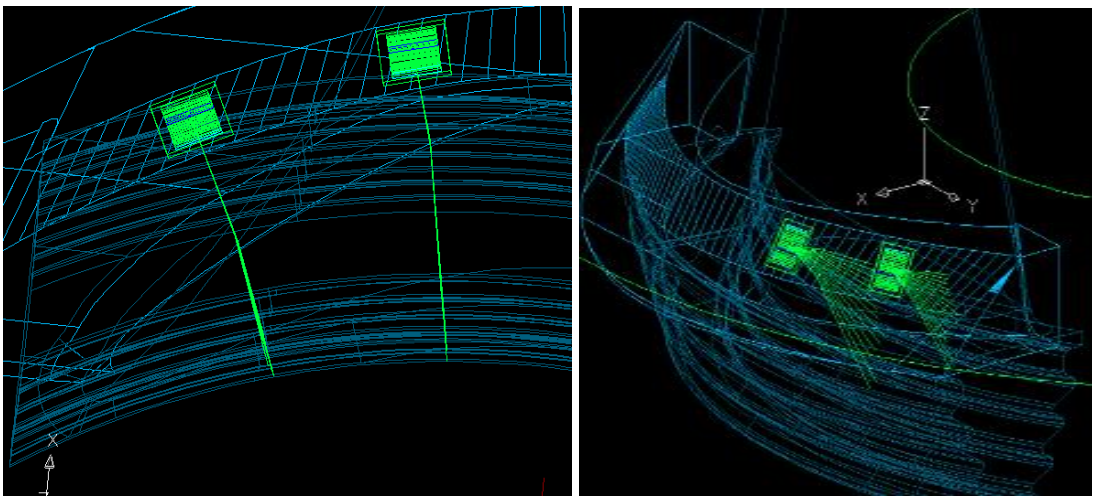

Figure 6-18 Phased array ray tracing simulation of convex wedge interrogating concave root

6.4 Conclusions

After carrying out the various simulations of the wedge models it was found that the desired properties of the wedge were successfully attained. Refracting shear waves into the volume of the blade root whilst creating skew deflection by the appropriate amount required at different positions around the scan had been achieved. As no skewing of the probe would be necessary, it was now conceivable that a probe scanned around the surface of the wedge could generate an encoded line scan. It was seen that in order to produce the roof angling of the wedges to produce the required skew deflection, the wedges had become significantly thicker in certain parts compared to others. This thickening of the wedge would create a challenge for the phased array laws which would, if programmed accurately, vary depending on position around the wedges. It was considered however that a nominal law could be used if the imaging of defects was not affected detrimentally; hence real prototypes were required to carry out experimental validation.

Final modelling of the wedges was carried out to trim away excess material and prepare them for final production. One of each wedge was manufactured from solid Rexolite using 5-axis CNC machining in the RWE npower workshop facility at Ferrybridge. Experimental validation of the wedges was then carried out as described in the following chapter.

Chapter 7. Experimental validation of the continuous wedge

7.1 Introduction

One convex and one concave continuous wedge were manufactured from Rexolite following successful simulation validation in the previous chapter, as seen in Figure 7-1 and Figure 7-2. Experiments were carried out to validate the function of the wedges against the reference blade containing EDM notches which was previously used in the experiments outlined in section 5.3.4 and seen in Figure 5-25 and Figure 5-26. The aim of these experiments was to measure the sensitivity to each notch compared to the centre reference notch and then compare the performance to the baseline results acquired in experiment 1 (section 5.3.4.5) and experiment 2 (section 5.3.4.6). In further experiments the bespoke scanning frame was used to enact encoded line scans of the reference blade, firstly with the traditional Rexolite wedges to acquire baseline measurements, followed by the continuous wedges to compare their performance. The results will show how practicable line scans were impossible using the traditional method whereas the continuous wedges performed as designed in a repeatable and sensitive manner.

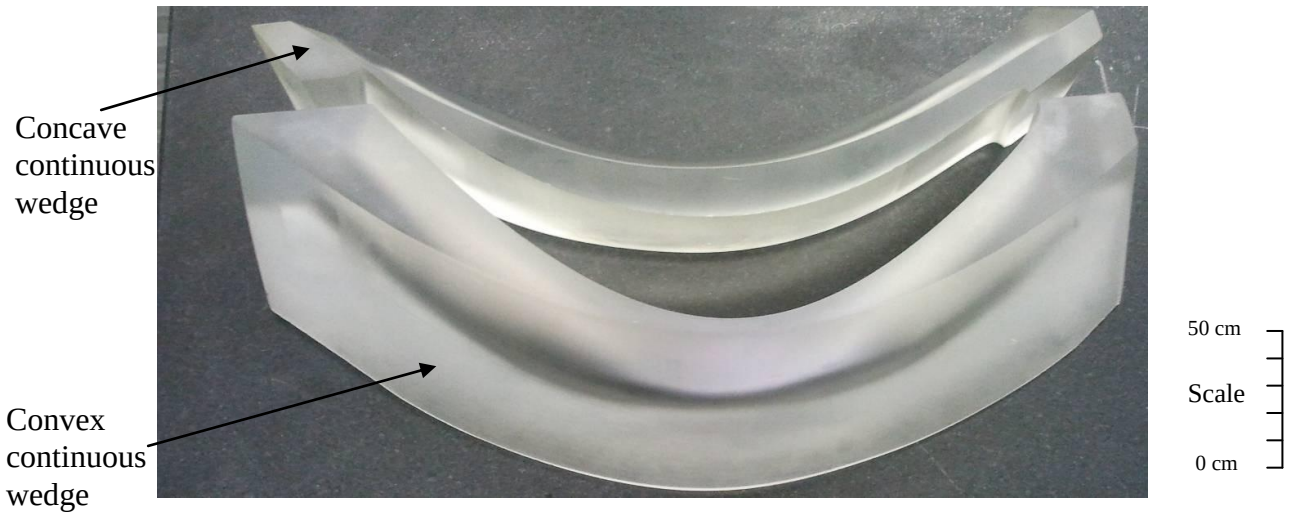

Figure 7-1 Rexolite continuous wedges – top view

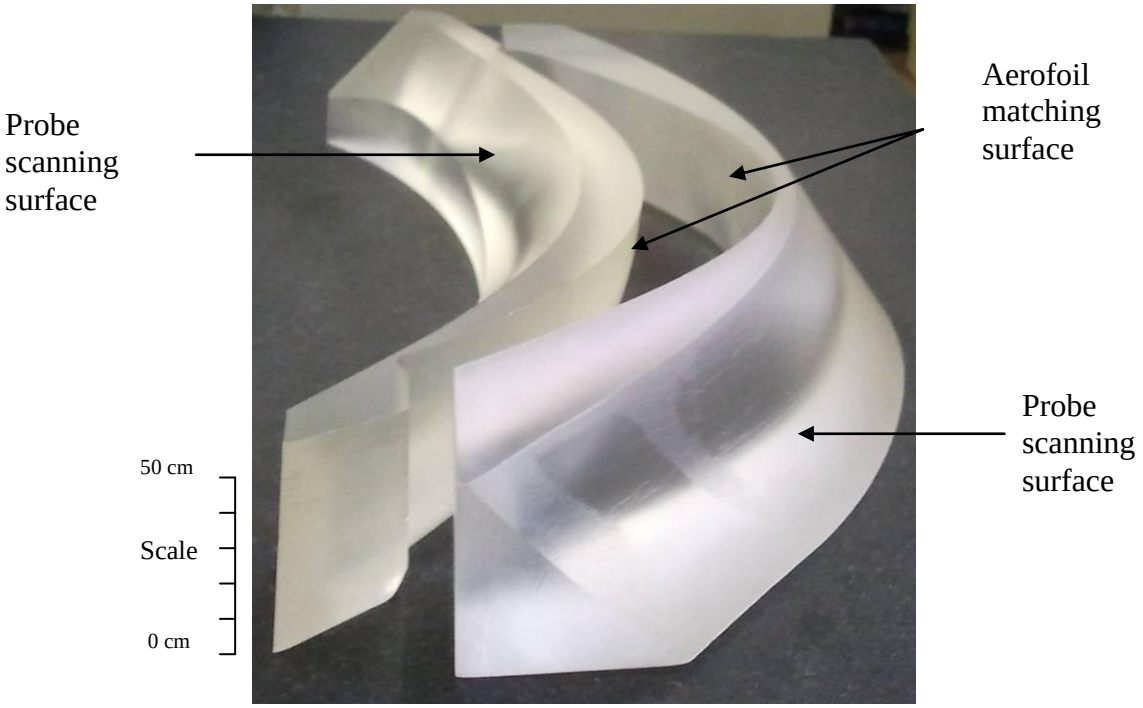

Figure 7-2 Rexolite continuous wedges – side view

7.2 Validation of skew deflection

In the following series of three experiments, the sensitivity to all the notches in the reference blade was tested to establish the extent to which the continuous wedges achieved the goal of producing skew defection. The effect on the thickness variation across the wedge was also tested experimentally to allow for accurate comparison to the baseline results found in experiments 1 and 2, sections 5.3.4.5 and 5.3.4.6 respectively.

7.2.1 Experimental equipment

Zetec Omniscan phased array unit (serial No NP1056), laptop running Ultravision 1.2R4, Imasonic 5L16E16-10 phased array probe (serial No L289C101), concave and convex continuous wedges, Rexolite test block (R1), Zetec bespoke scanning frame, reference sample S1, Sonagel couplant (watered down by 50 %).

7.2.2 Procedures for experiment 5 and 6

The continuous wedge was coupled to the relevant aerofoil of reference blade S1 using the watered down Sonagel couplant, carefully ensuring that all trapped air was evacuated by applying even pressure and viewing through the transparent Rexolite material to confirm. Reference sensitivity was set by maximising the response from the reference notch and calibrating to 80 % FSH. The gain level, beam angle, and depth were recorded. Responses from all notches were maximised in turn setting them to 80 % FSH; gain level, beam angle, and depth were recorded. Notches D, E, L and M were excluded as they are designed for a complementary inspection.

Screen shots of all sector scans were recorded.

7.2.3 Ultravision phased array parameters (Experiment 5 and 6)

Shear wave velocity in sample: 3230ms^{-1}, wedge longitudinal velocity: 2320ms^{-1}, wedge angle: 36°, Height of First Element (HoFE): 14 mm, scan axis offset: 7 mm, sector scan: 35° to 85° at 0.5° steps, focussing: true depth at 40 mm, band pass filters: 3.3 MHz to 7.5 MHz, number of elements: 16, element pitch: 1 mm, elevation: 10 mm, centre frequency: 5 MHz.

7.2.4 Experiment 5 – Continuous wedge scan of concave root from convex aerofoil

7.2.4.1 Reference sensitivity:

Notch E to 80 % full screen height (FSH)

7.2.4.2 Results:

The recorded sector scan of the reference Notch E can be seen in Figure 7-3 below and the recorded sector scans for each of the other notches can be found in Appendix E. Table 7-1 shows a summary of the results for each EDM notch.

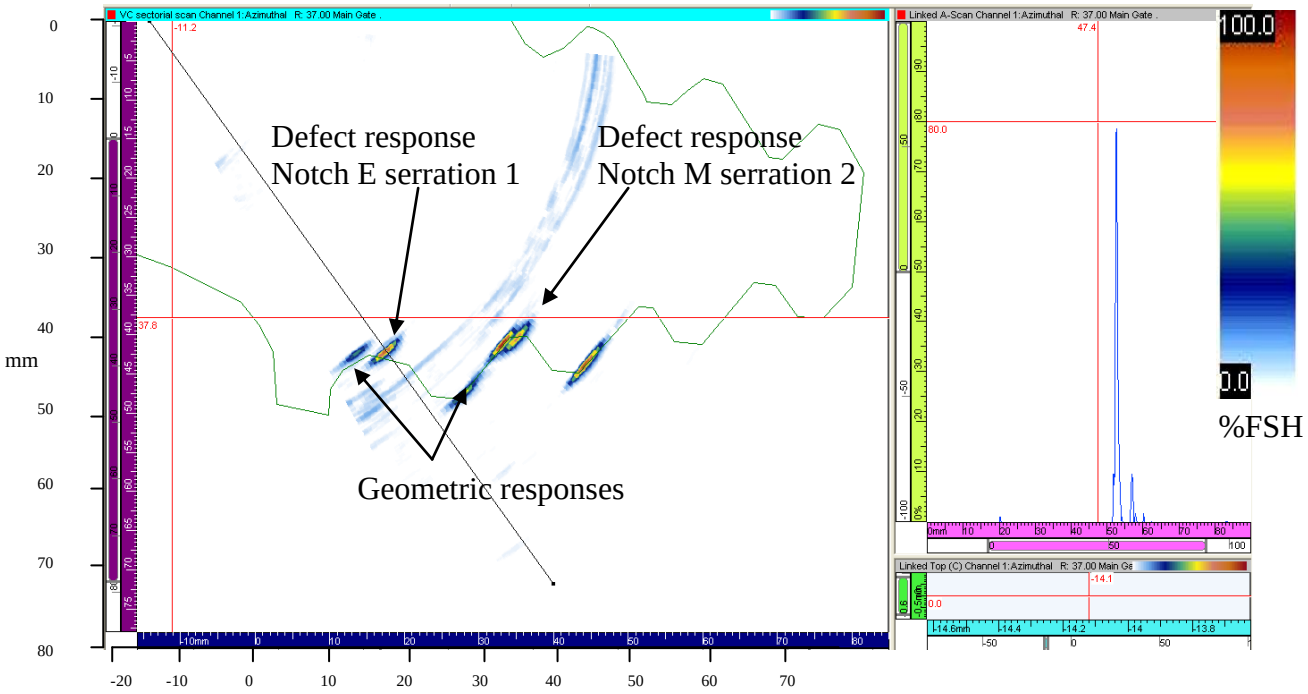

Figure 7-3 Continuous wedge Sector scan of concave Notch E – 80 % FSH, 20dB, 37°, and 42 mm deep

	Continuous wedge results - concave root from convex aerofoil					
	EDM Notch Position	Active angle used in PA law	Gain at 80 % FSH (dB)	Beam Angle (°)	Depth ±0.5 (mm)	Deviation from reference (dB)
Serration 1	A		No Detection out of range			
	B	26°	30	54.5	26.9	+10
	C	30°	22	42.5	37.7	+2
	E (reference)	36°	20	37	42	0
	F	30°	24	51	30.1	+3
	G	28°	30	62	20.5	+10
	H		No Detection out of range			
Serration 2	I		No Detection out of range			
	J		No Detection out of range			
	K	28°	28	58	32.2	+8
	M	36°	22	55.5	33.7	+2
	N	28°	29	65.5	24.2	+9
	O		No Detection out of range			
	P		No Detection out of range			

Table 7-1 Experiment 5 - continuous wedge results concave root

7.2.4.3 Discussion of results

It can be seen from Table 7-1 that the extent of coverage from the convex aerofoil was between notch B at the leading edge and notch G at the trailing edge in serration 1. Also the

limit of coverage in serration 2 was shown to extend past notch K but not as far as notch J at the leading edge and past notch N but not as far as notch O at the trailing edge. It was noted during the experiment that no skewing of the probe was required to acquire maximum responses from each notch and that the geometric responses from the serrations were detected throughout the scan range. This confirmed that the ultrasound was refracting at a trajectory which was normal to the root serrations and also meant that the same probe position which was sensitive to defects in serration 1 were also sensitive to defects in serration 2.

Sensitivity to defects in the first serration varied by 10dB compared to the reference sensitivity level from notch E and defects in the second serration varied by only 9dB. The decrease in sensitivity was due to the increasing beam angles presented to the inspection regions as the offset between the aerofoil and roots decreased towards the inlet and outlet ends. The thickness of the continuous wedge also contributed to the drop in sensitivity towards the ends of the scan due to attenuation in the Rexolite. Experiments were carried out to quantify the contribution made by the wedge thickness on sensitivity as seen in section 7.2.6, experiment 7.

It was found that the active angle associated with the wedge was not consistent around the full extent of the wedge and was altered to correct the image for each measurement taken. The inconsistency was due to an error in the wedge design which had not taken account of the change in slope of the aerofoil as it extended towards the inlet and outlet ends.

7.2.5 Experiment 6 – Continuous wedge scan of convex root from concave aerofoil

7.2.5.1 Reference sensitivity:

Notch D to 80 % Full screen height (FSH)

7.2.5.2 Results:

The recorded sector scan of the reference Notch D can be seen in Figure 7-4 below and the recorded sector scans for each of the other notches can be found in Appendix E. Table 7-2 shows a summary of the results for each EDM notch.

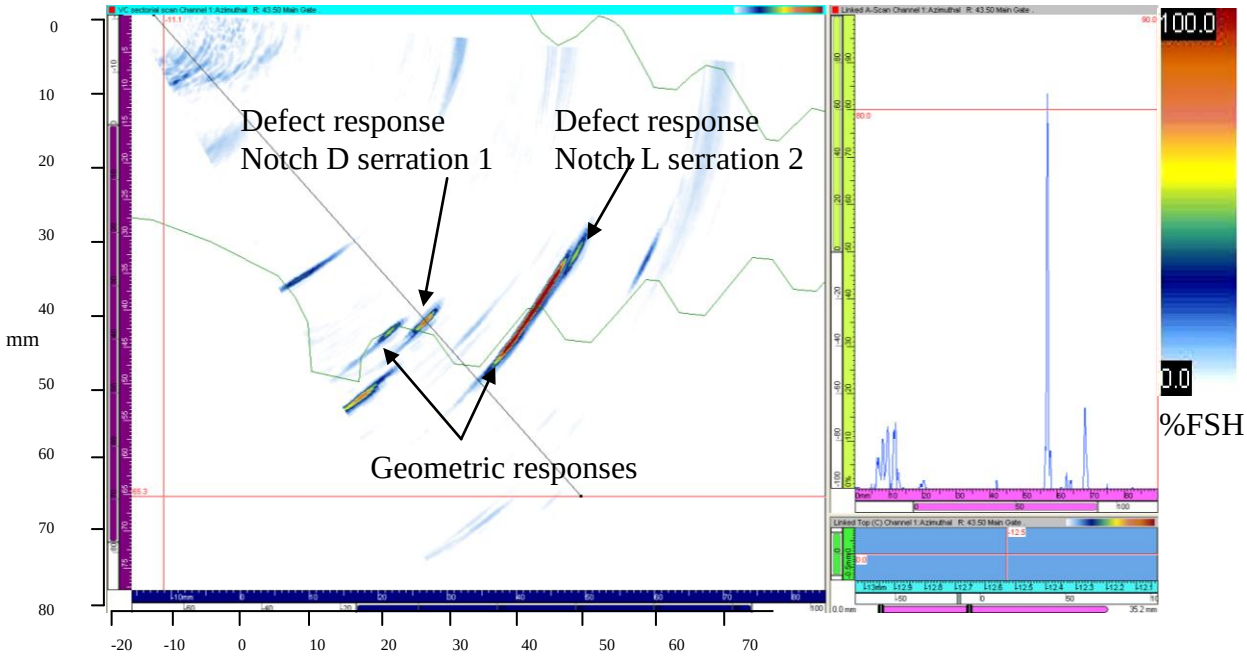

Figure 7-4 Continuous wedge Sector scan of convex Notch D – 80 % FSH, 22dB, 43.5°, and 41.4 mm deep

	Continuous wedge results - convex root from concave aerofoil					
	EDM Notch Position	Active angle used in PA law	Gain at 80 % FSH (dB)	Beam Angle (°)	Depth ±0.5 (mm)	Deviation from reference (dB)
Serration 1	A		No Detection out of range			
	B		No Detection out of range			
	C	30°	18	36	48.1	-4
	D (reference)	30°	22	43.5	41.4	0
	F	33°	17	45.5	39.6	-5
	G		No Detection out of range			
	H		No Detection out of range			
Serration 2	I	30°	30	44	49.7	+8
	J	30°	23	47.5	46.3	+1
	K	30°	22	49.5	44.6	0
	L	30°	24	59.5	33.5	+2
	N	30°	26	48.5	45.5	+4
	O	33°	26	44	49.2	+4
	P	33°	36	38	55	+14

Table 7-2 Experiment 6 - continuous wedge results convex root

7.2.5.3 Discussion of results

It can be seen from Table 7-2 that the extent of coverage from the concave aerofoil was between notch C at the leading edge and notch F at the trailing edge in serration 1. The main limitation was set by the overhang of the root platforms blocking the beam trajectories beyond these notches. The limit of coverage in serration 2 was shown to extend to all notches in the second serration although the response from notch P was very weak due to the platform overhang beginning to block the beam to the second serration.

It was again noted during the experiment that no skewing of the probe was required to acquire maximum responses from each notch and that the geometric responses from the serrations were detected throughout the scan range. This confirmed that the ultrasound was refracting at a trajectory which was normal to the root serrations.

The sensitivity to notches away from the centre of serration 1 was improved compared to the reference notch D where a variation of up to -5dB was measured. The variation in sensitivity to notches in the second serration was also very small apart from a variation of +8dB for notch I and +14dB for notch P where the platform began to block the beam.

It was again found that the active angle associated with the wedge was not consistent around the full extent of the wedge and was altered to correct the image for each measurement taken.

7.2.6 Experiment 7 – Attenuation measurement of Rexolite block

7.2.6.1 Ultravision phased array parameters:

Compression wave velocity (Rexolite): 2320ms^{-1}, wedge angle: 0°, Height of First Element (HoFE): 0 mm, scan axis offset: 0 mm, sector scan: -5° to 5° at 0.5° steps, focussing: true depth at 1000 mm, band pass filters: 3.3 MHz to 7.5 MHz, number of elements: 16, element pitch: 1 mm, elevation: 10 mm, centre frequency: 5 MHz.

7.2.6.2 Procedure:

The Rexolite test block (R1), which was machined from the same batch of material used for the manufacture of the continuous wedges, was used to assess the attenuation and transfer losses in all dimensions, see Figure 7-5.

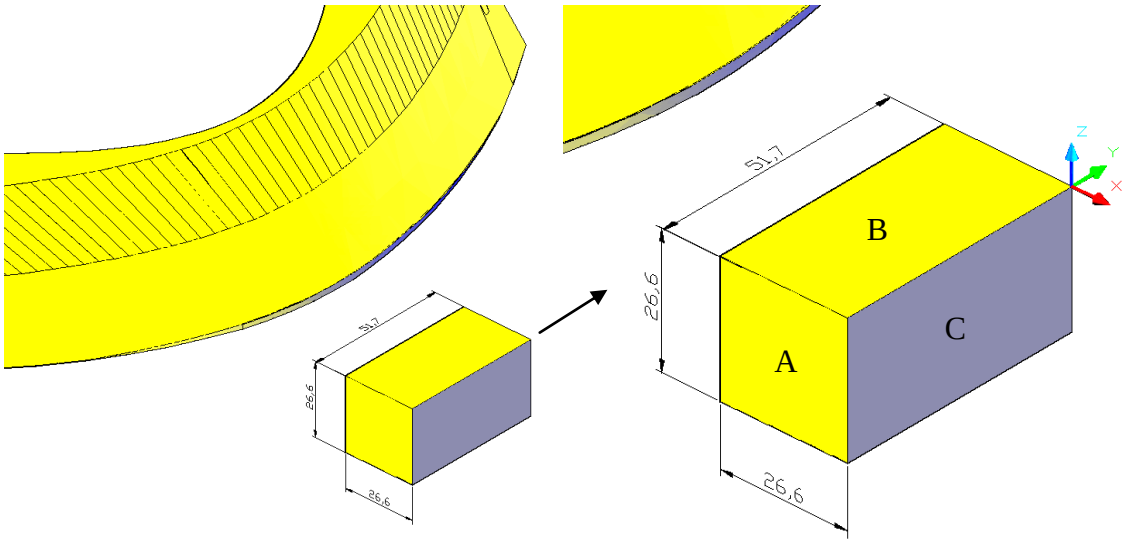

Figure 7-5 Rexolite test block (R1) – X = 26.6 mm, Z = 26.6 mm, Y = 51.7 mm

The phased array probe was coupled directly to face A of the Rexolite test block with a small amount of Sonagel couplant; the second back wall echo was maximised to 100 % full screen height (FSH) and the gain level recorded. The gain was increased to maximise the third back wall echo followed by the fourth back wall echo and the gain levels recorded for each at 100 % FSH. The experiment was then repeated from face B and face C. The gain difference between the subsequent echoes was used to approximate the combined attenuation and transfer losses in each dimension of the block.

7.2.6.3 Results:

Table 7-3 shows the results obtained from each of the dimensions of the Rexolite block and records the losses which consist of a combination of material attenuation and transfer losses through subsequent skips between the back wall and coupling interface. The calculation used for the attenuation approximation was as follows: -

$$\alpha = \Delta dB/2d$$

Where α = Attenuation,
ΔdB = change in gain between subsequent back wall (BW) echoes
d = thickness of sample

It is noted that this calculation provides an approximation of material attenuation and takes no account of the reflection coefficient at the probe/sample interface and transfer losses through the couplant layer.

	Rexolite test block (R1) attenuation checks				
	2nd BW gain (dB) ±0.5	3rd BW gain (dB) ±0.5	4th BW gain (dB) ±0.5	Attenuation 2nd to 3rd BW (dB/mm) ±0.02	Attenuation 3rd to 4th BW (dB/mm) ±0.02
Face A – Y coordinate (51.7 mm)	22	35	47	0.126	0.116
Face B – Z coordinate (26.6 mm)	10	20	30	0.188	0.188
Face C – X coordinate (26.6 mm)	10	19	28	0.169	0.169

Table 7-3 Experiment 7 – Rexolite attenuation measurement results

7.2.6.4 Discussion of results

It is clear from the results recorded in Table 7-3 that the losses measured in the X and Z coordinates were consistent. However the losses in the Y coordinate were measurably less than the other two dimensions. As the measurements in all dimensions were taken over the same number of back wall echoes (independently of beam path) then transfer losses would be approximately equal for each dimensional measurement. The Rexolite test block was machined in the orientation shown in Figure 7-5 compared to the continuous wedges; that means that the attenuation of the continuous wedges in the orientation of ultrasonic propagation is approximately 0.169dB/mm ±0.02.

7.3 Comparison of results experiments 5, 6, and 7

The sensitivity levels using the continuous wedges measured in experiments 5, 6 and 7 were compared to the results measured in experiments 1 and 2 (section 5.3.4) which provided the baseline results of sensitivity to each EDM notch in the reference blade. Due to

the thickness variation across the continuous wedge it was necessary to compensate for the attenuation in the Rexolite at different notch positions to provide an accurate comparison. Measurements of the Rexolite beam path (height of first element) in the continuous wedge for each notch position were made and used to calculate the approximate attenuation based on 0.17dB/mm as measured in experiment 7. Table 7-4 shows the beam path measurements for each notch and the attenuation calculated for the delta beam path compared to the reference notch beam path. It can be seen that the very thickest region of the convex wedge creates up to 8dB more attenuation of the ultrasound compared to the reference position in the middle of the wedge. These figures were rounded up or down to the nearest whole decibel and negated from the experimental results for the continuous wedges. Table 7-5 shows the deviation from reference sensitivity for the baseline results (section 5.3.4) compared to the attenuation adjusted continuous wedge results.

	Attenuation compensation for continuous wedges							
	Concave Wedge				Convex Wedge			
	Notch	Rexolite BP (mm)	ΔBP ($BP - BP_{ref}$) (mm)	Attenuation ($\alpha \times 2\Delta BP$) (dB)	Notch	Rexolite (BP) (mm)	ΔBP ($BP - BP_{ref}$) (mm)	Attenuation ($\alpha \times 2\Delta BP$) (dB)
Serration 1	A				A			
	B				B	26	19	6.46
	C	17	-2	-0.68	C	16	9	3.06
	D(BP_{ref})	19	0	0	E(BP_{ref})	7	0	0
	F	18	-1	-0.34	F	19	12	4.08
	G				G	30	23	7.82
	H				H			
Serration 2	I	7	-12	-4.08	I			
	J	12	-7	-2.38	J			
	K	17	-2	-0.68	K	16	9	3.06
	L	19	0	0	M	7	0	0
	N	18	-1	-0.34	N	19	12	4.08
	O	13	-6	-2.04	O			
	P	12	--7	-2.38	P			

Table 7-4 Attenuation compensation in continuous wedges

		Continuous wedge Sensitivity Comparison 80 % FSH (dB)					
	EDM Notch Position	Convex Root deviation from reference (dB)			Concave Root deviation from reference (dB)		
		Baseline	Concave Wedge	Δ dB	Baseline	Convex Wedge	Δ dB
Serration 1	A						
	B				+7	+4	3
	C	-5	-3	-2	0	-1	1
	D	0 (reference)	0 (reference)	0			
	E				0 (reference)	0 (reference)	0
	F	-3	-5	2	+2	-1	3
	G				+7	+2	5
	H						
Serration 2	I	+7	+12	-5			
	J	-1	+3	-4			
	K	0	+1	-1	+11	+5	6
	L	+5	+2	3			
	M				+4	+2	2
	N	+3	+4	-1	+13	+5	8
	O	-2	+6	-8			
	P	+8	+16	-8			

Table 7-5 Continuous wedge sensitivity comparison

Significant improvement in the sensitivity was acquired by the convex continuous wedge compared to the baseline results (highlighted in green) and in some regions using the concave continuous wedge. However, whilst showing a relative reduction in sensitivity, the results for the concave wedge were still comparable to the baseline results, only deviating significantly in notches I, O, and P where blocking by the platform affected sensitivity. The ability to push the probe down into the platform radius towards the ends of the aerofoil enabled the sensitivity to be improved when carrying out experiment 2 to get the baseline results; when using the continuous wedge, pushing the probe further down the scan face meant that sensitivity could be improved to notches I, O and P, but it did not represent a practical solution when the overall ideal scan height was higher up the wedge. The graphs in Figure 7-6 and Figure 7-7 show plots of all the notch sensitivity deviations for all experiments, including the baseline (experiments 1 and 2), bespoke scanner (experiments 3

and 4) and continuous wedge (experiments 5 and 6). Lower values for the deviation from reference represent higher sensitivity relative to the reference notch.

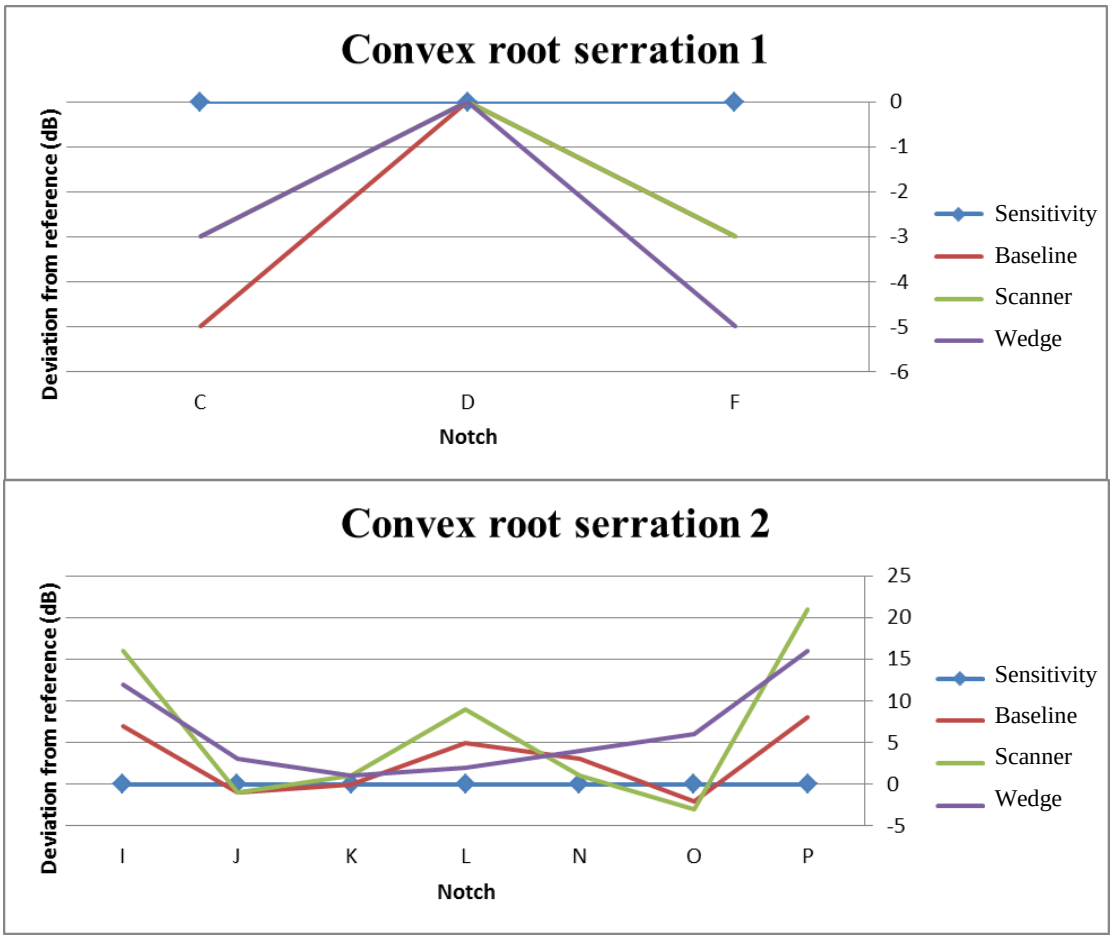

Figure 7-6 Plot of convex root sensitivity deviation comparing baseline, scanner, and continuous wedge results (ΔdB from Table 7-5)

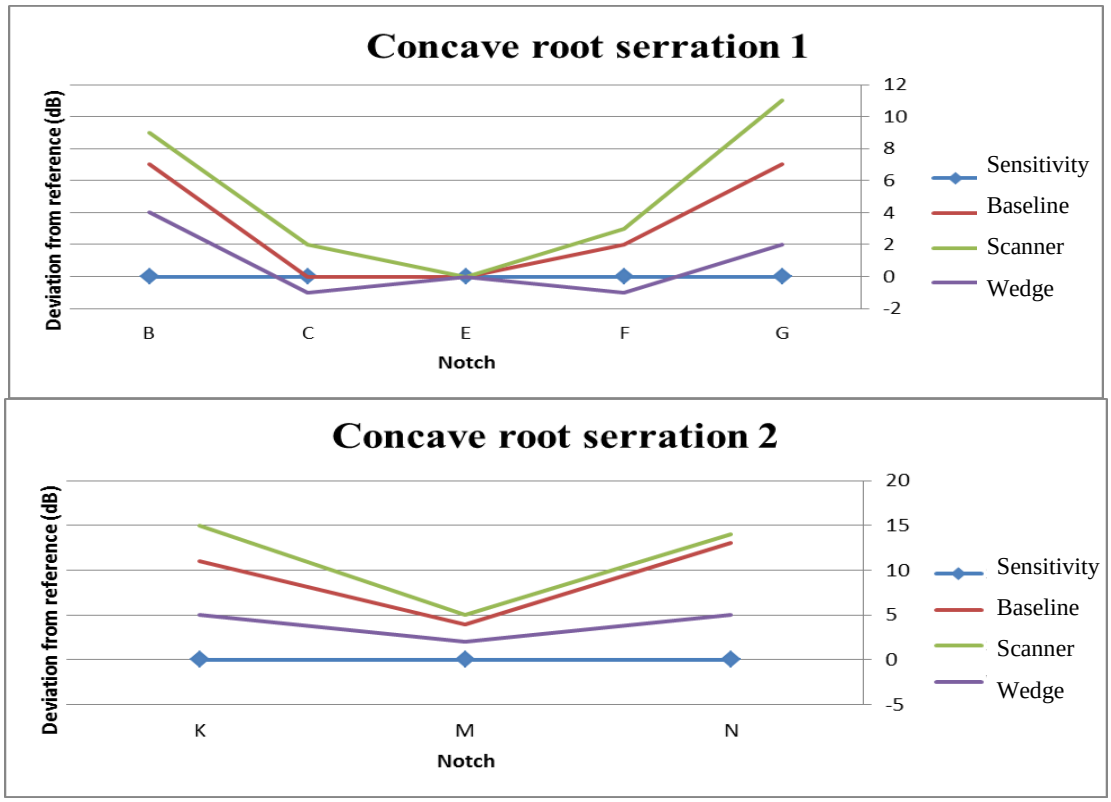

Figure 7-7 Plot of concave root sensitivity deviation comparing baseline, scanner, and continuous wedge results (ΔdB from Table 7-5)

The sensitivity to notches in the concave root is clearly improved whilst utilising the continuous wedge as seen as purple plots on the graphs in Figure 7-7. There is also a measureable evening out of the deviation from the reference level across the axial extent of the scan. The result in practice would be that the scan sensitivity, which is reference sensitivity plus an appropriate level of gain for search scanning, could be set at a lower value; this would prevent significant saturation of ultrasonic responses from geometry and defects in highly sensitive regions in comparison to those in less sensitive regions, and also improve the ability to resolve defects from geometric echoes.

The sensitivity to notches in serration 1 of the convex root using the continuous wedge is evenly matched to the baseline result; being 2 dB more sensitive towards the trailing edge near notch F, but 2 dB less sensitive than the baseline at the leading edge near notch C, see Figure 7-6. In serration 2 of the convex root however, the continuous wedge offers better

sensitivity in the centre but less towards the leading and trailing edges. The main reason for this decrease towards the ends is the blocking of beam propagation caused by the platforms. More significantly is the fact that the wedge has the effect of evening out the sensitivity across the axial extent of the scan and if the extreme outer notches were discounted the variation would be less than 5 dB. The result again would be that the scan sensitivity could be set at a lower value to prevent significant saturation of ultrasonic responses.

7.4 Encoded line scans

One of the aims of the research as outlined in section 1.4 was to establish techniques which overcome the engineering challenges of inspecting LP turbine last stage blades whilst in-situ, with the aim of increased coverage, sensitivity, repeatability and reliability. While it has been shown that increases in coverage and sensitivity have been achieved with in-situ access using precision jigs and bespoke scanning frames, the application of the inspections rely on the vigilance, skill level and integrity of the operator. Variation between operators can lead to different levels of detection of small defects, while manual manipulation of probes on complex surfaces in unsighted regions can lead to poor repeatability and reliability of the technique. The application of the bespoke scanning frames alleviates some of the variables but requires high levels of skill to manipulate the probe and achieve precise and repeatable coverage.

Experiments were carried out to show how combining the scanning frames, which offer precise and repeatable probe positioning on the component, with the continuous wedges, facilitated the application of encoded line scans. Using the line scanning technique ensures that the inspection area is comprehensively and accurately interrogated in a repeatable and reliable way. Moreover, data is collected for the whole scan region providing a finger print of every blade for the records and facilitating offline analysis of merged B, C, and D scans.

Cross checking and auditing of scan results is also improved therefore decreasing the likelihood of defects being missed.

7.4.1 Experimental equipment

Zetec Omniscan phased array unit (serial No NP1056), Laptop running Ultravision 1.2R4, Imasonic 5L16E16-10 phased array probe (serial No L289C101), 36° flat Rexolite wedge (HoFE 8 mm), 36° contoured Rexolite wedge (HoFE 8 mm), concave and convex continuous wedges, Zetec bespoke scanning frame, reference sample S1, Sonagel couplant (watered down by 50 %).

7.4.2 Ultravision phased array parameters

Shear wave velocity in sample: 3230ms^{-1}, wedge longitudinal velocity: 2320ms^{-1}, wedge angle: 36°, Height of First Element (HoFE): 8 mm, scan axis offset: 7 mm, sector scan: 35° to 85° at 0.5° steps, focussing: true depth at 40 mm, band pass filters: 3.3 MHz to 7.5 MHz, number of elements: 16, element pitch: 1 mm, elevation: 10 mm, centre frequency: 5 MHz.

7.4.3 Procedures for experiments 8, 9, 10 and 11

The bespoke scanning frame was configured to inspect as appropriate the convex or concave root as seen in Figure 5-30 in section 5.3.4.2 and Figure 5-31 in section 5.3.4.3. The height of the scanner was adjusted so that the front of the probe was measured at 15 mm from the top of the root platform. Reference sensitivity was set by maximising the response from the reference notches and calibrating to 80 % FSH while a further 8 dB were added for scan sensitivity. The probe skew adjustment mechanism was set to 0° and locked in position and the probe positioned with the centre line of the wedge lined up with the edge of the trailing of the aerofoil. The encoder output from the scanner was calibrated and couplant was applied to the scan path around the concave aerofoil. Ultravision was configured to perform a single line scan, triggered on the encoder input and collecting data every 0.5 mm,

and displaying an online B scan to monitor the progress of the scan. Ultravision was triggered and the probe was slowly driven around the aerofoil until the centre line of the wedge lined up with the leading edge of the aerofoil. The collected data was stored and volumetrically merged to produce B scan and C scan views of the full data volume. The scan was repeated a further three times.

7.4.4 Experiment 8 – Baseline encoded line scan of convex root from concave aerofoil using conventional wedges

7.4.4.1 Reference sensitivity:

Notch D to 80 % Full screen height (FSH)

7.4.4.2 Scan sensitivity:

Reference sensitivity plus 8dB

7.4.4.3 Results:

The volumetrically merged data scans can be seen in

to Figure 7-11 showing the merged C, merged B and sector scan of the section through the red measuring ruler. Where responses from notches have been identified they are labelled with their designated letter.

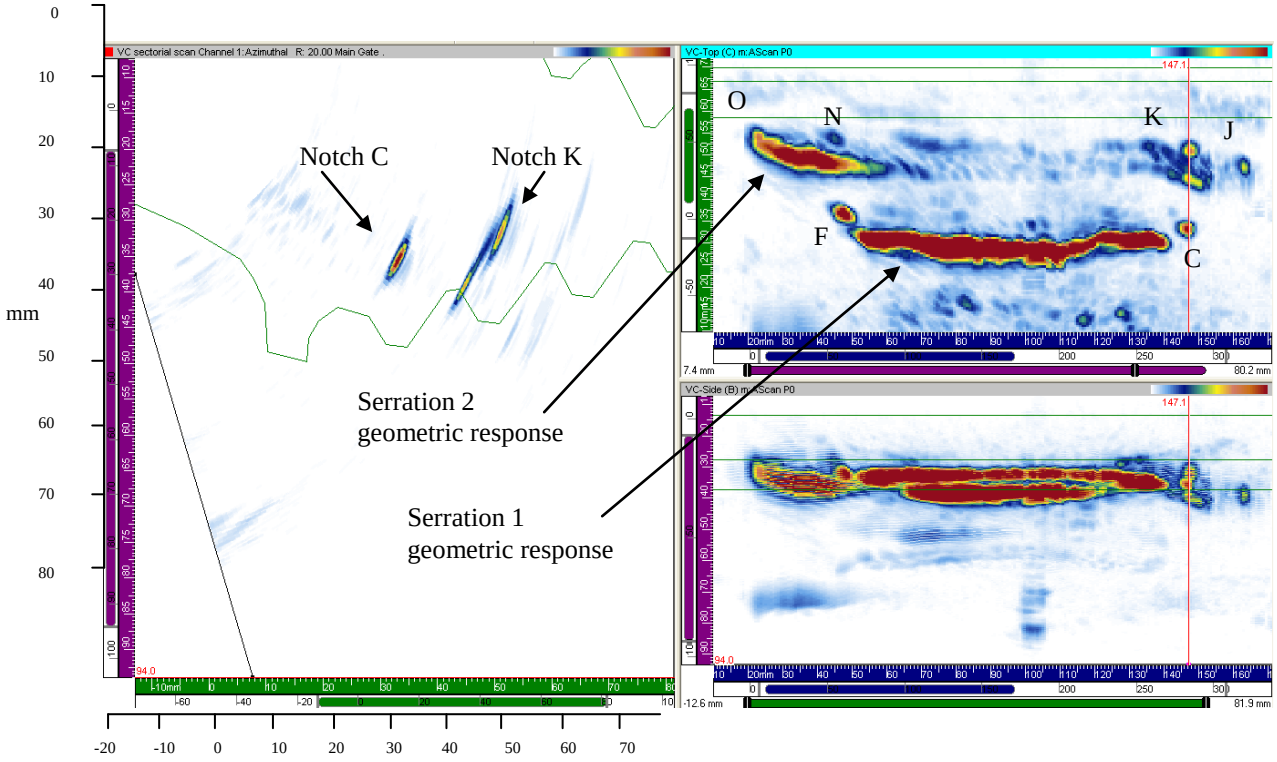

Figure 7-8 Experiment 8 – Convex root inspection with conventional wedge line scan 1

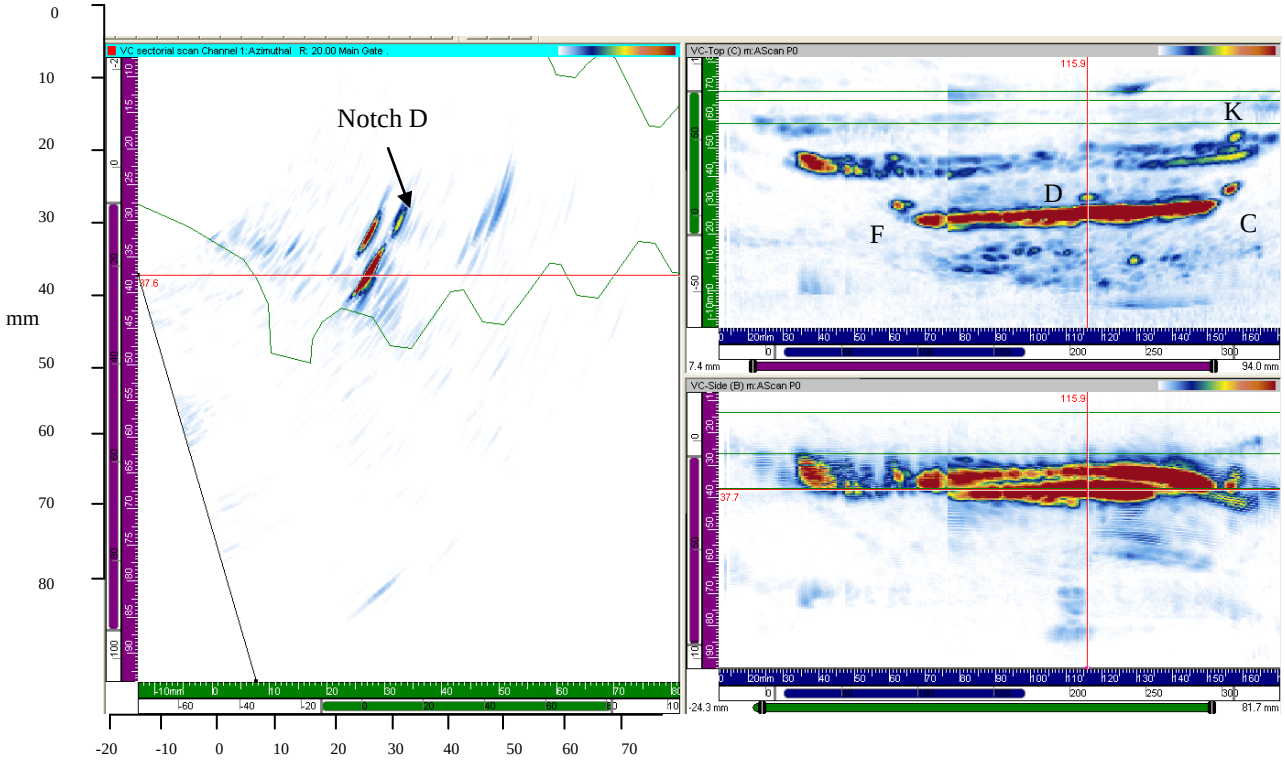

Figure 7-9 Experiment 8 – Convex root inspection with conventional wedge line scan 2

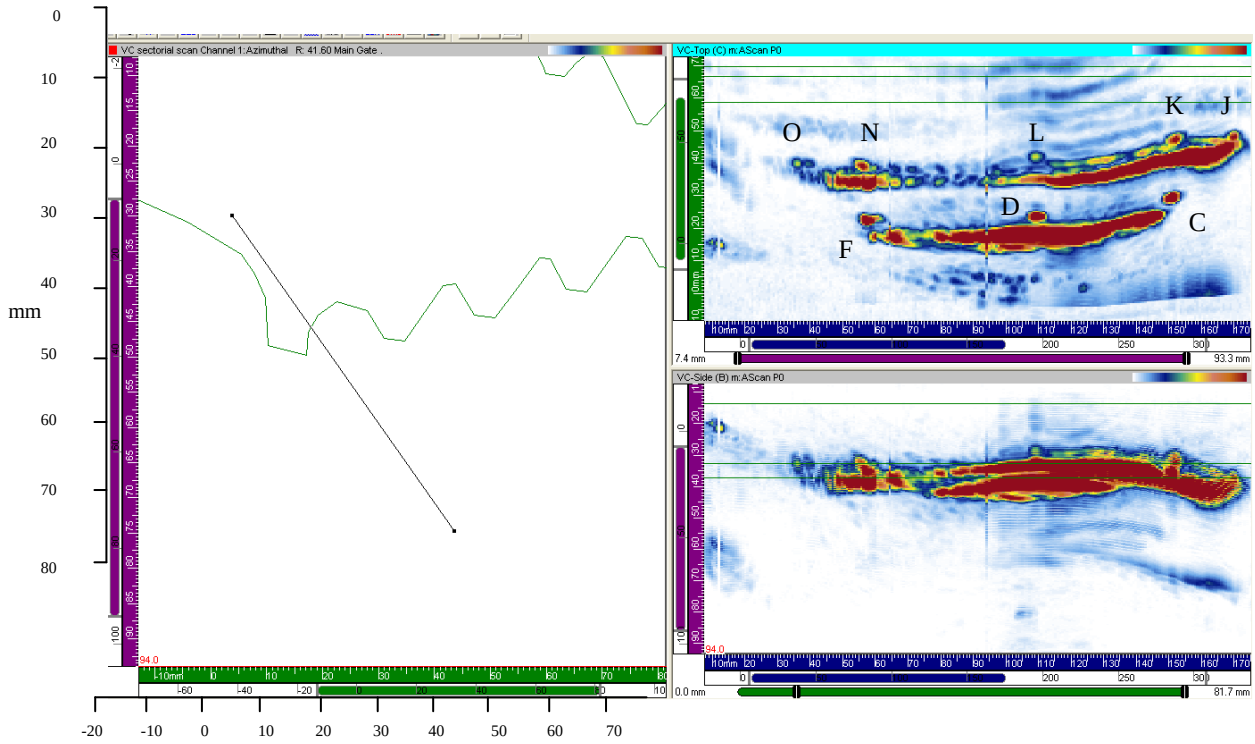

Figure 7-10 Experiment 8 – Convex root inspection with conventional wedge line scan 3

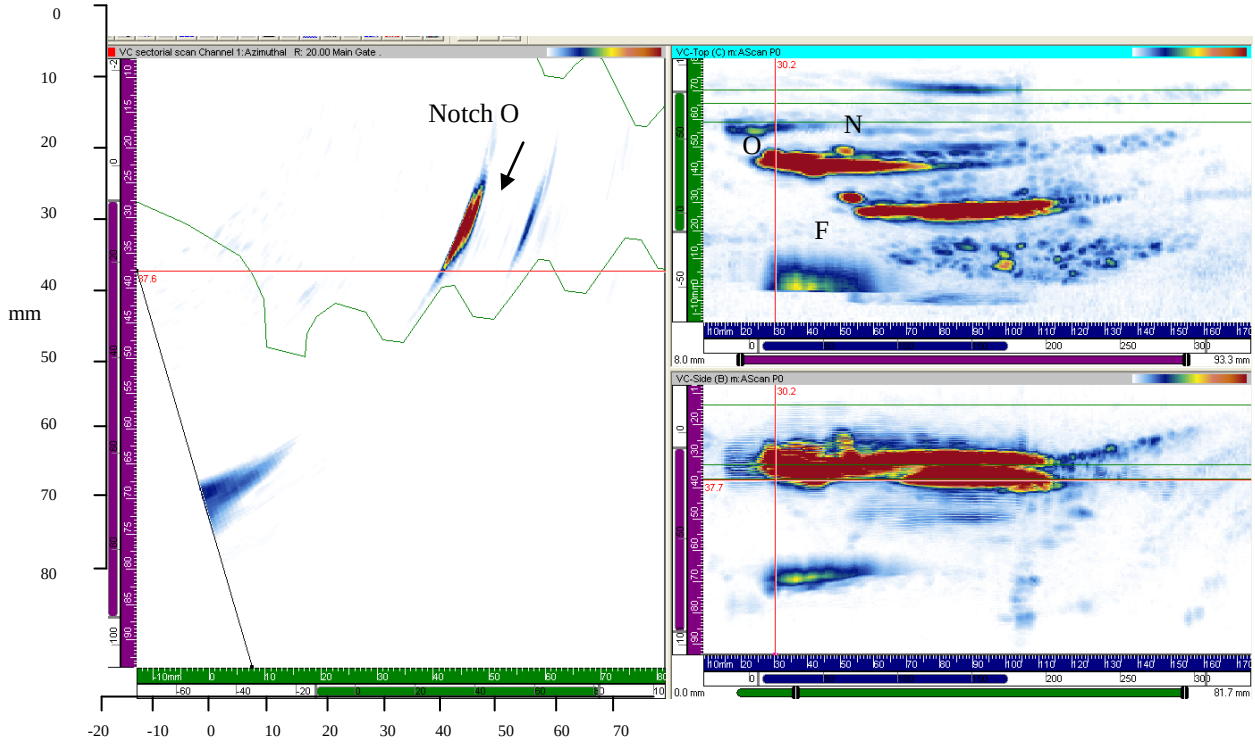

Figure 7-11 Experiment 8 – Convex root inspection with conventional wedge line scan 4

7.4.4.4 Discussion of results:

It can be seen in Figure 7-8 that scan 1 produced a consistent geometric responses from serration 1, indicating that coupling to the aerofoil was satisfactory. However, responses

from the serration 2 geometric were inconsistent and the scan failed to detect notches D and L in the critical centre regions; only weak responses from notches J, K, N and O were produced. Scan 2 (Figure 7-9) produced significantly less consistent coupling and failed to detect all but notch K in the second serration. Scan 3 (Figure 7-10) produced the best result and all notches were detected; inconsistent sensitivity across the scan and poor coupling were noted. Scan 4 (Figure 7-11) showed excellent sensitivity at the start of the scan at the trailing edge and detected notches F, N and O, but coupling was disrupted resulting in poor sensitivity and no further detection of geometric or defect responses.

The most notable issue with the application of this scan was the lack of repeatable coupling and inability to consistently detect all defects. The mechanical design of the scanner and refinement of the wedge profile might overcome some of the issues with coupling, but the requirement to skew the probe at various positions around the scan prevent it being a practicable solution.

7.4.5 Experiment 9 – Baseline encoded line scan of concave root from convex aerofoil using conventional wedges

7.4.5.1 Reference sensitivity:

Notch E to 80 % Full screen height (FSH)

7.4.5.2 Scan sensitivity:

Reference sensitivity plus 8dB

7.4.5.3 Results:

The volumetrically merged data scans can be seen in Figure 7-12 to Figure 7-15 showing the merged C, merged B and sector scan of the section through the red measuring ruler. Where responses from notches have been identified they are labelled with their designated letter.

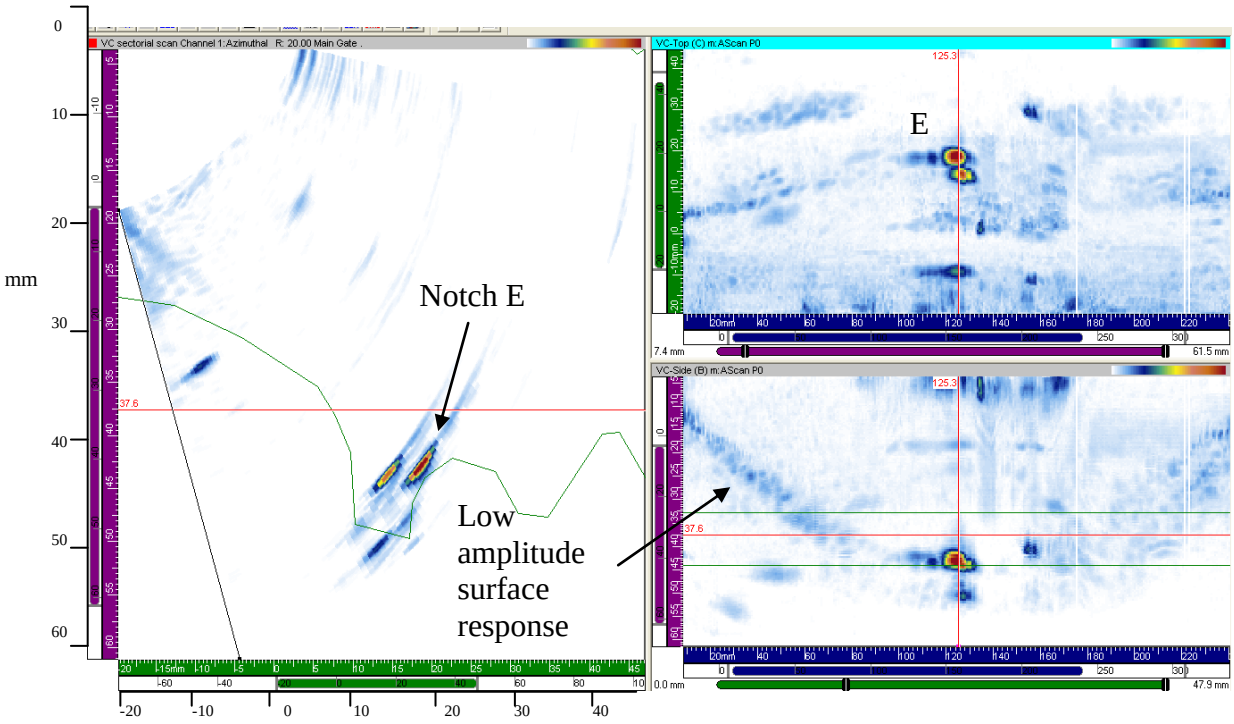

Figure 7-12 Experiment 9 – Concave root inspection with conventional wedge line scan 1

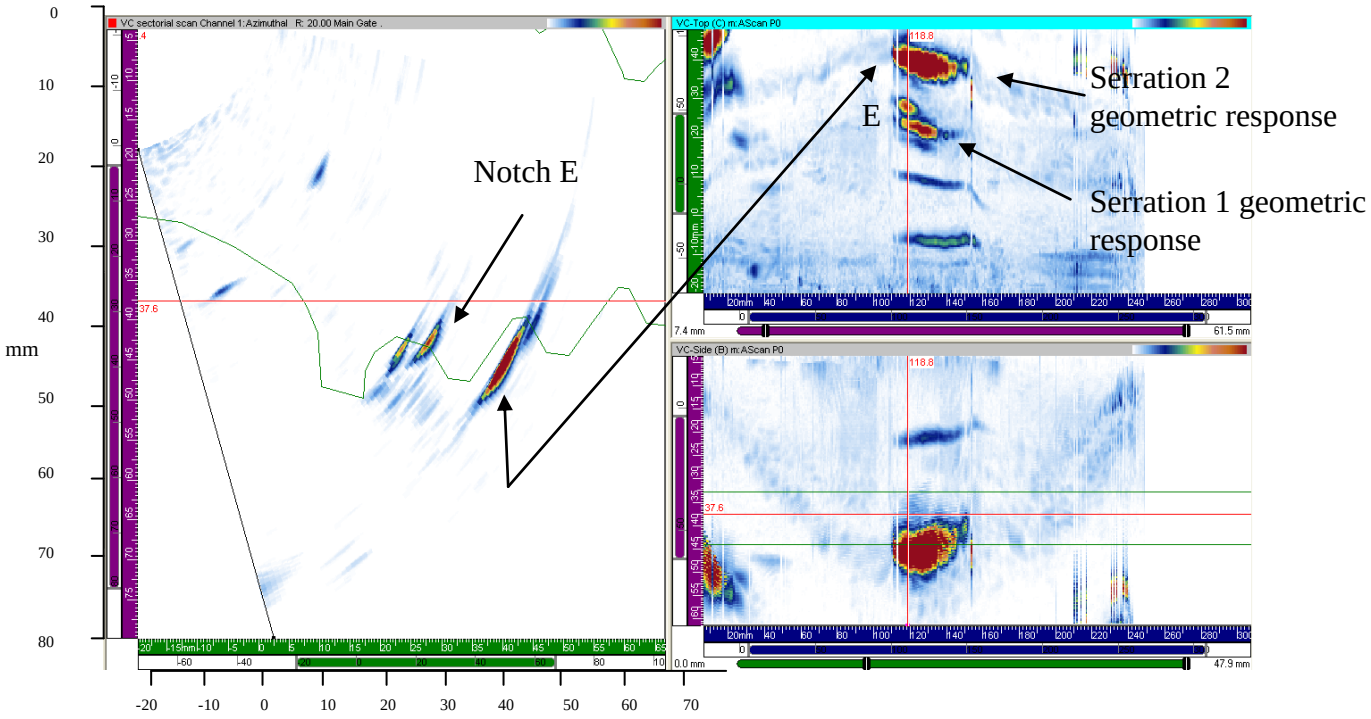

Figure 7-13 Experiment 9 – Concave root inspection with conventional wedge line scan 2

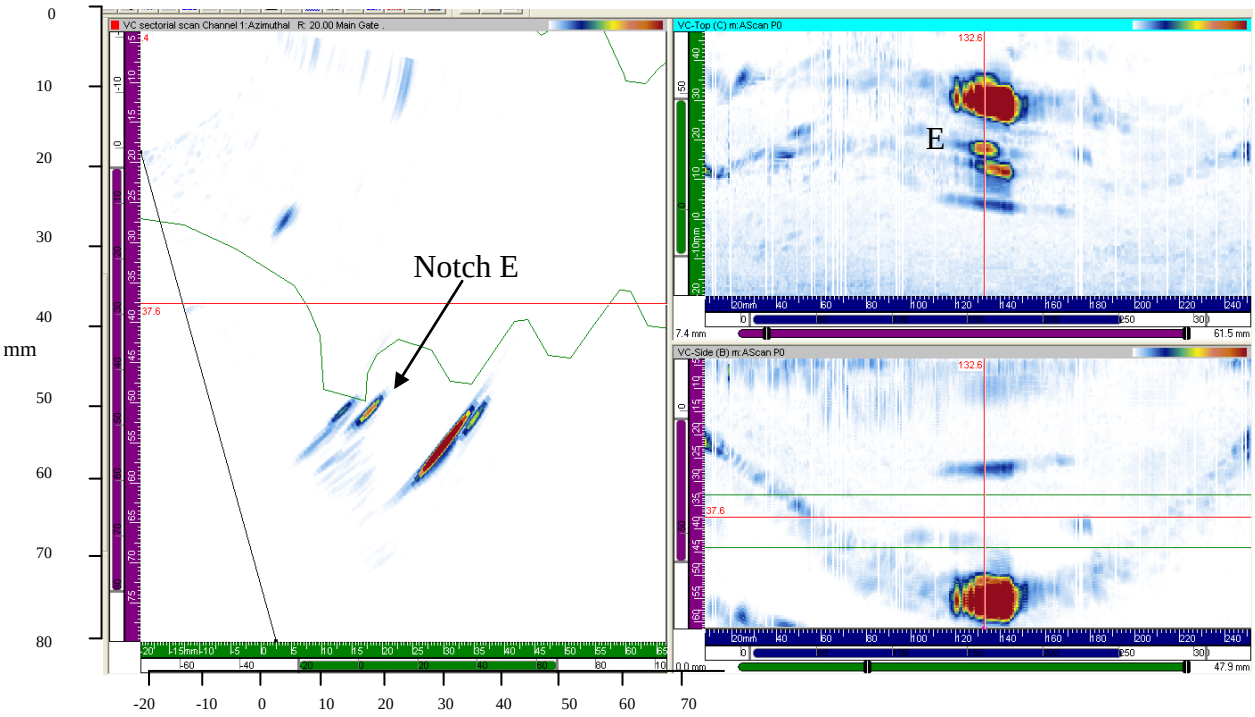

Figure 7-14 Experiment 9 – Concave root inspection with conventional wedge line scan 3

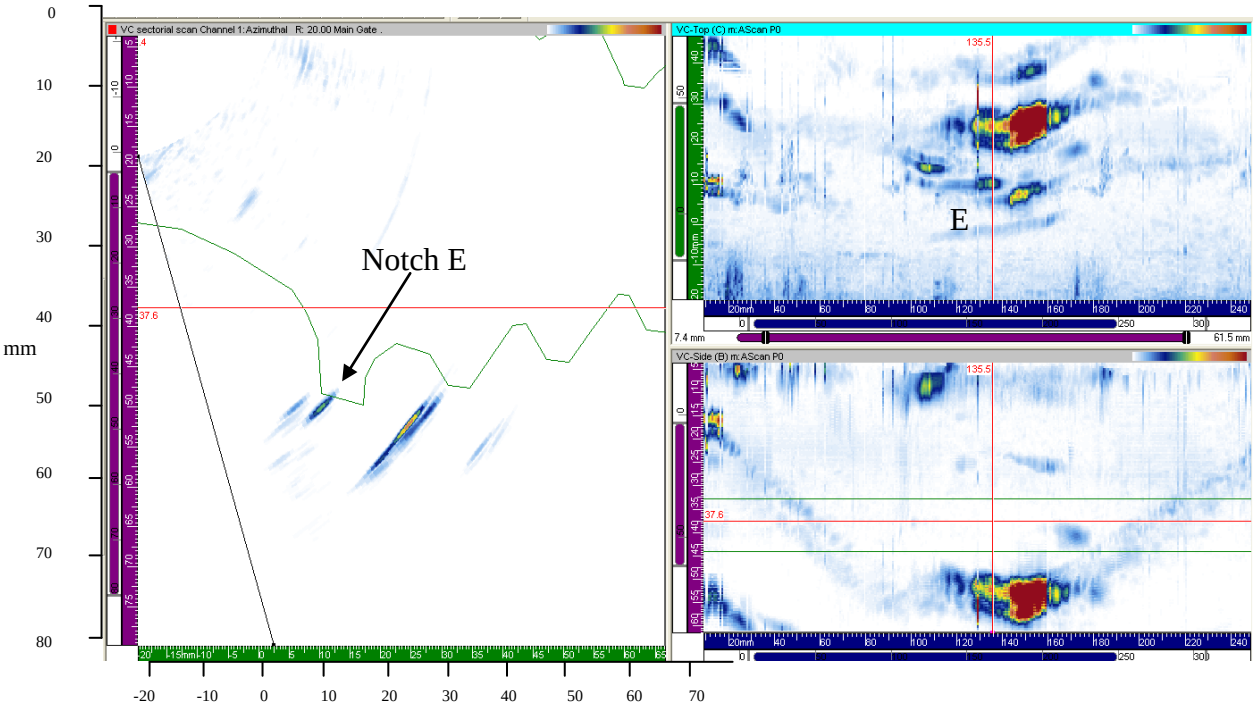

Figure 7-15 Experiment 9 – Concave root inspection with conventional wedge line scan 4

7.4.5.4 Discussion of results:

It is immediately clear from the four scans carried out that the omission of skewing has severely diminished the sensitivity of the technique. It can be seen that positive coupling

was achieved around the extent of the scans indicated by the low amplitude responses from serration 1 and marked in Figure 7-12. Good sensitivity was achieved at a very narrow axial extent at the centre of the scans, seen by the high amplitude responses from serration 2 and detection of notch E in all cases. No sensitivity to any defect or geometric was achievable outside of this narrow region rendering the technique inadequate.

7.4.6 Experiment 10 – Encoded line scan of convex root from concave aerofoil using continuous wedge

7.4.6.1 Reference sensitivity:

Notch D to 80 % Full screen height (FSH)

7.4.6.2 Scan sensitivity:

Reference sensitivity plus 8 dB

7.4.6.3 Procedure:

The concave continuous wedge was carefully coupled to the aerofoil using the watered down Sonagel, taking care to visually confirm that all trapped air was exhausted by looking through the transparent Rexolite. The bespoke scanning frame was configured to inspect the convex or concave root as seen in Figure 7-16. The height of the scanner was adjusted so that the back of the probe was level with the top of the continuous wedge. The active angle in the phased array law calculator was set to 30° to compensate for the wedge angle variation and the height of the first element to 14 mm. The procedure described in section 7.4.6.3 was then repeated. The scan was repeated once at the same height and two more times with the probe set 5 mm further down the wedge.

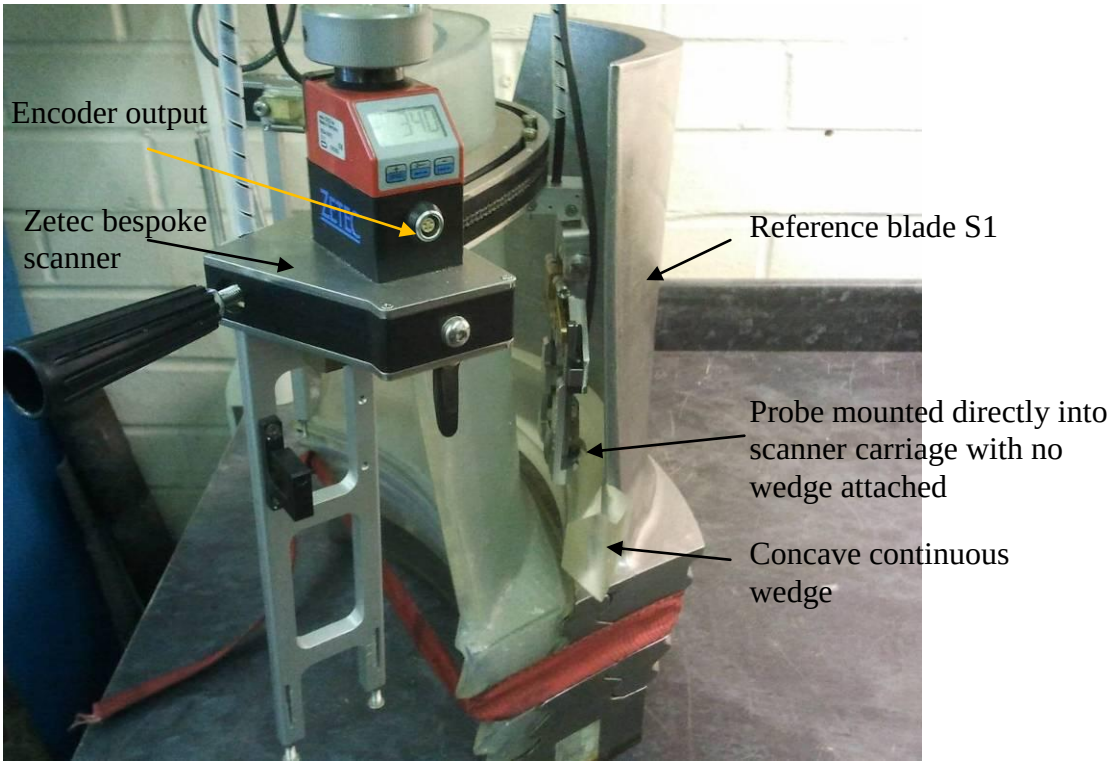

Figure 7-16 Concave continuous wedge and scanner configuration

7.4.6.4 Results:

The volumetrically merged data scans can be seen in Figure 7-17 to Figure 7-20 showing the merged C, merged B and sector scan of the section through the red measuring ruler. Where responses from notches have been identified they are labelled with their designated letter.

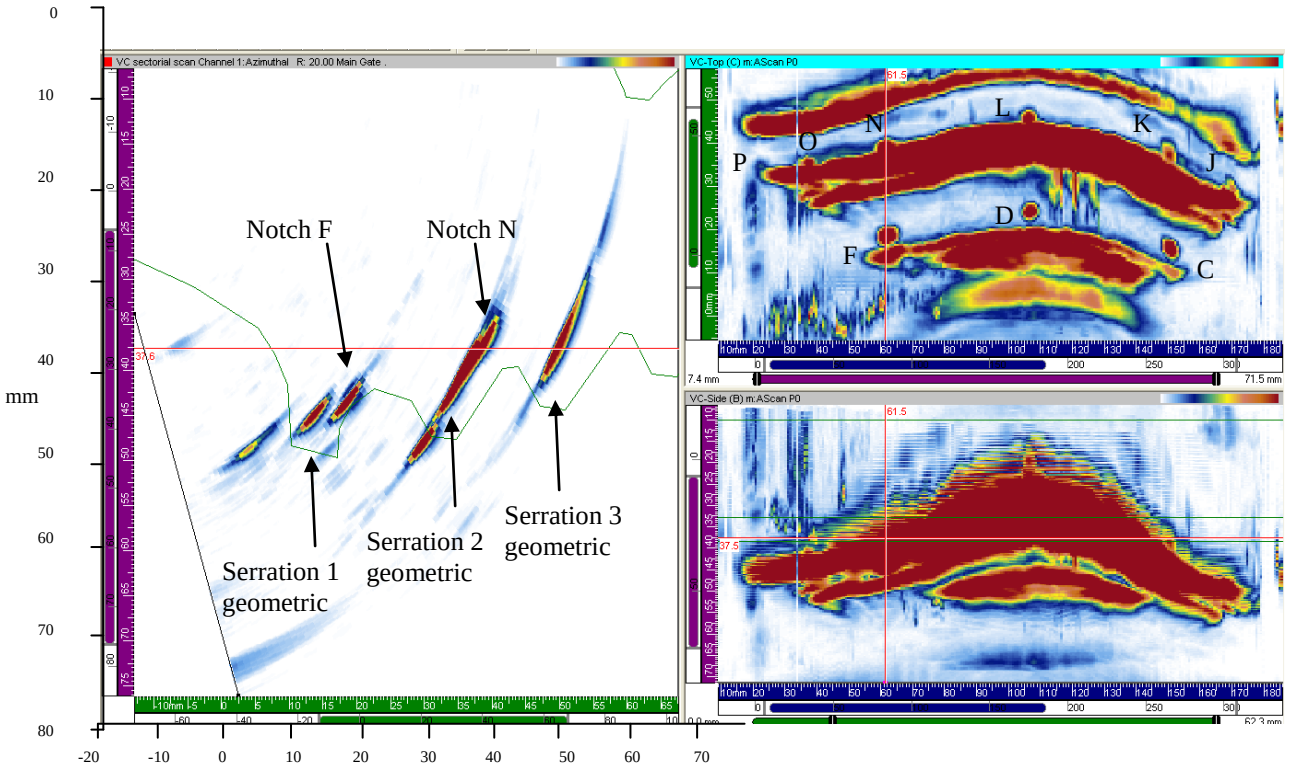

Figure 7-17 Experiment 10 – Convex root inspection with continuous wedge line scan 1

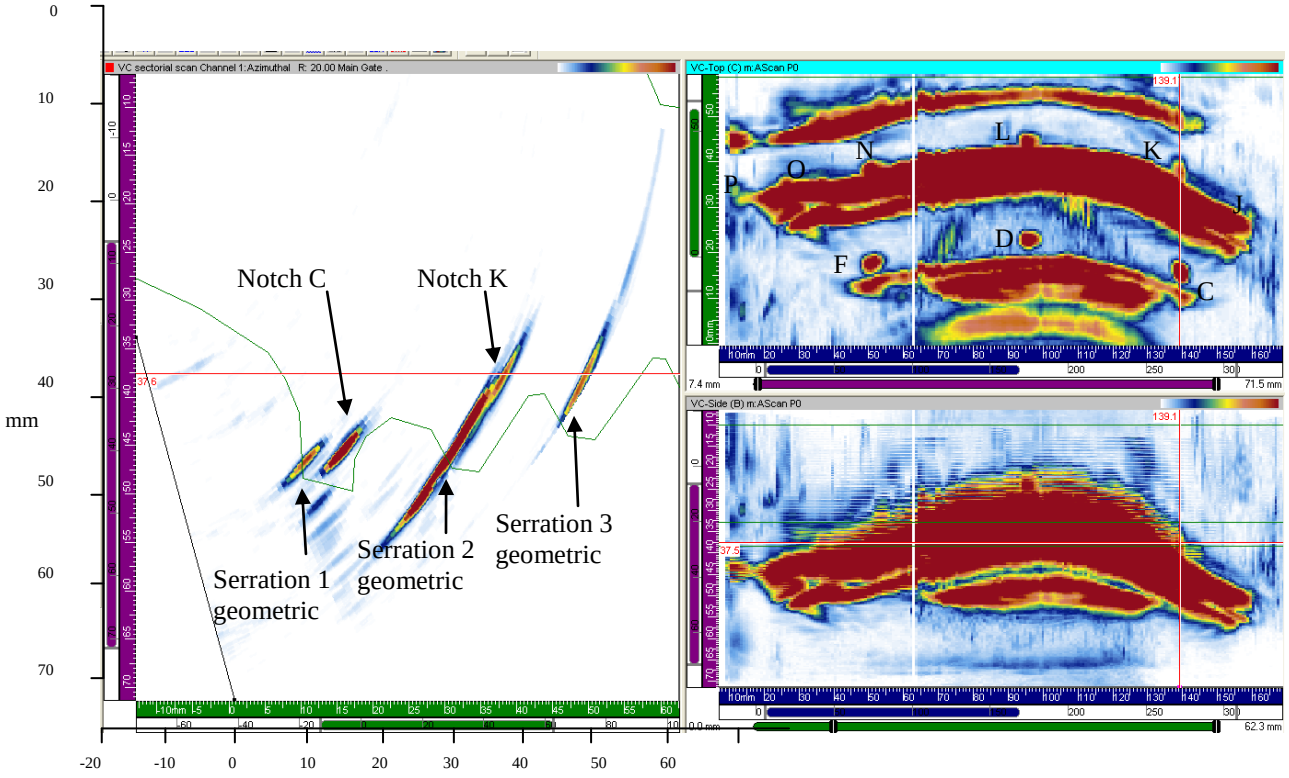

Figure 7-18 Experiment 10 – Concave root inspection with continuous wedge line scan 2

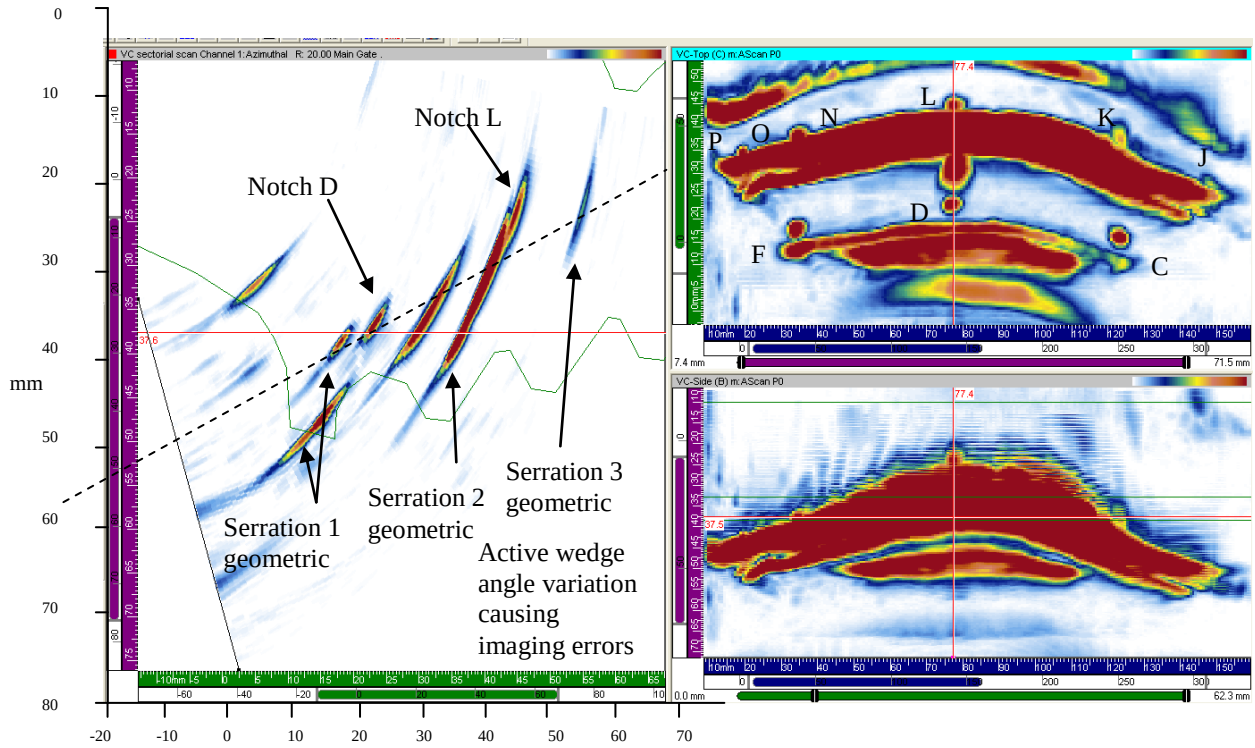

Figure 7-19 Experiment 10 – Concave root inspection with continuous wedge line scan 3 probe height reduced by 5 mm

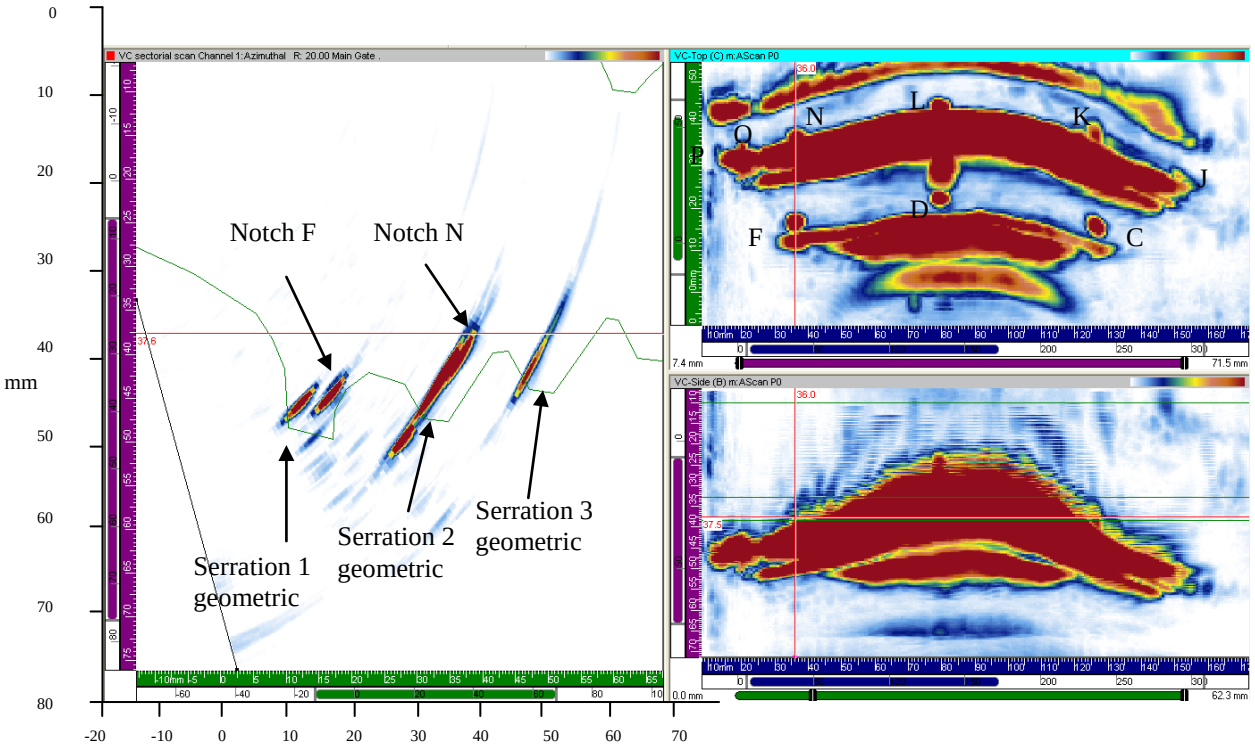

Figure 7-20 Experiment 10 – Concave root inspection with continuous wedge line scan 4 probe height reduced by 5 mm

7.4.6.5 Discussion of results:

It can be seen that the merged B scans offered little in the way of data analysis as the responses from defects are masked by the geometric responses. However the merged C scans did offer good separation from the geometric responses and the defects can be resolved and identified easily. In practice, a combination of the merged views and the linked sector scans would be used to analyse the data set to ensure that anomalies due to defects are identified. It is seen that the continuous wedge has significantly improved the sensitivity to defects around the extent of the axial scan and the consistency of coupling and repeatability between scans is marked. Notches C, D and F in serration 1were positively detected while notches J, K, L, N, O and P were also positively identified in serration 2. It is noted however that the sensitivity to notch P was significantly less than the others, correlating well with the results found in experiment 6, section 7.2.5. The significant result to note is the fact that the geometric responses from serrations 1, 2, and 3 are consistently detected around the full extent of the scan, proving that the beam trajectories have been normalised by application of skew deflection. This is in contrast to the results from experiment 8, section 7.4.4, where responses from serration 1 were consistent but inconsistent to serration 2 and absent for serration 3.

The variation in the active wedge angle due to errors in the design and modelling of the wedge can be seen marked by the dashed line in Figure 7-19. The angle required at the centre of the wedge should be 36° compared to the selected law parameter of 30° used for the scan. The angle of 30° suited the majority of the scan and so the compromise was made in the setup, resulting in the angled appearance of the sector scan at the centre.

7.4.7 Experiment 11 – Encoded line scan of concave root from convex aerofoil using continuous wedge

7.4.7.1 Reference sensitivity:

Notch E to 80 % Full screen height (FSH)

7.4.7.2 Scan sensitivity:

Reference sensitivity plus 8dB

7.4.7.3 Procedure:

The convex continuous wedge was carefully coupled to the aerofoil using the watered down Sonagel, taking care to visually confirm that all trapped air was exhausted by looking through the transparent Rexolite. The bespoke scanning frame was configured to inspect the concave root from the convex aerofoil through the continuous wedge as seen in Figure 7-21. The height of the scanner was adjusted so that the back of the probe was level with the top of the continuous wedge. The active angle in the phased array law calculator was set to 30° to compensate for the wedge angle variation and the height of the first element to 14 mm. The procedure described in section 7.4.6.3 was then repeated.

7.4.7.4 Results:

The volumetrically merged data scans can be seen in Figure 7-22 to Figure 7-25 showing the merged C, merged B and sector scan of the section through the red measuring ruler. Where responses from notches have been identified they are labelled with their designated letter.

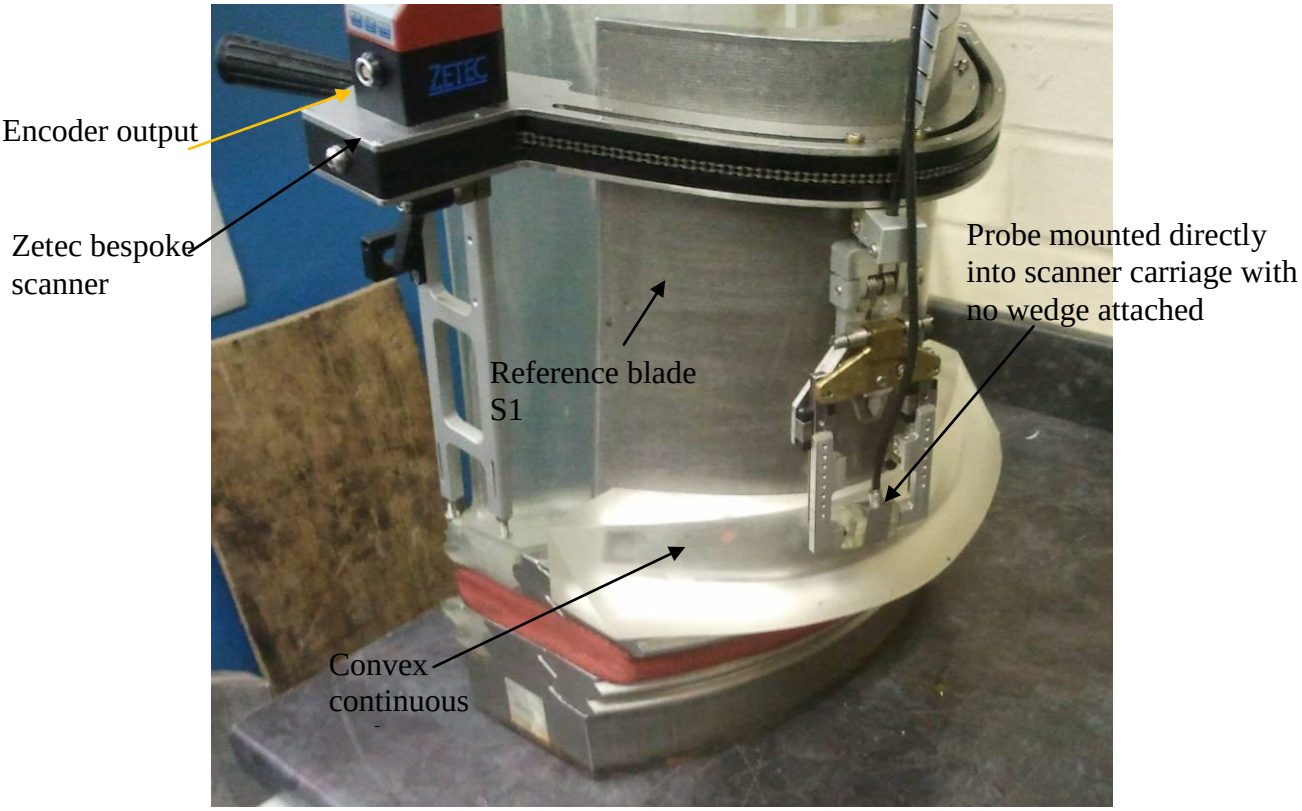

Figure 7-21 Convex continuous wedge and scanner configuration

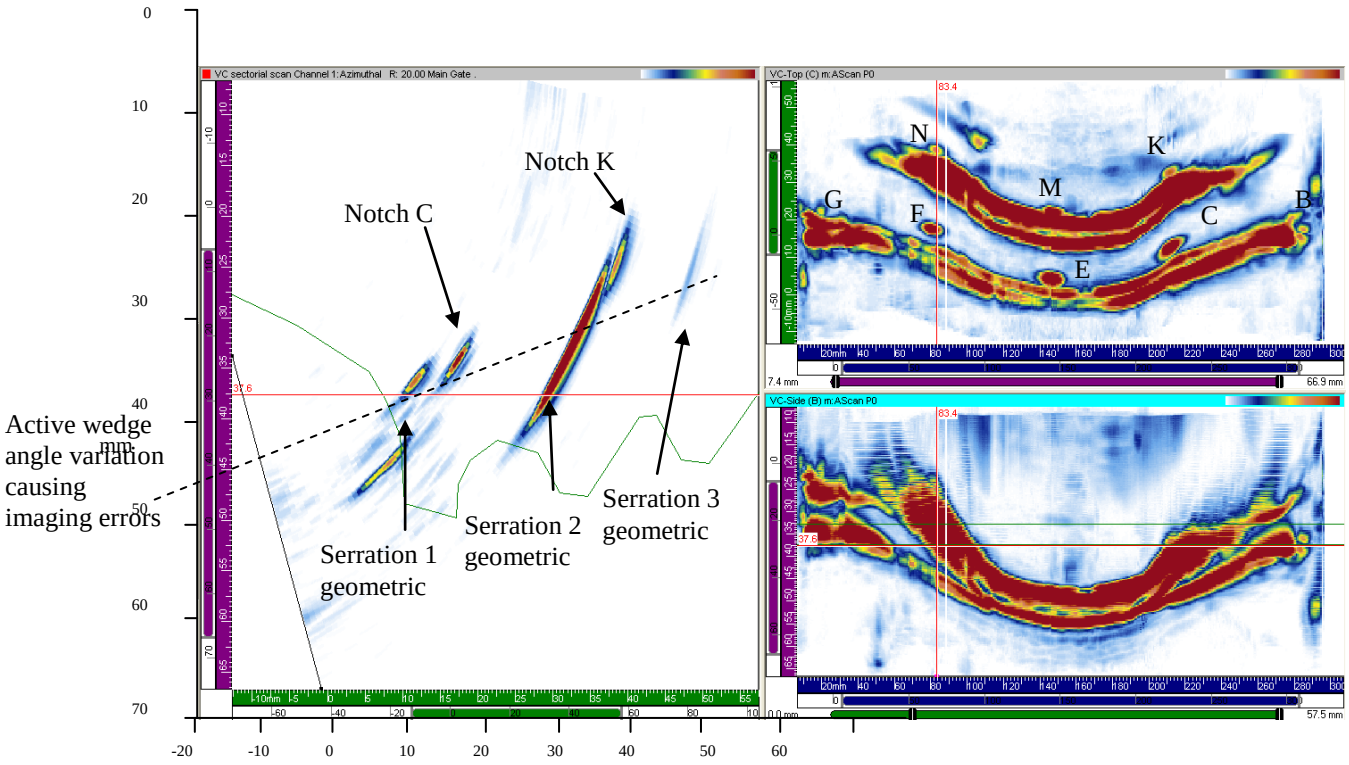

Figure 7-22 Experiment 11 – Concave root inspection with continuous wedge line scan 1

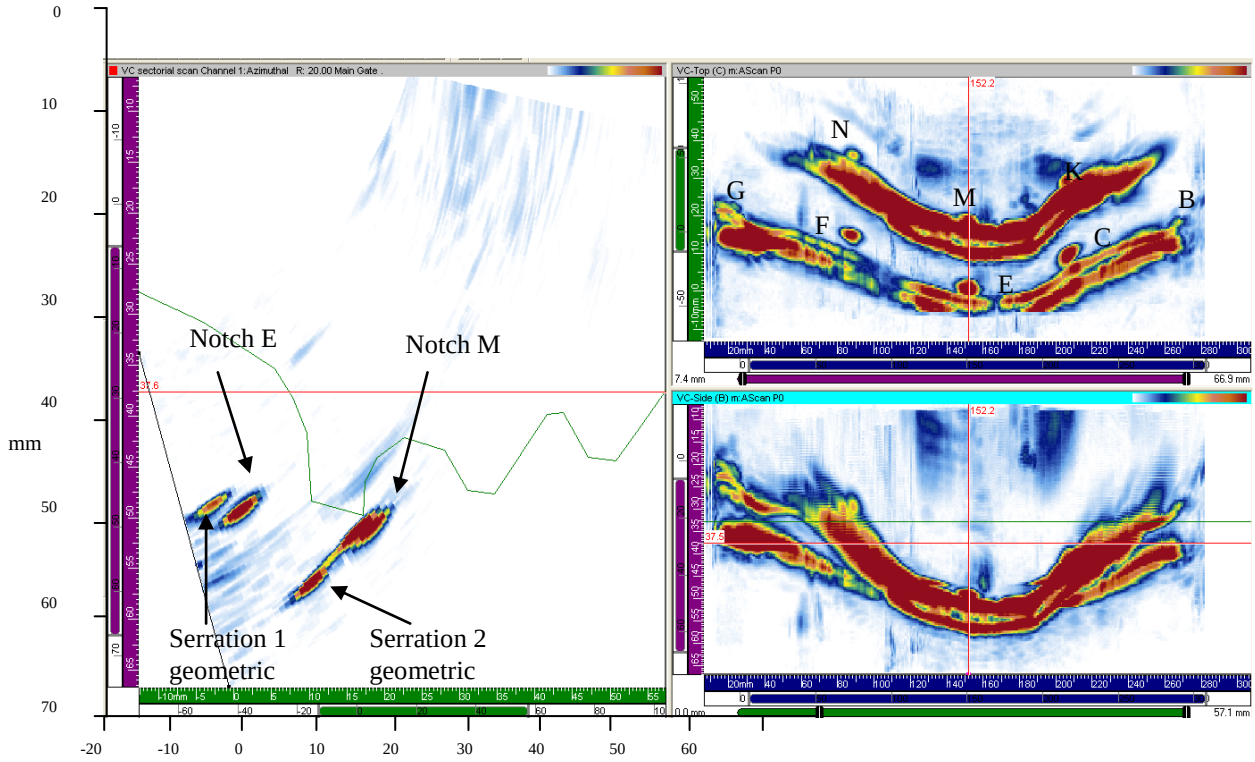

Figure 7-23 Experiment 11 – Concave root inspection with continuous wedge line scan 2

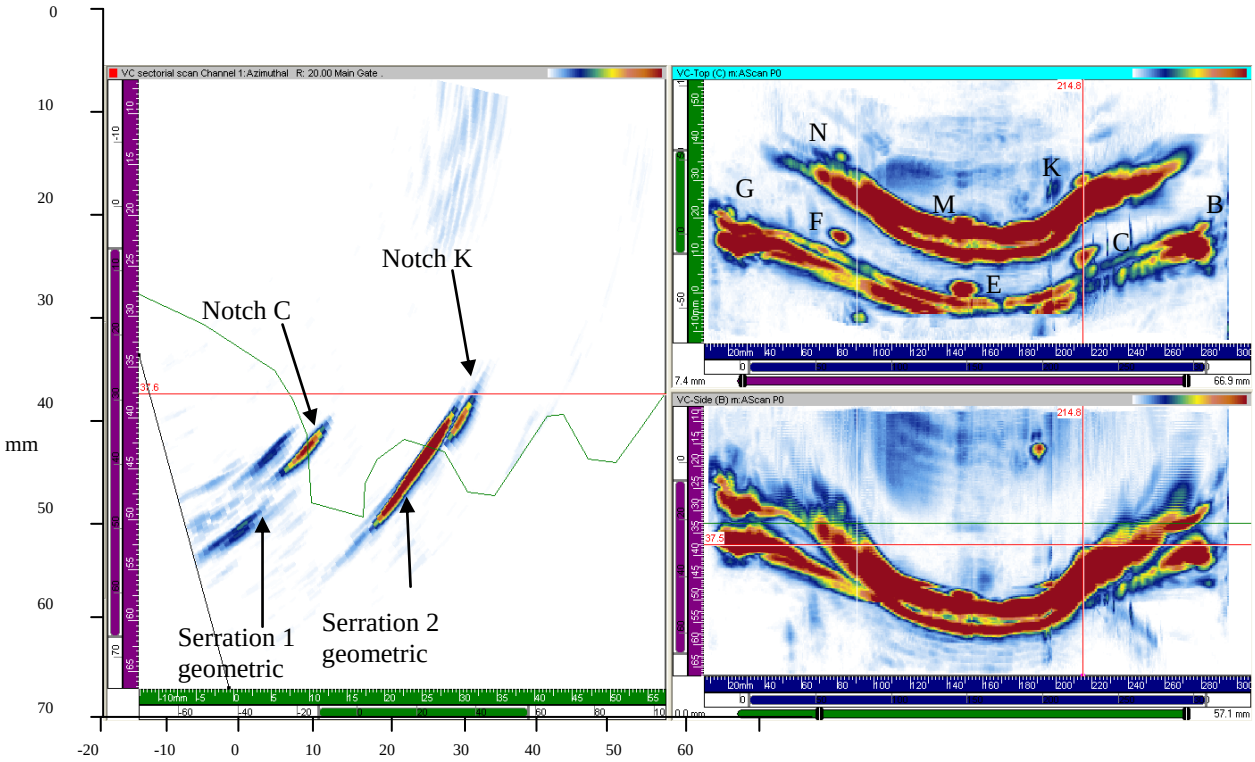

Figure 7-24 Experiment 11 – Concave root inspection with continuous wedge line scan 3

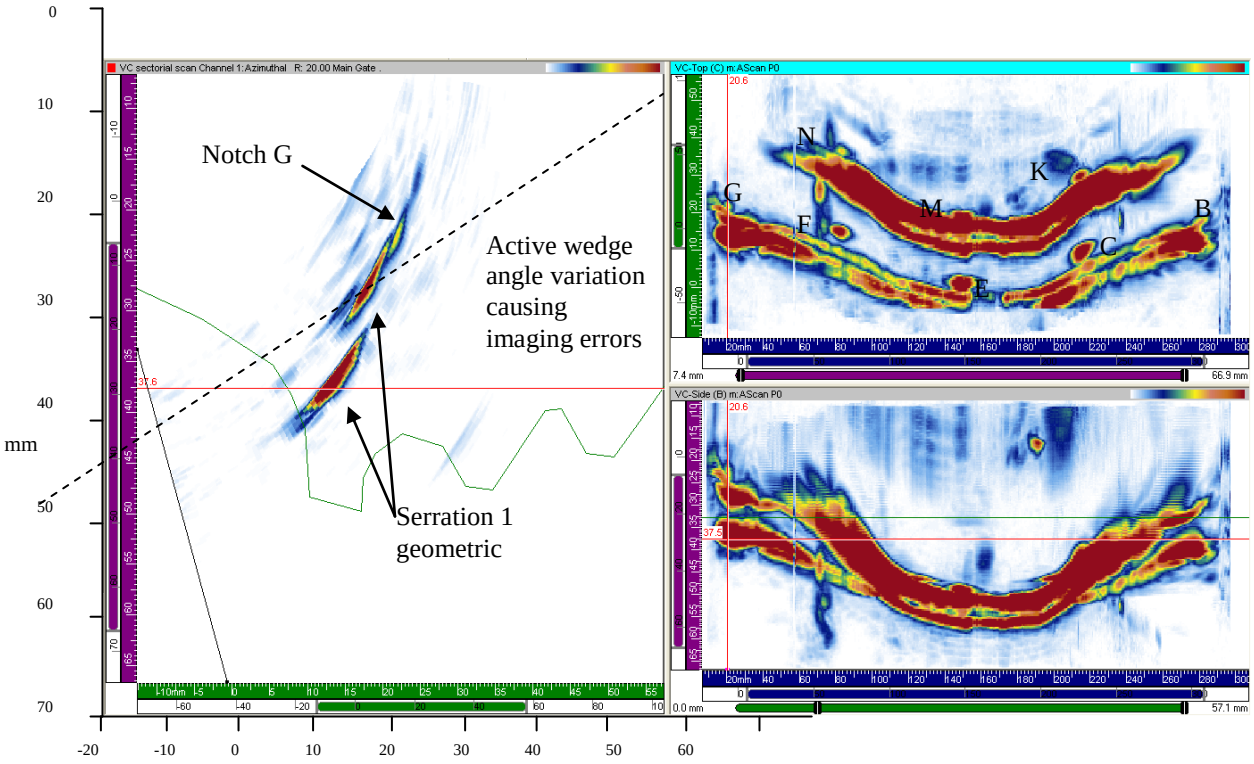

Figure 7-25 Experiment 11 – Concave root inspection with continuous wedge line scan 4

7.4.7.5 Discussion of results:

As with the results from experiment 10 it can be seen that the merged B scans offered little in the way of data analysis as the responses from defects are masked by the geometric responses. However the merged C scans did offer good separation from the geometric responses and the defects can be resolved and identified easily. It is seen that the continuous wedge has significantly improved the sensitivity to defects around the extent of the axial scan and the consistency of coupling and repeatability between scans is marked. Notches B, C, E, F and G in serration 1were positively detected while notches K, M and N were also positively identified in serration 2. It is noted however that the sensitivity to notches B and G was significantly less than the others, correlating well with the results found in experiment 5, section 7.2.4. The significant result to note is the fact that the geometric responses from serrations 1 and 2 are consistently detected around the full extent of the scan, proving that the beam trajectories have been normalised by application of skew deflection.

This is in contrast to the results from experiment 9, section 7.4.5, where no consistent responses were acquired from any of the serrations or defects other that notch E.

The variation in the active wedge angle due to errors in the design and modelling of the wedge were more problematic using the convex wedge, as seen in Figure 7-22 and Figure 7-25. The angle required at the centre of the wedge should be 36° compared to the selected law parameter of 30° used for the scan. The angles required toward the outer limits of the wedge were in the region of 26° and the sector scans were skewed as a result. However the error did not prevent positive detection of the defects and was only significant towards the ends near notches B and G which are covered by a complementary inspection from the platform, see section 4.4.5.

7.5 Conclusions

The aim of this chapter was to experimentally validate the function of the continuous wedge in producing the appropriate skew deflection for any position around the extent of the aerofoil. In that respect it has been shown that the wedge performed as designed and produced positive detection of all the defects in range of the scan; importantly no skewing of the phased array probe was required to maximise responses from notches in the reference blade.

It is noted that the experiments were in no way designed to validate the sizing capabilities of the technique; instead they were able to show that the relative sensitivity to the EDM notches at various positions around the blade root was improved. It can be seen however that the axial extent of defects could be measured with reasonable accuracy and that the 5mm long EDM notches resulted in 6 dB drop of sizes within 1mm. The through wall extent of 0.5 mm deep notches would be difficult to accurately measure and would be estimated based on an amplitude relative to reference notches, however defects in excess of 1.5 mm might be assessed using tip diffraction measurement techniques to a high level of accuracy.

The results of experiments 5 and 6 confirmed that the skew deflection parameters had been met, whilst taking account of the wedge attenuation from the results of experiment 7, the sensitivity to each notch compared favourably to the baseline results attained in experiments 1 and 2 (section 5.3.4).

Experiments 8 and 9 clearly illustrated how enacting encoded line scans of the aerofoil using traditional wedges led to inconsistency of coupling, poor sensitivity, and in the case of the convex wedge no detection of all but one notch in the concave root. Experiments 10 and 11 went on to prove that the continuous wedges facilitated accurate and repeatable line scans, detecting all notches in range of the aerofoil scans. A significant feature of the recorded line scans was the repeatable and continuous responses from the root serrations, further confirming that skew deflection was taking place and the appropriate normalisation of the ultrasonic beam was achieved.

The experiments carried out in this chapter did however illustrate a fundamental error that had been made in the design and modelling of the continuous wedges. It was found that the active refraction angle, designed to produce refraction of 36° along the full axial extent of the wedge, had not taken enough account of the variation in the slope of the aerofoil relative to the platform. The zero degree datum used to set the active angle during the modelling was taken through the vertical centre line of the blade; this was accurate in the centre of the blade aerofoil but was inaccurate towards the ends. Figure 7-26 and Figure 7-27 illustrate the slope of tangents taken at the incident point for different sections around the convex aerofoil and shows that the 0° datum from which the active 36° angle was measured was up to 8° out. However, despite this error the prototype wedges performed as designed in all other respects and simple changes to the model would rectify the issue.

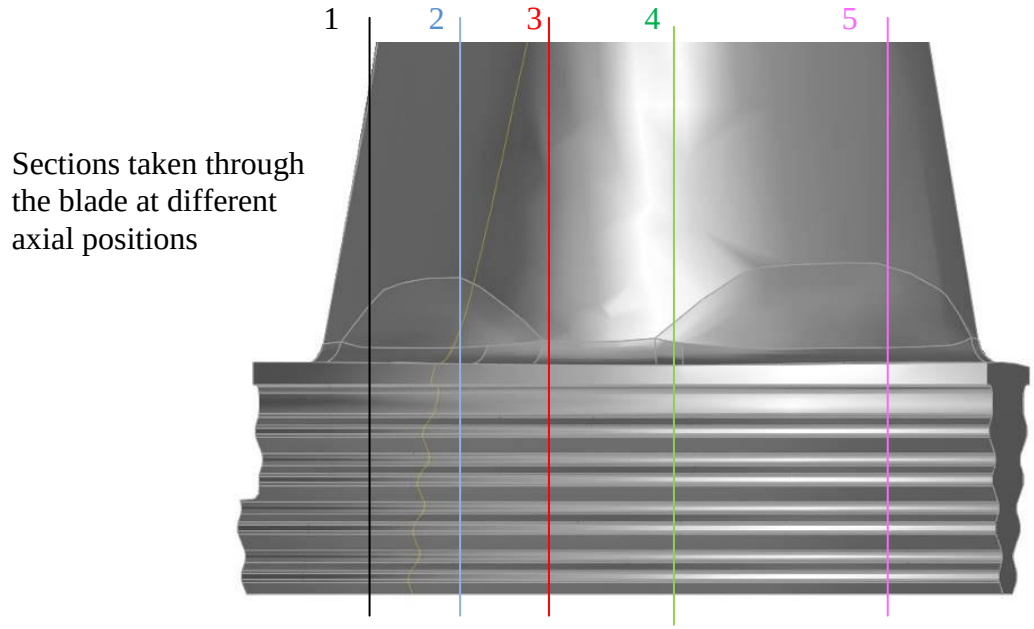

Figure 7-26 Section planes on blade aerofoil to illustrate inconsistent active refraction

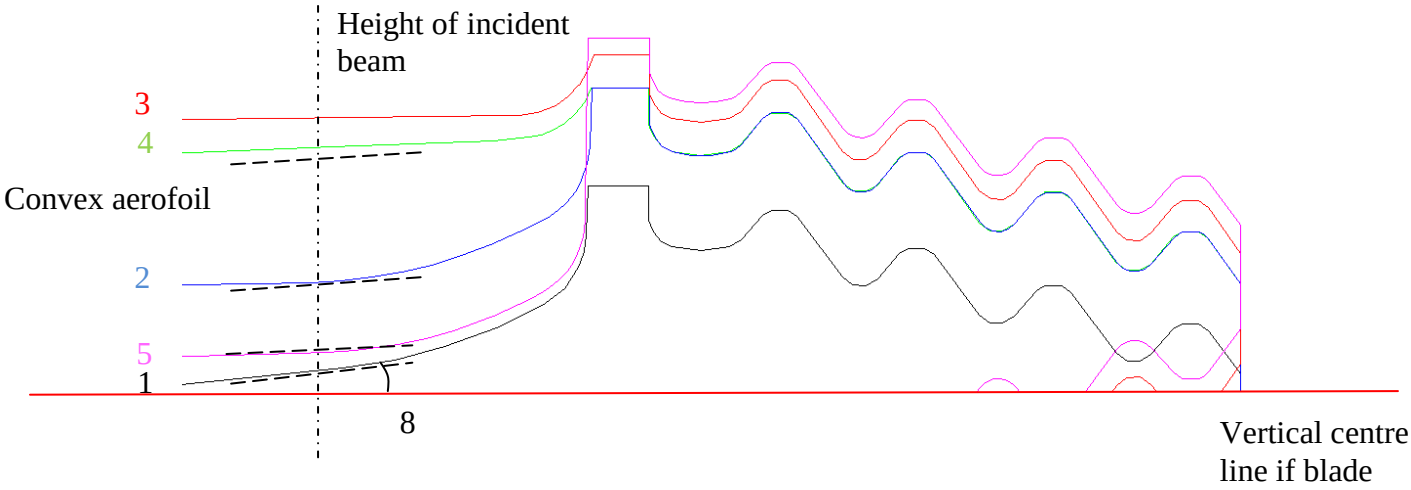

Figure 7-27 Sections taken through blade to illustrate inconsistent active refraction

Chapter 8. Conclusions and future work

8.1 Conclusions

The work carried out towards the presentation of this thesis was very specific in its aims to research and develop viable techniques for targeted inspections of steam turbine blade roots as used in the power industry. More specifically, the development and validation of several techniques has been successfully carried out for the inspection of pinned root and curved axial entry fir tree root designs; these different designs posed both individual and shared challenges which were addressed in a methodical and logical process. There were three major facets to the problem posed across the different blade root designs including: complex minimal inspection surfaces from which to refract ultrasound, restricted or limited access for probe manipulation, and geometric complexity preventing efficient and sensitive interrogation of the target inspection zones. By combining modern simulation techniques, the latest CAD modelling packages, bespoke phased array probes and rapid prototyping techniques, innovative solutions have been established which facilitate complex inspections which would otherwise be severely limited or impossible.

It was shown in section 4.2 that combining the small form factor of the Imasonic 20 element 10 MHz phased array probe with CNC machined Rexolite jigs, provided a successful solution for the inspection of pinned blade roots. These blade roots offered very limited flat land from which to refract ultrasound accurately, preventing inspection by traditional phased array UT techniques. It was seen that the Rexolite jigs offered simple and accurate placement of the probe whilst facilitating sensitive and repeatable interrogation of the target inspection regions. Several trials were carried out to validate the technique which led to the widespread deployment across RWE npower and customer sites.

It was shown however that there were some drawbacks to the methodology used in the design and manufacture of such jigs. Although it proved to be a novel and technically valid solution to the problem, there were concerns about production costs and lead times, ensuring that design changes were both costly and time consuming. Further concerns existed about the precision of the refracted beam; final probe positioning was set by optimising responses from EDM notches in the reference samples whilst moving the probe around on the partially finished wedge. On critically small geometry this method could lead to inconsistencies and did not guarantee the precision of the refracted beam.

Further concerns were raised about the accuracy of the component CAD models used to model the jigs. It was described how the re-engineering process used by RWE npower workshops produced components which were accurate to a high degree in the critical tolerance fit regions, but not so accurate in less critical regions such as the aerofoil-root block radii. For the production of precision jigs the radii in this region were required to be highly accurate. In order to overcome this issue the author successfully specified and procured an inexpensive solution in the NextEngine^{TM} laser scanning system. It was shown that CAD models of the target component could be made to an accuracy of ±0.125 mm which was proved to be sufficiently accurate for the production of jigs.

By utilising the precise CAD models with Zetec's 3D simulation tools within the CAD environment, it was shown how jigs could be modelled in a more robust and accurate way. By then taking advantage of modern rapid prototyping techniques a novel solution for jig production was developed. The shape of the jig, probe positioning and all complex features were set at the modelling stage thereby guaranteeing precision; the jig models were manufactured using Stereolithography and Rexolite blocks were retrofitted to facilitate ultrasonic refraction. Production costs and lead times were significantly reduced, offering the ability to quickly and cheaply enact design changes, whilst smaller items which were difficult to manufacture on CNC machines were easily produced.

The precision and ability to facilitate complex inspections was further utilised for the inspection of inaccessible and unsighted regions of CAEFTRs. The ability to produce accurate self locating jigs, which can be fed into physically restricted regions of last stage blades, has led to significant gains in coverage. As a result, the design methodologies developed through this project have been adopted in all such inspection techniques and have saved RWE npower an estimated £1M to date. The novelty and technical advantage gained by this design approach has also led to success in winning contracts to develop several inspections for external customers. These include an in-situ inspection for a major OEM turbine manufacturer, contracts in Australia and several developments for UK based power generators. In each case the ability to develop and validate the techniques in relatively short periods coupled with the advantages over traditional methods helped win the business. The work to date has generated an estimated £500K for RWE npower inspection management whilst saving the customers approximately £2M.

In Chapter 5 it was shown how the aerofoil of a CAEFTR offers a significant proportion of coverage of the roots. However the ability to manually manipulate a phased array probe is limited almost entirely by the inter-blade spacing. In partnering with Zetec to produce a bespoke scanning frame it was seen how coverage of the roots could be carried out remotely. The experiments carried out to validate the scanner showed it was capable of matching the sensitivity of the manually acquired baseline results within 4dB. The two exceptions were in serration 2 of the convex root, where the fixed probe height in the scanner prevented optimisation of the responses from the notches at the extreme inlet and outlet sides; manual manipulation in acquiring the baseline results allowed the probe to be pushed down the aerofoil to optimise responses from these notches. It was found that the scanning frame was less efficient than manual manipulation of the probe, due to coupling and instability issues when skewing the probe, requiring more time to acquire results. It did however offer a highly successful solution for the remote inspection of the roots where

manual scanning is severely restricted. Inspections using scanning frames of this design have been successfully deployed on three occasions on a customer rotor in Greece, where lack of access renders other methods impossible.

In addition to the scanning frames, Chapter 5 described how rapid prototyped jigs, discussed in Chapter 4, were used to complement the inspections from the aerofoil. It was shown how the jigs with Rexolite blocks offered extended coverage of the concave root towards the inlet and outlet ends; facilitating shear wave sector scanning from the platforms. Additionally it was shown how rapid prototyping was used to produce platform scanning jigs able to control a compression wave sector scan along the platform to cover the convex root towards the ends.

The inspection techniques described in Chapter 4 and Chapter 5 which were developed as a result of this research combine to provide comprehensive, sensitive and reliable coverage of both CAEFTR and pinned root blade designs. The design methodology is transferable between different rotor designs and root configurations and has facilitated the in-situ inspection of the last stage blades of low pressure rotors. By avoiding the costs of decommissioning, dismantling and blade removal for surface inspection NDT methods, outage downtime has been significantly reduced and an estimate £1M of savings have been achieved by RWE npower at the time of writing.

Chapter 6 introduced the concept of a single continuous wedge invention, designed to overcome the issues of poor coupling and probe stability on the changing geometry of the aerofoil while removing the requirement to skew the probe. The geometric mismatch between the aerofoil and roots resulted in the ultrasound trajectories not being normal to potential defects in the root serrations, thereby reducing sensitivity or non detection. Skewing of the probe was shown to compensate for the mismatch but complicated the coupling of profiled wedges, created instability when using the scanning frames and

prevented the application of single encoded line scans. The concept, which specified a single wedge which matched and coupled exactly to the root platform and aerofoil, would produce skew deflection at any given point with a probe scanned along its surface. The effect was that the ultrasound trajectories would be normal to the root profile for all axial positions and would therefore remove the need to physically skew the probe. After careful calculation of skew deflection required at different points around the aerofoil, the wedge concept was modelled. Simulations showed that successful skew deflection was produced to the degree required at any axial location around the scan. After production of a concave and convex side wedges from Rexolite, experiments outlined in Chapter 7 proved the concept against EDM notches in the reference blade. It was shown that all EDM notches could be optimised without the need to physically skew the probe, thereby proving that the required skew deflection was taking place. The results showed that the sensitivity to defects in the convex root was improved whilst the sensitivity in the concave root was comparable to the baseline results.

By removing the requirement to physically skew the probe it was shown how single line scans were facilitated by the continuous wedges. The results confirmed that the concept was valid and all defects were positively and repeatedly detected. There were significant benefits of the continuous wedge over previously applied techniques. A full scan of the blade root is accomplished by application of the wedge to the aerofoil, insertion of the scanner, and rapid continuous scan of the probe along the scan surface. Taking 1 to 2 minutes to apply it results in a recorded scan of the entire volume of the root (concave or convex) for further analysis. The tools available in Ultravision mean that the analysis is rapid and defects are positively and readily identifiable. A permanent record of the inspection is made which offers simple and efficient 100 % audit, where geometric features indicate the quality of the scan. The total scan time and analysis can be carried out in 2 to 3 minutes per blade root side. In contrast, the manual manipulation or manual scanner techniques require careful and

methodical application to achieve coverage of the root, requiring constant adjustment of skew and coupling. The resulting scans take 3 to 4 minutes to complete with no permanent record of the scan data and no guarantee that parts of the root were not passed over. Auditing requires re-inspection of a percentage of blades and operator skill and integrity are a more significant variable in the quality of the inspection.

In summary, the continuous wedge offers a more consistent, sensitive, and efficient method of inspecting the blade roots from the aerofoil, offering a time saving of up to 50 % while producing auditable documentary evidence of the scan data. The novelty and inventive step of the continuous wedge has been affirmed by the European patent office who requested only minor amendments to the wording in certain paragraphs of the patent application (see page 242).

The objectives laid out in Chapter 2 specified the development of reliable inspection of the critical regions of blade roots and listed the following: -

1. Research, and as far as practicable, evaluate the state of the art in the inspection of turbine blade root fixings. The main focus of such inspections should be on two common types of blade fixing which are historically prone to cracking:-
    a. Pinned Roots
    b. Curved Axial Entry Fir Tree Roots (CAEFTR)
2. Overcome the technical challenges of applying phased array ultrasonic techniques to complex geometry with limited refraction surfaces, and/or limited access.
3. Establish techniques which overcome the engineering challenges of inspecting LP turbine last stage blades whilst in-situ, with the aim of:-
    a. Increased coverage, sensitivity, repeatability, and reliability
    b. Utilising the current portfolio of RWE inspection equipment and retaining portability where possible
    c. Utilising, primarily but not exclusively, phased array technology

d. Developing mechanical means of access to inspection surfaces where manual manipulation is prohibitively space limited

4. Adopt a design and development methodology which is transferable between varying rotor designs, allowing rapid and controllable deployment of new application challenges

In the first point, as far as practicable the author researched and evaluated the state of the art in the inspection of blade root fixings. Identifying where published, techniques deployed across the industry for the inspection of pinned and CAEFTR roots. The challenges of inspecting complex geometry were well documented and evaluated as part of this research.

In the second point, development in conjunction with Imasonic led to the production of the 20 element 10 MHz phased array probe which offered a small form-factor suitable for deployment on severely limited geometry. In combination with the development of novel jigs, outlined in Chapter 4, it was shown how successful inspection of such geometry was facilitated. In these respects it can be concluded that the author succeeded in overcoming the technical challenges of applying phased array technology to such blade root configurations.

In the third point, which specifies a range of objective relating to the inspection of LP turbine last stage blades, a number of solutions were developed which met all the objectives. It was shown, through development and experimental validation, that a combination of bespoke jigs and scanning frames has increases the inspection coverage of blade roots, while offering methods by which inspections are carried out with rotors in-situ. The invention of the continuous wedge has led to more sensitive, reliable and repeatable inspection of the blade roots, while reducing the inspection time and producing a more rigorous audit trail with permanent records. This was all achieved using the current RWE npower portfolio of equipment using 1D phased array technology and sustained portability.

In the fourth point, regarding transferability of technology between differing rotor designs, a design process and development methodology has been created that has been successfully deployed across multiple projects. The steps taken in producing viable and

sensitive techniques are universal across projects; laser scanning, CAD model production, CAD based simulation and design of wedges, combined with modern rapid prototyping techniques have revolutionised the approach taken by the development team at RWE npower. The methodology has now been proven across many in-house and customer focussed projects where the quality and technical superiority of the solution has been key.

The objectives identified at the start of this research programme have largely been met. A combination of the invention and validation of the continuous wedge, novel manual scanning frames and novel jig development have led to significant steps forward in the inspection of complex blade root configurations. NDT forms a key role in the continued operation of both life-expired and modern power plants across the world. The techniques formed by this research have offered significant improvements in the ability of NDT to provide accurate and comprehensive data from which decisions can be made about the condition of safety critical plant items. It has also facilitated the deployment of inspection techniques on service rotors and removed the need to expensively decommission and dismantle such rotors for the purposes of inspection. The cost savings to generating companies are tangible and the benefits to the sponsoring company (RWE npower) and third party customers are far reaching.

8.2 Future work

A.1.1 Summary of future work

There are a number of areas where the research and applications described in this thesis would benefit from further work and briefly include:-

- Field trials of the continuous wedge to validate the consistency of coupling between multiple blades on a service rotor.

- Remodelling of the wedge prototypes to be tested and trialled on alternative blade root designs.
- Research into possible design of conformable continuous wedges which might overcome the problems of geometric variations should they arise.
- Research into wedge materials with good acoustic properties but lower acoustic velocity to increase the refraction coefficient and therefor reduce wedge thickness.
- Consider rapid prototyping techniques which could produce models with good acoustic properties for building the continuous wedge, thereby reducing production costs and design cycles.
- Adapt the continuous wedge concept to alternative applications such as nozzle weld inspections.

A.1.2 Future work in detail

Through the course of this research the methodology and concepts have been used across a variety of applications and have proven to be successful and crucial to achieving sensitive and repeatable inspections of complex blade root designs. These applications have included the deployment of the scanning frames and rapid prototyped jigs across various LP rotor last stage blades with both CAEFTR and pinned roots both in-situ and ex-situ. Successful deployment of the jigs has also enabled the inspection of smaller stage 4 LP rotor blades where the challenge has been lack of refracting surfaces and limited space.

Although the continuous wedges have been validated by both simulation and bench trials against a reference blade with EDM notches, it has not yet been deployed on a live inspection. The main reason for this is that the demand for inspection of the specific blade design used for the prototypes has not arisen, and therefore no opportunity has afforded itself. It was seen that mistakes were made at the modelling stage of the prototypes which meant that the active refraction angle of the wedge was inconsistent, see section 7.5. It is

intended that the next major inspection requirement for the inspection of CAEFTR will afford the opportunity to remodel the wedges to suit that particular configuration. Care will be taken to ensure that the slope variation of the aerofoil is considered, so removing the inconsistency found with the prototypes. Consistency and efficiency of the coupling interface between the wedge and the blade could then be tested across multiple blades which might have been subjected to hand blending when manufactured, or erosion in service. Either scenario could lead to anomalies in the geometric shape of the blade compared to the model and so compromise the coupling efficiency. Having established whether the variation might create a problem, further research into conformability of such wedges might be appropriate.

It is noted that the thickness of the wedges, which increases to produce the effective roof angle and thereby produce skew deflection, might render the concept void if sufficient spacing between blades is not available to accommodate the wedge. Research into alternative wedge materials should be carried out to establish an alternative which possesses good acoustic properties whilst having a lower velocity of sound. By reducing the velocity the refractive index is increased and therefore the amount of active and roof angles could be reduced. This would in turn lead to reduced size of the wedge and enable it to be utilised in situations where inter-blade spacing is much smaller.

The production costs of the prototype continuous wedges amounted to around £5000, taking account of the material cost and complex nature of the production process, using 5 axis CNC milling machines. An ideal scenario would be to produce the wedges using a rapid prototyping process similar to that used with the jigs. This would result in short lead times, reduced cost and facilitate iterative design changes such as the one required on the original wedges. However, no current rapid prototyping technique exists, to the knowledge of the author, which results in a material possessing good acoustic properties for use as an

ultrasonic wedge. Significant further research could be undertaken to find a material and process which could result in all the desired properties seen with Rexolite.

Finally, the concept of the continuous wedge is not restricted to applications targeted in this thesis; other application should be explored, which require skew deflection to normalise the ultrasonic beam to the target inspection regions. One such application that could benefit from such a concept is that of the inspection of nozzle welds to piped systems. These inspections require that the ultrasonic probe be skewed at different positions around the scan to compensate for the curvature of the parent pipe. Traditional scanning systems have a complex cam configuration to skew the probe or simpler mechanical systems require multiple scans at various fixed skews. More recent applications using 2D phased arrays have led to significant improvements in the control of the beam skew but require complex, expensive and often importable equipment to control and drive them. By careful design and modelling of the continuous wedge, skew deflection could be created to normalise the beam trajectories using standard portable phased array equipment. As no skewing would be required, the design of the scanning equipment could be simplified and the compromise to coupling of the probe when skewing removed. Other potential benefits would include reduced cost and inspection time, whilst potentially increasing sensitivity to small defect and improved defect sizing and characterisation.

References

1. **RWE Group,** 'About RWE', Available at http://www.rwe.com/web/cms/en/111466/rwe/rwe-group/about-rwe/, *[Accessed Sep 2011]*

2. **RWE npower, '**npower cogen', Available at http://www.rwe.com/web/cms/en/97676/rwe-npower/about-us/our-businesses/npower-cogen/, *[Accessed Sep 2011]*.

3. **Cogeneration.net,** 'What is cogeneration?' Available at http://cogeneration.net/, *[Accessed Sep2011]*.

4. **RWE npower,** 'Renewable energy (RWE npower renewable)', http://www.rwe.com/web/cms/en/284070/rwe-npower/about-us/our-businesses/renewable-energy/, *[Accessed Sep2011]*.

5. **Ambrosini, A.M.,** 'Life extension of coal-fired power plants', Profiles PF05-13, Dec 2005.

6. **Farley M.J., 2008,** 'Energy in the future – new challenges for NDT', 17th World Conference on Non-destructive Testing, 25-28 Oct 2008, Shanghai, China.

7. **The Royal Academy of Engineering, '**Forces on large steam turbine blades, RWE npower', Available at http://www.raeng.org.uk/education/diploma/maths/pdf/exemplars_advanced/22_Blade_Forces.pdf. *[Accesses Sep 2011]*

8. **Nuclear Engineering International, 1999, '**Dealing with turbine blade failures in India', Available at http://www.neimagazine.com/story.asp?storyCode=6067, *[Accessed Sep 2011]*

9. **Engelhardt G.[1], Macdonald D.[2] , Zhang Y.[2], Dooley B.[3];** 'Deterministic Prediction of Corrosion Damage in Low Pressure Steam Turbines', [1]OLI Systems Inc., [2]Centre for Electrochemical Science and Technology, The Pennsylvania State University, [3]Electric Power Research Institute, The Power Plant Chemistry Journal, issue 11, 2004.

10. **Mazur Z., Garcia-Illescas R., Aguirre-Romano J., Perez-Rodriguez N.; Instituto de Investidaciones Electricas Turboaquamarinia**,'Steam turbine blade failure analysis', Engineering Failure analysis, volume 15 issue 1-2, 2008.

11. **Stamps K.J, Chamberlain A., Edwards R., 2003,** 'TS717/001, UT Phased array GEC 945 mm Last Stage Blade Curved Roots', RWE Npower Technical Procedure.

12. **Clossen M., Opheys Dr M.F., Rauschenbach H., Siegel M.; Siemens Power Generation,** 'Lifetime Extension Through Advanced Non-Destructive Examination Methods', Power-Gen Europe 30th May to June 1st 2006, Cologne, Germany.

13. **Opheys Dr M.F., Rauchenbach H., Siegel M., Goode G.; Siemens AG Power Generation, Heinrich D.; Celgelec AT Gmbh & Co**, 'Blade Root / Blade Attachment Inspection by Advanced UT and Phased array Technique', 6th International Charles Parsons Turbine Conference, 16-18 September 2003, Trinity College, Dublin.

14. **Zetec Inc,** 'Turbine blade scanner, Phased array UT inspection of blades', Available at http://www.zetec.com/2010/06/blade-scanner/, *[Accessed Sep 2011]*

15. **Drax Group Plc,** 'Explore Drax, Boiler', Available at http://www.draxpower.com/explore_drax/power_station/?id=1873, *[Accessed Sep 2011]*.

16. **Nag P.K.,** 'Power plant engineering', Tata McGraw-Hill, 2002**.**

17. **Doosan Heavy Industries and Construction,** 'Products and Services', Available at http://www.doosan.com/doosanheavybiz/en/services/power/power_plant/turbine/products/steam_turbine.page, *[Accessed Sep 2011]*.

18. **Havakechian S., Greim R.; ABB Power Generation Ltd,** 'Aerodynamic design of 50 percent reaction turbines', Journal of Mechanical Engineering Science, Volume 213 no. 1, 1999.

19. **Mujezinovic A.; GE, Schenectady, NY, USA,** 'Bigger blades cut costs', Modern Power Systems, February 2003.

20. **Stringer J., Viswanathan R.; Electric Power Research Institute, Palo Alto, CA 95070,** 'Failure Mechanisms of High Temperature Components in Power Plants', Journal of Engineering Materials and Technology, JULY 2000, Vol. 122 / 255

21. **Shige T., Magoshi R., Itou S., Ichimura T., Kondou Y.; Mitsubishi Heavy Industries, Ltd.** 'Development of Large-Capacity, Highly Efficient Welded Rotors for Steam Turbines', Technical Review Volume.38 No.1, 2001.

22. **GE Energy; Schenectady, NY, USA,** 'Final report to the US Department of Energy, High Efficiency Steam Turbines with Extra Long Buckets', December 2005.

23. **Shaw N., RWE npower, '**TECH-PLI-08-DRO-200-000, Metallurgical analysis of cracking to Parsons 660MW IP rotor stage 6 pinned roots', RWE npower technical report.

24. **Stamps K.J., 2008,** 'TS717/044, UT inspection of pinned blade root stages 6,7 & 8 – inlet and outlet blade fingers', RWE npower Technical Procedure.

25. **Stuart D., 2008,** 'TECH-PLI-DRO-08-030-003, 'UT Inspection of Drax IP rotor Stage 6, 7, and 8 blade roots', RWE npower Inspection report.

26. **McSweeney F., 2008,** 'TECH-PLI-DRO-08-030-004, 'MPI Inspection of Drax IP rotor Stage 6 loose blade roots', RWE npower Inspection report.

27. **Jackson C., Ahmed A., Parry-Mills B.; British Energy,** 'E/PROC/ENG/BI/218 Revision 000, Procedure for the ultrasonic inspection of LP turbine blade root – area adjacent to fastener hole', February 2011.

28. **Rauschenbach H., Clossen M., Opheys Dr M., Siegel M.; Siemens Energy Sector,** 'Advanced Ultrasonic application for the inspection of turbine components', 10th ECNDT, Moscow 2010.

29. **Richard D., Reilly D., Berlanger J., Maes G.; Zetec Inc, 2010,** 'SimNDT, Software tools for the design of phased array UT inspection techniques', SimNDT 2010.

30. **ASME, 1989; '**ASME handbook on water technology for thermal power systems'.

31. **EPRI, 1986;** 'Interim consensus guidelines on fossil plant cycle chemistry'.

32. **Garraway K.; RWE npower, 2009** 'TECH-JJE-1047-09, Thessaloniki L-0 Blade contamination assessment', RWE npower technical report.

33. **P. Stanchi, D. Pellegatti, Ansaldo Energia,** 'K251-PA-001 Inspection of blade roots and steeple specification', August 2009.

34. **Turner S.; Alstom,** '945 Last stage LP moving blade maintenance issues', PSUK Customer conference, November 2005.

35. **Rauschenbach H., Opheys Dr M., Mann U., Achtzehn J.; Siemens Power Generation,** 'Advanced NDE inspection methods for field service at power plants', 8th ECNDT, Barcelona 2008.

36. **Ciorau P., Pullia L.; Ontario Power Generation,** 'How Reliable is Your Call? OPG Phased Array Ultrasonic Inspection, experience on Siemens- Parson Turbine Blade Roots 2001-2007', NDT.net e-journal issue 2007-09.

37. **Ciorau P, MacGillivray D., Hazelton T., Gilham L, Craig D.; Ontario Power Generation., Poguet J.; - Imasonic S.A,** 'In-situ examination of ABB L-0 blade roots and rotor steeple of low-pressure steam turbine, using phased array technology. Proof-of-principle results', 6th EPRI Steam Turbine/Generator Workshop and Vendor exposition - St Louis, Missouri, USA - August 1999.

38. **Ciorau P.; Ontario Power Generation,** 'A Contribution to Repeatability of 1-D Linear Array Probes Used on Large-Scale Inspection of Low-Pressure Turbine Components', NDT.net e-journal volume 11 No 10, September 2006.

39. **Ciorau P.; Ontario Power Generation, Chartier C, Mair K.; Acuren Canada,** 'A Contribution of Phased Array Ultrasonic Technology (PAUT) to Detection and Sizing Stress Corrosion Cracks', NDT.net e-journal issue 2008-10.

40. **Zayicek P.; EPRI,** 'Ultrasonic Inspection of Steam Turbine Blade Roots: Interim Report', December 2005.

41. **Cracknell A.P.,** 'Ultrasonics', Wykenham Publishers, 1980.

42. **Stockwell J.R.,** 'Application of air coupled ultrasonic systems and signal processing to the interrogation of concrete', Ph.D Thesis, University of Warwick, September 2004.

43. **Ensminger D.,** 'Ultrasonics : Fundamentals Technology Applications: Mechanical Engineering 65 (Mechanical Engineering)', Hardcover - 2 Sep 1988.

44. **Blitz J., Simpson G.,** 'Ultrasonic Methods of Nondestructive Testing', Hardcover - Nov 1995.

45. **Mason W.P**., 'Physical acoustics and the properties of solids', D.Van Nostrand Company Inc, 1958.

46. **Askeland D.R., Phulé P.P.,** 'The science and engineering of materials (5th ed.)', 2006.

47. **Beer F.P., Johnston E.R., Dewolf J., Mazurek D.,** 'Mechanics of Materials', McGraw Hill, 2009.

48. **Hartsuijker, C., Welleman J.W,** 'Engineering Mechanics 2', Springer, 2001.

49. **Oberg E, Jones F D, Horton H L, Ryffel H H, '**Machinery's Handbook', 26th Edition, 2011.

50. **Drinkwater B., Wilcox P., 2009,** 'Ultrasonics and Acoustics', EngD in NDE course.

51. **Rayleigh, J.W.S.,** 'The theory of sound', volume 1 of 2, second edition, Dover Publications, 1945.

52. **Rayleigh, J.W.S.,** 'On Waves Propagated along the Plane Surface of an Elastic Solid'. Proc. London Mathematical Society. s1-17 (1): 4–11, 1885.

53. **Juluri N., 2008,** 'Inspection of complex structures using guided waves', Thesis: Imperial College London.

54. **Adam J.A**., 'Mathematics in nature: modeling patterns in the natural world - The relation between the frequency of a wave and its wavelength λ', Princeton University Press, 2003.

55. Bekefi, G., Barrett A. H., 'Electromagnetic Vibrations, Waves, and Radiation - Waves in Dielectrics', Cambridge, MA: MIT Press, pp. 426-440, 1987.

56. **Sony B., Balasbramamian T., Pardikar R.J.,** 'Ultrasonic study for detection of inner diameter cracking in pipeline girth welds using creep waves', International journal of pressure vessels and piping, Volume 80, issue 2, pages 139-146, February 2002.

57. **Woo J.,** 'A short history of the development of ultrasound in obstetrics and gynaecology', Part 1, 1998.

58. **Gowda R., Khan I.A., Vasavadea B.C., Sacchi T.J., Patel R.,** 'History of the evolution of echocardiography', International journal of Cardiology, 97, pl-6, 2004.

59. **Povey M.J., McClements D.J,** 'Ultrasonics in food engineering. Part 1: Introduction and experimental methods', Journal of food engineering, 8, p212-245, 1988.

60. **Silk M S,** 'Estimates of the probability of detection of flaws in TOFD data with varying levels of noise', BINDT Journal INSIGHT vol. 38 no. 1 January 1996

61. **Avdiaj S., Setina J., Sala N.,** 'Modeling of the piezoelectric effect using the finite-element method (FEM)', Materials and technology 43 (2009) 6.

62. **Ribichini Dr R.,** 'Modelling of Electromagnetic Acoustic Transducers'**,** PhD Thesis, Imperial College, London, 2011.

63. **Machado G., Faguaga M., Moreno-Gobbi A., Aulet A., Nunez I.,** 'Design, Manufacture and Characterisation of Ultrasonic Transducers', Ferromagnetics Volume 386, Issue 1, 2009.

64. **Wang H., Ritter T., Cao W., Shung K.,** 'High frequency properties of passive materials for ultrasonic transducers', IEEE Transactions on Ultrasonics, Ferroelectrics and frequency control, vol 48 No1, 2011.

65. **Stepinski T., Lingvall F.; Uppsala University, 2000,** 'Automatic Defect Characterisation in Ultrasonic NDT', 15th World conference on NDT, Roma, Italy, 15th – 21 October 2000.

66. **Huygens C,** '*Traité de la lumiere'* (Leiden, Netherlands: Pieter van der Aa, 1690), Chapter 1.

67. **Enders P.; Ahornallee 11, D-15754 Senzig, Germany,** 'Huygens' Principle as Universal Model of Propagation', Latin-American Journal of Physics Education, Vol 3 No1, 2009.

68. **Copson E.T., Baker B.B.,** 'The Mathematical Theory of Huygens' Principle', Third Edition, Hardcover, 1987.

69. **Richard P.,** *'The Feynman Lectures on Physics',* Vol. 3. USA: Addison-Wesley. pp. 1–8, 1965.

70. **Sengupta D.L., Liepa V.V**., 'Applied electromagnetics and electromagnetic compatibility', John Wily & Sons Publications, Hoboken, NJ, USA, 2005.

71. **Schuhmacher S., Zanger P., Langenberg K.J.,** 'A system model to predict the results of ultrasonic scattering experiments', Journal of Nondestructive Evaluation, Volume 13 No 3, 1994.

72. **Conolly G.D.,** 'Modelling of the propagation of ultrasound through austenitic steel welds', PhD Thesis, The University of London, 2009.

73. **Howry D.H.,** 'The ultrasonic visualization of soft tissue structures and disease processes', J.Lab.Clin.Med., 40:812-813, 1952.

74. **Howry D.H., Bliss W.R.,** 'Ultrasonic visualization of soft tissue structures of the body', J.Lab.Clin.Med., 40, 1952.

75. **Howry D.H.,** 'Sound wave portrait in flesh', Lif Magazine, Volume 37, No 12, p174, September 1954.

76. **Thomas A., Banerjee A.K., Busch I.,** 'Classic papers in modern diagnostic radiology', Springer, 2005.

77. **Bom N., Lance C.T., Van Zweten G., Kloster F.E., Roelandt J.,** 'Multiscan Echocardiography 1, technical description', circulation 48:1066-1074, 1973.

78. **Mcnay M.B., Flemming E.E.,** 'Forty years of obstetric ultrasound 1957-1997 from A-scope to three dimensions', Ultrasound in medicine and biology, volume 25.1, 1999.

79. **Woo J.,** 'A short history of the development of ultrasound in obstetrics and gynaecology', Part 2, 1998.

80. **Thurstone F.L., Vonramm O.I.,** 'Acoustical imaging with linear phased array', Metals technology, pp73-74, 1975.

81. **Macovski A.,** 'Ultrasonic array for reflection imaging', Patent number US3918024, June 24 1974.

82. **Kossoff G.,** 'Cross array ultrasonic transducer', Patent number US3881164, September 1973.

83. **Beaver W.L.,** 'Signal processor for ultrasonic imaging', Patent number US4005382, August 1975.

84. **Becker F.L., Crow V.I.,** 'Development of an ultrasonic imaging system for inspection in nuclear reactor pressure vessels', EPRI, Palo Alto, Report number NP/1229, October 1979.

85. **Song S.J., Shin H.J., Jang Y.H.,** 'Development of an ultrasonic array system for non-destructive tests on nuclear power plant components', Nuclear engineering and design 214, pp151-161, 2002.

86. **McNab A., Campbell M.J.,** 'Ultrasonic phased arrays for non-destructive testing', NDT International, Volume 20 No6, December 1987.

87. **Mahaut S., Roy O., Beroni C., Rotter B.,** 'Development of phased array techniques to improve characterisation of defects located in components of complex geometry', Ultrasonics, volume 40, pp165-169, 2002.

88. **Erhard A., Schenk G., Houser T., Volz U.,** 'New applications using phased array techniques', Nuclear engineering and design, Volume 206, pp325-336, 2001.

89. **Hunter A.J., Drinkwater B.W., Wilcox P.D.,** 'The wavenumber algorithm for full matrix imaging using an ultrasonic array', IEEE Ultrasonics, Ferroelectrics and frequency control, volume 55, issue 11, 2008.

90. **Lane C.J.L., Dunhill A.K., Drinkwater B.W., Wilcox P.D.,** 'The inspection of anisotropic single-crystal components using 2D ultrasonic array', IEEE Ultrasonics, Ferroelectrics and frequency control, volume 57, issue 12, December 2010.

91. **Poguet J., Marguet J., Pichonnat F., Chupin L.; Imasonic S.A.,** 'Phased array technology: concepts, probes and applications', NDT.net Volume 7, No5, May 2002.

92. **Erhard A.**, **Wüstenberg H.**, **Schenk G**, **Möhrle** W.; Federal Institute for Materials Testing, 'Calculation and construction of phased array-UT probes', Nuclear Engineering and design, Volume 94 Issue 3, 1986.

93. **Olympus NDT,** 'Introduction to Phased array Ultrasonic Technology Applications', 2004.

94. **Edmonds P.D.,** 'Ultrasonics', Methods of experimental physics, Volume 19, 1981.

95. **Ginzel E.A.[1], Johnson D.[2],** 'Phased array Resolution Assessment Techniques', [1]Materials Research Institute Ontario, [2]Eclipse Scientific Products Ontario, NDT.net 2008.

96. **Fouts J.L.,** 'Forming Screen Effect on Ultrasonic Beam Field', MSc Thesis, School of Engineering, Georgia Institute of Technology, 2005.

97. **Clay A.C., Wooh S.C., Azar L., Wang J.Y.,** 'Experimental Study of Phased array Beam Steering Characteristics', Journal of Nondestructive Evaluation, Volume 18 No 2, 1999.

98. **Wooh S.C, Shi Y.,; MIT,** 'Optimisation of Ultransonic Phased arrays', Review of Progress in Quantitative Non-Destructive Evaluation, Volume 17, 1998.

99. **Ciorau, P., Ontario Power Generation Inc.,** 'A Contribution to Phased array Ultrasonic Inspection of Welds Part 1: Data Plotting for S- and B-Scan Displays', *CINDE Journal*- volume 28 no 5, 2007.

100. **Olympus NDT,** 'Advances in Phased array Ultrasonic Technology Applications', 2007.

101. **Maes G., Turgeon S., Reilly D., Kučik P.; Zetec Inc.,** 'Phased array UT inspection through wavy surfaces', NDE for Safety/Defektoskopie 2009, Prague, November 2009.

102. **Russell J., Cawley P.; Imperial College, UK. Long R.; Rolls-Royce, UK. '**Development of a Membrane Coupled Conformable Phased array', 7th International Conference on NDE in Relation to Structural Integrity for Nuclear and Pressurized Components, Yokohama, Japan, 12-15 May 2009.

103. **Myer K.,** 'Handbook of materials selection', John Wiley & Sons, 2002.

104. **Cinquin M., Le Ber L., Lonne S., Mahaut S.; Commissariat a l'Energie Atomique,** 'Results of 2006 UT modeling benchmark obtained with CIVA at CEA: beam modeling and flaw signal prediction', QNDE 2006 - Portland, Oregon.

105. **Raillon R., Bey S., Dubois A., Mahaut S., Darmon M.,** 'Results of the 2010 UT modeling benchmark obtained with CIVA: responses of backwall and surface breaking notches of various sizes', QNDE 2010 - San Diego, California.

106. **Issenmann B., Rougeron G., Mahaut S., Laborde S., '**UT phased array inspection of turbines components: experiments and simulation', QNDE 2010 - San Diego, California.

107. **Next Engine, Inc.,** 'The #1 selling 3D scanner', Available at http://www.nextengine.com/.

108. **Direct dimensions, Inc.,** 'Laser scanners', Available at http://www.dirdim.com/prod_laserscanners.htm, *[Accessed Sep 2011]*.

109. **Reilly D., Berlanger J., Maes G.,** 'On the use of 3D ray-tracing and beam simulation for the design of advanced UT phased array inspection techniques', Proceedings, 5th International Conference on NDE in Relation to Structural Integrity for Nuclear and Pressurized Components, San Diego, USA, May 2006.

110. **Richard D., Berlanger J., Maes G., Reilly D., '**Advanced Software Tools for Design and Implementation of Phased Array UT Inspection Techniques on Complex Components'**,** 8th International Conference on NDE in Relation to Structural Integrity for Nuclear and Pressurized Components, Berlin, May 2010**.**

111. Wohlers Report 2009, 'State of the Industry Annual Worldwide Progress Report on Additive Manufacturing', Wohlers Associates, 2009.

112. **Bartolo P.J.,** 'Stereolythography: Materials processes and applications', Springer, 2011.

113. **11th-hour-prototypes, '**Selective Laser Sintering', Available at http://www.11th-hour-prototypes.co.uk/SLS.html.

114. **Interpro**, 'Stereolithography (SLA) – Tolerances', Available at http://www.interpromodels.com/services/SLAstereo.html, *[Accessed Sep 2011]*.

115. RWE npower, 'Value added statement – June 2010', Npower engineering quarterly value statements signed off by station managers.

116. Silk M.J., 'Defect Sizing using Ultrasonic Diffraction', British Journal of NDT, 1979.

117. Davis J.M., Moles M., 'Resolving capabilities of phased array sectorial scans (S-scans) on diffracted tip signals', Insight Vol 48 No 4, 2006.

Publications and Patents arising from this thesis

BINDT conference Cardiff 2010

The paper contained in this appendix was submitted for presentation at the BINDT conference in Cardiff 2010 and subsequently won 'The William Gardner Award' for best paper for a person in the early stages of their career. It also simultaneously won 'The BINDT Annual Conference Paper Award' for best paper published by any author or team of authors. The paper was subsequently published in the 'Insight' journal, volume 53, No2 February 2011.

8th international conference Berlin 2010

A paper was also submitted and presented at the 8th international conference on 'NDE in relation to structural integrity for the nuclear and pressurised components'. This paper was subsequently published in the conference proceeding EUR 24824 EN- 2010.

Patent application No 10008308.8 - 1240

Patent application was submitted on August 10th 2010 for the invention of the continuous wedge described in Chapter 6. The European patent office examiner has accepted the novelty and inventive step of the invention and it should be published in December 2011.

Appendix B. Analysis of 20 element 10 MHz phased array probe

B.1 Introduction

As illustrated in section 4.1.1, the available scanning surfaces for the inspection of complex blade roots are acutely limited. A major obstacle to the development of phased array techniques associated with such finite inspection areas and limited access, has been the availability of miniature phased array probes. After various discussions with probe manufacturers one probe was developed which had a significantly small form-factor whilst offering enough elements and aperture to provide good phased array characteristics. Table B-1 shows the critical parameters of this probe with an aperture of 6.2 by 5 mm, but critically with a case size of only 9 by 7 mm and 28 mm long as seen in Figure B-1.

Parameter	Value
Centre Frequency (-6dB)	10 MHz
Acoustic Impedance Matching	Rexolite
Pulse Length (-20dB)	<350 ns
Bandwidth (-6dB)	>60 %
Array Type	Linear array
Number of Channels	20
Mechanical Focusing	None
Element Pitch	0.31 mm
Inter-Element Space	0.05 mm
Active Aperture	6.2 mm
Passive Aperture	5 mm

Table B-1 Imasonic 6822 E101 - 10 MHz, 20 element phased array probe parameters

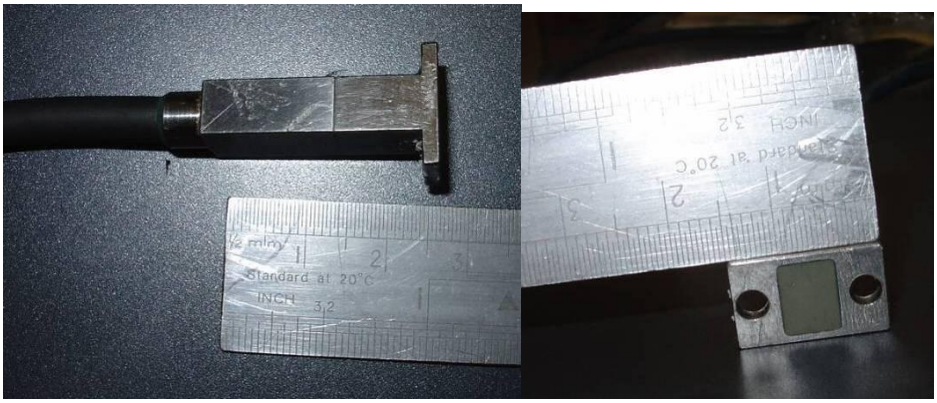

Figure B-1 Imasonic 6822 E101 - 10 MHz, 20 element phased array probe

B.2 Performance, 20 element, 10 MHz Probe

Taking some of the design parameters as described in section 3.4.4 it was possible to predict some of the functional specifications of the transducer ensuring that the layout of the elements would perform as expected. The probe aperture of 5 mm x 6.2 mm provided a solution for application to very limited refraction surfaces and limited access but would also have a detrimental effect on the focal power and potential performance of the transducer. A number of basic approximations and calculations were performed to assess the transducer performance against the requirement of the inspection using both compression and shear wave configurations.

B.2.1 Near Field compression waves

The near field or focal limit for compression waves can be approximated by equation (33) from section 3.4.4.1:-

$$N = \frac{A^2}{4\lambda} = \frac{38.44}{0.592 \times 4} = 16.28mm$$

Where: -

$$\lambda = \frac{v}{f}$$

Where: - v = Velocity of sound, f = *centre frequency*, A = Aperture, λ= Wavelength, N = Near Field

If a wedge is utilised, the equivalent ultrasound path in the wedge must be considered due to the effect on the near field calculation, see equation (38). The near field in the sample under test is reduced by the wedge steel path equivalent. Therefore, if a 12 mm thick wedge was utilised the equivalent focal limit, N_{equ}, in the sample would become:-

$$N_{equ} = \frac{A^2}{4\lambda} - \left(\frac{V_i}{V_r} \times BP_i \right) = \frac{38.44}{4 \times 0.59} - \left(\frac{2320}{5920} \times 12 \right) = 16.28 - 4.72 = 11.56mm$$

The distance to the region of interest from the platform of the pinned blade root was measured at 25 mm, see Figure B-2. It can therefore be seen that due to the small aperture

of the transducer the regions of interest are beyond the near field and so focussing is inappropriate. For this reason all inspection would be carried out in the far field of the beam and thus beam size at these distances is compromised.

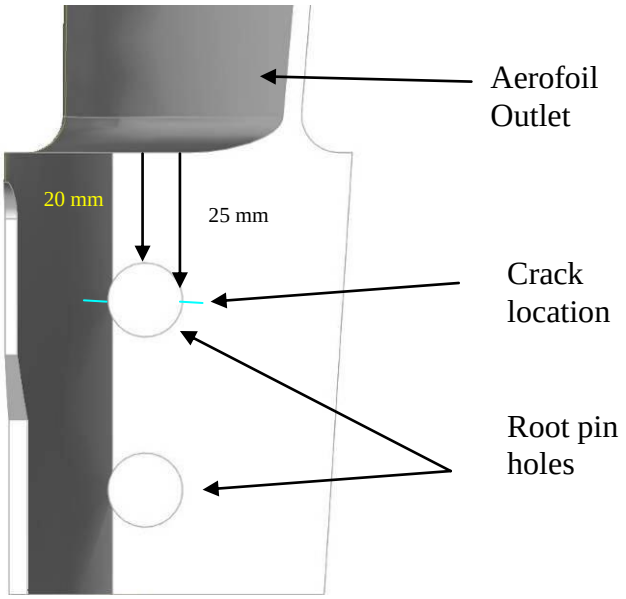

Figure B-2 IP Rotor Pinned Blade Root Compression Wave Inspection

B.2.2 Beam Spot Size for compression waves in the Far Field

The beam width (in the active plane) of an unfocused beam can be approximated using equation (51) whilst beam width in the passive plane can be approximated using equation (52). Note that the beam width approximations are only valid for beam path distances greater than the near field of the probe.

$$BW(\Delta X_{-6dB}) = k.\lambda \frac{BP}{A} \quad (51)$$

$$BW(\Delta Y_{-6dB}) = k.\lambda \frac{BP}{H} \quad (52)$$

Where:- BW = Beam Width, λ = Wavelength, BP = Beam path distance, A = Aperture, H = Passive elevation

k = Half angle beam divergence constant

The beam width in both the active and passive planes can be calculated at the natural near field focal point with no wedge. The half path beam divergence constant (k) was chosen based on Δ_{dB} = -6 dB, hence k = 0.884 [100].

B.2.2.1 Beam width at natural focus no wedge

Active $$BW(\Delta X_{-6dB}) = k.\lambda \frac{BP}{A} = 0.884 \times 0.59 \times \frac{16.28}{6.2} = 1.37mm$$

Passive $$BW(\Delta Y_{-6dB}) = k.\lambda \frac{BP}{H} = 0.884 \times 0.59 \times \frac{16.28}{5} = 1.7mm$$

The beam width in both active and passive planes can also be calculated at the beam path distance of 25 mm to the outer pin hole of the blade root with no wedge for comparison, see Figure B-2.

B.2.2.2 Beam width at outer pin hole no wedge

Active $$BW(\Delta X_{-6dB}) = k.\lambda \frac{BP}{A} = 0.884 \times 0.59 \times \frac{25}{6.2} = 2.1mm$$

Passive $$BW(\Delta X_{-6dB}) = k.\lambda \frac{BP}{H} = 0.884 \times 0.59 \times \frac{25}{5} = 2.6mm$$

Repeating these calculations whilst considering the effect of the beam travelling through the wedge in addition to the beam path to the hole results in the following: -

Beam width at outer pin hole with 12 mm high wedge

Equivalent beam path (BP_{equ}) including wedge is given by: -

$$BP_{equ} = BP + \left(BP_{wedge} \times \frac{vi}{v_r} \right) = 25 + \left(12 \times \frac{2320}{5920} \right) = 25 + 4.702 = 29.702mm \quad (53)$$

Hence the beam width at the hole is approximated by: -

Active $$BW(\Delta X_{-6dB}) = k.\lambda \frac{BP_{equ}}{A} = 0.884 \times 0.59 \times \frac{29.702}{6.2} = 2.49mm$$

Passive $$BW(\Delta X_{-6dB}) = k.\lambda \frac{BP}{H} = 0.884 \times 0.59 \times \frac{29.702}{5} = 3.09mm$$

As it can be seen the beam spot size at the outer pin hole has increased compared to the size at the natural focus and could lead to over sizing of defects smaller than 2.49 mm when using traditional drop-off sizing. However, if it is approximated that defects larger than half wavelength should be detectable, then detection of defects greater than 0.3 mm should be achievable and could be over sized due to the larger beam size. Using phased arrays however simplifies the detection of diffraction signals from the tips of defects and would improve sizing capabilities for sub-beam size defects.

B.2.2.3 Near field shear waves

In order to generate shear waves in steel at a given refraction angle it is necessary to utilise a Rexolite wedge with a mechanical angle calculated by Snell's law from equation (31) as follows:

$$\frac{\sin\theta_i}{\sin\theta_r} = \frac{v_i}{v_r}$$

Rearranged $$\theta_i = \sin^{-1}\left(\frac{v_i}{v_r}\sin\theta_r\right)$$

The refracted angle required to hit the centre of the inspection zone (position 2b) is approximately 45° (see Figure B-3); the required mechanical angle of the Rexolite wedge is calculated using compression wave velocity (v_i) of Rexolite equal to 2320 ms^{-1} and shear wave velocity (v_r) of steel equal to 3230 ms^{-1}

$$\theta_i = \sin^{-1}\left(\frac{2320}{3230} \times \sin 45\right) = 30.5^0$$

The distance to the region of interest from the available scanning platform of the pinned blade root was measured for the range of angles required to cover the outlet leg corner, see Figure B-3.

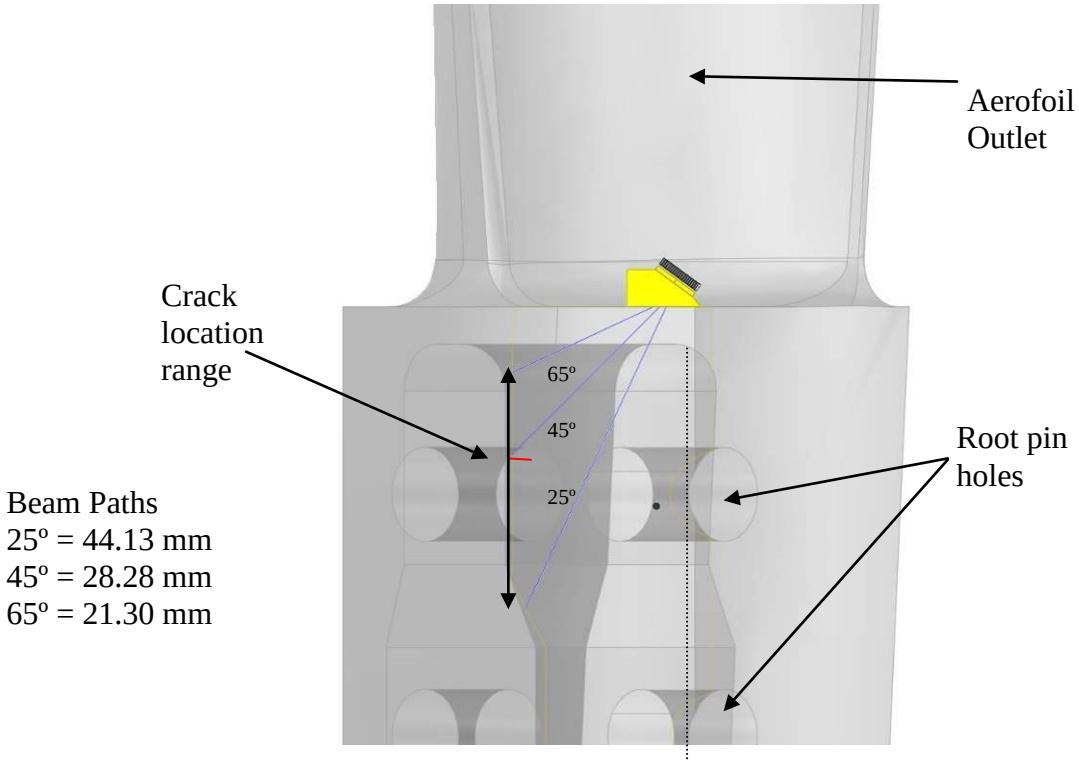

Figure B-3 IP Rotor Pinned Blade Root Shear Wave Inspection

Utilising the 30.5º Rexolite wedge to produce a natural refracted angle at 45º, the phased array laws would be required to steer the refracted beam ±20º to achieve the coverage required. The beam divergence (θ_{st}) calculated using equation (39) will establish that the transducer in question is capable of achieving the required range of angles. The range of incident angles within the wedge required to refract the ultrasound between 25° and 65° is calculated: -

@25° $$\theta_i = \sin^{-1}\left(\frac{2320}{3230}\times\sin 25\right) = 17.67^0$$

@65° $$\theta_i = \sin^{-1}\left(\frac{2320}{3230}\times\sin 65\right) = 40.61^0$$

Negative $\Delta\theta_i$ = 30.5° - 17.67° = 12.83°

Positive $\Delta\theta_i$ = 40.61° - 30.5° = 10.11°

The calculations show that the phased arrays are required to steer the beam within the Rexolite wedge by a minimum of 12.83° which is well within the capabilities of the transducer as shown by: -

$$\theta_{st} = \sin^{-1}(0.514\lambda/e)$$

$$\theta_{st} = \sin^{-1}(0.514 \times 0.232/0.26$$

$$\theta_{st} = 27.29°$$

where: wavelength (λ) for compression waves in the wedge = v/f = 2320/10000 = 0.232 mm

The near field of the probe is now dependent on the extent of the refracted angle due to a reduction in the effective aperture; from its maximum at the natural refracted angle of 45° set by the wedge, to its minimum at the highest refracted angle of 65°. The effective aperture for the transducer through the 30.5° wedge can be calculated for the limits of refracted angles using equation (37): -

$$A_{eff} = A\frac{\cos\theta_r}{\cos\theta_i}$$

θ_r = 25º $\quad A_{eff} = 6.2 \times \frac{\cos 25}{\cos 17.67} = 5.9mm$

θ_r = 45º $\quad A_{eff} = 6.2 \times \frac{\cos 45}{\cos 30.5} = 5.08mm$

θ_r = 65º $\quad A_{eff} = 6.2 \times \frac{\cos 65}{\cos 40.61} = 3.45mm$

The equivalent near field approximation is then done whilst taking account of the effective aperture and beam path within the wedge from equation (38). A nominal beam path of 10 mm in the wedge and a near field width to length correction factor (k) of 1.15[100] are used as follows: -

$$N = \frac{k \times A_{eff}{}^2}{4\lambda} - \frac{BP_i \times v_i}{v_r} \qquad (54)$$

θ_r = 25º $\qquad N_{equ} = \frac{1.15 \times 5.9^2}{4 \times 0.32} - \left(\frac{2320}{3230} \times 10 \right) = 22.7mm$

θ_r = 45º $\qquad N_{equ} = \frac{1.15 \times 5.08^2}{4 \times 0.32} - \left(\frac{2320}{3230} \times 10 \right) = 16mm$

θ_r = 65º $\qquad N_{equ} = \frac{1.15 \times 3.45^2}{4 \times 0.32} - \left(\frac{2320}{3230} \times 10 \right) = 3.51mm$

It can therefore be seen that the regions of interest are well outside the near field of the transducer at the different refracted angles and so focussing of the beam is inappropriate. All inspection will be carried out in the far field of the beam and thus beam size at these distances again becomes relevant.

B.2.3 Beam spot size for shear waves in the far field

The beam width in the active and passive planes of the unfocussed beam can again be approximated using equation (50) and equation (51) respectively.

B.2.3.1 Beam width at natural focus 25° shear

Equivalent beam path (BP_{equ}) including wedge is given by equation (53): -

$$BP_{equ} = BP + \left(BP_{wedge} \times \frac{vi}{v_r} \right) = 44.13 + \left(10 \times \frac{2320}{3230} \right) = 44.13 + 7.18 = 51.31mm$$

Hence the beam width at the inspection zone is approximated by: -

Active $\qquad BW(\Delta X_{-6dB}) = k.\lambda \frac{BP_{equ}}{A_{eff}} = 0.884 \times 0.32 \times \frac{51.31}{5.9} = 2.46mm$

Passive $\qquad BW(\Delta Y_{-6dB}) = k.\lambda \frac{BP_{equ}}{H} = 0.884 \times 0.32 \times \frac{51.31}{5} = 2.9mm$

B.2.3.2 Beam width at natural focus 45° shear

Equivalent beam path (BP_{equ}) including wedge is given by equation (53): -

$$BP_{equ} = BP + \left(BP_{wedge} \times \frac{vi}{v_r} \right) = 28.28 + \left(10 \times \frac{2320}{3230} \right) = 28.28 + 7.18 = 35.46mm$$

Hence the beam width at the hole is approximated by: -

Active $$BW(\Delta X_{-6dB}) = k.\lambda \frac{BP_{equ}}{A_{eff}} = 0.884 \times 0.32 \times \frac{35.46}{5.08} = 1.97mm$$

Passive $$BW(\Delta Y_{-6dB}) = k.\lambda \frac{BP_{equ}}{H} = 0.884 \times 0.32 \times \frac{35.46}{5} = 2.01mm$$

B.2.3.3 Beam width at natural focus 65° shear

Equivalent beam path (BP_{equ}) including wedge is given by equation (53): -

$$BP_{equ} = BP + \left(BP_{wedge} \times \frac{vi}{v_r} \right) = 21.3 + \left(10 \times \frac{2320}{3230} \right) = 21.3 + 7.18 = 28.48mm$$

Hence the beam width at the hole is approximated by: -

Active $$BW(\Delta X_{-6dB}) = k.\lambda \frac{BP_{equ}}{A_{eff}} = 0.884 \times 0.32 \times \frac{28.48}{3.45} = 2.33mm$$

Passive $$BW(\Delta Y_{-6dB}) = k.\lambda \frac{BP_{equ}}{H} = 0.884 \times 0.32 \times \frac{28.48}{5} = 1.61mm$$

The effective aperture decreases with increasing refracted angle so beam divergence increases. At the same time the equivalent beam path reduces so it can be seen that the passive beam size reduces with increasing steering angles due to reduced beam path whereas the active beam size remains similar in all cases.

If it is approximated that defects larger than half wavelength should be detectable, then detection of defects greater than 0.16 mm should be achievable but could be over sized due to the larger beam size. Sizing of small defects would have to be done using diffraction techniques[116 117]. Table B-2 shows the results of all the approximations calculated for both the compression wave and shear wave configurations of the 20 element 10 MHz transducer.

		Effective Aperture (mm)	Near Field N_{equ} (mm)	Beam Path equivalent to Inspection area within component (mm)	Beam width at Inspection Zone	
					$BW(\Delta X_{-6dB})$ (mm)	$BW(\Delta Y_{-6dB})$ (mm)
Compression (No Wedge)		6.2	16.28	25	2.1	2.6
Compression (12 mm Rexolite Wedge)		6.2	11.56	29.7	2.49	3.09
Shear (30.5º Rexolite Wedge)	**25º**	5.9	22.7	51.31	2.46	2.9
	45º	5.08	16	35.46	1.97	2.01
	65º	3.45	3.51	28.48	2.33	1.61

Table B-2 Focal Limits and beam widths of the 20 element, 10 MHz Phased array Probe

B.2.4 Resolution

Having approximated the beam dimensions at the inspection zones provides important information about the ability to resolve separate defects which are laterally oriented and defects which are axially oriented with respect to the beam.

Lateral resolution (Δd) is the minimum distance between two reflectors located at the same depth, which produce amplitudes clearly separated by more than 6dB from peak to valley[100]. This measure is taken with the transducer being moved over the defects and interrogated with a fixed beam angle (A-Scan). Lateral resolution is proportional to beam width and can be approximated by: -

$$\Delta d = \frac{BW_{\Delta X-6dB}}{4} \tag{55}$$

Angular resolution ($\Delta\theta$) relates the minimum angle between two A-Scans which produce amplitudes from two adjacent defects at the same depth, which can be resolved by a minimum of -6dB between peak to valley. This measure is taken with a static probe position of a phased array system using azimuthal sector scans. The minimum distance between defects shall be approximated in the same way as lateral resolution and the angular resolution can be derived by calculating the angle of a triangle formed between the two

defects spaced by Δd and the centre of the transducer as illustrated Figure B-4 and then calculated using equation (56):-

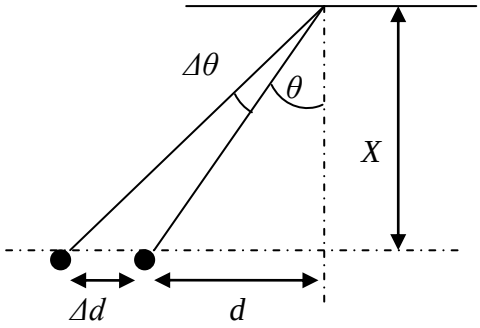

$\Delta\theta$ = Angular Resolution
θ = Refracted angle to first defect
X = True depth to defects
Δd = Lateral resolution

Figure B-4 Illustration of angular resolution ($\Delta\theta$)

$$\Delta\theta = Tan^{-1}\left(\frac{d+\Delta d}{X}\right) - \theta \qquad (56)$$

Axial resolution (Δz) is the minimum depth spacing along the acoustic axis, for which two adjacent defects at different depths are resolved more than 6dB peak to valley. Axial resolution will be dependent upon pulse duration as seen in equation (57), so highly damped broadband probes will yield better axial resolutions[100].

$$\Delta z = \frac{v_{sample} \times \Delta\tau_{-20d\mathbf{B}}}{2} \qquad (57)$$

Table B-3 shows the approximated lateral, angular, and axial resolutions for the 20 element 10 MHz phased array transducer in the proposed inspection configurations. It can be seen that the minimum spacing between adjacent defects in all configurations using shear waves would be less than 0.62 mm and for compression waves at low refraction angles of less than 0.63 mm. This relates in the case of the shear waves to an angular resolution of better than 0.7° and for compression waves better than 1.4°.

	Beam width at Inspection Zone		Lateral resolution (mm) Δd	Angular Resolution (degrees) $\Delta\theta$	Axial resolution (mm) Δz
	BW(ΔX_{-6dB}) (mm)	**BW(ΔY_{-6dB}) (mm)**	$\Delta d = \frac{BW_{\Delta X-6dB}}{4}$	$\Delta\theta = Tan^{-1}\left(\frac{d+\Delta d}{X}\right) - \theta$	$\Delta z = \frac{v_{sample} \times \Delta\tau_{-20dB}}{2}$
Compression (No Wedge) @ 5°	2.11	2.6	0.525	1.192	0.689
Compression (12 mm Rexolite Wedge) @ 5°	2.51	3.09	0.6225	1.412	
Shear (30.5º Rexolite Wedge)	2.46	2.9	0.615	0.6712	0.376
25º	1.97	2.01	0.4925	0.6968	
45º	2.33	1.61	0.5825	0.6153	
65º					

Table B-3 Lateral, angular, and axial resolution for the 20 element 10 MHz phased array probe

B.2.5 Discussion

It has been shown that the small aperture of the transducer has a limiting effect on the near field and therefore limits the ability to focus the ultrasound at the target inspection regions. However, significantly small defects of sub 0.5 mm should be easily detected with the ability to resolve adjacent defects which are less than 0.62 mm apart. Careful application of sizing techniques which utilise diffraction signals will be necessary for sub beam width defects, but due to the high resolution attained defect sizing of approximately 0.5 to 0.62 mm accuracy should be achievable.

Appendix C. Bench trials and validation of rexolite jigs for IP rotor inspections

As described in section 4.2.3 trials were carried out to validate the Rexolite jig designs both with known defective samples and blind inspection of a service rotor. This appendix reports the results of those trials.

C.1 Initial bench trials

Bench trial inspections were carried out to a total of 27 blades with the following properties;

- 2 with EDM slots
- 1 with mechanical damage
- 15 contained the cracking defects removed from a repaired rotor
- 9 were defect free blades.

Reference sensitivity was set for the compression wave inspections with the outer pin hole response maximised to 100 % full screen height (FSH); reference sensitivity was set for the shear wave inspection to the saddle geometric response maximised to 100 %FSH. Inspection sensitivity was set to reference sensitivity plus 6dB. The results were recorded in Table C-1 below.

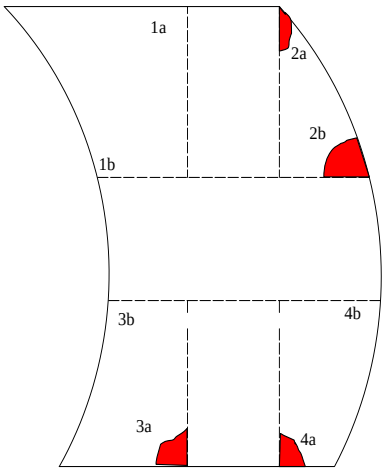

Blade No	4	3	2a	2b
1				
2				
3				
4				
5	ok	ok	ok	ok
6				
7				
8				
9				
10				
11				
12	ok	ok	def	ok
13				
14				
15				
16	ok	ok	def	def
17	ok	ok	ok	ok
18	ok	ok	ok	def
19				
20				
21				
22				
23				
24				
25				
26				
27				
28				
29	ok	ok	ok	def
30				
31				
32				
33				

Blade No	4	3	2a	2b
34				
36	ok	ok	ok	def
37				
38				
39				
40				
41				
42				
43				
44				
45				
46	ok	ok	def	def
47	ok	ok	def	def
48	ok			def
49				
50				
51	def	def	ok	ok
52	slot	slot	ok	ok
53	slot	slot	slot	ok
54				
55				
56				
57	ok	ok	def	def
58				
59	ok	ok	ok	ok
60				
61				
62	ok	ok	ok	ok
63				
64	ok	ok	ok	ok
65				
66	ok	ok	ok	def

Blade No	4	3	2a	2b
67	ok	ok	def	def
68				
69	ok	ok	def	def
70				
71	ok	ok	ok	ok
72				
73				
74				
75	ok	ok	ok	ok
76				
77	ok	ok	def	def
78				
79				
80	ok	ok	ok	ok
81				
82				
83	ok	ok	ok	ok
84				
85				
86				
87	ok	ok	def	def
88	ok	ok	def	def
89				
90				
91				
92				
93				
94				
95				
96				
97				
98				

Table C-1 Results of steam end initial bench trial

C.1.1 Discussion of trial results

All defective blades were identified correctly with positive responses from defects in all positions. Figure C-1 shows damage to the 2b position of blade 29 which consisted of a <0.5 mm notch inflicted on the blade during original assembly of the rotor, and corrosion damage to the inner saddle face. The sector scan of blade 29, recorded during the trial, can be seen in Figure C-2; the scan illustrates the sensitivity of the shear wave technique to very small flaws, and the need to carefully characterise defects based on the response and amplitude.

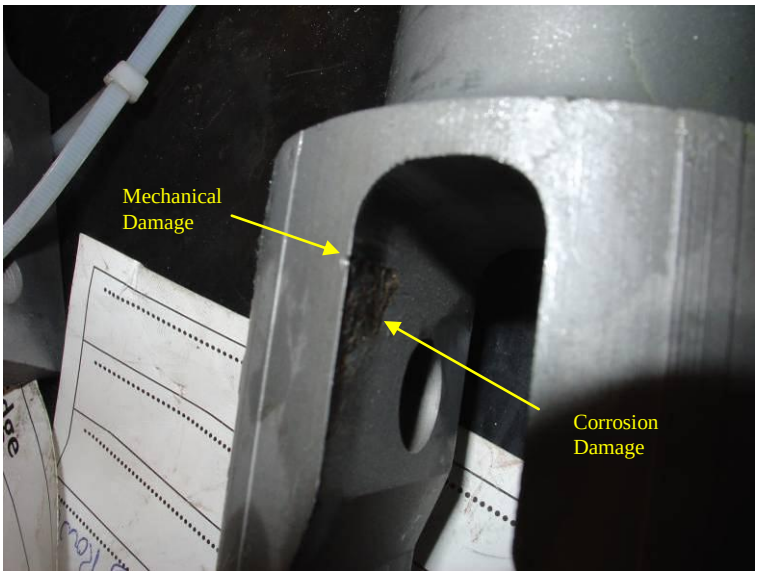

Figure C-1 Mechanical damage to saddle edge of blade 29

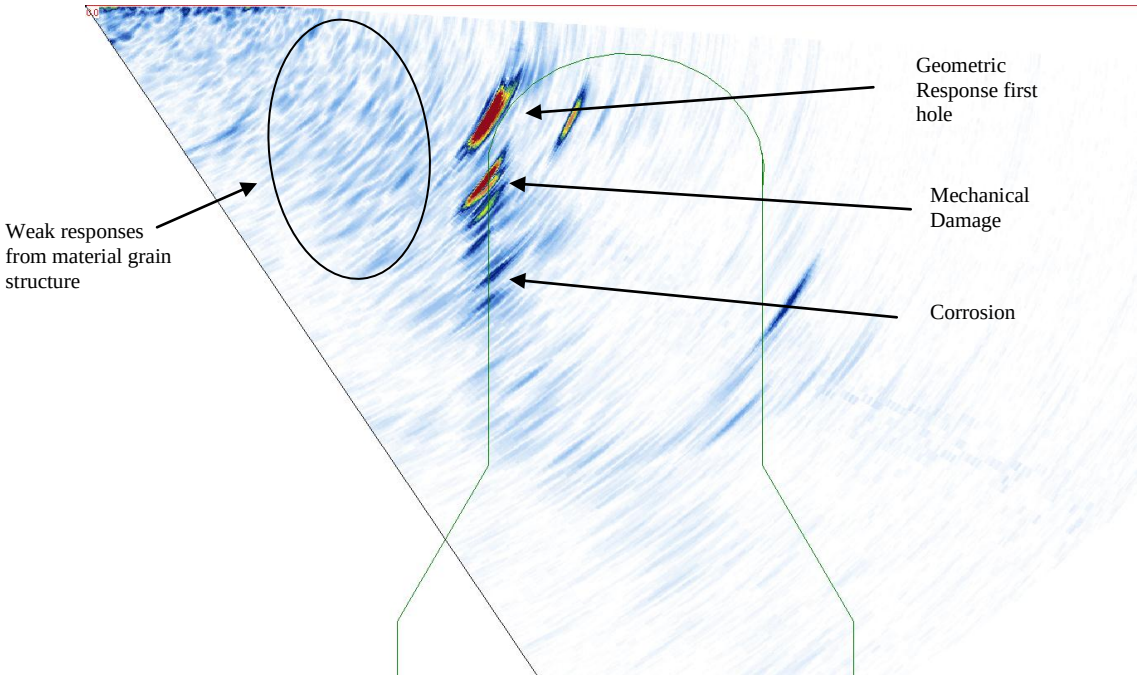

Figure C-2 Ultravision sector scan of blade 29

All EDM slots were positively detected in blades 52 and 53 but the slot at the 7o'clock position (Figure C-7) from zone 3, gave very weak responses and illustrated the limit of detection for defects shadowed by the hole. Figure C-3 and Figure C-4 show the recorded sector scans for Blade 53 Zone 3, and blade 53 Zone 4 respectively; this blade contained EDM slots in the 9 o'clock position round the pin hole. Figure C-5 and Figure C-6 show

the sector scans for blade 52 Zone 3, and blade 52 Zone 4 respectively; these blades contained EDM slots in the 7o'clock position round the pin holes.

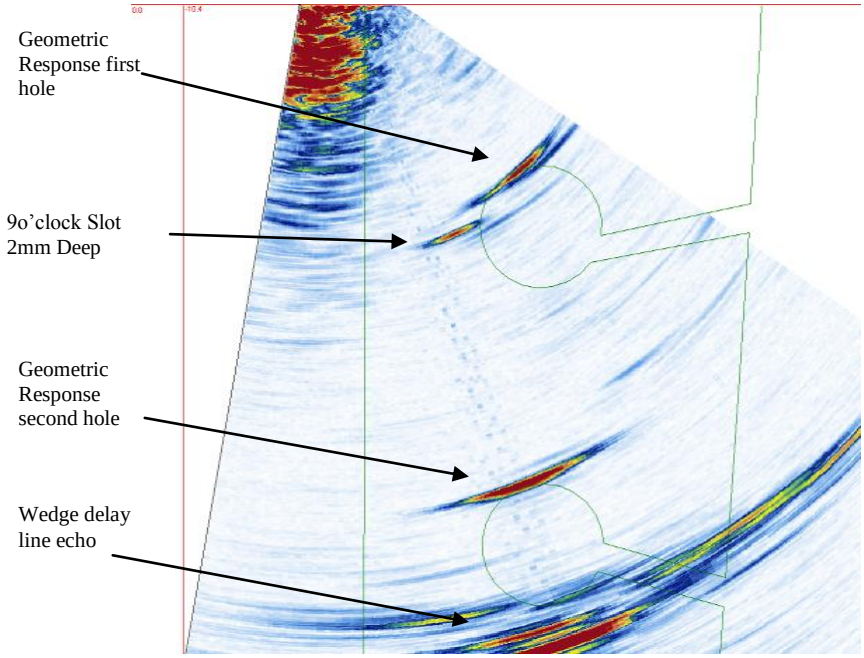

Figure C-3 Sector scan of EDM slot from blade 53 zone 3

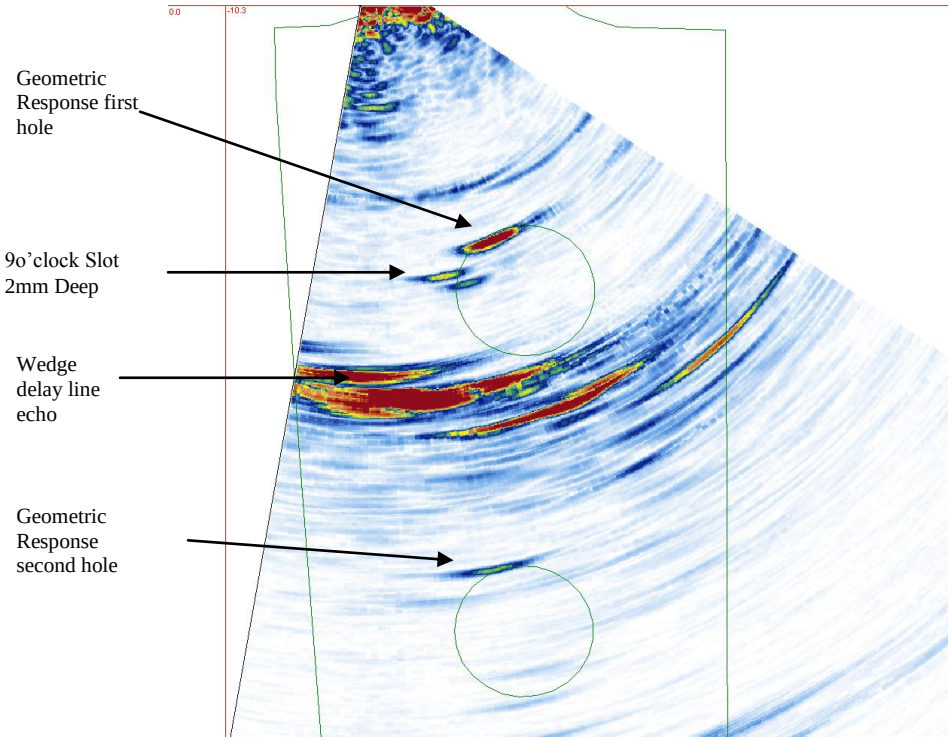

Figure C-4 Sector scan of EDM slot from blade 53 zone 4

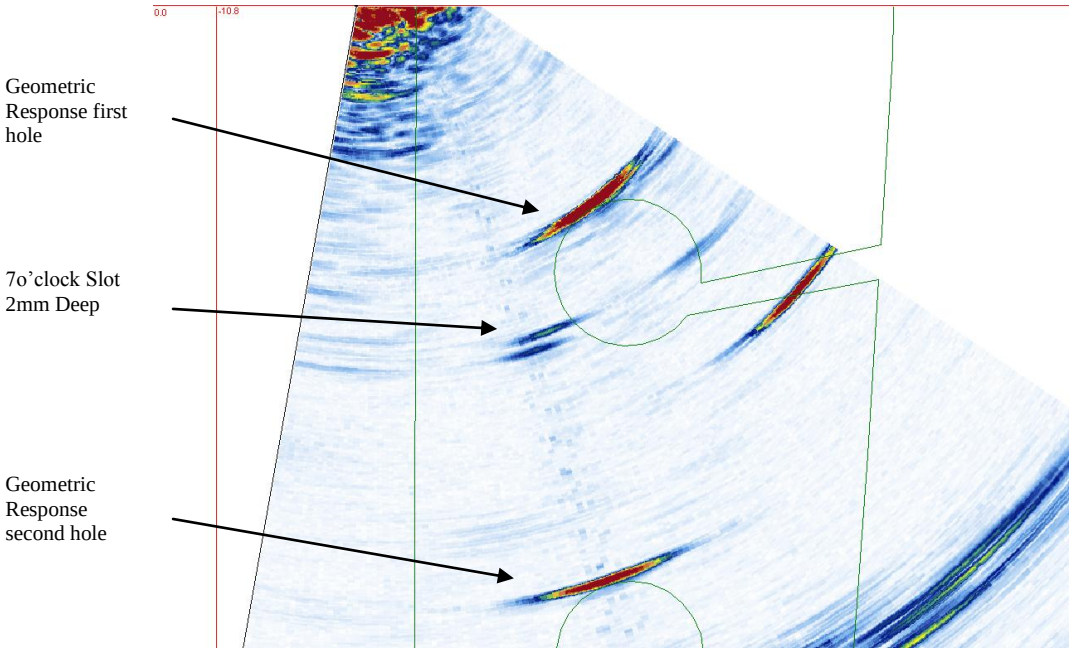

Figure C-5 Sector scan of EDM slot from blade 52 zone 3

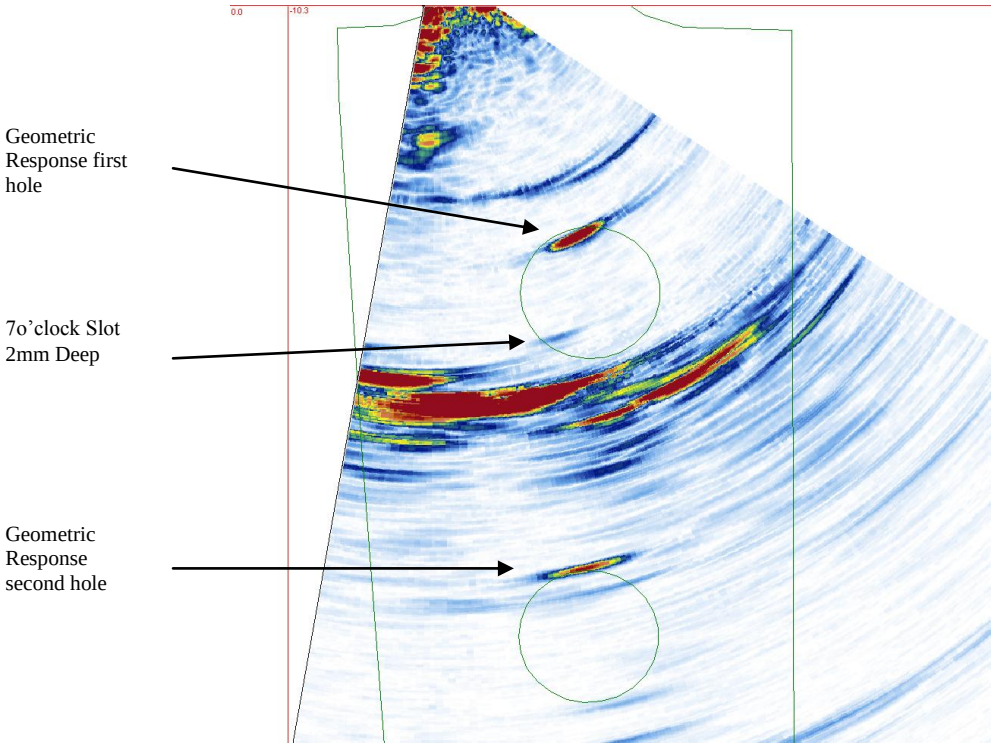

Figure C-6 Sector scan of EDM slot from blade 52 zone 4

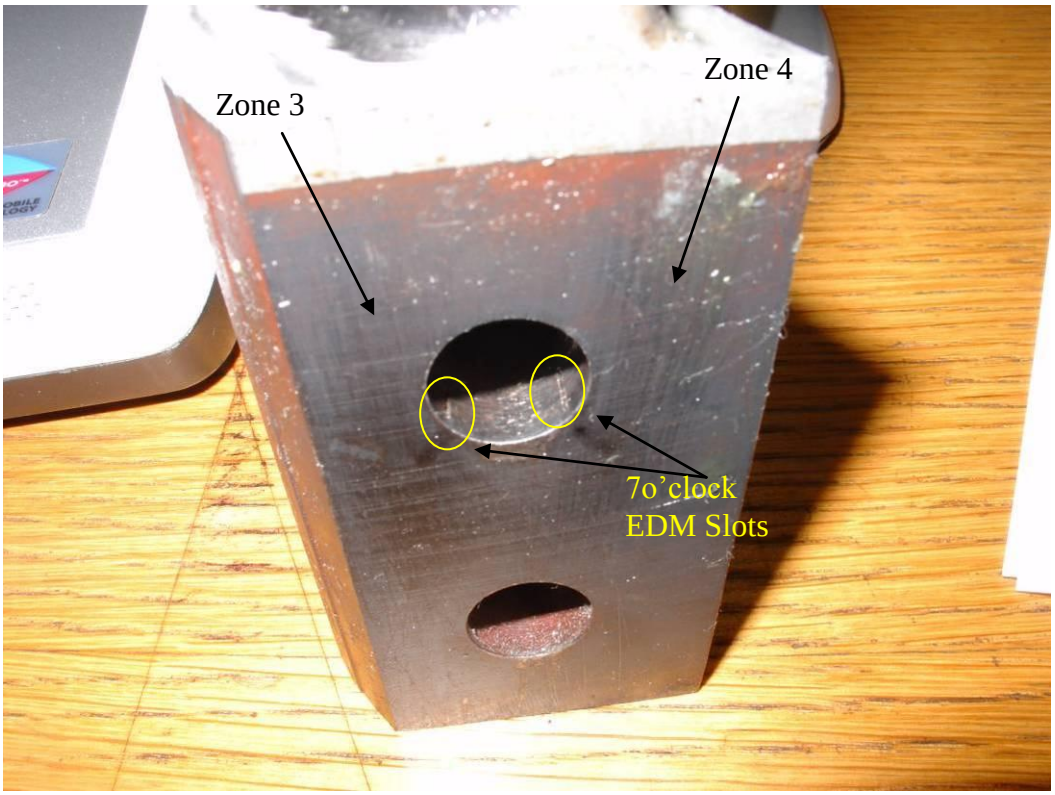

Figure C-7 Positioning of blade 52 7o'clock slots

It was noted in section 2.2.2.3 that two blades (one of which was blade 66) were difficult to detect using the manual single element inspection technique, mainly due to the inability to resolve the crack response from the geometric response. Figure C-8 shows the improvement in detection capability in this position when utilising the phased array technique. The defect was easily resolved from the geometric response and the extent of the crack could be measured from the tip diffraction and facets along its depth.

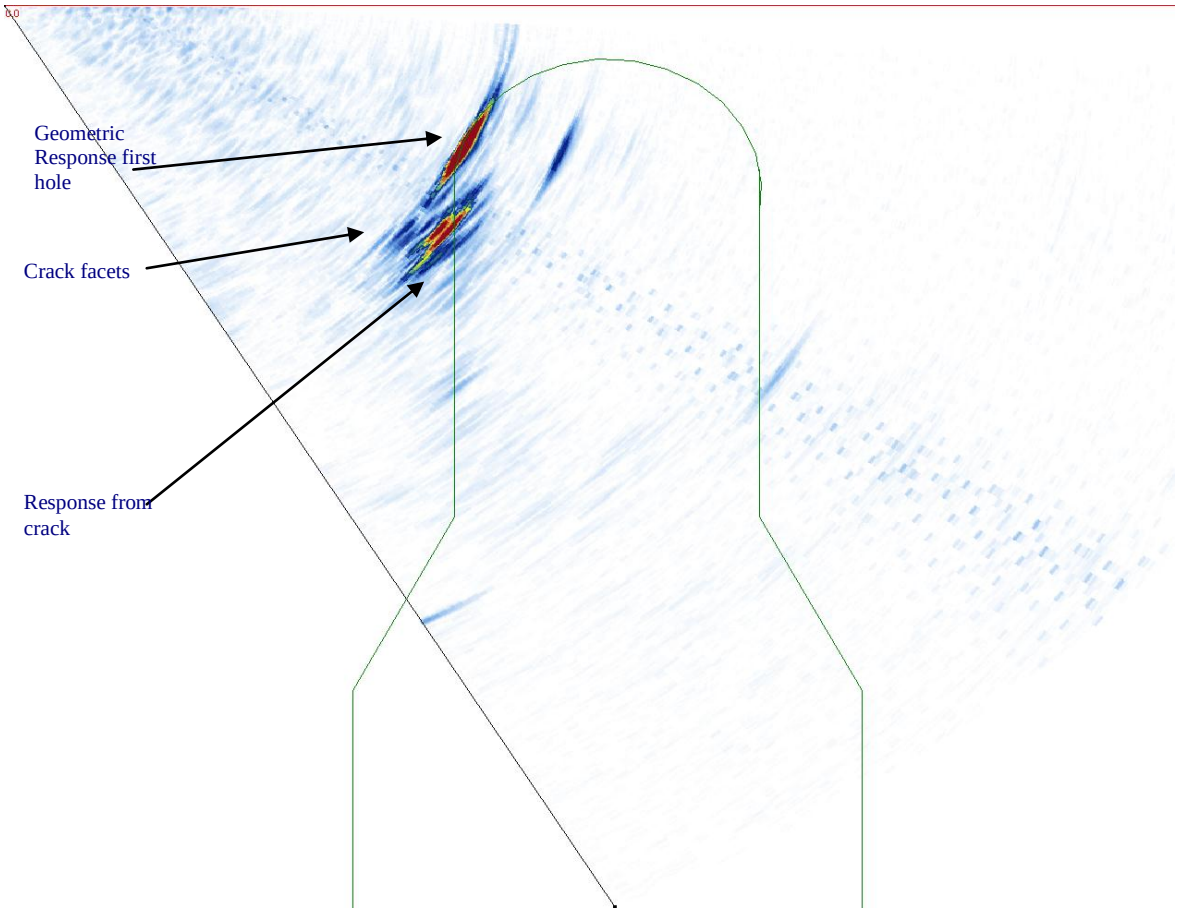

Figure C-8 Blade 66 sector scan of defect

C.1.2 Conclusion of initial bench trials

It was shown through the initial bench trial that successful detection was achieved of all confirmed defects in blades removed from the steam end of the parson's 660MW steam turbine. It was also seen that high sensitivity to small flaws to the saddle corner (2b zone) was achieved; careful characterisation would be required to distinguish mechanical damage from cracks as seen with blade 29. However, the flaw in blade 29 would be considered a significant stress raising point, which could lead to crack propagation.

The advanced imaging of the phased array sector scan, providing high sensitivity to small defects, coupled with the ability to place the probe in the correct position, meant that this inspection yielded more positive detection of the defects. The manual single element inspection required a high level of dexterity of the operator, in manipulating, tilting, and

skewing the probe to achieve coverage. The CNC wedges ensured that the phased array probe could be placed quickly and accurately in the correct position for every blade, whilst the phased array laws ensured coverage of the inspection zone by electronically steering the ultrasonic beam. The inspection of each zone could be carried out in approximately a quarter of the time, with less couplant to contaminate the rotor, providing recordable accurate detection of defects.

Shadowing of defects which propagate from below the 7o'clock position of the root pin hole would limit detectability of small defects in those positions.

It is clear that there are huge advantages to the approach using CNC profiled jigs as the basis of this type of inspection. The inspections at each zone were very repeatable and sensitive to small flaws in the blade root areas.

C.1.3 Inspection validation of Parsons 660MW IP turbine

Further to the initial bench trials, the opportunity was taken to complete a full blind trial validation of the phased array technique on a service rotor. The phased array technique, in conjunction with the original single element manual inspection technique (Technique sheet NP/WI/NDT017), was utilised to carry out inspection of 6 wheels, each containing 100 blades; the inspection consisted of 600 blades from stages 6, 7, and 8 of both the steam end and alternator end of the rotor, see Figure C-9. No defects were found to stages 6 or 8 of both ends of the rotor, however more than 50 % of the blades in stage 7 of both ends produced responses that were indicative of cracking.

The phased array inspection results correlated directly with the single element inspection results, but a large proportion of defects were reported to the 2b position (see Figure C-10) which was not covered in the manual technique. A rotor with such a high proportion of defective blades could not be economically repaired by replacement of just the defective blades; hence the decision was made to re-blade the entire wheel of blades on stage 7 at both

ends. The wheels of blades were extracted intact by removal of the root pins followed by sponge blasting in preparation for full surface inspection utilising fluorescent magnetic particle inspection (FMPI). All defects were characterised by location and size and compared to the phased array inspection results.

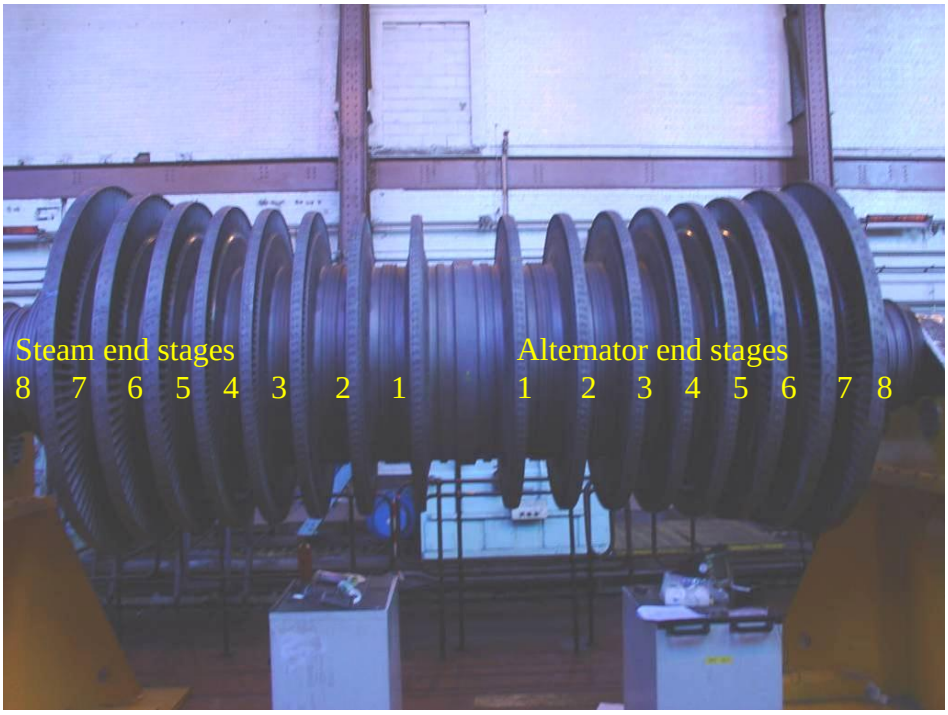

Figure C-9 Service IP rotor inspection

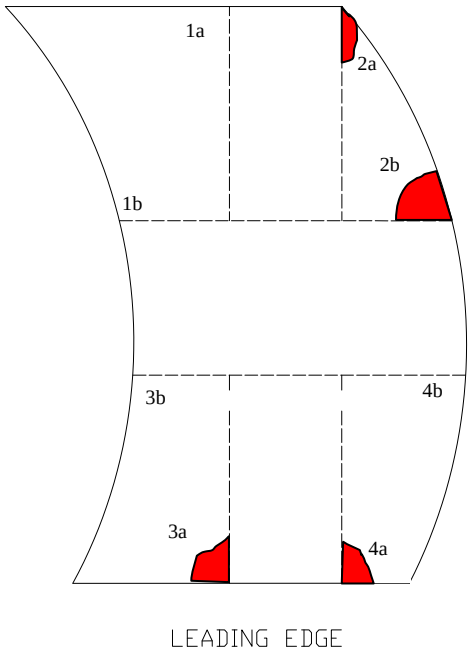

Figure C-10 Defect locations of pinned blade roots

C.1.4 Validation analysis

Defects previously not experienced were found in zones 3b and 4b (Figure C-10) during the FMPI inspection. However 97 % of the blades cracked in zone 4b had major defects in zone 2b which were detected and would be removed for repair. The addition of a shear wave inspection, similar to that utilised to inspect zone 2b regions, was developed and all defects in this zone 4b were subsequently detected. A technique to detect defects in zone 3b was not possible due to the absence of a suitable scanning platform. Out of the 10 blades found to contain defects in zone 3b, only 2 would have been left undetected had selective repairs been carried out due to major defects detected in other zones. A total of 14 blades with defects in zone 2b were misinterpreted and reported as corrosion, and a further 6 blades with cracks in zone 2b were missed during the live inspection. The analysis of zone 2b highlighted the need to allow some tilting of the probe/wedge on the blade root, this allowed better coverage of the corner geometry and increase the ability to characterise defects. When the 20 blades were re-tested after removal from the rotor, with no inter-blade spacing restriction, 14 out of the 20 could be positively characterised as cracked. A further 4 of these were detectable but very difficult to characterise, and 2 were out of the useful range of the inspection and could not be positively detected. All results and analysis can be found in a comprehensive validation report produced by the author (reference RCNDE-EngD-18 Month Report).

C.1.5 Final statistics for blade detection performance.

Taking account of all the defects found and reported, with slight modification to the shear wave PA technique (tilting), 10 blades would have been left in the rotor had there been selective repairs because: either there was no test for that position and no defects were found in other positions, and/or the current technique has no detection capability, see Table C-2.

After the successful addition of a shear wave inspection to the 4b position, assuming 100 % detection of these defects, only 4 blades would remain undetected. With modification to the wedges and probe position, to increase focal depth and therefore sensitivity to lower down defects, detection of 2 further defects in zone 2b might be achieved. Only 2 defects would be left undetected in zone 3b due to lack of inspection capability, highlighted in red in Table C-2 below.

Stm Blade	1A	1B	2A	2B	3A	3B	4A	4B
56				1x2		3x5		
60								6x2
76								6x3
81				3x7				
Alt Blade	**1A**	**1B**	**2A**	**2B**	**3A**	**3B**	**4A**	**4B**
43						3x2		
46								12x4
68								5x3
70						4x2		
77								10x2
88								12x3

Table C-2 Blades with defects not detected in all positions

Appendix D. Experiment 1 to 4 results

Contained within this appendix are all the recorded phased array scans carried out through experiments 1 to 4 in section 5.3.4 of Chapter 5.

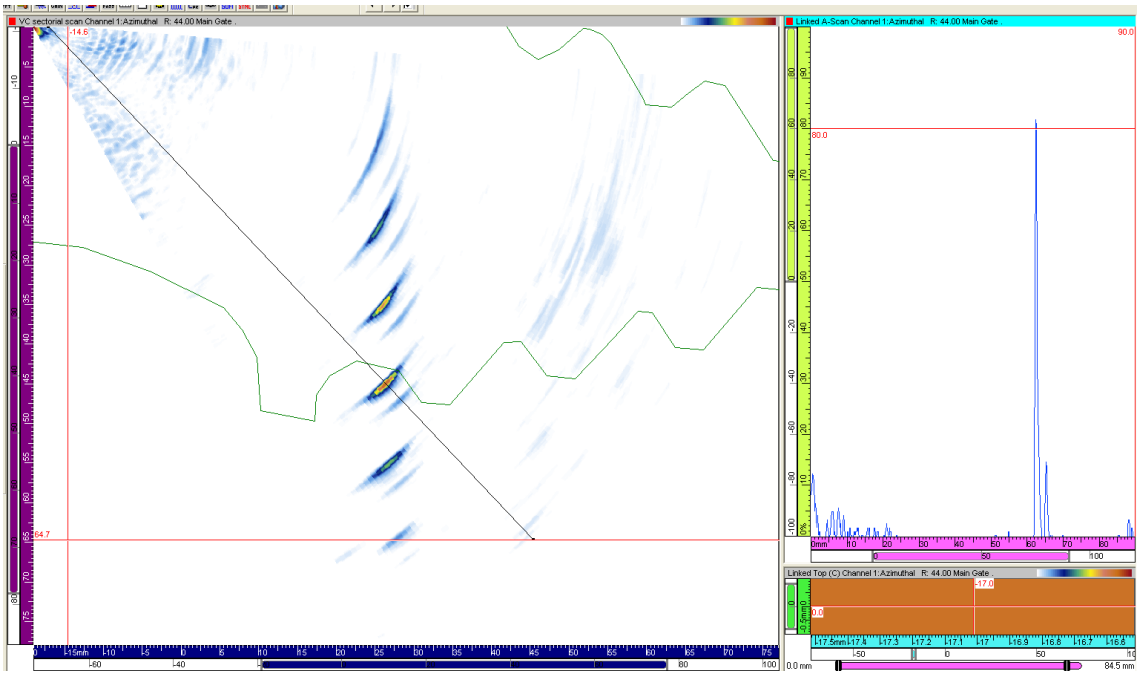

Figure D-1 Experiment 1 - SDH– 80 % FSH, 24dB, 44°, and 45 mm deep

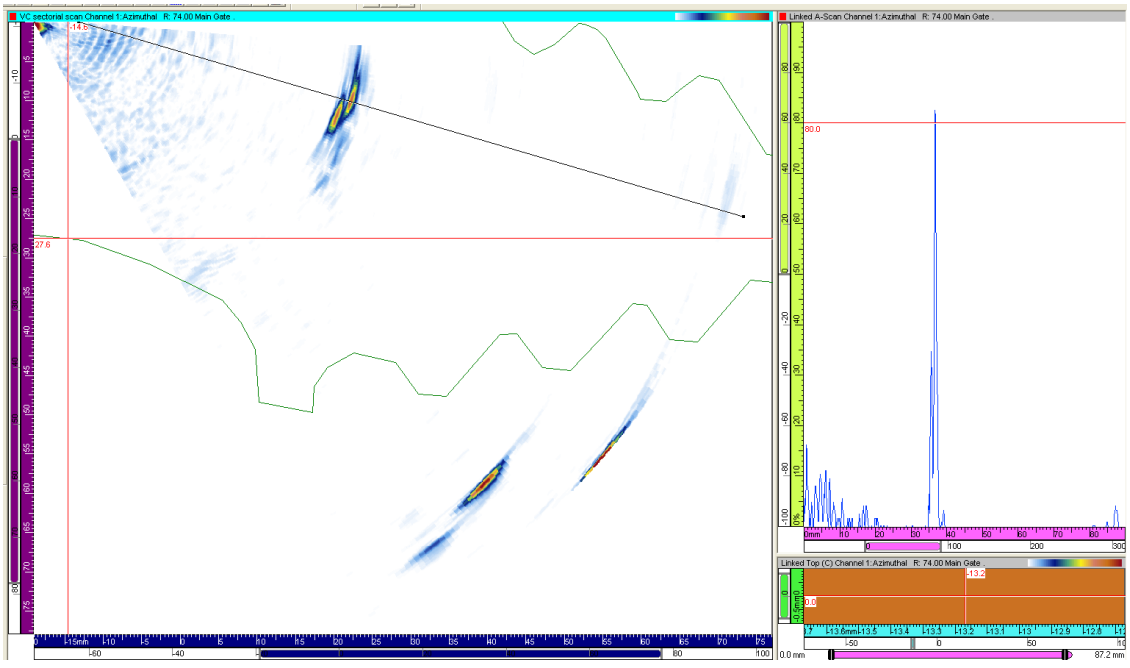

Figure D-2 Experiment 1 – Concave Notch B – 80 % FSH, 28dB, 73.5°, and 10.4 mm deep

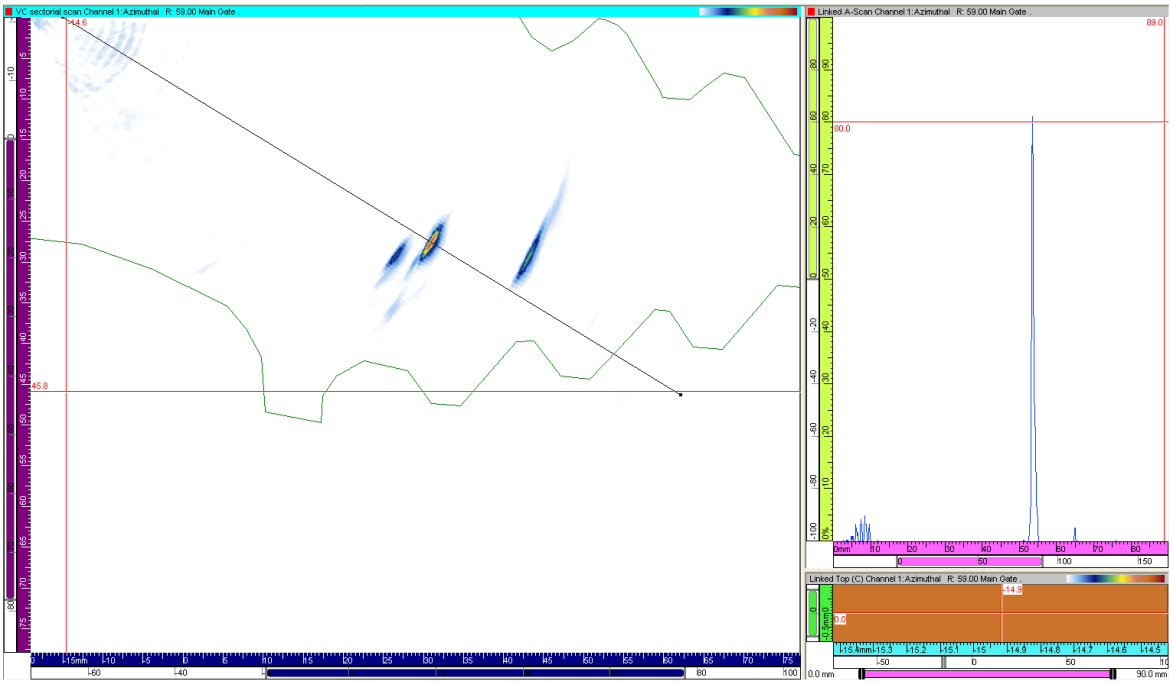

Figure D-3 Experiment 1 – Concave Notch C – 80 % FSH, 21dB, 59°, and 27.6 mm deep

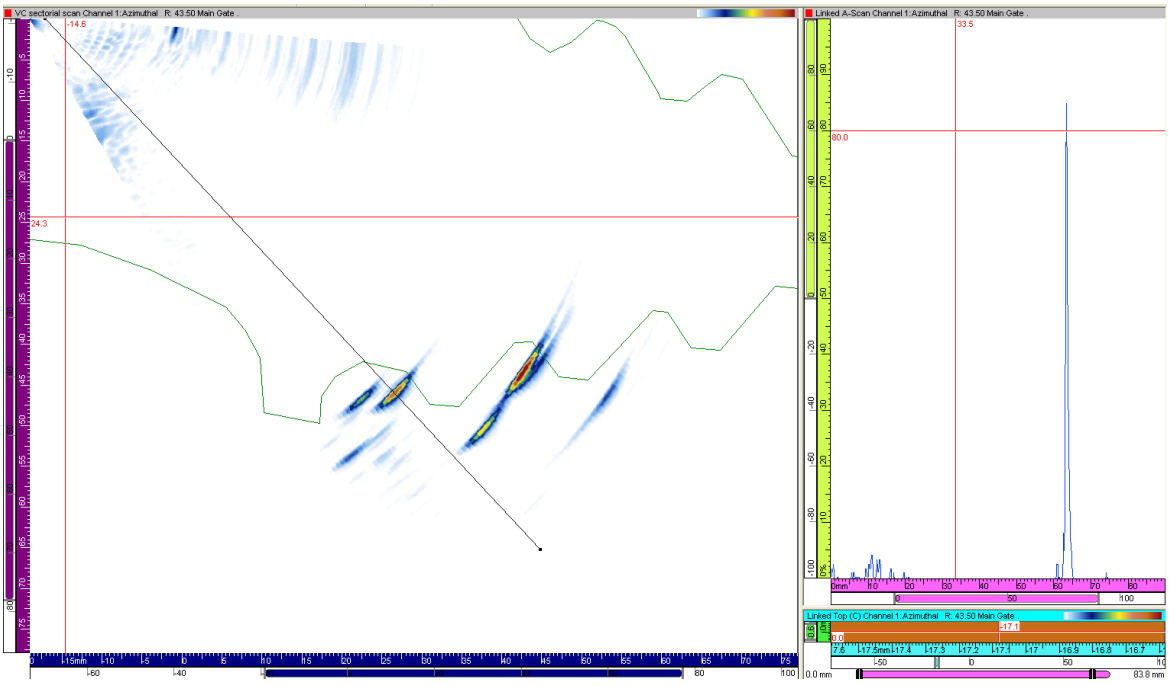

Figure D-4 Experiment 1 – Concave Notch E (reference) – 80 % FSH, 21dB, 44°, and 45 mm deep

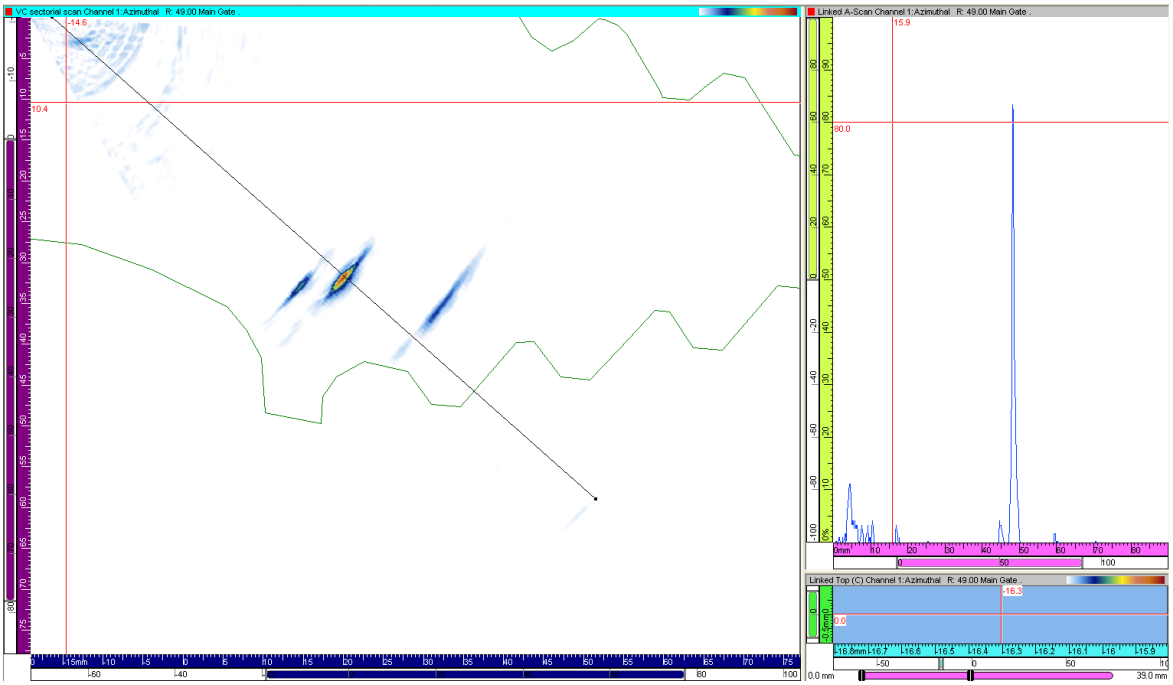

Figure D-5 Experiment 1 – Concave Notch F – 80 % FSH, 23dB, 49°, and 32 mm deep

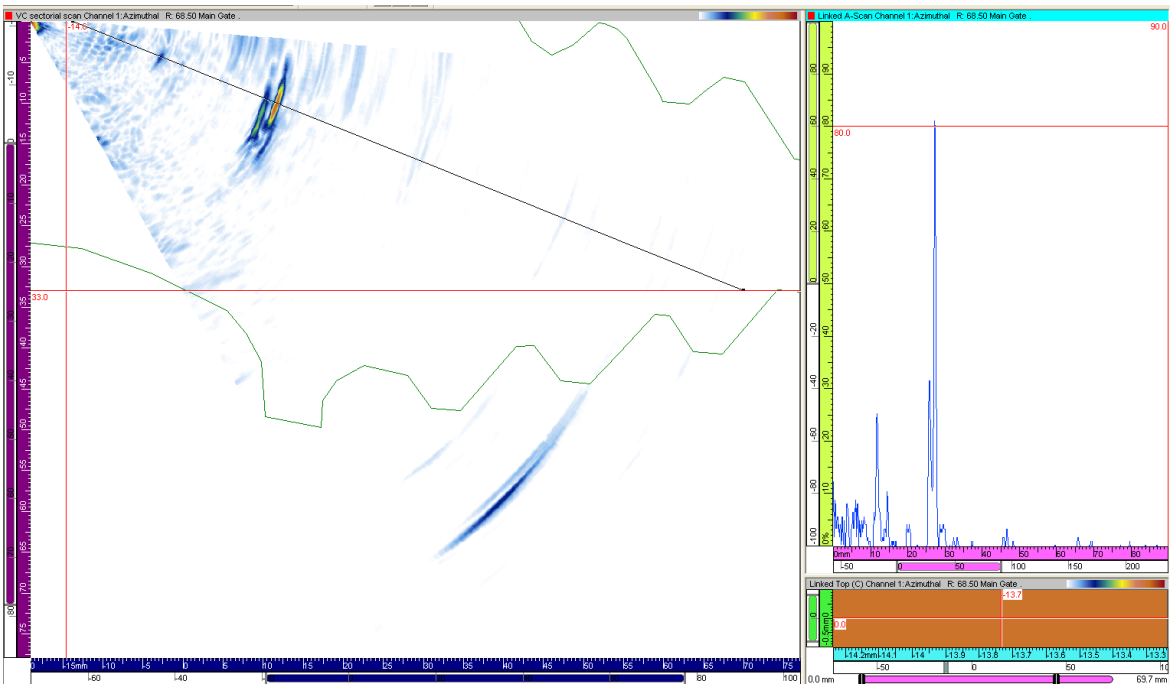

Figure D-6 Experiment 1 – Concave Notch G – 80 % FSH, 28dB, 68.5°, and 10.1 mm deep

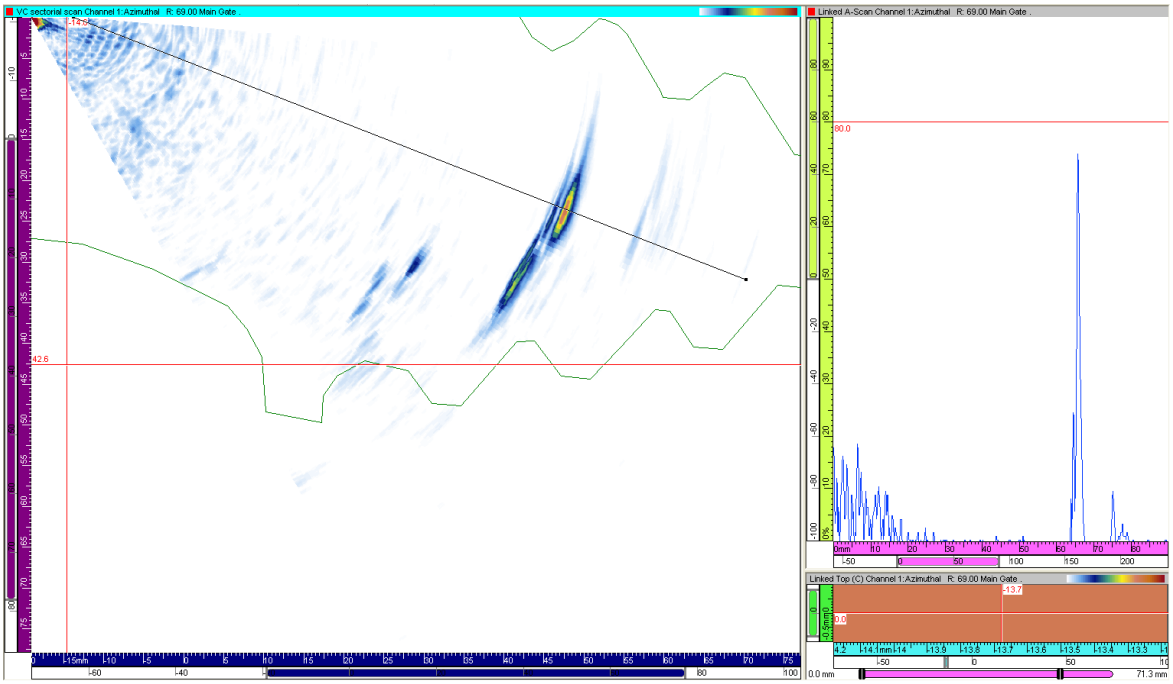

Figure D-7 Experiment 1 – Concave Notch K – 80 % FSH, 32dB, 69°, and 23.7 mm deep

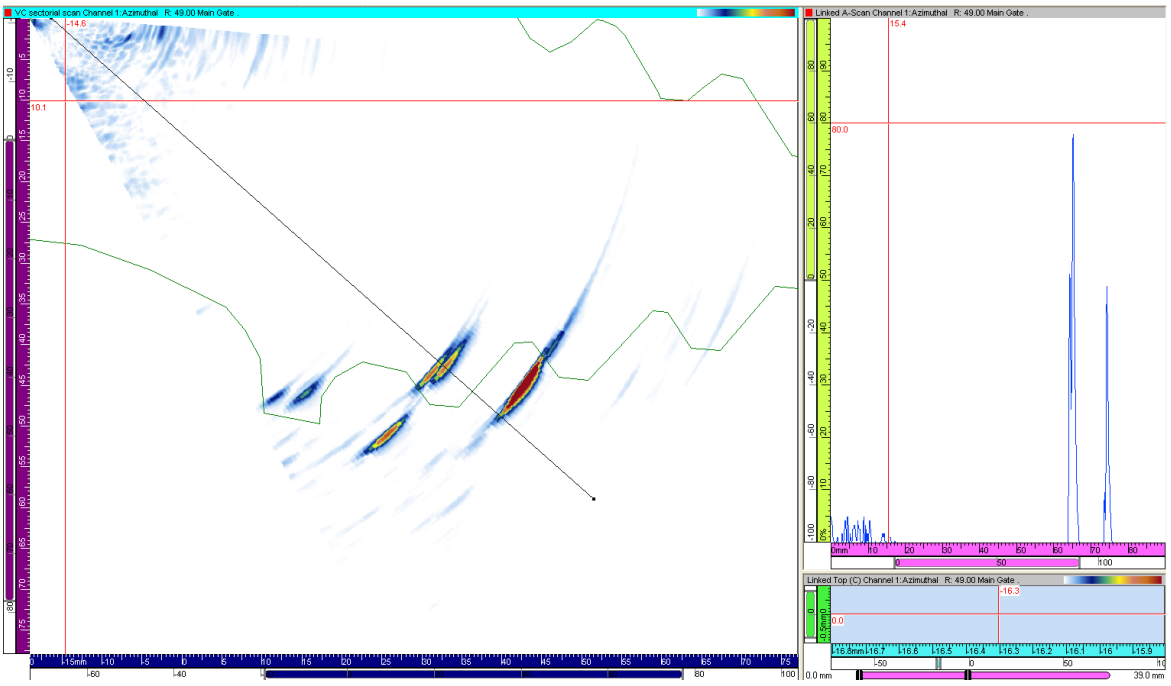

Figure D-8 Experiment 1 – Concave Notch M – 80 % FSH, 25dB, 49°, and 42.6 mm deep

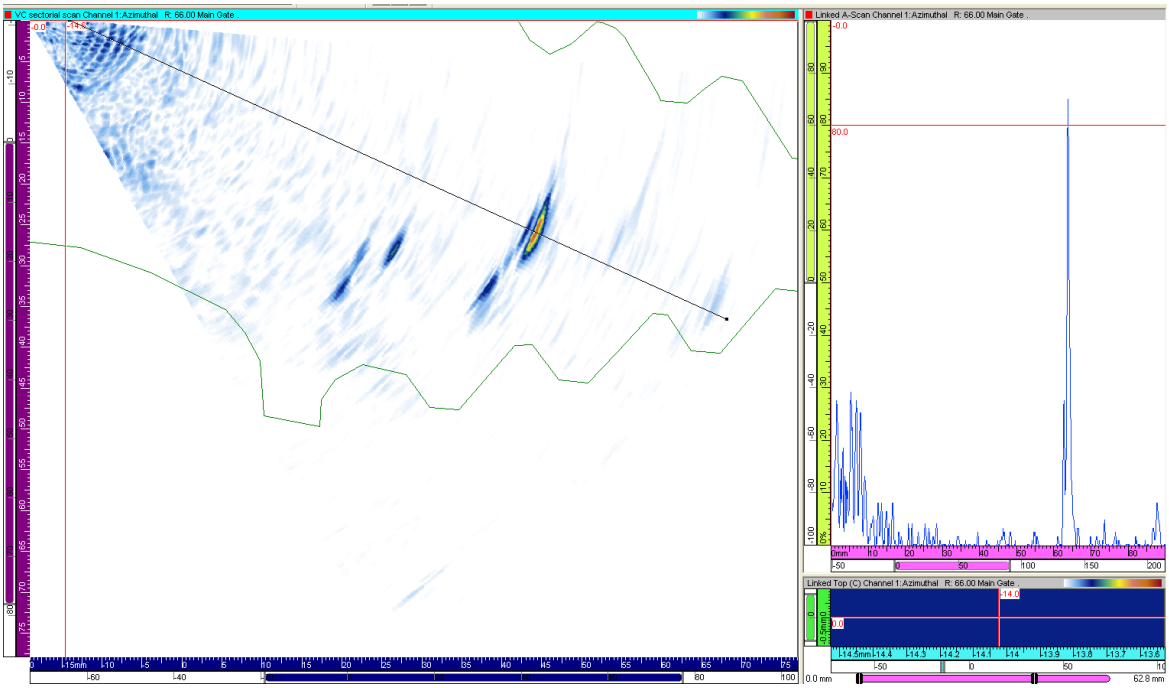

Figure D-9 Experiment 1 – Concave Notch N – 80 % FSH, 34dB, 66°, and 26.1 mm deep

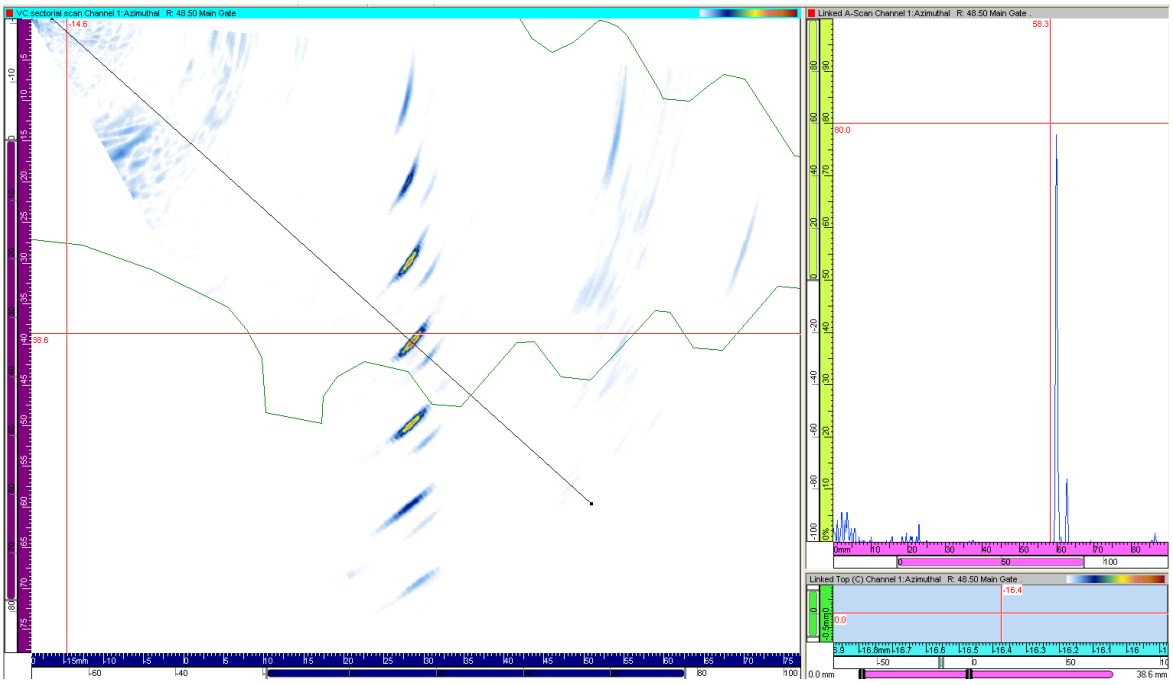

Figure D-10 Experiment 2 – SDH – 80 % FSH, 25dB, 48.5°, and 40 mm deep

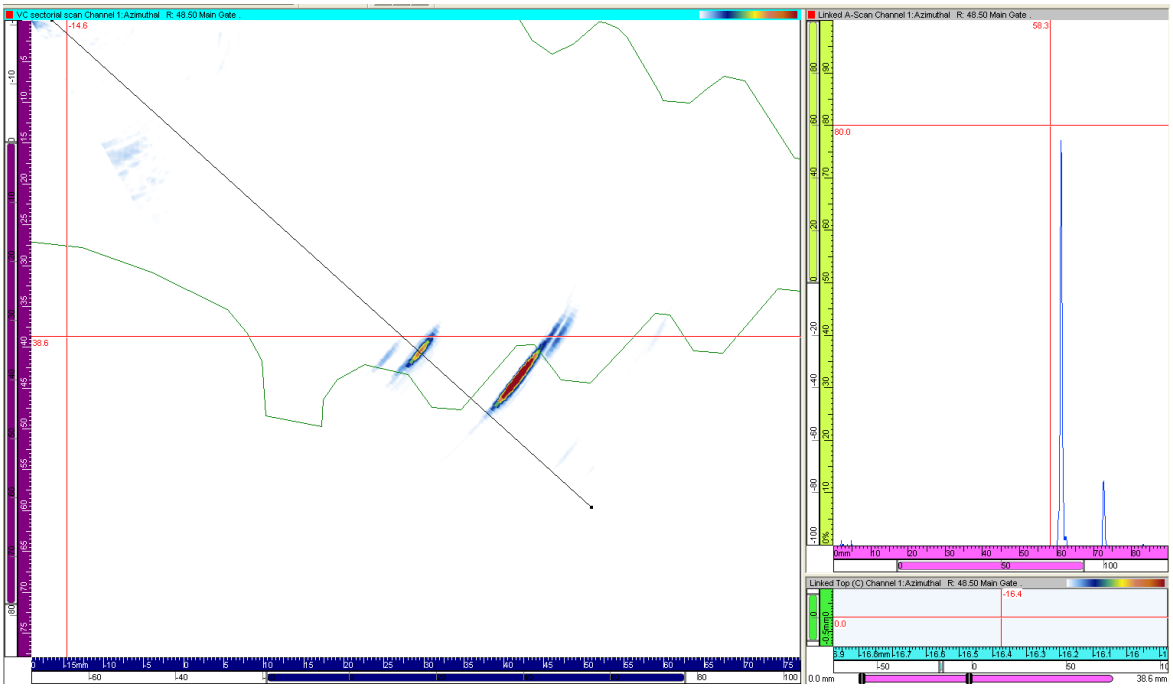

Figure D-11 Experiment 2 – Convex Notch C – 80 % FSH, 17dB, 48.5°, and 40 mm deep

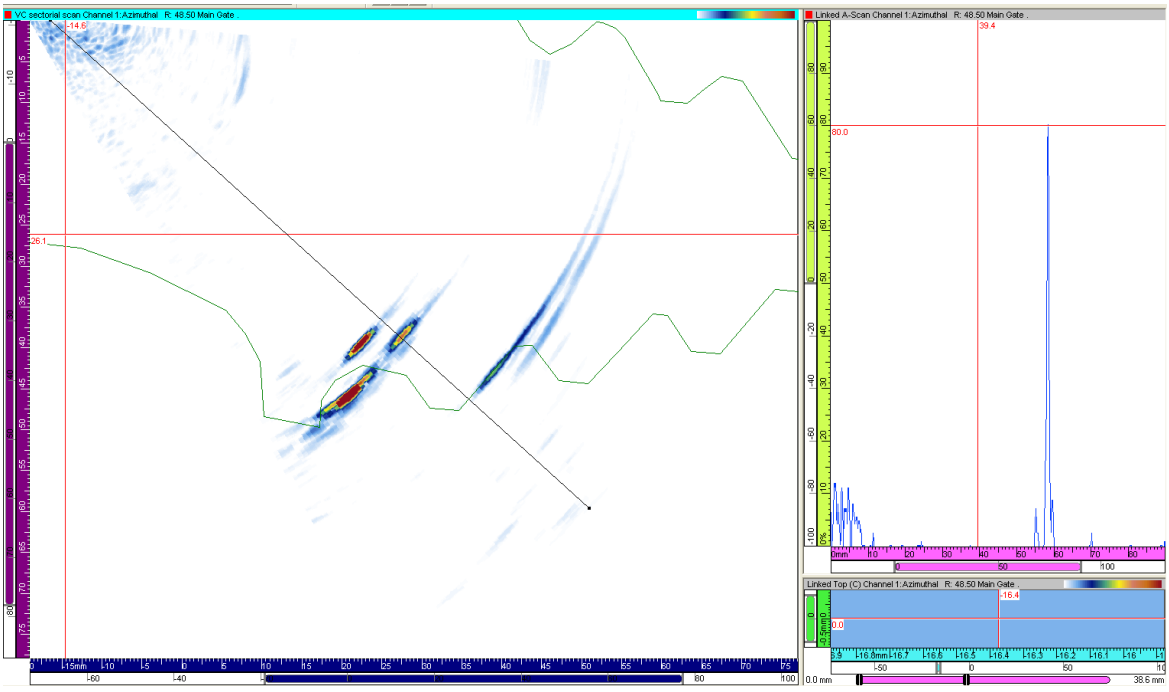

Figure D-12 Experiment 2 – Convex Notch D (reference) – 80 % FSH, 22dB, 48.5°, and 38.6 mm deep

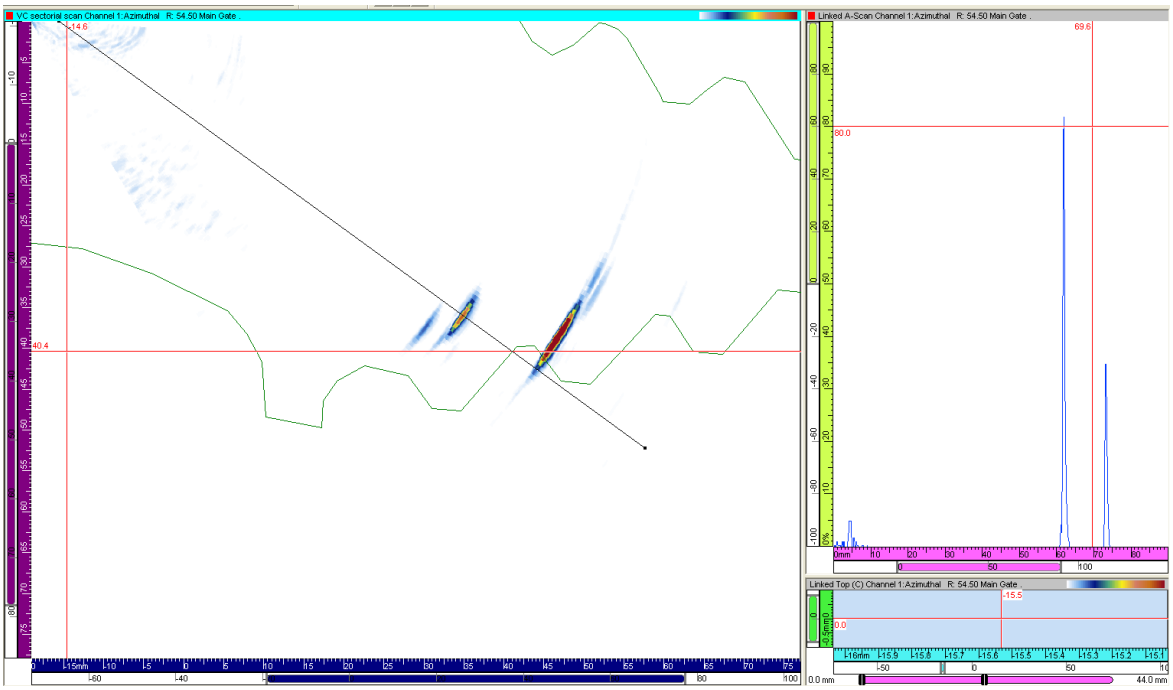

Figure D-13 Experiment 2 – Convex Notch F – 80 % FSH, 19dB, 54.5°, and 36.1 mm deep

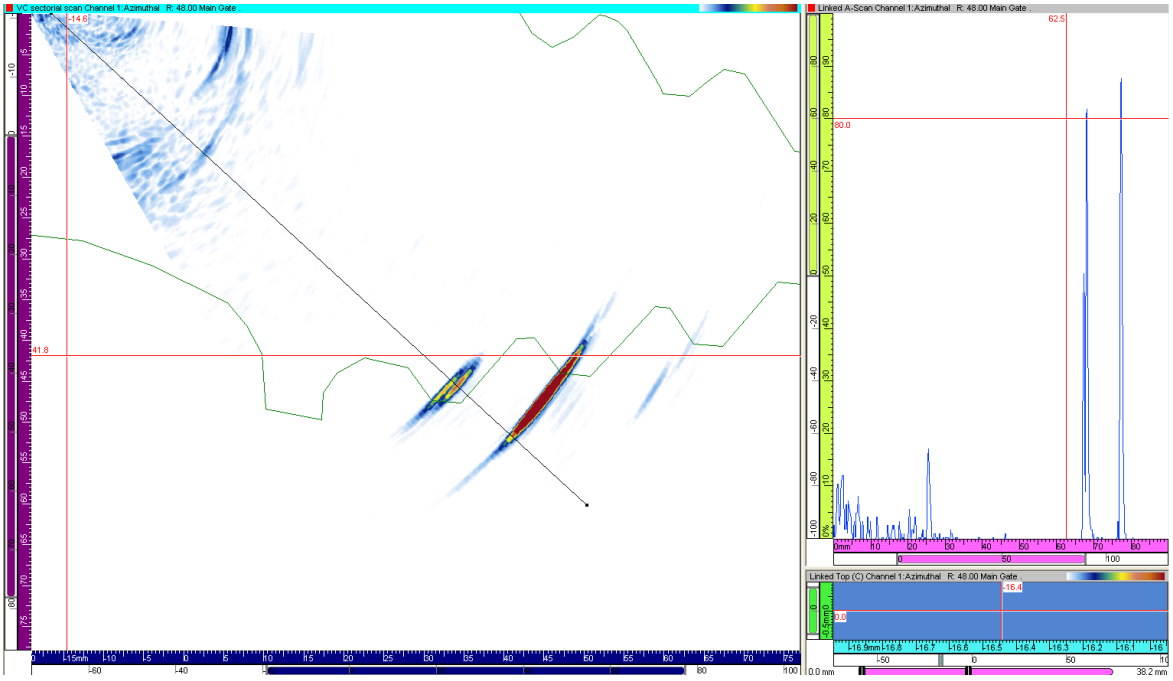

Figure D-14 Experiment 2 – Convex Notch I – 80 % FSH, 29dB, 48°, and 45 mm deep

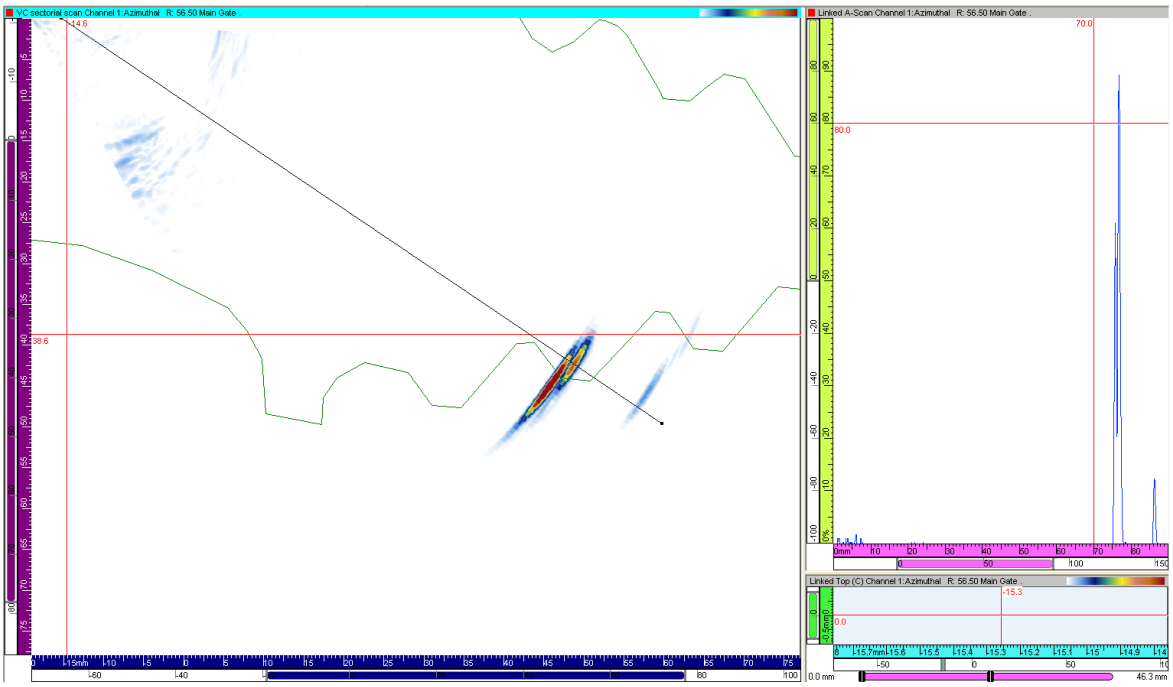

Figure D-15 Experiment 2 – Convex Notch J – 80 % FSH, 21dB, 57°, and 41.5 mm deep

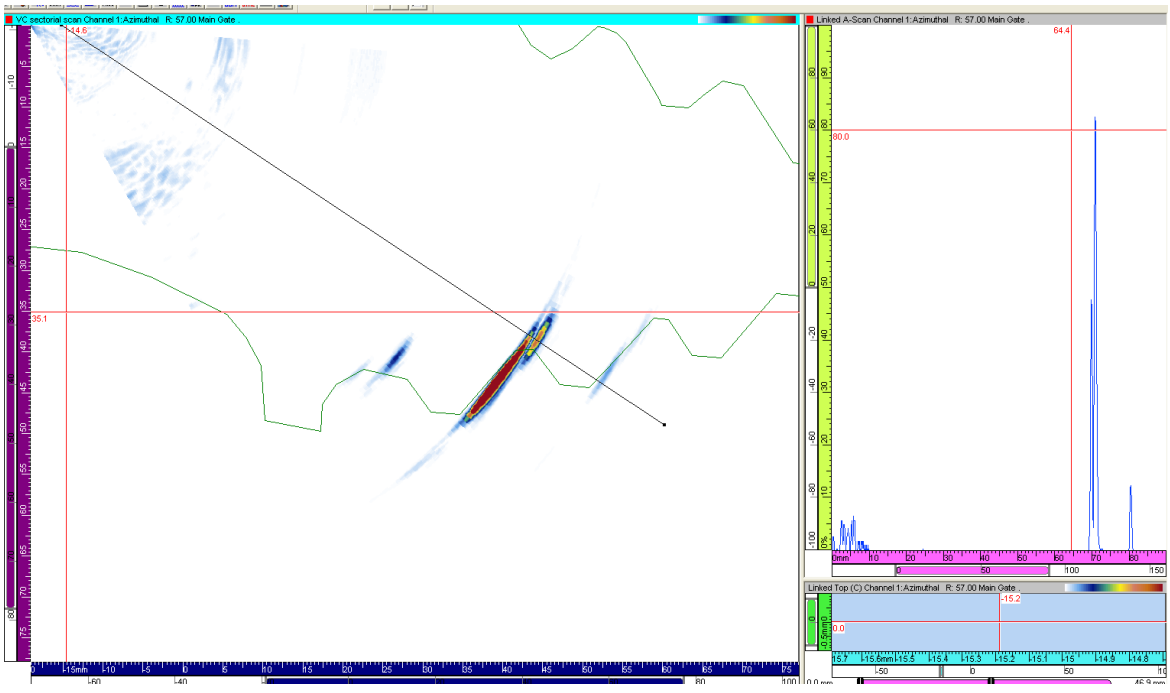

Figure D-16 Experiment 2 – Convex Notch K – 80 % FSH, 22dB, 57°, and 38.6 mm deep

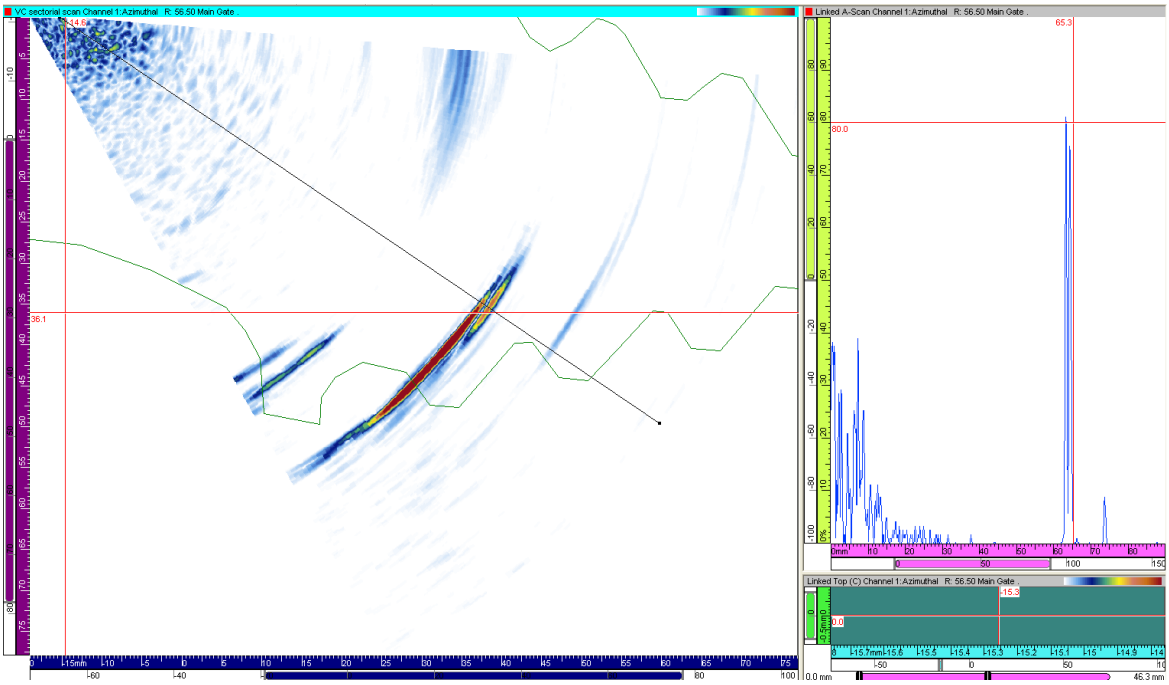

Figure D-17 Experiment 2 – Convex Notch L – 80 % FSH, 27dB, 57°, and 35 mm deep

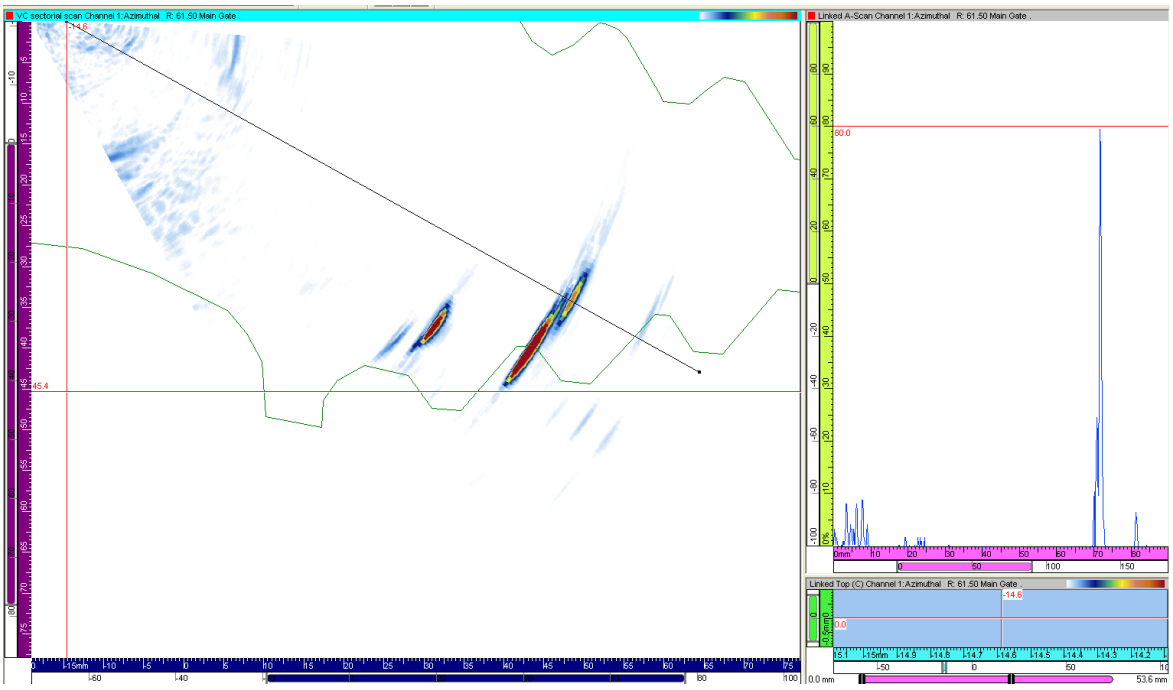

Figure D-18 Experiment 2 – Convex Notch N – 80 % FSH, 25dB, 61.5°, and 34 mm deep

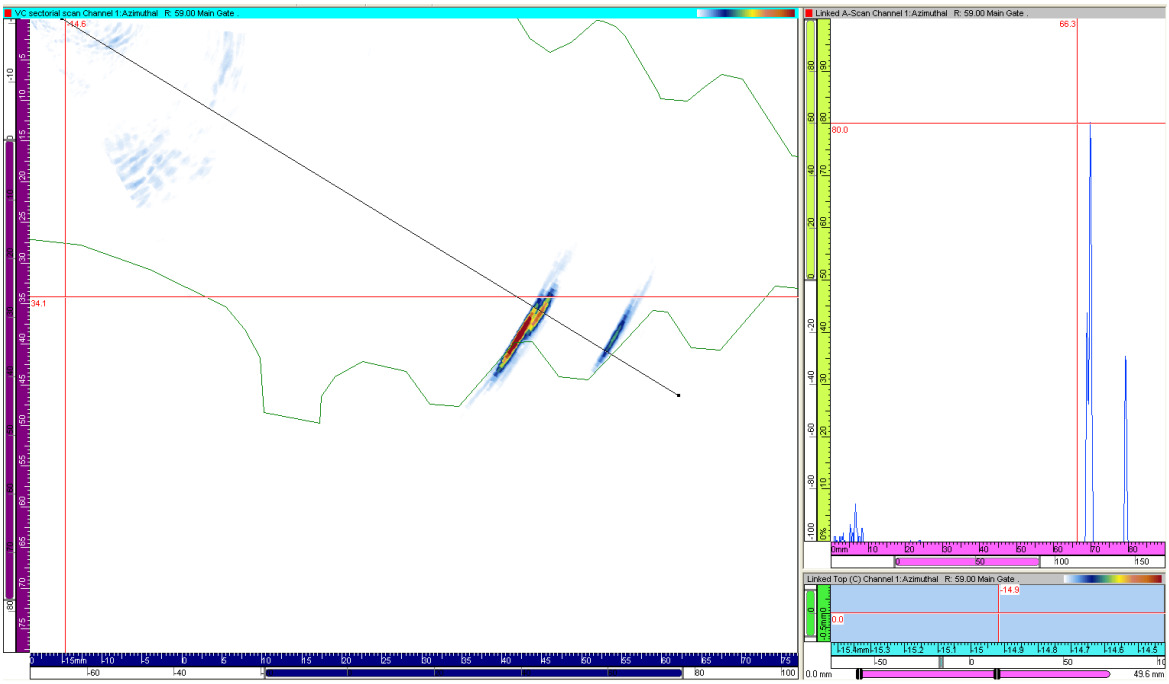

Figure D-19 Experiment 2 – Convex Notch O – 80 % FSH, 20dB, 59°, and 36.1 mm deep

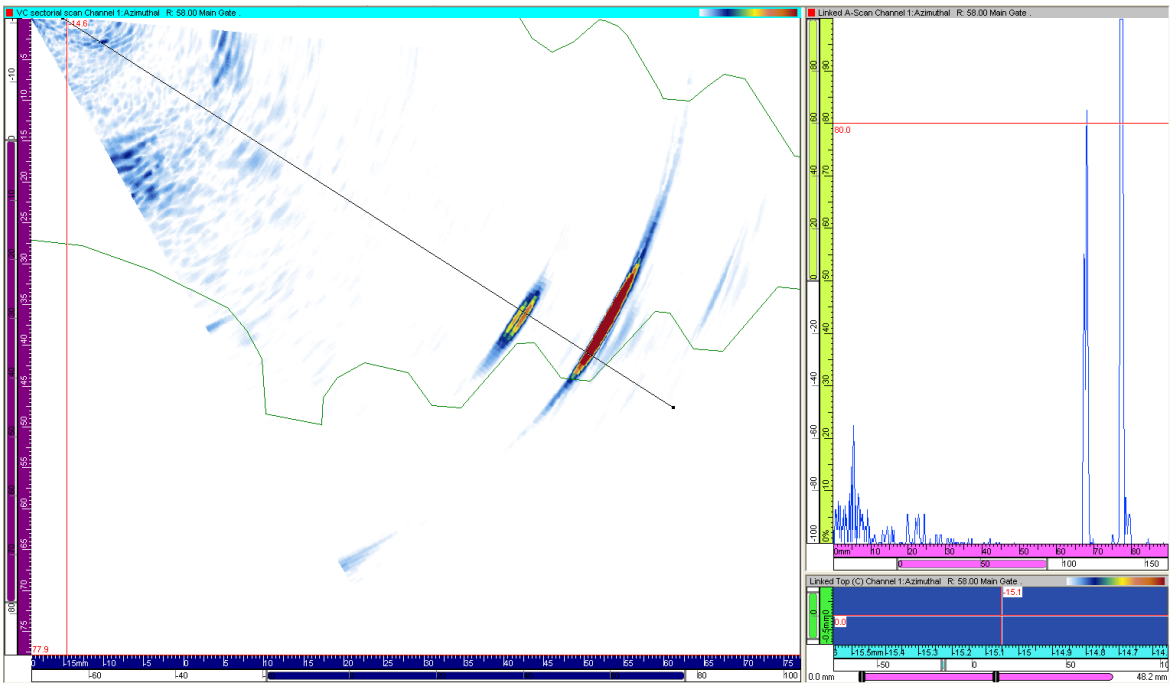

Figure D-20 Experiment 2 – Convex Notch P – 80 % FSH, 30dB, 57.5°, and 36.7 mm deep

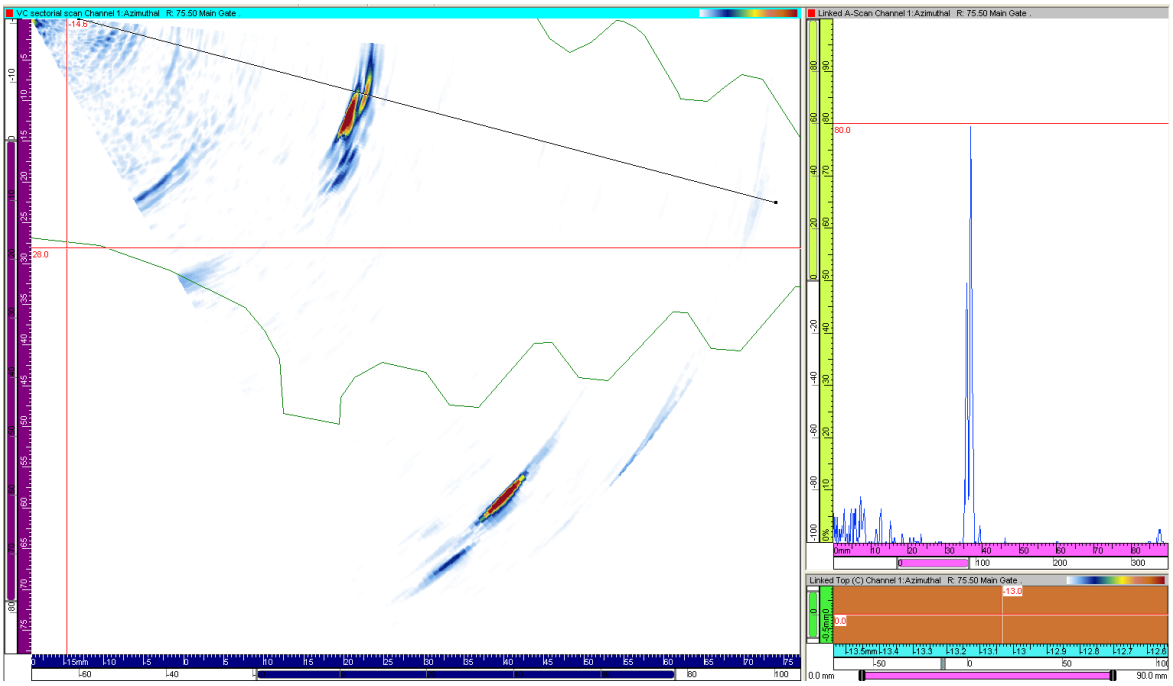

Figure D-21 Experiment 3 – Concave Notch B – 80 % FSH, 30dB, 76°, and 9 mm deep

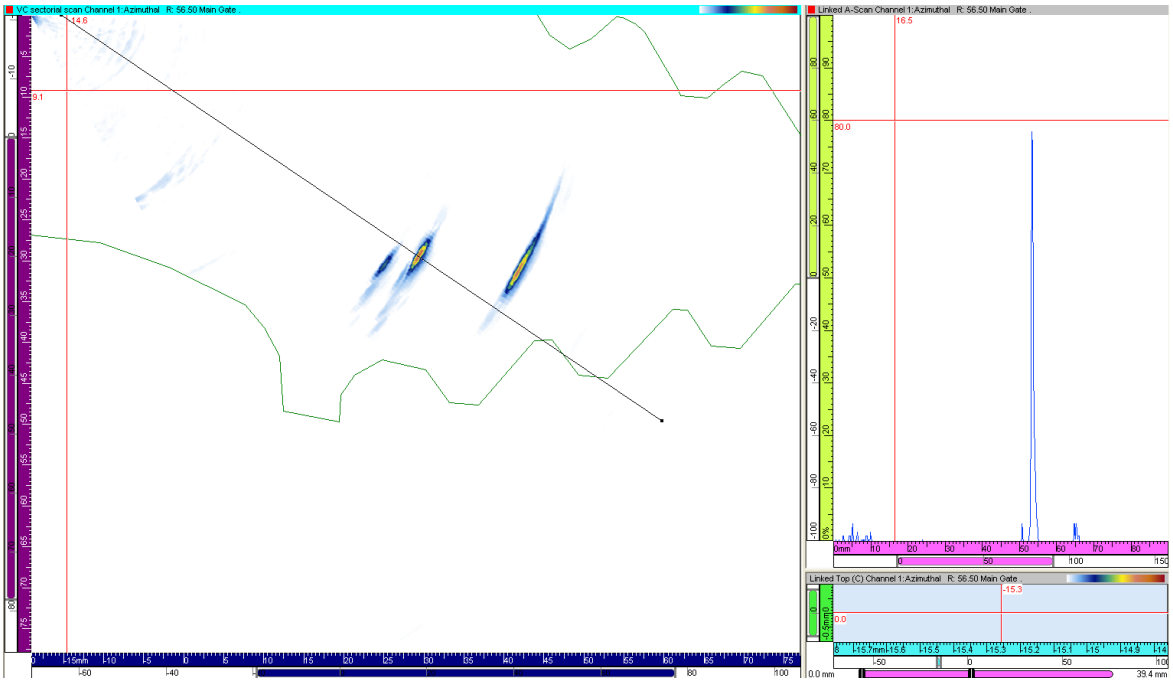

Figure D-22 Experiment 3 – Concave Notch C – 80 % FSH, 23dB, 56°, and 29 mm deep

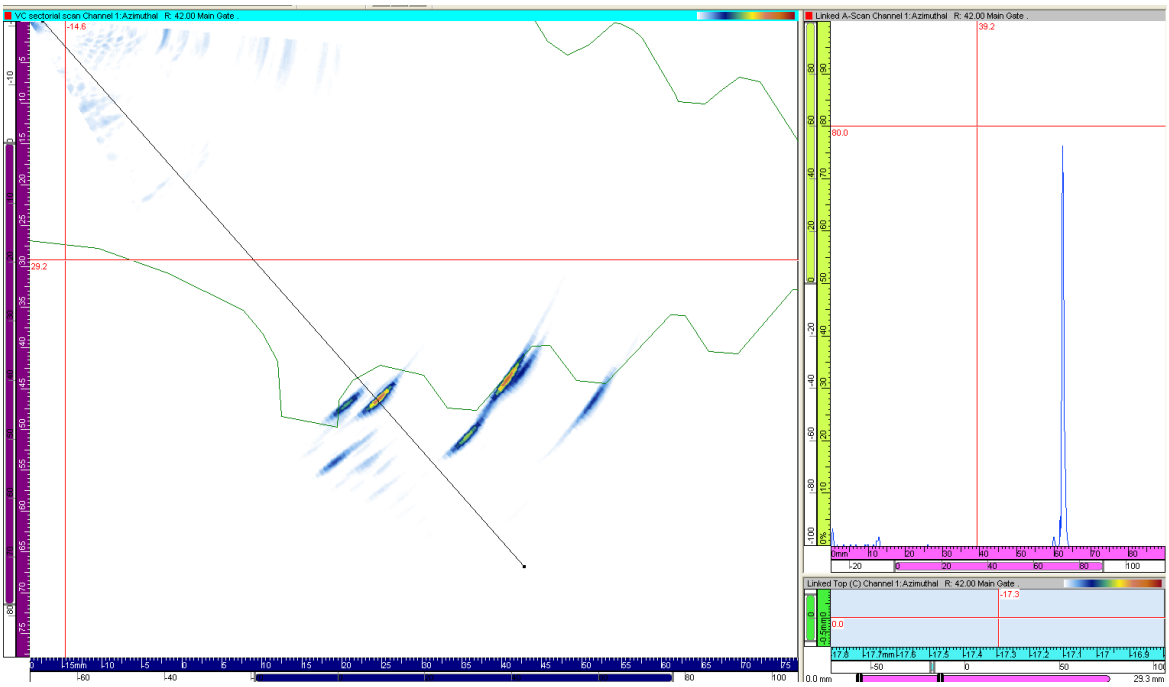

Figure D-23 Experiment 3 – Concave Notch E (reference) – 80 % FSH, 21dB, 42°, and 46 mm deep

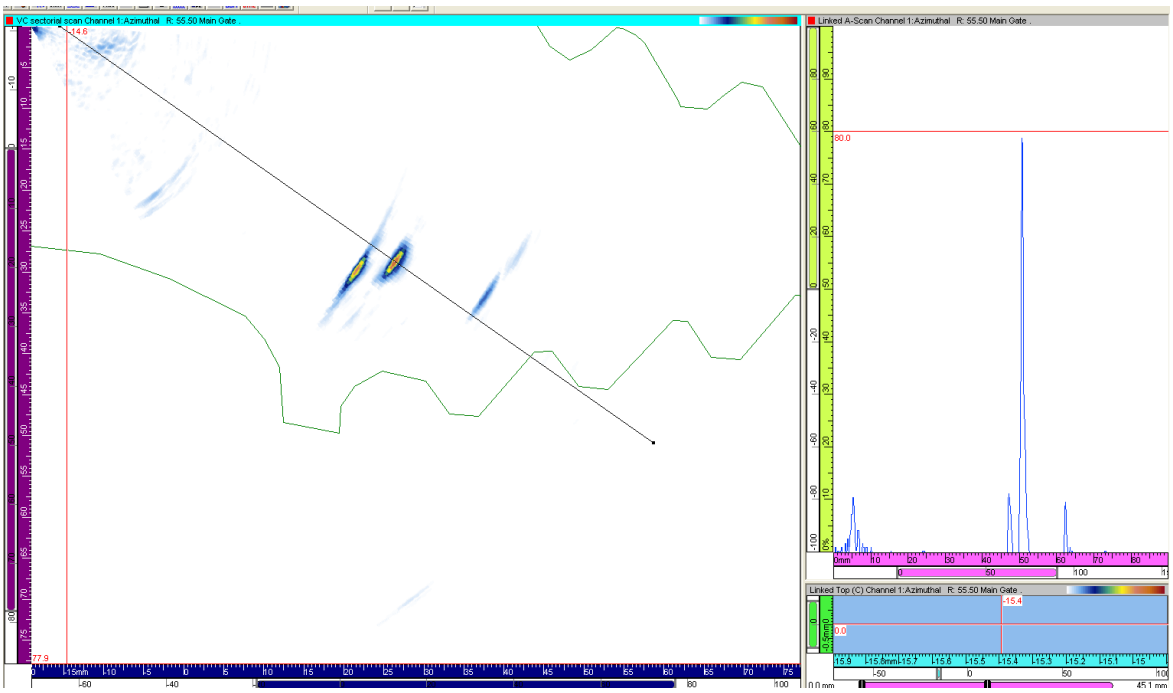

Figure D-24 Experiment 3 – Concave Notch F – 80 % FSH, 24dB, 59°, and 28 mm deep

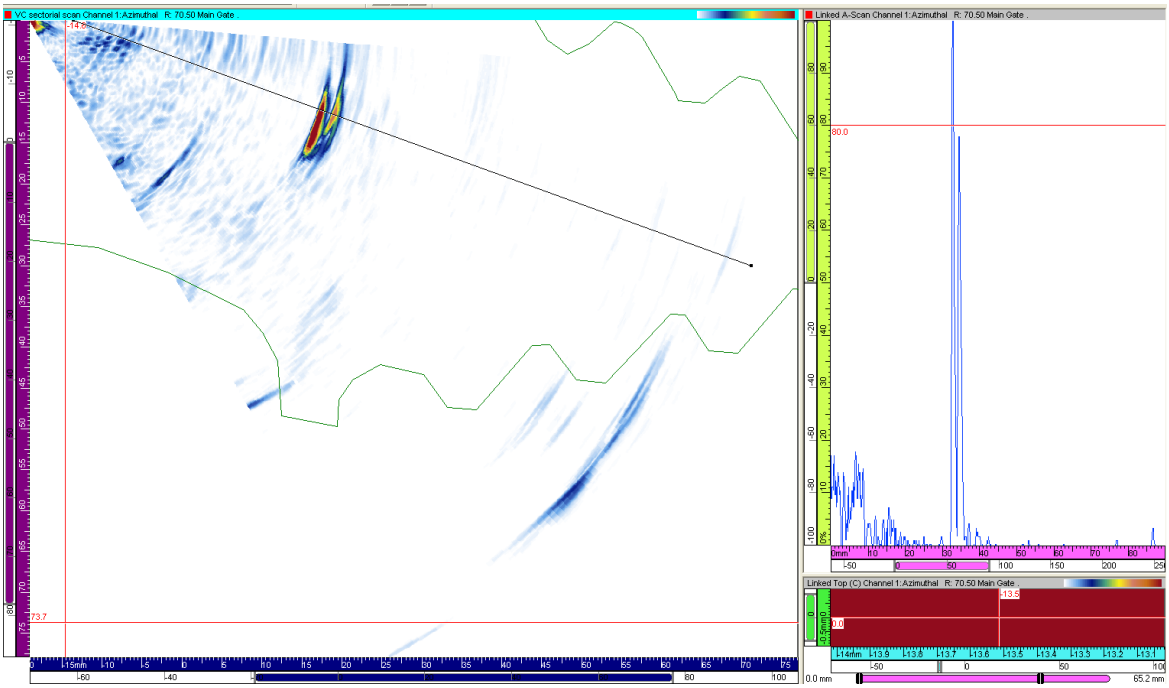

Figure D-25 Experiment 3 – Concave Notch G – 80 % FSH, 32dB, 70°, and 9 mm deep

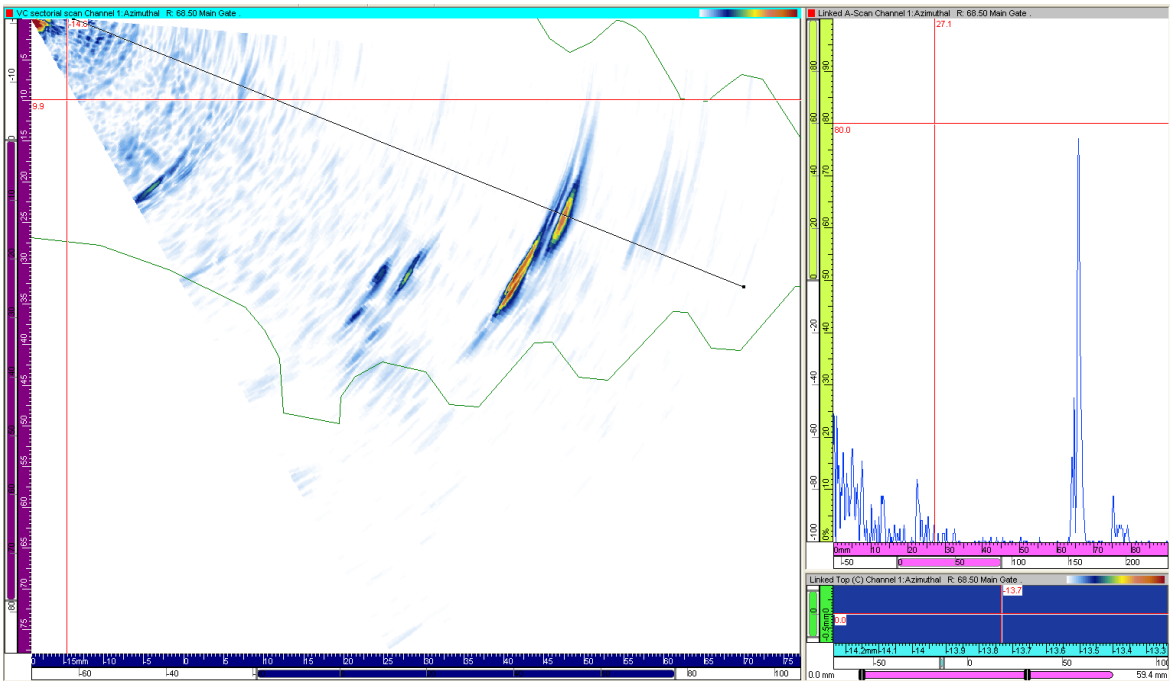

Figure D-26 Experiment 3 – Concave Notch K – 80 % FSH, 36dB, 68°, and 25 mm deep

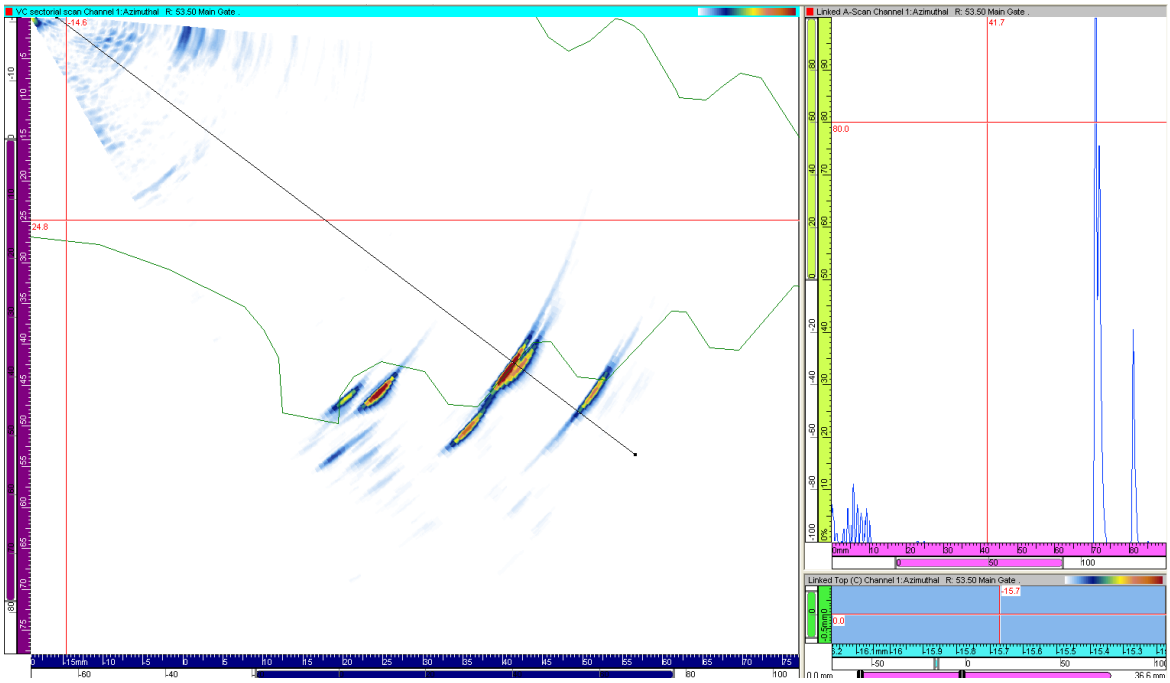

Figure D-27 Experiment 3 – Concave Notch M – 80 % FSH, 26dB, 42°, and 43 mm deep

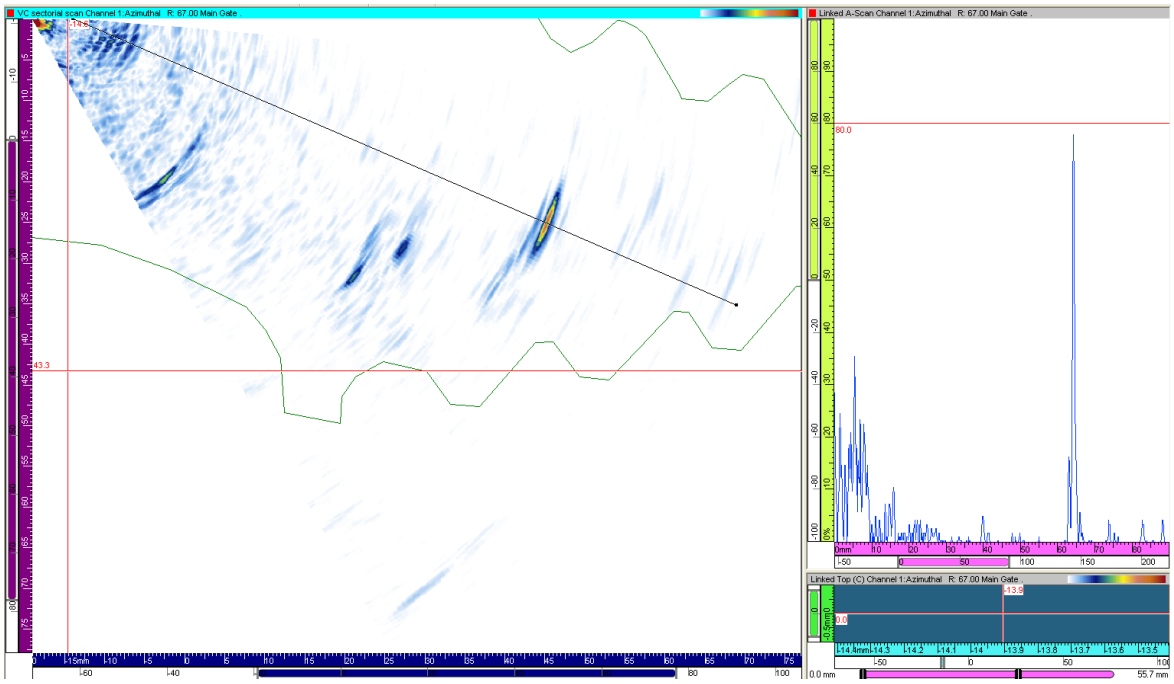

Figure D-28 Experiment 3 – Concave Notch N – 80 % FSH, 35dB, 67°, and 25 mm deep

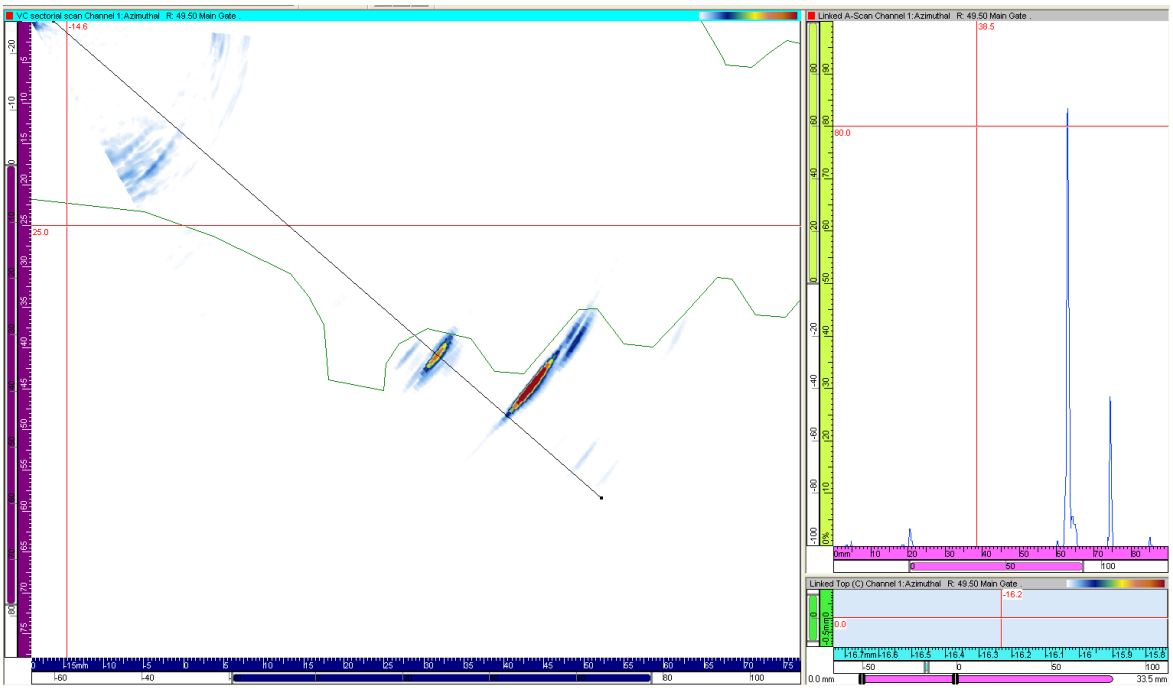

Figure D-29 Experiment 4 – Convex Notch C – 80 % FSH, 21dB, 49.5°, and 41 mm deep

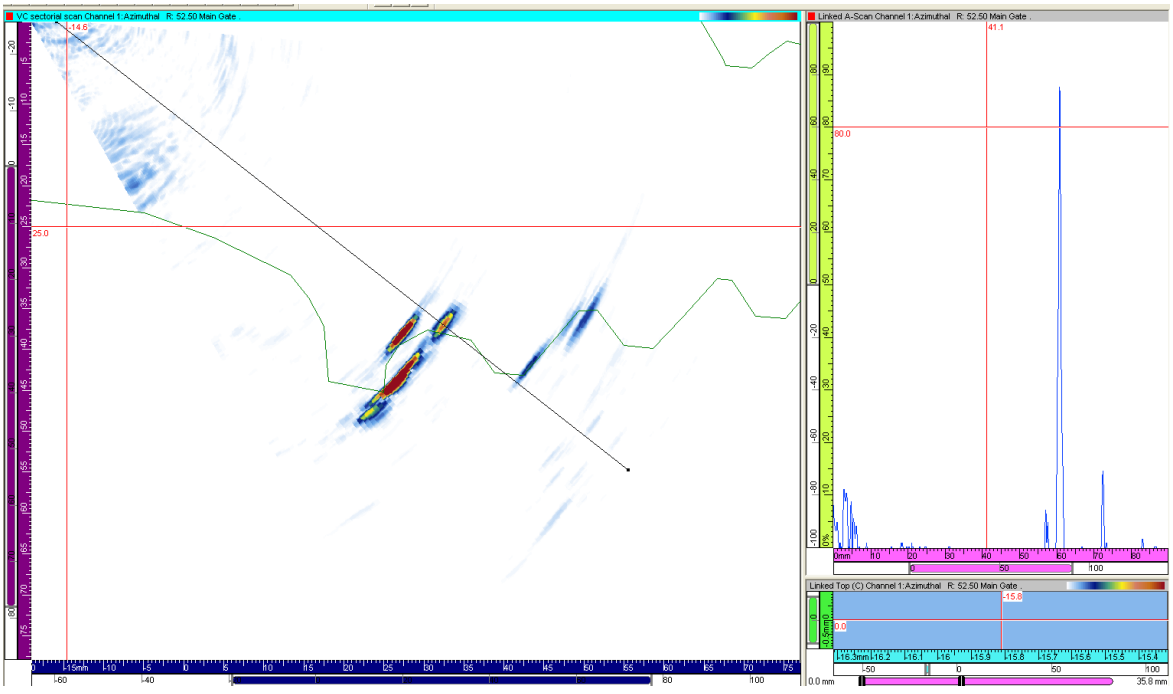

Figure D-30 Experiment 4 – Convex Notch D (reference) – 80 % FSH, 24dB, 52.5°, and 37 mm deep

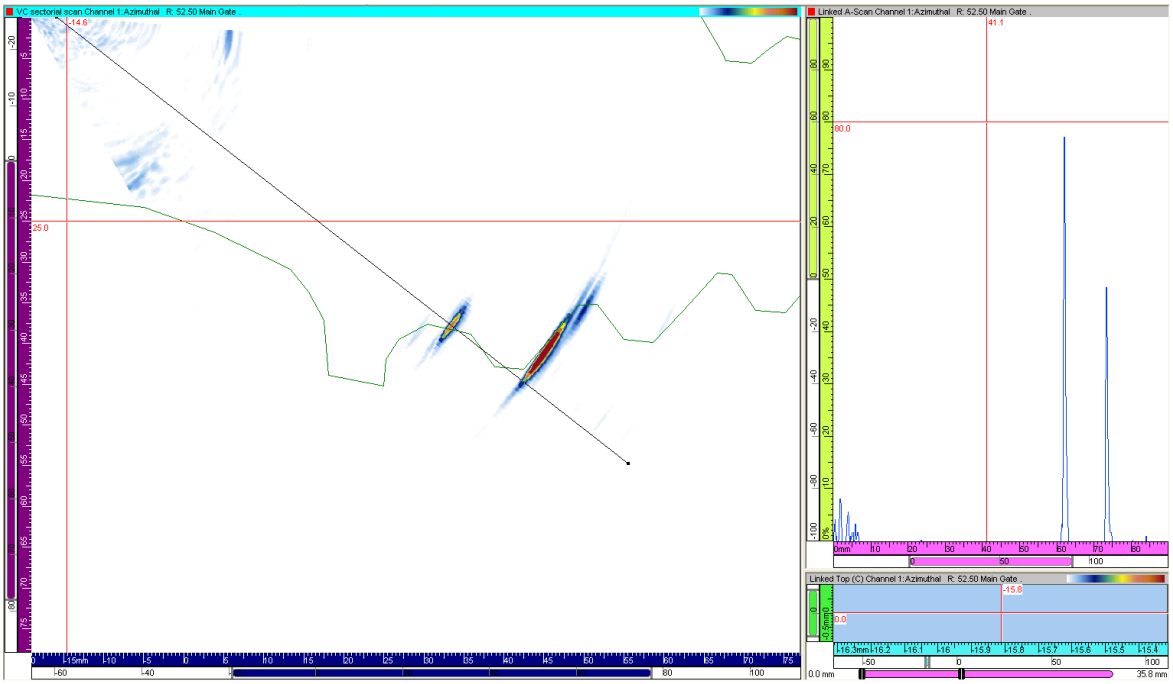

Figure D-31 Experiment 4 – Convex Notch F – 80 % FSH, 21dB, 52.5°, and 37 mm deep

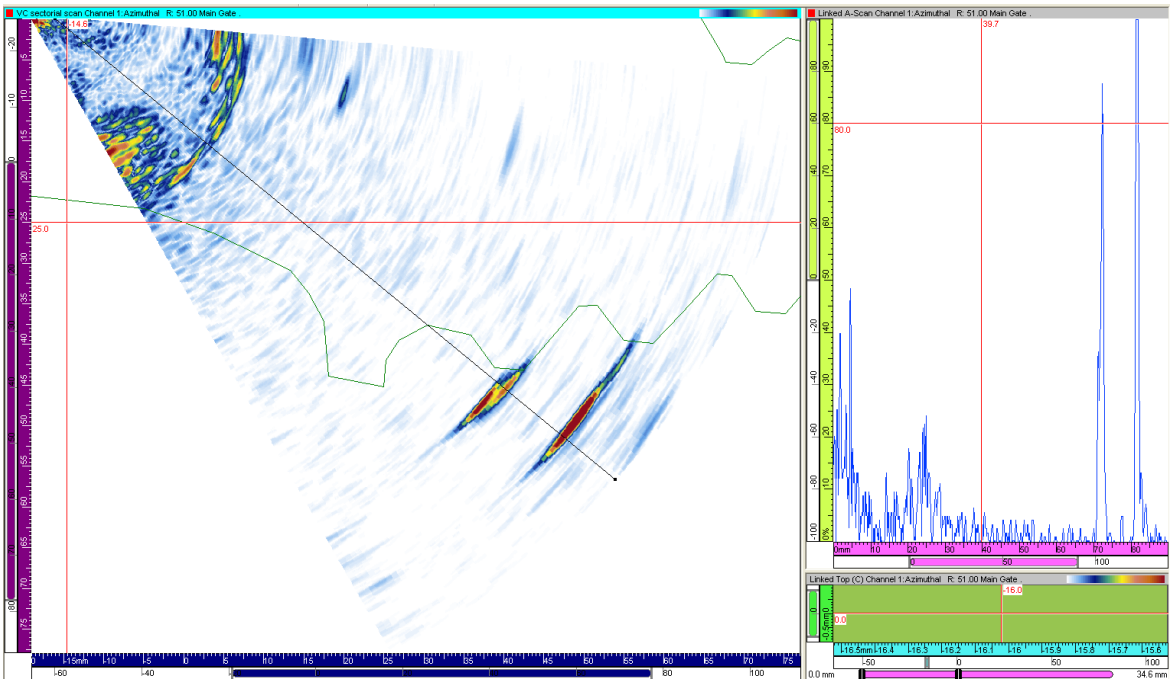

Figure D-32 Experiment 4 – Convex Notch I – 80 % FSH, 40dB, 51°, and 45 mm deep

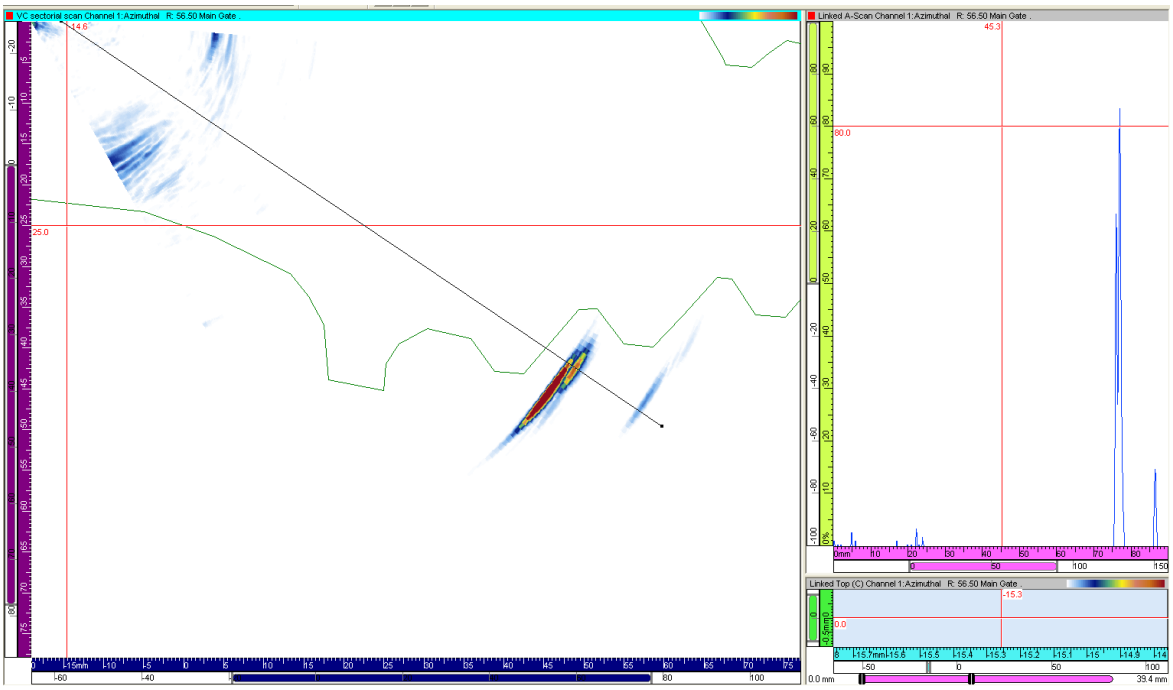

Figure D-33 Experiment 4 – Convex Notch J – 80 % FSH, 23dB, 56.5°, and 42 mm deep

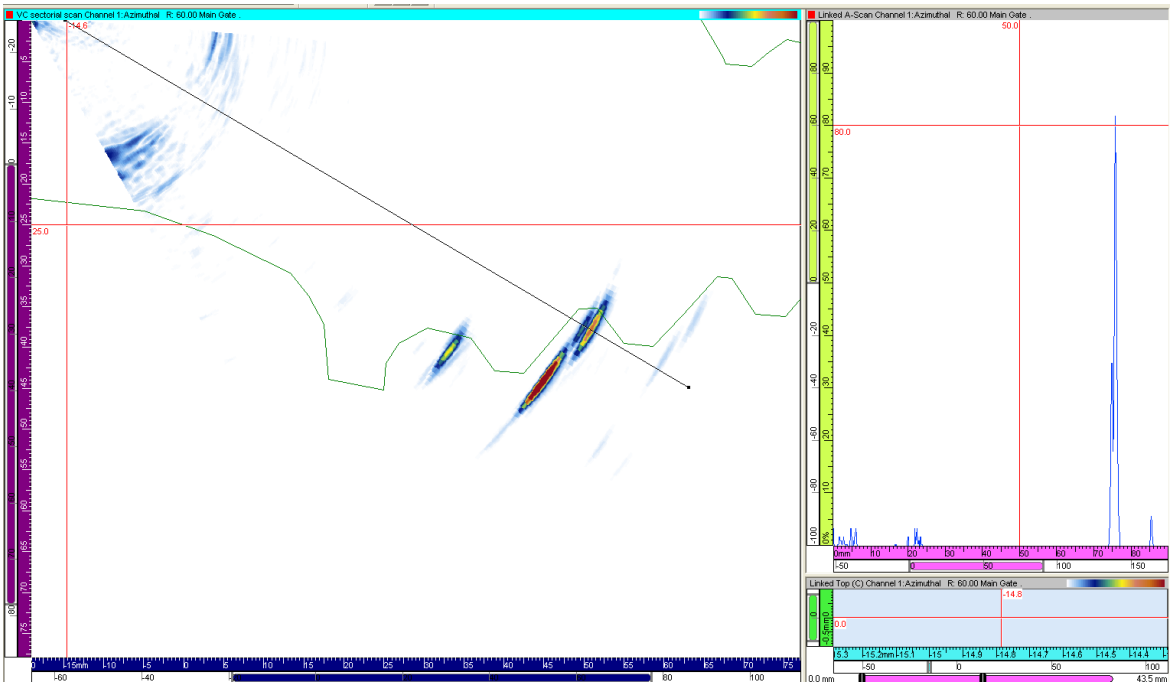

Figure D-34 Experiment 4 – Convex Notch K – 80 % FSH, 25dB, 60°, and 38 mm deep

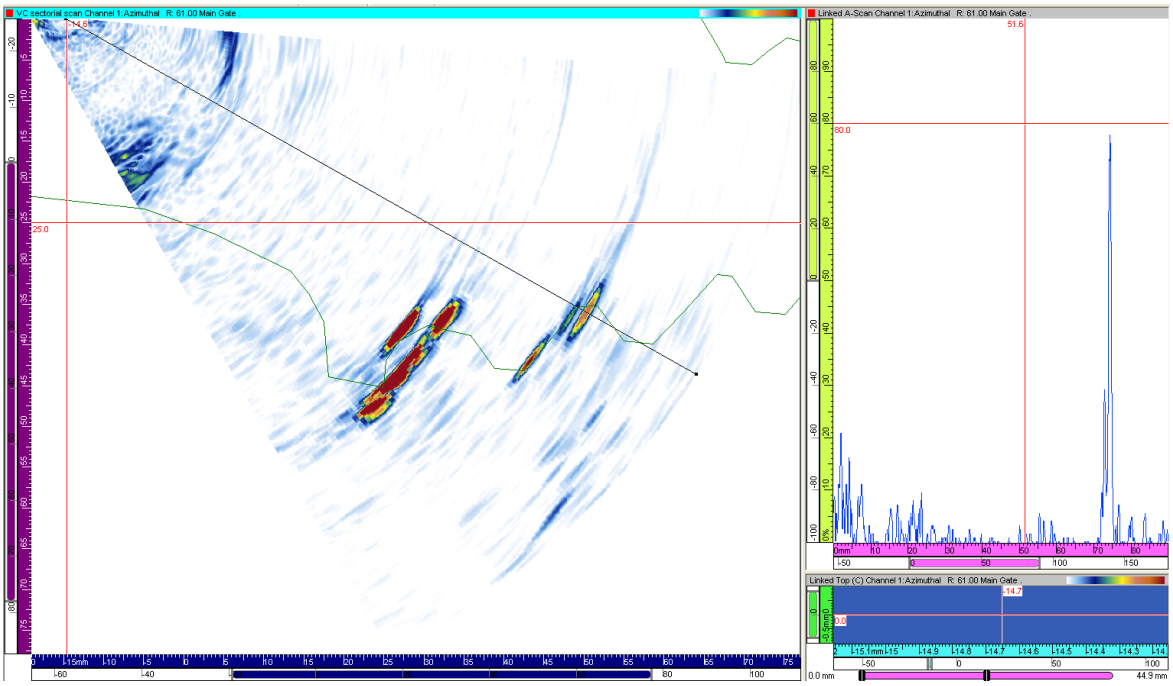

Figure D-35 Experiment 4 – Convex Notch L – 80 % FSH, 33dB, 61°, and 36 mm deep

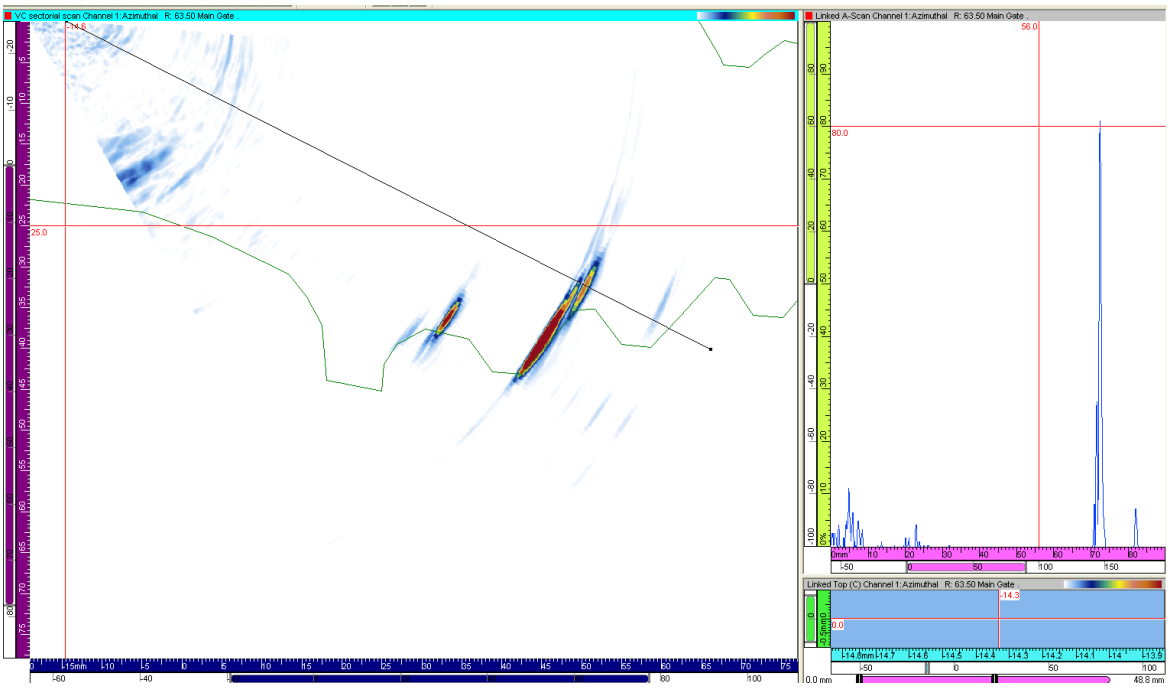

Figure D-36 Experiment 4 – Convex Notch N – 80 % FSH, 26dB, 63°, and 33 mm deep

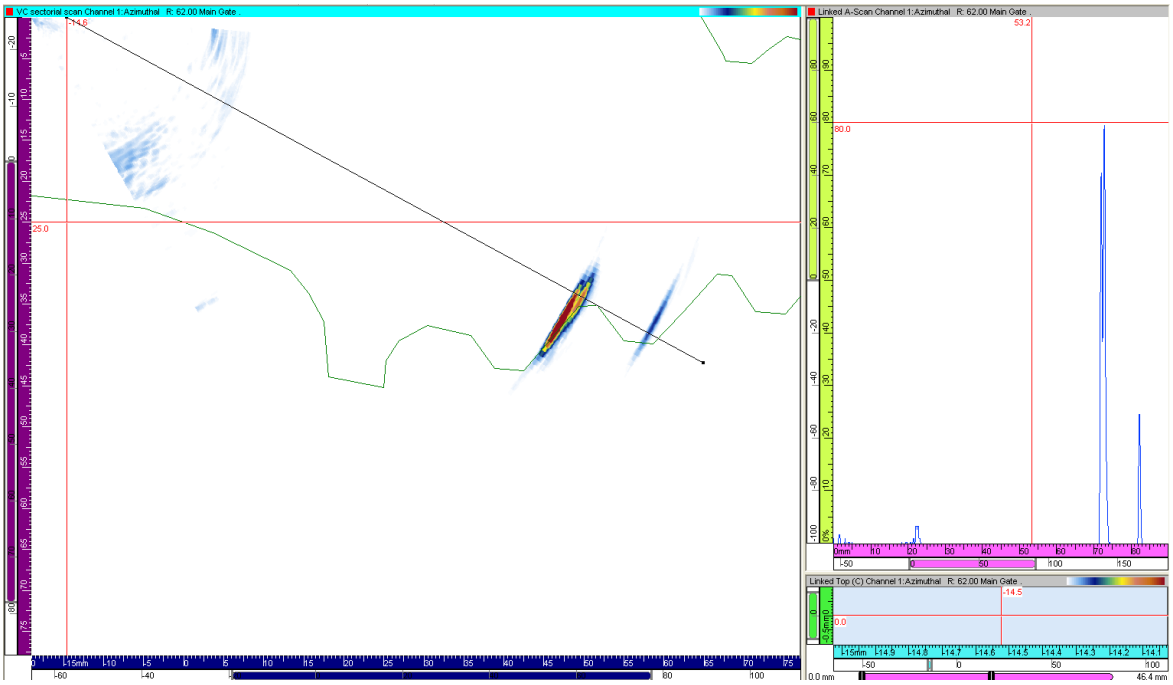

Figure D-37 Experiment 4 – Convex Notch O – 80 % FSH, 22dB, 62°, and 35 mm deep

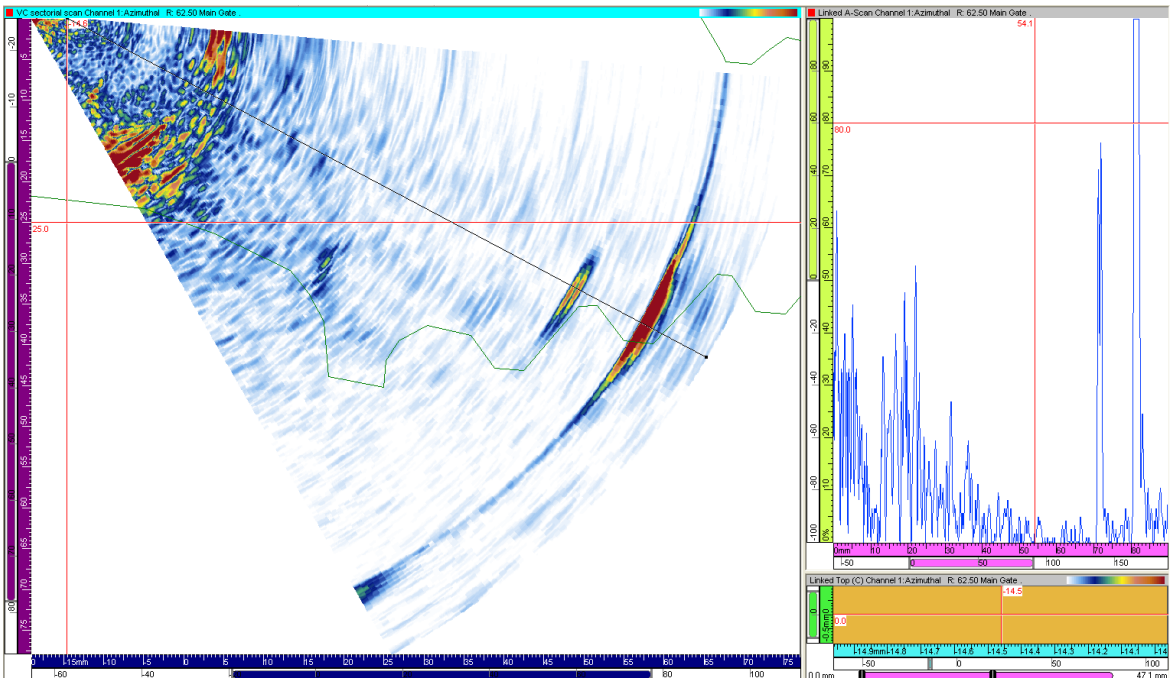

Figure D-38 Experiment 4 – Convex Notch P – 80 % FSH, 45dB, 62.5°, and 33 mm deep

Appendix E. Experiment 5 and 6 results

Contained within this appendix is all the recorded phased array scans carried out in experiments 5 and 6 in section 7.2 of Chapter 7.

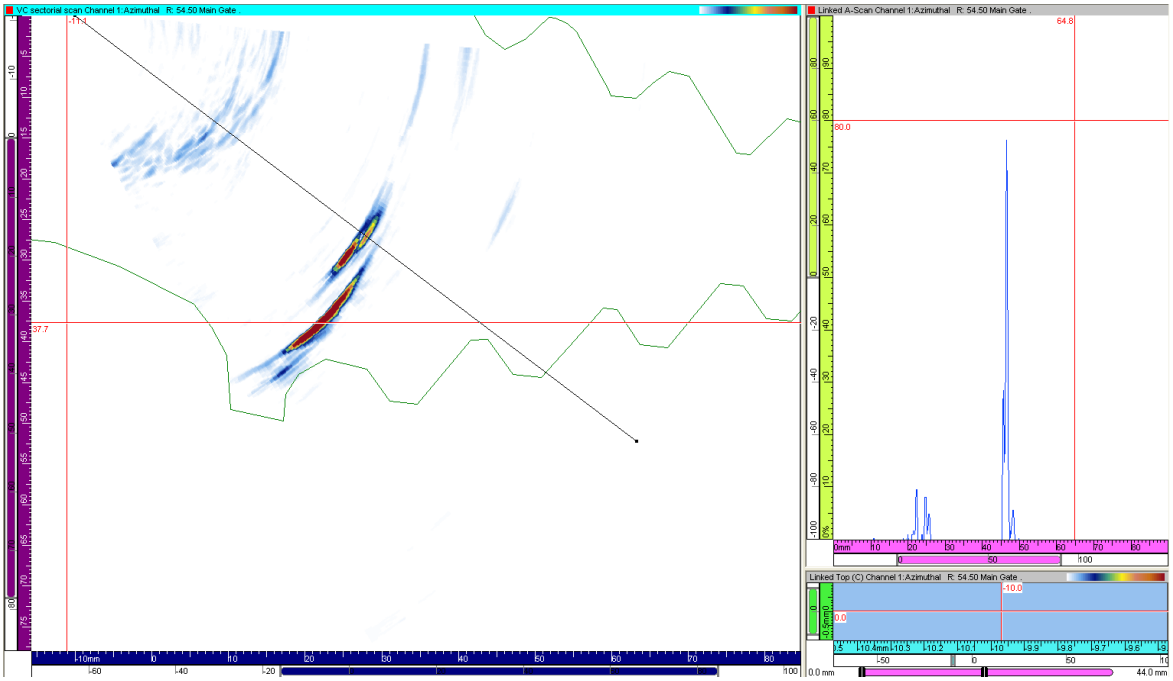

Figure E-1 Experiment 5 – Concave Notch B – 80 % FSH, 30dB, 54.5°, and 26.9 mm deep

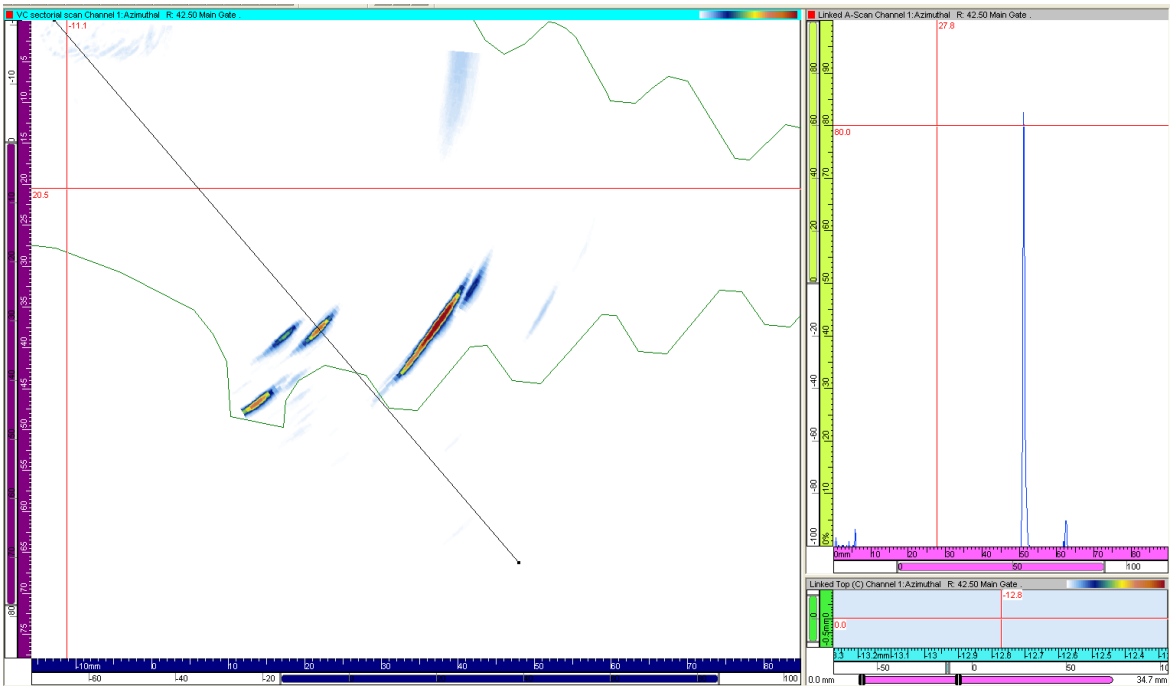

Figure E-2 Experiment 5 – Concave Notch C – 80 % FSH, 22dB, 42.5°, and 37.7 mm deep

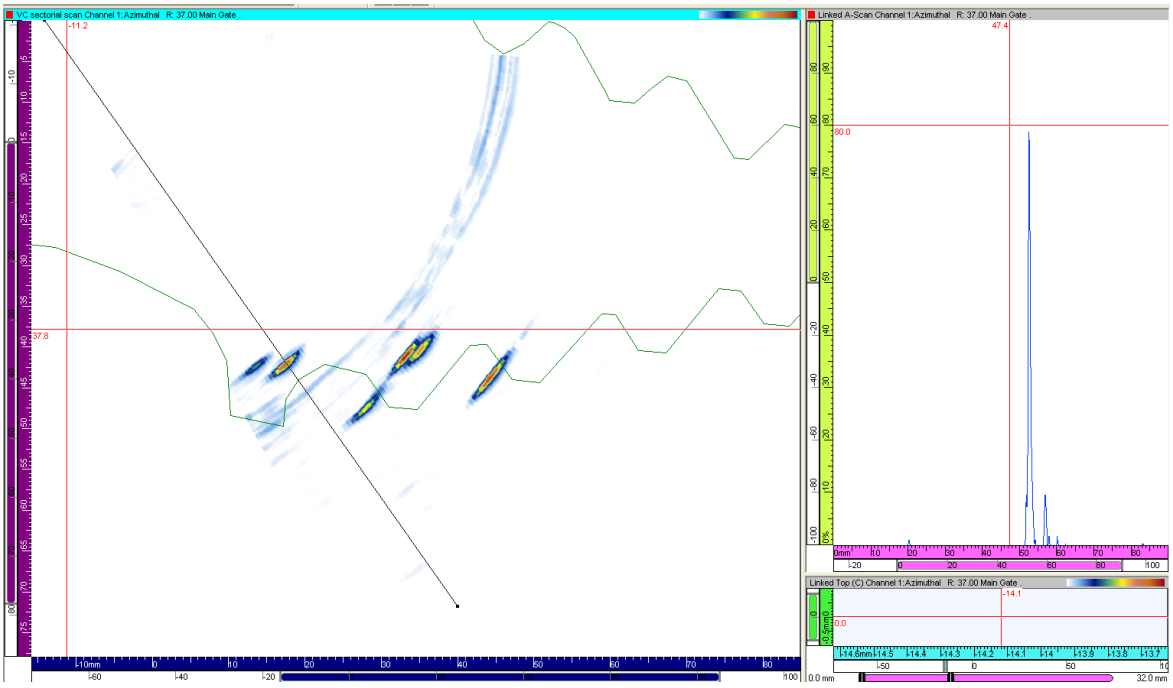

Figure E-3 Experiment 5 – Concave Notch E (reference) – 80 % FSH, 20dB, 37°, and 42 mm deep

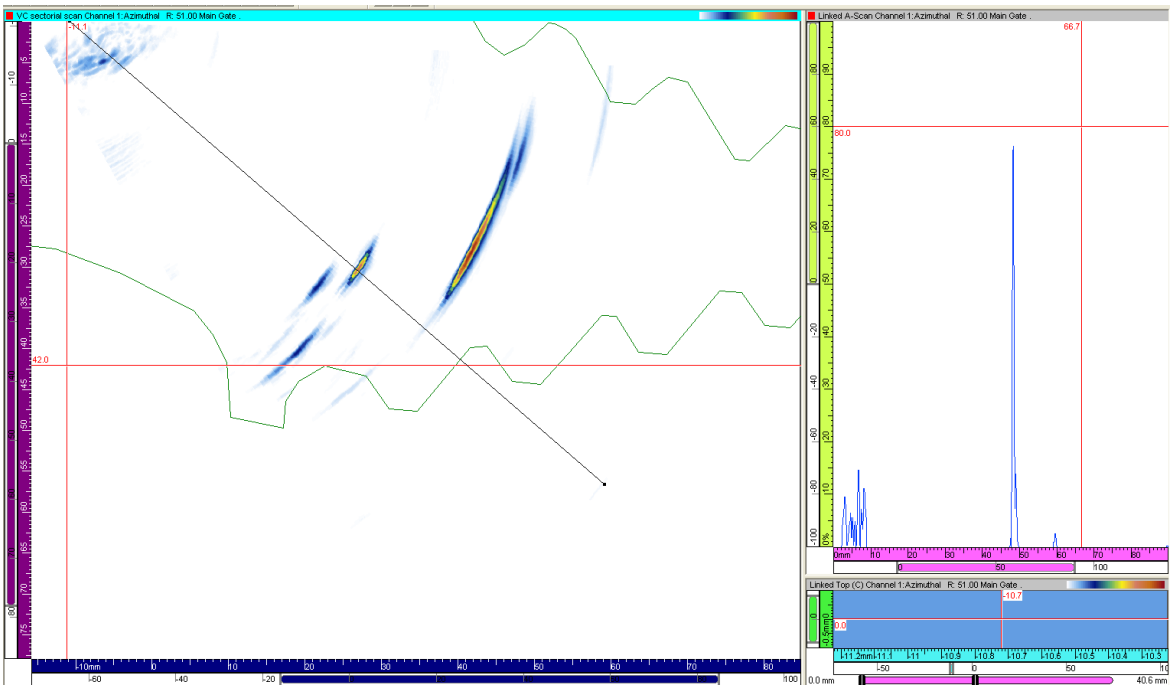

Figure E-4 Experiment 5 – Concave Notch F – 80 % FSH, 24dB, 51°, and 30.1 mm deep

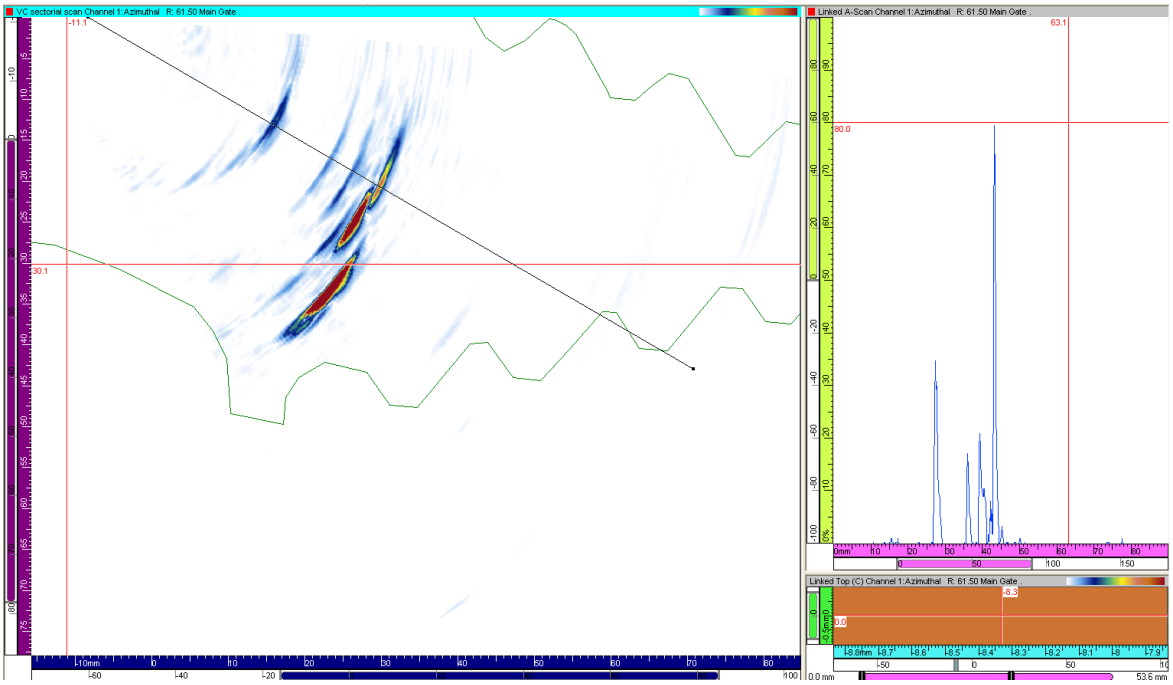

Figure E-5 Experiment 5 – Concave Notch G – 80 % FSH, 30dB, 62°, and 20.5 mm deep

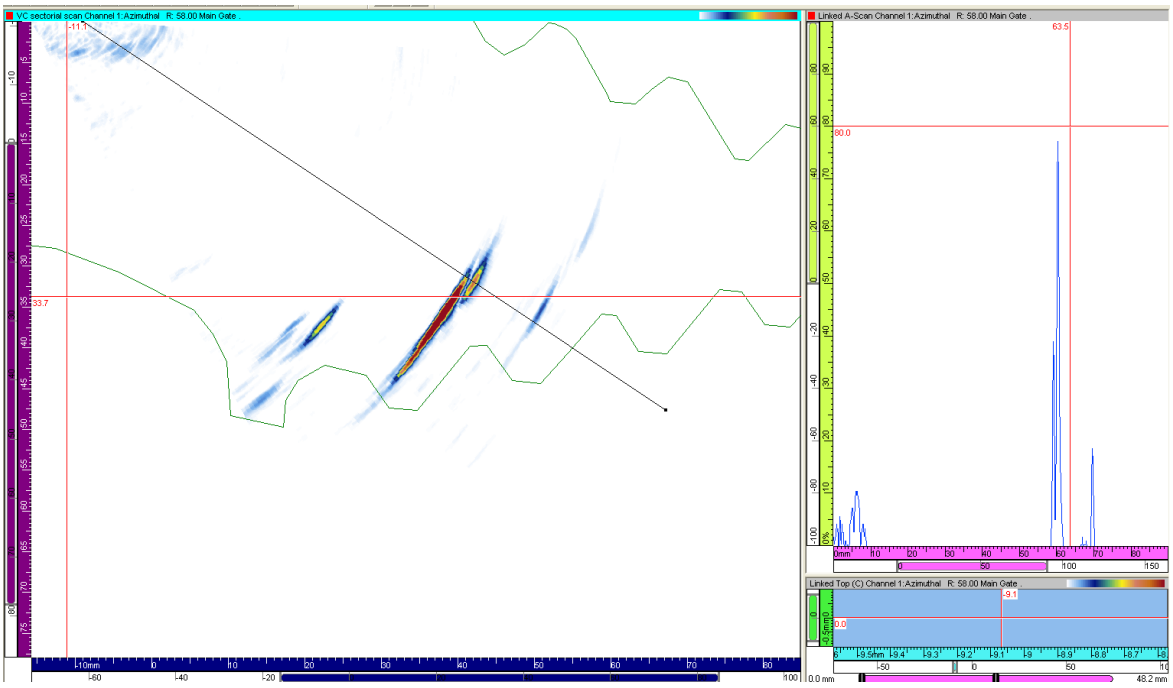

Figure E-6 Experiment 5 – Concave Notch K – 80 % FSH, 28dB, 58°, and 32.2 mm deep

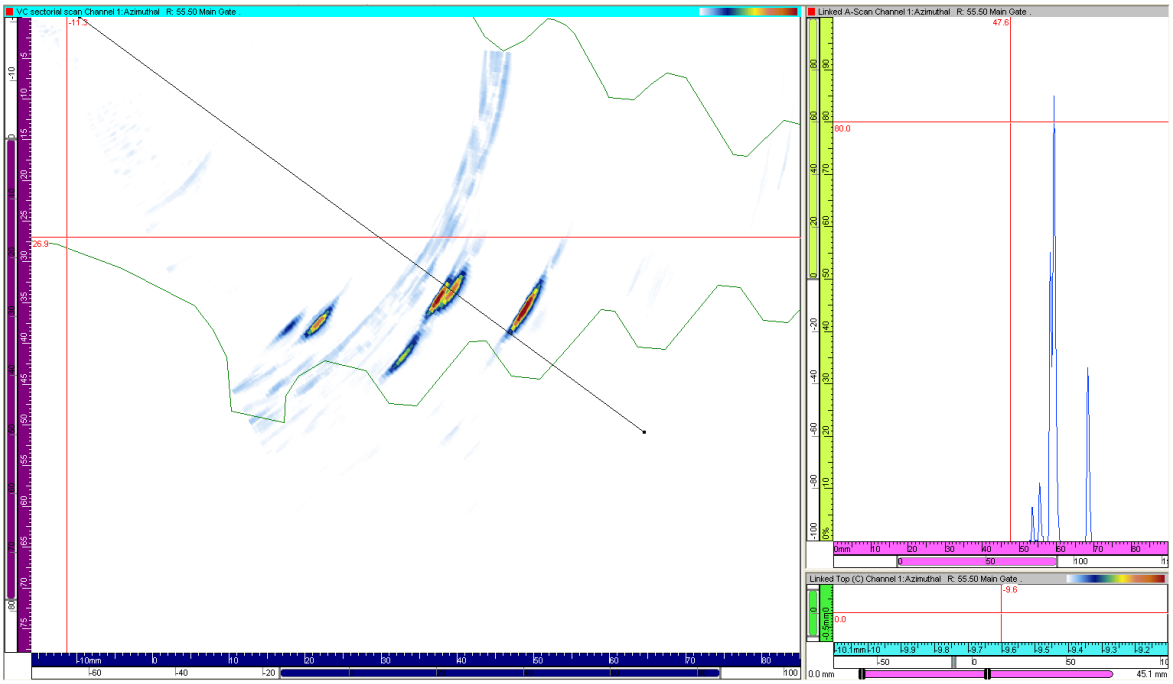

Figure E-7 Experiment 5 – Concave Notch M – 80 % FSH, 22dB, 55.5°, and 33.7 mm deep

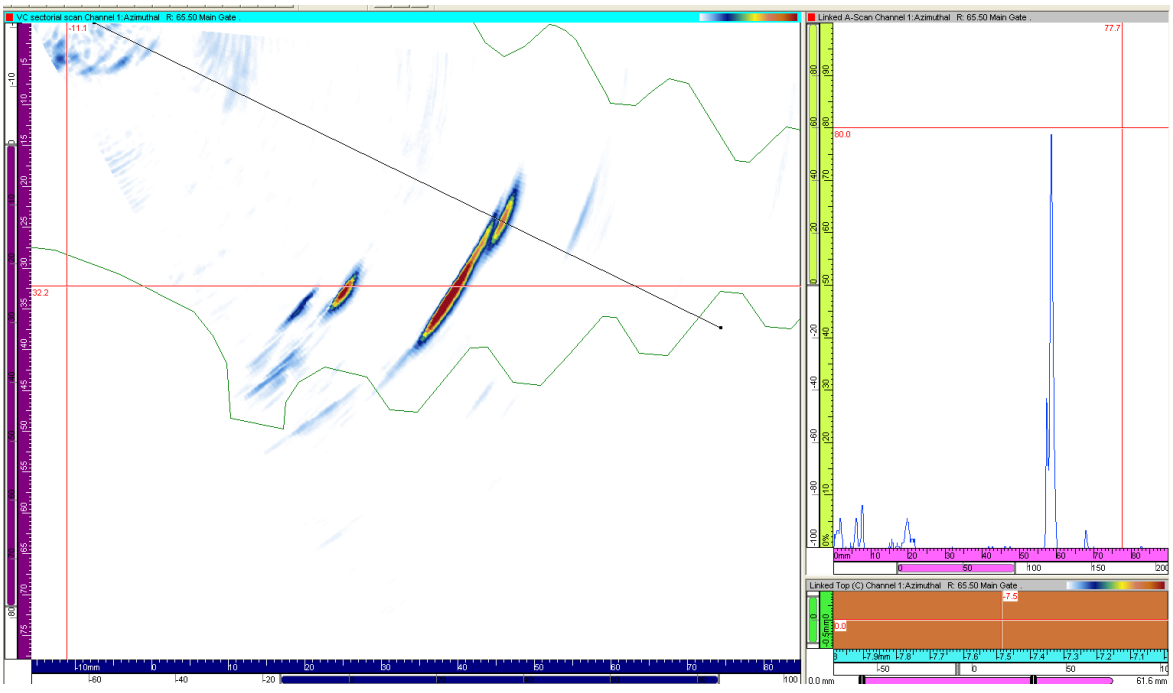

Figure E-8 Experiment 5 – Concave Notch N – 80 % FSH, 29dB, 65.5°, and 24.2 mm deep

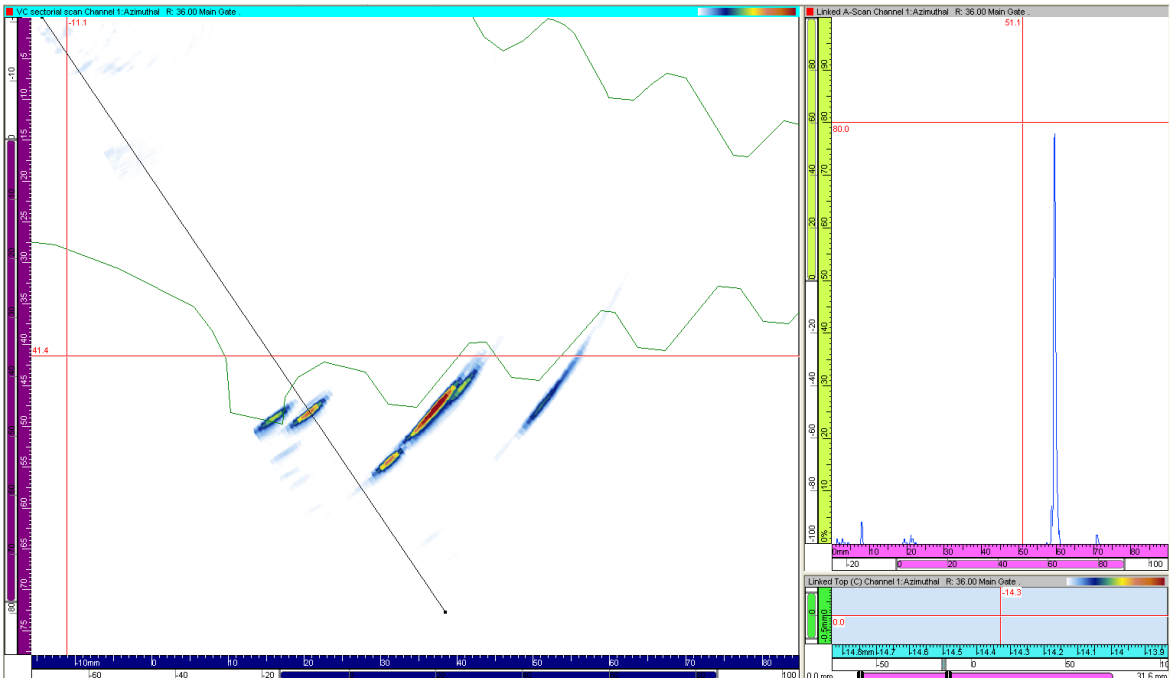

Figure E-9 Experiment 6 – Convex Notch C – 80 % FSH, 18dB, 36°, and 48.1 mm deep

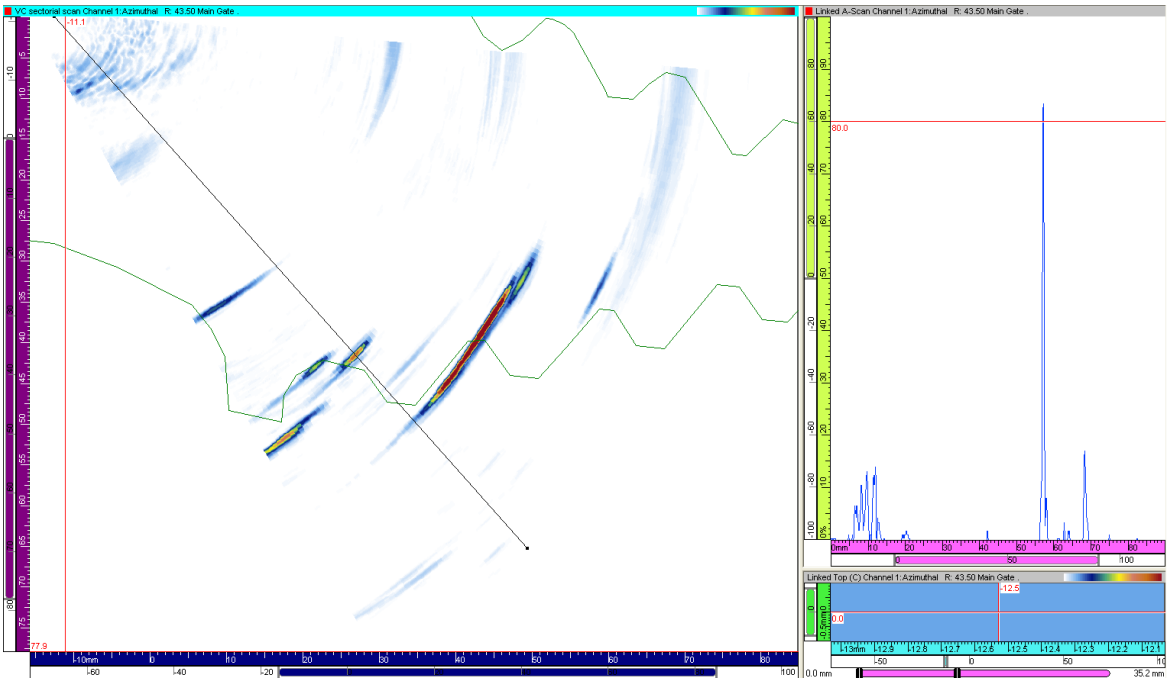

Figure E-10 Experiment 6 – Convex Notch D (reference) – 80 % FSH, 22dB, 43.5°, and 41.4 mm deep

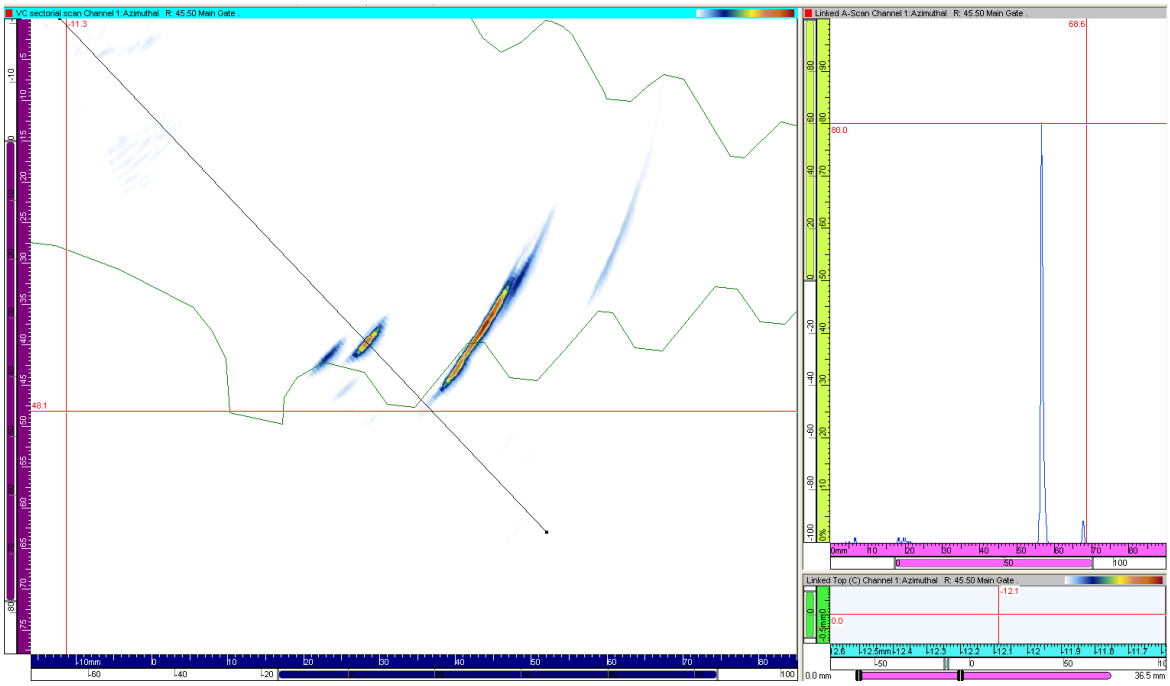

Figure E-11 Experiment 6 – Convex Notch F – 80 % FSH, 17dB, 45.5°, and 39.6 mm deep

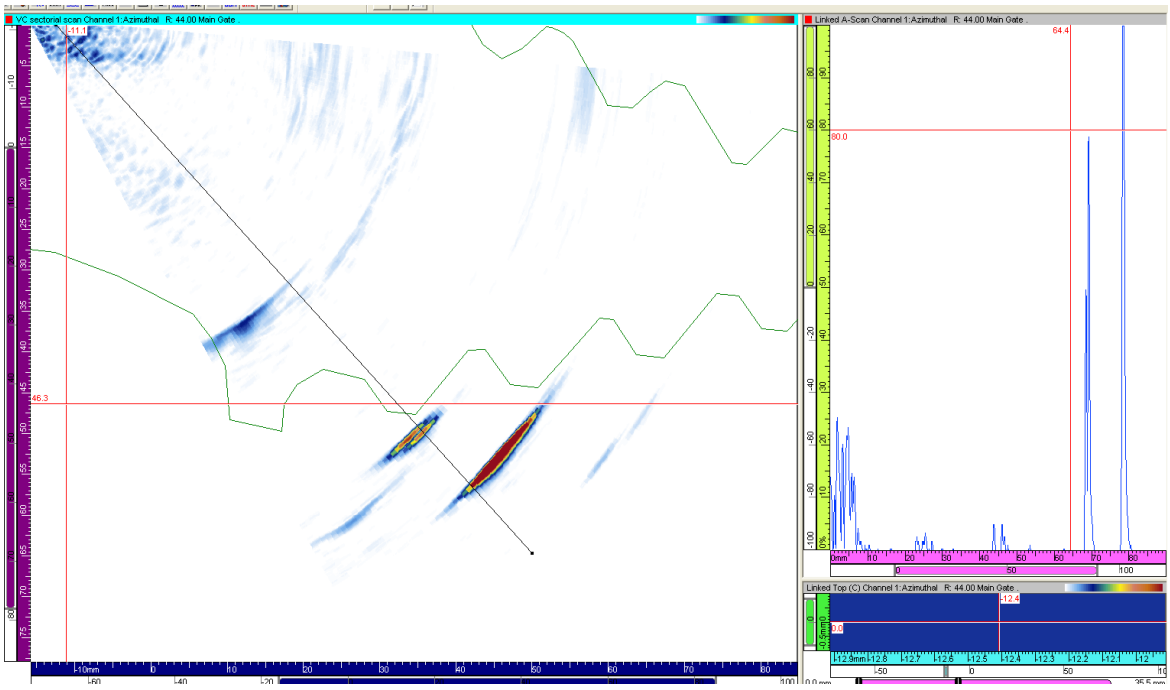

Figure E-12 Experiment 6 – Convex Notch I – 80 % FSH, 30dB, 44°, and 49.7 mm deep

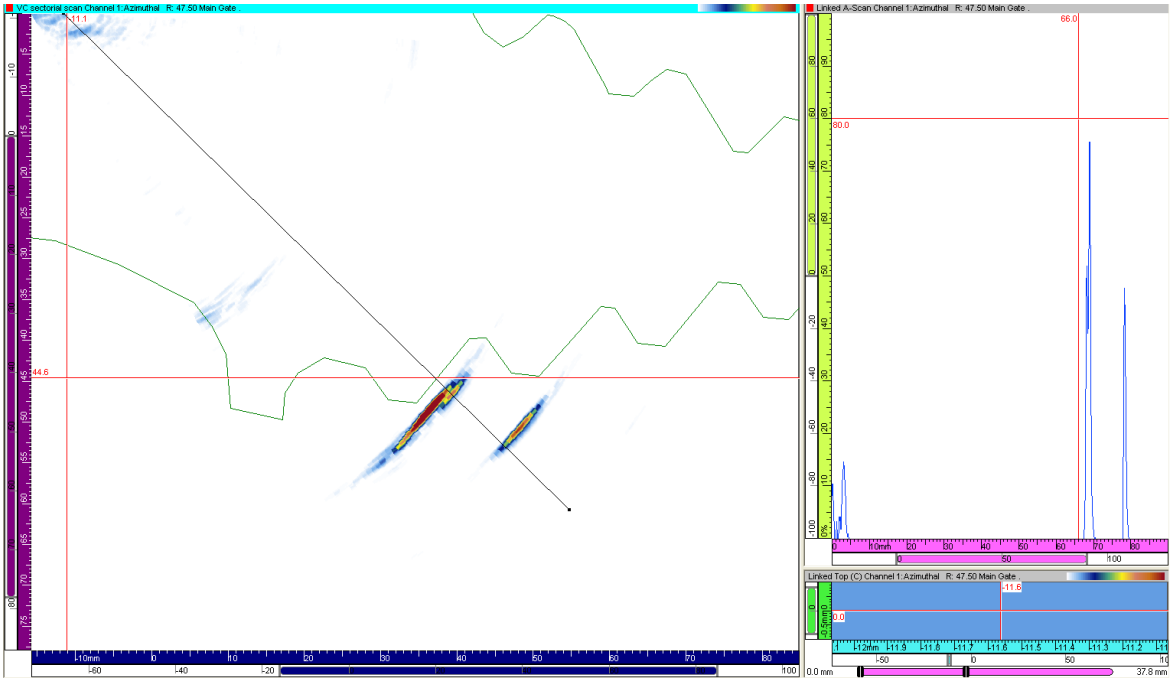

Figure E-13 Experiment 6 – Convex Notch J – 80 % FSH, 23dB, 47.5°, and 46.3 mm deep

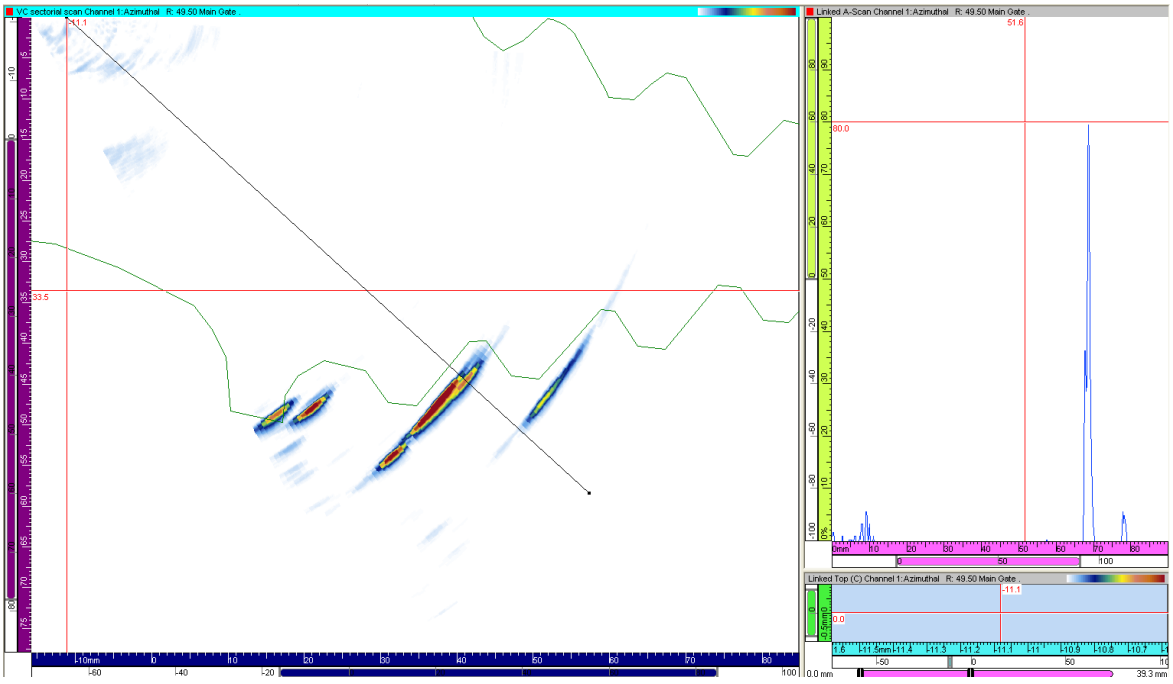

Figure E-14 Experiment 6 – Convex Notch K – 80 % FSH, 22dB, 49.5°, and 44.6 mm deep

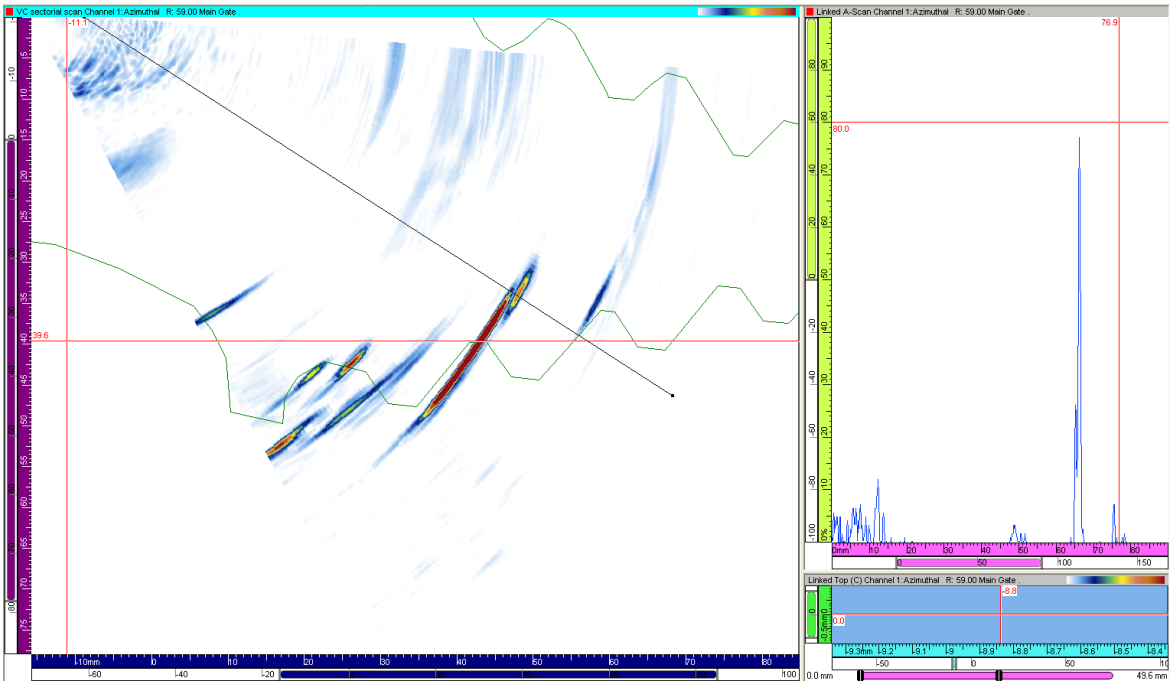

Figure E-15 Experiment 6 – Convex Notch L – 80 % FSH, 24dB, 59.5°, and 33.5 mm deep

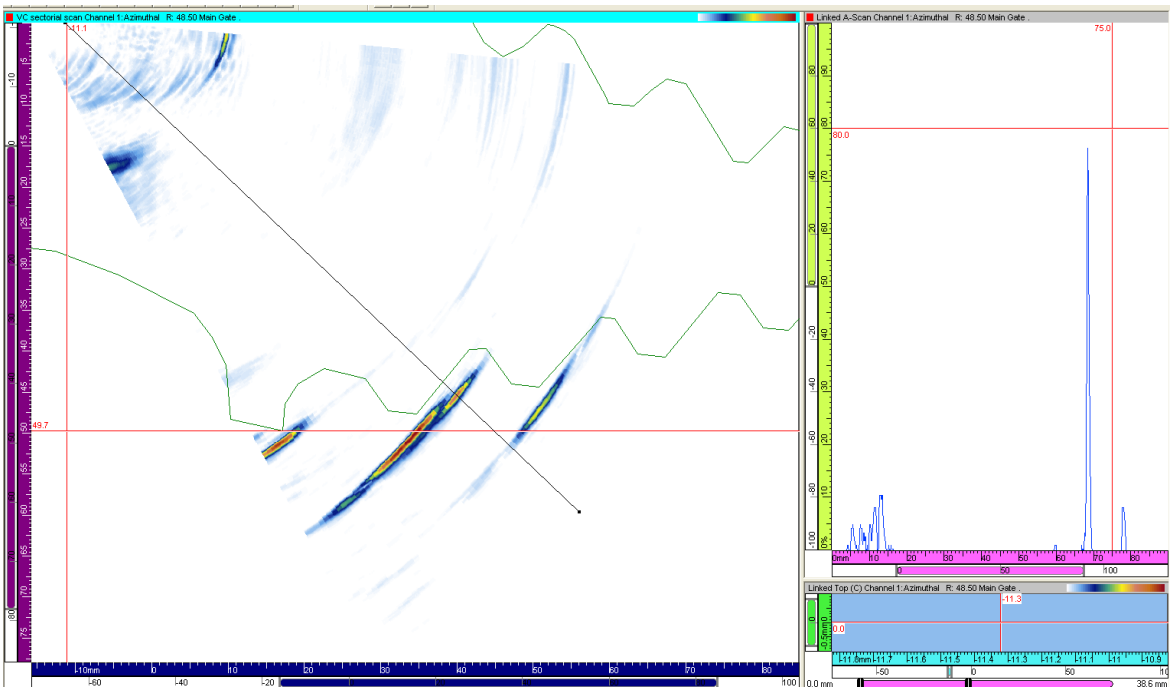

Figure E-16 Experiment 6 – Convex Notch N – 80 % FSH, 26dB, 48.5°, and 45.5 mm deep

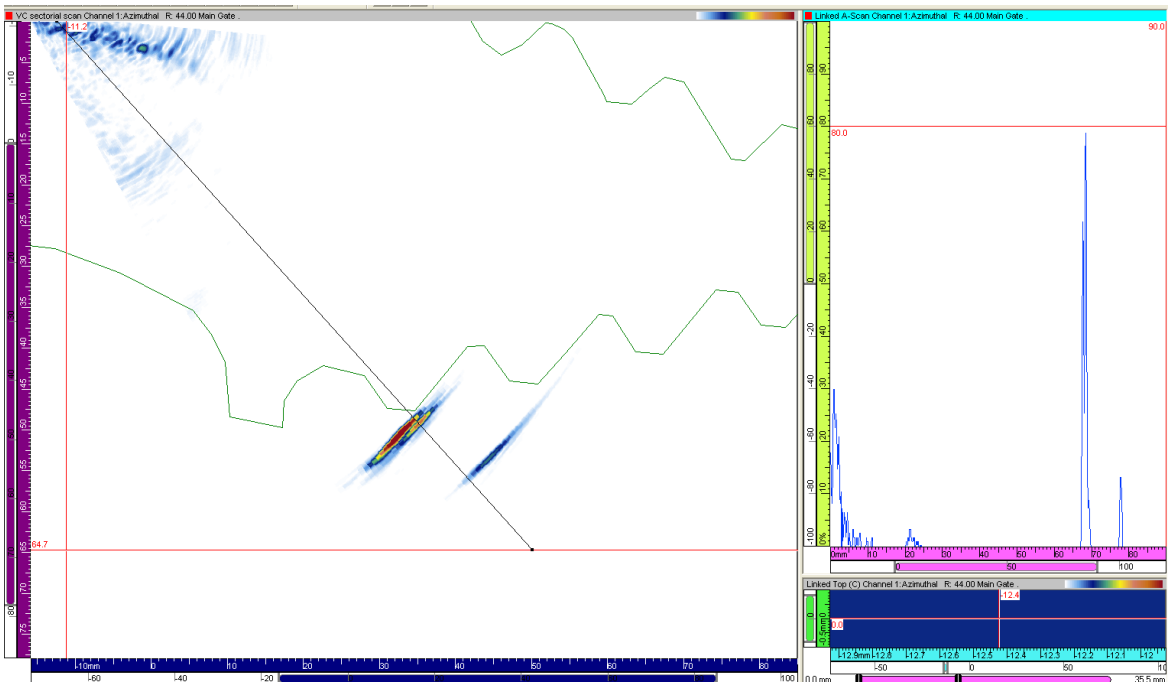

Figure E-17 Experiment 6 – Convex Notch O – 80 % FSH, 26dB, 44°, and 49.2 mm deep

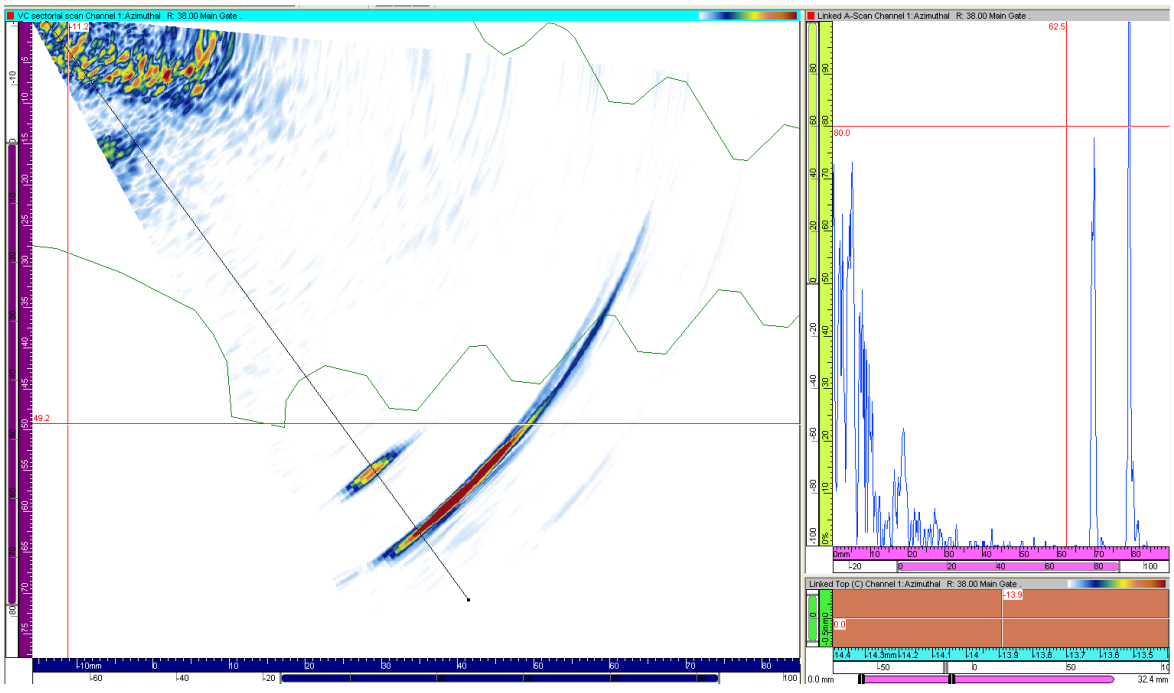

Figure E-18 Experiment 6 – Convex Notch P – 80 % FSH, 36dB, 38°, and 55 mm deep